

University of Windsor

Scholarship at UWindor

Electronic Theses and Dissertations

Theses, Dissertations, and Major Papers

2008

Analysis of fixed-pitch straight-bladed VAWT with asymmetric airfoils

Mazharul Islam
University of Windsor

Follow this and additional works at: <https://scholar.uwindsor.ca/etd>

Recommended Citation

Islam, Mazharul, "Analysis of fixed-pitch straight-bladed VAWT with asymmetric airfoils" (2008). *Electronic Theses and Dissertations*. 7977.

<https://scholar.uwindsor.ca/etd/7977>

This online database contains the full-text of PhD dissertations and Masters' theses of University of Windsor students from 1954 forward. These documents are made available for personal study and research purposes only, in accordance with the Canadian Copyright Act and the Creative Commons license—CC BY-NC-ND (Attribution, Non-Commercial, No Derivative Works). Under this license, works must always be attributed to the copyright holder (original author), cannot be used for any commercial purposes, and may not be altered. Any other use would require the permission of the copyright holder. Students may inquire about withdrawing their dissertation and/or thesis from this database. For additional inquiries, please contact the repository administrator via email (scholarship@uwindsor.ca) or by telephone at 519-253-3000ext. 3208.

Analysis of Fixed-Pitch Straight-Bladed VAWT with Asymmetric Airfoils

by
Mazharul Islam

A Dissertation
Submitted to the Faculty of Graduate Studies
through Department of Mechanical, Automotive and Materials Engineering
in Partial Fulfillment of the Requirements for
the Degree of Doctor of Philosophy at the
University of Windsor

Windsor, Ontario, Canada
2008

© 2008 Mazharul Islam



Library and
Archives Canada

Bibliothèque et
Archives Canada

Published Heritage
Branch

Direction du
Patrimoine de l'édition

395 Wellington Street
Ottawa ON K1A 0N4
Canada

395, rue Wellington
Ottawa ON K1A 0N4
Canada

Your file Votre référence
ISBN: 978-0-494-42382-0
Our file Notre référence
ISBN: 978-0-494-42382-0

NOTICE:

The author has granted a non-exclusive license allowing Library and Archives Canada to reproduce, publish, archive, preserve, conserve, communicate to the public by telecommunication or on the Internet, loan, distribute and sell theses worldwide, for commercial or non-commercial purposes, in microform, paper, electronic and/or any other formats.

The author retains copyright ownership and moral rights in this thesis. Neither the thesis nor substantial extracts from it may be printed or otherwise reproduced without the author's permission.

AVIS:

L'auteur a accordé une licence non exclusive permettant à la Bibliothèque et Archives Canada de reproduire, publier, archiver, sauvegarder, conserver, transmettre au public par télécommunication ou par l'Internet, prêter, distribuer et vendre des thèses partout dans le monde, à des fins commerciales ou autres, sur support microforme, papier, électronique et/ou autres formats.

L'auteur conserve la propriété du droit d'auteur et des droits moraux qui protègent cette thèse. Ni la thèse ni des extraits substantiels de celle-ci ne doivent être imprimés ou autrement reproduits sans son autorisation.

In compliance with the Canadian Privacy Act some supporting forms may have been removed from this thesis.

Conformément à la loi canadienne sur la protection de la vie privée, quelques formulaires secondaires ont été enlevés de cette thèse.

While these forms may be included in the document page count, their removal does not represent any loss of content from the thesis.

Bien que ces formulaires aient inclus dans la pagination, il n'y aura aucun contenu manquant.


Canada

Declaration of Co-Authorship / Previous Publication

I. Co-Authorship Declaration

I hereby declare that this dissertation incorporates material that is result of joint authorship of the following publications:

- [1]. Mazharul Islam, David S-K Ting and Amir Fartaj. 2007. Assessment of Small-Capacity Straight-bladed VAWT for Sustainable Development of Canada. International Journal of Environment Studies. Vol 64, No 4, pp 489–500. (Chapter 1)
- [2]. Mazharul Islam, M. Ruhul Amin, David S-K. Ting and Amir Fartaj. 2007. Aerodynamic Factors Affecting Performance of Straight-bladed Vertical Axis Wind Turbines. ASME International Mechanical Engineering Congress and Exposition (IMECE) 2007, Seattle, Washington, USA. November 10-16. IMECE2007-41346. pp 1-11. (Chapter 2)
- [3]. Mazharul Islam, M. Ruhul Amin, David S-K. Ting and Amir Fartaj. 2007. Aerodynamic Factors Affecting Performance of Smaller-Capacity Fixed-Pitch Straight-bladed Vertical Axis Wind Turbines. ASME Journal of Solar Energy Engineering. SOL-08-1006. In review. (Chapter 2)
- [4]. Mazharul Islam, David S-K Ting and Amir Fartaj. 2008. Aerodynamic Models for Darrieus Type Straight-bladed Vertical Axis Wind Turbines. Renewable & Sustainable Energy review, Elsevier. Vol 12, No 4, pp 1087-1109. (Chapter 3)
- [5]. Mazharul Islam, M. Ruhul Amin, David S-K. Ting and Amir Fartaj. 2008. Performance Analysis of a Smaller-capacity Straight-bladed VAWT with

- Prospective Airfoils. Proceedings of the 46th AIAA Aerospace Sciences Meeting and Exhibit & 27th ASME Wind Energy Symposium, January 2008, Reno, Nevada, USA. AIAA 2008-1333. pp 1-17. (Chapter 4 & 5)
- [6]. Mazharul Islam, David S-K Ting and Amir Fartaj. 2007. Desirable Airfoil Features for Smaller-Capacity Straight-Bladed VAWT. Wind Engineering. Vol 31, No 3, pp 165–196. (Chapter 5)
- [7]. Mazharul Islam, M. Ruhul Amin, David S-K. Ting and Amir Fartaj. 2008. Selection of Airfoils for Straight-Bladed Vertical Axis Wind Turbines Based on Desirable Aerodynamic Characteristics. ASME International Mechanical Engineering Congress and Exposition (IMECE) 2008, Boston, Massachusetts, USA. October 31-November 6. IMECE2008-66027. In review. (Chapter 6)
- [8]. Mazharul Islam, David S-K Ting and Amir Fartaj. 2008. Design of a Special-purpose Airfoil for Smaller-Capacity Straight-Bladed VAWT. Wind Engineering. Vol 32, No 1, pp 27–54. (Chapter 7)
- [9]. Mazharul Islam, M. Ruhul Amin, David S-K. Ting and Amir Fartaj. 2008. A New Airfoil for the Supporting Struts of Smaller-capacity Straight-Bladed VAWT. 12th AIAA/ISSMO Multidisciplinary Analysis and Optimization Conference, 10 - 12 September, Victoria, British Columbia, Canada. (Chapter 8)
- [10]. Mazharul Islam, Firoz Uddin Ahmed, David S-K. Ting and Amir Fartaj. 2008. Design Analysis of Fixed-pitch Straight-bladed Vertical Axis Wind Turbines with an Alternative Material. 7th Annual World Wind Energy Conference to be held June 24-26. Kingston, Ontario, Canada. (Chapter 8)

It should be noted that, none of the above-mentioned publications has been used in their entirety in any single chapter of this dissertation. Selected portion of texts or figures (referenced in the caption of the figures) from these publications are contained in the chapters shown above within the parenthesis. In all the cases,

the key ideas, primary contributions, literature survey, computational analysis, experimental designs, data analysis and interpretation, and manuscript preparations were performed by the author. Contributions of the co-authors were primarily in the supervision or editorial level.

I am aware of the University of Windsor Senate Policy on Authorship and I certify that I have properly acknowledged the contribution of other researchers to my dissertation, and have obtained permission from each of the above-mentioned co-author(s) to include the above material(s) in my dissertation.

I certify that, with the above qualification, this dissertation, and the research to which it refers, is the product of my own work.

II. Declaration of Previous Publication

This dissertation includes materials from 10 original papers as listed in "Section I" above that have been previously published/submitted for publication in peer reviewed journals and conferences.

I certify that I have permissions from the copyright owner(s) to include the above published material(s) in my dissertation. I certify that the above material describes work completed during my registration as graduate student at the University of Windsor.

I declare that, to the best of my knowledge, my dissertation does not infringe upon anyone's copyright nor violate any proprietary rights and that any ideas, techniques, quotations, or any other material from the work of other people included in my dissertation, published or otherwise, are fully acknowledged in

accordance with the standard referencing practices. Furthermore, to the extent that I have included copyrighted material that surpasses the bounds of fair dealing within the meaning of the Canada Copyright Act, I certify that I have obtained permission from the copyright owner(s) to include such material(s) in my dissertation.

I declare that this is a true copy of my dissertation, including any final revisions, as approved by my dissertation committee and the Graduate Studies office, and that this dissertation has not been submitted for a higher degree to any other University of Institution.

Abstract

Selection of the airfoil is crucial for better aerodynamic performance and dimensions of a smaller-capacity fixed-pitch SB-VAWT. Most of the earlier research works with SB-VAWT mainly utilized symmetric airfoils as its blade shape, but several research works indicated that the performance of fixed pitch SB-VAWT with asymmetric blades have the potential to exhibit superior characteristics at low Reynolds numbers (RN). However, currently there is lack of comprehensive information in the public domain regarding the desirable aerodynamic and geometric features of prospective asymmetric airfoils for SB-VAWTs. Against this backdrop, this research has been undertaken with an objective to perform detail systematic investigative analysis with asymmetric airfoils appropriate for smaller-capacity fixed-pitch SB-VAWT with optimum design configuration.

A computational method has been developed in the present study after identifying and considering the main aerodynamic challenges of smaller-capacity SB-VAWT using theoretical coefficients rather than using rarely available expensive experimental results. After conducting literature survey and detail performance analyses with available asymmetric airfoils, it has been found that there is a need for designing special-purpose airfoils for smaller-capacity SB-VAWT. Under this circumstance, a new airfoil "MI-VAWT1" has been designed and it has been found that its performance is much superior to other prospective asymmetric airfoils and conventionally used symmetric NACA 0015 at low RN and low tip speed ratio ranges. Another airfoil, named as "MI-STRUT1", has been designed for blade supporting struts to reduce the detrimental parasitic drag losses. After considering the design parameters and detailed sensitivity analyses with selected important parameters, a new class of 3kW SB-VAWT (named as "MI-VAWT 3000") has been proposed.

Acknowledgements

The author would like to sincerely praise and thank The Almighty God, The Most Gracious and The Most Merciful, for enabling him to initiate and complete this task.

Many individuals and organizations helped me in different stages of the research work by different means. I would like to humbly recognize their contributions in the subsequent paragraphs below.

The author is appreciative to Dr. David S-K Ting and Dr. Amir Fartaj, his co-supervisors, for their supervisions. I would also like to thank University of Windsor and Ontario Ministry of Training, Colleges and Universities for granting me the scholarships for the present work. Also, several staffs of the University of Windsor helped me throughout the period of the research works and I am grateful for their helps. Special thanks go to the internal reviewers (Dr. Ronald Barron, Dr. Nader Zamani & Dr. Edward Carriveau) and the external examiner (Dr. David Wood) for their comments and suggestions.

The author would also like to acknowledge the works of the individuals and organizations that are listed in the bibliography section of this dissertation. The author utilized numerous free software or freewares (including XFLR5, XFOIL, Photofiltre, GIMPshop, WinTopo, Engauge) for the present work and he is grateful to the developers of these excellent tools.

Last, but not the least, my sincere gratitude goes to my family members - my mother, my wife and my two sons. Special thanks to my adored wife Tazina for her constant encouragement, supports and nice VAWT sketches.

Table of Contents

Declaration of Co-Authorship / Previous Publication	<i>iii</i>
Abstract	<i>vii</i>
Acknowledgements	<i>viii</i>
List of Figures	<i>xiv</i>
List of Tables	<i>xxiv</i>
Nomenclature	<i>xxvi</i>
Chapter 1: Introduction	1
<hr/>	
<i>1.1. Historical Background of Wind Turbines</i>	<i>3</i>
<i>1.2. Modern VAWT Types</i>	<i>3</i>
<i>1.3. Major VAWTs Related Programs</i>	<i>7</i>
<i>1.4. About Fixed-pitch Straight-bladed VAWTs (SB-VAWTs)</i>	<i>11</i>
<i>1.5. Objectives</i>	<i>21</i>
<i>1.6. Scopes of the Dissertation</i>	<i>22</i>
<i>1.7. Significance of the Research</i>	<i>24</i>

**Chapter 2: Aerodynamic Challenges of Smaller-
capacity Fixed-pitch SB-VAWTs** 27

<i>2.1. Aerodynamics of SB-VAWTs</i>	27
<i>2.2. Self-starting Problem of SB-VAWTs</i>	29
<i>2.3. Major Aerodynamic Challenges</i>	32
<i>2.4. Summary of the Chapter</i>	53

**Chapter 3: Review of Aerodynamic Computational
Models** 56

<i>3.1. General Mathematical Expressions for Aerodynamic Analysis of Fixed-pitch SB-VAWTs</i>	56
<i>3.2. Computational Models for Performance Analysis of VAWTs</i>	60
<i>3.3. Summary of the Chapter</i>	77

**Chapter 4: Computational Scheme for Performance
Analysis of SB-VAWT** 78

<i>4.1. Fundamentals of Cascade Model for Straight-bladed VAWT</i>	80
<i>4.2. Input of Airfoil Aerodynamic Characteristics</i>	95
<i>4.3. Modeling of Dynamic Stall Effect</i>	107
<i>4.4. Modeling of Flow Curvature Effect</i>	111
<i>4.5. Modeling of the Effect of Parasitic Drag</i>	114
<i>4.6. Comparisons of Performance Curves between Experimental and XFOIL Datasets</i>	115

4.7. Validation of the Computational Scheme	117
4.8. Summary of the Chapter	119
Chapter 5: Desirable Airfoil Features for Smaller-Capacity SB-VAWT	121
<hr/>	
5.1. Previously Utilized General-Purpose Airfoils for SB-VAWTs	122
5.2. Specially Designed Airfoils for SB-VAWTs	130
5.3. Desirable Aerodynamic Characteristics of SB-VAWT Airfoil	133
5.4. Desirable Geometric Features of SB-VAWT Airfoil	148
5.5. Performance Analysis with Candidate Asymmetric Airfoils	158
5.6. Summary of the Chapter	162
Chapter 6: Selection of Prospective Asymmetric Airfoils	165
<hr/>	
6.1. Criteria for Selection of Prospective Asymmetric Airfoils	165
6.2. Selection of Candidate Airfoils Based on Experimental Results	166
6.3. Performance of the Candidate Airfoils	167
6.4. Analysis of Selected Prospective Airfoils through Performance Indices	170
6.5. Selection of the Best Prospective Asymmetric Airfoil	176
6.6. Summary of the Chapter	177

**Chapter 7 : Design of a Special-purpose Airfoil for
Smaller-Capacity SB-VAWT** 182

*7.1. Sensitivity Analysis with Geometric Features of NASA LS(1)-
0417* 182

7.2. New Special-Purpose SB-VAWT Airfoil – “MI-VAWT1” 193

7.3. Summary of the Chapter 196

**Chapter 8 : Design Analysis of a Smaller-capacity SB-
VAWT** 200

8.1. Design Parameters 201

8.2. Analytical Tool for Design Analysis of SB-VAWT 234

8.3. Sensitivity Analyses with Selected Design Parameters 238

8.4. Specifications of a New Class of SB-VAWT – “MI-VAWT 3000” 248

8.5. Summary of the Chapter 251

Chapter 9: Experimentation of a SB-VAWT Prototype 253

9.1. Fabrication of a SB-VAWT Prototype 253

9.2. Instrumentation 257

9.3. Experimental Setup 260

9.4. Results and Discussions 262

9.5. Summary of the Chapter 265

Chapter 10 : Concluding Remarks **269**

10.1. Research Outcomes **269**

10.2. Recommendations for Further Research Works **276**

References **277**

Appendices **295**

Appendix A: Flow Diagram of Computational Scheme **296**

Appendix B: Flow Diagram of Design Analysis **299**

Appendix C: XFOIL **301**

Appendix D: Coordinates of MI-VAWT1 **315**

Appendix E: Coordinates of MI-STRUT1 **316**

Appendix F: Determination of Bending Moment and Bending Stress **317**

Appendix G: Selected Pictures of the Blade Fabrication Process **322**

Vita Auctoris **325**

List of Figures

<i>Figure 1.1: Savonius-type VAWT</i>	4
<i>Figure 1.2: Curved-blade (or “Egg-beater” type) Darrieus VAWT</i>	5
<i>Figure 1.3: Straight-bladed VAWT (SB-VAWT)</i>	6
<i>Figure 1.4: H-Rotor Type VAWT</i>	8
<i>Figure 1.5: Schematic of a Typical Straight-bladed VAWT Stand-alone Electric System</i>	13
<i>Figure 1.6: Schematic of a Typical Straight-bladed VAWT Grid-connect Electric System</i>	14
<i>Figure 1.7: Schematic of a Typical Straight-bladed VAWT Mechanical Pumping System</i>	15
<i>Figure 1.8: Scopes of Different Chapters of the Dissertation</i>	26
<i>Figure 2.1: Flow Velocities around SB-VAWT</i>	28
<i>Figure 2.2: Variation of Angle of Attack with Azimuthal Position at Different Tip Speed Ratios of a SB-VAWT</i>	29
<i>Figure-2.3: C_p-λ Curves of SB-VAWT with NACA 0015 Airfoil</i>	31
<i>Figure 2.4: C_Q-λ Curves of SB-VAWT with NACA 0015 Airfoil</i>	31
<i>Figure 2.5: Structural Components of A Typical SB-VAWT and Their Associated Aerodynamic Challenges</i>	33
<i>Figure 2.6: Low-Reynolds Number Airfoil Performance</i>	34
<i>Figure 2.7: Structure of Laminar Separation Bubble</i>	35
<i>Figure 2.8: Effect of Laminar Bubble on Lift-Drag Polar</i>	36
<i>Figure 2.9: Variation of C_r-α Curves at Different Reynolds Number</i>	38

<i>Figure 2.10: Schematic Showing Unsteady Airloads and Flow Physics for a Two-Dimensional Airfoil Undergoing Dynamic Stall</i>	40
<i>Figure 2.11: Comparison of Experimental and Computational Non-dimensional Tangential Forces</i>	42
<i>Figure 2.12: Comparison of Experimental and Computational Non-dimensional Normal Forces</i>	42
<i>Figure 2.13: Typical Variation of Relative Velocity and Angle of Attack along Chordwise Direction</i>	43
<i>Figure 2.14: Qualitative Illustration of Conformal Transformation</i>	44
<i>Figure 2.15: Mean Values of Camber and Incidence at Different C/R</i>	45
<i>Figure 2.16: Variation of Virtual Camber and Incidence with Blade Orbital Position</i>	45
<i>Figure 2.17: Comparison Between C_p-λ Curves of Experimental And Computational Results of an Experimental SB-VAWT</i>	47
<i>Figure 2.18: Velocity Contour around a Vertical Axis Wind Turbine at $\lambda=6.0$</i>	49
<i>Figure 2.19: Stream Lines around a Vertical Axis Wind Turbine at $\lambda=6.0$</i>	50
<i>Figure 3.1: Flow Velocities of SB-VAWT</i>	58
<i>Figure 3.2: Force Diagram of a Blade Airfoil</i>	59
<i>Figure 3.3: Schematic of Single Streamtube Model</i>	62
<i>Figure 3.4: Schematic of Multiple Streamtube Model</i>	65
<i>Figure 3.5: Schematic of Double-Multiple Streamtube Model</i>	68
<i>Figure 3.6: Vortex System for a Single Blade Element</i>	70
<i>Figure 3.7: Velocity Induced at a Point by a Vortex Filament</i>	71
<i>Figure 3.8: Development of Blade into a Cascade Configuration</i>	74

<i>Figure 3.9: Horizontal Section of a SB-VAWT with Flow Velocities in the Upstream and Downstream Sides</i>	76
<i>Figure 4.1: Comparison of Experimental and Analytical Power-coefficients by Different Computational Models</i>	79
<i>Figure 4.2: Velocity Diagram on a Blade Airfoil</i>	83
<i>Figure 4.3: Force Diagram on a Blade Airfoil</i>	88
<i>Figure 4.4: C_L-α Curve of NACA 0015 at $RN=360,000$</i>	96
<i>Figure 4.5: C_D-α Curve of NACA 0015 at $RN=360,000$</i>	96
<i>Figure 4.6: C_M-α Curve of NACA 0015 at $RN=360,000$</i>	97
<i>Figure 4.7: C_L-α Curve of Gö 420 at $RN=420,000$</i>	97
<i>Figure 4.8: C_D-α Curve of Gö 420 at $RN=420,000$</i>	98
<i>Figure 4.9: C_m-α Curve of Gö 420 at $RN=420,000$</i>	98
<i>Figure 4.10: Flow Diagram of the Computational Scheme for Performance Analysis of SB-VAWTs</i>	101
<i>Figure 4.11: Comparison of C_L-α Curves of Experimental Datasets and FoilCheck Results</i>	103
<i>Figure 4.12: Comparison of C_D-α Curves of Experimental Datasets and FoilCheck Results</i>	104
<i>Figure 4.13: Typical Variation of Relative Velocity and Angle Of Attack Along Chord-wise Direction</i>	111
<i>Figure 4.14: Geometry to Determine Camber of Circular Arc</i>	112
<i>Figure 4.15: Comparisons of $C_{p,net}$-λ Curves Based on Experimental and XFOIL Airfoil Datasets at $RN=100,000$</i>	116
<i>Figure 4.16: Comparisons of $C_{p,net}$-λ Curves Based on Experimental and XFOIL Airfoil Datasets at $RN=300,000$</i>	116
<i>Figure 4.17: Comparison of Experimental and Computational C_P-λ Curves at $RN=164,948$</i>	118

<i>Figure 4.18: Comparison of Experimental and Computational C_F-λ Curves at $RN=219,931$</i>	118
<i>Figure 4.19: Comparison of Experimental and Computational C_F-λ Curves at $RN=274,914$</i>	119
<i>Figure 5.1: Geometry of Conventionally used NACA Symmetric Airfoils</i>	123
<i>Figure 5.2: Two Types of Configurations for Attaching Cambered Airfoils with the Supporting Struts</i>	126
<i>Figure 5.3: Geometries of Selected Asymmetric Airfoils</i>	127
<i>Figure 5.4: C_F-α Curves of Selected Asymmetric Airfoils at $RN=100,000$ & $\mu=10$</i>	128
<i>Figure 5.5: C_F-α Curves of Selected Asymmetric Airfoils at $RN=300,000$ & $\mu=10$</i>	129
<i>Figure 5.6: Lift Curves of Selected Asymmetric Airfoils at $RN=100,000$</i>	134
<i>Figure 5.7: Lift Curves of Selected Asymmetric Airfoils at $RN=300,000$</i>	135
<i>Figure 5.8: Drag Buckets of Selected Asymmetric Airfoils at $RN=100,000$</i>	137
<i>Figure 5.9: Drag Buckets of Selected Asymmetric Airfoils at $RN=300,000$</i>	138
<i>Figure 5.10: C_l/C_d Ratio of Selected Asymmetric Airfoils at $RN=100,000$</i>	139
<i>Figure 5.11: C_l/C_d Ratio of Selected Asymmetric Airfoils at $RN=300,000$</i>	140
<i>Figure 5.12: Deep Stall Characteristic on the Upper Surfaces of Selected Prospective Airfoils</i>	142
<i>Figure 5.13: Deep Stall Characteristic on the Lower Surfaces of Selected Prospective Airfoils</i>	142
<i>Figure 5.14: Comparison of Sound Pressure Levels (SPL) of Selected Prospective Airfoils</i>	146

<i>Figure 5.15: Pitching Moment Coefficient of Selected Asymmetric Airfoils at $RN=100,000$</i>	147
<i>Figure 5.16: Pitching Moment Coefficient of Selected Asymmetric Airfoils at $RN=300,000$</i>	148
<i>Figure 5.17: Geometric Features of a Typical Asymmetric Airfoil</i>	151
<i>Figure 5.18: C_r-α Curves of LS(1) 0417MOD & LS(1) 0421MOD at $RN=100,000$</i>	154
<i>Figure 5.19: C_r-α Curves of LS(1) 0417MOD & LS(1) 0421MOD at $RN=300,000$</i>	155
<i>Figure 5.20: $C_{P,ne\tau}$-λ Curves of SB-VAWTs with Selected Asymmetric Airfoils at $RN=50,000$</i>	159
<i>Figure 5.21: $C_{Q,ne\tau}$-λ Curves of SB-VAWTs with Selected Asymmetric Airfoils at $RN=50,000$</i>	159
<i>Figure 5.22: $C_{P,ne\tau}$-λ Curves of SB-VAWTs with Selected Asymmetric Airfoils at $RN=100,000$</i>	160
<i>Figure 5.23: $C_{Q,ne\tau}$-λ Curves of SB-VAWTs with Selected Asymmetric Airfoils at $RN=100,000$</i>	160
<i>Figure 5.24: $C_{P,ne\tau}$-λ Curves of SB-VAWTs with Selected Asymmetric Airfoils at $RN=300,000$</i>	161
<i>Figure 5.25: $C_{Q,ne\tau}$-λ Curves of SB-VAWTs with Selected Asymmetric Airfoils at $RN=300,000$</i>	161
<i>Figure 6.1: C_r-α Curves of Selected Airfoils Based on Experimental Results at $95,000 \leq RN \leq 160,000$</i>	169
<i>Figure 6.2: C_r-α Curves of Selected Airfoils Based on Experimental Results at $295,000 \leq RN \leq 360,000$</i>	169
<i>Figure 6.3: Selection Process of the Most-Promising Airfoil for the Design of a Special-Purpose Airfoil</i>	181
<i>Figure 7.1: Geometric Features of an Asymmetric Airfoil</i>	183
<i>Figure 7.2: Geometry of Candidate Airfoil for Sensitivity Analysis</i>	184

<i>Figure 7.3: Power Coefficients of LS-0417 with Different Cambers at RN=100,000</i>	185
<i>Figure 7.4: Power Coefficients of LS-0417 with Different Cambers at RN=300,000</i>	185
<i>Figure 7.5: Torque Coefficients of LS-0417 with Different Cambers at RN=100,000</i>	186
<i>Figure 7.6: Torque Coefficients of LS-0417 with Different Cambers at RN=300,000</i>	186
<i>Figure 7.7: Power Coefficients of LS-0417 with Different Thicknesses at RN=100,000</i>	188
<i>Figure 7.8: Power Coefficients of LS-0417 with Different Thicknesses at RN=300,000</i>	188
<i>Figure 7.9: Torque Coefficients of LS-0417 with Different Thicknesses at RN=100,000</i>	189
<i>Figure 7.10: Torque Coefficients of LS-0417 with Different Thicknesses at RN=300,000</i>	189
<i>Figure 7.11: Power Coefficients of LS-0417 with Different Leading Edge Radius (R_{LE}) at RN=100,000</i>	191
<i>Figure 7.12: Power Coefficients of LS-0417 with Different Leading Edge Radius (R_{LE}) at RN=300,000</i>	191
<i>Figure 7.13: Torque Coefficients of LS-0417 with Different Leading Edge Radius (R_{LE}) at RN=100,000</i>	192
<i>Figure 7.14: Torque Coefficients of LS-0417 with Different Leading Edge Radius (R_{LE}) at RN=300,000</i>	192
<i>Figure 7.15: Power Coefficients of LS-0417 with Different Trailing Edge Thicknesses (t_{TE}) at RN=100,000</i>	194
<i>Figure 7.16: Power Coefficients of LS-0417 with Different Trailing Edge Thicknesses (t_{TE}) at RN=300,000</i>	194
<i>Figure 7.17: Torque Coefficients of LS-0417 with Different Trailing Edge Thicknesses (t_{TE}) at RN=100,000</i>	195

<i>Figure 7.18: Torque Coefficients of LS-0417 with Different Trailing Edge Thicknesses (t_{TE}) at $RN=300,000$</i>	195
<i>Figure 7.19: Geometry of MI-VAWT1</i>	196
<i>Figure 7.20: $C_{P,net}$-λ Curves of a SB-VAWT with MI-VAWT1 at $RN=50,000$</i>	197
<i>Figure 7.21: $C_{Q,net}$-λ Curves of a SB-VAWT with MI-VAWT1 at $RN=50,000$</i>	197
<i>Figure 7.22: $C_{P,net}$-λ Curves of a SB-VAWT with MI-VAWT1 at $RN=100,000$</i>	198
<i>Figure 7.23: $C_{Q,net}$-λ Curves of a SB-VAWT with MI-VAWT1 at $RN=100,000$</i>	198
<i>Figure 7.24: $C_{P,net}$-λ Curves of a SB-VAWT with MI-VAWT1 at $RN=300,000$</i>	199
<i>Figure 7.25: $C_{Q,net}$-λ Curves of a SB-VAWT with MI-VAWT1 at $RN=300,000$</i>	199
<i>Figure 8.1: The Main Components of a Typical SB-VAWT</i>	202
<i>Figure 8.2: Three Different Types of Blade Supports of SB-VAWTs</i>	206
<i>Figure 8.3: Eppler 862 Non-lifting Supporting Strut</i>	207
<i>Figure 8.4: Newly Designed MI-STRUT1</i>	208
<i>Figure 8.5: Comparison Between the C_{do} of Eppler 862 and MI-STRUT1 at Different Reynolds Number</i>	208
<i>Figure 8.6: $C_{P,net}$-λ Curves of a SB-VAWT with Different Shapes of Supporting Struts at $RN=100,000$</i>	209
<i>Figure 8.7: $C_{P,net}$-λ Curves of a SB-VAWT with Different Shapes of Supporting Struts at 300,000</i>	210
<i>Figure 8.8: Power Coefficients of a 1kw Fixed-pitch Straight-bladed VAWT at Different Solidities</i>	212
<i>Figure 8.9: Torque Coefficients of a 1kw Fixed-pitch Straight-bladed</i>	213

<i>VAWT at Different Solidities</i>	
<i>Figure 8.10: $C_{p,net}-\lambda$ Curves of a SB-VAWT at Different Aspect Ratio</i>	214
<i>Figure 8.11: $C_{Q,net}-\lambda$ Curves of a SB-VAWT at Different Aspect Ratio</i>	215
<i>Figure 8.12: MI-VAWT1 Blade with Winglets</i>	217
<i>Figure 8.13: MI-VAWT1 Blade with Endplates</i>	218
<i>Figure 8.14: Elliptical MI-VAWT1 Blade with Sectional View</i>	219
<i>Figure 8.15: Illustration of a Typical Power Curve of a 3kW SB-VAWT</i>	220
<i>Figure 8.16: Illustration of a Design Power Coefficient and Tip Speed Ratio</i>	222
<i>Figure 8.17: $C_{P,net}-\lambda$ Curves of a SB-VAWT with Different Fixed Pitch Angle</i>	224
<i>Figure 8.18: $C_{P,net}-\lambda$ Curves of a SB-VAWT with Different Fixed Pitch Angle</i>	224
<i>Figure 8.19: Cross-Section Principle of a Wind Turbine Blade Giving the Nomenclature of the Different Blade Construction Elements</i>	227
<i>Figure 8.20: Number of Load Cycles of Different Mechanical Applications</i>	228
<i>Figure 8.21: Schematic S-N Diagram for Various Fatigue-critical Structures</i>	228
<i>Figure 8.22: Diagram Showing Stiffness Versus Density for all Materials</i>	229
<i>Figure 8.23: MI-VAWT with Skin and Rib Areas</i>	235
<i>Figure 8.24: SB-VAWT with Three New Design Features</i>	249
<i>Figure 9.1: The Selected Symmetric and Asymmetric Airfoils for SB-VAWT Prototype</i>	254
<i>Figure 9.2: SB-VAWT Prototype with 2 Blades</i>	255

<i>Figure 9.3: SB-VAWT Prototype with 3 Blades</i>	255
<i>Figure 9.4: Torque Measurement Setup</i>	258
<i>Figure 9.5: Data Acquisition System</i>	259
<i>Figure 9.6: Experimental Setup for SB-VAWT Prototype</i>	261
<i>Figure 9.7: Torque Produced by the SB-VAWT Prototype equipped with NACA 0021</i>	263
<i>Figure 9.8: Torque Produced by the SB-VAWT Prototype equipped with NACA 4415</i>	263
<i>Figure 9.9: Comparison Between NACA 0021 & NACA 4415 equipped with 2-blades</i>	266
<i>Figure 9.10: Comparison Between NACA 0021 & NACA 4415 equipped with 3-blades</i>	266
<i>Figure 9.11: Comparison Between the Computational and Experimental Results of SB-VAWT Equipped with 2-blades of NACA 0021</i>	267
<i>Figure 9.12: Comparison Between the Computational and Experimental Results of SB-VAWT Equipped with 3-blades of NACA 0021</i>	267
<i>Figure 9.13: Comparison Between the Computational and Experimental Results of SB-VAWT Equipped with 2-blades of NACA 4415</i>	268
<i>Figure 9.14: Comparison Between the Computational and Experimental Results of SB-VAWT Equipped with 3-blades of NACA 4415</i>	268
<i>Figure C1: Comparison of Experimental Data with XFOIL Results for S1210 at $RN=100,000$</i>	306
<i>Figure C2: Comparison of Experimental Data with XFOIL Results for S1210 at $RN=300,000$</i>	307
<i>Figure C3: Comparison of Experimental Data with XFOIL Results for S1223 at $RN=100,000$</i>	308

<i>Figure C4: Comparison of Experimental Data with XFOIL Results for S1223 at RN=300,000</i>	309
<i>Figure C5: Comparison of Experimental Data with XFOIL Results for S8037at RN=100,000</i>	310
<i>Figure C6: Comparison of Experimental Data with XFOIL Results for S8037at RN=300,000</i>	311
<i>Figure C7: Comparison of Experimental Data with XFOIL Results for SG6040 at RN=100,000</i>	312
<i>Figure C8: Comparison of Experimental Data with XFOIL Results for SG6040 at RN=300,000</i>	313
<i>Figure C9: Comparison of Experimental Data with XFOIL Results for DU_06-W-200 at RN=300,000</i>	314
<i>Figure F1: Section of a Straight-Bladed Wind Turbine Showing Forces on the SB-VAWT Blade</i>	317
<i>Figure F2: Bending Moment Diagram of an Overhang Supported Beam</i>	318
<i>Figure F3: Bending Moment Diagram of a Simply Supported Beam</i>	320
<i>Figure G1: Cutting of Styrofoam using CNC machine for NACA 4415 Blades</i>	322
<i>Figure G2: Initial Painting of the Blades with a Water-based Color</i>	322
<i>Figure G3: Styrofoam Blade Cores & Fibre Glass Clothing before Lamination Process</i>	323
<i>Figure G4: Applying Fiberglass Resin Along With Hardener</i>	323
<i>Figure G5: Blades before Sanding Process</i>	324
<i>Figure G6: SB-VAWT with the Blades after Final Painting</i>	324

List of Tables

<i>Table 1.1: Major Advantages of Small-scale Fixed-pitch Straight-bladed Vertical Axis Wind Turbine (VAWT) over Horizontal Axis Wind Turbine (HAWT)</i>	11
<i>Table 4.1: Computational Scheme for Performance Analysis of SB-VAWTs</i>	120
<i>Table 5.1: Roughness Sensitivity of Selected Airfoils at $Re=100,000$</i>	145
<i>Table 5.2: Roughness Sensitivity of Selected Airfoils at $Re=300,000$</i>	145
<i>Table 5.3: Ratings of Candidate Airfoils Based on Desirable Aerodynamic Characteristics</i>	149
<i>Table 5.4: Three Types of Airfoils for Generating Lift</i>	150
<i>Table 5.5: Geometric Features of Selected Airfoils</i>	157
<i>Table 6.1: Selected Candidate Airfoils Based on Experimental Results</i>	168
<i>Table 6.2: Performance Index of Selected Prospective Airfoils Based on Equal Weight</i>	179
<i>Table 6.3: Performance Index of Selected Prospective Airfoils Based on Unequal Weight</i>	180
<i>Table 8.1: Different Design Parameters of a SB-VAWT Powered Application</i>	202
<i>Table 8.2: Engineering Properties of Pultruded FRP and Extruded Aluminum</i>	233
<i>Table 8.3: Different Fixed & Variable Parameters Considered in the Design Analyses</i>	237
<i>Table 8.4: Matrix of Design Parameters for the Sensitivity Analyses</i>	238
<i>Table 8.5: Design Analyses of Different Types of Blade Supports</i>	240

<i>Table 8.6: Sensitivity Analysis with Solidity</i>	241
<i>Table 8.7: Design Configurations with Aluminum and FRP</i>	243
<i>Table 8.8: Results of Sensitivity Analysis with Blade Airfoil</i>	245
<i>Table 8.9: Results of Sensitivity Analysis with Blade Support Shape</i>	247
<i>Table 8.10: Specifications of the Salient Design Features of MI-VAWT 3000</i>	250
<i>Table 8.11: Summary of the Innovative Design Concepts for SB-VAWTs</i>	252
<i>Table 9.1: Dimensions of SB-VAWT Prototype with Symmetric Airfoil</i>	254

Nomenclature

A	Area swept by turbine
A_b	total blade sectional area
A_r	area of blade rib
A_s	area of blade skin
ABL	atmospheric boundary layer
b	a factor
c	blade chord
C_1	distance along chord from leading edge point to blade fixing point
C_2	distance along chord from trailing edge point to blade fixing point
C_d	blade drag coefficient
C_{dd}	blade drag coefficient due to dynamic stall effect
C_{di}	induced drag coefficient
C_{do}	zero-lift-drag coefficient
C_D	turbine overall drag coefficient = $F_D / \frac{1}{2} \rho A V_\infty^2$
C_{DD}	rotor drag coefficient = $F_D / \frac{1}{2} \rho A V_\infty^2$
$C_{d,st}$	drag coefficient of supporting struts of SB-VAWTs
C_l	blade lift coefficient
C_m	blade pitching moment coefficient
C_n	normal force coefficient
C_P	turbine overall power coefficient = $P_o / \frac{1}{2} \rho A V_\infty^3$
$C_{P,net}$	net power coefficient
C_Q	turbine overall torque coefficient = $Q / \frac{1}{2} \rho A V_\infty^2 R$
$C_{Q,net}$	net torque coefficient
C_t	tangential force coefficient
D	blade drag force
ECN	Energy research Centre of the Netherlands
f	maximum camber of imaginary circular arc
F	force on blade airfoil
F_{cf}	centrifugal force
F_D	turbine overall drag force
F_f	a factor for lift correction due to flow curvature

F_n	normal force (in radial direction)
F_{net}	net normal force (in radial direction)
F_{nid}	force appearing in frictionless flow
F_{nv}	force due to pressure loss
F_n^+	non-dimensional normal force = $C_n (W/V_\infty)^2$
F_t	tangential force
F_{ta}	average tangential force
F_t	non-dimensional tangential force = $C_t (W/V_\infty)^2$
g	acceleration due to gravity
h_d	rotor height diameter ratio = $H/2R$
H	height of turbine
HAWT	horizontal axis wind turbines
I	area moment of inertia
\bar{I}	centroidal area moment of inertia
I_r	moment of inertia of blade rib
I_s	moment of inertia of blade skin
k_1	an empirical constant
k_c	a constant
k_i	exponent in the induced velocity relation
K	factor to include dynamic stall
L	blade lift force
L_{id}	lift force appearing in frictionless flow
L_v	lift force contributed by pressure loss
M	meter
\dot{m}	mass flow rate
m_b	blade mass per unit length
M	blade pitching moment
M_{bn}	bending moment due to net normal force in Nm
M_{bt}	bending moment due to net tangential force in Nm
n	an exponent
N	number of blades
NACA	National Advisory Committee for Aeronautics
p	static pressure
P_f	a factor in prestall condition
P_o	overall power

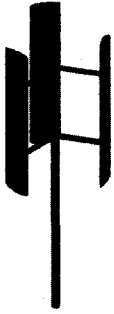
P_∞	atmospheric pressure
PI	performance index
PIV	Particle Image Velocimetry
PM	particulate matter
PV	photovoltaic
Q	overall torque
Q_s	starting torque
R	turbine radius
R_{LE}	leading edge radius
Re_t	turbine speed Reynolds number = $R\omega c/\nu$
Re_w	wind speed Reynolds number = $V_\infty c/\nu$
RETs	renewable energy technologies
RN	local Reynolds number = Wc/ν
S_a	allowable stress in N/mm^2
S_{bn}	bending stress due to net normal force in N/mm^2
S_{bt}	bending stress due to tangential force in N/mm^2
S_m	maximum value of blade stress in each revolution in N/mm^2
$S_{\dot{\alpha}}$	sign of rate of change of angle of attack
SB-VAWT	straight-bladed vertical axis wind turbine
SPL	sound pressure level
t	blade spacing = $(2\pi R/N)$
t_c	maximum blade thickness as a fraction of chord
t_{max}	maximum thickness of airfoil
t_s	blade skin thickness
t_{TE}	trailing edge thickness
V	centre line velocity along freestream velocity direction
V_a	induced velocity
V_c	chordal velocity component
V_{cut}	cutout speed
V_e	wake velocity in upstream side
V_n	normal velocity component
V_r	radial velocity component
V_w	wake velocity in downstream side
V_I	velocity contributed by circulation
V_∞	wind velocity

$V_{cut\ out}$	cut-out speed
V_{design}	design wind speed
VAWT	vertical axis wind turbines
W	relative flow velocity
α	effective blade angle/angle of attack for finite wing
$\dot{\alpha}$	instantaneous rate of change of α
α_c	incidence correction angle due to flow curvature
α_i	induced angle of attack
α_m	modified angle of attack due to dynamic stall
α_o	angle of attack for infinite wing
α_s	stalling angle
β	$(\alpha_e - \alpha_i)$
γ	an empirical constant
γ_p	blade pitch angle
Γ	circulation per unit length
δ	correction factor for induced drag
Δp_{ov}	total pressure loss term (total cascade loss)
ε	= D/L
θ	azimuth angle
λ	tip speed ratio = $R\omega/V_\infty$
μ	aspect ratio = H/c
ν	kinematic viscosity
ρ	fluid density
σ	solidity = Nc/R
τ	correction factor for induced angle
ω	angular velocity of turbine in rad/s

SUBSCRIPTS

d	downstream side / design point
e	trailing edge point
eq	equivalent condition due to flow curvature
i	leading edge point
u	upstream side
x	x-axis

y	y-axis
1	cascade inlet
2	cascade outlet



Chapter 1

Introduction

Among all the environmentally benign renewable energy technologies (RETs), wind energy plays a vital role. It has been increasing approximately 32% a year globally over the last five years [CanWEA 2008]. At the end of 2007, the total global wind power installed capacity was over 94 GW [GWEC 2008]. In 2007, the total value of new wind power generating equipment installed was about US\$36 billion [GWEC 2008].

Wind energy is considered as one of the leading renewable energy sources which has zero emissions and has minimal impact on watersheds, landscapes, and biodiversity. Also, it does not contribute to increased toxins in our environment [Clean Air Renewable Energy Coalition 2002]. Application of wind energy promotes sustainable development, meeting the needs of the present without compromising the ability of future generations to meet their needs [WCED 1987].

The main culprits obstructing sustainable development are the conventional fossil fuel and nuclear energy technologies that are accompanied by environmental degradation at local, regional, and global levels that threaten human well-being now and well into the future. This degradation threatens human health and quality of life in the short term, and affects ecological balance and biological diversity in the long term. On the other hand, wind energy harnessed from the

natural ecosystem is environmentally benign and inexhaustible. Due to increasing efforts by the global communities to combat greenhouse gas emissions from conventional fossil fuel technologies, wind energy technologies will be playing a progressively more significant role in the coming years.

Currently there are two main categories of modern wind turbines, namely Horizontal Axis Wind Turbines (HAWT) and Vertical Axis Wind Turbines (VAWT), which are used primarily for electricity generation and water pumping. For the HAWT machines, the axis of rotation of blades is horizontal and for the VAWT, the axis of rotation is vertical. Unlike HAWT, VAWTs are insensitive to direction of wind and thus they don't need any complicated yawing mechanisms. VAWTs are potentially more efficient and more economical, but those with fixed pitch straight-blades have hitherto been regarded as unsuitable for stand-alone use due to their lack of starting torque.

Most of the earlier research works carried out by Sandia National Laboratory, NRCan and several commercial straight-bladed VAWT (SB-VAWT) models used only symmetric airfoils which were unable to self-start properly. According to the computational research works by Kirke [1998], the performance of fixed pitch VAWT with asymmetric airfoils (whose top and bottom halves are not the same) using newly developed high-lift airfoils exhibit superior characteristics at low Reynolds numbers (RN) and results indicate that fixed pitch VAWT using these blade sections should self-start reliably. However, no comprehensive research work could be found from the literature regarding the viability of applying low RN high-lift asymmetric airfoils for alleviating the drawbacks of the smaller capacity SB-VAWTs. Against this backdrop, the proposed research aims to perform detailed systematic investigative analysis with alternative low-drag, high-lift asymmetric airfoils appropriate for better performance of smaller capacity fixed-pitch SB-VAWT.

1.1. Historical Background of Wind Turbines

Wind energy systems have been used for centuries as a source of energy for mankind. According to historic sources, the Babylonian emperor Hammurabi used windmills for an ambitious irrigation project as early as the 17th century BCE [ITDG 2006]. Later, Persian inventors developed a wind-power machine, a more advanced windmill than that developed by the Babylonians [PSIGATE 2006]. Arab geographers traveling in Afghanistan in the 7th century wrote descriptions of windmills, which resembled our modern revolving doors [Vogel 2005]. Vertical windmills of this category were still used in some parts of Iran and Afghanistan in the late 1980's, and it was estimated that they generated about 75 horsepower and can grind a ton of wheat every 24 hours [Lunde 1980]. The earliest European windmills appeared in France and England in the 12th century and quickly spread throughout Europe. These early wood structures, called post mills, were rotated by hand around a central post to bring the sails into the wind. By the late part of the 13th century the typical 'European windmill' had been developed and this became the norm until further developments were introduced during the 18th century. At the end of the 19th century there were more than 30,000 windmills in Europe, used primarily for the milling of grain and water pumping [ITDG 2006].

1.2. Modern VAWT Types

There have been many designs of vertical axis windmills over the centuries and currently the vertical axis wind turbines can be broadly divided into three basic types, namely (1) Savonius type, (2) Darrieus type, and (3) H-Rotor type. Brief descriptions of these VAWT types are given below.

1.2.1. Savonius Wind Turbine

The Savonius type VAWT, as shown in Figure 1, was invented by Finnish engineer S. J. Savonius in 1929 [Savonius 1931]. It is basically a drag force driven wind turbine with two cups or half drums fixed to a central shaft in

opposing directions. Each cup/drum catches the wind and so turns the shaft, bringing the opposing cup/drum into the flow of the wind. This cup/drum then repeats the process, causing the shaft to rotate further, thus completing a full rotation. This process continues all the time the wind blows and the turning of the shaft is used to drive a pump or a small generator. Though typical values of maximum power coefficient for other types of wind turbines vary between 0.3 to 0.45, those for the Savonius turbines are typically not more than 25% according to most investigators [Kirke 1998]. This type of turbine is suitable for low power applications and they are commonly used for wind speed instruments.

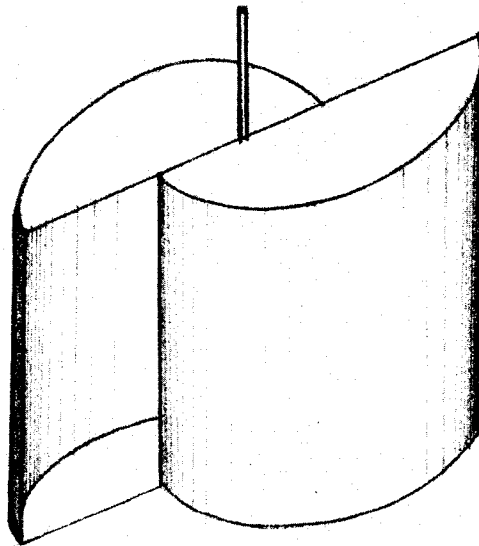


Figure 1.1: Savonius-type VAWT [Islam et. al 2008a]

1.2.2. Darrieus Wind Turbines

The modern Darrieus Vertical Axis Wind Turbine was invented by French engineer George Jean Mary Darrieus. He submitted his patent in 1931 [Darrieus 1931] in the U.S.A. which included both the “Eggbeater (or Curved-bladed)” and “Straight-bladed” VAWTs. Sketches of these two variations of Darrieus concepts are shown in Figures 1.2 and 1.3 respectively. The Darrieus type VAWTs are basically lift force driven wind turbines. The turbine consists of two or more

aerofoil shaped blades which are attached to a rotating vertical shaft. The wind blowing over the aerofoil contours of the blade creates aerodynamic lift and actually pulls the blades along. The troposkien shape eggbeater type Darrieus VAWT, which minimizes the bending stress in the blades, were commercially deployed in California in the past.

In the small scale wind turbine market, the simple straight-bladed Darrieus VAWT, often called giromill or cyclo-turbine, is more attractive for its simple blade design. This configuration falls into two categories: fixed pitch and variable pitch. It has been found from previous research activities that fixed pitch SB-VAWTs provide inadequate starting torque [Kirke 1998]. Contemporary variable pitch blade configuration has potential to overcome the starting torque problem but it is overly complicated, rendering it impractical for smaller capacity applications.

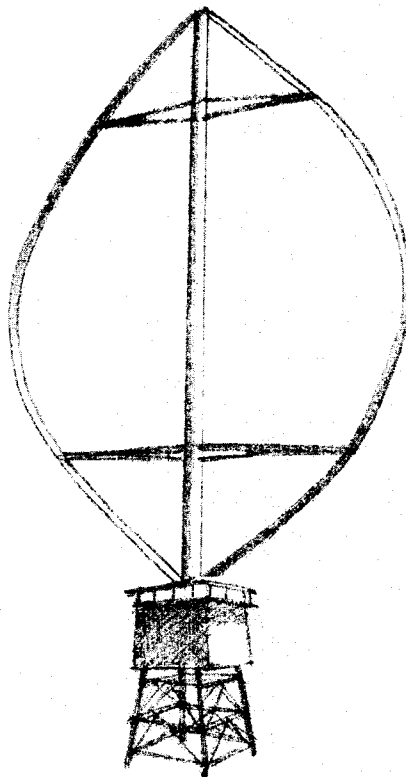


Figure 1.2: Curved-blade (or “Egg-beater” type) Darrieus VAWT [Islam et. al 2008a]

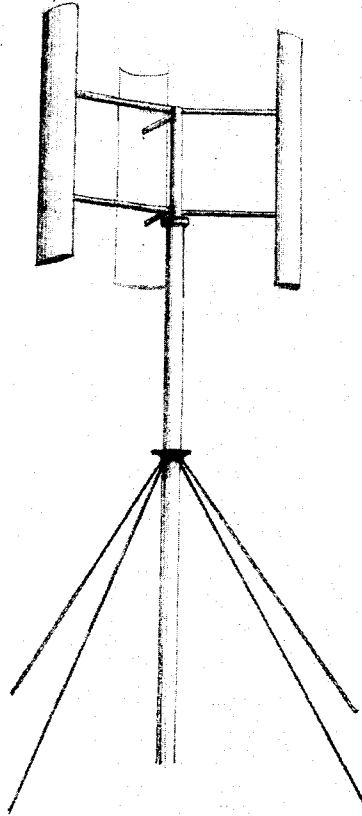


Figure 1.3: Straight-bladed VAWT (SB-VAWT)

The majority of previously conducted research activities on VAWT focused on SB-VAWTs equipped with symmetric airfoils (like NACA 4-digit series of 0012, 0015, 0018) which were unable to self-start. This lack of self-starting capability is due to several factors (including technical, inadequate research work & funding), and the most dominant ones are due to the aerodynamic aspects. According to Internet survey, there are a handful of commercial SB-VAWTs products, but no reliable information could be obtained from an independent source regarding the performance of these products and the claims made by the manufacturers are yet to be authentically verified.

At present, development of large scale SB-VAWT is limited to the research stage only, although large eggbeater Darrieus wind turbines had reached the market

commercially in the past before disappearing later. However, in the small scale wind turbine market, the simple straight-bladed Darrieus seems to be more cost effective than the eggbeater Darrieus as few companies had marketed this type of wind turbine before, e.g. the Pinson/Asi cycloturbine which utilized an end tail for changing pitch. This particular giromill model was stated in Drees' research paper [Drees 1978] as having 3.6m diameter and 2.4m height. With 3 blades at chord length of 29cm, the rotor has solidity of 0.24. Another pitch changing research prototype was built by Grylls et. al [1978]. It has a diameter of 2.4m and a height of 1.6m. Using 3 blades with a chord length of 14.5cm only, the rotor has a solidity of 0.18. Wind tunnel results for this prototype indicated the rotor was able to self-start at wind speed of 3.5m/s, provided the pitch angle change is larger than ± 4 degrees.

1.2.3. H-Rotors

H-Rotors, as shown in Figure 1.4, were developed in the UK through the research carried out during the 1970s - 1980s when it was established that the elaborate mechanisms used to feather the straight-bladed Darrieus VAWT blades were unnecessary. It was found that the drag/stall effect created by a blade leaving the wind flow would limit the speed that the opposing blade (in the wind flow) could propel the whole blade configuration forward. The H-Rotor was therefore self-regulating at all wind speeds reaching its optimal rotational speed shortly after its cut-in wind speed.

1.3. Major VAWTs Related Programs

Although there were major research programs and installations of VAWT in the USA and Canada during the seventies and eighties, their popularity gradually declined due to more economical fossil fuels resources. Most of the wind turbines installed today are HAWT largely due to significant investments made by many countries over the last ten years that have overshadowed progress in VAWT

technology. A brief overview of national VAWT related programs undertaken in Canada, USA and UK is given below.

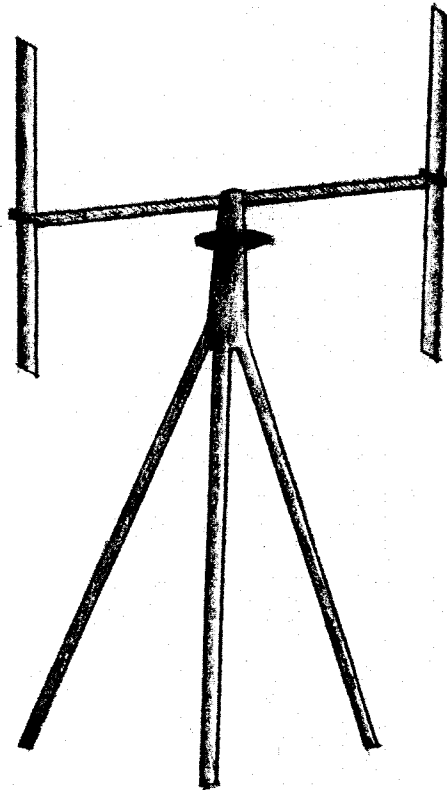


Figure 1.4: H-Rotor Type VAWT [Islam et. al 2008a]

1.3.1. Canada

Research on wind energy systems began in the Low Speed Aerodynamics Laboratory of National Research Council (NRC), Canada in 1966 [Chappell 1986]. At that time aerodynamic research engineers in NRC thought about a reliable inexpensive means of providing relatively small amounts of energy for pumping water, lighting and communications to aid developing countries in combating drought, famine, and isolation in rural areas. Later, NRC devised a VAWT configuration with non-adjustable hoop-shaped airfoils that had higher efficiency than conventional high-solidity VAWTs. Attempts to patent the new wind turbine in 1967 uncovered the work of G. J. M. Darrieus in France about 40.

years earlier. In fact, NRC had reinvented the Darrieus VAWT and had developed and proved its performance well beyond the work of Darrieus.

Early wind tunnel tests conducted by NRC had shown that the VAWT has power coefficient comparable with the HAWT. Researchers at NRC were convinced that the VAWT design, due to its simplicity, had the potential to be more economical than HAWT. It was then decided to start transferring the VAWT technology to the industry. Subsequently, NRC built strong relationships with the industry and completed designing and manufacturing of small and medium size VAWT. Later, during the early eighties, there was interest in Megawatt size VAWT. It was found that it was feasible to construct a VAWT up to 10 MW size. Subsequently, the dream of building multi-megawatt VAWT was fulfilled through the implementation of the project EOLE. EOLE is the largest VAWT in the world, located in Quebec, Canada.

The Atlantic Wind Test Site Inc. (AWTS) is a national facility in Canada for testing and development of wind energy technology. AWTS has also been a key participant in the Canadian wind energy program since it was established in 1980. The most promising VAWT related research conducted by AWTS has been dynamically soft Darrieus rotors, a concept which computer models predict will dramatically reduce structural loads [Soft VAWT Project 2007]. To investigate this, AWTS has initiated a project designed to validate the computer models used to predict the structural responses and aerodynamic modeling and then, with the aid of several consultants, designed a VAWT rotor, that could be fabricated at low cost, and could function as a Soft VAWT.

1.3.2. U.S.A.

VAWT related R&D works in the USA have been carried out by the Sandia National Laboratories (SNL) under the sponsorship of Department of Energy (DOE) [Sandia National Laboratory 2006]. SNL has developed computer codes to model and analyze the structural and aerodynamic performance of VAWT.

VAWT related R&D activities of SNL were culminated through the installation of a 34-m test VAWT for gathering more field data for analysis. SNL has always maintained a close relationship with NRC, Canada for its strong R&D capability. There were a number of commercial wind farms built in the US using the Darrieus design of machine, most of which were built by The Flow Wind Corporation. On the whole the machines proved to be quite efficient and reliable, however there was a problem with fatigue on the blades. The aerofoil blades were designed to flex, allowing for the extra centrifugal forces in high wind and blade speeds. Unfortunately this flexing of the blades led to premature fatigue of the blade material, leading to a number of blade failures [Peace 2003].

1.3.3. United Kingdom

During the late 1970's there was an extensive research programme carried out in the UK led by P. J. Musgrove at Reading University. The purpose of the project was to attempt to rationalize the geometry of the blades by straightening out the blades of a Darrieus type wind turbine, creating a SB-VAWT or H-Rotor configuration. However, at the time it was thought that a simple H-blade configuration could become dangerously unstable in high wind speeds. It was therefore proposed by Musgrove, that a reefing mechanism be incorporated in the machines design thus allowing the blades to be feathered in high winds. These earlier machines with feathering blades were known as Variable Geometry Vertical Axis Wind Turbines.

UK VAWT related activities included wind tunnel tests and the building of a few prototype machines of 40 kW – 100 kW range. This preliminary work culminated in a final reefing arrowhead blade design for a large 25m, 130 kW rated machine, to be located in Carmarthen Bay in South Wales. This machine, known as the VAWT 450, was built by a consortium of Sir Robert McAlpine and Northern Engineering Industries (Vertical Axis Wind Turbines Limited) in 1986. The project was funded by the UK Department of Trade and Industry.

1.4. About Fixed-pitch Straight-bladed VAWTs (SB-VAWTs)

Though HAWTs work well in rural settings with steady uni-directional winds, SB-VAWTs have numerous advantages over them. Some of these advantages are outlined in Table 1.1. It can be understood from this table that unlike HAWTs, fixed-pitch SB-VAWTs are mechanically simpler. They do not require additional components (like yaw mechanics, pitch control mechanism, wind-direction sensing device). Furthermore, almost all of the components requiring maintenance are located at the ground level, facilitating the maintenance work appreciably. It is a fact that the maintenance cost is minimal with SB-VAWT in comparison to diesel gensets typically used as a backup or off-grid power source. They also eliminate the costs (both initial and recurring maintenance) of these additional components and risks associated with the failure or malfunction of these components. Judging all these factors, it can be said that SB-VAWT can be ideal candidate for rooftop (rural and urban) and certain mechanical applications.

Table 1.1: Major Advantages of Small-scale Fixed-pitch Straight-bladed Vertical Axis Wind Turbine over Horizontal Axis Wind Turbine [Islam et. al 2007a]

Horizontal Axis Wind Turbine	Straight-bladed Vertical Axis Wind Turbine
Complex blade geometry.	Simplest blade geometry.
Sensitive to wind direction, and thus require “yaw mechanism” and “wind-direction sensing device” to orient the rotor towards wind.	Insensitive to the wind direction.
Generators are mounted with the rotor high above the ground, thus require the tower to be tilted for maintenance work.	Generator can be placed on the ground.
Require complex pitching mechanism.	Do not require any pitch control device.
Require costly, complex, control & safe breaking devices to avoid ‘runaway’.	Low-cost, simple & self-regulating, using their inherent geometry to prevent ‘runaway’ without special controls.
Can not be directly coupled with mechanical devices (like pump, fan) situated on the ground to generate useful torque,	Can be directly coupled with mechanical devices (like pump, fan) situated on the ground to generate useful torque.

1.4.1. Technical Aspects of Different System Configurations

SB-VAWT can be utilized through different configurations to deliver useful electrical or mechanical energies. Technical aspects of these different configurations are briefly discussed in the following headings.

Electric Systems

One of the major applications of SB-VAWT is to generate electricity. They can operate in both off-grid and on-grid configurations. The system can also incorporate other energy sources (like solar photovoltaic, micro hydro or diesel) to utilize hybrid configuration. Hybrid systems are quite useful where an existing energy technology, such as a conventional generator, is already in use and fuel is expensive. They can also be an option if the cost of storage (i.e. lead acid battery) is high due to large loads.

“Off-grid system” (commonly known as stand-alone configuration) means that the SB-VAWT and the load it serves (e.g. a house or business entity) are not connected with an electrical network (or grid). As the wind is usually an intermittent energy resource, off-grid configurations are typically installed with some form of energy storage device. As shown in Figure 1.5, this configuration usually consists of a (i) generator; (ii) charge controller; (iii) DC source centre; and (iv) lead acid battery bank. The generator is directly coupled with the VAWT central shaft and typically all small wind turbines use permanent magnet DC generators which can directly be used for charging the battery bank. The lead-acid battery bank stores the excess electricity generated by wind which can be supplied to the load (e.g. household appliances like lights, refrigerators etc.) when there is insufficient wind. There can be several other energy storage options, which are in the early stage of commercial phase, that use flywheels or compressed air, or that electrolyze water to produce hydrogen [NRCan 2005]. The charge controller is used to regulate the battery charging. In order to obtain AC current from this configuration, an inverter has to be included in the system.

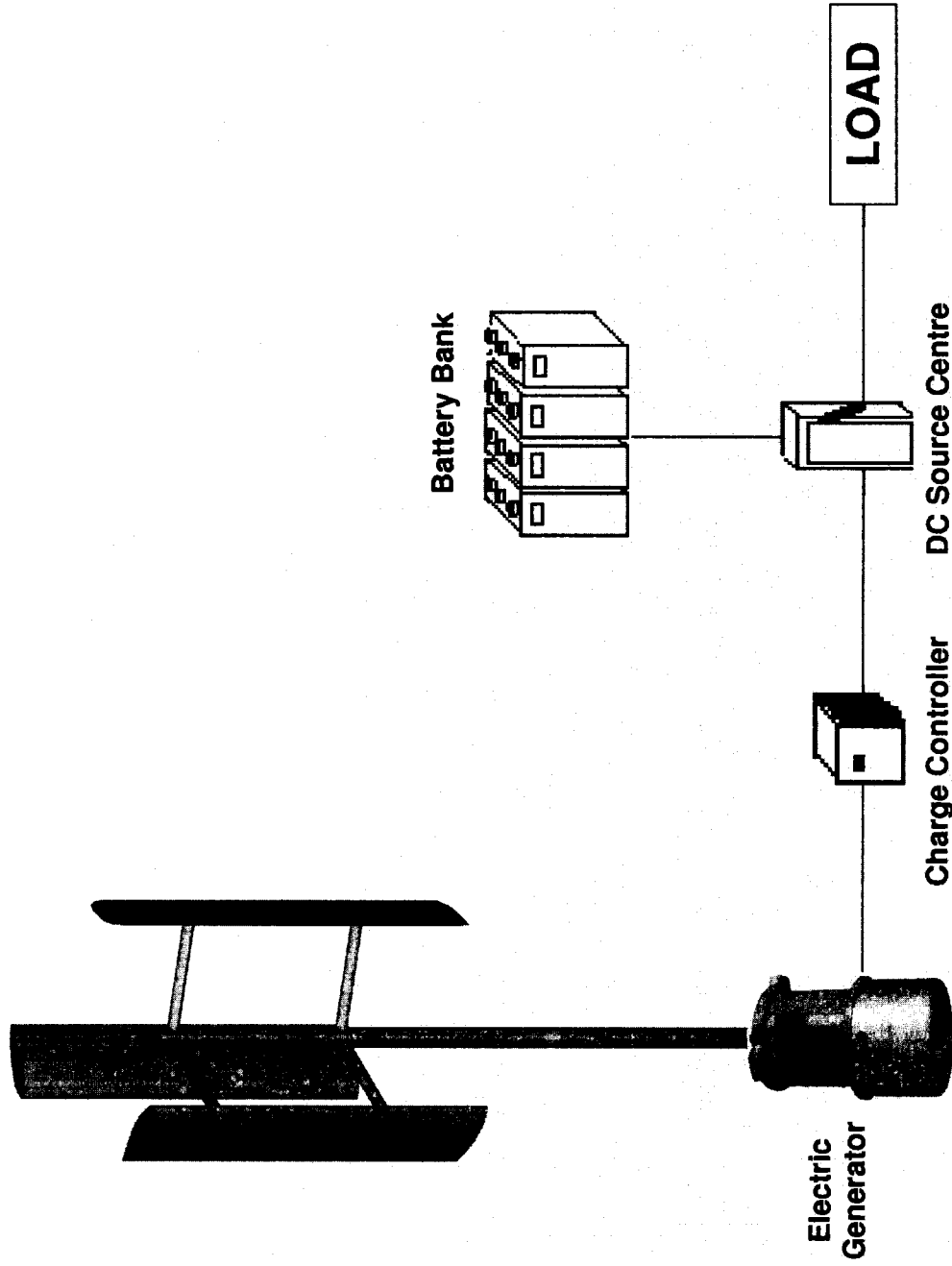


Figure 1.5: Schematic of a Typical SB-VAWT Stand-alone Electric System [Islam et. al 2007a]

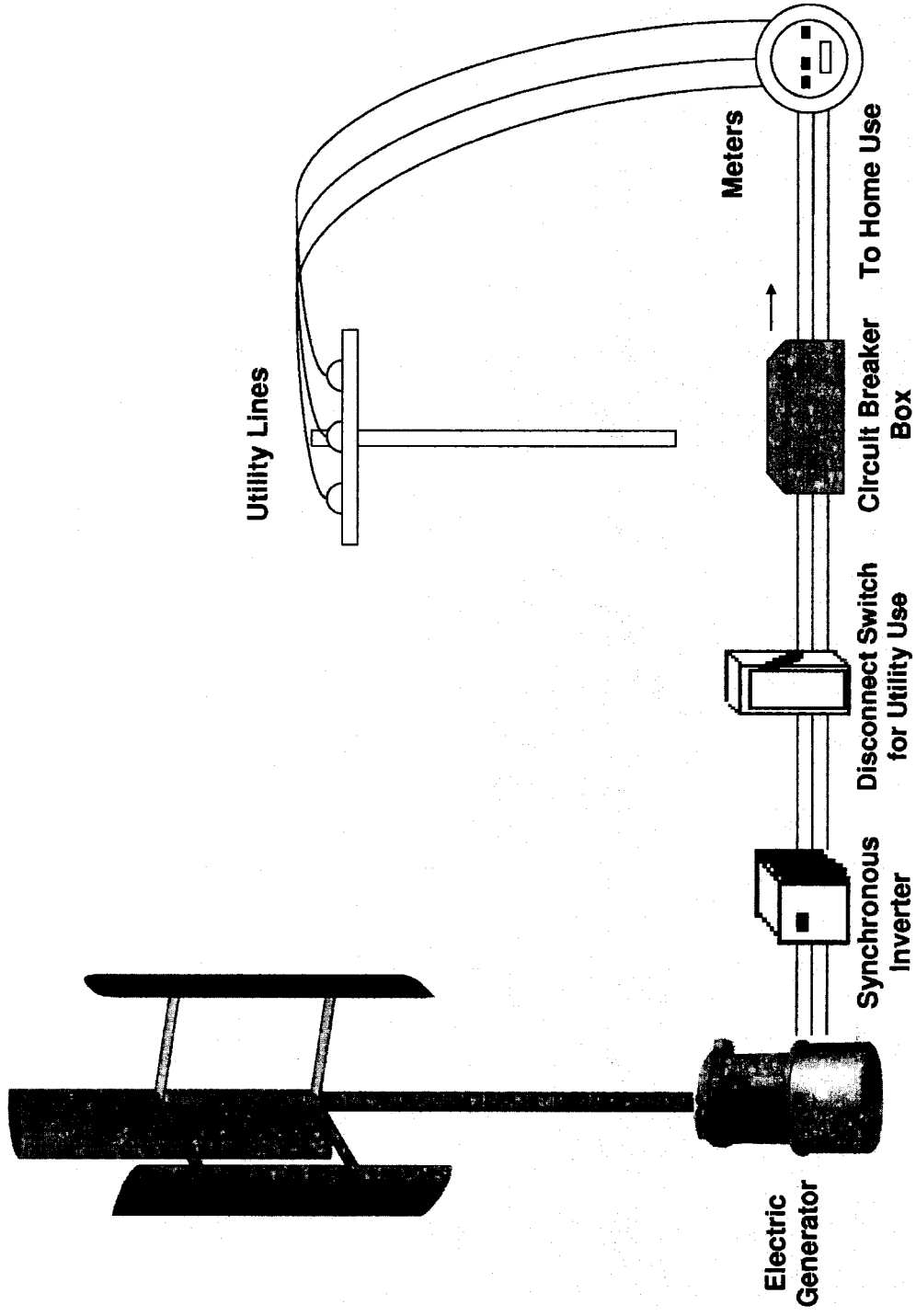


Figure 1.6: Schematic of a Typical SB-VAWT Grid-connect Electric System [Islam et. al 2007a]

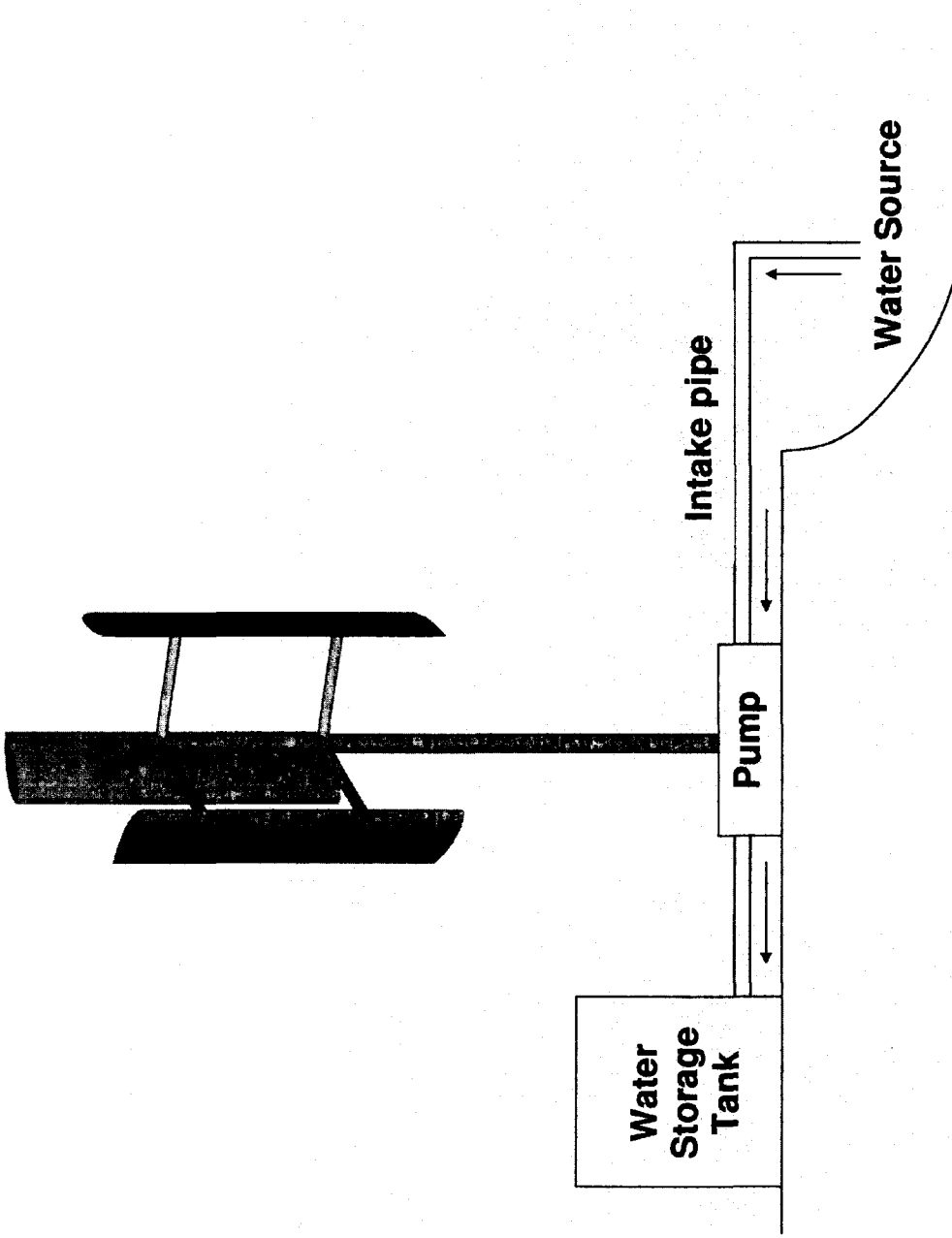


Figure 1.7: Schematic of a Typical SB-VAWT Mechanical Pumping System [Islam et. al 2007a]

As shown in Figure 1.6, “on-grid systems” are connected directly to an external electricity network or grid. In this configuration, a house typically receives its electricity from the SB-VAWT when wind is available, and from the grid whenever supplemental power is required. If arrangement can be made with the utility, the excess electricity can be sold back to the grid under a ‘net metering’ scheme which can significantly improve the cost effectiveness of this type of system.

Mechanical Systems

Figure 1.7 shows a SB-VAWT driven mechanical simple systems where a device (like pump, fan etc.) can be directly coupled with the central shaft to acquire wind energy. This type of systems can be utilized to aerate ponds, pump water for livestock, irrigate or drainage, ventilate air, and to supply water to remote households, farms and small communities. More than a million mechanical systems are said to be in use today, mostly in farms [NRCan 2003]. Several applications of mechanical systems are described in the next section.

1.4.2. Prospective Applications of SB-VAWTs

From the past experiences, it is evident that wind turbines can compete with conventional sources in niche markets (such as off-grid electrification and pumping), and lower costs make them affordable options in increasingly large markets. Cost-effective smaller capacity SB-VAWT can be utilized for an array of applications to provide mechanical, electrical and heat energy. Some of the marketable environmentally benign applications are briefly described under the subsequent headings.

Electrification of Remote Communities

Remote off-grid communities can be found in most of the countries in the world, e.g. there are about 300 remote communities in Canada that are not connected with the electricity grid [You and Leng 2003]. These communities are ideal consumers of sustainable energy sources such as wind. At present, expensive diesel or propane driven gensets are used for supplying electricity and heat in

these locations. In these remote areas, generating electricity with diesel generators can range from \$0.25 to \$1.00 per kilowatt hour [CANRen 2006]. So, in prospective sites, electricity generated by the wind is clearly cost effective.

When compared to the money that is charged by electrical companies, wind energy costs are nearly competitive even without accounting for the environmental and health benefits. Furthermore, the transport of the fuel to the remote areas is costly and labour intensive. Solar Photovoltaic (PV) installations, on the other hand, are reliable, but they provide very little output in the winter in northern countries like Canada. And this can be reduced to zero if they are covered with snow. In this situation, hybrid power plant of wind and solar PV can be opted, along with the possibility of keeping a reduced capacity genset for emergencies. Installations of wind turbines with a vertical axis are particularly suitable for areas with such extreme weather conditions. For this purpose, the turbine should not only produce less noise and be insensitive to wind direction, but also should have the lowest possible maintenance expenditures.

Electrification of Urban Cities (or Built Environment)

Urbanization is a sign of modernization, industrialization and mobility. According to Research Group on the Global Future [2006] - urban population in North America is about 70% and in Europe it is more than 60%. In the future, most of the people in the world will live in urban areas [Research Group on the Global Future 2006]. Due to this process, increasing amount of cleaner energy technologies, like wind energy, are required for the urban population for sustainable human development. Smaller capacity SB-VAWT has a clear niche market in the urban areas due to their low levels of noise and the independence from the wind direction [Hannes 2003].

It is expected that if a cost-effective SB-VAWT is designed, it will make valuable contributions to the renewable component of an urban area's power supply. This new market is potentially enormous. Feeding power directly into the building's

own electrical circuits avoids costs otherwise associated with a separate connection to the local utility electrical distribution network [Blanch 2002]. The economic value of the energy is equal to that otherwise charged by the client's electrical supplier, which is considerably higher than would normally be paid for wind energy supplied directly to the grid. Furthermore, wind energy has a stable cost which is not subject to the same volatility as fossil fuel supplies. In fact, the cost of wind energy production is approximately stable for the entire life of the facility, up to 25 years. Many urban consumers in North America and Europe are choosing wind power for this reason, as insurance against spikes in electricity prices caused by volatility in fossil fuel supply.

Pumping Water

Wind energy was used to pump water long before the discovery of electricity. Many different approaches to wind energy water pumping are still in use around the world today [NRCan 2003]. Historically, the Babylonian emperor Hammurabi used VAWT windmills for an ambitious irrigation project as early as the 17th century BCE [ITDG 2006]. A smaller capacity SB-VAWT can be utilized to drive a rotating or reciprocating pump. It has particular advantage of locating the pump at the ground level which can be directly coupled with the rotating shaft and thus eliminates the need for a gearbox or belt-drive. Furthermore, these turbines can be used to drive a pump indirectly where the turbine generator can provide electricity for a remotely located electricity-driven pump.

Remote Telecommunication

Another niche market for smaller capacity SB-VAWT is remote telecommunication stations or light towers. Supplying an isolated telecommunication station exclusively with a diesel or propane driven genset is very expensive due to very high transportation costs of fuel and recurrent maintenance problems. It has been found with tests of horizontal axis wind turbines that not all these equipment could fulfill the expectations with regard to low maintenance and resilience in extreme conditions [Hannes 2003]. Due to this

fact different companies are searching for especially robust systems that can deal with the difficult conditions of these locations. A Bosnian Telecom company invited tender comprised the energy supply for 7 remote GSM-stations. This lot was won by a smaller capacity SB-VAWT manufacturer with a project for a hybrid system consisting of one VAWT of 3kW rated power and 1 kW of PV-panels [Hannes 2003].

Heating, Ventilation and Air-conditioning

In the future, smaller capacity SB-VAWT can also be deployed for heating and air-conditioning applications. During the winter months, it is possible to use wind energy directly for heating purposes. In this application, instead of arrangement of generator and gearbox, the wind turbine contains a brake that directly warms up water in an insulated tank by whirling [Grauthoff 1991]. The thermal inertia of the system being heated provides energy storage. This system can offer good torque-speed matching and efficient energy conversion [Kirke 1998]. Several heating systems are already in use in Japan for converting wind power for heating greenhouses [Nagai et. al 1986].

Recently, smaller capacity SB-VAWT has also been applied for ventilation purpose. Ove Arup, an Australia-based company, has developed a wind turbine able to rival electricity as a power source for ventilation. The cost of installing their VAWT is similar to that for conventional ventilation. But they have found it less noisy and in some conditions, a building can cool and ventilate itself [Ove Arup & Partners 2003]. Hot air rises in a room and, as it leaves at the top, draws in cool air at the bottom. Their SB-VAWT basically drives a fan for ventilation and have been installed at Africa University on the Mozambique border and at the Mediterranean Shipping company's Zimbabwean headquarters. Arup believes the international market for such devices could easily number thousands per year [ASHRAE Journal 2003].

It is also possible to couple a wind turbine directly with the compressor of a refrigeration unit. From a feasibility study funded by the European Union, it appeared that the application of wind energy driven cooling systems can be economically justified, especially when used as an autonomous system in remote areas [Foellings et. al 1985]. This type of system has prospect for community cold storages in remote islands and coastal areas.

Mechanical Aeration for Ponds, Lakes & Wastewater Treatment Plants

Aeration improves water quality by maintaining good dissolved oxygen levels throughout all of the water, including the bottom. This is very important because once the lake or pond has oxygen near the bottom, new insect larvae, snails, and other fish food can begin to live there. One can accomplish proper aeration through the use of an aerator, creating waterfalls or fountains. Without the use of one of these units, water reservoirs become stagnant and smelly. In areas where there are harsh winters, use of an aerator in addition to a pond de-icer can keep an area of the pond from freezing (particularly for small backyard ponds). This open area allows toxic gases caused from decomposing organic matter, fish wastes, sludge, leaves, etc. to escape from the pond as well as allows an entrance for fresh oxygen.

Among different categories of surface aerators, low-speed vertical axis types are among the more energy-efficient ones [ASCE 1988, Eckenfelder 1989]. So, these vertical axis type surface aerators can directly be coupled with smaller capacity SB-VAWT for the above-mentioned low intensity aeration applications, requiring no gearing or right-angle drives [Kirke 1995]. Such arrangements could have considerable advantages over HAWT or conventional electric motor-powered units in capital, operating and maintenance costs at sites where wind conditions are suitable.

Desalination and Water Purification

Desalination and water purification are also promising applications for smaller capacity SB-VAWT. At present, there are several ways to desalinate brackish or saline water and also to remove other contaminants such as pathogenic bacteria. The traditional desalination method requires heat and/or reduced pressure. In most situations electro dialysis or reverse osmosis is the most economical desalination system [Smith and Swinton 1988, Fell 1985]. Electro dialysis requires electrical current but reverse osmosis requires only a pressure difference, which is provided by pumping. SB-VAWTs can provide energy for each of these methods of desalination and decontamination, but wind-powered reverse osmosis in particular appears to merit further investigation [Kirke 1998].

1.5. Objectives

- Selection of appropriate asymmetric airfoils suitable for fixed-pitch SB-VAWTs for critical computational analysis;
- Achievement of clear insights regarding the aerodynamic parameters affecting the performance of fixed-pitch SB-VAWTs;
- Performance analysis of fixed-pitch SB-VAWTs equipped with asymmetric airfoils using existing appropriate computational models;
- Sensitivity analysis of salient geometric features of prospective low-speed asymmetric airfoils to enhance aerodynamic performance at low speed;
- Investigation of the viability of using asymmetric airfoils for a self-starting fixed-pitch SB-VAWT;
- Design of a cost-effective fixed-pitch SB-VAWT using a prospective asymmetric airfoil with an appropriate blade material and compare its performance with a conventionally used symmetric airfoil; and
- Experimental investigation with a SB-VAWT prototype and analyze its production of torque at low wind speeds.

1.6. Scopes of the Dissertation

In this dissertation, both theoretical and experimental investigations were performed to assess the viability of asymmetric airfoils for better performance and self-starting of fixed-pitch SB-VAWT. The overall scopes of the dissertation can be better understood from Figure 1.8 and they are briefly described below.

In **Chapter 1**, the general introduction about wind energy utilization with special emphasis on SB-VAWT is discussed. The objectives and scopes of the research are also outlined.

Chapter 2 analyzes the aerodynamics of a smaller-capacity fixed-pitch SB-VAWT. Despite uncomplicated components and easy manufacturing processes, the aerodynamics related to SB-VAWTs is complex and needs special considerations during performance and design analysis. Its performance is affected by several aerodynamic factors which are related with the different structural components (like blades, supporting struts, central shaft) and surroundings (like the atmosphere). The main aerodynamic challenges encountered by a smaller-capacity SB-VAWT are determined in this chapter.

In recent time, there has been resurgence of interests regarding SB-VAWTs as several universities and research institutions have carried out extensive research activities and developed numerous designs based on several aerodynamic computational models. These models are crucial for optimum design parameters and also for predicting the performance before fabricating the physical models or prototypes. **Chapter 3** presents review of these existing aerodynamic theories and their extensions. The advantages and disadvantages of the theories are also discussed.

In order to do the performance and design analysis, a computational scheme has been developed using the Cascade Model and XFOIL, a subsonic airfoil design and analysis tool developed at MIT. **Chapter 4** describes different models of the computational scheme which have been utilized to address the main aerodynamic challenges discussed in Chapter 2.

Chapter 5 contains the outcome of the analysis with desirable features of SB-VAWT airfoil for self-starting SB-VAWT with optimum performance. Nine aerodynamic features have been identified which would contribute to self-starting SB-VAWT. After identification of these aerodynamic features, an attempt is made to select the desirable geometric features. Furthermore, six selected airfoils are analyzed through performance analysis using the computational models described in Chapter 4.

In **Chapter 6**, an attempt has been made to shortlist prospective airfoils based on experimental and analytical airfoil characteristics. Nine performance indices have been defined in this chapter in light of desirable aerodynamic characteristics to select best performing airfoil. Then, ten prospective airfoils are analyzed through their performance indices.

Chapter 7 presents the sensitivity analysis of a prospective asymmetric airfoil to enhance its performance (increase in lift coefficient, decrease in drag coefficient, increase in the stall angle, etc) by changing the geometric features (thickness, camber, leading edge radius, trailing edge thickness). This analysis resulted in the design of a special-purpose airfoil named as "MI-VAWT1".

Chapter 8 illustrates detail design analysis of a smaller-capacity SB-VAWT using the MI-VAWT1. The overall dimensions and performance of a fixed-pitch SB-VAWT are obtained from the analysis.

Chapter 9 presents the experimental investigation with a SB-VAWT prototype with both symmetric and asymmetric airfoils. Two different solidities have been explored in the study by changing the number of the blades of the prototype.

Finally in the **Chapter 10**, conclusions and remarks are drawn based on the research outcomes of the preceding chapters. Also, recommendations for the future works are presented in this chapter.

1.7. Significance of the Research

The present research has been undertaken because of the current lack of comprehensive understanding regarding the application of asymmetric airfoils for efficient and self-starting fixed-pitch SB-VAWT. This dissertation is meant to fill this gap as much as possible. Key findings of the research works are published in journals and presented in conferences, seminars and workshops for dissemination purpose.

A computational method (based on available aerodynamic models) has been developed in the present study after identifying and considering the main aerodynamic challenges of SB-VAWT using theoretical coefficients rather than using rarely available expensive experimental results. This scheme conforms reasonably well to the experimental results. This modified scheme can be utilized for performance analysis of SB-VAWT equipped with both symmetric and asymmetric airfoils. This computational scheme has a potential to be utilized for investigating other prospective airfoils in the future for enhanced performance without low RN experimental datasets.

A new special-purpose SB-VAWT blade airfoil, named as MI-VAWT1, has been designed in the present study after considering the desired characteristics.

Another thick airfoil, named MI-STRUT1, has been designed for the shape of blade supporting struts to reduce the detrimental parasitic drag losses. The selection of these two new airfoils are expected to enhance the performance and starting torque production of SB-VAWTs.

After considering 22 design parameters and detailed sensitivity analyses with 5 of these parameters, a new class of 3kW SB-VAWT with alternative light-weight and long-lasting material has been proposed in the present study. It is also expected that the results of this design analyses can be utilized by the designers of fixed-pitch SB-VAWTs to develop cost-effective, efficient and self-starting SB-VAWT which can be utilized in mitigation of environmental insults. It is expected that smaller-capacity SB-VAWT will compete with the conventional sources in niche markets and can be utilized for an array of applications, including (i) electricity generation; (ii) pumping water; (iii) purifying and/or desalinating water by reverse osmosis; (iv) heating and cooling using vapor compression heat pumps; (v) mixing and aerating water bodies; and (vi) heating water by fluid turbulence.

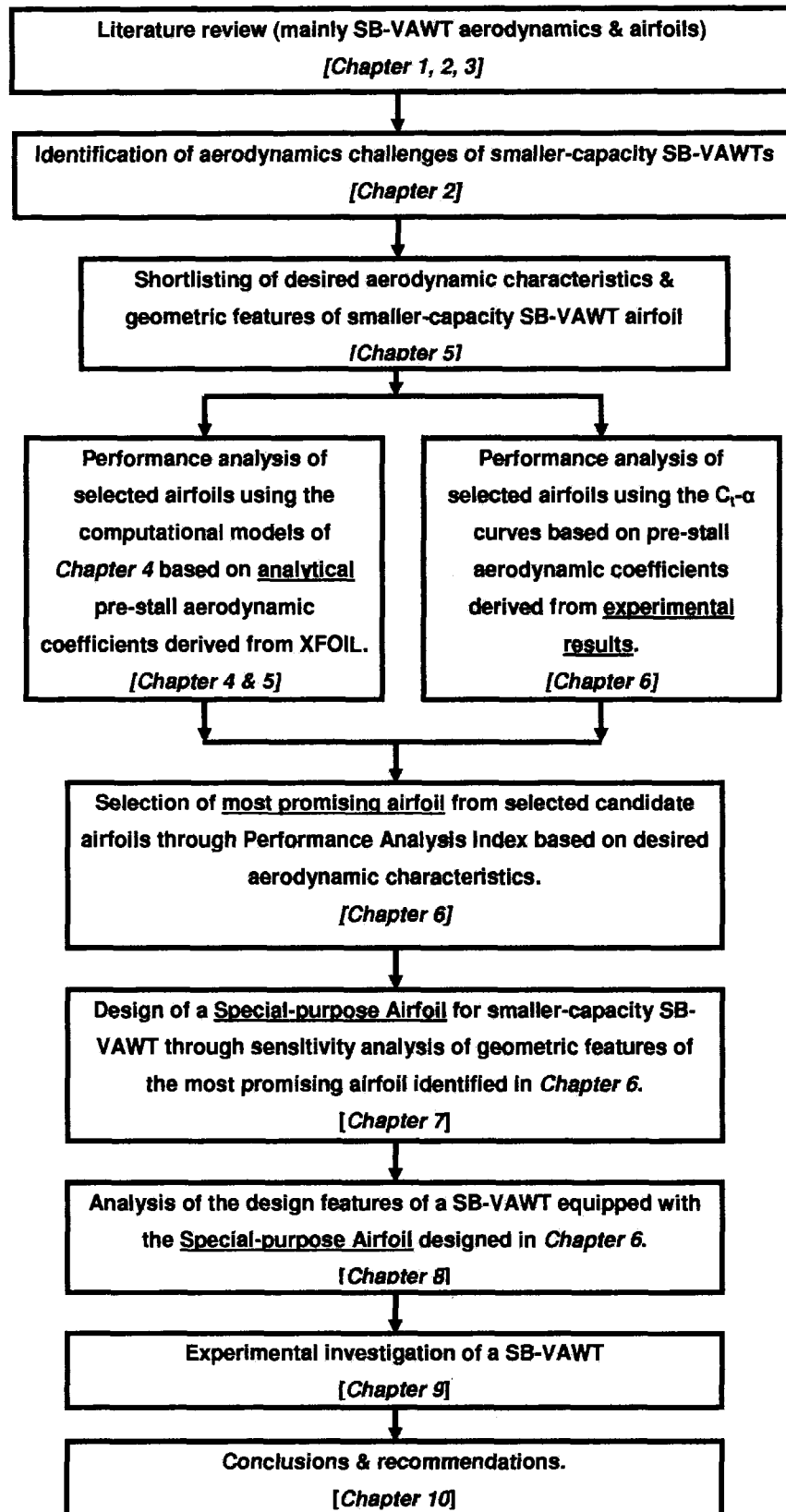


Figure 1.8: Scopes of Different Chapters of the Dissertation

Chapter 2

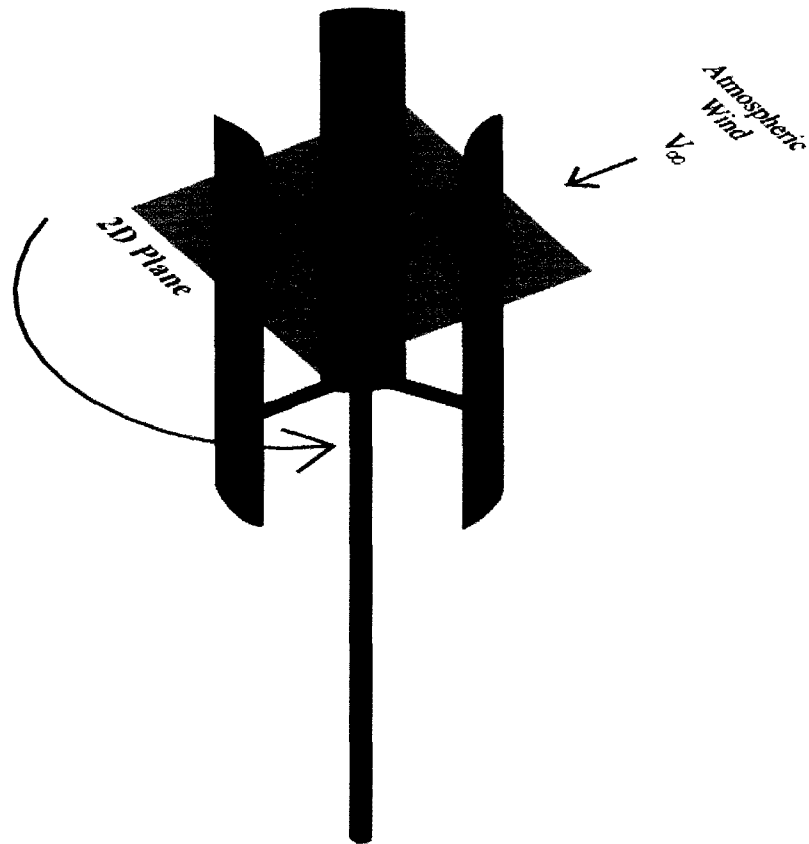
Aerodynamic Challenges of Smaller-capacity Fixed-pitch SB-VAWTs

Smaller-capacity fixed-pitch SB-VAWT has the simplest structural features. However, its rotor's aerodynamics is very complex. In this section, seven major aerodynamic factors are analyzed before developing a computation scheme for aerodynamic performance analyses of fixed-pitch SB-VAWT.

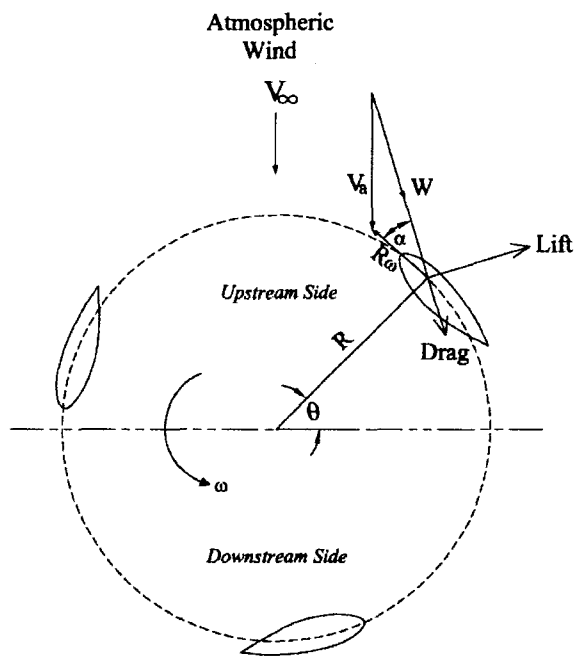
2.1. Aerodynamics of SB-VAWTs

The smaller-capacity fixed-pitch SB-VAWT is a lift force driven wind turbine consisting of two or more airfoil shaped blades which are attached to a rotating vertical shaft as shown in Figure 2.1. The wind blowing over the airfoil contours of the blade creates aerodynamic lift and pulls the blades along.

In Figure 2.1, a SB-VAWT blade's circular path is shown with both the 3D and 2D representations. As this blade rotates, it experiences a varying relative flow velocity (W), which is the vector sum of the local induced wind speed and the blade speed. The lift force generated by the blade has a tangential component in the direction of rotation. If the contribution of the drag force is smaller than that of the lift force, the blade contributes positive torque which drives a load connected with the central rotating shaft. The orbital position of the blade is called azimuth (θ) and both relative flow velocity and the local angle of attack (α) vary with θ .



(a) 3D Model



(b) 2D Plan View

Figure 2.1: Flow Velocities around SB-VAWT [Islam et. al 2007b]

The amplitude of this variation is related to a non-dimensional parameter known as tip speed ratio (λ). The variation of α with θ at different λ is shown in Figure 2.2 for a SB-VAWT with NACA 0015. It can be seen from this figure that α changes through positive and negative values in each revolution of the blade at different λ and as the turbine speed increases, more energy is extracted and the flow is decelerated.

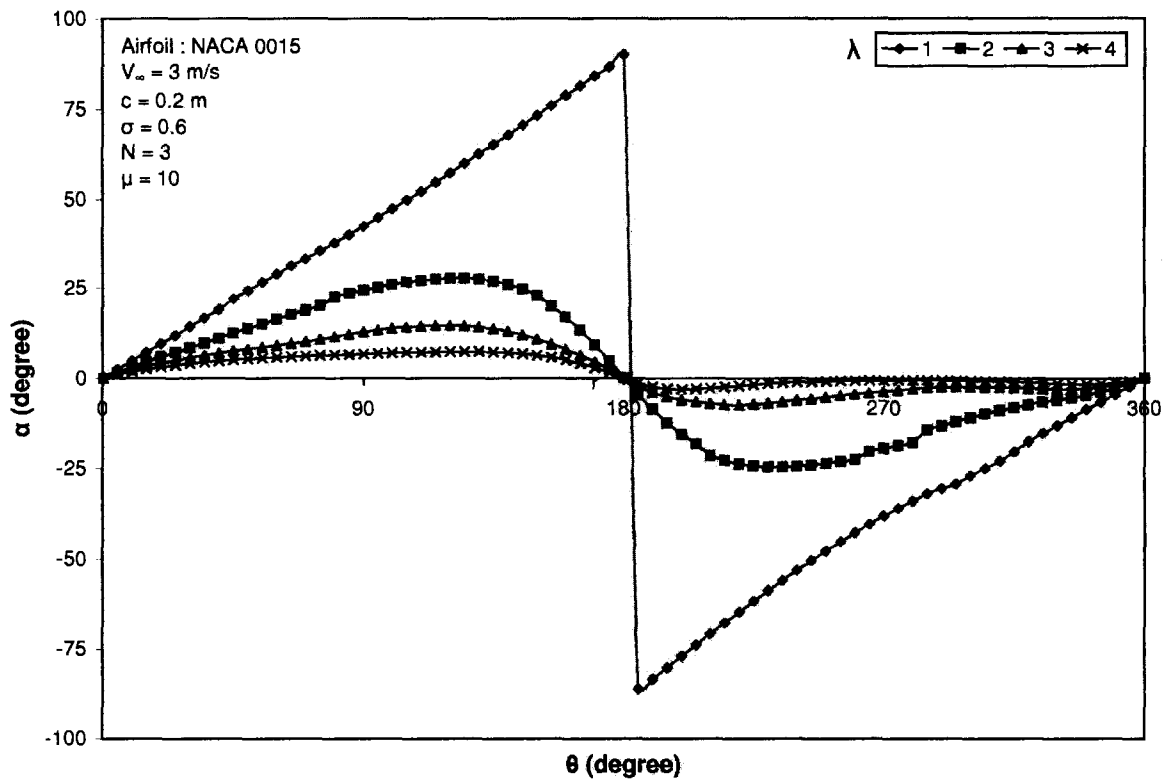


Figure 2.2: Variation of Angle of Attack with Azimuthal Position at Different Tip Speed Ratios of a SB-VAWT

2.2. Self-starting Problem of SB-VAWTs

It is commonly believed that small-capacity SB-VAWTs are inherently unable to self-start properly. This notion is true for older designs which were constructed by utilizing old symmetric NACA airfoils. According to Watson [1979], the inability of Darrieus type VAWTs to self-start is due to a band of tip speed ratios below

operating condition for which the net amount of energy collected by each blade in each revolution is negative. To achieve self-starting, SB-VAWT must be altered so that a net positive amount of torque is produced at all tip speed ratios up to the operating point. As shown in Figure 2.2, at low values of λ , the blades of SB-VAWT encounter a wide range of α and thus fluctuate between stalled and unstalled conditions. At low λ , the blade is stalled at almost all azimuth angles. As a result, most fixed-pitch SB-VAWT do not reliably self-start and it is only at higher values of λ , above about 3, that the blades remain unstalled and the turbine can achieve high efficiency [Kirke 1998].

The inability of SB-VAWTs to self-start can be better understood from Figures 2.3 and 2.4, which illustrate the power (C_P) and torque (C_Q) coefficients of a 1kW SB-VAWT at 3m/s. The cascade model, proposed by Hirsch and Mandal [1987] was utilized for producing these curves. The original source of the aerodynamic characteristics of the airfoil used here is Sheldahl and Klimas [1981] which has been synthesised from a combination of experimental results and computer calculations by Lazauskas [Cyberiad 2007] for eliminating data anomalies. Both of these curves depict negative C_P and C_Q values at low tip speed ratios.

These negative regions were described by Baker [1983] as the “dead band” which is an undesirable phenomenon. A turbine with this kind of C_P - λ characteristic may just start but will not generally accelerate through the dead band to its optimum working speed unless the wind speed happens to drop suddenly in such a way that λ jumps from a value below the dead band to a value above it, and then increases gradually so the turbine can accelerate up to working speeds [Kirke 1998]. Kentfield [1996], who developed a form of self-starting variable-pitch VAWT, stated that – “*The Darrieus turbine is inherently non self-starting*” after realizing this undesirable feature of SB-VAWT.

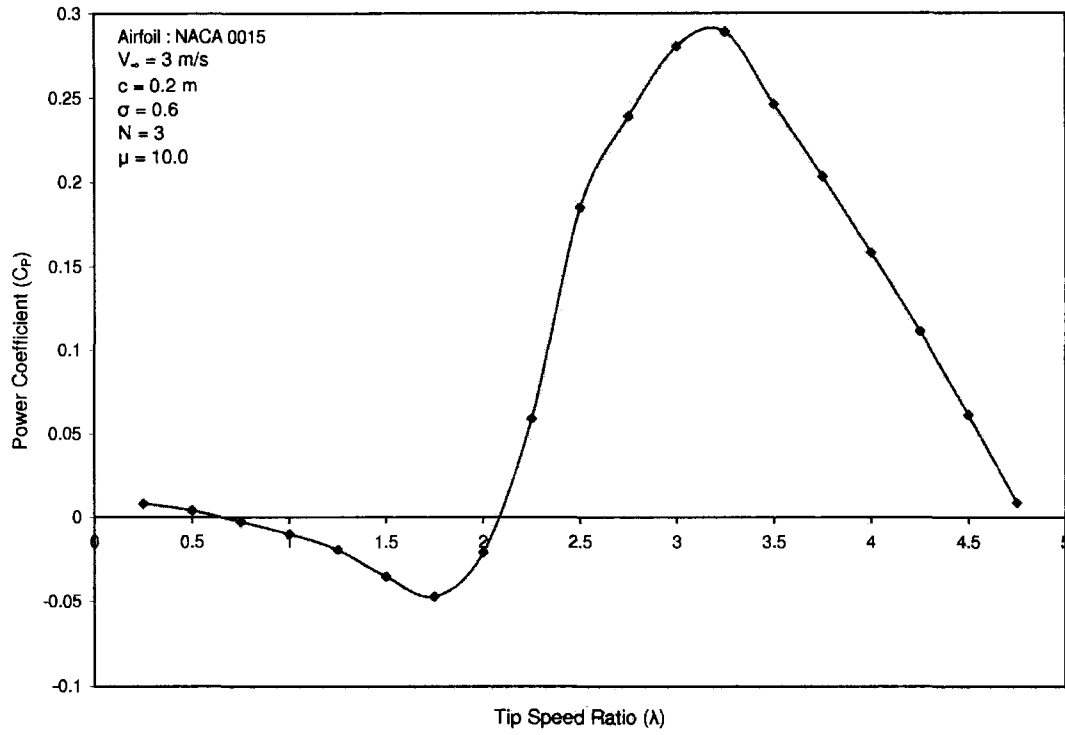


Figure-2.3: C_p - λ Curves of SB-VAWT with NACA 0015 Airfoil

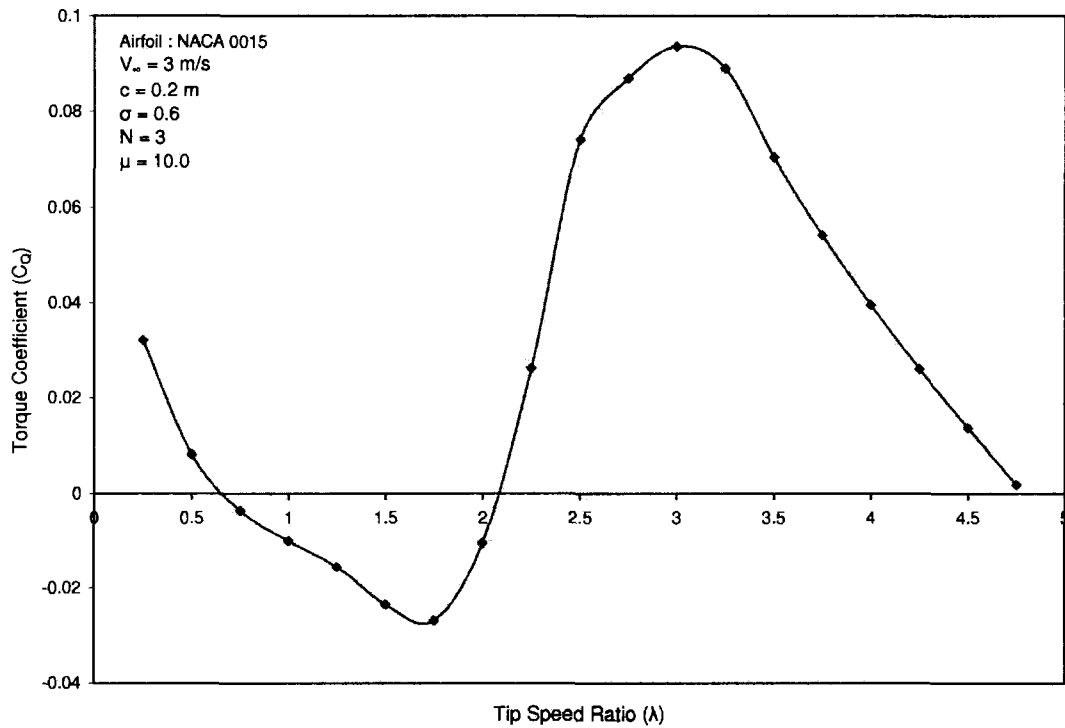


Figure 2.4: C_q - λ Curves of SB-VAWT with NACA 0015 Airfoil

The problem of self-starting can be alleviated by (i) using high-lift low-drag special-purpose airfoil; and (ii) by incorporating a Savonius rotor or torque tube [Islam et. al 2007c]. Self-starting problems can be overcome electrically if the SB-VAWT is coupled with a synchronous alternator or a DC generator which can function as a motor and can be used to drive the turbine up to operating speed. Although motor starting is common in grid-connected wind turbines and could be done with smaller-capacity wind turbines, it is not a common practice.

A detailed investigation of self-starting features of SB-VAWT was performed by Kirke [1998]. Using the assembled airfoil data, both experimental and estimated, he used a double multiple streamtube theory based mathematical model to predict the performance of both fixed and variable-pitch VAWTs. He investigated the performance of fixed-pitch VAWTs with cambered blades using newly developed profiles that exhibit superior characteristics at low Reynolds numbers and his results indicate that fixed-pitch VAWTs using these blade sections should self-start reliably [Kirke 1998].

2.3. Major Aerodynamic Challenges

Though SB-VAWT has very simple structural features, its rotor's aerodynamics is very complex. Its performance is affected by several aerodynamic factors which are related with the different structural components (like blades, supporting arms, central shaft) and surroundings (like the atmosphere) as shown in Figure 2.5. The seven main aerodynamic challenges encountered by a smaller-capacity SB-VAWTs are identified in this research after rigorous analysis and literature survey, which are: (i) low RN operation; (ii) post-stall operation; (iii) unsteady effects; (iv) rotational effects; (v) operation of the blades in the wake region; (vi) parasitic drag losses due to the supporting struts; and (vii) atmospheric turbulence. These challenges are discussed in the subsequent sections.

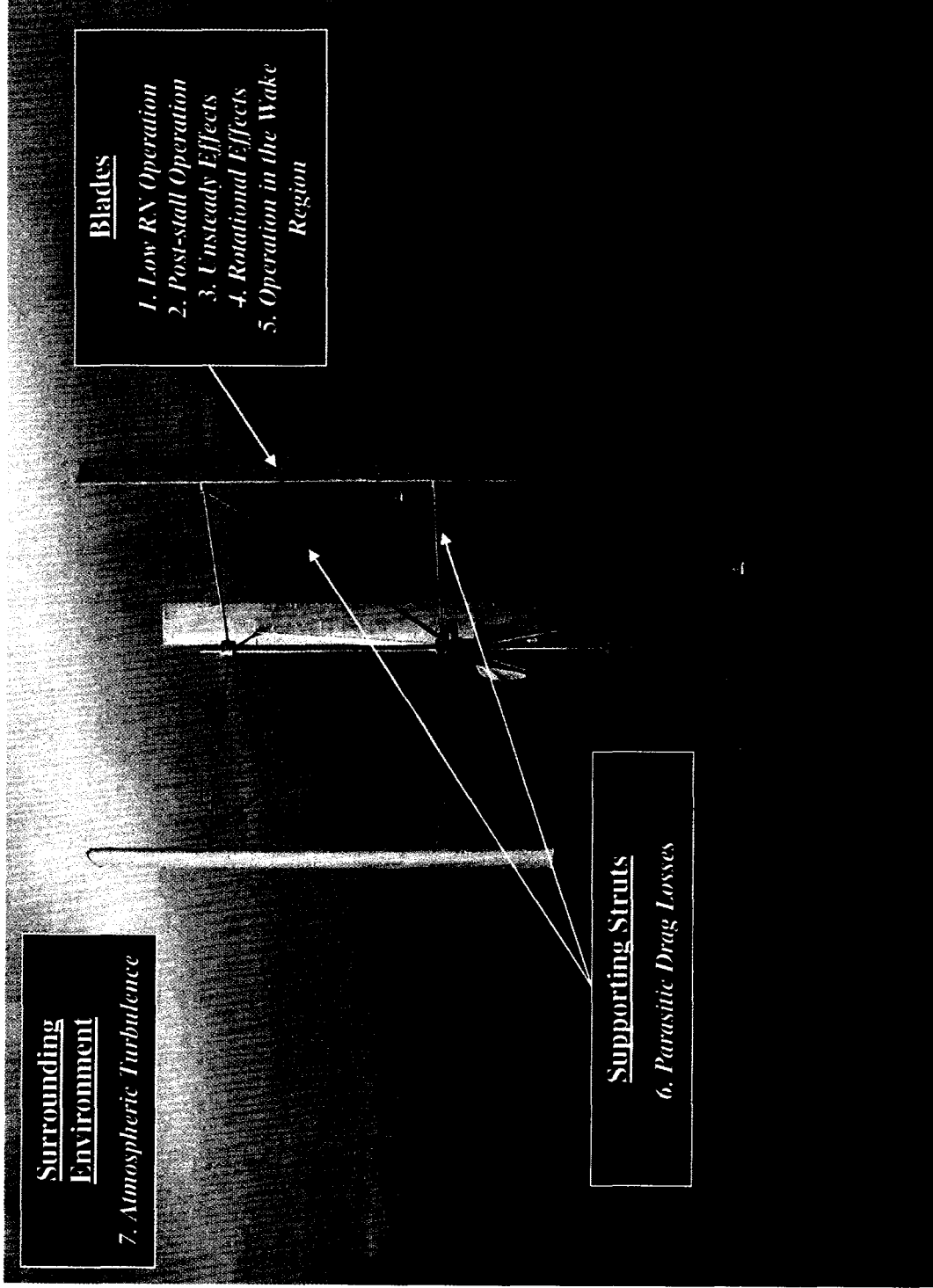


Figure 2.5: Structural Components of A Typical SB-VAWT and Their Associated Aerodynamic Challenges

2.3.1. Low Reynolds Number (RN) Operation

The small-scale VAWTs are usually designed to operate in a wind speed range of 4 to 15 m/s. The chord length of the blades for small-sized wind turbines are usually around 0.2 to 0.3 m. As a result, considering the chord length as characteristic length, the operating Reynolds number ($\rho V_\infty c / \mu$) of interest is restricted between 100,000 to 500,000, which is considered as Low RN [Sahin 2004]. In this range of RN, very complex flow phenomena take place within a short distance on the upper surface of the blade [Hak 1990]. At lower Reynolds numbers the viscous effects are relatively large, causing high drags and limiting the maximum lift, while at the higher values the lift-to-drag ratio improves [Lissaman 1983]. There is a critical Reynolds number of about 70,000 at which this performance transition takes place which can be seen most vividly in Figure 2.6.

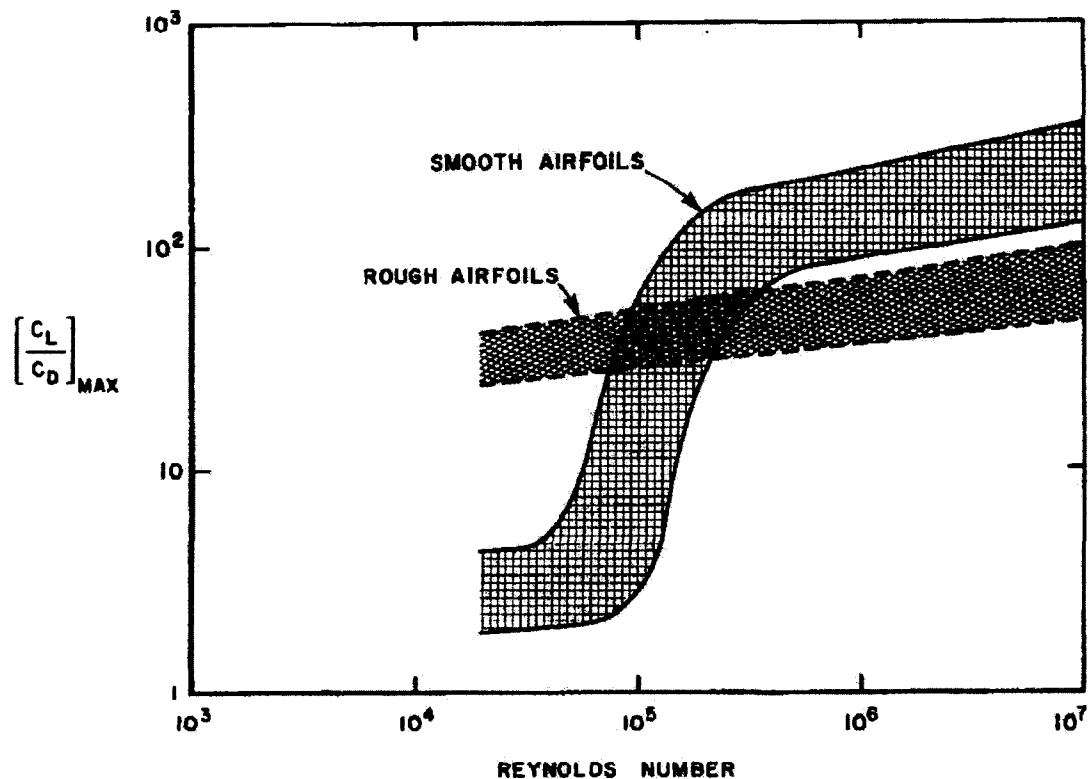


Figure 2.6: Low-Reynolds Number Airfoil Performance [Reprinted, with permission, from the Annual Review of Fluid Mechanics, Volume 15 © 1983 by Annual Reviews.

www.annualreviews.org

A laminar separation bubble commonly forms in the low RN range, which plays an important role in determining the boundary layer behavior and the stalling characteristics of the blade [Hak 1990 and Tani 1964]. Figure 2.7 shows the general geometric structure of a laminar bubble. After laminar separation, the flow proceeds at an approximately constant separation angle and the processes of transition occur. As turbulence develops, the increased entrainment causes reattachment. After reattachment, the turbulent boundary layer reorganizes itself to form an approximately normal turbulent profile [Lissaman 1983]. It is this behavior of short- and long-bubble formation, and bursting with angle of attack and Reynolds number, that causes such striking differences in performance of various airfoil shapes [Lissaman 1983]. Figure 2.8 illustrates the effect of the laminar bubble on lift-drag polar on two different airfoils at a Reynolds number of 50,000. This figure shows the detrimental effect of the laminar bubble on lift-drag ratio of two typical airfoils.

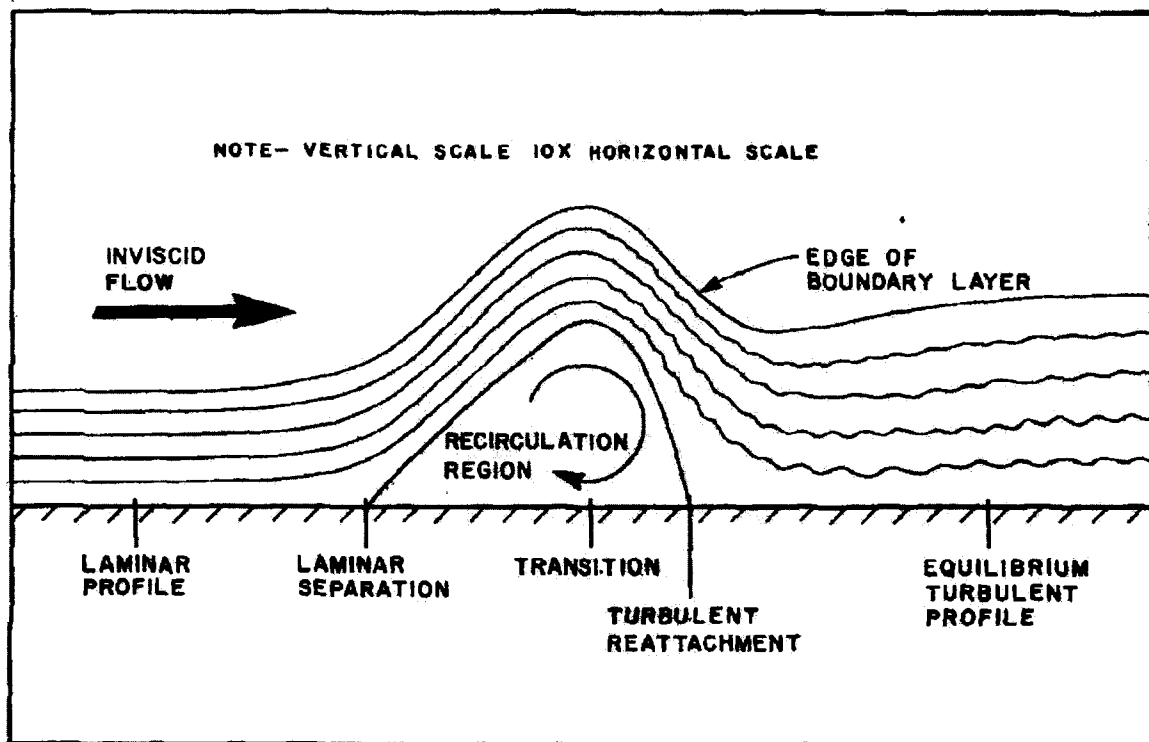


Figure 2.7: Structure of Laminar Separation Bubble [Reprinted, with permission, from the Annual Review of Fluid Mechanics, Volume 15 © 1983 by Annual Reviews.

www.annualreviews.org

The low RN affects mainly the boundary layer and hence skin friction drag and, through influence of the separation, the stall and the maximum lift coefficient [Jesch and Walton 1980]. An airfoil with $RN < 50,000$ will experience laminar separation with no subsequent reattachment [Carmicheal 1981]. As the RN increases and approaches 200,000, it becomes more likely that the laminar separation bubble can be avoided [Lissaman 1983]. Since boundary layer transition and separation of blades are also affected by surface roughness, there is a complicated interaction between the boundary layer and outside airstream. Generally, as chord size increases, or as air velocity is increased, airfoil characteristics improve [Jesch and Walton 1980].

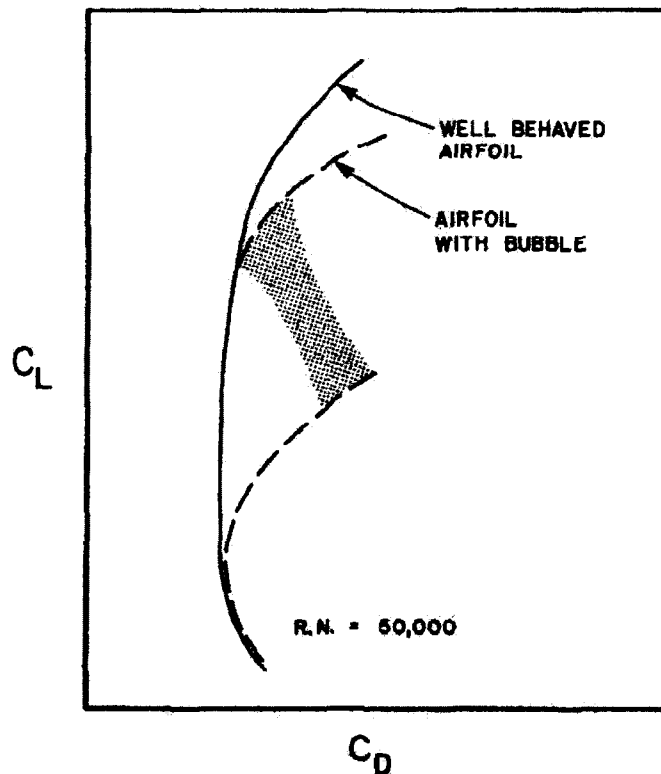


Figure 2.8: Effect of Laminar Bubble on Lift-Drage Polar [Reprinted, with permission, from the Annual Review of Fluid Mechanics, Volume 15 © 1983 by Annual Reviews.

www.annualreviews.org

For a small fixed-pitch VAWT to self-start it is necessary that the airfoil produces at least moderately high lift and low drag at RN between about 80,000 and 150,000 [Kirke 1998]. The symmetrical sections usually used on VAWTs perform poorly in this RN range and do not achieve self-starting [Kirke 1998]. Figure 2.9 shows the variation of tangential force coefficient (C_t), which generates useful torque, with angle of attack at three different RNs . It is clear from this figure that the maximum value of C_t increases with RN .

2.3.2. Post-stall Operation of the Blades

In Figure 2.1, a SB-VAWT blade's circular path is shown with both the 3D and 2D representations. It has been stated earlier that as the blades of SB-VAWT rotate, they face different relative flow velocity (W). When the turbine starts and as the rotational speed increases, the blades even experience back flow [Claessens 2006]. In this situation, the effective angle of attack can be above the stall angle and thus the air flow detaches (or separates) from the upper side (known as the suction side) of the blade [Hoerner and Borst 1985].

The variation of α with θ at different λ has already been shown in Figure 2.2 which depicts that at low values of λ , the blade of SB-VAWT encounters a wide range of α and thus fluctuates between stalled and unstalled conditions. The behavior of lift and drag coefficients in the post-stall regimes has serious consequence for fixed-pitch SB-VAWT which can be observed at Figure 2.9 where the variation of tangential force coefficient is shown. It can be seen from this figure that at a range of angles of attack, C_t becomes negative. This is one of the main reasons for low or negative starting torque at low tip speed ratios where the blades are stalled at almost all the azimuth angles.

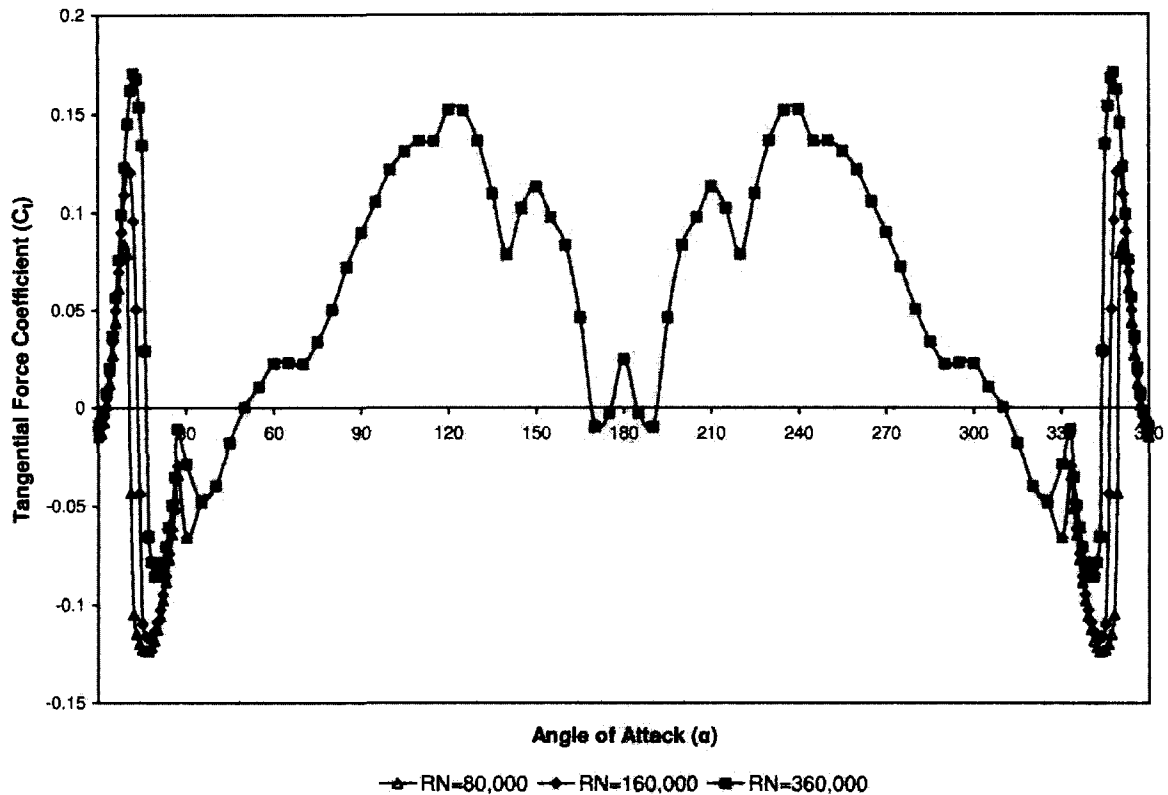


Figure 2.9: Variation of C_T - α Curves at Different Reynolds Number

2.3.3. Unsteady Effects

In real life situation, the flow over streamlined lifting surfaces always encounters unsteady effects which have often been ignored. Studies of unsteady airfoil flows have been motivated mostly by efforts to avoid or reduce such undesirable effects like dynamic stall, vibrations, gust response etc [McCroskey 1982]. This requires predicting the magnitude and phase (or time lag) of the unsteady fluid-dynamic loads on thin lifting surfaces. Some attention has also been given to potentially beneficial effects of unsteadiness, such as the propulsive efficiency of flapping motion, controlled periodic vortex generation, and stall delay, and to improving the performance of turbomachinery, helicopter rotors, and wind turbines by controlling the unsteady forces in some optimum way.

Among all the unsteady effects, the most important one which is related to VAWT is the dynamic stall effect which is briefly discussed in this section. The parameters affecting the dynamic behavior of an airfoil under periodic variations of inflow conditions are: amplitude of the oscillation, mean angle of attack, reduced frequency, Reynolds and Mach numbers, airfoil shape (thickness, leading edge radius, etc.), surface roughness, and free stream turbulence [Aerodyn 2005]. If the oscillation due to dynamic stall occurs around a mean angle of attack close to $C_{l,max}$ (static stall) the viscous effect become predominant. Figure 2.10 shows an example of lift, drag and pitching moment hysteresis curves for an airfoil oscillating around $C_{l,max}$.

In the case of Darrieus type SB-VAWT the local angle of attack changes continuously with time during its operation. When the angle of attack of VAWT remains constant or varies slowly with time, it encounters the static stall. But when the angle of attack changes rapidly with time, it experiences the dynamic stall. Dynamic stall is more difficult to analyze and predict than static stall due to its dependence on a much larger number of parameters including airfoil shape, amplitude and oscillation frequency of angle of attack, type of motion, turbulence level and three-dimensional effects. On the other hand, static stall depends almost exclusively on the angle of attack and the RN [Allet et. al 1997].

Dynamic stall prediction methods used by the helicopter, turbomachinery, aircraft and wind turbine industries are largely based on empirical or semi-empirical approaches [Ham and Garelick 1968, Ekaterinaris and Platzer 1997]. Presence of the dynamic stall has been observed by Laneville and Vittecoq [1986] when they measured the unsteady fluid forces acting on the rotating blade in a wind tunnel. Recently, Fujisawa and Shibuya [2001] has also studied this phenomenon in the flow field around a Darrieus wind turbine blade through flow visualization and particle image velocimetry (PIV) measurement in stationary and rotating frames of reference.

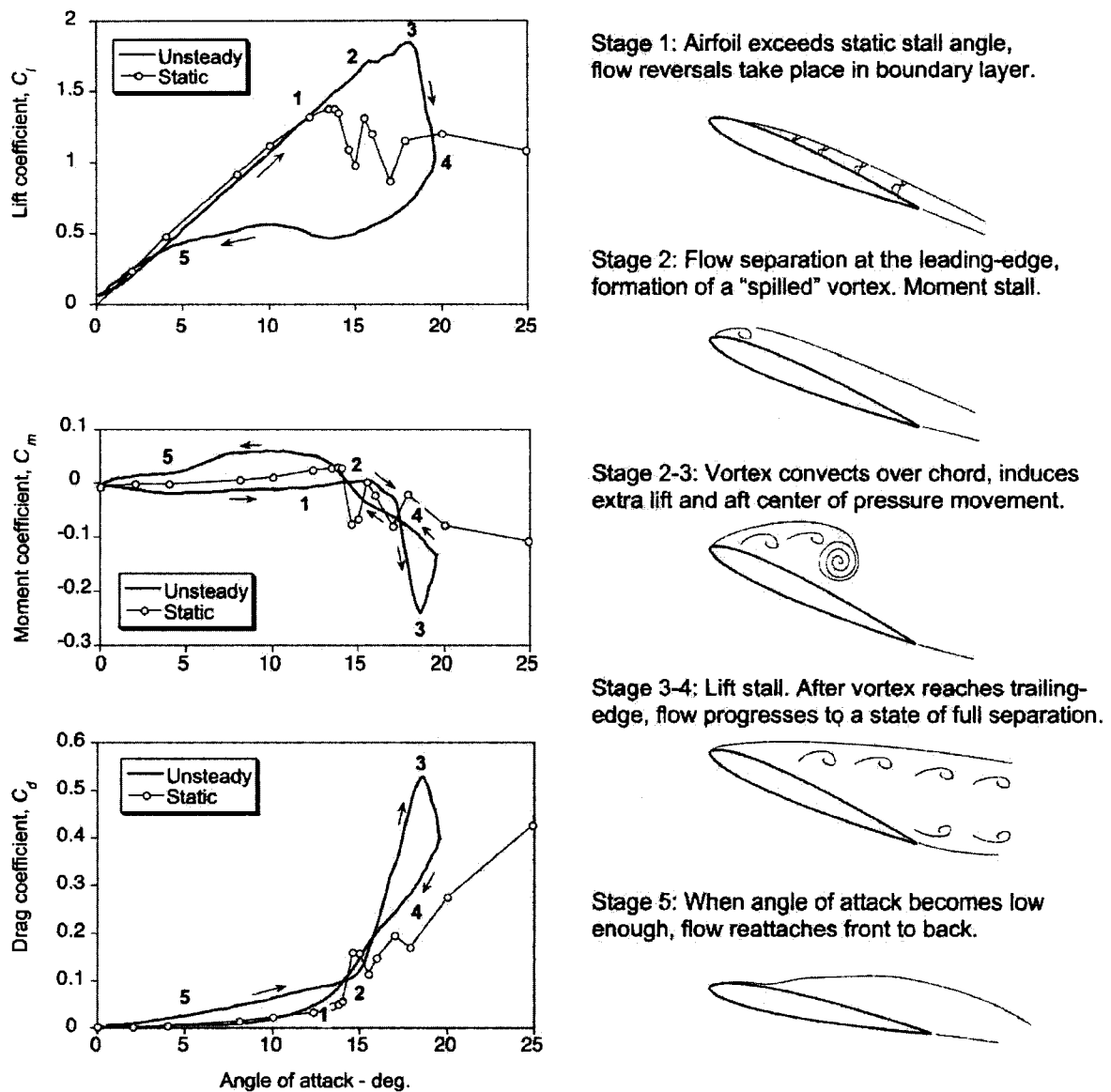


Figure 2.10: Schematic Showing Unsteady Airloads and Flow Physics for a Two-Dimensional Airfoil Undergoing Dynamic Stall [Reproduced, with permission, from Leishman 2002]

The main feature of dynamic stall, when compared with static stall, is the shedding of a distinct vortex on the upper side of the airfoil that detaches from the leading-edge region and convects downstream over the surface. The

convection of this vortex produces a rearward motion of the centre of pressure and a corresponding negative peak in pitching moment about the quarter chord [Pawsey 2002]. When this dynamic stall vortex moves through the trailing edge of the airfoil, lift force drops sharply and the flow becomes full separated. When α returns to lower values, reattachment of the flow may be delayed to a significantly lower values of α than that at which separation occurred. A schematic showing these characteristics of unsteady airloads and flow physics for a two-dimensional airfoil undergoing dynamic stall is shown in Figure 2.10 which has been reproduced from Leishman [2002].

Computational & Experimental Investigations of Dynamic Stall Effect

Figures 2.11 and 2.12 depict the comparison of experimental results of non-dimensional tangential and normal forces [Vittecoq and Laneville 1983] with that of computational analyses carried out in this research. In the present work the cascade model with Boeing-Vertol dynamic stall model [Mandal and Burton 1994] has been used to obtain the computational results shown in these figures. The aerodynamic characteristics of the NACA 0018 airfoil have been taken from Cyberiad [2007].

It can be seen from Figures 2.11 and 2.12 that the cascade model with dynamic stall effects gives reasonable correlation with the experimental datasets, especially in regard to the peak values. It can be concluded from this analysis that there are substantial differences between the characteristics of the static and dynamic stalls. Aerodynamic forces due to dynamic stall may be much higher than those due to static stall. As a result, for the performance prediction of Darrieus turbines, especially for the local forces, there can be substantial differences between the experimental data and the calculated values unless the dynamic stalling effect is added.

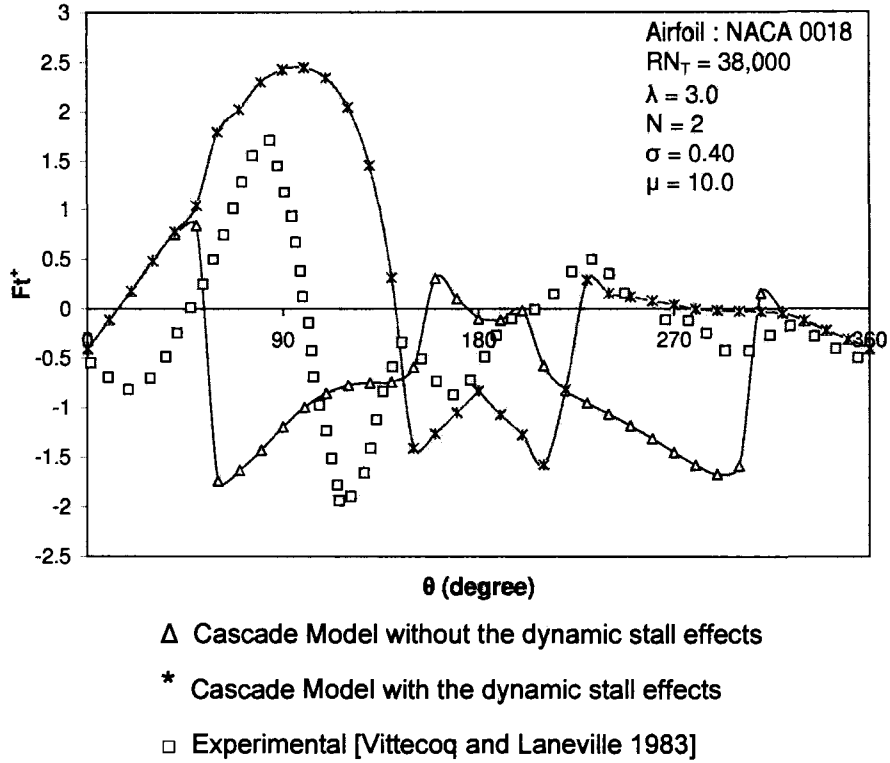


Figure 2.11: Comparison of Experimental and Computational Non-dimensional Tangential Forces

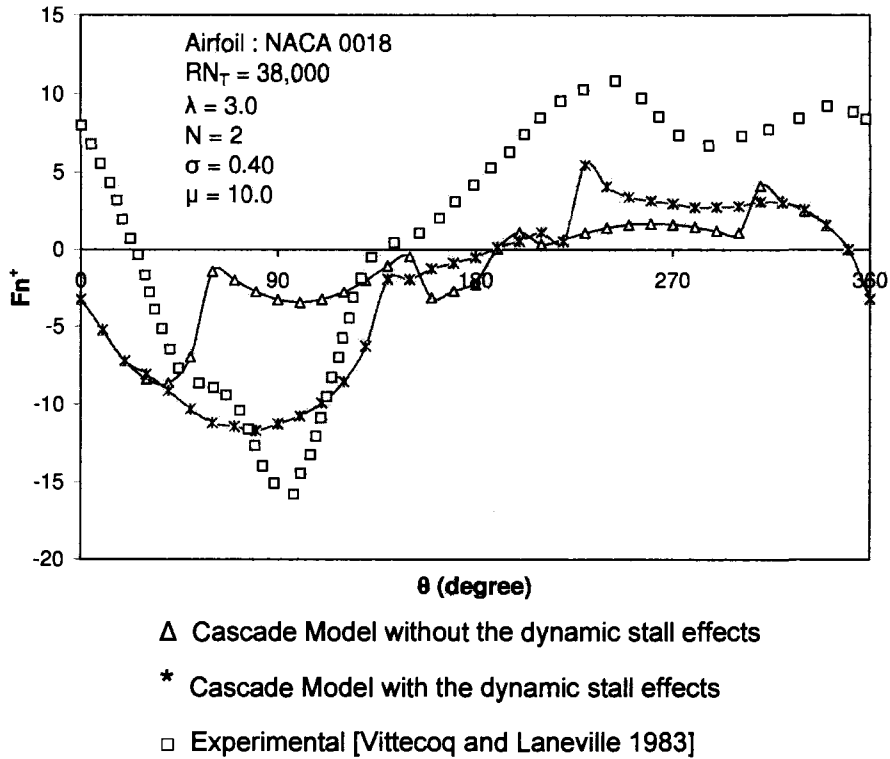


Figure 2.12: Comparison of Experimental and Computational Non-dimensional Normal Forces

2.3.4. Rotational Effects

When the VAWT blade rotates in a circular path, the direction of rotational velocity varies continuously along the chord, making the flow over the blade airfoil that of a curvilinear nature. It can be seen from Figure 2.13 that the relative velocity W and the angle of incidence are not constant along the chord-wise direction, which cause the phenomenon of flow curvature effect. It can have significant influence on the lift-drag characteristics of the blade airfoil of VAWT.

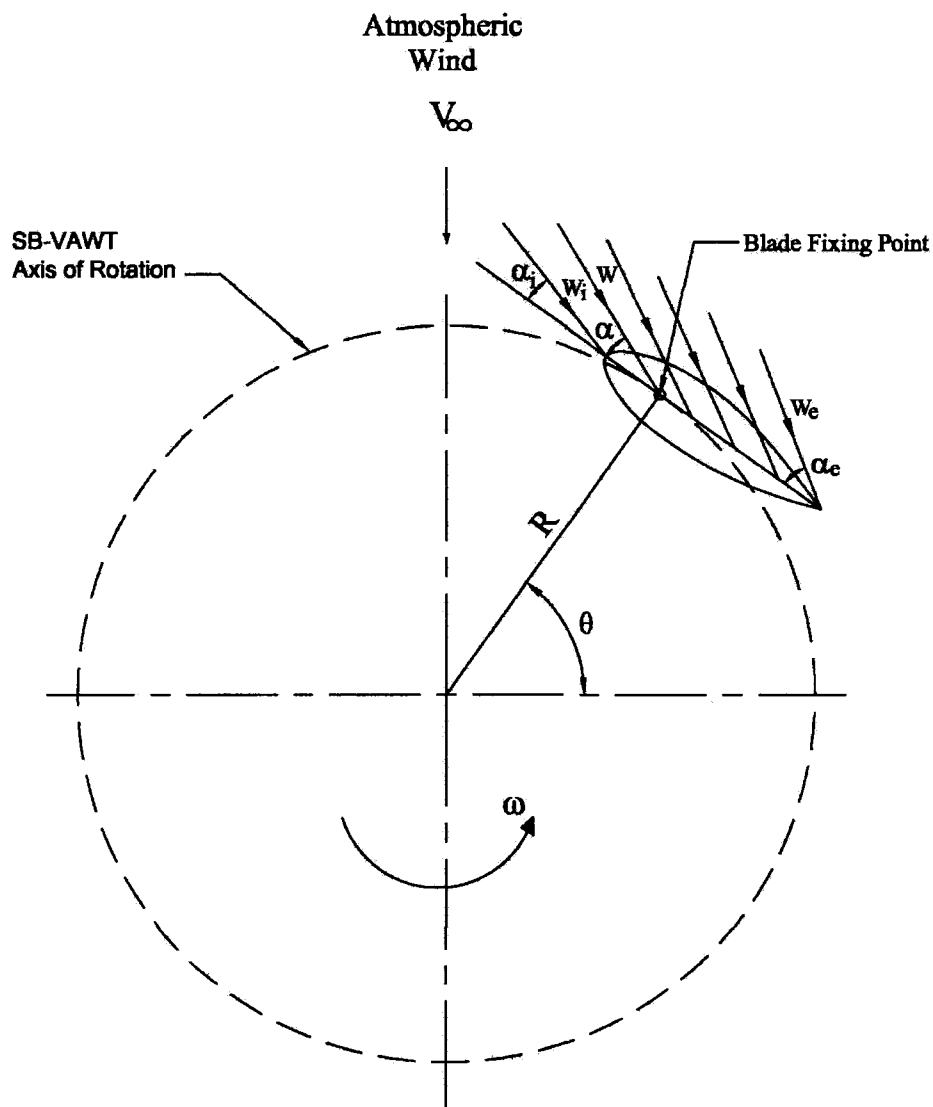


Figure 2.13: Typical Variation of Relative Velocity and Angle of Attack along Chordwise Direction

Migliore et. al [1980] performed an elaborate study of the flow curvature effect on the performance characteristics of a SB-VAWT. In their method, they considered the curved flow consisting of concentric streamlines pattern on the turbine blade airfoils (geometric airfoils). As shown in Figure 2.14, by conformal mapping techniques the geometric airfoil is transformed into a virtual airfoil with change in camber and incidence angle appearing in the rectilinear flow. They observed strong influence of the flow curvature on the performance characteristics of a Darrieus wind turbine, especially when the chord-radius ratio is high as shown in Figure 2.15.

Migliore et. al [1980] also noted that under most circumstances the flow curvature effect has a detrimental influence on the blade aerodynamic efficiency. However, they suggested that consideration of airfoils whose virtual equivalents really are cambered would enhance the turbine performance. They have also found that the virtual camber and virtual incidence due to flow curvature varies with blade orbital position or azimuthal angle as shown in Figure 2.16.

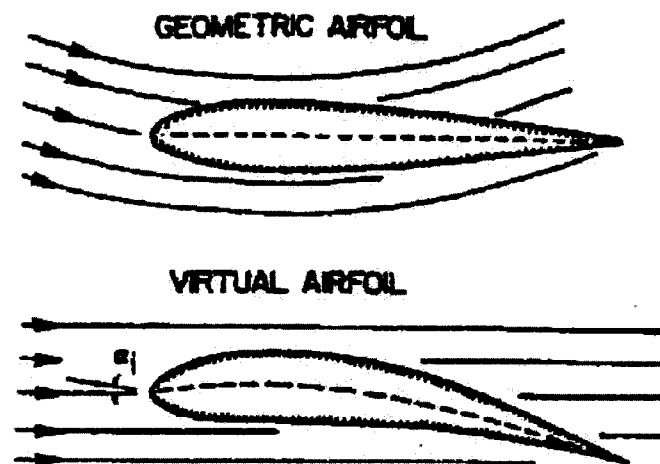


Figure 2.14: Qualitative Illustration of Conformal Transformation [Reproduced, with permission, from Migliore et. al 1980]

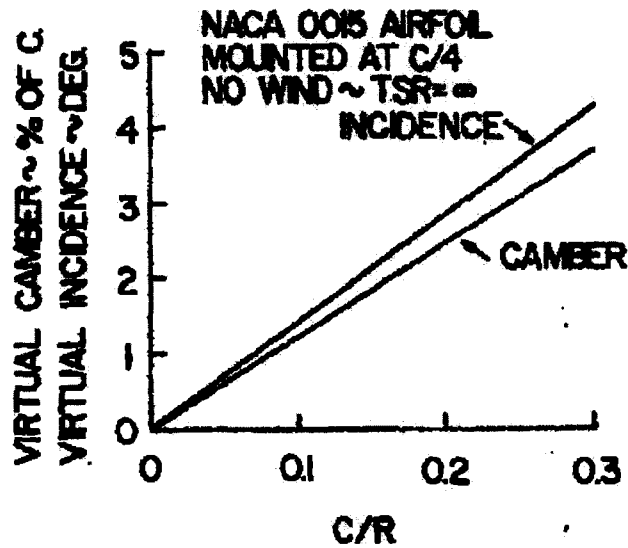


Figure 2.15: Mean Values of Camber and Incidence at Different C/R [Reproduced, with permission, from Migliore et. al 1980]

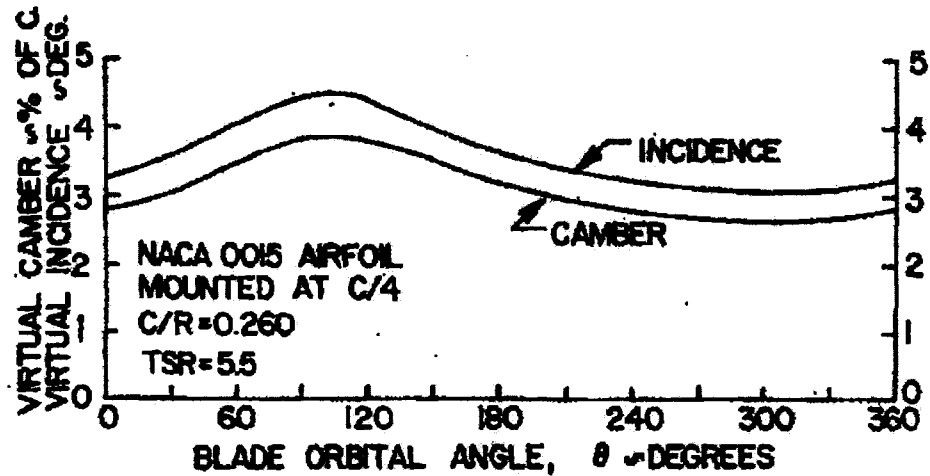


Figure 2.16: Variation of Virtual Camber and Incidence with Blade Orbital Position [Reproduced, with permission, from Migliore et. al 1980]

Since flow curvature effects become more pronounced as the blade chord to radius ratio (c/R) increases, they can be expected to be more important for turbines of relatively high solidity. The compensation for the flow curvature effects can produce better performance characteristics for VAWTs [Zervos

1988a]. Flow curvature effects have been described by Migliore et. al [1980], Hirsch and Mandal [1984], Zervos and Roucos [1988] and Mandal and Burton [1994]. The four major impacts of flow curvature effect on VAWTs are described below.

(i) Virtual Camber: It was demonstrated by Migliore et al. [1980] that a symmetrical blade travelling in a curved path acquires “virtual camber,” i.e. its behavior is similar to that of an otherwise similar airfoil but with camber, traveling in a straight line. They showed that for $c/R = 0.260$, a NACA 0015 blade mounted at $c/4$ has about 3% virtual camber. As a result of the virtual camber, the lift curve of the airfoil is shifted downwards and an aerodynamic moment is introduced [Zervos 1988a]. Migliore et al. [1980] assumed that symmetrical blades would be preferable over cambered blades and proposed that the simplest way to alleviate this problem is to fabricate geometric airfoils whose virtual equivalents are the symmetric airfoils originally chosen. However, it has been argued by Zervos [1988a] that the use of non-symmetric airfoils with a curvature in the opposite sense, having a lift curve shifted upwards and to the left, should diminish the loading upstream and increase it downstream.

(ii) Virtual Incidence: Flow curvature causes a change along the blade chord and the pitching moment effects will not be zero for a symmetrical blade. For NACA 0015 blades mounted at $c/4$ with $c/R = 0.26$, Migliore et al. [1980] calculated a virtual incidence of about 3° . As a result of virtual incidence, the lift curve of the airfoil shifts to the right [Zervos 1988a].

(iii) Change in Zero-Lift Drag Coefficient (C_{d0}): Hirsch and Mandal [1984] showed that C_{d0} is dependent on c/R , and that the application of simple analytic expressions to allow for this and for virtual incidence gave more accurate predictions than those based on the work of Migliore et al [1980].

(iv) Asymmetric Loading: Zervos [1988a] identified that due to the impact of this phenomenon, more lift is produced in the upstream than the downstream locations of the azimuthal position. This results in an asymmetric loading and it can cause premature stalling. Zervos also found that because of the wake produced in the upstream side of the rotor, the effective angle of incidence is smaller in the downstream side, accentuating the asymmetric loading.

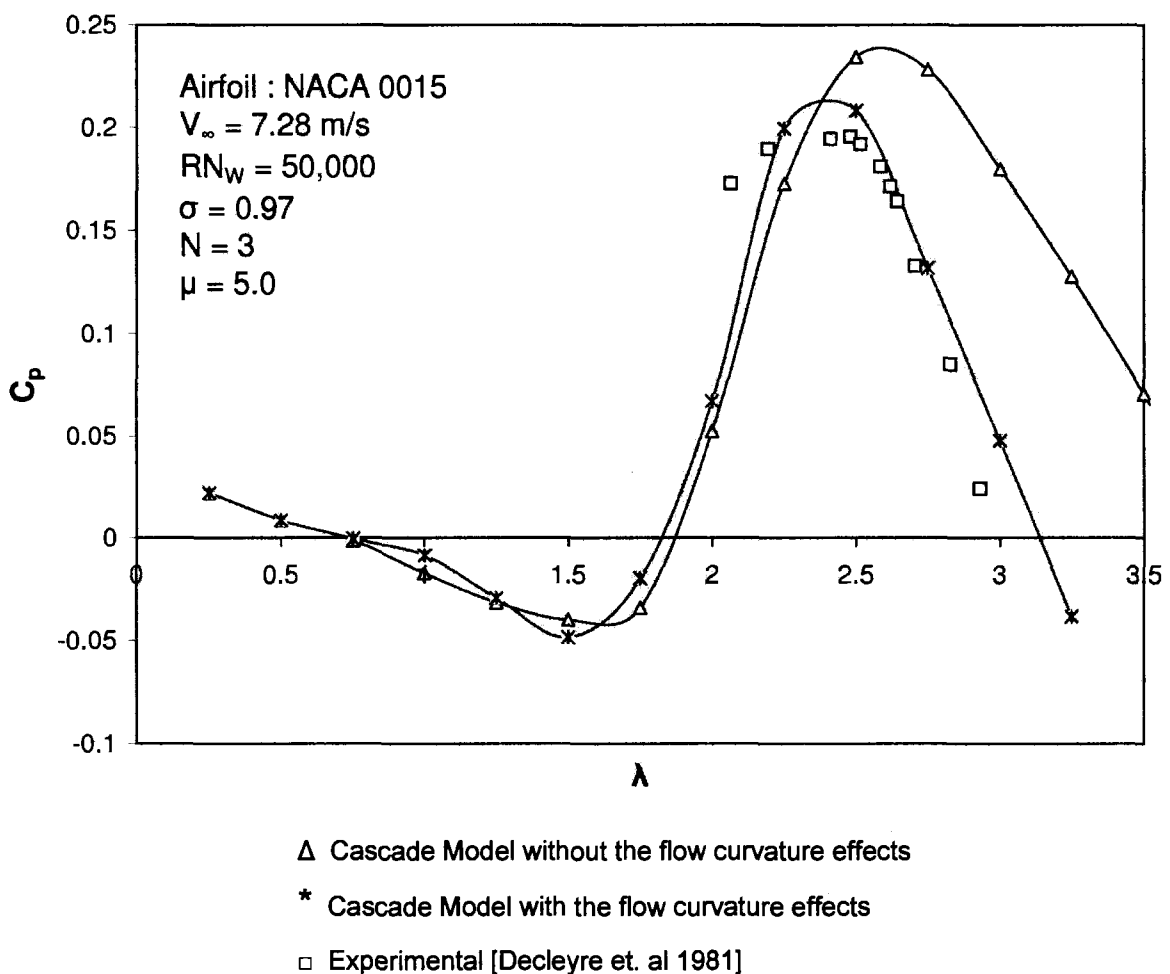


Figure 2.17: Comparison Between C_p - λ Curves of Experimental And Computational Results of an Experimental SB-VAWT [Islam et. al 2007c]

Computational Investigation of Flow Curvature Effect

To elucidate the effect of flow curvature, in the present work the Cascade Model [Hirsch and Mandal 1987] described earlier has been used to do the performance analysis. The aerodynamic characteristics of the NACA 0015 airfoil have been taken from Cyberiad [2007]. In Figure 2.17, the C_p - λ curves of an experimental SB-VAWT are shown. It can be seen from the figure that incorporation of flow curvature effects gives better results which conforms quite well with the experimental results of Decleyre et. al [1981] over the higher values of λ . However, at the lower values of λ , the effect is not pronounced.

2.3.5. Operation of the Blades in the Wake Region

For all VAWTs, the blade/blade wake interaction presents the most fundamental modeling problem [Klimas 1982]. All the VAWT performance prediction models need to take special care for calculating the induced velocities in the upstream ($0^\circ \leq \theta \leq 180^\circ$) and downstream ($180^\circ \leq \theta \leq 360^\circ$) sides. It has been found that most of the power is extracted from the wind during the upstream side of a VAWT [Kirke 1998]. According to Baker [1983], even a small difference between velocities experienced by the upstream and downstream blades will have a significant effect on the relative amounts of power available to each side.

In recent times, attempts have been made by different researchers in different parts of the world to understand the blade/blade wake interaction of SB-VAWT using the state-of-the-art computational techniques like computational fluid dynamics (CFD). As the angles of attack of SB-VAWT are widely fluctuating during rotor rotation, the large scale separation and interaction between the turbulent wake and moving airfoils are usually encountered. Therefore, unsteady and high accuracy simulation is usually needed to simulate flow around the VAWT [Iida et. al 2005]. Iida et. al [2005] attempted to simulate flow around a VAWT with Large Eddy Simulation (LES) with overset technique to solve the

complicated flow around the VAWT. The numerical results show that large separation occurred and unsteady aerodynamic forces were observed in the wake of VAWT. In the case of high tip-speed ratio, the predicted results by Iida et. al (as shown in Figures 2.18 and 2.19) reasonably agree with those of the momentum theory.



Figure 2.18: Velocity Contour around a Vertical Axis Wind Turbine at $\lambda=6.0$
[Reproduced, with permission, from Iida et. al 2005, © Copyright: Japan Society of Mechanical Engineering]

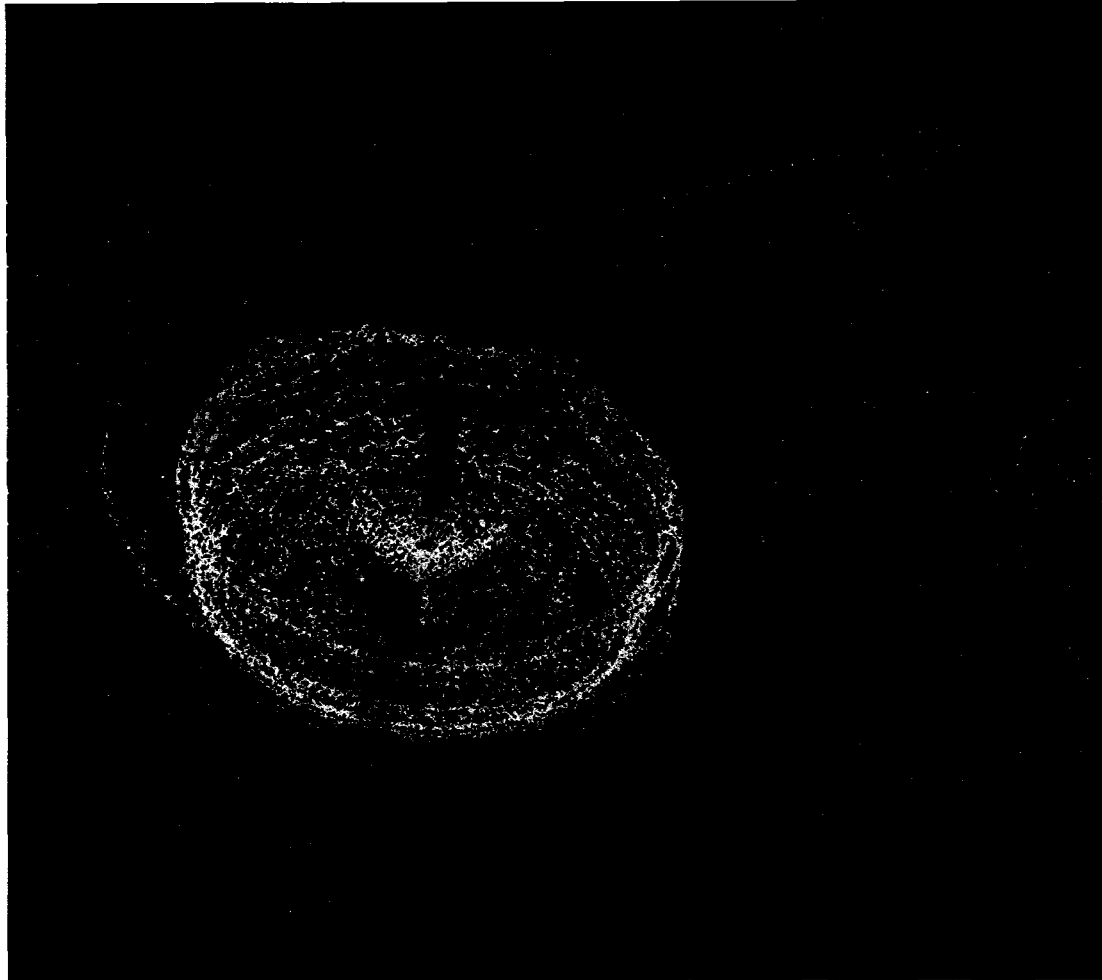


***Figure 2.19: Stream Lines around a Vertical Axis Wind Turbine at $\lambda=6.0$
[Reproduced, with permission, from Iida et. al 2005, © Copyright: Japan Society of
Mechanical Engineering]***

The vortex flow model of Duremberg [1979] finds that the velocity difference across a three-bladed turbine is about 0.55, i.e. the downstream blades receive wind at a speed of 0.55 times of the upstream side. About 90 or 95% of the energy is extracted from the upstream pass and this proportion depends on various factors including σ and λ [Kirke 1998]. Loth and McCoy [1983] have shown that a trade-off exists between energy extraction on the upstream and downstream passes and the more power extracted on the upstream pass, the

less energy is available on the downstream pass. Also the total energy that can be extracted is about the same regardless of whether it is extracted mostly on the upwind pass or not [Kirke 1998].

2.3.6. Parasitic Drag Losses due to the Supporting Struts

The primary source of drag for SB-VAWTs are the blades which are also responsible for generating lift. As shown in Figure 2.5, the supporting struts (or radial arms) which connect the blades with the central rotating column (or rotor) are also responsible for generating additional parasitic drag which reduce the overall power output. By definition, parasitic drag is the drag on the parts of the rotor that is not associated with any lifting surface and which detracts from the overall performance of the rotor [Global Energy Concepts 2003]. It is one of the major disadvantages of the straight-bladed VAWTs. The loss of power due to its effect is proportional to the cube of tip speed ratio. It has been determined by Mandal [1986] that at supporting strut drag coefficient of 0.25, the peak power of a straight-bladed VAWT drops by about 30%.

The design of supporting struts involves a trade-off between aerodynamic and structural requirements. To minimize the parasitic drag, one strut per blade is preferred for aerodynamic reasons with a low drag, non-lifting airfoil profile, but the strut must be strong enough to resist the loads and stiff enough to prevent excessive deflection and oscillation, both in flexure and torsion [Kirke 1998]. For small turbines with high blade bending moments due to centripetal acceleration, two struts per blade are preferable. Also airfoil performance deteriorates as the aspect ratio (μ) decreases and it is desirable to use long slender blades for high μ . Such blades generally require two points of support for structural reasons [Kirke 1998].

2.3.7. Atmospheric Turbulence

The wind varies along the earth surface and also above it in an indefinite pattern and strength due to inhomogeneous terrain, different surface roughness, and variation in atmospheric thermal stratification, which is called turbulence (or gusts) [Rohatgi and Barbezier 1999]. Atmospheric wind is always turbulent with continuous variation in intensities. So, wind turbines, operating in open terrains, usually operate in high turbulence with lower layer atmospheric turbulence or wakes of other wind turbines [Devinant et. al 2002]. The variations in the wind flow consist of gusts accompanied by small changes in its direction, which are commonly ascribed to eddies embedded in the general steady flow. In so far as these eddies are visualized, they are supposed to consist of more or less circular disturbances with the wind [Sahin 2004]. If the flow is an eddy and coincides with the wind direction, the velocity increases leading to a gust.

The wind over the earth may be regarded as composed of an average wind speed (U), proportional to “gradient wind”, with the superposition of an unsteady, continuously unstable and randomly varying component (u). These variations are responsible for the vertical transport of horizontal momentum by which surface shear stress is transmitted through the atmospheric or planetary boundary layer [Rohatgi 1996]. There is also a significant amount of turbulence in areas with a very uneven terrain surface, and behind obstacles (such as buildings). Study of atmospheric turbulence effect on wind turbine performance is crucial because it always decreases the energy output of any aerodynamic energy converters like wind turbines and it also imposes more wear and tear [DWIA 2007a]. It causes random fluctuating loads and stresses over the whole structure, resulting in power fluctuations and fatigue life of the wind turbine.

In wind engineering applications, turbulent variations of the wind speed are typically expressed by standard deviation of velocity fluctuations measured over 10–60 min. The variation in this ratio is caused by a large natural variability. This

concept cannot be explained by Gaussian processes. Turbulence occurs at atmospheric boundary layer as a result of interaction between surface and atmosphere [Sahin 2004].

As per computational analysis of Pawsey [2002], the performance of fixed-pitch SB-VAWT is reduced significantly due to atmospheric turbulence. However, though turbulent fluctuations have effect on the performance of wind turbines, its effect is not quantifiable without a detailed unsteady CFD analysis. The calculations shown here are likely to be considerably modified if a detailed study is performed that accounts for both the real impinging wind and the real turbulent wake effects.

2.4. Summary of the Chapter

Despite uncomplicated components and easy manufacturing processes, the aerodynamics related to SB-VAWTs is quite complex and needs special considerations for designing a self-starting SB-VAWT with optimum performance. Different aerodynamic factors discussed in this Chapter significantly affect the performance of SB-VAWT. One of the most problematic aspects of the complex aerodynamics of SB-VAWT is that they produce very little starting torque when conventional airfoils are used and one of the main reasons of the inability to self-start is due to a band of tip speed ratios below operating condition for which the net amount of energy collected by each blade in each revolution is negative. To achieve self starting, SB-VAWT must be altered so that a net positive amount of torque is produced at all tip speed ratios up to the operating point.

The performance of SB-VAWT is affected by several aerodynamic factors which are related to the different structural components and the surroundings. The seven main aerodynamic challenges have been identified in this Chapter, which are:

- (i) Low RN Operation: They operate in the low Reynolds number (RN) regime which is a highly sensitive unstable region with high probability of separation. In this range of RN, very complex flow phenomena take place within a short distance of the leading edge on the upper surface of the blade and the laminar separation bubble that commonly forms in this range plays an important role in determining the boundary layer behavior and the stalling characteristics of the blade.
- (ii) Post-stall Operation: Unlike the conventional aerodynamic applications, VAWTs encounter a wide range of angle of attack, especially at low tip speed ratios. The behavior of lift and drag coefficients in the post-stall regimes has serious consequence for fixed-pitch SB-VAWT and at a range of angles of attack, the tangential force coefficient becomes negative. This is one of the main reasons for low or negative starting torque at low tip speed ratios.
- (iii) Unsteady Effects: Because of the oscillating α , the SB-VAWT blades always produce a fluctuating force, even in steady conditions. Consequently, undesirable dynamic stall, vibrations, gust response etc. may result. The effects of dynamic stall on the performance of a SB-VAWT have been analyzed with Cascade model, developed by Hirsh and Mandal [1987]. It is observed from the analysis that aerodynamic forces due to dynamic stall are higher than those due to static stall. As a result, for the performance prediction of straight-bladed VAWTs, especially for the local forces, there can be substantial differences between the experimental data and the calculated values unless the dynamic stall effect is added.
- (iv) Rotational Effects: When the SB-VAWT blade rotates in a circular path, the direction of rotational velocity varies continuously along the chord, making the flow over the blade airfoil of a curvilinear nature and thus it encounters flow curvature effects if the chord/radius ratio is high. It can have significant influence on the lift-drag characteristics of the blade airfoil of VAWT, especially

at higher tip speed ratios. The effects of flow curvature on the performance of a SB-VAWT have been analyzed in this chapter with Cascade model.

- (v) Operation of the Blades in the Wake Region: Blades of SB-VAWTs on the downstream pass operate in their own wakes shed by blades on the upstream pass and for all the VAWTs, the blade/blade wake interaction presents the most fundamental modelling problem. All the VAWT performance prediction models need to take special care for calculating the induced velocities on the upstream and downstream sides.
- (vi) Parasitic Drag of the Supporting Struts: The primary source of drag for SB-VAWTs are the blades, which are also responsible for generating lift. The supporting struts (or radial arms) which connect the blades with the central rotating column (or rotor) are also responsible for generating additional parasitic drag which reduce the overall power output.
- (vii) Atmospheric Turbulence: SB-VAWTs mostly operate in turbulent atmospheric conditions. As per a detailed computational analysis, their performance can be reduced significantly due to atmospheric turbulence.

All these factors collectively make the thorough analysis of SB-VAWT a challenging undertaking and detailed analyses of these factors described in this Chapter are of great importance for better aerodynamic performance and dimensions of a smaller-capacity SB-VAWT.

Chapter 3

Review of Aerodynamic Computational Models

In the past, several universities and research institutions have carried out research activities related to SB-VAWTs and published reports, journal papers and conference papers. Many of these documents were collected during the present research work and attempt has been made to develop a comprehensive understanding of previous SB-VAWT related research activities, including experimental results from test models and prototypes, aerodynamic theories and special-purpose airfoils designed for VAWT use. In this chapter, a comprehensive review has been made of the main available aerodynamic computational models which are used for performance analysis of SB-VAWTs.

3.1. General Mathematical Expressions for Aerodynamic Analysis of Fixed-pitch SB-VAWTs

Before comparative analysis of the main aerodynamic models, the general mathematical expressions which are common to most of the aerodynamic models are described in this section.

3.1.1. Variation of Local Angle of Attack

The flow velocities in the upstream and downstream sides of the Darrieus type VAWTs are not constant as seen in Figure 3.1. From this figure one can observe that the flow is considered to occur in the axial direction. The chordal velocity

component V_c and the normal velocity component V_n are respectively obtained from the following expressions

$$V_c = R\omega + V_a \cos \theta \quad (3.1)$$

$$V_n = V_a \sin \theta \quad (3.2)$$

where V_a is the axial flow velocity (i.e. induced velocity) through the rotor, ω is the rotational velocity, R is the radius of the turbine, and θ is the azimuth angle.

Referring to Figure 3.1, the angle of attack (α) can be expressed as

$$\alpha = \tan^{-1}\left(\frac{V_n}{V_c}\right) \quad (3.3)$$

Substituting the values of V_n and V_c and non-dimensionalizing

$$\alpha = \tan^{-1}\left[\frac{\sin \theta}{\left(\frac{R\omega}{V_\infty} / \frac{V_a}{V_\infty}\right) + \cos \theta}\right] \quad (3.4)$$

where V_∞ is the freestream wind velocity. If we consider blade pitching then

$$\alpha = \tan^{-1}\left[\frac{\sin \theta}{\left(\frac{R\omega}{V_\infty} / \frac{V_a}{V_\infty}\right) + \cos \theta}\right] - \gamma \quad (3.5)$$

where γ is the blade pitch angle.

3.1.2. Variation of Local Relative Flow Velocity

The relative flow velocity (W) can be obtained as (Figure 3.1)

$$W = \sqrt{V_c^2 + V_n^2} \quad (3.6)$$

Inserting the values of V_c and V_n (Equations 3.1 and 3.2) in to Equation (3.6), one can find velocity ratio as

3.1.3. Variation of Tangential and Normal Forces

The directions of the lift and drag forces and their normal and tangential components are shown in Figure 3.2. The tangential force coefficient (C_t) is basically the difference between the tangential components of lift and drag forces. Similarly, the normal force coefficient (C_n) is the difference between the normal components of lift and drag forces. The expressions of C_t and C_n can be written as

$$C_t = C_l \sin \alpha - C_d \cos \alpha \quad (3.8)$$

$$C_n = C_l \cos \alpha + C_d \sin \alpha \quad (3.9)$$

The net tangential and normal forces can be defined as

$$F_t = C_t \frac{1}{2} \rho c H W^2 \quad (3.10)$$

$$F_n = C_n \frac{1}{2} \rho c H W^2 \quad (3.11)$$

where ρ is the air density, c is the blade chord and H is the height of the turbine.

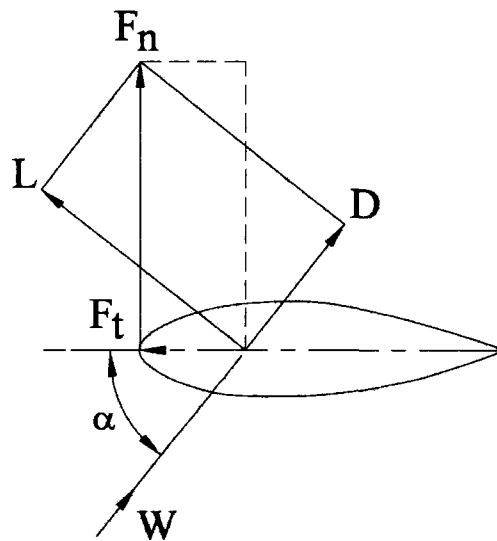


Figure 3.2: Force Diagram of a Blade Airfoil

3.1.4. Calculation of Total Torque

Since, the tangential and normal forces represented by Equations (3.10) and (3.11) are for any azimuthal position, they are considered as a function of azimuth angle θ . Average tangential force (F_{ta}) on one blade can be expressed as

$$F_{ta} = \frac{1}{2\pi} \int_0^{2\pi} F_t(\theta) d\theta \quad (3.12)$$

The total torque (Q) for the number of blades (N) is obtained as

$$Q = NF_{ta}R \quad (3.13)$$

3.1.5. Power Output

The total power (P) can be obtained as

$$P = Q \cdot \omega \quad (3.14)$$

3.2. Computational Models for Performance Analysis of VAWTs

In the past, several mathematical models, based on several theories, were prescribed for the performance prediction and design of Darrieus type VAWTs by different researchers. The key components of all the computational models can be broadly described as:

- Calculations of local relative velocities and angles of attack at different tip speed ratios and azimuthal (orbital) positions;
- Calculation of ratio of induced to freestream velocity ($\frac{V_a}{V_\infty}$) considering the blade/blade-wake interaction;
- Mathematical expressions based on different approaches (Momentum, Vortex or Cascade principles) to calculate normal and tangential forces;
- 'Pre-stall airfoil characteristics' (C_l , C_d & C_m) for the attached regime at different Reynolds numbers;

- 'Post-stall model' for stall development and fully stalled regimes;
- 'Finite aspect ratio consideration';
- 'Dynamic Stall Model' to account for the unsteady effects;
- 'Flow Curvature Model' to consider the circular blade motion.

According to the literature survey, the most studied and best validated models can be broadly classified into three categories - (1) Momentum model, (2) Vortex model and (3) Cascade model. It should be noted that not all the models consider all the key components described above. Descriptions of these three main categories of VAWT computational models are presented below.

3.2.1. Momentum Model

Different momentum models (also specified as Blade Element/Momentum or BEM model) are basically based on calculation of flow velocity through a turbine by equating the streamwise aerodynamic force on the blades with the rate of change of momentum of air, which is equal to the overall change in velocity times the mass flow rate. The force is also equal to the average pressure difference across the rotor. Bernoulli's equation is applied in each streamtube. The main drawback of these models is that they become invalid for large tip speed ratios and also for high rotor solidities because the momentum equations in these particular cases are inadequate [Paraschivoiu, 2002]. Over the years, several approaches were attempted to utilize this concept, which are discussed briefly under the following headings.

Single Streamtube Model

In 1974 Templin proposed the single streamtube model which is the first and simplest prediction method for the calculation of the performance characteristics of a Darrieus type VAWTs [Templin, 1974]. In this model the entire turbine is

assumed to be enclosed within a single streamtube as shown in Figure 3.3. This model first incorporated the concept of the windmill actuator disc theory into the analytical prediction model of a Darrieus type VAWT. In this theory the induced velocity (rotor axial flow velocity) is assumed to be constant throughout the disc and is obtained by equating the streamwise drag with the change in axial momentum.

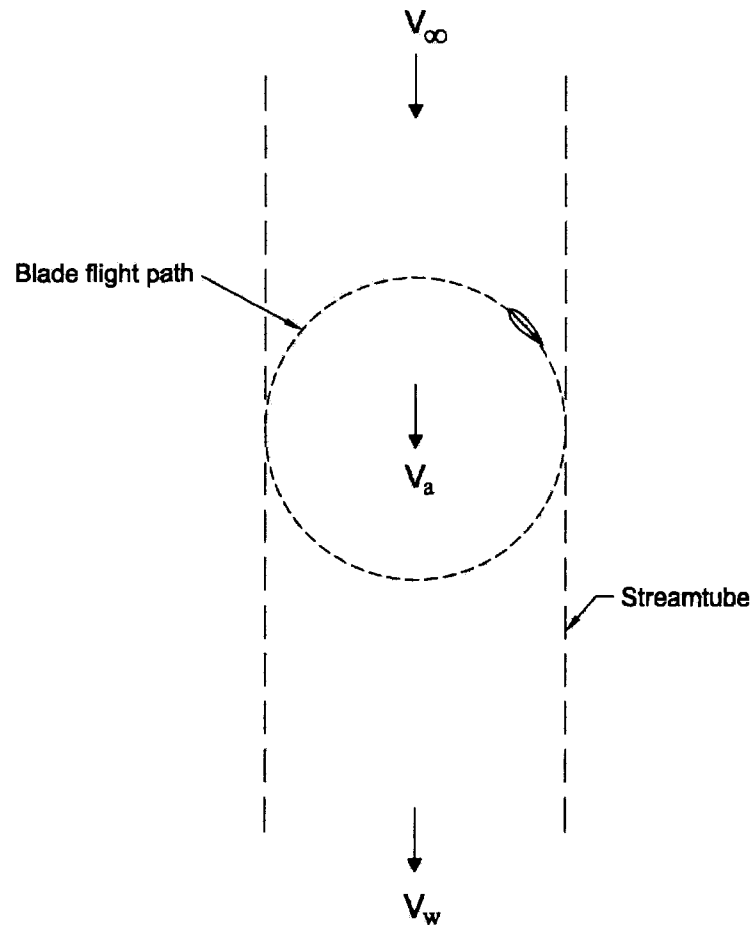


Figure 3.3: Schematic of Single Streamtube Model

The actuator disc is considered as the surface of the imaginary body of revolution. It is assumed that the flow velocity is constant throughout the upstream and downstream side of the swept volume. This theory takes into account the effect of airfoil stalling on the performance characteristics. The

effects of geometric variables such as blade solidity and rotor height-diameter ratio have been included in the analysis. The effect of zero-lift-drag coefficient on the performance characteristics has also been included. Wind shear effect cannot be incorporated into the model.

Now, according to Glauert's actuator disk theory [1935], the expression of the uniform velocity through the rotor is

$$V_a = \frac{V_\infty + V_w}{2} \quad (3.15)$$

where V_w is the wake velocity. All the calculations in this model are performed for a single blade whose chord equals the sum of the chords of the actual rotor's blades. The streamwise drag force (F_D) due to the rate of change of momentum is

$$F_D = \dot{m} \cdot (V_\infty - V_w) \quad (3.16)$$

where \dot{m} is the mass flow rate. The rotor drag coefficient (C_{DD}) is defined as

$$C_{DD} = \frac{F_D}{\frac{1}{2} \rho A V_a^2} \quad (3.17)$$

From Equations (3.15), (3.16) and (3.17), we can find that,

$$C_{DD} = 4 \left(\frac{V_\infty - V_a}{V_a} \right) \quad (3.18)$$

and

$$\frac{V_a}{V_\infty} = \left(\frac{1}{1 + \frac{C_{DD}}{4}} \right) \quad (3.19)$$

The overall torque and power coefficient of the VAWT can be determined from Equations (3.13) and (3.14) by utilizing the expression of $\frac{V_a}{V_\infty}$ derived in Equation (3.19) above.

This model can predict the overall performance of a lightly loaded wind turbine, but it always predicts higher power than the experimental results. It does not predict the wind velocity variations across the rotor. These variations gradually increase with the increase of the blade solidity and tip speed ratio. Noll and Ham presented an analytical method for the performance prediction of a cyclically pitched SB-VAWT using the single streamtube model [Noll and Ham 1980]. They added the effect of strut drag, turbulent wake state and dynamic stall to their analytical method.

Multiple Streamtube Model

Wilson and Lissaman [1974] introduced the multiple streamtube model which was an improvement over the single streamtube model. In this model the swept volume of the turbine is divided into a series of adjacent, aerodynamically independent parallel streamtubes as shown in Figure 3.4. The blade element and momentum theories are then employed for each streamtube. In their model they considered the flow as inviscid and incompressible for the calculation of the induced velocity through the streamtube. As a result, only the lift force appears in the calculation of the induced velocity. Wilson and Lissaman [1974] considered the theoretical lift for their calculation, which is given by

$$C_l = 2\pi \sin \alpha \quad (3.20)$$

In this model, the induced velocity ratio can be found from the following expression,

$$\frac{V_a}{V_\infty} = 1 - \left(\frac{k}{2} \cdot \frac{Nc}{R} \cdot \frac{R\omega}{V_\infty} \cdot \sin\theta \right) \quad (3.21)$$

where k is a factor found through iteration. In this model, the induced velocity varies over the frontal disc area both in the vertical and horizontal directions [Mandal 1986]. Atmospheric wind shear can be included in this model. However, this model still is inadequate in its description of flow field and it can be applied only for a fast running lightly loaded wind turbine.

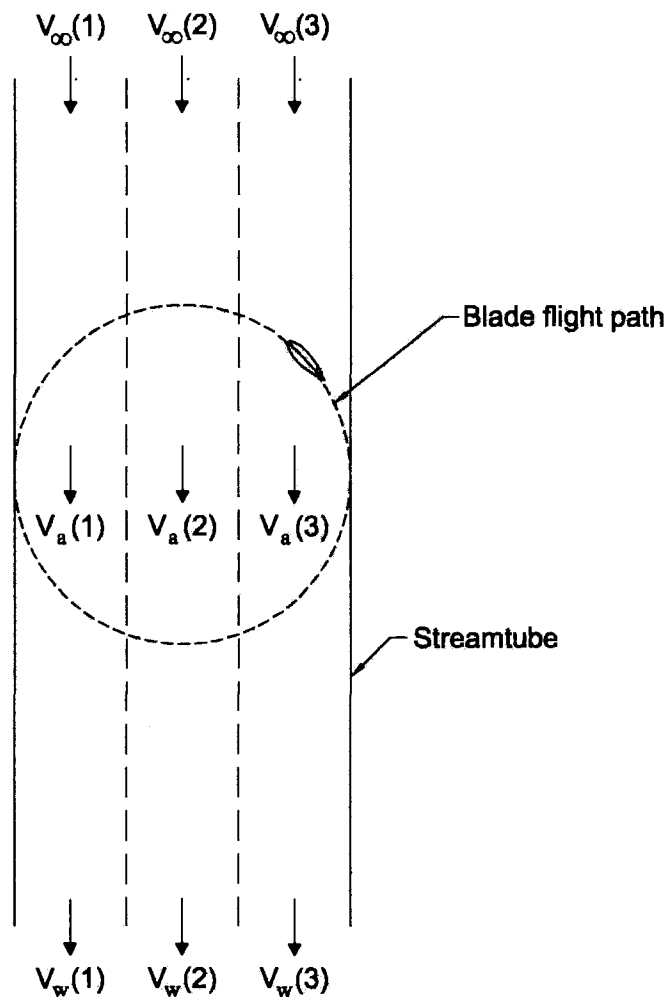


Figure 3.4: Schematic of Multiple Streamtube Model

Strickland [1976] presented another multiple streamtube model for a Darrieus type VAWT. In this model, induced velocity is found by equating the blade elemental forces (including airfoil drag) and the change in the momentum along each streamtube. The wind shear effects have also been included in the calculation of the model. This model predicts the overall performance reasonably well, especially when the rotor is lightly loaded. It displays improvement over the single streamtube model.

The basic difference between Wilson's and Strickland's models is that Wilson used the theoretical lift force only in the calculation of induced velocity while Strickland added the effect of drag force as well for the similar calculation. Among these two models, Wilson's model gives fast convergence while Strickland's model gives slower convergence due to added complexity.

Another theory based on the multiple streamtube model including the effects of airfoil geometry, support struts, blade aspect ratio, turbine solidity and blade interference was presented by Muraca et. al [1975]. They derived an expression for lift distribution on the plate with the variable angle of attack from the leading to the trailing edge points of the flat plate and averaged the distributed lift force over the whole surface of the flat plate. They found that, the effect of flow curvature on the performance characteristics is insignificant for a low chord to radius ratio.

Sharpe [1977] gave an elaborate description of the multiple streamtube model. The principal idea of his model is similar to Strickland's model. Additionally, he incorporated the effect of Reynolds number into the calculation [Sharpe 1977].

Another improved version of the extended multiple streamtube model was presented by Read and Sharpe [1980] for VAWT. In their model the parallel streamtube concept is dispensed with and the expansion of the streamtube is

included. It is strictly applicable to low solidity lightly loaded wind turbines with large aspect ratio (H/c). It can predict the instantaneous aerodynamic blade forces and the induced velocities better than those by the conventional multiple streamtube model, but the prediction of overall power coefficients cannot be made with reasonable accuracy. It usually gives lower power than that obtained experimentally.

Double Multiple Streamtube Model

Paraschivoiu [1981] introduced double multiple streamtube theory for the performance prediction of a Darrieus wind turbine. As shown in Figure 3.5, in this model the calculation is done separately for the upstream and downstream half-cycles of the turbine. At each level of the rotor, the upstream and downstream induced velocities are obtained using the principle of two actuator discs in tandem. The concept of the two actuator discs in tandem for a Darrieus wind turbine was originally given by Lapin [1975]. For both the upstream and downstream half-cycles, vertical variation of the induced velocity (like that in the multiple streamtube model) is considered, while in the horizontal direction induced velocity is assumed to be constant (like that of a single streamtube model). For the upstream half-cycle, the wake velocity is represented by,

$$V_e = V_{\infty i} \left(2 \frac{V_{au}}{V_{\infty i}} - 1 \right) = V_{\infty i} (2u_u - 1) \quad (3.22)$$

where $V_{\infty i}$ is the local ambient wind velocity (which is different at different heights of the turbine blade due to the effect of wind shear) and $u_u (= \frac{V_{au}}{V_{\infty i}})$ is the interference factor for the upstream half-cycle. For the downstream half-cycle of the rotor, V_e is the input velocity. The induced velocity for the downstream half-cycle is V_{ad} which can be written as

$$V_{ad} = u_d V_e = u_d (2u_u - 1) V_{\infty i} \quad (3.23)$$

where $u_d (= \frac{V_{ad}}{V_e})$ is the interference factor for the downstream half-cycle. The streamtube induced velocity is calculated by a double iteration, one for each part of the rotor.

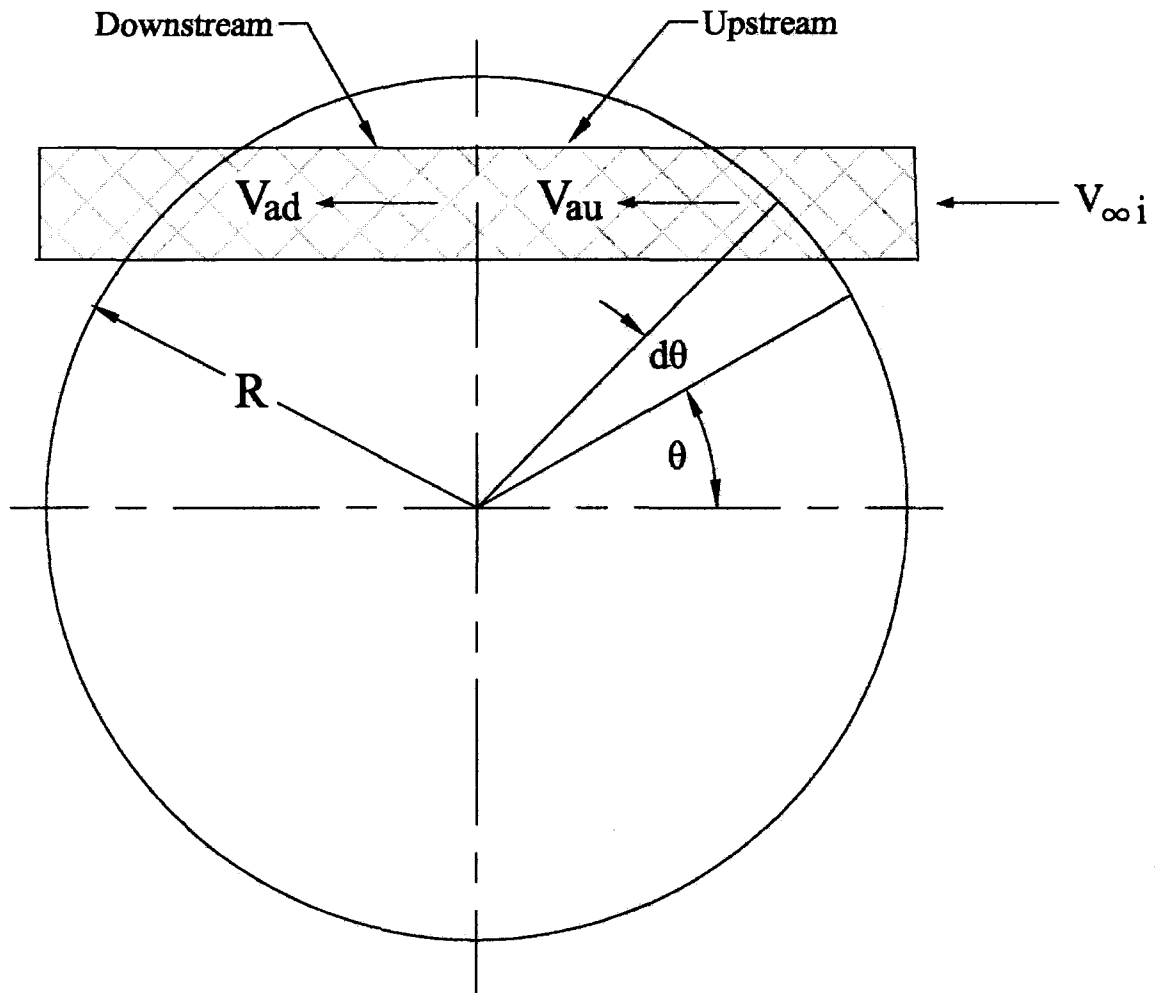


Figure 3.5: Schematic of Double-Multiple Streamtube Model

The double multiple streamtube model with constant and variable interference factors (induced velocity ratios), including secondary effects for a Darrieus wind

rotor was examined by Paraschivoiu et. al [1983]. They found a relatively significant influence of the secondary effects, namely the blade geometry and profile type, the rotating tower and the presence of struts and aerodynamic spoilers, especially at high tip speed ratios. They considered the variation of the induced velocity as a function of azimuth angle, which gives a more accurate calculation of the aerodynamic loads. In the paper presented by Paraschivoiu and Delclaux [1983], they made improvements in the double multiple streamtube model. They considered the induced velocity variation as a function of the azimuth angle for each streamtube.

The double multiple streamtube model gives better correlation between the calculated and experimental results, especially for the local aerodynamic blade forces, than the multiple streamtube models. However, this model overpredicts the power for a high solidity turbine and there appears to be a convergence problem for the same type of turbine, especially in the downstream side and at the higher tip speed ratios.

3.2.2. Vortex Model

The vortex models are basically potential flow models based on the calculation of the velocity field about the turbine through the influence of vorticity in the wake of the blades. The turbine blades are represented by bound or lifting-line vortices whose strengths are determined using airfoil coefficient datasets and calculated relative flow velocity and angle of attack. A simple representation of the vortex system associated with a blade element is shown in Figure 3.6. The VAWT blade element is replaced by a “bound” vortex filament, sometimes called “substitution” vortex filament or a lifting-line. The strengths of the bound vortex and each trailing tip vortex are equal as a consequence of the Helmholtz theorems of vorticity [Currie 1974]. According to Figure 3.6, the strengths of the shed vortex systems have changed on several occasions. On each of these occasions, a

spanwise vortex is shed whose strength is equal to the change in the bound vortex strength as dictated by Kelvin's theorem [Currie 1974].

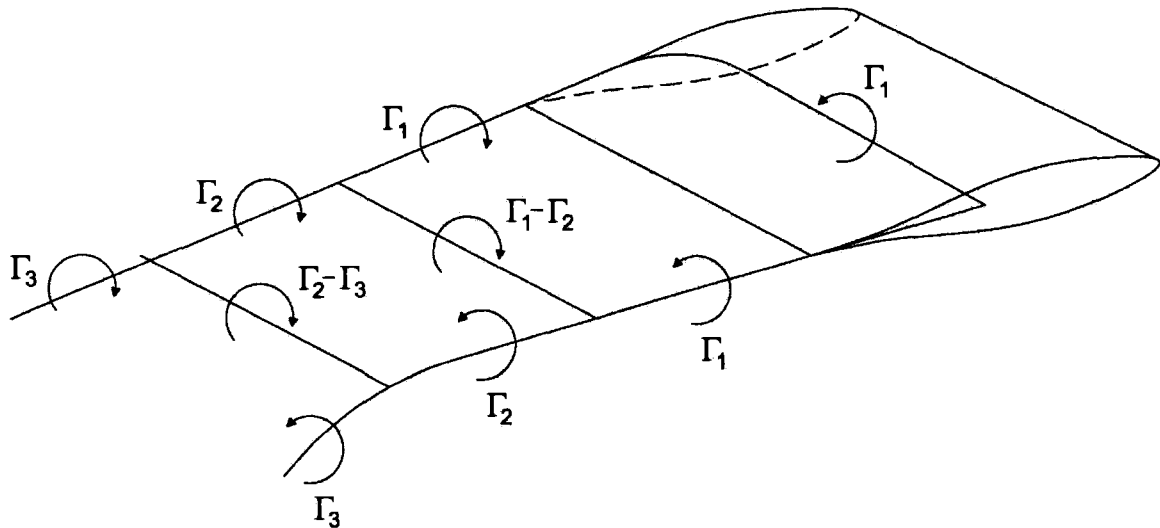


Figure 3.6: Vortex System for a Single Blade Element

The fluid velocity at any point in the flow field is the sum of the undisturbed wind stream velocity and the velocity induced by the entire vortex filaments in the flow field. The velocity induced at a point in the flow field by a single vortex filament can be obtained from the Biot-Savart law, which relates the induced velocity to the filament strength. Referring to the case shown in Figure 3.7, for a straight vortex filament of strength Γ and length l , induced velocity \vec{V}_p at a point P on the filament is given by

$$\vec{V}_p = \vec{e} \frac{\Gamma}{4\pi d} (\cos\theta_1 - \cos\theta_2) \quad (3.24)$$

where d is the minimum distance of the point P from the vortex filament, \vec{e} and \vec{r} are the unit vectors. It should be noted that if point P should happen to lie on the vortex filament, Equation (3.24) yields indeterminate results, since \vec{e} can not be

defined and the magnitude of \vec{V}_p is infinite. The velocity induced by a straight filament on itself is, in fact, equal to zero.

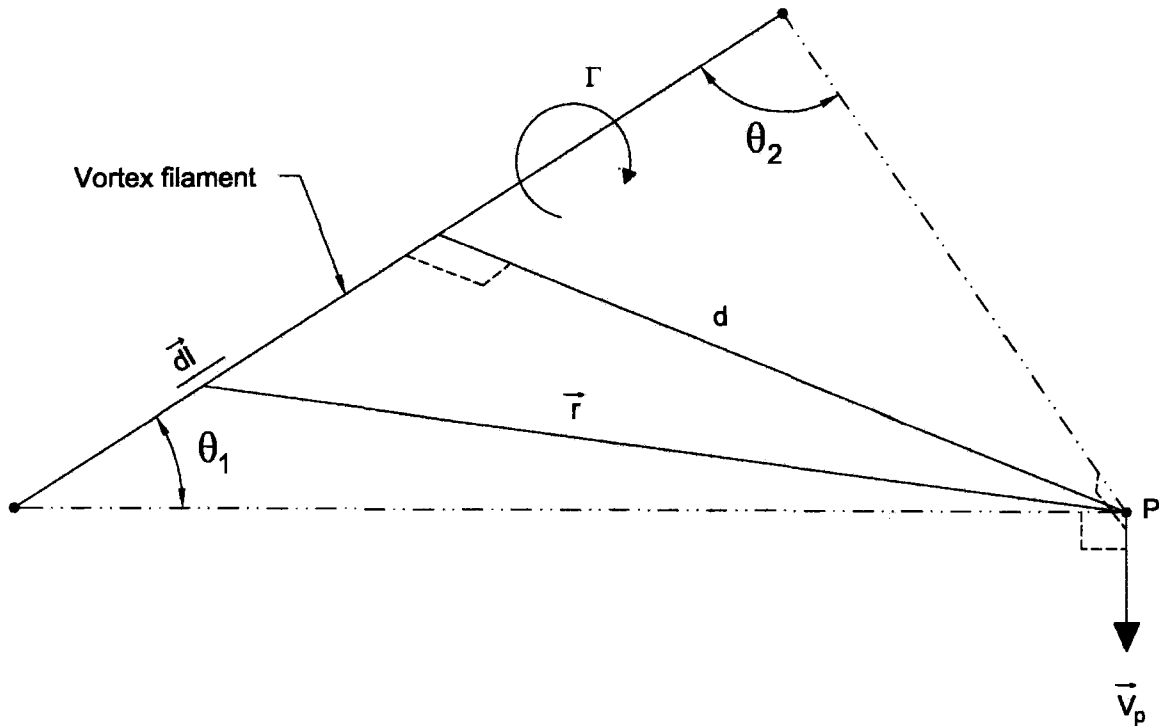


Figure 3.7: Velocity Induced at a Point by a Vortex Filament

In order to allow closure of the vortex model, a relationship between the bound vortex strength and the velocity induced at a blade segment must be obtained. A relationship between the lift (L) per unit span on a blade segment and the bound vortex strength Γ_B is given by the Kutta-Joukowski law. The lift can also be formulated in terms of the airfoil lift coefficient (C_l). Equating these two expressions for the lift yields the required relationship between the bound vortex strength and the induced velocity at a particular blade segment as

$$\Gamma_B = \frac{1}{2} c C_l W \quad (3.25)$$

where c is the blade chord. After determining the induced velocity distribution, it becomes straight-forward to obtain performance characteristics of VAWT as described in Section 3.1.

Larsen [1975] first introduced the idea of vortex model. He used his vortex model for the performance prediction of a cyclogiro windmill. His model is a two-dimensional one but if the vortex trailing from the rotor blade tips is considered, it may be said that it is not strictly two-dimensional. However, in his model angle of attack is assumed small and, as a result, the stall effect is neglected.

Fanucci and Walters [1976] presented a two-dimensional vortex model applicable to a SB-VAWT. In their analysis they considered the angle of attack very small, which eliminates the stall effect.

Holme [1976] presented a vortex model for a fast running vertical-axis wind turbine having a large number of straight, very narrow blades and a high height-diameter ratio (in order to make a two-dimensional flow assumption). The analysis is valid for a lightly loaded wind turbine only.

Wilson [1980] also introduced a two-dimensional vortex analysis to predict the performance of a giromill. In his method he did not take the stall effect into account, because the angle of attack was assumed to be small.

Strickland et. al [1979] presented a three-dimensional extension of the vortex model, and the aerodynamic stall is incorporated into the model. They presented the experimental results for a series of two-dimensional rotor configurations. Their calculated values show more or less good correlation with the experimental results for the instantaneous blade forces and the near wake flow behind the

rotor. Strickland et. al [1981] made improvements on the prior vortex model (quasi-steady vortex model). The latest model is termed as the dynamic vortex model since, in this model, the dynamic effects are included. The improvements over the prior model are that it includes the dynamic stall effect, pitching circulation and added mass effect. They repeated the experiment with the test model as is mentioned in reference [1979] and found appreciable variations with the prior results. The correlation with their calculated values by the dynamic vortex model and the latest experimental results of the local blade forces and wake velocities seem to be reasonable in some cases.

Cardona [Cardona 1984] incorporated the effect of flow curvature following the method given by Migliore et. al [1980] into the original aerodynamic vortex model presented by Strickland et. al [1979]. He also added a modified form of the dynamic stall effects. He found an improved correlation with the calculated and experimental results for the instantaneous aerodynamic blade forces and the overall power coefficients.

The main disadvantage of vortex model is that it takes too much computation time. Furthermore, these models still rely on significant simplifications, like potential flow is assumed in the wake and the effect of viscosity in the blade aerodynamics is included through empirical force coefficients [Pawsey 2002].

3.2.3. Cascade Model

The periodic equidistant arrangement of several blades or vanes of turbomachineries is called a cascade. Hence, the cascade is the basic element of the turbomachine, and cascade flow is the essential physical phenomenon for the operation of the machine [Scholz 1977]. The cascade model was proposed by Hirsch and Mandal [1987], who were the first to apply the cascade principles, widely used for turbomachines, for the analysis of VAWTs.

In this model, the blade airfoils of a turbine are assumed to be positioned in a plane surface (termed as the cascade) with the blade interspace equal to the turbine circumferential distance divided by the number of blades as shown in Figure 3.8. The relationship between the wake velocity and the free stream velocity is established by using Bernoulli's equation while the induced velocity is related to the wake velocity through a particular semi-empirical expression.

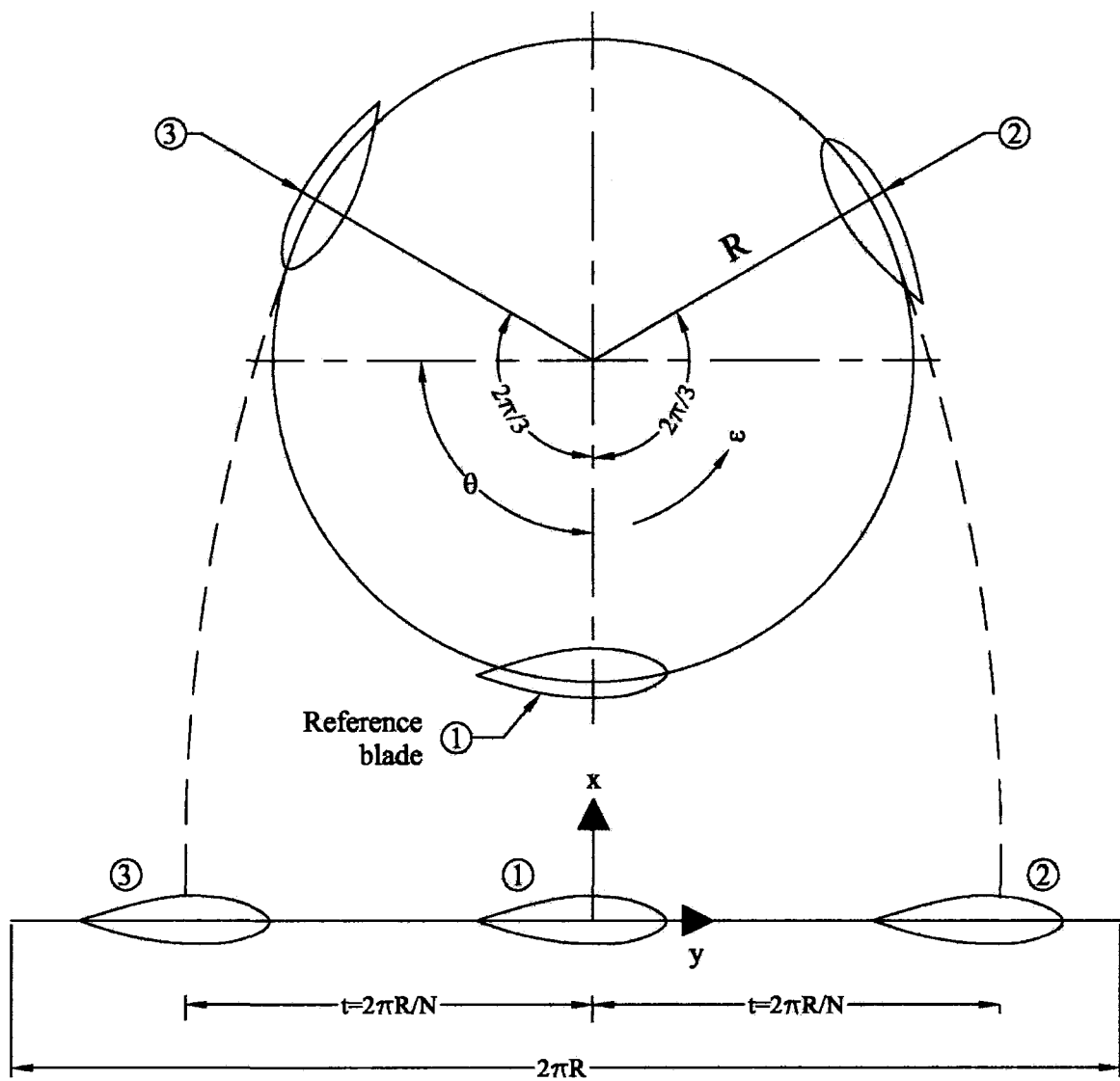


Figure 3.8: Development of Blade into a Cascade Configuration

In this model, the aerodynamic characteristics of each element of the blade are obtained independently (like the double multiple streamtube theory), for the upwind and downwind halves of the rotor, considering the local Reynolds number and the local angle of attack as shown in Figure 3.9. After determination of the local relative flow velocity and the angle of attack, the VAWT is developed into a cascade configuration that is shown in Figure 3.8. The cascade is considered in a plane normal to the turbine axis. If the blade represented by (1) at an azimuth angle θ is considered as the reference blade, the flow conditions on the other two blades represented by (2) and (3), are assumed to be equal to those of the reference blade. This process is continued for one complete revolution of the reference blade, with a step of $\delta\theta$.

To find the induced velocity, a relationship between the wake velocity and the induced velocity is introduced. For the upstream side this is expressed as

$$\frac{V_{au}}{V_{\infty}} = \left(\frac{V_e}{V_{\infty}}\right)^{k_i} \quad (3.26)$$

and for the downstream side, this is expressed as

$$\frac{V_{ad}}{V_e} = \left(\frac{V_w}{V_e}\right)^{k_i} \quad (3.27)$$

where V_e and V_w are the wake velocities in the upstream and downstream side. The value of the exponent k_i is found from a fit of experimental results. The induced velocity ratio for the downstream side can be written in the form,

$$\frac{V_{ad}}{V_{\infty}} = \frac{V_{ad}}{V_e} \frac{V_e}{V_{\infty}} = \frac{V_e}{V_{\infty}} \left(\frac{V_w}{V_e}\right)^{k_i} \quad (3.28)$$

The expression of the exponent k_i is written in accordance with Hirsch and Mandal [1987] as

$$k_i = (0.425 + 0.332\sigma) \quad (3.29)$$

where $\sigma = \frac{Nc}{R}$. The final expression for the overall torque is found from,

$$Q = \rho R^3 \frac{H}{R} \int_0^{2\pi} (W_2^2 \sin \alpha_2 \cos \alpha_2 - W_1^2 \sin \alpha_1 \cos \alpha_1) d\theta \quad (3.30)$$

where W_1 and W_2 are the relative velocities in the cascade inlet and outlet. α_1 and α_2 are the angles of attack in the cascade inlet and outlet. Detailed description of this model can be found from Hirsh and Mandal [1987].

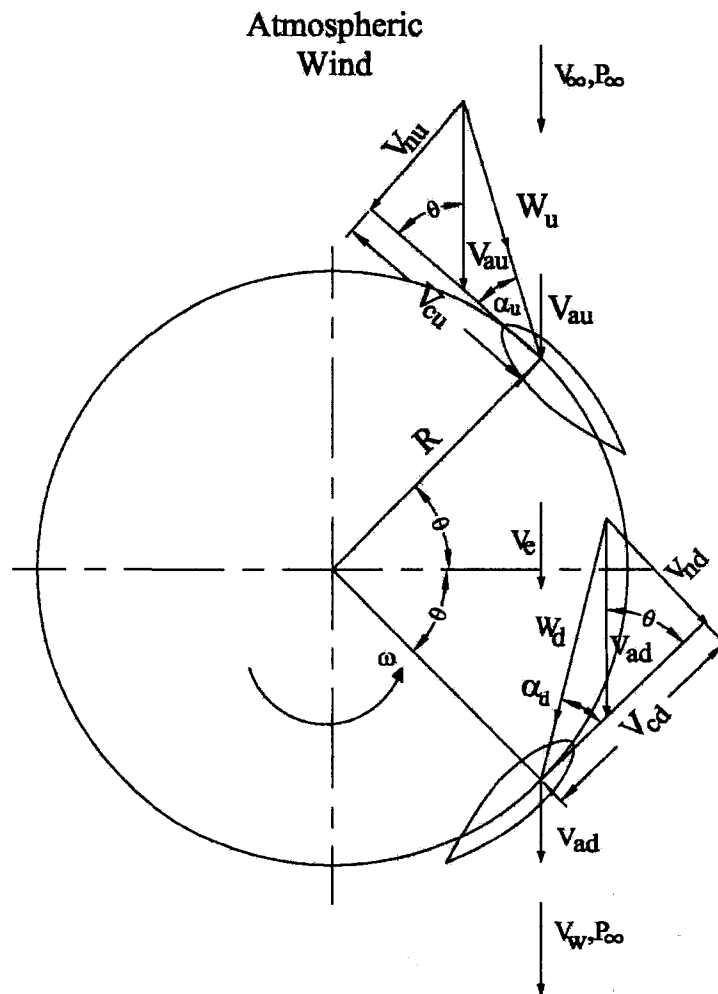


Figure 3.9: Horizontal Section of a SB-VAWT with Flow Velocities in the Upstream and Downstream Sides

3.3. Summary of the Chapter

Several aerodynamic models have been analyzed in this chapter which are applied for better performance prediction and design analysis of SB-VAWT. At present the most widely used models are the double multiple streamtube model, free-vortex model and the cascade model. It has been found that, each of these three models has their strengths and weaknesses. Among these three models, the vortex models are considered to be the most accurate models according to several researchers, but they are computationally very expensive and in some cases they suffer from convergence problem. It has also been found that the double multiple streamtube model is not suitable for high tip speed ratios and high solidity SB-VAWTs. On the other hand, the cascade model gives smooth convergence even for high tip speed ratios and high solidity SB-VAWTs with reasonable accuracy [Islam et. al 2008a].

Chapter 4

Computational Scheme for Performance Analysis of SB-VAWT

In this chapter, the original cascade model and the modifications required for its applicability for performance analysis of SB-VAWTs equipped with both symmetric and asymmetric airfoils are discussed. To choose an appropriate model for the present study, the available major aerodynamic models have been investigated in the previous chapter. Based on the findings of the previous chapter, it has been decided that the cascade model, proposed by Hirsch and Mandal [1987], is most appropriate for the present research mainly due to the following factors:

- (i) It is based on an established “Cascade Principle” which is widely applied for the analysis of conventional turbomachines [Scholz 1977];
- (ii) It provides smooth convergence and is much faster than streamtube (including the double and multiple streamtube models) and complex vortex models [Mandal 1986, Hirsch and Mandal 1987, Mandal 1994, Mandal and Burton 1994];
- (iii) It can be coupled with a sophisticated flow-curvature model (which was developed by the same researchers who developed the cascade model) that is critical for the present analysis with asymmetric airfoils with cambered shapes [Mandal 1994, Mandal and Burton 1994];
- (iv) It considers the effect of dynamic stall through the widely accepted Boeing-Vertol model [Mandal 1994, Mandal and Burton 1994];

(v) It considers several other vital aerodynamic factors, including finite aspect ratio, local RN effects [Mandal 1986, Hirsch and Mandal 1987, Mandal 1994, Mandal and Burton 1994]; and

(vi) It gives reasonable correlations with experimental datasets [Mandal 1986, Hirsch and Mandal 1987, Mandal 1994, Mandal and Burton 1994]. In the past, several researchers have validated the cascade model and compared the results with other available computational models like the vortex and streamtube models. These comparisons have been published in reputed journals like Wind Engineering [Hirsch and Mandal 1987, Mandal and Burton 1994]. It can be seen from all these published articles that the cascade model gives reasonable correlations with experimental results.

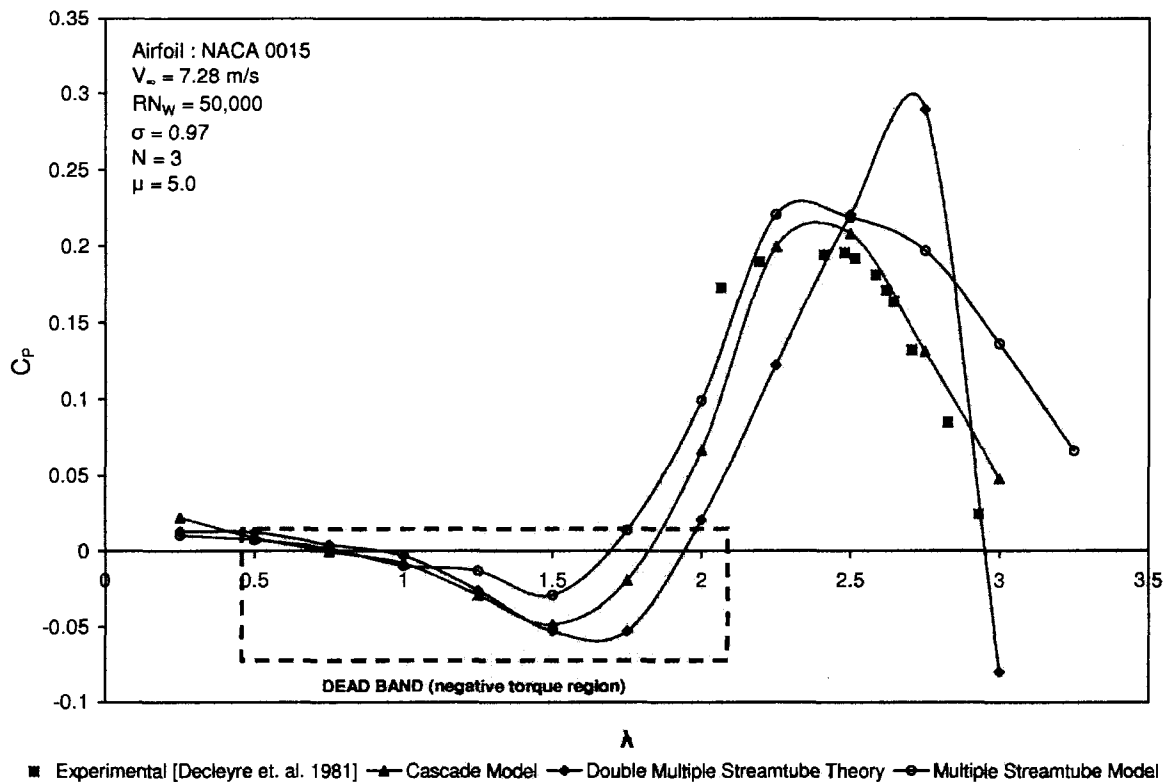


Figure 4.1: Comparison of Experimental and Analytical Power-coefficients by Different Computational Models

A comparative study on three popular computational models has been investigated in the present study. Results obtained from these three models are compared with the experimental datasets of Decleyre et. al [1981] in Figure 4.1. It can be seen from this figure that all the models overpredicts the power coefficient. Among the three mathematical models, the values predicted by the cascade model conform best with the experimental datasets. An important phenomenon can also be observed from this figure, namely the negative C_p values at low tip speed ratios ($\lambda=R\omega/V_\infty$). This region of negative torque, described by Baker [1983] as the “dead band” is an undesirable phenomenon as described in section 2.2.

4.1. Fundamentals of the Cascade Model for SB-VAWT

The basic principle of any turbomachine (like SB-VAWT) is the dynamic force exchange between the fluid and the rotor blades. The periodic equidistant arrangement of several blades or vanes of turbomachinaries is called a cascade. Hence, the cascade is the basic element of the turbomachine, and cascade flow is the essential physical phenomenon for the operation of the machine [Scholz 1977]. Cascade principles have been widely utilized for analysis of turbomachinaries.

Hirsch and Mandal [1987] were the first to apply the cascade principles for the analysis of VAWTs. In this model, the blade airfoils of a turbine are assumed to be positioned in a plane surface (and hence termed as the cascade) with the blade interspace equal to the turbine circumferential distance divided by the number of blades. The relationship between the wake velocity and the free stream velocity is established by using Bernoulli's equation while the induced velocity is related to the wake velocity through an assumed analytical expression.

As mentioned in the previous section, the cascade model gives reasonable correlation with the available experimental data. It can predict the overall values

of both low and high solidity turbines quite well and it takes reasonable computation time. Moreover, the problem of convergence associated with the momentum and vortex theories can be eliminated by using the cascade theory [Mandal and Burton 1994]. In order to strengthen the capability of this model, in 1989 Muniruzzaman and Mandal [1989] included the effect of dynamic stall with cascade theory that gives improved correlation. Mandal and Burton [1994] furthered this work at the Reading University, UK with the effect of dynamic stall including flow curvature that produces significantly better predictions.

4.1.1. Basic Assumptions

To apply the cascade theory for the determination of the performance analysis of a SB-VAWT, the following assumptions are made in order to simplify the analysis:

- (1) The blades on the cylindrical surface are assumed to be developed into a plane surface and this configuration is known as the rectilinear cascade.
- (2) One of the blades is considered as the reference blade and at any instant, power is calculated with the supposition that each of the blades sees the same flow and produces the same power as those of the reference blade. This process is continued at every station with the reference blade for one complete revolution of the turbine. Later the average power is obtained.
- (3) The wake velocity of the upstream side is assumed to act in the axial direction and behave as the free stream velocity on the downstream blade that is positioned behind the upstream blade. The pressure in the wake region of the upstream side is assumed equal to the atmospheric pressure.
- (4) While finding the wake velocity, the flow is assumed to be steady, one-dimensional, incompressible and rotationally symmetric.

4.1.2. Blade Element Angles and Velocities

The flow velocities in the upstream and downstream sides of the SB-VAWTs are not constant, which can be seen in Figure 3.9. From this figure one can observe that the flow is considered to occur in the axial direction. The chordal velocity component V_{cu} and the normal velocity component V_{nu} are respectively obtained from the following expressions

$$V_{cu} = R\omega + V_{au} \cos\theta \quad (4.1)$$

$$V_{nu} = V_{au} \sin\theta \quad (4.2)$$

Referring to Figure 3.9, the angle of attack α_u for the upstream side can be expressed as

$$\alpha_u = \tan^{-1}\left(\frac{V_{nu}}{V_{cu}}\right) \quad (4.3)$$

Introducing the values of V_{nu} and V_{cu} and non-dimensionalizing

$$\alpha_u = \tan^{-1}\left[\frac{\sin\theta}{\left(\frac{R\omega}{V_\infty} / \frac{V_{au}}{V_\infty}\right) + \cos\theta}\right] \quad (4.4)$$

The relative flow velocity W_u for the upstream side is obtained as (Figure 3.2)

$$W_u = \sqrt{V_{cu}^2 + V_{nu}^2} \quad (4.5)$$

Inserting the values of V_{cu} and V_{nu} in Equation (4.5), and non-dimensionalizing, one can find

$$\frac{W_u}{V_\infty} = \frac{W_u}{V_{au}} \cdot \frac{V_{au}}{V_\infty} = \frac{V_{au}}{V_\infty} \sqrt{\left[\left(\frac{R\omega}{V_\infty} / \frac{V_{au}}{V_\infty}\right) + \cos\theta\right]^2 + \sin^2\theta} \quad (4.6)$$

Following the same procedure, similar expressions are obtained for the downstream side. Hence, to determine the angle of attack α_d and the relative

flow velocity W_d for the downstream side, subscript u is replaced by d in Equations (4.4) and (4.6) respectively.

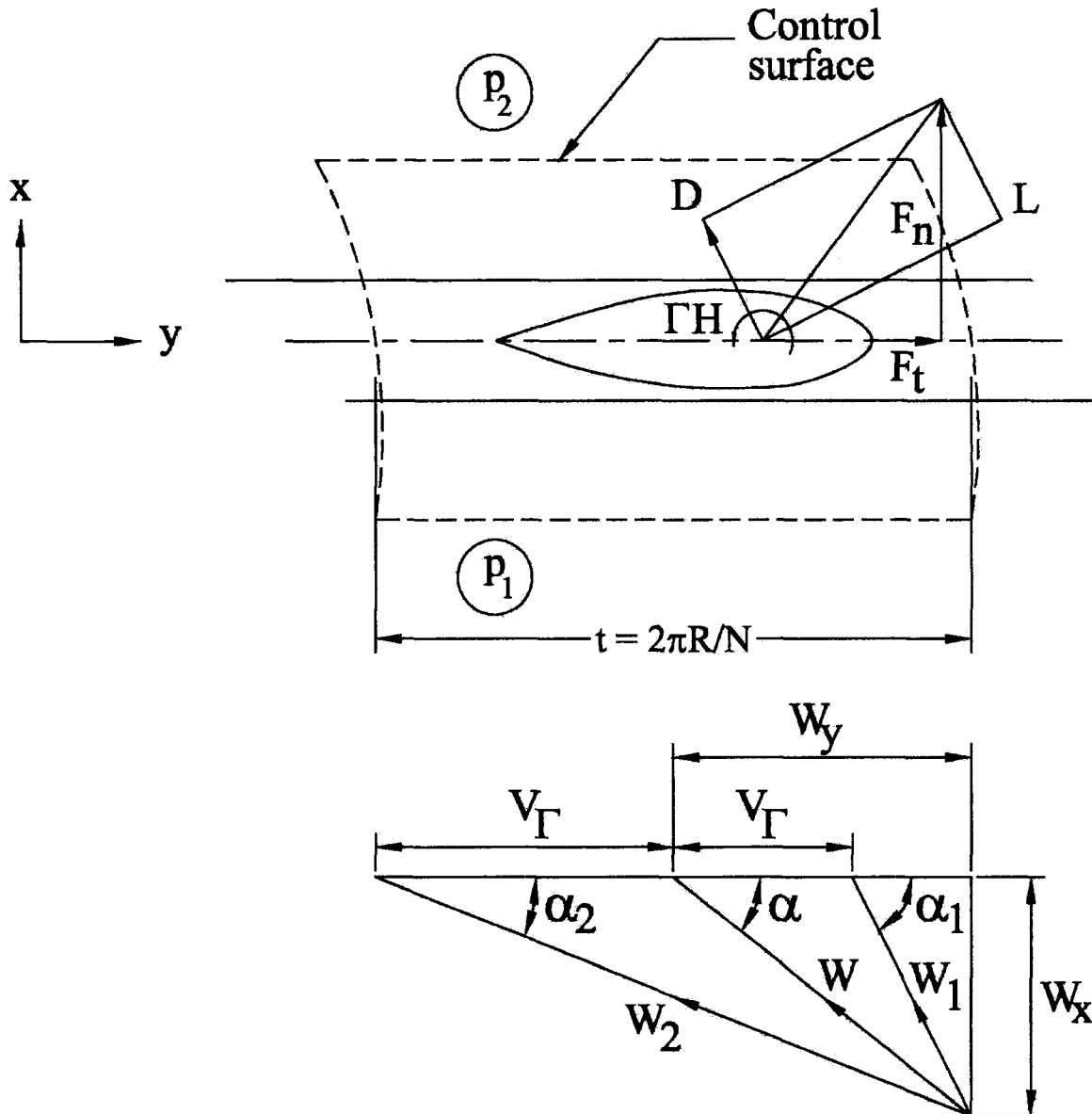


Figure 4.2: Velocity Diagram on a Blade Airfoil

As discussed in Section 3.2.3, the SB-VAWT is developed into a cascade configuration that is shown in Figure 3.8 after determination of the local relative flow velocity and the angle of attack. The cascade is considered in a plane normal to the turbine axis.

In the following analysis, the general mathematical expressions are derived for the upstream and downstream sides by omitting the subscripts u and d. These general expressions can be applied for both the upstream and downstream sides by subscripting the variable parameters (dependent on sides of the turbine) with u for upstream and d for downstream.

Figure 4.2 shows the velocity diagram on the reference blade of the cascade configuration for a SB-VAWT. To perform the analysis a control surface is chosen as shown in this figure. The control surface consists of two lines parallel to the cascade front and two identical streamlines having interspace t . This figure also shows velocities in reference to the blade in the cascade. Referring to Figure 4.2, the expressions of these velocities are obtained as

$$\frac{W_y}{V_\infty} = \frac{W}{V_\infty} \cos \alpha \quad (4.7)$$

$$\frac{W_x}{V_\infty} = \frac{W}{V_\infty} \sin \alpha \quad (4.8)$$

$$\frac{W_1^2}{V_\infty^2} = \frac{W_x^2}{V_\infty^2} + \frac{(W_y - V_\Gamma)^2}{V_\infty^2} \quad (4.9)$$

$$\frac{W_2^2}{V_\infty^2} = \frac{W_x^2}{V_\infty^2} + \frac{(W_y + V_\Gamma)^2}{V_\infty^2} \quad (4.10)$$

where

$$V_\Gamma = \frac{\Gamma H}{2t} = \frac{N\Gamma H}{4\pi R} \quad (4.11)$$

Here W_x and W_y are the components of the relative flow velocity W , in the x - and y - directions respectively where x is chosen along the perpendicular direction and y is chosen along the parallel direction of the cascade front (Figure 4.2). W_1 and W_2 are the relative flow velocities respectively, at the cascade inlet and outlet. The blade airfoil upstream and downstream sides are termed as the cascade inlet and outlet respectively. V_Γ is the velocity contributed by circulation ΓH . The blade spacing is $t=2\pi R/N$. The angles of attack at the cascade inlet α_1 and outlet α_2 are respectively expressed as

$$\alpha_1 = \tan^{-1} \left[\frac{W_x / V_\infty}{(W_y - V_\Gamma) / V_\infty} \right] \quad (4.12)$$

$$\alpha_2 = \tan^{-1} \left[\frac{W_x / V_\infty}{(W_y + V_\Gamma) / V_\infty} \right] \quad (4.13)$$

4.1.3. Aerodynamic Forces

Along the bounding streamlines (Figure 4.2) the pressure forces are cancelled; viscous forces can be neglected outside the boundary layers. There exists only the momentum flux through the straight lines parallel to the cascade front. So, the force in the tangential direction due to the rate of change of momentum is obtained as

$$F_t = \dot{m}(W_2 \cos \alpha_2 - W_1 \cos \alpha_1) \quad (4.14)$$

Applying the continuity equation, the mass flow rate \dot{m} can be determined as

$$\dot{m} = \rho H t W_1 \sin \alpha_1 = \rho H t W_2 \sin \alpha_2 = \rho H t W_x \quad (4.15)$$

From Equations (4.14) and (4.15), one can obtain the expression of F_t as

$$F_t = \rho H t (W_2^2 \sin \alpha_2 \cos \alpha_2 - W_1^2 \sin \alpha_1 \cos \alpha_1) \quad (4.16)$$

The force in the normal direction to the cascade can be found as

$$F_n = \dot{m}(W_1 \sin \alpha_1 - W_2 \sin \alpha_2) + Ht(p_1 - p_2) \quad (4.17)$$

where p_1 and p_2 are respectively the pressures at the cascade inlet and outlet. Introducing the value of \dot{m} from Equation (4.15), Equation (4.17) can be written as

$$F_n = \rho Ht(W_1^2 \sin^2 \alpha_1 - W_2^2 \sin^2 \alpha_2) + Ht(p_1 - p_2) \quad (4.18)$$

Considering the total cascade loss by a total pressure loss term ΔP_{ov} and using Bernoulli's equation between the cascade inlet and outlet, one finds,

$$\frac{p_1}{\rho g} + \frac{W_1^2}{2g} = \frac{p_2}{\rho g} + \frac{W_2^2}{2g} + \frac{\Delta P_{ov}}{\rho g} \quad (4.19)$$

Rearranging,

$$p_1 - p_2 = \frac{\rho}{2}(W_2^2 - W_1^2) + \Delta P_{ov} \quad (4.20)$$

Introducing $W_1 \sin \alpha_1 = W_2 \sin \alpha_2$ (Figure 4.2), one can obtain the expression of normal force from Equations (4.18) and (4.20) as

$$F_n = \frac{\rho Ht}{2}(W_2^2 - W_1^2) + Ht \Delta P_{ov} \quad (4.21)$$

The expressions of the normal force coefficient C_n and the tangential force coefficient C_t are written as

$$C_n = C_l \cos \alpha + C_d \sin \alpha \quad (4.22)$$

$$C_t = C_l \sin \alpha - C_d \cos \alpha \quad (4.23)$$

The non-dimensional tangential force coefficient F_t^+ and normal force coefficient F_n^+ can be defined as

$$F_t^+ = \frac{F_t}{\frac{1}{2} \rho c H V_\infty^2} \quad (4.24)$$

$$F_n^+ = \frac{F_n}{\frac{1}{2} \rho c H V_\infty^2} \quad (4.25)$$

The tangential and normal forces can be defined as

$$F_t = C_t \frac{1}{2} \rho c H W^2 \quad (4.26)$$

$$F_n = C_n \frac{1}{2} \rho c H W^2 \quad (4.27)$$

Now from Equations (4.24), (4.25), (4.26) and (4.27), one can obtain

$$F_t^+ = C_t \frac{W^2}{V_\infty^2} \quad (4.28)$$

$$F_n^+ = C_n \frac{W^2}{V_\infty^2} \quad (4.29)$$

4.1.4. Velocity Contributed by Circulation

The circulation about the blade profile is defined by,

$$\Gamma = \oint_s \vec{W} d\vec{s} \quad (4.30)$$

Its contribution along the streamlines is cancelled by virtue of the opposing directions of s , while the contribution along the parallel direction of the cascade front is retained. As a result, the circulation becomes,

$$\Gamma = t(W_2 \cos \alpha_2 - W_1 \cos \alpha_1) \quad (4.31)$$

From Equations (4.14), (4.15) and (4.31), one can obtain

$$F_t = \rho H W_x \Gamma \quad (4.32)$$

Referring to Figure 4.3, the lift force can be written as

$$L = L_{id} + L_v \quad (4.33)$$

where L_{id} and L_v are respectively the lift force appearing in the frictionless flow and the lift force due to pressure loss.

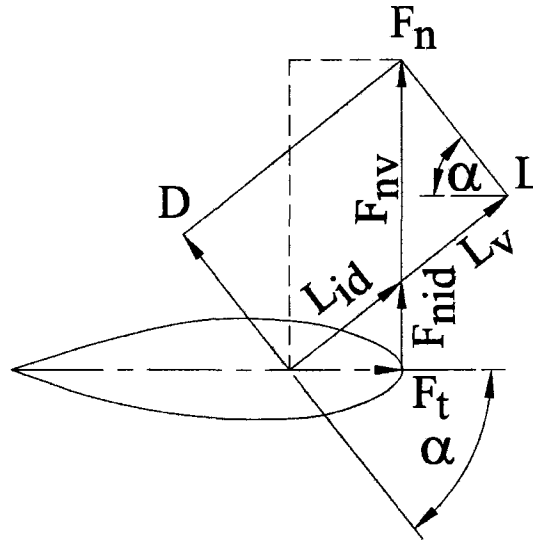


Figure 4.3: Force Diagram on a Blade Airfoil

According to Figure 4.3, L_{id} and L_v can be expressed as

$$L_{id} = \frac{F_t}{\sin \alpha} \quad (4.34)$$

$$L_v = D \cot \alpha \quad (4.35)$$

where D is the drag force on the blade airfoil.

From Equations (4.33), (4.34) and (4.35), one can find

$$L = \frac{F_t}{\sin \alpha + D \cot \alpha} \quad (4.36)$$

Dividing both sides of Equation (4.36) by L , introducing $\varepsilon = D/L$ and arranging

$$\frac{F_t}{L \sin \alpha} = (1 - \varepsilon \cot \alpha) \quad (4.37)$$

or

$$L = \frac{F_t}{\sin \alpha} \frac{1}{(1 - \varepsilon \cot \alpha)} \quad (4.38)$$

Introducing the value of F_t from Equation (4.32), the lift force L becomes,

$$L = \frac{\rho H W_x}{\sin \alpha} \frac{\Gamma}{(1 - \varepsilon \cot \alpha)} \quad (4.39)$$

Since $W_x = W \sin \alpha$ according to Figure 4.2, the lift force can be expressed as ,

$$L = \rho H W \frac{\Gamma}{(1 - \varepsilon \cot \alpha)} \quad (4.40)$$

The lift force L is defined as

$$L = \frac{1}{2} C_l \rho W^2 c H \quad (4.41)$$

From the above two equations (4.40 and 4.41), the expression for the circulation is obtained as

$$\Gamma = \frac{1}{2} C_l c W (1 - \varepsilon \cot \alpha) \quad (4.42)$$

One can obtain the expression of V_Γ from Equations (4.11) and (4.42) as

$$V_\Gamma = \frac{1}{8\pi} C_l \frac{Nc}{R} W (1 - \varepsilon \cot \alpha) H \quad (4.43)$$

Non-dimensionalizing gives

$$\frac{V_\Gamma}{V_\infty} = \frac{1}{8\pi} C_l \frac{Nc}{R} \frac{W}{V_\infty} (1 - \varepsilon \cot \alpha) H \quad (4.44)$$

4.1.5. Total Pressure Loss Term

From Figure 4.3, the normal force can be expressed as

$$F_n = F_{nid} + F_{nv} \quad (4.45)$$

where F_{nid} is the force appearing in the frictionless flow and F_{nv} is the force due to pressure loss. Referring to Figure 4.3, F_{nv} can be expressed as

$$F_{nv} = \frac{D}{\sin \alpha} \quad (4.46)$$

The force F_{nv} can also be expressed as

$$F_{nv} = tH\Delta P_{ov} \quad (4.47)$$

From Equations (4.46) and (4.47), one obtains

$$\Delta P_{ov} = \frac{D}{tH \sin \alpha} \quad (4.48)$$

The drag force D is defined as

$$D = \frac{1}{2} C_d \rho W^2 cH \quad (4.49)$$

As a result, one can find the pressure loss term from Equations (4.48) and (4.49) as

$$\Delta P_{ov} = \frac{\rho}{2} \frac{C_d}{\sin \alpha} \frac{c}{t} W^2 \quad (4.50)$$

where,

$$\frac{c}{t} = \frac{Nc}{2\pi R} = \frac{1}{2\pi} \frac{Nc}{R} \quad (4.51)$$

Now from the above two equations, one obtains

$$\Delta P_{ov} = \frac{\rho}{2} \frac{C_d}{\sin \alpha} \frac{1}{2\pi} \frac{Nc}{R} W^3 \quad (4.52)$$

or, in the non-dimensionalized form

$$\frac{\Delta P_{ov}}{\rho V_{\infty}^2} = \frac{1}{4\pi} \frac{C_d}{\sin \alpha} \frac{1}{2\pi} \frac{Nc}{R} \frac{W^2}{V_{\infty}^2} \quad (4.53)$$

4.1.6. Velocity Ratios

Applying Bernoulli's equation with absolute velocity in front and behind the cascade, one obtains for the upstream side

$$\frac{V_{\infty}^2}{2g} + \frac{p_{\infty}}{\rho g} = \frac{V_{au}^2}{2g} + \frac{p_{1u}}{\rho g} \quad (4.54)$$

$$\frac{V_e^2}{2g} + \frac{p_{\infty}}{\rho g} = \frac{V_{au}^2}{2g} + \frac{p_{2u}}{\rho g} \quad (4.55)$$

where V_{au} and V_e are respectively the induced velocity and the wake velocity for the upstream side, p_{1u} and p_{2u} are the static pressures respectively at the cascade inlet and outlet for the upstream side. In the wake region of the upstream side with the velocity V_e , the pressure is assumed equal to the atmospheric pressure (Figure 4.1). Subtracting Equation (4.55) from Equation (4.54), one finds,

$$\frac{V_{\infty}^2}{2g} - \frac{V_e^2}{2g} = \frac{p_{1u}}{\rho g} - \frac{p_{2u}}{\rho g} \quad (4.56)$$

After rearranging

$$(p_{1u} - p_{2u}) = \frac{\rho}{2} (V_{\infty}^2 - V_e^2) \quad (4.57)$$

Now subscripting the variable parameters in Equation (4.20) by u for the upstream side and balancing with Equation (4.57), one obtains

$$\frac{\rho}{2} (V_{\infty}^2 - V_e^2) = \frac{\rho}{2} (W_{2u}^2 - W_{1u}^2) + \Delta P_{ov_u} \quad (4.58)$$

Again subscripting the variable parameters in Equation (4.52) by u for the upstream side, introducing into Equation (4.58) and dividing throughout by $\rho/2$, one can find

$$V_{\infty}^2 - V_e^2 = (W_{2u}^2 - W_{1u}^2) + \frac{1}{2\pi} \frac{Nc}{R} \frac{C_{d_u}}{\sin \alpha_u} W_u^2 \quad (4.59)$$

From Equation (4.59), the expression of the wake velocity in the non-dimensionalized form for the upstream side can be expressed as

$$\frac{V_e}{V_{\infty}} = \sqrt{1 - (W_{2u}^2 - W_{1u}^2) - \frac{1}{2\pi} \frac{Nc}{R} \frac{C_{d_u}}{\sin \alpha_u} \frac{W_u^2}{V_{\infty}^2}} \quad (4.60)$$

Similarly, the expression of the wake velocity in the non-dimensionalized form for the downstream side can be found as

$$\frac{V_w}{V_e} = \sqrt{1 - \left(\frac{W_{2d}^2}{V_e^2} - \frac{W_{1d}^2}{V_e^2} \right) - \frac{1}{2\pi} \frac{Nc}{R} \frac{C_{d_d}}{\sin \alpha_d} \frac{W_d^2}{V_e^2}} \quad (4.61)$$

The wake velocity ratio for the downstream side can be related as

$$\frac{V_w}{V_{\infty}} = \frac{V_w}{V_e} \frac{V_e}{V_{\infty}} \quad (4.62)$$

In the cascade model to find the induced velocity a relationship between the wake velocity and the induced velocity is introduced. For the upstream side this is expressed as

$$\frac{V_{au}}{V_{\infty}} = \left(\frac{V_e}{V_{\infty}} \right)^{k_i} \quad (4.63)$$

and for the downstream side, this is expressed as

$$\frac{V_{ad}}{V_e} = \left(\frac{V_w}{V_e} \right)^{k_i} \quad (4.64)$$

The value of the exponent k_i is found from a fit of experimental results. The induced velocity ratio for the downstream side can be written in the form,

$$\frac{V_{ad}}{V_\infty} = \frac{V_{ad}}{V_e} \frac{V_e}{V_\infty} = \frac{V_e}{V_\infty} \left(\frac{V_w}{V_e} \right)^{k_i} \quad (4.65)$$

The expression of the exponent k_i is written in accordance with Hirsch and Mandal [1987] as

$$k_i = (0.425 + 0.332\sigma) \quad (4.66)$$

where $\sigma = \frac{Nc}{R}$

4.1.7. Rotor Power Coefficient

General expressions are given in this section for the upstream and downstream sides thereby omitting the subscripts u and d. The same expressions can be used for the upstream and downstream sides by subscripting the variable parameters with u (upstream) and d (downstream).

Equations (4.16) and (4.21) can be expressed in the following form after inserting $t=2\pi R/N$.

$$F_t(\theta) = \frac{2\pi}{N} \rho R^2 \frac{H}{R} (W_2^2 \sin\alpha_2 \cos\alpha_2 - W_1^2 \sin\alpha_1 \cos\alpha_1) \quad (4.67)$$

$$F_n(\theta) = \frac{\pi}{N} \rho R^2 \frac{H}{R} (W_2^2 - W_1^2) + \frac{2\pi}{N} R^2 \frac{H}{R} \Delta P_{ov} \quad (4.68)$$

Since the tangential and normal forces represented by Equations (4.67) and (4.68) are for any azimuthal position, they are considered as a function of azimuth angle θ .

Average tangential force on one blade can be expressed as

$$F_{ta} = \frac{1}{2\pi} \int_0^{2\pi} F_t(\theta) d\theta \quad (4.69)$$

The torque for the number of blades N is obtained as

$$Q = NF_{ta}R \quad (4.70)$$

From Equations (4.67), (4.69) and (4.70), one can find

$$Q = \rho R^3 \frac{H}{R} \int_0^{2\pi} (W_2^2 \sin \alpha_2 \cos \alpha_2 - W_1^2 \sin \alpha_1 \cos \alpha_1) d\theta \quad (4.71)$$

The turbine torque coefficient is defined by

$$C_Q = \frac{Q}{\frac{1}{2} \rho A V_\infty^2 R} \quad (4.72)$$

After inserting $A=2RH$ into (4.71) and substitution into (4.72), the expression for torque coefficient becomes

$$C_Q = \int_0^{2\pi} \left(\frac{W_2^2}{V_\infty^2} \sin \alpha_2 \cos \alpha_2 - \frac{W_1^2}{V_\infty^2} \sin \alpha_1 \cos \alpha_1 \right) d\theta \quad (4.73)$$

The turbine overall power coefficient is obtained from the expression

$$C_p = C_Q \cdot \lambda \quad (4.74)$$

where $\lambda = \frac{R\omega}{V_\infty}$ is the tip speed ratio. In order to determine the turbine overall torque coefficient, numerical integration is performed by the help of Simpson's rule.

4.2. Input of Airfoil Aerodynamic Coefficients

For performance analysis of SB-VAWTs, one of the critical tasks is to input the characteristics of airfoils in terms of lift, drag and moment coefficients. In order to run the cascade model, airfoil characteristic datasets have to be fed into the main program for $0^\circ \leq \alpha \leq 360^\circ$.

Typical C_l - α , C_d - α and C_m - α curves for a symmetrical NACA 0015 and asymmetric GÖ420 airfoil are shown from Figures 4.4 to 4.9. It can be seen from Figure 4.4 and 4.7 that, up to the stall angle, C_l varies approximately linearly with α and this slope is called the lift slope. In this region the flow moves smoothly over the airfoil and is attached over most of the surface [Anderson 2001]. C_l starts with zero lift at zero incidence for the symmetrical sections (such as the NACA 0015 as shown in Figure 4.4) and with positive lift at zero incidence for cambered sections (such as the GÖ 420 as shown in Figure 4.7).

Usually, the slope of this lift-line curve in the pre-stall regime is approximately 0.1 per degree [Kuhlman and Kuhlman 1995]. As stall is approached, the slope decreases until at stall C_l reaches a peak value of 0.8 – 1.45 for the conventional airfoils (like NACA and GÖ airfoils), and up to 2 for some airfoils, depending on the airfoil shape and RN [Kirke 1998]. As α becomes large, the flow tends to separate from the top surface of the airfoil, creating a large wake of relatively “dead air” behind the airfoil where flow is recirculating and part of the flow is actually moving in a direction opposite to the free stream [Anderson, 2001].

To facilitate the input process, two-dimensional airfoil lift and drag coefficients below and above the stall angle have been treated separately in the present computational scheme. Furthermore, the effect of aspect ratio due to finite length of the SB-VAWT blades is also considered in the present study to improve the accuracy of the analysis.

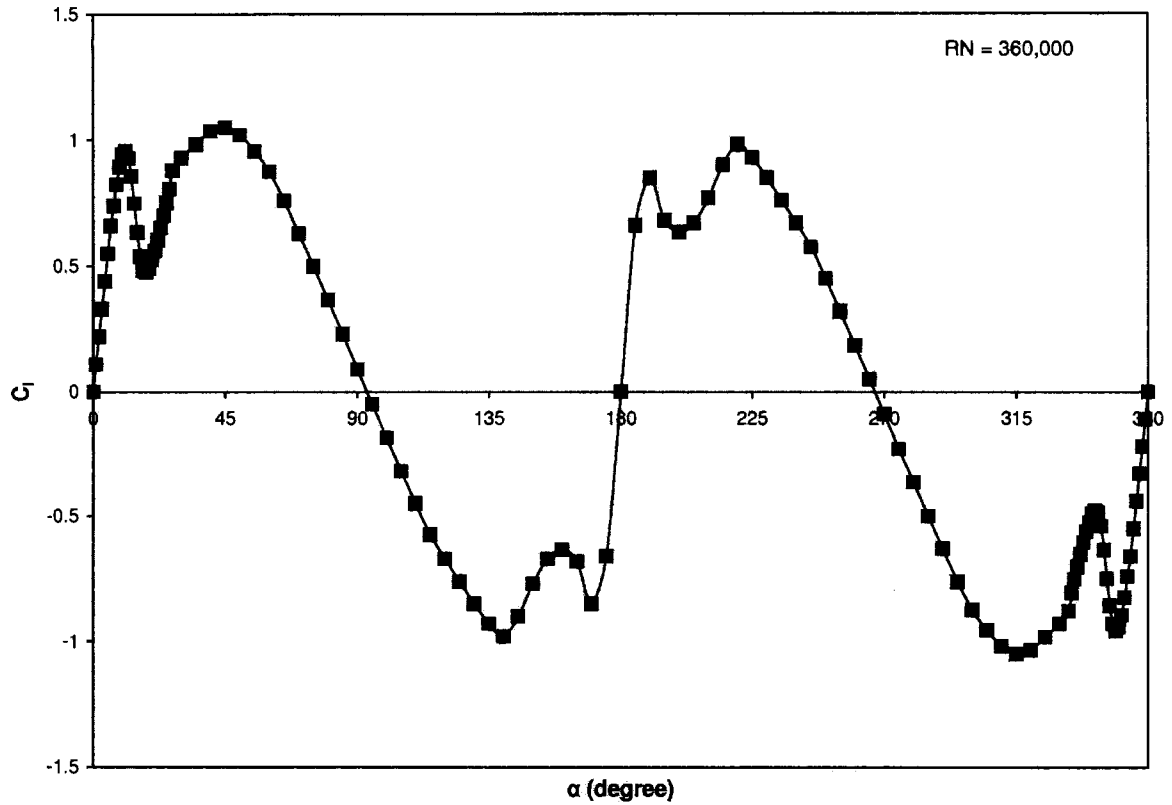


Figure 4.4: C_l - α Curve of NACA 0015 at $RN=360,000$ [Based on datasets of Cyberiad 2007]

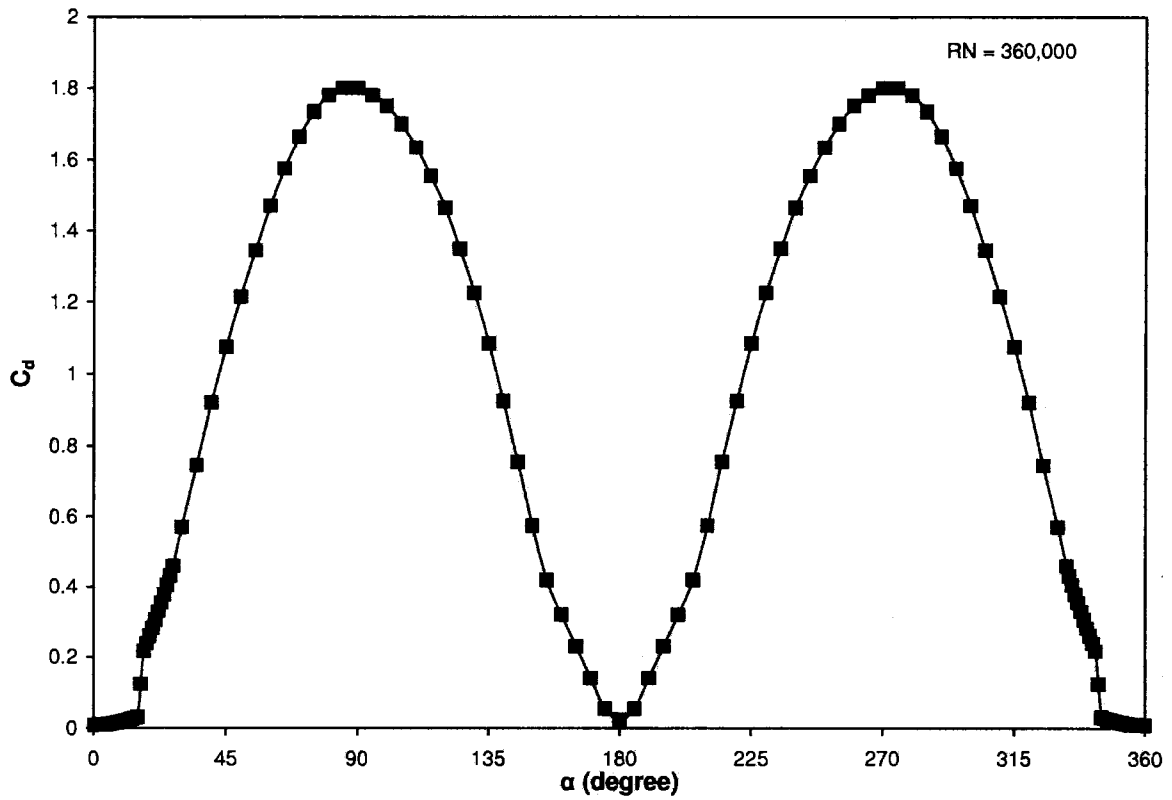


Figure 4.5: C_d - α Curve of NACA 0015 at $RN=360,000$ [Based on datasets of Cyberiad 2007]

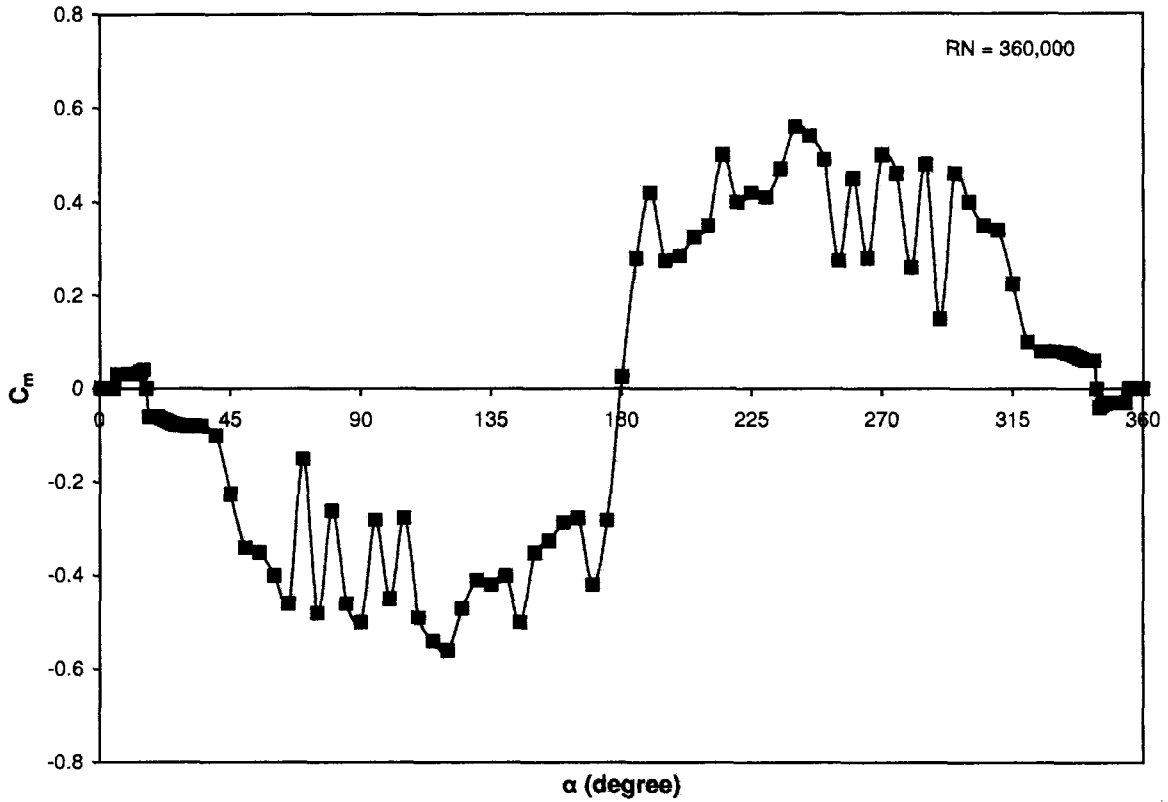


Figure 4.6: C_m - α Curve of NACA 0015 at $RN=360,000$ [Based on datasets of Cyberiad 2007]

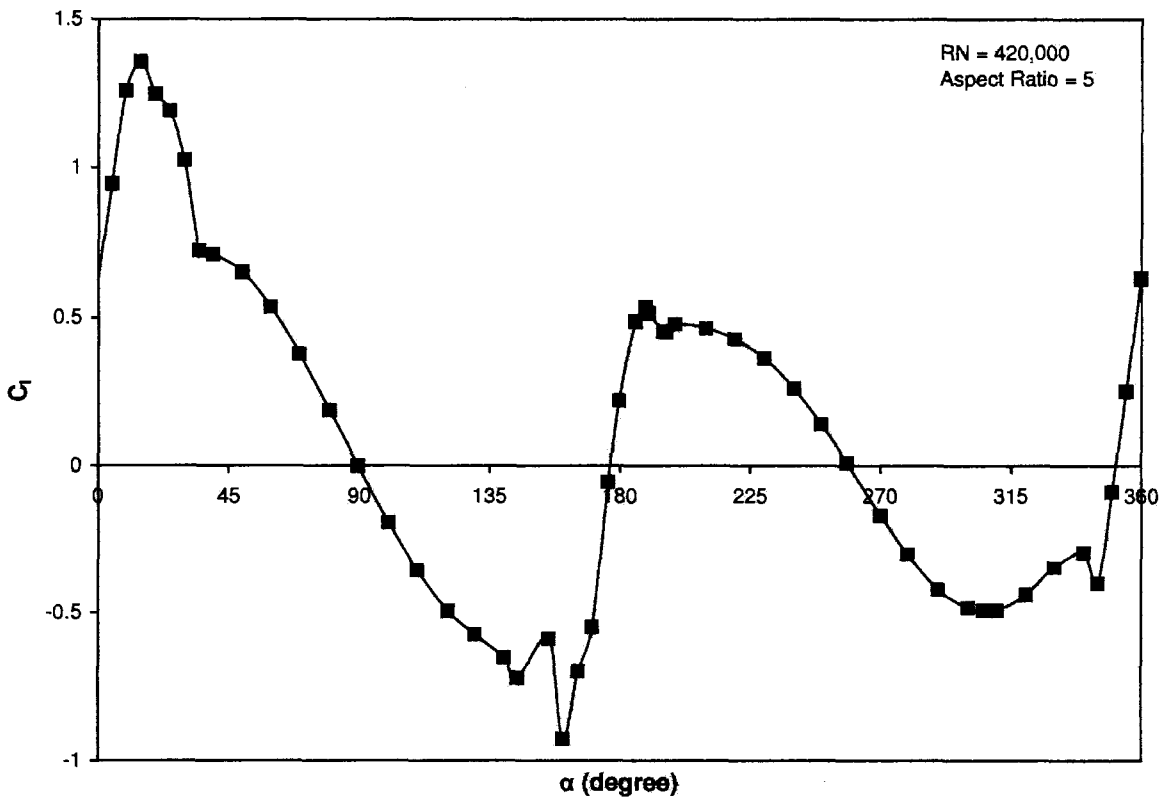


Figure 4.7: C_l - α Curve of Gö 420 at $RN=420,000$ [Based on datasets of Riegels 1961]

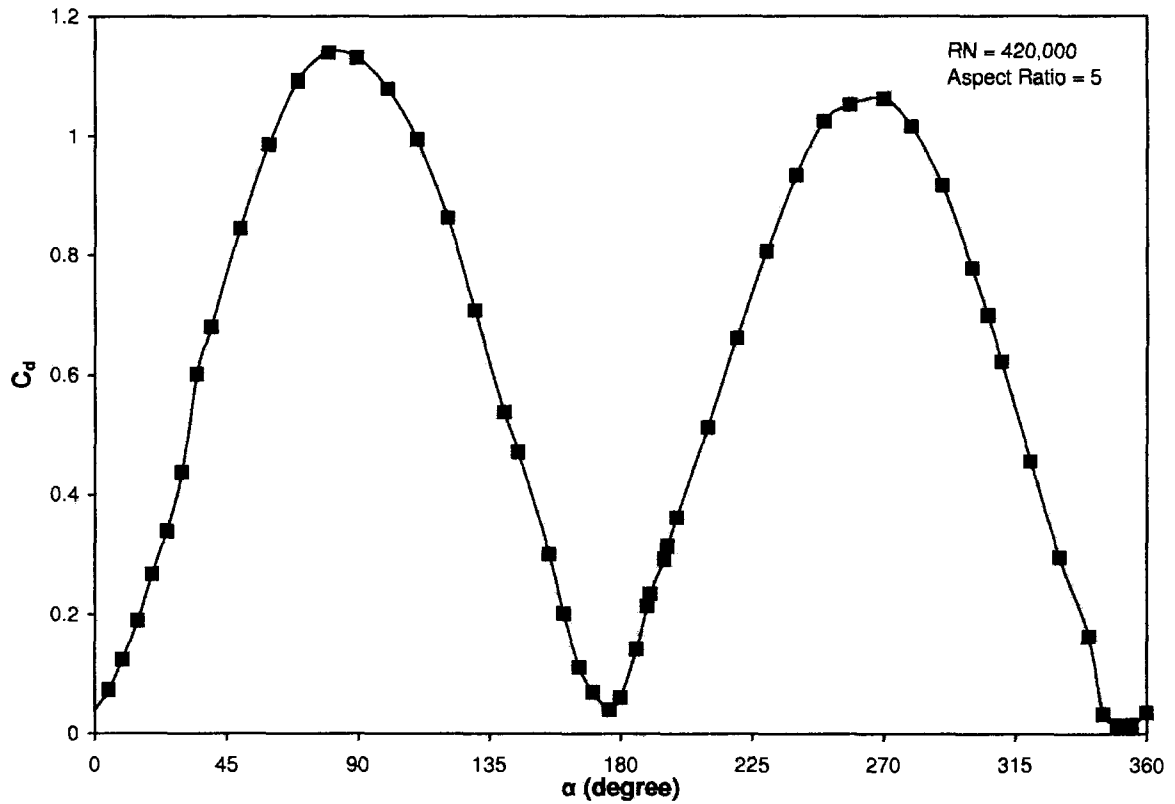


Figure 4.8: C_d - α Curve of Gö 420 at $RN=420,000$ [Based on datasets of Riegels 1961]

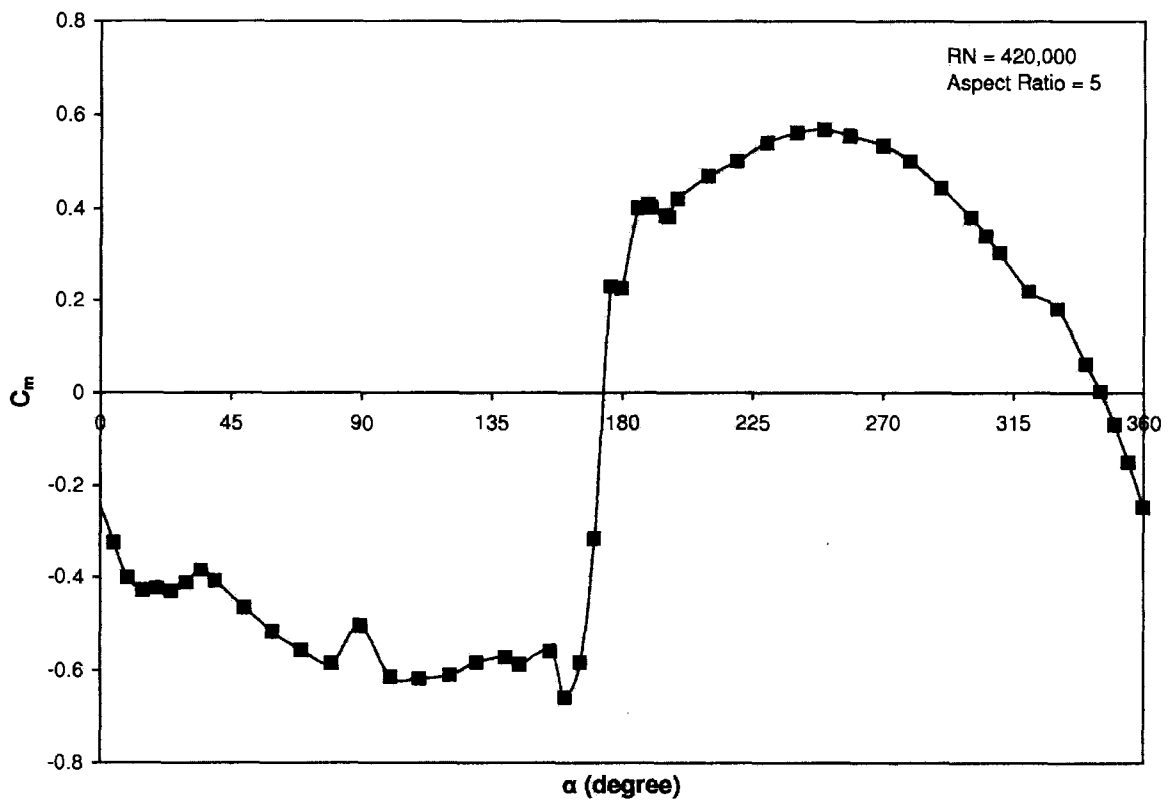


Figure 4.9: C_m - α Curve of Gö 420 at $RN=420,000$ [Based on datasets of Riegels 1961]

4.2.1. Two-dimensional Pre-Stall Input Datasets

In the original cascade model [Hirsch and Mandal 1987], the values of lift and drag characteristics of only two airfoils (namely NACA 0012 and NACA 0015) were used. The two-dimensional lift and drag coefficients for these two symmetric airfoils were taken from different sources including Jacob and Sherman [1937], Sheldahl and Blackwell [1976] and Willmer [1979]. The variation of lift and drag coefficients in the pre-stall regime for NACA 0015 were used in the original cascade model. The airfoil characteristics (i.e. lift and drag coefficients) were fed into the model by analytical expressions derived through linear regression of experimental data for a wide range of different Reynolds numbers. Mandal also considered the effect of finite aspect ratio as outlined in Section 4.2.3.

At present there is a lack of experimental results of airfoils at low RN. A comprehensive search for low RN airfoil lift, drag and moment coefficient data done by Kirke [1998] over a wide range of α yielded only a very limited range of useful information. Kirke [1998] found the following gaps in the low RN airfoil data:

- “(i) No actual test data are available for solid, rigid aerofoil sections (as distinct from cambered plates and sails) at high incidence and RN below 250,000;*
- “(ii) No data are available for cambered sections through the full 360° incidence;*
- “(iii) Only two sources of post stall C_M data are available, and of these, only one covers the full 360° incidence;*
- “(iv) Given that tests on nominally identical aerofoils under nominally identical conditions in different wind tunnels frequently give inconsistent results, especially at low RN where the formation and collapse of laminar separation bubbles makes performance hard to predict, the lack of comparisons between aerofoils of differing camber in the same wind tunnel is of particular concern.”*

Apart from the above bleak scenario of non-availability of low RN datasets, experimental results at low RN ranges are highly problematic [Hepperle 2007] as well. According to Hepperle - *“The scatter of the experimental data is just a matter of fact, caused by the underlying physics”*. According to McGhee and Walker [1989] - *“Experimental results obtained on various airfoils at low Re in different wind tunnels have shown large differences in airfoil performance ... This is not surprising because of the sensitivity of the airfoil boundary layer to free-stream disturbances, model contour accuracy, and model surface roughness. ... At Re of 100,000 or less, the flow phenomena are dominated by the presence of large laminar separation bubbles...”*.

McCrosky [1987] has shown that even nominally identical sections tested at similar RN in different wind tunnels may give different results [Kirke 1998]. Factors contributing to this variability have been discussed by McGhee and Walker [1989]. The formation of a laminar separation bubble, which markedly affects performance, is sensitive to factors such as surface roughness, inaccuracies in profile, and air turbulence, all of which may vary between a wind tunnel model, a field prototype and a commercially produced turbine [Kirke 1998]. McCrosky [1987] compared all available data for the NACA 0012 section (which is probably the most studied section of all) and concluded that – *“the scatter in the total ensemble of data is unacceptable in the author’s view, and it is not readily apparent which of these results are correct”*.

Because of the above-mentioned two critical factors: (a) non-availability of low RN airfoil datasets and (b) problematic low RN experimentation process, an alternative way was sought in the present study to obtain airfoil datasets which is described in the subsequent paragraphs.

In the pre-stall regime, which can also be interpreted as attached flow regime for $-15^\circ \leq \alpha \leq 15^\circ$, the general behavior of airfoils are well understood. According to Lissaman [1994] – *“Airfoil behavior in this regime can be very accurately*

estimated by the wealth of theory and data accumulated in half-century of refining two-dimensional airfoil theory for application of wings. Methods exist for accurate analytical estimation of the lift and drag forces in this regime, and there is also an extensive literature presenting experimental data". Realizing this fact, attempts have been made for the present analysis to acquire datasets for this regime from both experimental results and the analytical tool XFOIL as shown in Figure 4.10.

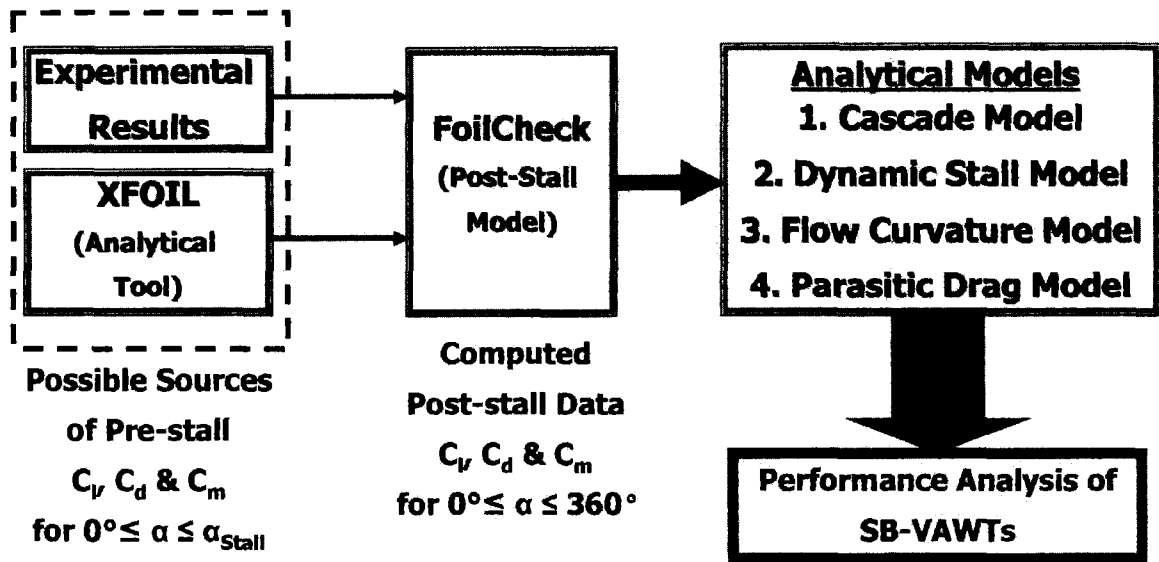


Figure 4.10: Flow Diagram of the Computational Scheme for Performance Analysis of SB-VAWTs

XFOIL [2007] has been used in this study to generate the required 2D datasets of lift, drag and moment coefficients in the pre-stall regime. XFOIL is an interactive program developed at MIT by Mark Drela [Drela 1989] for the design and analysis of subsonic isolated airfoils and it has been widely utilized for low RN airfoil analysis by renowned wind turbine related research organizations including NREL [Somers and Maughmer 2002], Risoe [Dahl and Fuglsang 1998, Dahl 1999] and Delft University [Timmer and Rooy 1992]. Details about XFOIL have been presented in Appendix C.

4.2.2. Modeling of Post-stall Airfoil Behavior

It has been mentioned in Section 2.3.2 that airfoil behavior in the post-stall regime is very important for proper analysis of SB-VAWTs. However, airfoil lift, drag and moment characteristics at high angles of attack (i.e. the post-stall regime) are not available for many airfoils of interest to wind turbine analysts [Hansen and Butterfield 1993] and in this regime the flow becomes less dependent on the airfoil shape and behaves similar to high angle of attack flow around flat plates.

Obtaining experimental results of airfoil lift, drag and moment coefficients up to angles of attack of 90° is quite unusual. Most tables or graphs of airfoil aerodynamic behavior only go up to the stall angle or a little higher and usually end at between 15° and 20° . Due to this lack of experimental datasets for post-stall region, designers are forced to adopt different types of semi-empirical models to generate data. In his original cascade model, Mandal took the values of post-stall lift and drag coefficients of symmetric NACA 0012 and NACA 0015 airfoils from the two-dimensional datasets of Sheldahl and Klimas [1981]. Due to this, an effort has been made to find a suitable post-stall model for the present study.

In the past, several researchers, like Beans and Jakubowski [1983], Kirke [1998] and Viterna-Corrigan [1981], attempted to model the airfoil behavior in the post-stall regimes by extrapolating the available airfoil data across the entire 360° range of potential angles of attack [Jonkman 2003]. An elaborate comparative study was carried out by Kirke [1998] between his approach and that of Beans and Jakubowski [1983]. However, it was found from the literature survey that the approach of Viterna-Corrigan [1981] has become the most widely used post-stall model at the moment which conforms well to the experimental results [Lissaman 1994]. This model can be used to predict the lift and drag coefficients

in the post-stall regimes of any airfoil just by using only a few pieces of experimental or computed data in the pre-stall regime [Lissaman 1994].

For the present analysis, the FoilCheck program of NREL's NWTC [NWTC Design Codes 2007] has been utilized to generate different airfoil characteristics between $0 \leq \alpha \leq 360^\circ$ using the computational 2D results obtained from XFOIL in the pre-stall regime as shown in Figure 4.10. FoilCheck uses a combination of wind tunnel data and the Viterna-Corrigan model equations for deep stall to generate airfoil data for all angles from a limited set of measurements. Details of FoilCheck can be found in the reference [NWTC Design Codes 2007].

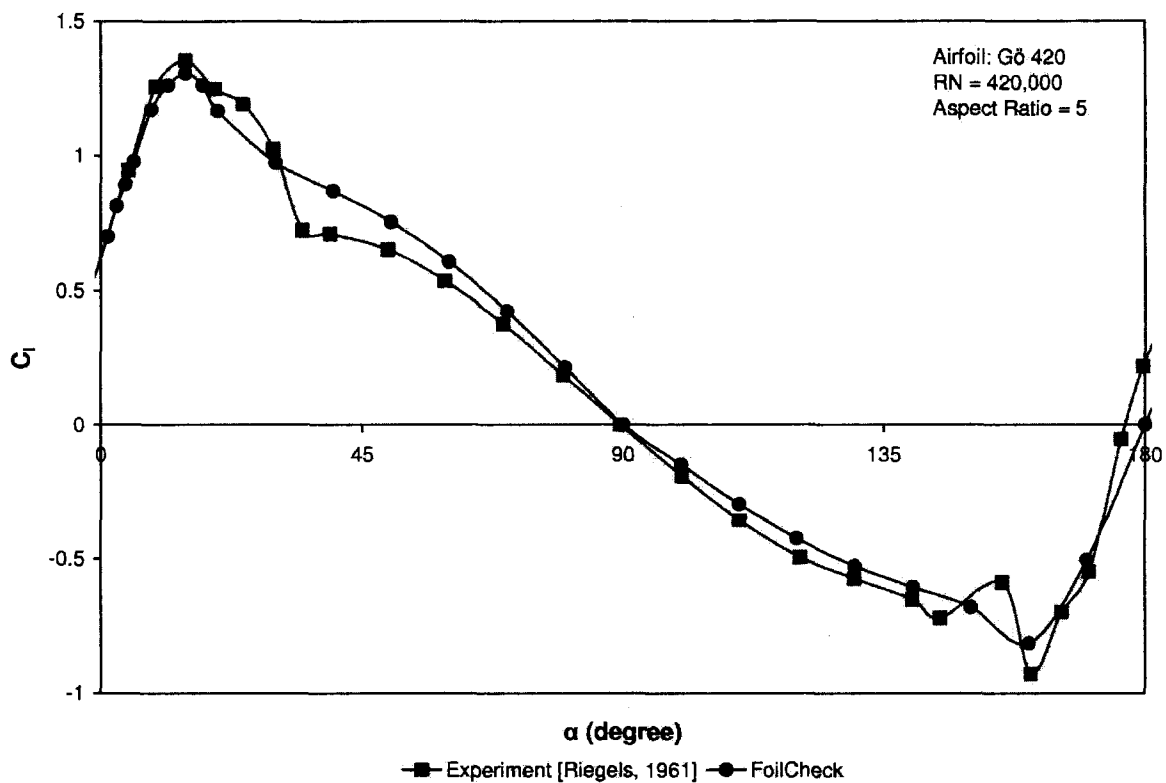


Figure 4.11: Comparison of C_l - α Curves of Experimental Datasets and FoilCheck Results

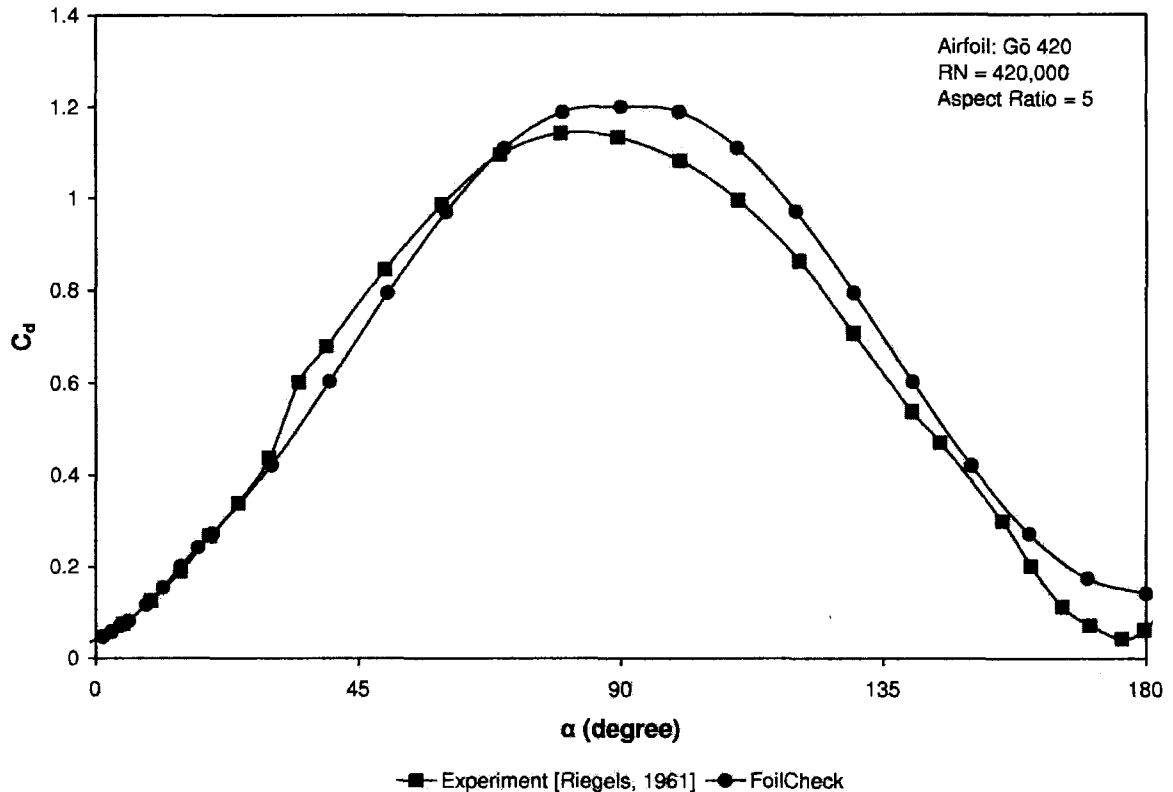


Figure 4.12: Comparison of C_d - α Curves of Experimental Datasets and FoilCheck Results

In Figures 4.11 and 4.12, comparison of C_l - α and C_d - α curves of experimental results of Göt 420 have been compared with the FoilCheck results. Here, XFOIL outputs obtained for the pre-stall (or attached) regime has been used for obtaining the Foilcheck results. It can be seen from Figure 4.11 that FoilCheck results for C_l conform reasonably to the experimental results. However, the C_d - α curve of FoilCheck is slightly higher in the post-stall regimes, as seen from Figure 4.12.

4.2.3. Effect of Aspect Ratio

Two dimensional lift and drag characteristics are normally presented based on an infinite aspect ratio. So, these characteristics cannot be directly used to find the performance of a SB-VAWT whose blades are finite. Hence, corrections for the finite aspect ratio are necessary before using those airfoil characteristics for the

performance analysis. Since the finite wing and finite blade of a SB-VAWT are of similar pattern, so, wing theory may be applied for the finite aspect ratio corrections of airfoil characteristics before using them for the performance analysis of SB-VAWT.

For the wing of finite span, there always occurs downwash (which is the velocity component in the downward direction of the wing) and power required to induce downwash is expressed in terms of the induced drag. The downwash velocity is created by the presence of tip vortices.

The total drag coefficient of a finite wing is given by

$$C_D = C_D' + C_{Di} \quad (4.75)$$

where C_D' is the profile drag coefficient for the infinite aspect ratio while C_{Di} is the induced drag coefficient. C_{Di} is expressed as

$$C_{Di} = \frac{C_l^2}{\pi\mu} \quad (4.76)$$

where μ indicates the aspect ratio of the turbine blade. Introducing the value of C_{Di} into Equation (4.75),

$$C_D = C_D' + \frac{C_l^2}{\pi\mu} \quad (4.77)$$

The angle of attack corrected for the finite aspect ratio effect is obtained as

$$\alpha = \alpha' + \alpha_i \quad (4.78)$$

where α' indicates the angle of attack for the infinite wing and α_i is the induced angle. The expression of the induced angle α_i is

$$\alpha_i = \frac{C_l}{\pi\mu} \quad (4.79)$$

Substituting Equation (4.79) into Equation (4.78), one finds

$$\alpha = \alpha' + \frac{C_l}{\pi\mu} \quad (4.80)$$

The above two equations (4.77) and (4.80) are developed on the assumption of uniform distribution of downwash, and they are explicitly valid only for wings possessing an elliptic lift distribution. However, other cases are dealt with by considering appropriate correction factors. Letting τ be the correction factor for the induced angle and δ is the correction factor for the induced drag, the expressions of C_D and α become

$$C_D = C_D' + \frac{C_l^2}{\pi\mu}(1 + \delta) \quad (4.81)$$

$$\alpha = \alpha' + \frac{C_l}{\pi\mu}(1 + \tau) \quad (4.82)$$

For a rectangular wing there are two limiting cases. When the chord is large compared with the span, aspect ratio approaches zero and in this case loading becomes an elliptical distribution. However, as the aspect ratio increases to infinity the loading approaches a rectangular distribution. The values of τ and δ are obtained from Milne-Thompson [1973] and Riegels [1961].

In the present analysis, the above mentioned expressions are only applied in the pre-stall drag coefficient and angle of attack to consider the finite aspect ratio of the blades of SB-VAWT. For the post-stall airfoil behavior, the aspect ratio is considered by the FoilCheck.

4.3. Modeling of Dynamic Stall Effect

As discussed in Section 2.3.3, when the angle of attack remains constant or varies slowly with time, the SB-VAWT encounters the static stall. But when the angle of attack changes rapidly with time, the turbine experiences the dynamic stall which is a complex and unsteady flow phenomenon. Aerodynamic forces due to dynamic stall may be much higher than those due to static stall. As a result, for the performance analysis of SB-VAWTs, especially for the local forces, there can be substantial differences between the experimental data and the calculated values unless the dynamic stalling effect is added [Mandal and Burton 1994].

There are several empirical methods for predicting the effect of dynamic stall and among them are those based on numerical correlations of dynamic stall delay such as the Boeing-Vertol method by Gormont [1973]. The Boeing-Vertol model was developed for helicopter rotor blades and several researchers have modified the original model for VAWTs [Mandal and Burton 1994, Paraschivoiu 2002]. It is currently the most popular model for its simplified approach with reasonable accuracy.

Strickland et. al [1980] were among the first to propose an adaptation of the Boeing-Vertol model for VAWTs. In their adaptation, the simplified Boeing-Vertol model is applied only when α is in the post-stall regime. Mandal and Burton [1994] also utilized the modified Boeing-Vertol model with their cascade model and they applied the Boeing-Vertol model when the angle of attack α is greater than the static stall angle or when the angle of attack decreases after having been above the stall angle. In their model [Mandal and Burton 1994] the Boeing-Vertol stall is turned off when the angle of attack is below the stall angle and increasing. Mandal and Burton [1994] also considered the dynamic stalling effect in the pre-stall condition from $\alpha=5$ degree up to the stall angle in the similar manner as that of ECN [Bultee! 1987-88], and they found the instantaneous blade forces and wake velocities downstream of the VAWT are calculated

reasonably well by their dynamic stall model and flow curvature model with the cascade model [1994].

It has been reported by some researchers that the Boeing-Vertol model tends to overpredict the effects of dynamic stall at large angles of attack [Paraschivoiu 2002]. To overcome this limitation, Masse [1981] and Berg [1983] introduced a modification factor which linearly interpolates the lift and drag values at static and dynamic conditions. In the present research, this modified version of Boeing-Vertol model suggested by Berg [1983], which satisfactorily correlates with experimental results [Paraschivoiu 2002], has been applied with the original cascade model for better performance analysis of SB-VAWT. Additionally, the modifications of lift and drag coefficients are done in the pre-stall regime in accordance with Mandal and Burton [1994]. The dynamic stall model of Mandal and Burton [1994], Masse [1981] and Berg [1983] are briefly described in the subsequent headings.

4.3.1. Dynamic Stall Model of Mandal and Burton [1994]

To include the effect of dynamic stall in the design process, the Boeing-Vertol stall model [Gormont 1973] was applied by Mandal and Burton [1994] in their cascade model with a view to determining the lift characteristics of the airfoil. This formulation is applied when the angle of attack is greater than the static stall angle. The Boeing-Vertol stall model is turned off when the angle of attack is below the stall. To simplify the analysis and eliminate the deficiency associated with the original Boeing-Vertol stall model, some modifications are done: one for lift characteristics in the pre-stall condition and another for the drag characteristics [Mandal and Burton 1994].

In the model of Boeing-Vertol, the blade angle is modified. The modified angle of attack α_m is determined from the following relation,

$$\alpha_m = \alpha - \gamma \cdot k_t \left(\sqrt{\frac{c\dot{\alpha}}{2W}} \right) S_{\dot{\alpha}} \quad (4.83)$$

where α is the effective blade angle of attack, γ and k_1 are empirical constants, $\dot{\alpha}$ denotes the instantaneous rate of change of α , $S_{\dot{\alpha}}$ is the sign of $\dot{\alpha}$ and W is the relative flow velocity. This modified angle of attack is used to calculate the lift coefficient due to the dynamic stalling effect (C_{ld}) in the following manner,

$$C_{ld} = \left(\frac{\alpha}{\alpha_m - \alpha_o} \right) C_l(\alpha_m) \quad (4.84)$$

where $C_l(\alpha_m)$ is the lift value chosen corresponding to the modified angle of attack α_m , and α_o is the angle of zero lift. For low Mach numbers and for airfoil thickness to chord ratios greater than 0.1, the value of γ is,

$$\gamma = 1.4 - 6(0.06 - t_c) \quad (4.85)$$

where t_c is the maximum airfoil thickness ratio. The k_1 value changes with the sign of the effective angle of attack and this is obtained from the relation,

$$k_1 = 0.75 + 0.25xS_{\dot{\alpha}} \quad (4.86)$$

This formulation is applied [Gormont 1973] when the angle of attack α is greater than the static stall angle or when the angle of attack is decreasing after having been above the stall angle. The Boeing-Vertol stall is turned off when the angle of attack is below the stall angle and increasing. In the present analysis in the pre-stall condition, the dynamic stalling effect is also encountered from $\alpha=5$ degree up to the stall angle in the similar manner as that of ECN [Bulteel 1987-88]. The dynamic lift C_{ld} is calculated by using the Boeing-Vertol model and the lift coefficient in the pre-stall condition (C_{lp}) is obtained according to the ECN model from the relation,

$$C_{lp} = P_f C_{ld}(\alpha_m) + (1 - P_f) C_l(\alpha) \quad (4.87)$$

where the factor P_f is determined from the following linear equation,

$$P_f = \frac{\alpha - 5}{\alpha_s - 5} \quad (4.88)$$

where α_s is the stalling angle. This equation means that at $\alpha=5$ degree, $P_f = 0$ and at $\alpha = \alpha_s$, $P_f = 1.0$, which means that at $\alpha=5$ degree, the contribution of C_{ld} is zero while that at $\alpha = \alpha_s$ the contribution of C_{ld} is maximum.

To consider the effect of drag characteristics due to dynamic stall in the analysis, the following empirical relation [Muniruzzaman and Mandal 1993] is used,

$$C_{dd} = \frac{C_{ld}}{C_l(\alpha)} C_d(\alpha) K \quad (4.89)$$

where K is a factor, chosen as 1.0 in the expression. Equation (4.89) signifies that the dynamic drag characteristic is proportional to the dynamic lift characteristic.

4.3.4. Modified Boeing-Vertol Model by Masse [1981] and Berg [1983]

Masse [1981] proposed the computation of modified dynamic coefficients based on a linear interpolation between the dynamic coefficient predicted by Gormont's model [1973] and the static coefficient as follows:

$$C_{ld}^{\text{mod}} = \begin{cases} C_l + \left[\frac{A_M \alpha_{ss} - \alpha}{A_M \alpha_{ss} - \alpha_{ss}} \right] (C_{ld} - C_l), & \text{when } \alpha_{ss} \leq A_M \alpha_{ss} \\ C_l & \text{when } \alpha > A_M \alpha_{ss} \end{cases}$$

$$C_{dd}^{\text{mod}} = \begin{cases} C_d + \left[\frac{A_M \alpha_{ss} - \alpha}{A_M \alpha_{ss} - \alpha_{ss}} \right] (C_{dd} - C_d), & \text{when } \alpha_{ss} \leq A_M \alpha_{ss} \\ C_d & \text{when } \alpha > A_M \alpha_{ss} \end{cases}$$

where $A_M=1.8$ is an empirical constant. Starting with the above modification by Masse, Berg [1983] proposed the use of $A_M=6$ which satisfactorily correlates the

predicted and experimental performance of Sandia 17-m VAWT [Paraschivoiu 2002]. The details of the original Boeing-Vertol model and its subsequent modifications by Masse [1981] and Berg [1983] can be found in Paraschivoiu [2002].

4.4. Modeling of Flow Curvature Effect

As discussed in Section 2.3.4, analysis of the performance of a VAWT with blades of a given airfoil section is complicated further by the fact that a blade describing a curvilinear path behaves differently from the same blade moving in a straight line, so that static tests in a wind tunnel do not necessarily give an accurate guide to the behavior of a VAWT blade. The curvilinear behavior of an airfoil is shown in Figure 4.13 where the typical variation of relative velocity (W) and angle of attack is illustrated along the chord-wise direction.

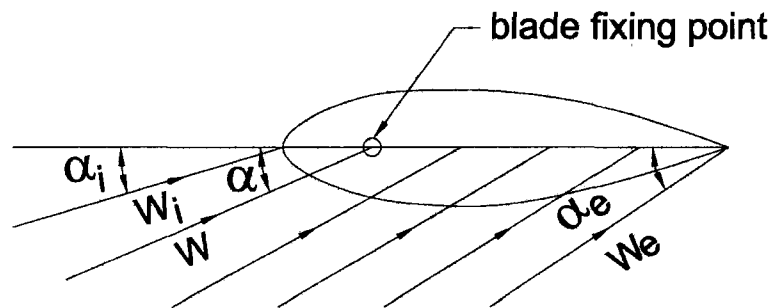


Figure 4.13: Typical Variation of Relative Velocity and Angle Of Attack Along Chord-wise Direction

An analytical method developed by Mandal and Burton [1994] is used to take into account of the curvilinear nature of flow. In the present analysis, to account for the flow curvature effect, the airfoil is assumed to be of cambered nature and the lift is corrected but the relative flow velocity is preserved.

In order to take its effect the thin airfoil theory is applied on an equivalent cambered airfoil having a mean camber line like that of the shape of a circular

where R_1 is the radius of the circular arc and h_1 is the maximum distance between the chord and the centre of the circular arc. The maximum camber of the circular arc f is found as

$$f = R_1 - h_1 \quad (4.93)$$

From Equations (4.91), (4.92) and (4.93), one can find the following expression,

$$\frac{2f}{c} = \frac{1 - \cos(\beta/2)}{\sin(\beta/2)} \quad (4.94)$$

The incidence correction angle is,

$$\alpha_c = \tan^{-1}\left(\frac{2f}{c}\right) \quad (4.95)$$

Introducing the value of $(2f/c)$ from Equation (4.94), one can find,

$$\alpha_c = \tan^{-1}\left[\frac{1 - \cos(\beta/2)}{\sin(\beta/2)}\right] \quad (4.96)$$

According to the thin airfoil theory, the lift characteristic of such a circular arc airfoil can be obtained from,

$$C_{lc} = 2\pi \sin(\alpha + \alpha_c) = 2\pi(\alpha + \alpha_c) \quad (4.97)$$

The lift characteristic of a thin airfoil with zero camber is determined from,

$$C_l = 2\pi \sin \alpha = 2\pi\alpha \quad (4.98)$$

It is obvious from the above two equations that due to the effect of the flow curvature, the lift needs to be corrected by a factor that is obtained from,

$$F_f = \frac{C_{lc}}{C_l} = \frac{(\alpha + \alpha_c)}{\alpha} \quad (4.99)$$

In the present analysis, the static lift is first corrected for the dynamic stalling effect, later this dynamic lift is corrected for the flow curvature effect with the multiplying factor F_f . For the upstream side of the turbine, $F_f > 1.0$ and for the

downstream side $F_f < 1.0$, since α_c is positive for the upstream side and negative for the downstream side.

4.5. Modeling of the Effect of Parasitic Drag

It has been discussed in Section 2.3.6 that parasitic drag losses generated by the supporting struts is one of the major disadvantages of the SB-VAWTs and the loss of power due to its effect is proportional to the cube of tip speed ratio. In order to calculate the parasitic losses due to supporting struts of SB-VAWT, the model developed by Mandal [1986] has been utilized in the present study. According to the model of Mandal [1986], the strut power coefficient can be expressed by,

$$C_{P,st} = \frac{1}{8} C_{d,st} N_{st} \frac{b_{st}}{H} \lambda^3 f_m \quad (4.100)$$

where,

$$f_m = 1 + \frac{1}{\lambda^2} \frac{V_a^2}{V_\infty^2} \quad (4.101)$$

and $C_{d,st}$ is the average drag coefficient of the supporting strut profile, b_{st} is the width of the strut, N_{st} is the number of supporting struts and H is the height of the SB-VAWT.

At low tip speed ratio (λ), V_a/V_∞ is nearly 1, as a result $f_m = 1 + 1/\lambda^2$, while at high λ , $V_a/V_\infty < 1$ and the factor f_m approaches 1. So, the expression of the strut power coefficient at high λ can be written in the form,

$$C_{P,st} = \frac{1}{8} C_{d,st} N_{st} \frac{b_{st}}{H} \lambda^3 \quad (4.102)$$

4.6. Comparisons of Performance Curves between Experimental and XFOIL Datasets

As shown in Figure 4.10, the pre-stall C_l , C_d and C_m datasets required by the FoilCheck (which is the post-stall model selected for this research) can be either obtained from experimental results or from an analytical tool like XFOIL. In this section, an effort has been made to compare the performance curve of a SB-VAWT, generated by the computational scheme (as described in the previous headings) developed in this chapter, with both possible sources of the pre-stall C_l , C_d and C_m datasets (i.e. experimental results and XFOIL).

In Figures 4.15 and 4.16, $C_{p,net}-\lambda$ curves of a SB-VAWT based on the XFOIL datasets have been compared with experimental results of Lyon et. al [1997]. The airfoil is SG6040 in both figures and solidity (Nc/R) of SB-VAWT is 0.2. The SB-VAWT used for this analysis has 3 blades with aspect ratio ($\mu=H/c$) of 10 and each of them are connected with the central shaft via two supporting struts. In both figures, the effect of parasitic drag losses, which depends on the drag coefficient and length of the supporting struts, are also shown. Usually, the value of $C_{d,st}$ varies between 0.1 and 0.5 [Kirke 1998]. Here a modest $C_{d,st}$ value of 0.1 has been used to illustrate the significance of parasitic drag losses.

It can be seen from Figures 4.15 and 4.16 that $C_{p,net}-\lambda$ curves based on XFOIL results are higher at both $Re=100,000$ and $300,000$. This is because of the fact that XFOIL usually over predict lift and under predict drag consistently at all angles of attack as discussed in Appendix C. However, since XFOIL is relatively consistent in its overpredictions of L/D (i.e. one can assume that similar bias for different types of airfoils) [Kellogg and Bowman 2004] and since in the present research XFOIL has been utilized for comparative study, XFOIL's over predictions should not pose a significant inaccuracy for deriving qualitative conclusions. Furthermore, to see the validity of the overall computational scheme developed in the present study, the results are compared with experimental results of SB-VAWT model in the next section.

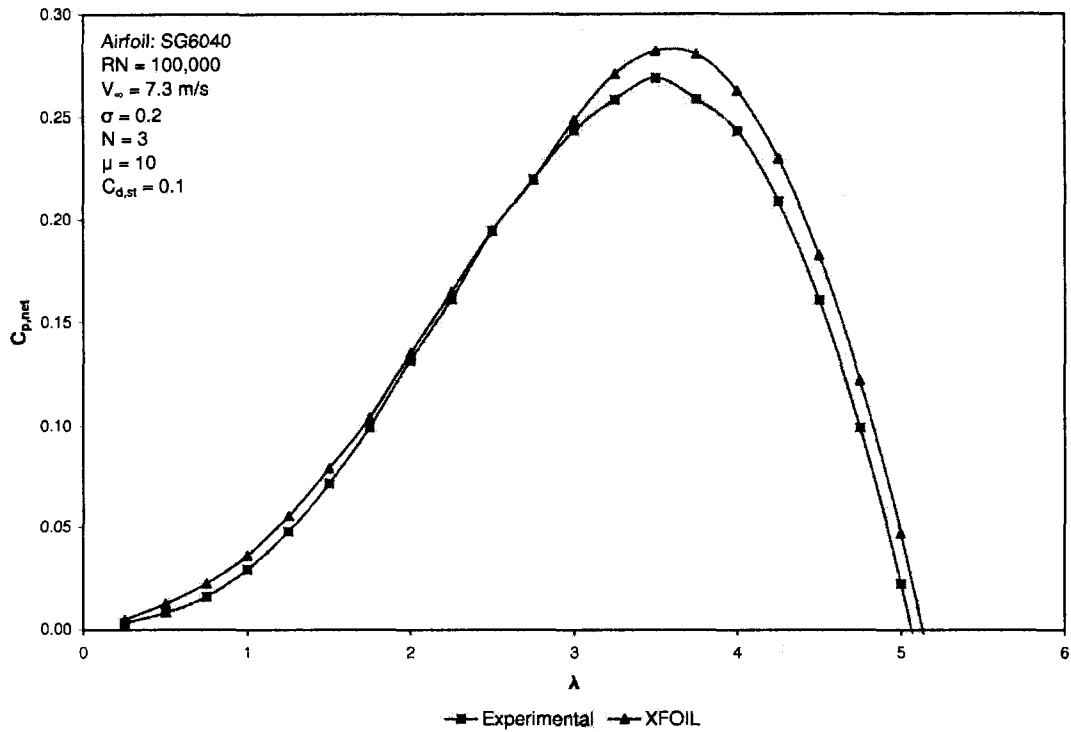


Figure 4.15: Comparisons of $C_{p,net}$ vs λ Curves Based on Experimental and XFOIL Airfoil Datasets at $RN=100,000$

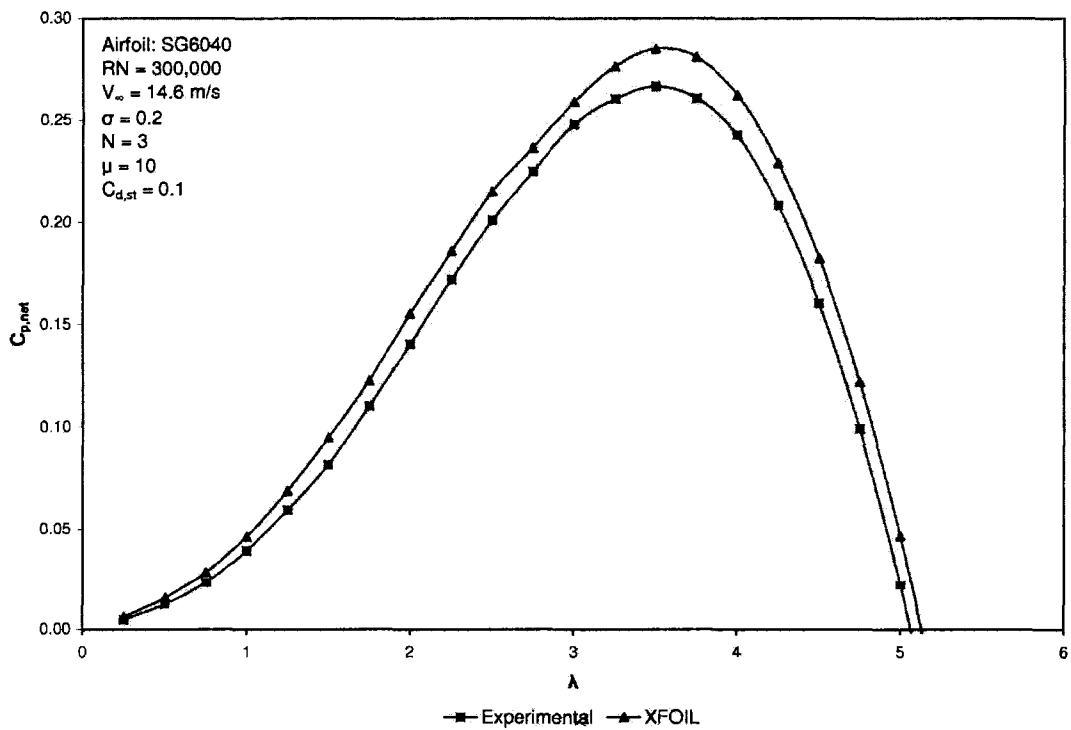


Figure 4.16: Comparisons of $C_{p,net}$ vs λ Curves Based on Experimental and XFOIL Airfoil Datasets at $RN=300,000$

4.7. Validation of the Computational Scheme

In Figures 4.17 to 4.19, experimental results [Bravo et. al 2007] have been compared with both the original cascade model and its modified version developed under the present study as described above. The airfoil is NACA 0015 in all the figures and solidity of SB-VAWT is 0.96. The SB-VAWT has 3 blades with aspect ratio of 7.5 and each of them is connected with the central shaft via two supporting struts. In all the figures, the effect of parasitic drag losses is also shown. Here $C_{d,st}$ value of 0.1 has been used to illustrate the significance of parasitic drag losses.

In Figure 4.17, C_p - λ curves at $V_\infty=6$ m/s are shown. It can be seen that results obtained from the cascade model using the XFOIL and FoilCheck airfoil characteristics conform better to the experimental results of Bravo et. al [2007] than the original cascade model with experimental characteristics. As described earlier, the original cascade model utilized the 2D airfoil characteristics from different sources including Jacob and Sherman [1937], Sheldahl and Blackwell [1976] and Willmer [1979] which were the products of experimental investigations. It can also be seen from Figure 4.12 that the results obtained from computational models overpredict the C_p values at different λ .

In Figure 4.18, C_p - λ curves are shown at $V_\infty=8$ m/s. At this RN better correlation can be seen between the experimental results and present modified cascade model with XFOIL and FoilCheck characteristics. The C_p - λ computed by the original cascade model is shifted towards higher λ . In Figure 4.19, C_p - λ curves at $V_\infty=10$ m/s are depicted. Like Figure 4.18, similar trends can be observed and the present computational scheme performs better than the original cascade model. From these figures one can conclude that the cascade model with the analytically derived airfoil characteristics obtained from XFOIL and FoilCheck produces performance curves which conform reasonably to the experimental results.

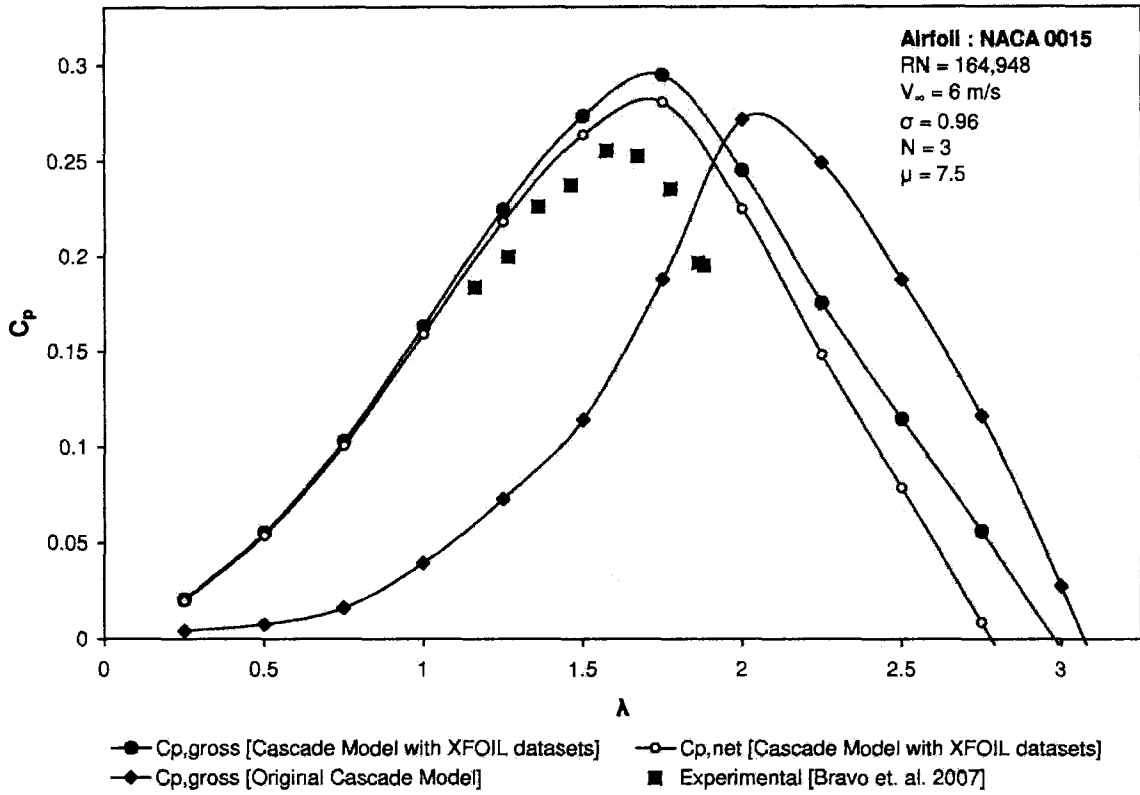


Figure 4.17: Comparison of Experimental and Computational C_p - λ Curves at $RN=164,948$

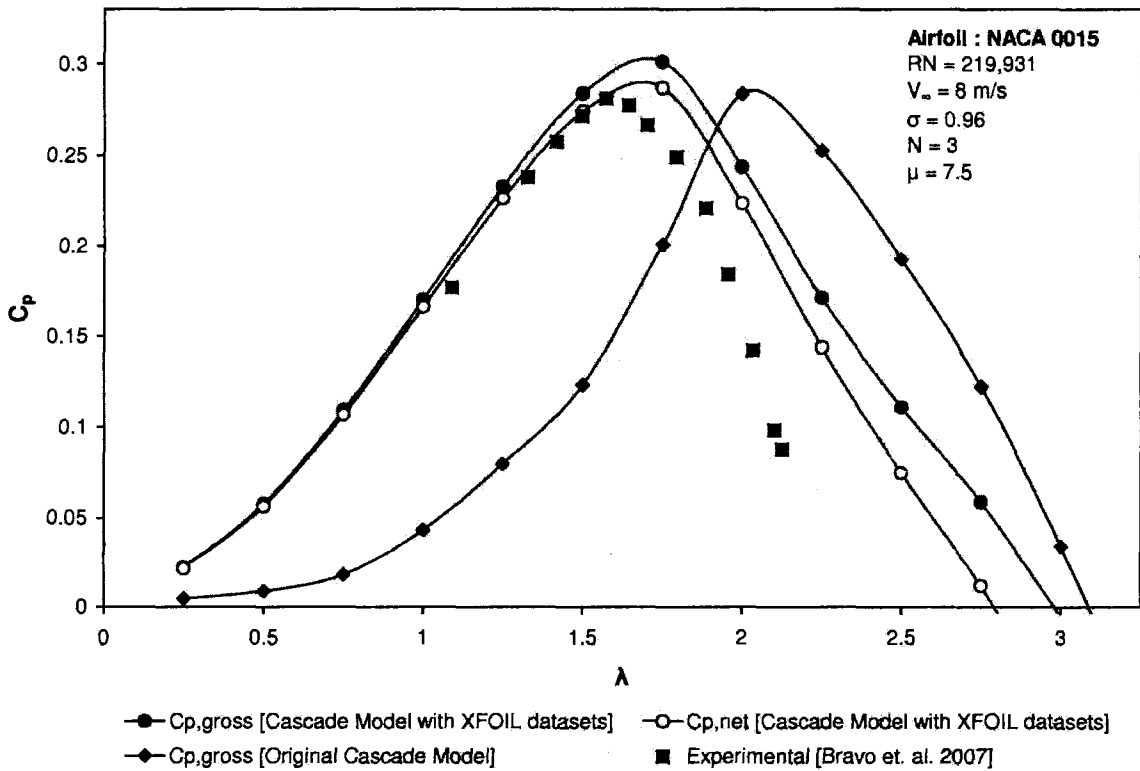


Figure 4.18: Comparison of Experimental and Computational C_p - λ Curves at $RN=219,931$

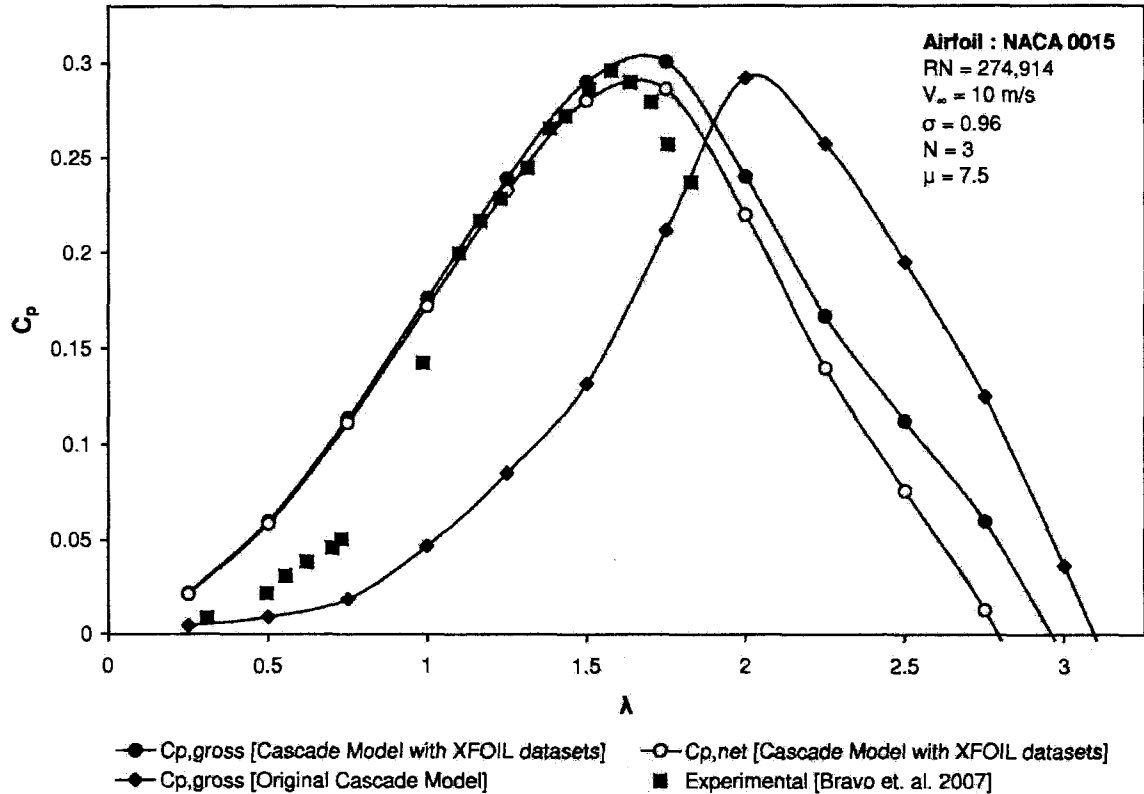


Figure 4.19: Comparison of Experimental and Computational C_p - λ Curves at $RN=274,914$

4.8. Summary of the Chapter

Based on the findings of the previous chapter, the cascade model, proposed by Hirsch and Mandal [1987] has been selected for the present research for performance analysis of SB-VAWTs. Different established models have been investigated and selected for considering the main aerodynamic challenges of SB-VAWT described in Chapter 2. Details of the overall computational scheme to consider some of the main aerodynamic challenges are presented in this chapter.

It has been established that the results from the computational models conform reasonably well to the experimental results. In Table 4.1, comparison between the modified computational scheme developed for this present study and that of earlier approach by Mandal (who developed the original cascade model) are shown.

Table 4.1: Computational Scheme for Performance Analysis of SB-VAWTs

Factor	Approach of Original Cascade Model	Approach undertaken in the present study
Calculations of local relative velocities and angle of attacks at different tip speed ratios and azimuthal (orbital) positions	Calculated for upstream and downstream separately [Hirsh and Mandal 1987]	Calculated for upstream and downstream separately [Hirsh and Mandal 1987]
Calculation of ratio of induced to freestream velocity ($\frac{V_a}{V_\infty}$) considering the blade/blade-wake interaction	Empirical formula [Hirsh and Mandal 1987]	Empirical formula [Hirsh and Mandal 1987]
Mathematical expressions to calculate normal and tangential forces	Cascade Principle [Hirsh and Mandal 1987]	Cascade Principle [Hirsh and Mandal 1987]
'Pre-stall airfoil characteristics' (C_l , C_d and C_m) for the attached regime at different Reynolds numbers	Incorporated only the characteristics of NACA 0012 and NACA 0015 based on experimental results	Correlations, based on either experimental results or theoretical values from XFOIL, for symmetric and asymmetric airfoils
'Post-stall Model' for stall development and fully stalled regimes	Based on experimental results	Obtained from FoilCheck which utilizes the pre-stall datasets obtained from either experimental results or XFOIL
'Dynamic Stall Model' to account for the unsteady effects	(a) Model for pre-stall regime [Mandal 1986] (b) Modified Boeing-Vertol Model [Mandal and Burton 1994, Mandal 1994] for post-stall regimes	(a) Model for pre-stall regime [Mandal 1986] (b) Modified Boeing-Vertol Model [Masse, 1981] for post-stall regimes
'Flow Curvature Model' to consider the circular blade motion	Mandal and Burton [1994]	Mandal and Burton [1994]
Parasitic drag of supporting struts	Mandal [1986]	Mandal [1986]

Chapter 5

Desirable Airfoil Features for Smaller-Capacity SB-VAWT

Selection of airfoil is the most critical factor in achieving better aerodynamic performance and in determining the optimum dimensions of a SB-VAWT. Airfoil related design changes also have the potential for increasing the cost effectiveness of VAWTs [Klimas 1985]. All the earlier research works carried out by Sandia National Laboratory, Natural Resources Canada and several commercial SB-VAWT models used mainly symmetric airfoils, that were developed for the aviation applications, but were unable to self-start properly. If this problem of self-starting could be overcome without a big increase in cost, SB-VAWTs could make a significant contribution in the field of stand-alone power supply systems [Kirke 1998].

Against the above-mentioned background, this chapter aims to perform detailed systematic investigative analysis with recently developed asymmetric airfoils appropriate for self-starting and better performance of smaller capacity fixed-pitch SB-VAWT through critical examination of their salient aerodynamic factors. In Chapter 2, the main aerodynamic challenges of SB-VAWTs have been presented. Realizing these challenges in mind, literature survey and computational analysis were conducted to identify and shortlist the desired aerodynamic characteristics of the airfoil suitable for smaller-capacity self-starting SB-VAWT with optimum performance. At the end, desired geometric features of an airfoil suitable for smaller capacity SB-VAWT are discussed.

5.1. Previously Utilized General-Purpose Airfoils for SB-VAWTs

Since its early stage of design and development, both the straight-bladed and curved-bladed Darrieus type VAWTs were mostly made with blades of the symmetric airfoils from the NACA 4-digit series, like NACA 0012, 0015, 0018 as shown in Figure 5.1, which were originally developed for high Reynolds number aviation applications. These airfoils have presumably been used mainly because only for these airfoils was there sufficient information on performance and loading [Zervos 1988b], including low RN data. Their lift, drag and pitching moment characteristics are the most well documented and thus making validation of the theoretical predictions easier [Kirke 1998]. However, Migliore [1983] has shown that the use of NACA 6-digit airfoils can improve the performance of the curved-blade VAWTs operating at Reynolds number of 3×10^6 . But, their application at lower RN is yet to be investigated. In 1980, Sandia National Laboratory (the main organization devoted to VAWT related research and development works in the US) developed a family of airfoil sections specifically tailored for use in the Egg-beater type Darrieus VAWTs [Klimas 1985], but like NACA 6-digit airfoils, suggested by Migliore, their application for smaller capacity VAWTs is yet to be analyzed.

In the late seventies, Healy [1978b] performed a theoretical study of the performance of VAWTs with NACA 0018 and eight cambered airfoils (namely Gö 460, Gö 676, Gö 738, Gö 735, Gö 746, Gö 741, Gö 744 and Gö 420). From his investigation, Healy concluded that “*the closer the airfoil is to symmetric, the more satisfactory its power output.*” Baker [1983] found satisfactory performance with the moderately cambered Gö 420 (also known as GOE 420) which is described below. Furthermore, Kirke [1998] questioned Healy’s conclusion by putting forward several valid arguments in favor of cambered airfoils for self-starting SB-VAWT.

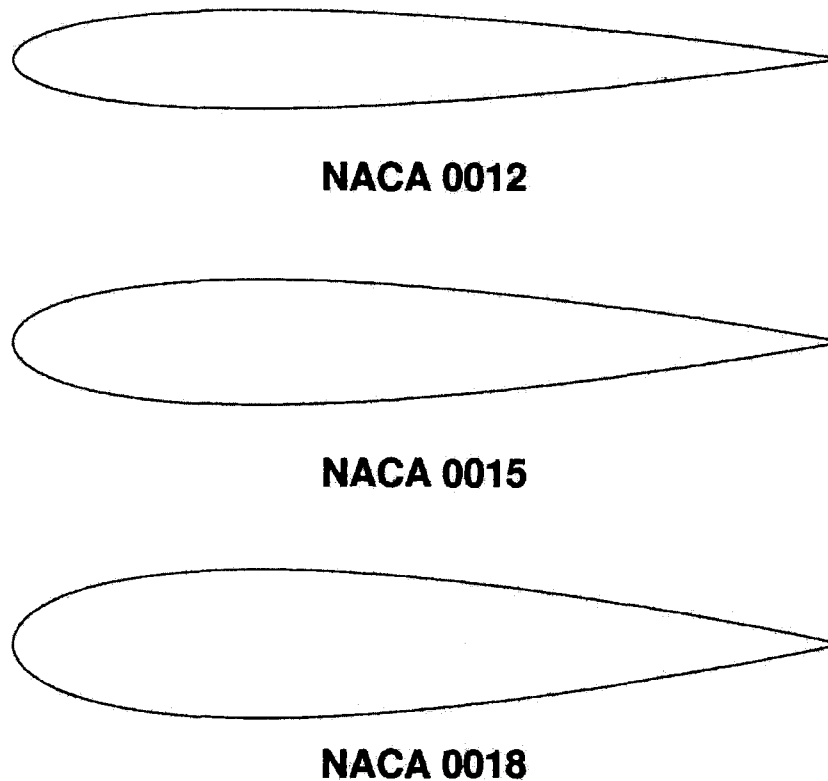


Figure 5.1: Geometry of Conventionally used NACA Symmetric Airfoils [Islam et. al 2007b]

In the mid-nineties, Kirke [1998] performed detailed computational works related to fixed-pitch SB-VAWT and he argued that – “for a small fixed pitch VAWT to self-start it is necessary that the aerofoils produce at least moderately high lift and low drag at Reynolds number between about 80,000 and 150,000. The symmetrical sections usually used on VAWTs perform poorly in this RE range and do not achieve self-starting, but thin cambered sections perform much better - at least at positive incidence. Unlike symmetrical sections, thin cambered sections can produce moderate lift at positive incidence even with a totally laminar boundary layer, i.e. at very low RE [Miley 1982]. Although cambered sections at negative incidence develop little lift and have a low stall angle, it is possible that their much superior performance at positive incidence could result in superior overall performance at low Re”.

Subsequently, Kirke performed simulation with NACA 4415 and one of the recently developed asymmetric airfoils (S1210) and commented that - *“performance of fixed pitch VAWTs with cambered blades using newly developed profiles that exhibit superior characteristics at low Reynolds numbers. Results indicate that fixed pitch VAWTs using these blade sections should self-start reliably”*. However, Kirke also found out that the S1210 blades would cost no more to produce than NACA 0015 blades and their only drawback for high speed loads would be the fact that maximum C_p occurs at lower λ with S1210 blades than with NACA 0015 blades.

In the early eighties, Kadlec [1982] of Sandia National Laboratory suggested that the power coefficient can be increased by using cambered airfoils on blades with little or no cost increases and he envisaged that the continued investigation of these alternative airfoils will determine their feasibility in advanced VAWTs. It was also acknowledged by Klimas [1985] that cambered blades appeared to offer some advantages in VAWT design.

Zervos [1988b] evaluated six airfoils (namely NACA 0012, NACA 0015, NACA 0018, NACA 63-015, GAW-1 and NLF0416) and found that the results of instantaneous power coefficient, normal force coefficient, and tangential force coefficient show a net advantage for GAW(1), also known as LS-0417, and NLF0416 both in pressure distribution (smaller adverse pressure gradients) and instantaneous loading (a more symmetric distribution with smaller peaks of normal and tangential forces during the cycle). Based on these results, he suggested that “judicious use of non-symmetric airfoils could produce better performance characteristics”.

Baker [1983] investigated the cause of the inability of low solidity fixed-pitch SB-VAWT to self start and suggested the utilization of blades having airfoil sections

that strongly exhibit the laminar separation bubble phenomena below the stall and that have low immediate post-stall drag. He investigated the performance of NACA 0012, Gö 420 and Wortmann FX63-137. He found superior performance of Gö 420 in comparison to NACA 0012 and the performance of FX63-137 was unsatisfactory. Baker commented that the inferior performance of FX63-137 is due to its very sharply angled trailing edge which exhibited noisy stall from positive angles of attack, accompanied by a sudden deceleration. The inferior performance of FX63-137 can also be attributed to its large camber which can be counterproductive. It was commented by Dereng [1981] that excessive camber or lack thereof will eliminate initial start-up capability and severely degrade or eliminate the ability to traverse the intermediate tip speed ratios.

It should be added that, cambered airfoils can be attached with the supporting struts of fixed-pitch SB-VAWT in two configurations based on the concave curvature of the camber line. These configurations are- (i) Concave-out; and (ii) Concave-in configurations as shown in Figures 5.2(a) and 5.2(b) respectively. If the concave side of a cambered blade faces outwards (i.e. the Concave-out configuration), it experiences positive incidence on the upstream pass and negative incidence on the downstream side as shown in Figure 5.2(a). As SB-VAWTs extract more energy on the upstream side, reduced amount of energy is available on the downstream side and as a result α for an unpitched blade is less on the downstream side than on the upstream side [Kirke 1998]. According to Kirke [1998], this configuration ensures maximum power extraction from the undisturbed flow on the upstream side. When the concave side of the cambered airfoil faces inward (i.e. Concave-in configuration), negative incidence occurs on the upstream side and positive incidence occurs on the downstream side as can be seen from Figure 5.2(b). For SB-VAWTs with large chord-to-radius ratio, the concave-out configuration results in addition of the virtual camber with the actual camber due to flow curvature effects. On the other hand, virtual camber for concave-in configuration will tend to cancel out the actual camber.

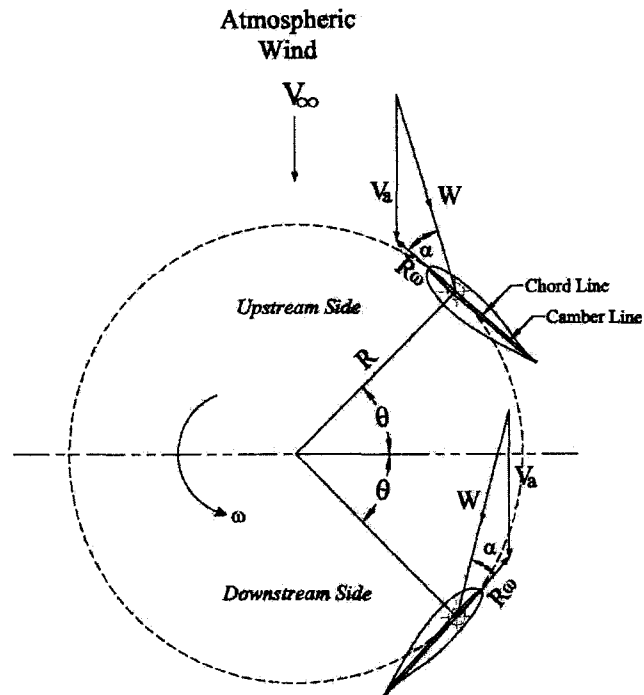


Figure 5.2(a): Concave-out Configuration

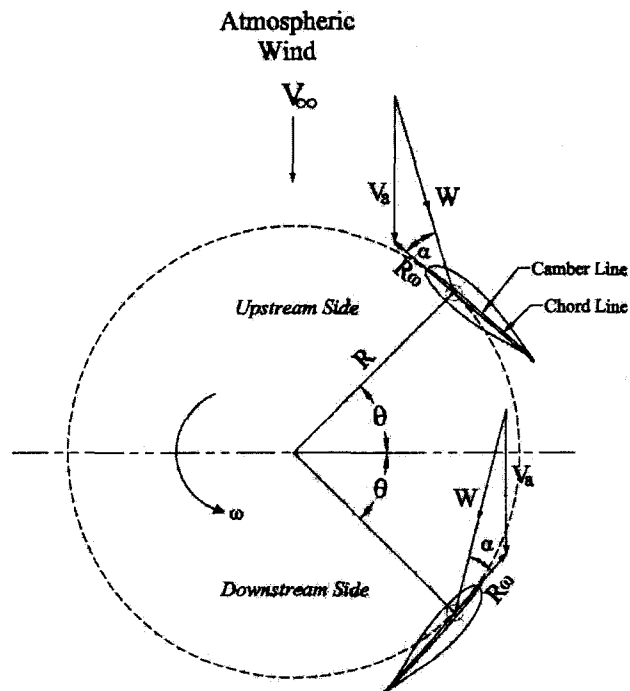


Figure 5.2(b): Concave-in Configuration

Figure 5.2: Two Types of Configurations for Attaching Cambered Airfoils with the Supporting Struts [Islam et. al 2007b]

5.1.1. Comparison of Performance of Selected Asymmetric Airfoils

Based on the literature survey, only the prospective airfoils (as shown in Figure 5.3) which are available in the public domain are investigated in this section to compare their performance. The selected airfoils are (i) Gö 420 or GOE 420 [Baker 1983], (ii) NACA 4415 [Kirke 1998] (iii) LS(1)-0417 or commonly known as GAW-1 [Zervos 1988b], (iv) NLF(1)-0416 [Zervos 1988b], and (v) S1210 [Kirke 1998]. The Reynolds number of the present analysis is limited between 100,000 and 300,000 which is the typical operating condition of smaller-capacity SB-VAWTs. Performance of these five selected airfoils is also compared with the NACA 0015 which has been extensively applied as a blade shape in the past.

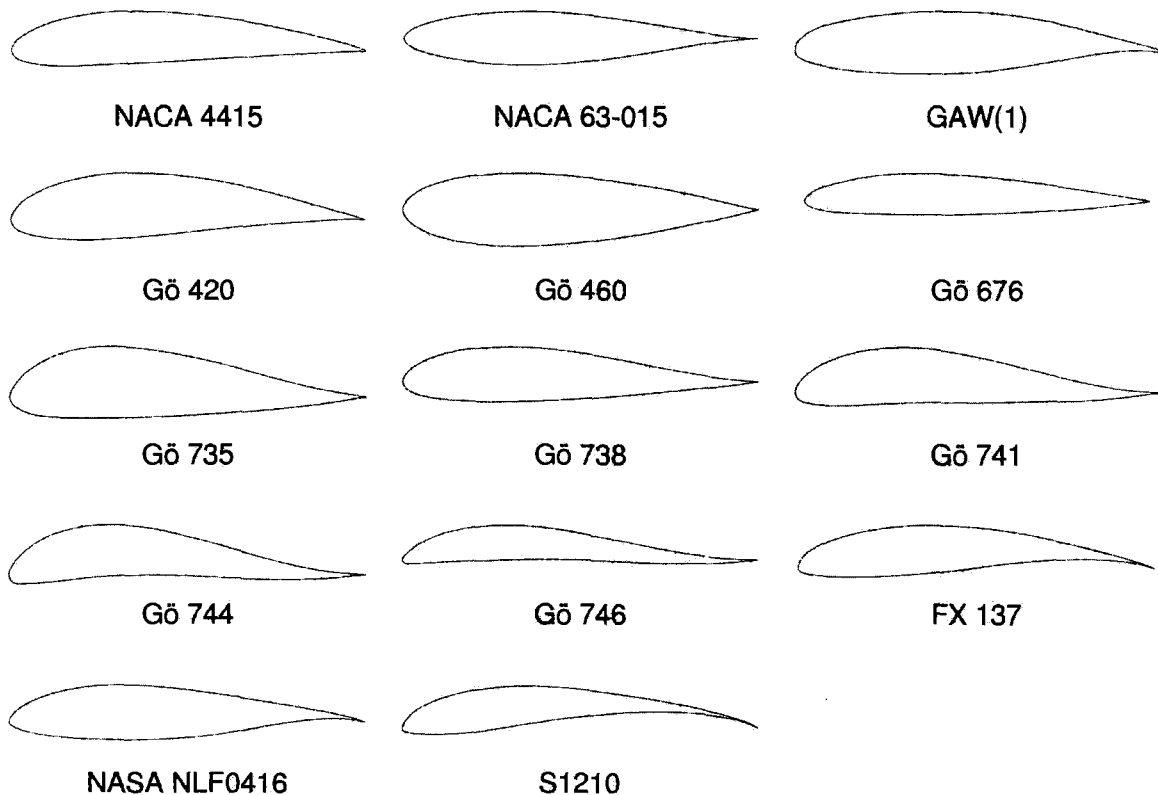


Figure 5.3: Geometries of Selected Asymmetric Airfoils [Islam et. al 2007b]

In Figures 5.4 and 5.5, the tangential force coefficient (C_t) versus angle of attack curves for 5 selected asymmetric airfoils are compared with NACA 0015 at $Re=100,000$ and $300,000$ respectively. For obtaining these curves, XFOIL [2007] was used to generate the required 2D datasets of lift and drag coefficients around $-20^\circ \leq \alpha \leq 20^\circ$.

For the present analysis, the FoilCheck program of NWTC [NWTC Design Codes 2007] has been utilized to generate different airfoil characteristics between $0^\circ \leq \alpha \leq 360^\circ$ using the computational 2D results obtained from XFOIL. However, it should be mentioned that this is a simplistic approach and in reality the situation might be more complex. The effects of free stream turbulence, as stated at the end of Section 2, are typically detrimental [Devinant et. al 2002] .

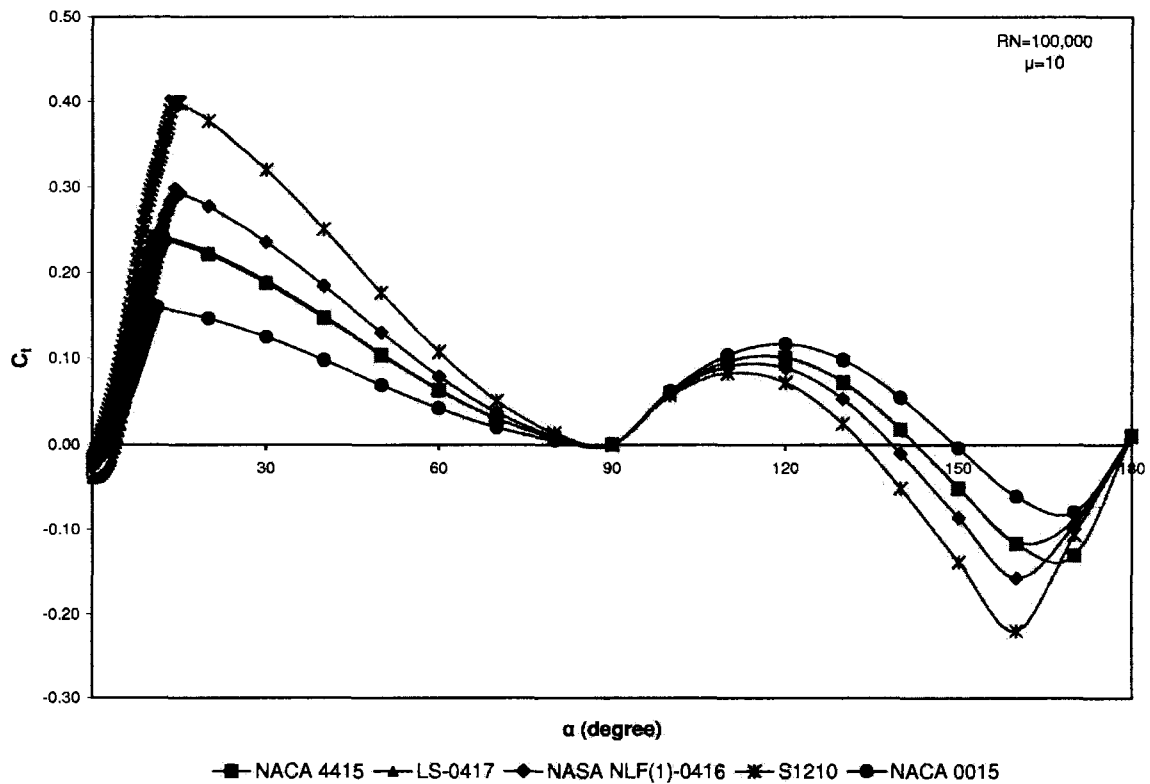


Figure 5.4: C_t - α Curves of Selected Asymmetric Airfoils at $Re=100,000$

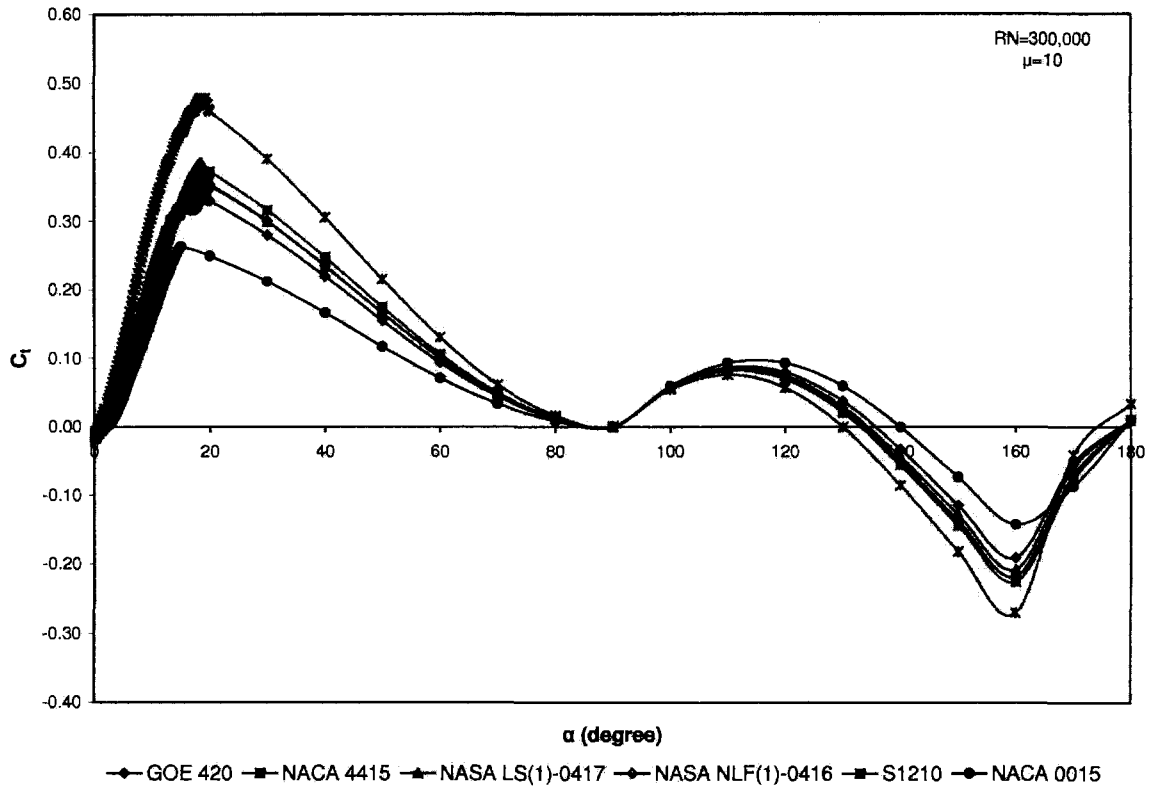


Figure 5.5: C_t - α Curves of Selected Asymmetric Airfoils at $RN=300,000$

For SB-VAWTs, when C_t value of an airfoil shape is positive, the blade will produce forward tangential or thrust force. Instantaneous torque produced by the blades can be calculated when the thrust force is multiplied by the blade radius (R). It can be seen from Figure 5.4 that C_t values of NACA 4415, NASA LS(1)-0417, NLF(1)-0416 and S1210 are much superior than that of conventional NACA 0015 at $RN=100,000$ for $0^\circ \leq \alpha \leq 90^\circ$. However, for $90^\circ \leq \alpha \leq 180^\circ$, the C_t values of NACA 0015 are greater than the asymmetric airfoils. Due to convergence problem, the aerodynamic characteristics of Gö 420 could not be generated from XFOIL at $RN=100,000$, possibly due to laminar separation bubbles typically encountered by airfoils at low RN . As a result, C_t values of Gö 420 could not be shown in Figure 5.4.

For $RN=300,000$, there was no problem of convergence and lift and drag coefficients could be generated for all the asymmetric airfoils and their

corresponding C_t values are shown in Figure 5.5. This figure also shows the superiority of asymmetric airfoils over NACA 0015 for $0^\circ \leq \alpha \leq 90^\circ$ degrees. Among all the asymmetric airfoils, the performance of S1210 is the best for $0^\circ \leq \alpha \leq 90^\circ$ degrees and thus confirming Kirke's [1998] claim that a fixed pitch SB-VAWT using this low RN airfoil should self-start satisfactorily.

5.2. Specially Designed Airfoils for SB-VAWTs

Rather than applying existing airfoils designed for aviation industry, several researchers have attempted to explore different types of asymmetric airfoils (mainly by modifying the existing airfoils) and claimed that they perform better than the conventional airfoils designed for the aviation applications. Kato et. al [1981a], Dereng [1981] and Seki [2005] utilized special-purpose asymmetric airfoils in their US patented SB-VAWTs. From literature survey, four other special-purpose asymmetric airfoils could also be found which were developed for SB-VAWTs. These four airfoils are briefly described below.

5.2.1. "TWT Series" of Tokai University, Japan

In the early eighties, Seki et. al. [1985] and Kato et. al [1981b] developed a family of asymmetric airfoils for SB-VAWT that are called TWT series which have partly positive and partly negative camber. They utilized the single streamtube model to develop this series of asymmetric airfoils. The researchers claimed that these airfoils are better performing than the NACA 4-digit series and they presented a performance comparison of one of their airfoils with NACA 0012. Subsequently, they constructed two prototypes for electricity generation and heating of a greenhouse [Kato et. al 1981b and Seki et. al 1985]. However, these prototypes are equipped with a Savonius rotor and a starter motor, indicating their inability to self-start. No information regarding the coordinates or experimental datasets of these TWT series airfoils could be found from the literature.

5.2.2. “ARC Series” of University of Athens, Greece

In the late eighties, Zervos of University of Athens [Zervos 1988b, Zervos 1988c, Zervos et. al 1989 and Zervos and Morfiadakis 1990] developed the Arc series specifically intended for VAWT. This series was basically developed by modifying the NACA 4-digit airfoils (like NACA 0015 or 0018) which were essentially designed for high speed applications. Like the TWT series, the coordinates or experimental datasets of these airfoils could not be found from the literature. Also, Zervos et al. did not present any discussion about the self-starting characteristics of the experimental fixed-pitch SB-VAWTs they made out of these airfoils and their plots do not include the behavior of these experimental models at low tip speed ratios [Zervos 1988b, Zervos 1988c, Zervos et. al 1989 and Zervos and Morfiadakis 1990].

5.2.3. “Transformed NACA 0018” of Maeda Corporation & Tokai University, Japan

Recently, Maruyama et. al. [2001] have attempted to utilize a special-purpose airfoil by transforming existing NACA 0018 by curving the chord line along the rotating circumference. They fabricated a full-scale model with this airfoil and conducted experimental investigations. They found that the performance of the transformed NACA 0018 is better than the unmodified one under no-load condition. No information could be found regarding the starting characteristics of the full-scale model.

5.2.4. DU 06-W-200 of Delft University

Claessens [2006] conducted a design analysis of special-purpose airfoil for VAWT under the scope of his Masters thesis. The analyses were conducted between the RN of 300,000 and 700,000. Claessens' design process was developed with the purpose of improving the NACA 0018 airfoil. He also investigated VAWT aerodynamics to find the design goals for the airfoil

characteristics. At the end, he designed a special-purpose VAWT airfoil named “DU 06-W-200” which is a laminar, 20% thick airfoil with 0.8% camber. To be able to compare the performance of NACA 0018 and DU 06-W-200, wind tunnel measurements were performed at the Delft University of Technology.

It was found by Claessens that (i) The 20% thickness adds to the blade strength without decreasing the performance; (ii) The added camber of 0.8% increases the performance with respect to a symmetric airfoil; (iii) The DU 06-W-200 performance equals the NACA 0018 for negative angles of attack; (iv) The DU 06-W-200 has a much higher $C_{l,max}$ for positive angles of attack, resulting in a wider drag bucket; (v) Deep stall occurs at higher angles of attack with a smaller drop in lift coefficient; (vi) In contrast to the NACA 0018 the DU 06-W-200 does not have laminar separation bubbles which extend over the trailing edge; (vii) The increase in turbine performance at the operating tip speed ratio of $\lambda = 3$ is 8% in clean conditions and twice as much when dirty.

Based on the published documents, the following points can be inferred regarding the above-mentioned four dedicated airfoils for SB-VAWTs:

- All of these airfoils are asymmetric airfoils;
- The main emphasis was to improve the overall performance of the turbine (at higher tip speed ratios) rather than developing a self-starting SB-VAWT.
- None of these airfoils were designed for the low RN (between 100,00 and 300,000) operation typically encountered by smaller capacity SB-VAWTs;
- Except the ARC series and DU 06-W-200, the other airfoils have not been designed considering the unsteady (dynamic stall) and rotational effects (flow-curvature).

5.3. Desirable Aerodynamic Characteristics of SB-VAWT Airfoil

In this section, an attempt will be made to short list the desirable aerodynamic characteristics of a self-starting and optimum performing SB-VAWT based on previous researches and computational analysis. The asymmetric airfoils analyzed in Section 5.1.1 are investigated using XFOIL. The airfoils described in Section 5.2 could not be incorporated in the analysis due to non availability of coordinates and copyright related issues. The analysis of the performance of the asymmetric airfoils is performed on different aerodynamic characteristics for Reynolds number 100,000 and 300,000. It should be pointed that it was not possible to generate the aerodynamic coefficients for GOE 420 at RN=100,000 due to convergence problem. However, at higher RN of 300,000 there was no such problem of convergence with any of the airfoils investigated in this section.

5.3.1. High Stall Angle at Low Reynolds Number

It has been discussed earlier that, behavior of lift and drag coefficients in the post-stall conditions at low λ has serious consequence for fixed-pitch SB-VAWT and their lack of starting torque is due to the cyclical change in α with θ . As at low λ , α exceeds the stall angle for much of the blades' travel path. Thus stalled blades generally contribute negatively to the driving torque so that the net work output per revolution may be negative for some values of λ . If the stall angle can be increased, this situation will be improved as the blades are stalled for a smaller proportion of their travel. So, it is clear that the stall angle of the airfoil sections for fixed-pitch SB-VAWT should be as large as possible in the low RN operation, typically encountered by SB-VAWT, in order to minimize separation at low tip speed ratios [Kirke 1998].

In Figures 5.6 and 5.7, the lift curves of the selected prospective airfoils are shown at RN=100,000 and 300,000 respectively. It can be seen from Figure 5.6 that at positive incidence stall angles (α_{stall}) of S1210 is best, and it is followed by NACA 4415, NLF-0416 and LS(1)-0417 at RN=100,000. Figure 5.7 shows that

α_{stall} of all the five prospective airfoils are similar at $RN=300,000$ and higher than NACA 0015 which justifies their superior performance in the positive incidences.

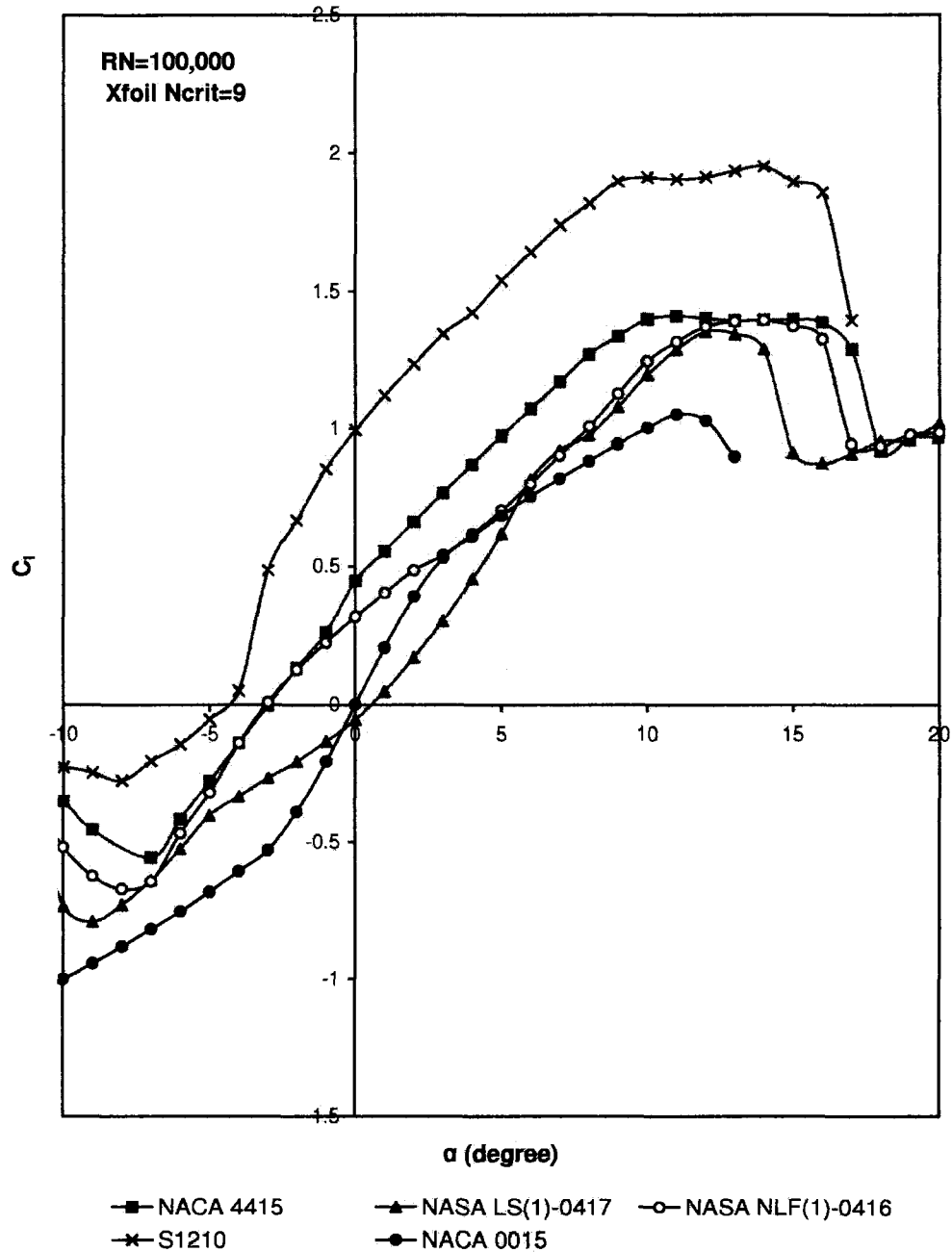


Figure 5.6: Lift Curves of Selected Asymmetric Airfoils at $RN=100,000$

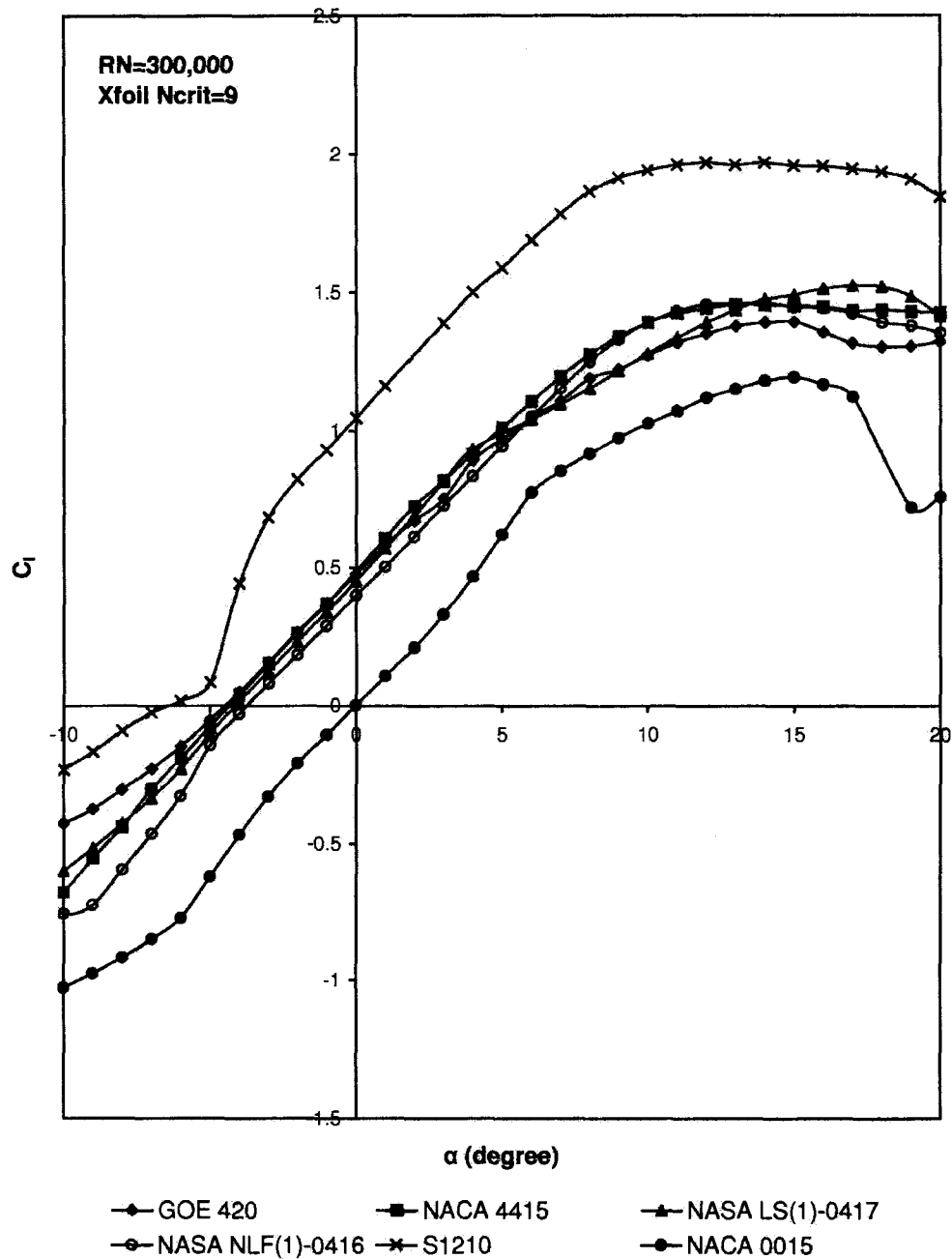


Figure 5.7: Lift Curves of Selected Asymmetric Airfoils at $RN=300,000$

It is also evident from Figures 5.6 and 5.7 that performance of NACA 0015 is better than the other asymmetric airfoils at RN of 100,000 and 300,000 in the negative incidences. But, as illustrated in Figure 2.2, SB-VAWT airfoils encounter

negative incidences in the downstream side ($180^\circ \leq \theta \leq 360^\circ$) where lesser amount of energy is available for harnessing as most of the power is extracted from the wind during the upstream side of a VAWT [Kirke 1998]. It has already been mentioned that the velocity difference across a three bladed turbine is about 0.55, i.e. the downstream blades receive wind at a speed of 0.55 times of the upstream side [Duremberg 1979] and about 90 or 95% of the energy is extracted from the upstream pass. Furthermore, the more power is extracted on the upstream pass, the less energy is available on the downstream pass [Loth and McCoy 1983]. So, though asymmetric airfoils produce lesser amount of lift in comparison to the symmetric airfoils at negative incidences and have a lower stall angle, their better performance at positive incidence can result in superior overall performance at low RN if the concave out configuration (shown in Figure 5.2) is used [Kirke 1998].

5.3.2. Wide Drag Bucket

Generally, airfoils exhibit the lowest drag over a narrow range of angle of attack called the "drag bucket" and the airfoil shape determines the nature and position of the drag bucket [CRRRC 2007]. Klimas [1985] identified that wide drag bucket is one of the desirable characteristics of VAWTs. It was also commented by Claessens [2006] that increased width of drag bucket is required to maintain performance over a larger range of α .

In Figures 5.8 and 5.9, drag polar (C_d-C_l curves) of selected asymmetric airfoils are shown at $Re=100,000$ and $300,000$. It can be seen in Figure 5.8, that the width of the drag bucket of NLF-0416 is the largest among all the analyzed airfoils. However, at higher Re of $300,000$, as shown in Figure 5.9, the widths of the drag bucket of LS-0417 and NLF-0416 are similar and not much different from that of NACA 0015.

5.3.3. Low Zero-lift-drag Coefficient

The desired airfoil should have the least amount of drag, especially the zero-lift-drag coefficient (C_{d0}) should be very low [Jesch and Walton 1980, Seki et. al 1985]. Seki et. al [1985] also suggested that zero-lift angle and minimum drag coefficient angles of a better performing airfoil should coincide or the difference should be small.

Basically, the zero-lift drag coefficient is reflective of parasitic drag which makes it very useful in understanding how "clean" or streamlined a VAWT's aerodynamics is [Wikipedia 2007a]. It can be observed from Figures 5.8 and 5.9 that C_{d0} of NACA 0015 is the lowest among all the airfoils considered. However, it will be shown in Section 5.3.7 that NACA 0015 is very sensitive to roughness.

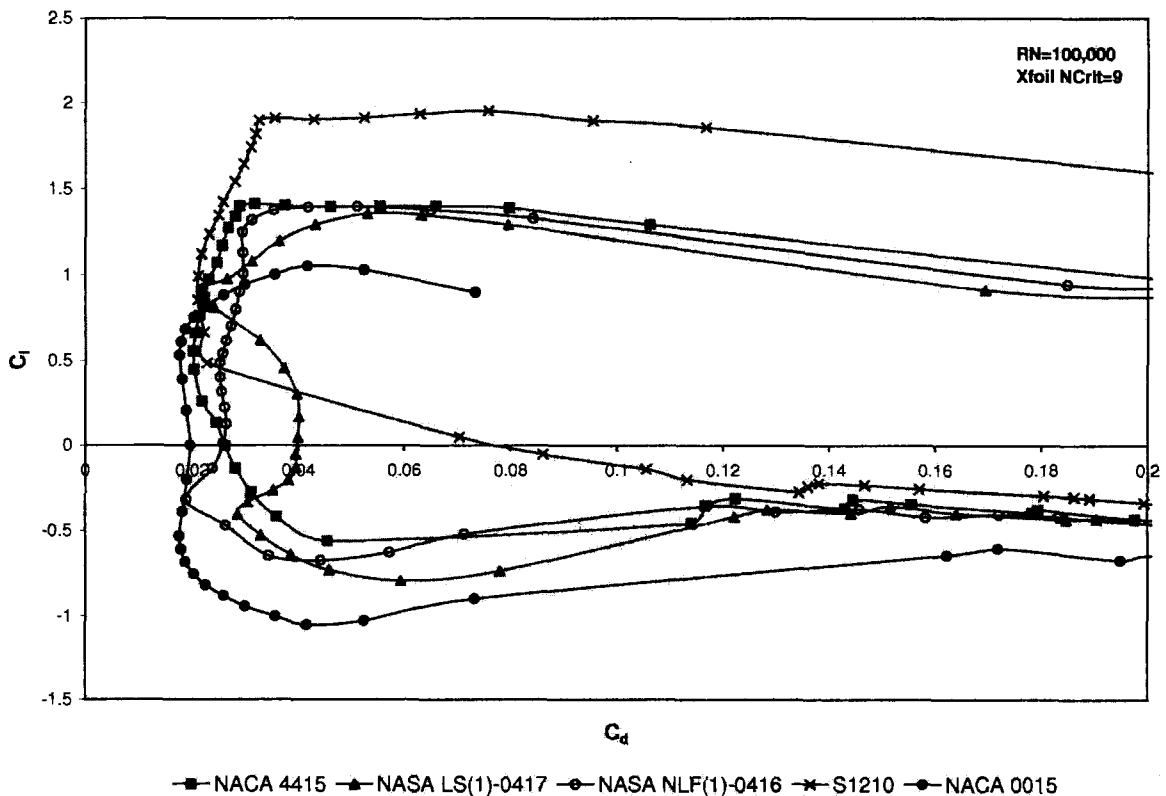


Figure 5.8: Drag Buckets of Selected Asymmetric Airfoils at $RN=100,000$

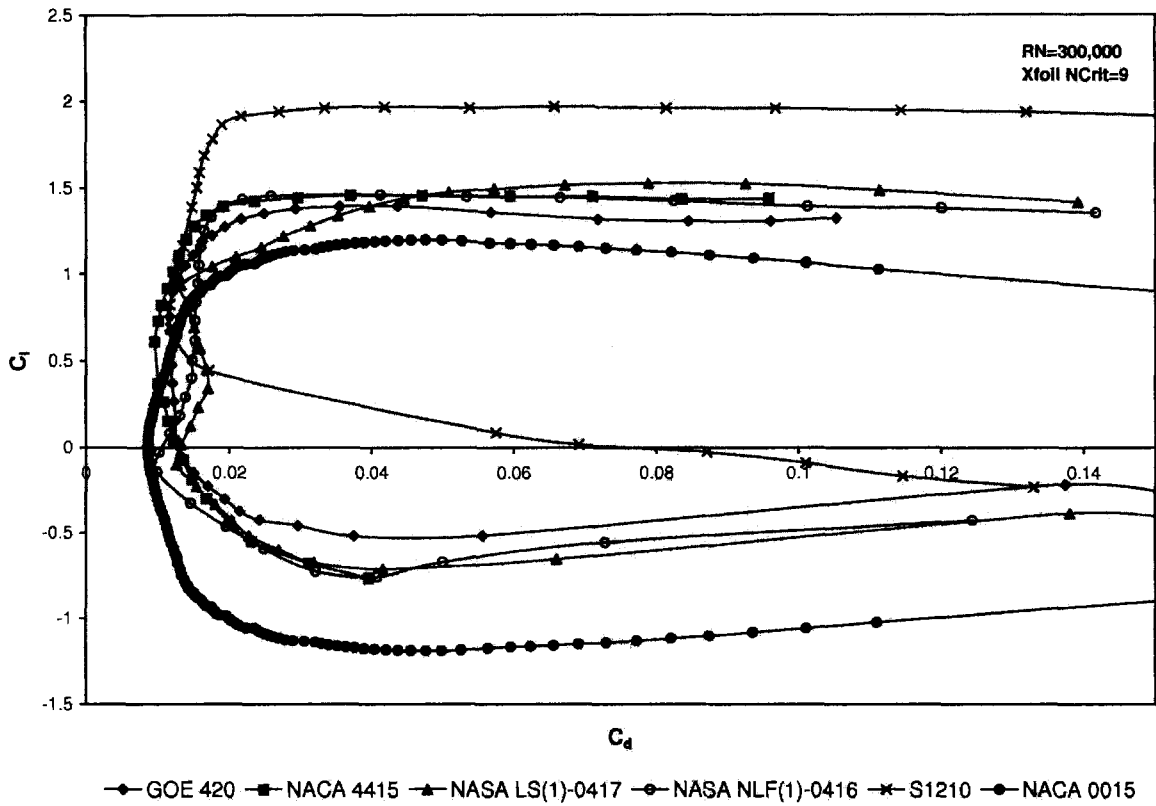


Figure 5.9: Drag Buckets of Selected Asymmetric Airfoils at RN=300,000

5.3.4. High C_l/C_d Ratio

The C_l/C_d ratio indicates the overall efficiency of any airfoil and naturally it is desirable to have higher ratio over a wide range of α for improving the aerodynamic performance of a VAWT [Dereng 1981 and Lissaman 1994] by increasing the tangential force coefficient which is defined as

$$C_t = C_l \sin \alpha - C_d \cos \alpha \tag{5.1}$$

It can be seen in Figure 5.10 that the C_l/C_d ratio of S1210 and NACA 4415 is much higher over a wide range of positive incidence in the pre-stall range than NACA 0015 at $RN=100,000$, clearly demonstrating their superiority at positive incidences. However, at negative incidences the reverse is true. But it has already been established in Section 5.3.1 that relatively the contribution of airfoils at positive incidences is more important than that of negative incidences for the concave-out configuration. At positive incidence and higher RN , the C_l/C_d ratios of all the asymmetric airfoils, except LS-0417, are better than that of NACA 0015, but again the situation is reversed at negative incidences.

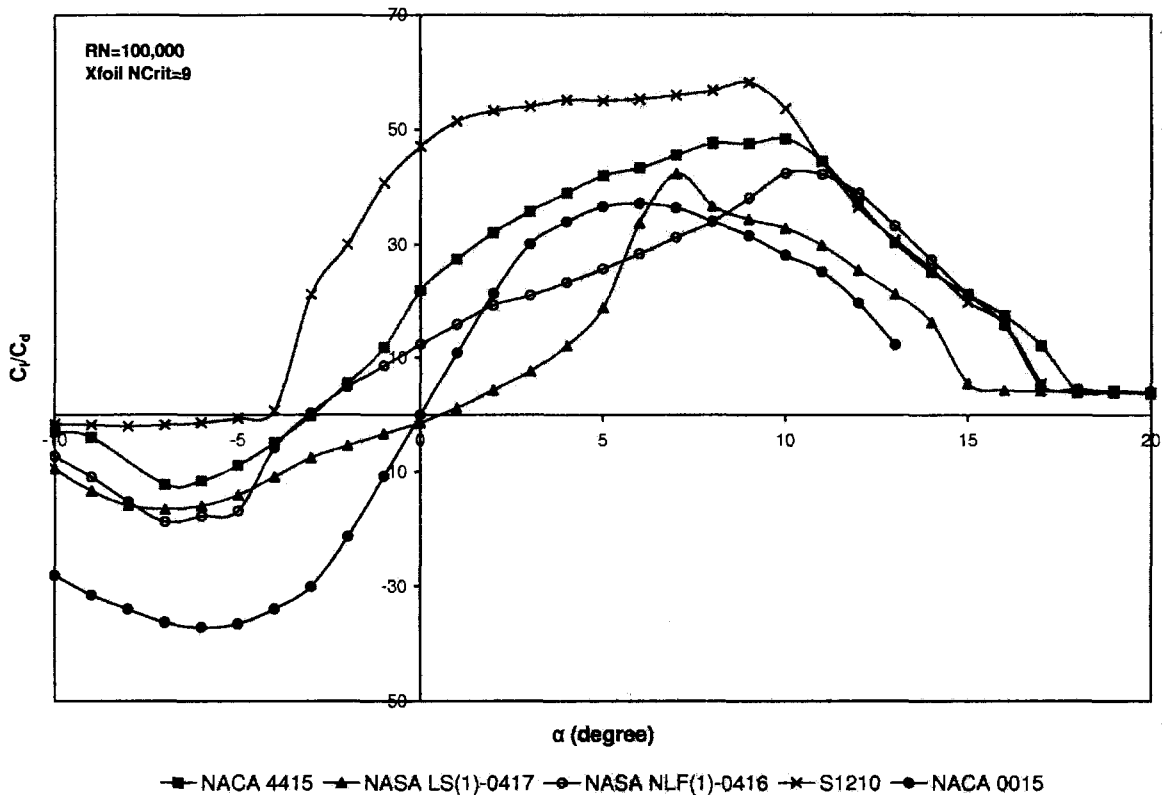


Figure 5.10: C_l/C_d Ratio of Selected Asymmetric Airfoils at $RN=100,000$

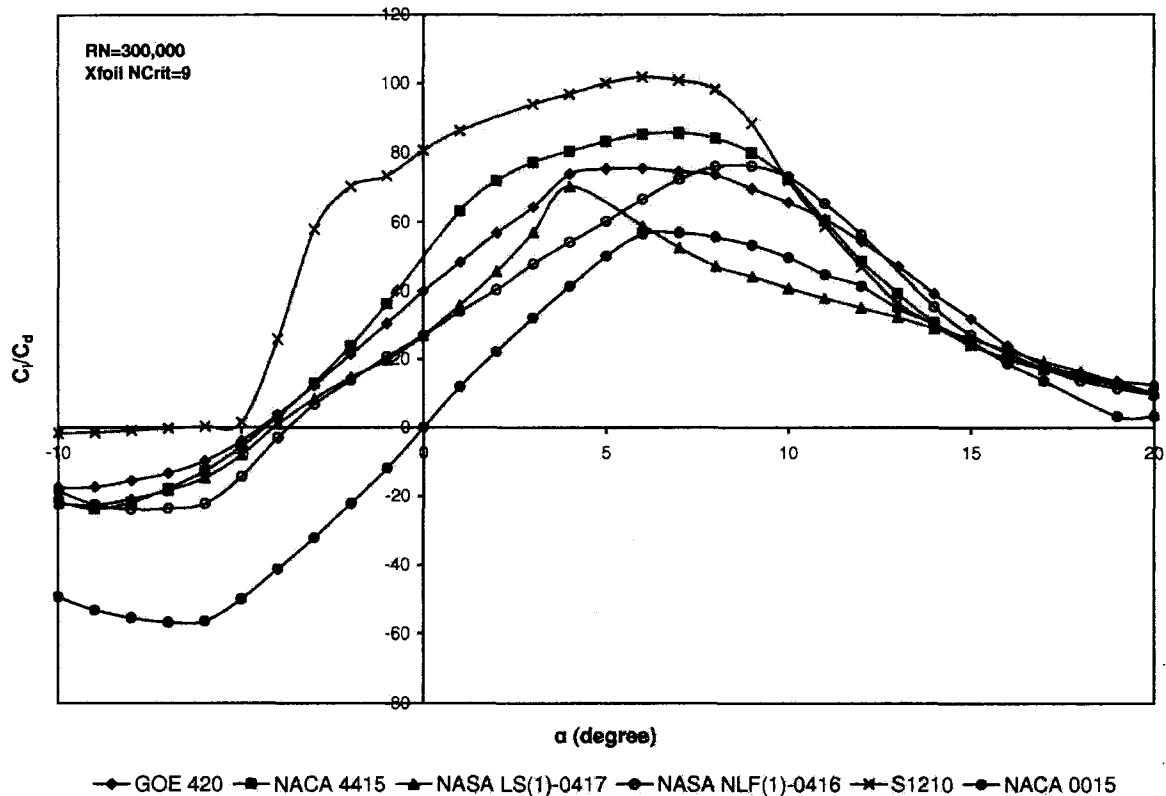


Figure 5.11: C_l/C_d Ratio of Selected Asymmetric Airfoils at $RN=300,000$

5.3.5. High Maximum Lift-Coefficient

If the airfoil shape of a smaller-capacity SB-VAWT has higher $C_{l,max}$, more positive torque will be generated in the pre-stall regime. This feature will also enhance the starting torque. Both high lift and stall angle are therefore desirable for SB-VAWTs. Furthermore, $C_{l,max}$ should be relatively insensitive to the changes of RN . The $C_{l,max}$ of asymmetric airfoils at positive α are usually much better than the symmetric profiles like NACA 0015 which is depicted in Figures 5.6 and 5.7 for RN of 100,000 and 300,000 respectively. Seki et. al [1985] suggested that the slope of the lift curve of SB-VAWT airfoil should be steeper for improved efficiency.

5.3.6. Delayed Deep-stall Property

Deep stall has negative influence on the performance of SB-VAWT. According to Claessens [2006], deep stall characteristics of airfoil are important for VAWTs and he suggested that:

- (i) deep stall should be postponed to a larger angle of attack;
 - (ii) hysteresis loop of the deep stall should be as small as possible; and
 - (iii) the drop of lift coefficient should be as small as possible at deep stall.
- The angle at which deep stall occurs depends on RN and the nose radius.

Timmer [2003] correlated the available data with the thickness of the airfoil nose, defined as the y/c value at $x/c=0.0125$, following the work of Gault [1957], in which the stalling characteristics of a large number of low-speed airfoils have been correlated. Timmer measured the deep stall characteristics of multiple profiles. He found a linear relation between the thickness of the nose and the deep-stall angle and the resulting straight line can be translated to the following relation between the thickness of the nose and the deep stall angle:

$$\alpha_{deep-stall} = 1114 \left(\frac{y}{c} \right)_{\frac{x}{c}=0.0125} \quad (5.2)$$

Using the above equation, the deep-stall characteristics of NACA 0015 and the selected asymmetric airfoils have been investigated in the present analysis and results are presented in Figures 5.12 and 5.13 for the upper and lower surfaces of the airfoils.

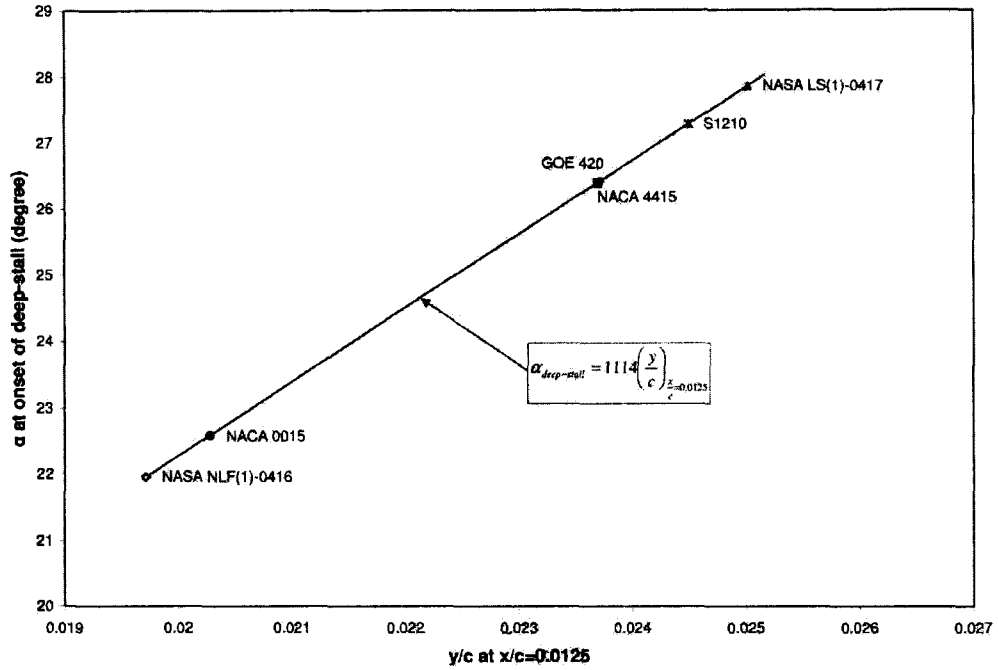


Figure 5.12: Deep Stall Characteristic on the Upper Surfaces of Selected Prospective Airfoils [Islam et. al 2007b]

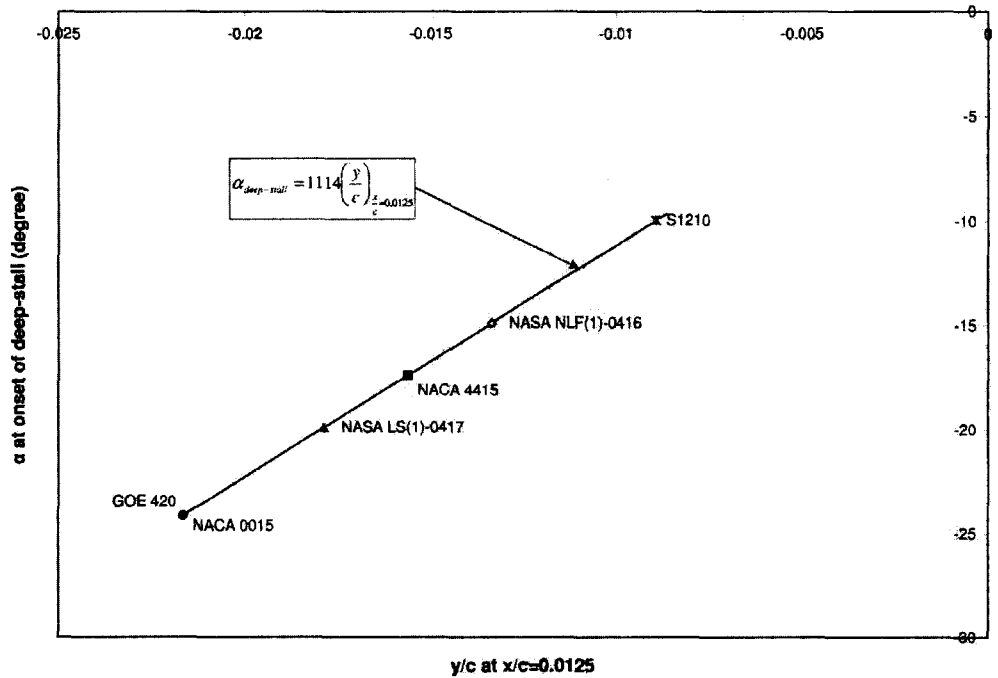


Figure 5.13: Deep Stall Characteristic on the Lower Surfaces of Selected Prospective Airfoils [Islam et. al 2007b]

It is seen in Figure 5.12 that except NLF-0416, the onset of deep-stall on the upper surface is delayed for the other asymmetric airfoils in comparison to NACA 0015. In Figure 5.13, the negative values in x/c denote lower surface ordinates and it can be seen that onset of deep-stall of NACA 0015 and GOE 420 are the lowest. It would be worthwhile to highlight that the analysis performed by Timmer [2003] is done at high RN range of 1 million and its applicability to low RN range typically encountered by smaller capacity SB-VAWT should be investigated further.

5.3.7. Low Roughness Sensitivity

The airfoil should have least amount of roughness sensitivity as wind turbines operate at diversified climatic conditions and its maintainability and performance deteriorate with surface roughness due to dust, dirt, rain or insect debris [Hansen and Butterfield 1993]. Because of surface roughness the boundary layer of the blades will turn turbulent near the nose, which results in a turbulent boundary layer over the airfoil [Claessens 2006].

Surface roughness generally decreases $C_{l,max}$ and increases C_{do} and these effects become more pronounced as RN increases [Miley 1982]. According to Lissaman [1994], $C_{l,max}$ of the NACA 230XX series airfoils are very sensitive to surface fouling, and their performance deteriorates with increased thickness more rapidly than that of other airfoils.

Lissaman [1994] also commented that NACA 63-2XX series airfoils have demonstrated the best overall performance characteristics of the NACA families, and they give reasonable resistance to roughness losses. Airfoils in the LS(1)-04XX series were designed to tolerate surface fouling, but HAWTs with these airfoils have experienced large power losses induced by roughness [Lissaman 1994].

To analyze the roughness sensitivity of airfoils in the wind tunnel, zigzag tape is usually applied at locations near to the leading edge of the airfoil. This situation can be simulated in XFOIL by imposing fixed transition near to the leading edge portion.

To compare the roughness sensitivity of the candidate airfoils for SB-VAWT, a trip is used at 10% chord length downstream of the leading edge at $RN=100,000$ and $300,000$. The results of the simulation at 10% fixed transition are compared with the salient characteristics of these airfoils at free transition and they are presented in Tables 5.1 and 5.2.

It can be seen from Table 5.1 that for all the airfoils, α_{stall} have increased, whereas $C_{l,max}$ and C_l/C_d ratio have decreased. Mixed trends have been observed for C_{do} and C_m of these airfoils at $RN=100,000$. However, at $RN=300,000$ (as shown in Table 5.2), α_{stall} and C_{do} of all the airfoils have increased, whereas C_l/C_d and C_m have decreased. In this case, mixed trends have been observed for $C_{l,max}$.

It can be inferred from these results that C_{do} , which is a very important parameter for SB-VAWT, is most affected due to roughness and it increases appreciably with RN . Among all the airfoils, C_{do} of LS(1)-0417 is found to be least sensitive to roughness both at $RN=100,000$ and $300,000$ which is consistent with the comment of Lissaman [1994] stated above. It is also found that C_{do} of NACA0015 is severely affected at $RN=300,000$ because of roughness.

Table 5.1: Roughness Sensitivity of Selected Airfoils at $RN=100,000$ [Islam et. al 2007b]

Airfoil	α_{stall} (degree)		$C_{l,max}$		C_{do}		C_l/C_d		C_m	
	Free Transition	Fixed Transition	Free Transition	Fixed Transition	Free Transition	Fixed Transition	Free Transition	Fixed Transition	Free Transition	Fixed Transition
NACA 0015	11.00	13	1.05	1.0196	0.0196	0.0204	37.42	28.99	-0.0423	-0.0463
NACA 4415	10.60	14	1.41	1.1994	0.0262	0.0221	48.96	32.01	-0.1073	-0.0798
LS(1)-0417	12.20	14.6	1.35	1.3052	0.0398	0.0229	42.31	28.87	-0.1238	-0.1263
NLF-0416	11.20	13.8	1.34	1.1486	0.0258	0.0216	43.13	33.50	-0.1219	-0.1076
S1210	9.60	14.4	1.91	1.6416	0.0745	0.1171	58.27	45.81	-0.2505	-0.2333

Table 5.2: Roughness Sensitivity of Selected Airfoils at $RN=300,000$ [Islam et. al 2007b]

Airfoil	α_{stall} (degree)		$C_{l,max}$		C_{do}		C_l/C_d		C_m	
	Free Transition	Fixed Transition	Free Transition	Fixed Transition	Free Transition	Fixed Transition	Free Transition	Fixed Transition	Free Transition	Fixed Transition
NACA 0015	15.00	15.2	1.20	1.2197	0.0086	0.0151	57.75	43.08	-0.0440	-0.0247
NACA 4415	13.00	16.2	1.46	1.3935	0.0126	0.0163	85.59	46.58	-0.1063	-0.0858
LS(1)-0417	14.80	16.8	1.49	1.5059	0.0130	0.0168	73.76	41.93	-0.1066	-0.0919
NLF-0416	13.20	16.2	1.47	1.3516	0.0106	0.0159	76.66	50.87	-0.0946	-0.0872
S1210	11.00	14	1.96	1.843	0.0797	0.1252	101.72	64.25	-0.2456	-0.2319

5.3.8. Low Trailing Edge Noise Generation

The laminar separation bubbles that extend over the trailing edge of the airfoil cause the blades to vibrate and are a source of noise. As SB-VAWTs have prospects to operate in the urban environments, noise emission should be kept as low as possible. According to Claessens [2006], an airfoil with smooth stall characteristics is desirable for reducing the trailing edge noise. In order to assess the trailing edge noise generated by the candidate airfoils, NAFNoise (which stands for NREL AirFoil Noise) has been utilized in the chapter.

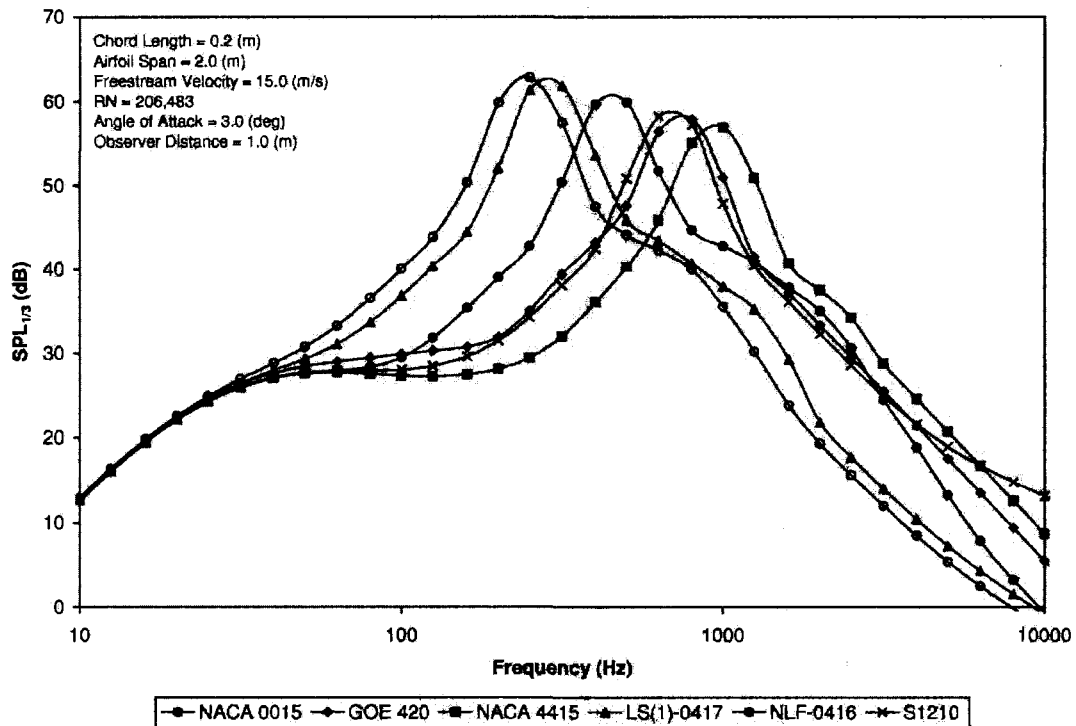


Figure 5.14: Comparison of Sound Pressure Levels (SPL) of Selected Prospective Airfoils [Islam et. al 2007b]

NAFNoise is a program that predicts the noise of any airfoil shape for different types of noise sources, including trailing-edge noise [Moriarty 2005]. Empirical models for the trailing edge noise sources were originally developed by Brooks, Pope and Marcolini [Brooks et. al 1989] and it models any airfoil shape by using

the boundary layer calculations of XFOIL which can be used as inputs into the models of Brooks, Pope, and Marcolini. In Figure 5.14, sound pressure level (SPL) at 1/3rd octave of candidate airfoils are shown. It can be seen from this figure that among all the airfoils, NLF(1)-0416 and NACA 4415 are generating highest and lowest amounts of noise respectively.

5.3.9. Large Negative Pitching Moment

Kato et. al [1981b] utilized a theory of simple tube of flow and found that pitching moment coefficient (C_m) of a SB-VAWT airfoil should be large in negative values for high efficiency. In their publication, they produced C_P - λ curve which shows better performance of an airfoil with $C_m=0.05$ relative to an airfoil with $C_m=0$ at higher TSR (>3.5) range. The variations of C_m of the selected airfoils are shown in Figures 5.15 and 5.16 for RN of 100,000 and 300,000. For both cases, the values of C_m for S1210 are most negative and they fluctuate around zero for NACA 0015.

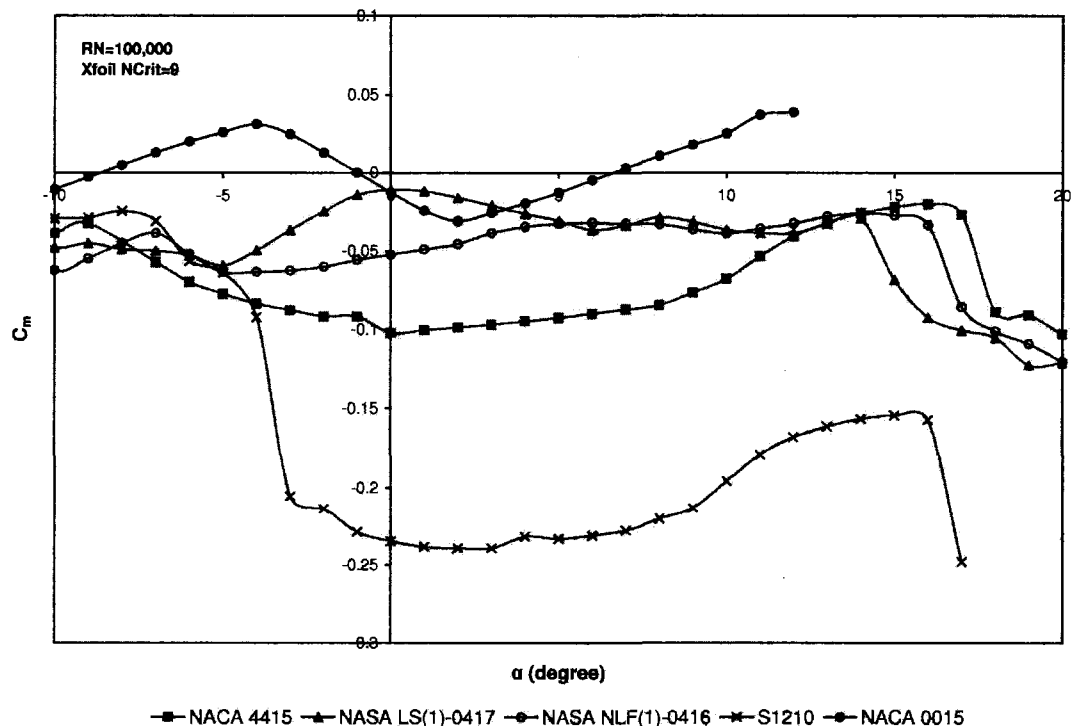


Figure 5.15: Pitching Moment Coefficient of Selected Asymmetric Airfoils at RN=100,000

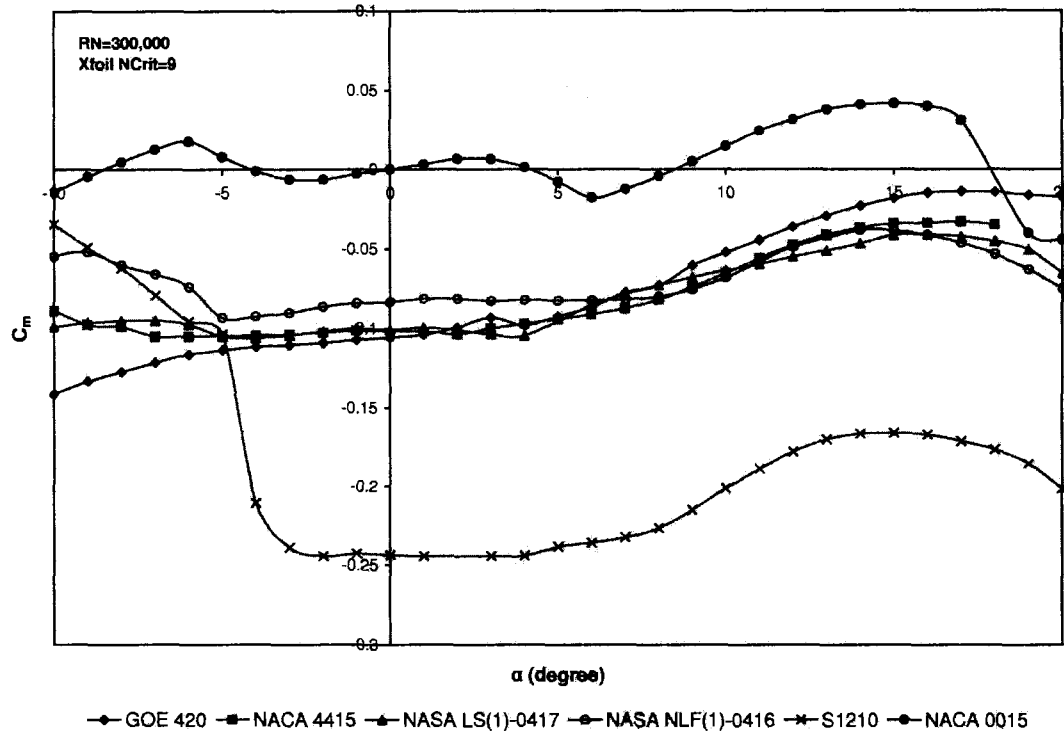


Figure 5.16: Pitching Moment Coefficient of Selected Asymmetric Airfoils at $RN=300,000$

In this section, nine desirable aerodynamic characteristics are identified and performance of the selected candidate airfoils is determined. All these characteristics are summarized in Table 5.3 for overall comparison and each candidate airfoil is rated (as shown within the parenthesis) based on each desirable characteristic for quick reference.




5.4. Desirable Geometric Features of SB-VAWT Airfoil

Desirable aerodynamic characteristics described in the previous section results from the different geometric features of an airfoil as shown in Figure 5.17. So, it is of profound importance to identify the required geometric features which is done in this section. A designer of small-scale SB-VAWT should consider these features while selecting an airfoil and a judicious choice should be made. Also, performance analysis of a SB-VAWT equipped with the selected airfoil as a blade shape should be done using one of the available computational models [Islam et. al 2008] before field applications.

Table 5.3: Ratings of Candidate Airfoils Based on Desirable Aerodynamic Characteristics [Islam et. al 2007b]

Airfoil	Stall Angle (degree)		Drag Bucket		C _{do}		(C _f /C _l) _{max}		C _{l,max}		Deep Stall (degree)		Roughness Sensitivity (% Change in C _{do} due to Trip)		C _{m,min}		SPL _{1/3,max} (dB)
	RN=100,000	RN=300,000	RN=100,000	RN=300,000	RN=100,000	RN=300,000	RN=100,000	RN=300,000	RN=100,000	RN=300,000	Upper Surface	Lower Surface	RN=100,000	RN=300,000	RN=100,000	RN=300,000	
NACA 0015	11.0 (3)	15.0 (1)	Large (1)	Large (1)	0.0196 (1)	0.0086 (1)	37.42 (5)	57.75 (6)	1.05 (5)	1.20 (6)	22.59 (5)	-24.12 (1)	4.08 (4)	75.58 (5)	-0.0423 (5)	-0.044 (6)	59.90 (4)
GOE420	-	14.4 (3)	-	Medium (3)	-	0.0127 (4)	-	75.45 (4)	-	1.40 (5)	26.41 (3)	-24.09 (2)	-	-	-	-0.1496 (2)	57.90 (2)
NACA 4415	10.6 (4)	13.0 (5)	Medium (2)	Medium (2)	0.0258 (2)	0.0126 (3)	48.96 (2)	85.59 (2)	1.41 (2)	1.46 (4)	26.39 (4)	-17.38 (4)	-15.65 (3)	29.37 (2)	-0.1073 (4)	-0.1063 (4)	56.95 (1)
LS(1)-0417	12.2 (1)	14.8 (2)	Small (5)	Small (6)	0.0398 (4)	0.013 (5)	42.31 (4)	73.76 (5)	1.35 (3)	1.49 (2)	27.87 (1)	-19.89 (3)	-42.46 (1)	29.23 (1)	-0.1238 (2)	-0.1066 (3)	61.92 (5)
NLF(1)-0416	11.2 (2)	13.2 (4)	Medium (3)	Medium (4)	0.0258 (3)	0.0106 (2)	43.1291 (3)	76.66 (3)	1.34 (4)	1.47 (3)	21.95 (6)	-14.87 (5)	-16.28 (2)	50.00 (3)	-0.1219 (3)	-0.0946 (5)	62.88 (6)
S1210	9.6 (5)	11.0 (6)	Medium (4)	Medium (5)	0.0745 (5)	0.0797 (6)	58.2696 (1)	101.72 (1)	1.91 (1)	1.96 (1)	27.29 (2)	-9.84 (6)	57.18 (5)	57.09 (4)	-0.2505 (1)	-0.2456 (1)	58.27 (3)

Table 5.4: Three Types of Airfoils for Generating Lift [Islam et. al 2007b]

	Type-1	Type-2	Type-3
Geometry			
Adverse pressure gradient (APG)	Requires strong APG on the upper surface	Upper surface requires strong APG (like Type-1), but lower surface required moderate APG.	Require moderate APG.
$C_{L,max}$ as RN decreases	Decreases appreciably	Decreases appreciably	Decreases moderately
α_{Stall} as RN decreases	Decreases appreciably	Decreases appreciably	Decreases moderately
Roughness sensitivity	More sensitive and there is loss of lift and increase in drag	More sensitive and there is loss of lift and increase in drag	Less sensitive and there is loss of lift and increase in drag
Applicability	-	Suitable for aviation applications.	Suitable for Low RN applications and used extensively for model aircraft and small low-speed fans.

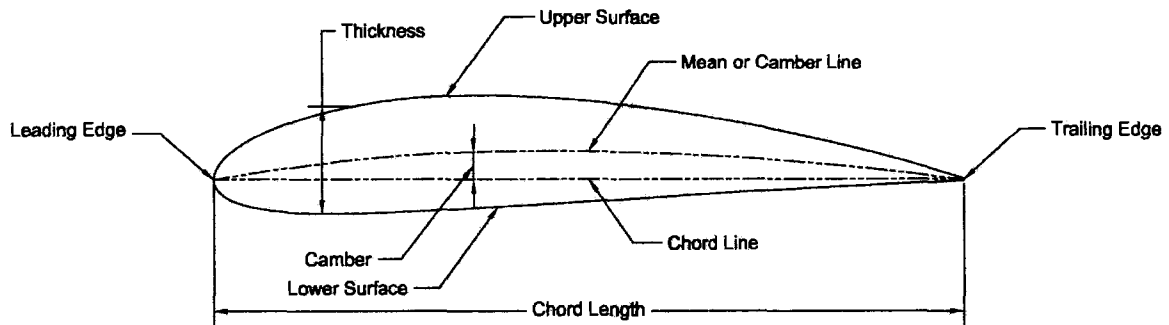


Figure 5.17: Geometric Features of a Typical Asymmetric Airfoil [Islam et. al 2007b]

5.4.1. Camber

Baker [1983] compared the theoretical performance of a moderately cambered Göttingen 420 aerofoil with that of a symmetrical NACA 0012 aerofoil with similar thickness. His modeling indicated that the cambered section would produce a higher tangential thrust (i.e. torque) over a wider range of α and more energy per “cycle” (i.e. per revolution) than the symmetrical section, and that a VAWT using the cambered blades would self-start, unlike the same turbine with the symmetrical blades. Kirke [1998] also found that a turbine with cambered NACA 4415 blades of 0.32 m chord should easily self-start in a 10 m/s wind ($Re = 200,000$), unlike an otherwise identical turbine with symmetrical NACA 0015 blades.

Kirke measured and compared the lift curves obtained for three airfoils, namely NACA 0015 (symmetric), NACA 4215 (asymmetric) & NACA 4415 (asymmetric), at three low values of Reynolds number – (i) 85,000; (ii) 124,000; and (iii) 213,000. He found that at the lowest Reynolds number value of 85,000 - “*the more highly cambered NACA 4415 section develops much higher lift at positive incidence than the other two sections, while at negative incidence there is little difference between the three curves, i.e. the cambered section is greatly superior at positive incidence and not much inferior at negative incidence and so is likely*”

to give superior starting performance". He also found that as RN increases, the superiority of the cambered sections in terms of lift at positive incidence becomes less pronounced. The four net advantages of cambered asymmetric airfoils over symmetric ones can be summarized as:

(i) Higher lift at low RN: In general, cambered blade sections produce higher lift at low RN and positive incidence than do symmetrical sections. The small-scale SB-VAWTs are usually designed to operate between chord RN of 100,000 to 300,000, which is considered as the Low RN regime. Miley [1982] remarked that at low RN, the laminar boundary layer is more stable and resistant to transition. The turbulent boundary layer is weak, and is able to tolerate only mild adverse pressure gradients (APG). There must be a large APG on either the upper or lower surface of an airfoil to generate lift and usually it is done in one of the three ways as described in Table 5.4. It can be concluded from Miley's investigation that for low RN operation, the type-3, which is basically a cambered airfoil, produces lift from high pressure on the lower surface and its APG is most moderate of the 3 types. Thus type-3 airfoils are less prone to separation which causes loss of lift and increase in drag.

(ii) Lesser roughness sensitivity: The type-3 cambered airfoils are also less sensitive to roughness because the behavior of the boundary layer is less critical for the realization of the lift producing pressure distribution. The increase in drag is common to all the three types of airfoils described above, but for type-3 the loss of lift is generally less [Miley 1982].

(iii) Higher stall angle: The stall angle of asymmetric cambered airfoils is higher than symmetric airfoils

(iv) Large negative pitching moment: Asymmetric airfoils usually produce large negative pitching moment (unlike symmetric airfoils), they are expected to show better performance in the higher λ range according to the study of Kato et al. [1981b].

5.4.2. Larger Thickness

Blades with thicker airfoils shapes have at least five advantages for small-scale SB-VAWTs, which are:

(i) Improvement of performance: Theoretical work by Healy [1978a] indicated that thicker sections, at least up to 18%, offer better performance at RN around 200,000-300,000. Also, Angell et. al. [1988] showed that sections up to about 20% thickness may be used with no loss in performance at RN of the order of 1.5 million.

(ii) Increase in Starting Torque: They also tend to increase starting torque according to modelling by Simhan [1994]. This apparently occurs because the drop in C_l associated with stall occurs less suddenly and sharply than with thinner sections. Dereng [1981] suggested that – “Airfoils of 19 percent chordal thickness have shown the most desirable start-up and traverse characteristics.” Seki [2005] also suggested a maximum thickness of the 2D blade between 20 and 25 percent of the chord thickness for improving the turbine self-starting performance and the efficiency of his straight wing type wind and water turbine which was patented in the USA.

(iii) Increase in Width of the Drag Bucket: In some airfoil series, larger thickness makes a wider drag bucket to maintain performance over a larger range of α [Claessens 2006].

(iv) Lower Radiated Sound: According to experiments conducted at Dutch national aerospace laboratory [Parchen et. al 1997], It has been found out that the radiated sound decreases with an increasing blade thickness.

(v) Improvement of Structural Strength: Blades with thicker airfoil shape can be made structurally stronger [Hansen and Butterfield 1993] with little increase in cost.

The above-mentioned advantages are due to several factors, including (i) soft stall or trailing edge stall which delays separation; (ii) higher amount of torque

and (iii) wide range for $C_{l,max}$ [Kirke 1998, Healy 1978a]. It has also been identified by Claessens [2006] that a thicker airfoil will in general also have deep stall at a higher angle of attack and they have generally a larger drop in lift at deep stall. It was also pointed out by Zervos [1988a] that the effect of thickness on detrimental unsteady loading was found to be very small. However, there is a limit to the benefits to be gained by using very thick airfoils at very low RN. Sato and Sunada [1995] have shown that airfoils of 28.5% thickness may fail to develop any useful lift at very low RN of the order of 33,000.

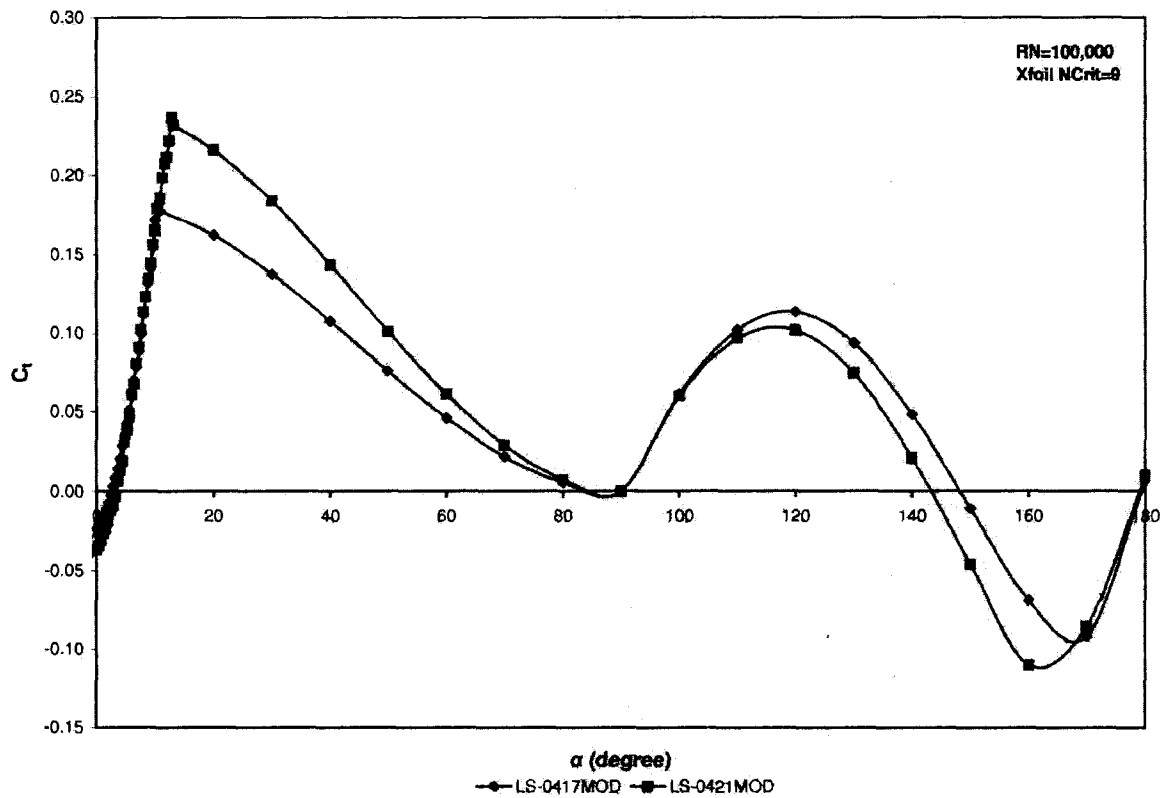


Figure 5.18: C_r - α Curves of LS(1) 0417MOD & LS(1) 0421MOD at RN=100,000 [Islam et. al 2007b]

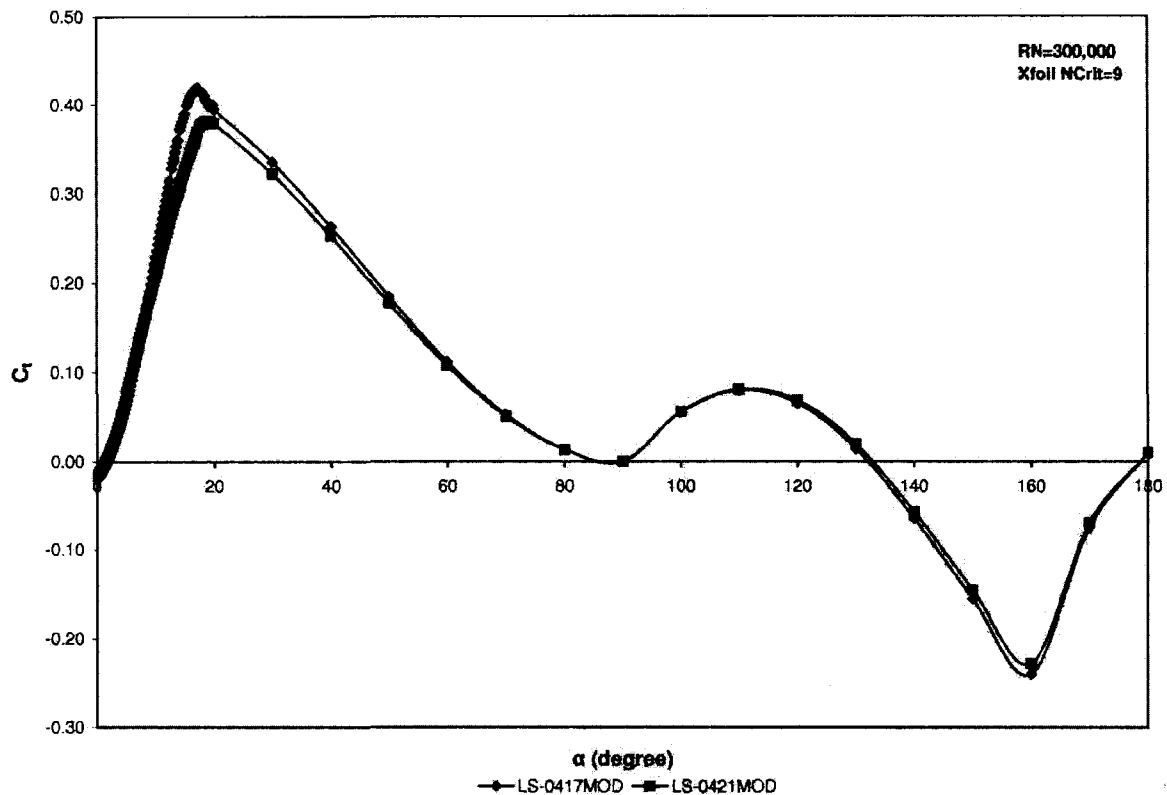


Figure 5.19: C_t - α Curves of LS(1) 0417MOD & LS(1) 0421MOD at $RN=300,000$ [Islam et. al 2007b]

To elucidate the performance of a low-speed asymmetric airfoil at different thickness, C_t - α curves of NASA LS-0417MOD and LS-0421MOD at $RN=100,000$ and $300,000$ are shown in Figures 5.18 and 5.19 respectively. It can be seen from Figure 5.18 that C_t values of NASA LS-0421MOD is higher in the post-stall regimes at $RN=100,000$. At $RN=300,000$, as shown in Figure 5.19, the C_t values of both the airfoils are similar.

5.4.3. Large Leading Edge Radius

Fupeng et. al [2001] suggested that larger leading edge radius is desirable as they are less sensitive to roughness which is a desirable aerodynamic characteristic for smaller capacity SB-VAWT as mentioned in Section 5.3.7. So,

larger leading edge radius will result in improved energy harness by SB-VAWT under dirty blade conditions owing to the accumulation of insect debris and also to increases of the lift-drag ratio of airfoil at large angle of attack. As described in Section 5.3.6, deep stall characteristic of an airfoil also depends on leading edge radius. It is worthwhile to mention here that Dereng [1981] suggested well rounded airfoils for VAWTs.

5.4.4. Moderate Trailing Edge Thickness

A study of trailing edge treatment was carried out by Sandia National Laboratory on SAND 0018/50, an airfoil specifically designed for VAWT, using extruded aluminum alloy model and it was found out that sharp trailing edge significantly reduced the minimum drag coefficient [Paraschivoiu 2002]. However, the SAND 0018/50 airfoil was developed for high RN operation unlike the present case of low RN.

Sato and Sunada [1995] had conducted wind-tunnel tests of five thick airfoils at low RN of 33,000, 66,000 and 99,000 and they measured lift and drag forces. They [Sato and Sunada 1995] found that by cutting off the trailing edge of the section and by making its trailing edge blunt at low Reynolds numbers – (i) the total drag can be reduced; (ii) the maximum lift increased; (iii) the linearity of lift curve with incidences improved; and (iv) the maximum lift-to-drag ratio increased. In Chapter 7, computational investigation has been performed to show that trailing edge thickness has positive effect on performance of SB-VAWT at low RN.

Though a smaller amount of trailing edge thickness is beneficial performance wise, but it should not be excessive for SB-VAWT blades. It should also be pointed out that fabrication of sharp trailing edges is often quite difficult and costly. It is easier to make the airfoil structurally stronger and more rigid by admitting thickness at the trailing edge [Sato and Sunada 1995].

For comparison purpose, the salient geometric features of the selected candidate airfoils that have been analyzed in the previous section are presented and rated according to the findings of this section in Table 5.5. However, it should be mentioned that the optimum camber for self-starting and better performing SB-VAWT is related to chord-radius ratios because of flow curvature effects and it should be judiciously chosen.

Table 5.5: Geometric Features of Selected Airfoils [Islam et. al 2007b]

Airfoil	Camber (% of c)	Thickness (% of c)	Leading Edge Radius (% of c)	Trailing Edge Thickness (% of c)
NACA 0015	0.00 (6)	15.00 (4)	2.37 (3)	0.32 (2)
GOE420	4.31 (2)	18.76 (1)	2.70 (2)	0.00 (3)
NACA 4415	4.00 (3)	15.00 (4)	2.22 (4)	0.32 (2)
LS(1)-0417	2.17 (5)	16.98 (2)	2.97 (1)	0.71 (1)
NLF(1)-0416	2.44 (4)	15.95 (3)	1.36 (6)	0.00 (3)
S1210	7.20 (1)	11.99 (5)	1.80 (5)	0.00 (1)

5.5. Performance Analysis with Candidate Asymmetric Airfoils

In this section, detail performance analyses of a SB-VAWT equipped with five of the candidate airfoils are further analyzed using the computational models described in the Chapter 4. The analyses are carried out between RN of 50,000 and 300,000.

In Figure 5.20, $C_{P,net}-\lambda$ curves of SB-VAWTs with the selected airfoils are shown at RN=50,000. It can be seen from this figure that at low λ , $C_{p,net}$ value of all the asymmetric airfoils are higher than NACA 0015. However, at $\lambda>3$ NACA 0015 generates more power at certain wind velocity. It is also observed from Figure 5.20 that at $\lambda<0.6$, NASA NLF(1)-0416 does not produce positive value of $C_{p,net}$ which is very undesirable. Among all the asymmetric airfoils, $C_{P,net}$ values of S1210 is very low at all λ in comparison to the other airfoils. One of the reasons for poor performance of S1210 can be attributed to its large maximum camber of 7.2% because of which it is producing lesser power in the downstream side. In Figure 5.21, $C_{Q,net}-\lambda$ curves of SB-VAWTs with the selected airfoils are shown at RN=50,000. All the asymmetric airfoils are producing more torque than NACA 0015 at low λ range. But, performance of NACA 0015 is better than the asymmetric airfoils at $\lambda>3$.

In Figure 5.22, $C_{P,net}-\lambda$ curves of SB-VAWTs with the selected airfoils are shown at RN=100,000. It can be seen from this figure that at low λ , $C_{P,net}$ of all the asymmetric airfoils are higher than NACA 0015. However, at $\lambda>2.5$ NACA 0015 generates more power. Among all the asymmetric airfoils, $C_{P,net}$ values of S1210 is very low at all λ in comparison to the other airfoils. In Figure 5.23, $C_{Q,net}-\lambda$ curves of SB-VAWTs with the selected airfoils are shown at RN=100,000. All the asymmetric airfoils are producing more torque than NACA 0015 at low λ range. But, performance of NACA 0015 is much better at higher λ . Among all the asymmetric airfoils, $C_{Q,net}$ values of LS-0417 are the highest up to $\lambda=3.5$ and that of S1210 are the least.

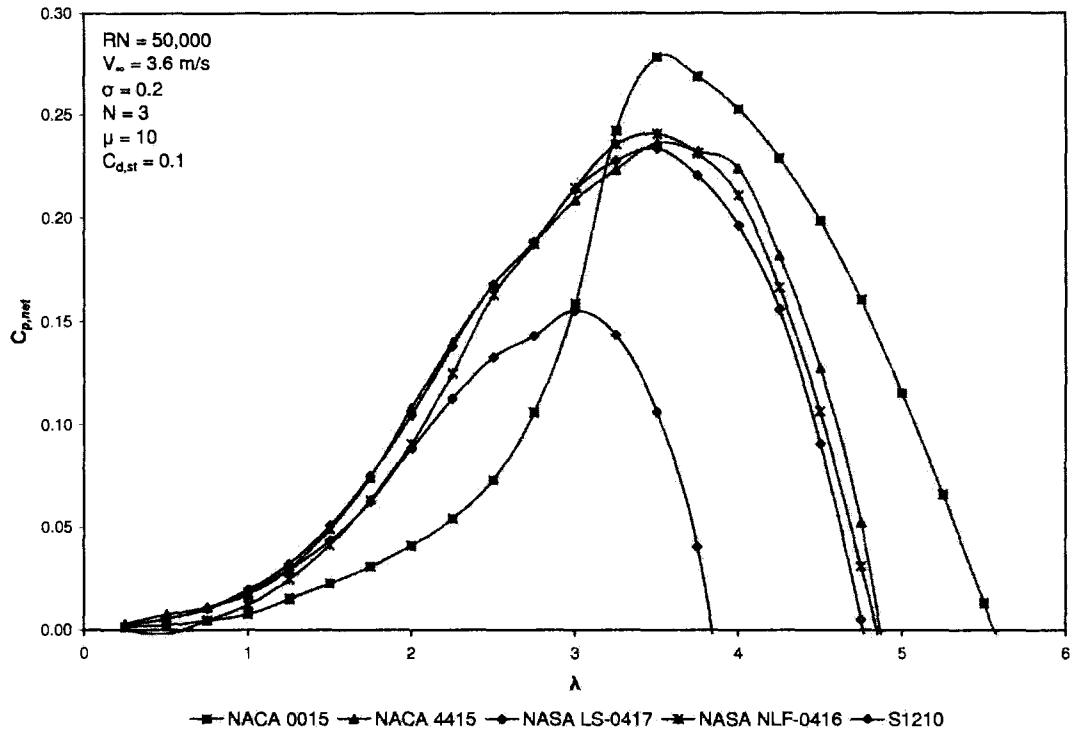


Figure 5.20: $C_{P,net}$ - λ Curves of SB-VAWTs with Selected Asymmetric Airfoils at $RN=50,000$

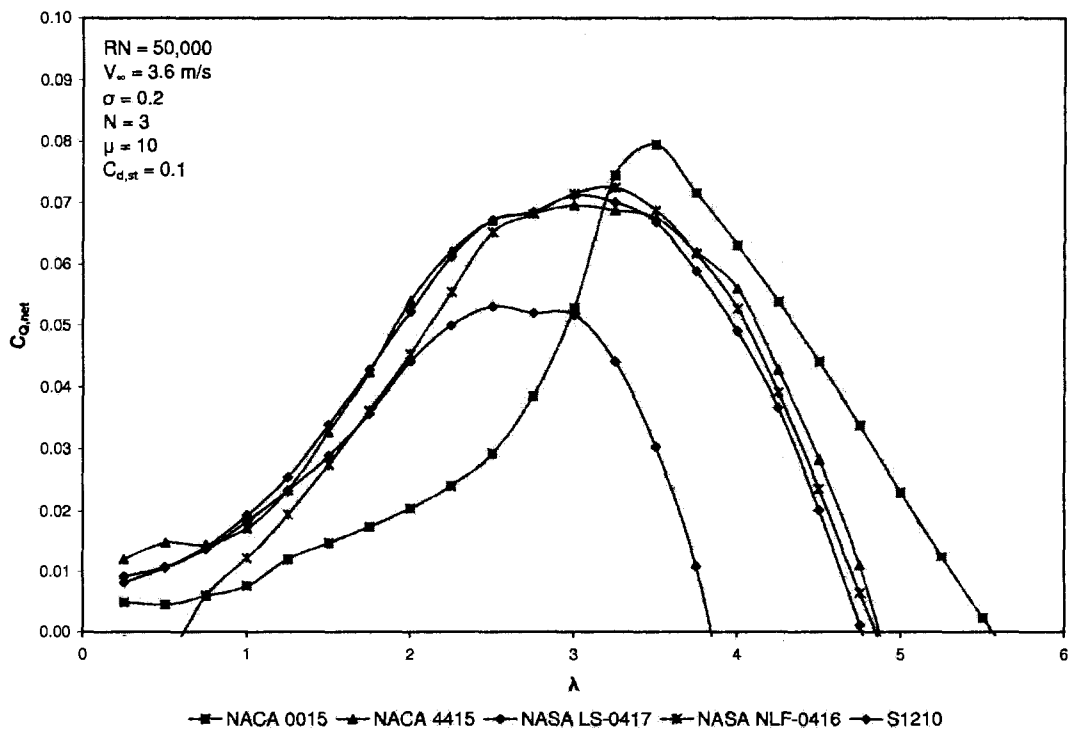


Figure 5.21: $C_{Q,net}$ - λ Curves of SB-VAWTs with Selected Asymmetric Airfoils at $RN=50,000$

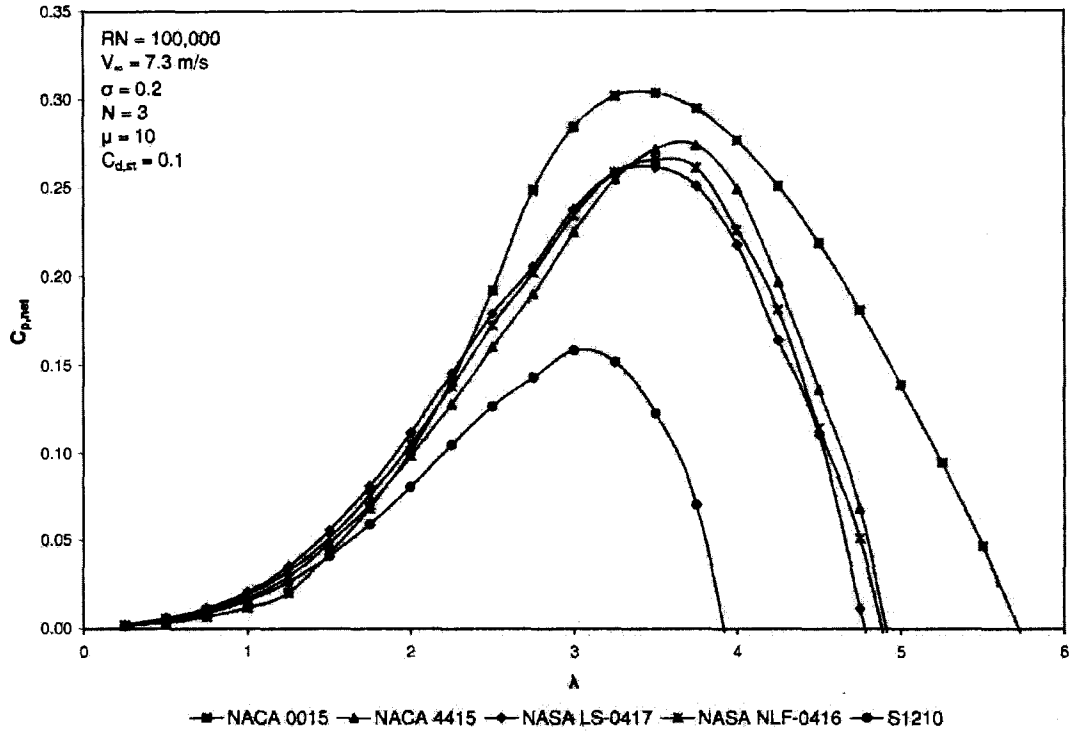


Figure 5.22: $C_{p,net}$ - λ Curves of SB-VAWTs with Selected Asymmetric Airfoils at $RN=100,000$
[Islam et. al 2007b]

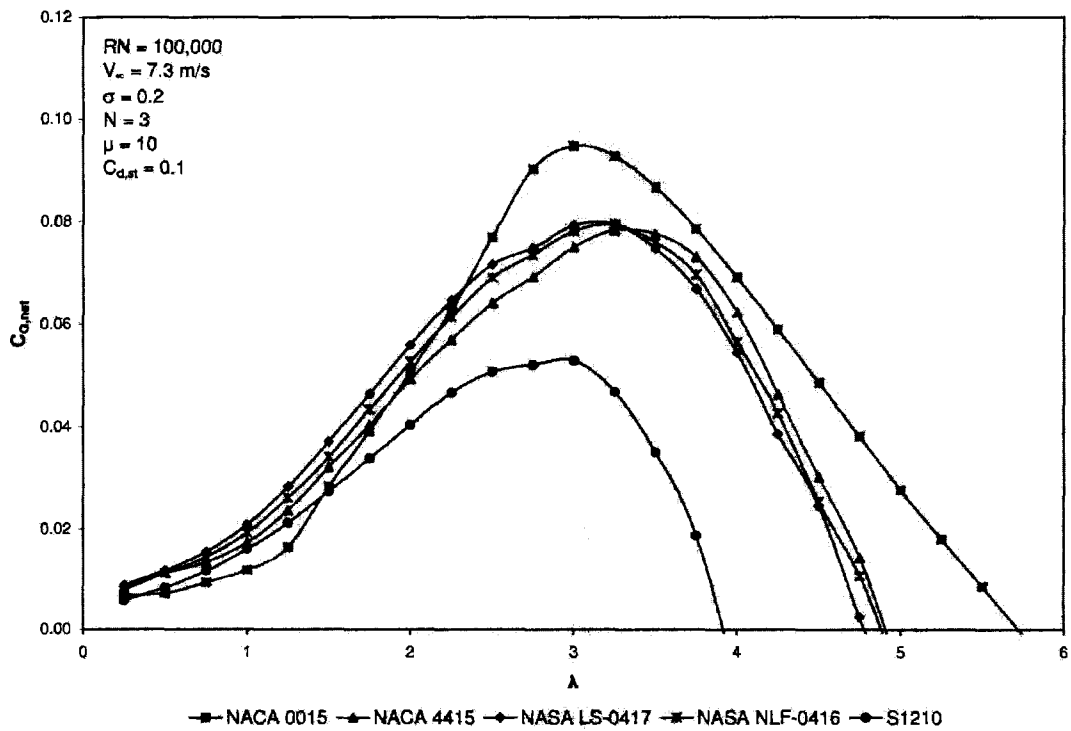


Figure 5.23: $C_{q,net}$ - λ Curves of SB-VAWTs with Selected Asymmetric Airfoils at $RN=100,000$
[Islam et. al 2007b]

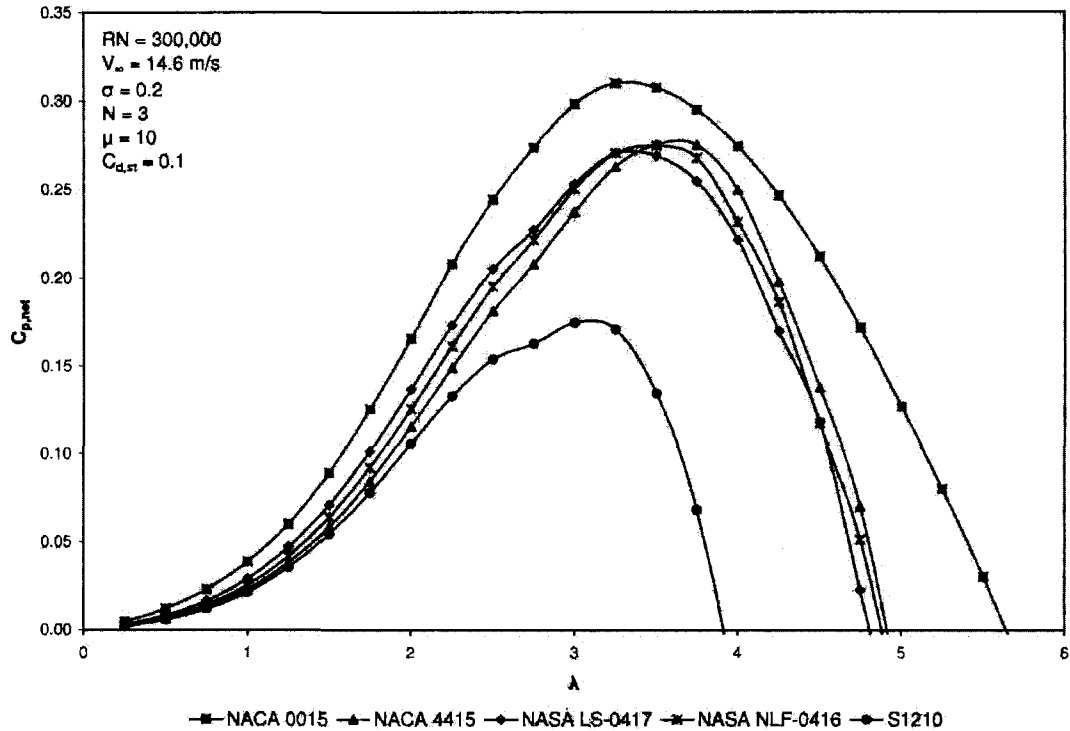


Figure 5.24: $C_{p,net}$ - λ Curves of SB-VAWTs with Selected Asymmetric Airfoils at $RN=300,000$ [Islam et. al 2007b]

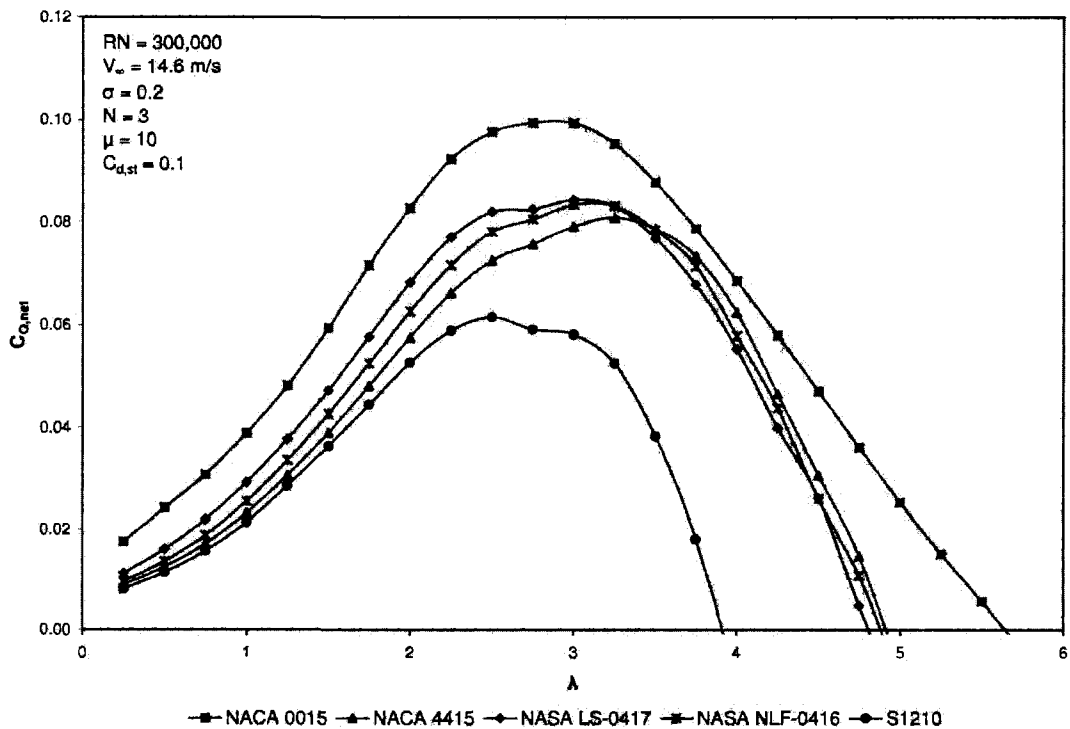


Figure 5.25: $C_{q,net}$ - λ Curves of SB-VAWTs with Selected Asymmetric Airfoils at $RN=300,000$ [Islam et. al 2007b]

In Figure 5.24, $C_{P,net}-\lambda$ curves of SB-VAWTs with the selected airfoils are analyzed at $Re=300,000$. At this Re $C_{P,net}$ values of NACA 0015 is higher than all the asymmetric airfoils at all the λ . Among all the asymmetric airfoils, $C_{P,net}$ values of LS-0417 are the highest up to $\lambda=3.25$, whereas that of S1210 are the lowest for all the values of λ considered. In Figure 5.25, $C_{Q,net}-\lambda$ curves are shown at $Re=300,000$. All the asymmetric airfoils are producing more torque than NACA 0015 at low λ . But, performance of NACA 0015 is much better at higher λ . Among all the asymmetric airfoils, $C_{Q,net}$ values of LS-0417 are the highest up to $\lambda=3.5$ and that of S1210 are the least.

It can be concluded from Figures 5.20 to 5.25 that the maximum value of $C_{P,net}$ and $C_{Q,net}$ of NACA 0015 are higher than all the asymmetric airfoils between $Re=50,000$ and $300,000$. Among all the asymmetric airfoils, the $C_{P,net}$ and $C_{Q,net}$ values of LS-0417 are better than the other asymmetric airfoils up to peak values which are the typical operating ranges of SB-VAWTs.

5.6. Summary of the Chapter

Selection of the airfoil is crucial for better aerodynamic performance and dimensions of a smaller-capacity SB-VAWT which can compete with conventional energy sources in niche markets like urban areas and off-grid remote applications for diversified applications. The aim of this chapter is to identify the desirable features of an ideal airfoil for smaller capacity SB-VAWT to improve its starting characteristics and overall performance.

An attempt has been made to shortlist several aerodynamic characteristics of the desirable airfoil and subsequently the required geometric features to achieve the short listed characteristics have also been determined. It has been found out in this chapter that conventionally used old NACA 4-digit symmetric airfoils are not suitable for smaller capacity SB-VAWTs. Rather, it will be advantageous to utilize

a high-lift and low-drag asymmetric thick airfoil suitable for low speed operation typically encountered by SB-VAWT.

In this chapter, nine aerodynamic features which would contribute to self-starting are identified, these are: (i) high stall angle at low Reynolds number, (ii) wide drag bucket, (iii) low zero-lift-drag coefficient, (iv) high C_l/C_d ratio, (v) high maximum lift-coefficient, (vi) delayed deep-stall property, (vii) low roughness sensitivity, (viii) low trailing edge noise generation, and (ix) large negative pitching moment.

After identification of these aerodynamic features, attempt has been made to select the desirable geometric features. It has been found that an airfoil for self-starting SB-VAWT with optimum performance should have camber, high thickness, large leading edge radius and moderate trailing edge thickness.

Four special-purpose asymmetric airfoils, designed for SB-VAWTs, have also been identified from the literature but could not be investigated due to non-availability of their geometry and copyright related issues. However, none of these special-purpose airfoils seems to be designed for the low RN operation and their main emphasis was on better performance.

Based on literature survey five asymmetric airfoils, designed mainly for the aviation purposes, found in the public domain were identified as potential candidates for SB-VAWTs by other researchers in the past. These candidate airfoils are investigated in this chapter and it has been found that none of these airfoils has all the desirable characteristics or geometric features.

Detail performance analyses of a SB-VAWT equipped with five of the candidate airfoils are further analyzed using the computational models described in the Chapter 4 and the results are compared with symmetric NACA 0015, which is

considered as an ideal airfoil for VAWTs [Paraschivoiu 2002]. The analyses are carried out at $Re=50,000$, $100,000$ and $300,000$.

It has been found that at $Re=50,000$, $C_{P,net}$ of all the asymmetric airfoils are higher than NACA 0015 in the low tip speed ratios (where the problem with the dead band responsible for self-starting problem occurs with conventional NACA airfoils). However, at $\lambda > 3$ NACA 0015 generates more power at certain wind velocity. Similar trend has been observed at $Re=100,000$ and $C_{P,net}$ of all the asymmetric airfoils are better than NACA 0015. However, at $\lambda > 2.5$ NACA 0015 generates more power. At $Re=300,000$, $C_{P,net}$ values of NACA 0015 is higher than all the asymmetric airfoils at all the λ which indicates that the candidate asymmetric airfoils can not perform better at $Re \approx 300,000$. Among all the asymmetric airfoils, $C_{P,net}$ values of LS-0417 are the best.

Chapter 6

Selection of Prospective Asymmetric Airfoils

Airfoils are specifically designed to generate lift force while keeping the drag force minimum. Selection of airfoil is crucial for better aerodynamic performance and design of aerodynamic applications such as wind turbine and aircrafts. In the previous chapter, five asymmetric airfoils which were investigated by other researchers in the past have been analyzed. Subsequently, several desirable characteristics of a SB-VAWT airfoil have been identified. Based on the criterion, an attempt has been made in this chapter to shortlist several other prospective candidate airfoils based on both experimental and analytical airfoil characteristics. New performance indices have been defined in the light of desirable aerodynamic characteristics to select best performing airfoil. After determining and rating of the candidate airfoils, the most promising airfoil is selected.

6.1. Criteria for Selection of Prospective Asymmetric Airfoils

Based on the finding of Chapter 5, the following aerodynamic and geometric criteria are used for finding more prospective airfoils from the public domain.

Aerodynamic Characteristic Features:

- (i) High stall angle at low Reynolds number,
- (ii) Wide drag bucket,
- (iii) Low zero-lift-drag coefficient,
- (iv) High C_l/C_d ratio,

- (v) High maximum lift-coefficient,
- (vi) Delayed deep-stall property,
- (vii) Low roughness sensitivity,
- (viii) Low trailing edge noise generation, and
- (ix) Large negative pitching moment.

Geometric Features:

- (i) Cambered
- (ii) High thickness
- (iii) Large leading edge radius and
- (iv) Moderate trailing edge thickness.

6.2. Selection of Candidate Airfoils Based on Experimental Results

An attempt have been made in the present research to investigate the experimental results of different types of airfoils which meet the ideal characteristics of the desired airfoil as described in the previous section. The airfoil datasets available in the public domain describe airfoils numerically in terms of coefficients such as lift, drag and pitching moment coefficients over various wind speed ranges, and are used as input into the computational performance analysis and design tools for SB-VAWT. The candidate is only interested in the experimental datasets for low speed applications which are often referred to as low Reynolds number conditions. These lower speed datasets proved to be difficult to find since most public domain datasets are for high Reynolds numbers as discussed in Section 4.2.1. The Reynolds number range of the experimental results is limited between 100,000 and 300,000 which is the typical operating condition of smaller-capacity SB-VAWTs. A sufficient sample size of the required datasets are needed to be identified, then they are

required to be retrieved in paper format, and subsequently digitized and converted into electronic format.

A comprehensive survey on the available low RN airfoil experimental results has been done by several researchers, including Miley [1980] and Kirke [1998]. These studies helped significantly in the present research. To find out prospective airfoils based on the criterion set in the previous section, the following series of airfoil datasets were investigated:

- (i) Gottingen Series
- (ii) NACA 4, 5 & 6 digit series
- (iii) Eppler low RN airfoils
- (iv) Wortmann FX series
- (v) NASA LS series
- (vi) NASA NLF series
- (vii) UIUC low RE airfoils

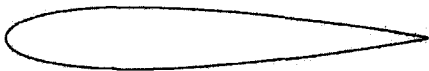
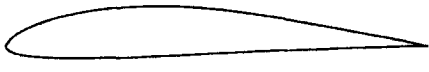
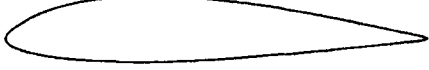


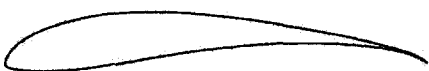
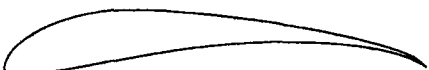
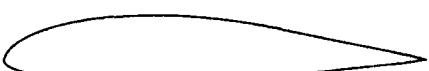
After doing meticulous screening process based on the criteria, seven low RN airfoils have been selected for preliminary analysis. The geometry and the source of the experimental results of the selected airfoils are shown in Table 6.1. For comparison purpose, NACA 0015 is also included in the preliminary analysis.

6.3. Performance of the Candidate Airfoils

In Figures 6.1 and 6.2, the tangential force coefficient (C_t) versus angle of attack curves for 7 selected asymmetric airfoils are compared with NACA 0015 at $RN \approx 100,000$ and $300,000$ respectively. For obtaining these curves, experimental results of lift and drag coefficients of these selected airfoils have been used. As discussed in Chapter 4, the lift and drag data of these airfoil are not available for

high angle of attacks (i.e. the post-stall regime) where the flow becomes less dependent on the airfoil shape and behaves similar to high angle of attack flow around flat plates. For the present analysis, the FoilCheck program of NWTC [NWTC Design Codes 2007] has been utilized to generate different airfoil characteristics between $0^\circ < \alpha < 180^\circ$ using the experimental results of pre-stall regime.

Table 6.1: Selected Candidate Airfoils Based on Experimental Results

Name	Geometry	Source	Remarks
NACA 0015		[Cyberiad, 2007]	NACA symmetric airfoil
E193		[Selig et. al 1989]	Eppler low RN asymmetric airfoil
GEMINI		[Selig et. Al 1995]	R/C sailplane asymmetric airfoil
MB253515		[Selig et. Al 1989]	Mike Bame low RN asymmetric airfoil
SG6040		[Lyon et. al 1997]	Giguere wind turbine asymmetric airfoil
S1210		[Selig et. al 1995]	Selig high lift low RN asymmetric airfoil
S1223		[Selig et. al 1995]	Selig high lift low RN asymmetric airfoil
S8037		[Lyon et. al 1997]	Selig low RN asymmetric airfoil

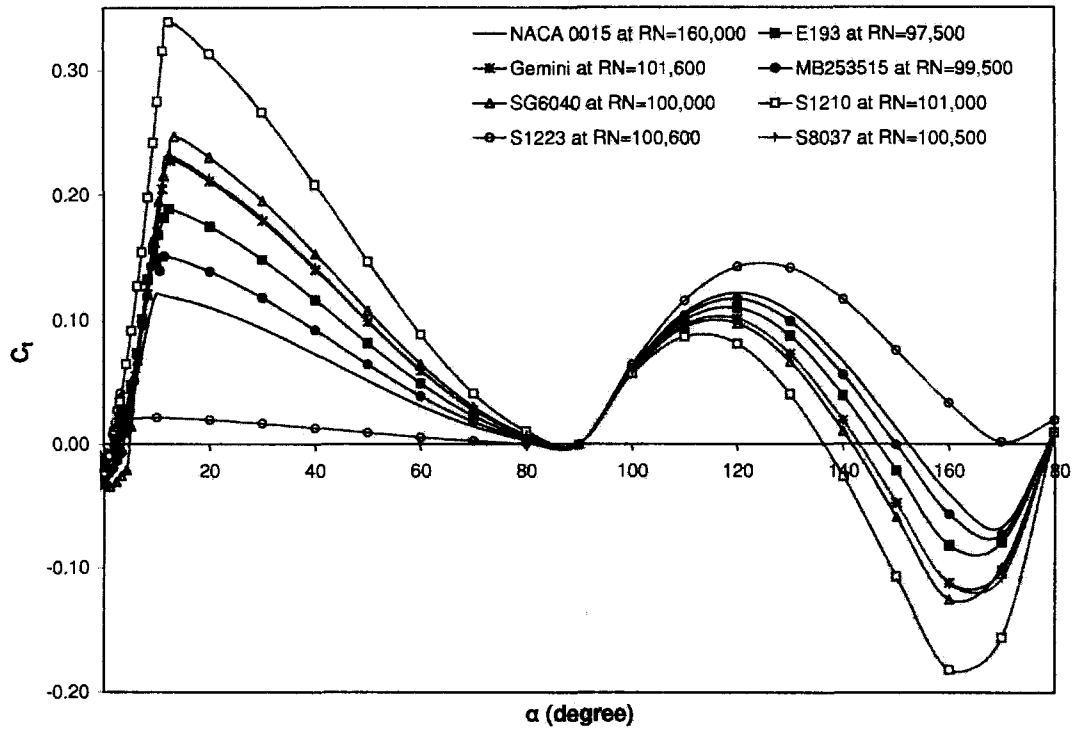


Figure 6.1: C_r - α Curves of Selected Airfoils Based on Experimental Results at $95,000 \leq RN \leq 160,000$

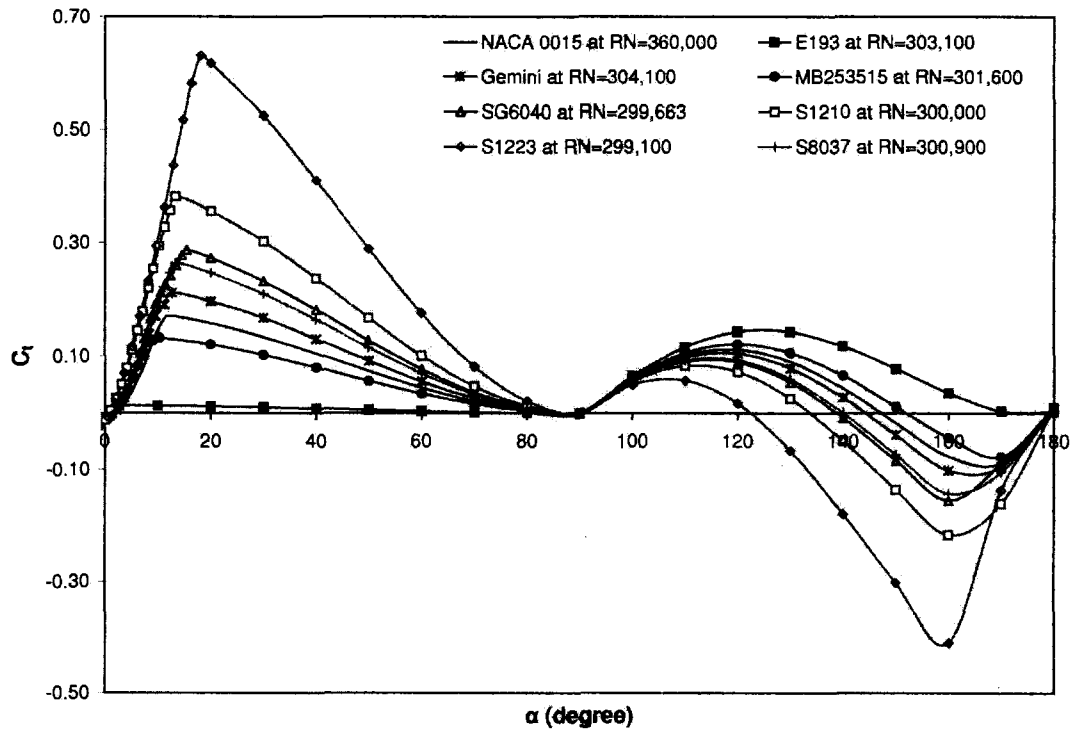


Figure 6.2: C_r - α Curves of Selected Airfoils Based on Experimental Results at $295,000 \leq RN \leq 360,000$

As discussed in the previous chapter, when C_t value of an airfoil shape is positive, the blades of SB-VAWT will produce forward tangential or thrust force. Instantaneous torque produced by the blades can be calculated when the thrust force is multiplied by the blade radius (R). It can be seen from Figure 6.1 that except S1223, C_t values of all the selected asymmetric airfoils are much superior to that of conventional NACA 0015 at $Re \approx 100,000$ for $0^\circ \leq \alpha \leq 90^\circ$. However, for $90^\circ \leq \alpha \leq 180^\circ$, the C_t values of NACA 0015 are greater than all the asymmetric airfoils except S1223.

Figure 6.2 shows that except E193 and MB253515, all the other five asymmetric airfoils are performing better than NACA 0015 for $0^\circ \leq \alpha \leq 90^\circ$ degrees. Among all the asymmetric airfoils, the performance of S1210 is the best for $0^\circ \leq \alpha \leq 90^\circ$ degrees at $Re \approx 100,000$ as illustrated in Figure 6.1. However at $Re \approx 300,000$, performance of S1223 is the best among all the airfoils for $0 \leq \alpha \leq 90$ degrees as can be seen from Figure 6.2. It can also be seen from both figures that though performance of GEMINI is moderate for $0^\circ \leq \alpha \leq 90^\circ$ degrees, its performance is better than most of the airfoils for $90^\circ \leq \alpha \leq 180^\circ$ degrees. Furthermore, the overall performance of SG6040 is only surpassed by S1210 at $Re \approx 100,000$. Judging all these factors, four airfoils (S1210, S1223, SG6040 and GEMINI) are selected from this preliminary analysis for further detailed performance index analysis in the next section.

6.4. Analysis of Selected Prospective Airfoils through Performance Indices

In this section, ten prospective airfoils are analyzed through their performance indices. Five airfoils (namely NACA 0015, NACA 4415, LS(1)-0417, NLF(1)-0416 and S1210) which were investigated of Chapter 5 are included in this analysis. Also, three other new prospective airfoils from the previous section are also included in this section. Furthermore, two more airfoils, namely LS(1)-0421MOD and LS(1)-0417MOD, which are also found to be prospective based on the

criteria are also selected. To conduct the performance index (PI) analysis, nine PI equations have been developed based on desirable aerodynamic characteristic features shortlisted in Section 6.1. These PI equations are described in the subsequent headings.

For obtaining the PI index of Stall Angle, Zero-Lift Drag Coefficient, $(C_l/C_d)_{max}$, $C_{l,max}$, Roughness Sensitivity, drag bucket, $C_{m,min}$, XFOIL [2007] has been used to generate the required 2D datasets of lift, drag and moment coefficients at $-20^\circ \leq \alpha \leq 20^\circ$. The FoilCheck program of NWTC [NWTC Design Codes 2007] has been utilized to generate different airfoil characteristics between $0^\circ < \alpha < 360^\circ$ using the pre-stall results obtained from XFOIL. As mentioned in the previous chapter, due to convergence problem the aerodynamic characteristics of Gö 420 could not be generated from XFOIL at $RN=100,000$ and possible reason for this is the laminar separation bubbles typically encountered by airfoils at low RN . In order to determine the PI of airfoil noise, NAFNoise has been utilized in the present analysis [Moriarty 2005].

6.4.1. PI for Stall Angle

Importance of higher stall angle for SB-VAWT airfoils has already been discussed in Section 5.3.1. It has been demonstrated that the stall angle of the airfoil sections for fixed-pitch SB-VAWT should be as large as possible in the low RN operation in order to minimize separation at low tip speed ratios [Kirke 1998]. PI for stall angle (W_{Stall}) indicates the percentage of the ratio between the stall angle of certain airfoil with respect to the maximum value of stall angle found among the selected airfoils. Mathematically,

$$W_{Stall} = \frac{\alpha_{Stall, Airfoil}}{\alpha_{Stall, Maximum}} \times 100\% \quad (6.1)$$

Average PI for stall angle (\overline{W}_{Stall}) is determined by averaging the values at $RN=100,000$ and $300,000$.

$$\overline{W}_{Stall} = \frac{W_{Stall, RN=100,000} + W_{Stall, RN=300,000}}{2} \quad (6.2)$$

6.4.2. PI for Zero-Lift Drag Coefficient

As discussed in Section 5.3.3., the desired SB-VAWT airfoil should have very low zero-lift-drag coefficient or C_{do} [Jesch and Walton 1980, Seki et. al 1985]. PI for C_{do} ($W_{C_{do}}$) is defined as the percentage of the ratio between the minimum value of C_{do} found among all the candidate airfoils to that of certain airfoil at the same RN. Mathematically,

$$W_{C_{do}} = \frac{C_{do, Minimum}}{C_{do, Airfoil}} \times 100\% \quad (6.3)$$

Average PI for Zero-Lift Drag Coefficient ($\overline{W}_{C_{do}}$) is determined by averaging the values at RN=100,000 and 300,000.

$$\overline{W}_{C_{do}} = \frac{W_{C_{do}, RN=100,000} + W_{C_{do}, RN=300,000}}{2} \quad (6.4)$$

6.4.3. PI for Maximum C_l/C_d

The C_l/C_d ratio indicates the overall efficiency of any airfoil and it is desirable to have higher ratio over a wide range of α for improving the aerodynamic performance of a SB-VAWT [Dereng 1981 and Lissaman 1994]. PI for stall angle (W_{C_l/C_d}) indicates the percentage of the ratio between the C_l/C_d of certain airfoil with respect to maximum value of C_l/C_d found among the selected airfoils at the same RN. Mathematically,

$$W_{C_l/C_d} = \frac{(C_l/C_d)_{max, Airfoil}}{(C_l/C_d)_{max, Maximum}} \times 100\% \quad (6.5)$$

Average PI for $(C_l/C_d)_{max}$ (\overline{W}_{C_l/C_d}) is determined by averaging the values at RN=100,000 and 300,000.

$$\overline{W}_{Cl/Cd} = \frac{W_{Cl/Cd, RN=100,000} + W_{Cl/Cd, RN=300,000}}{2} \quad (6.6)$$

6.4.4. PI for Maximum C_l

As mentioned in Section 5.3.5., higher maximum lift coefficient ($C_{l,max}$) is desirable for SB-VAWTs, because if the airfoil has higher $C_{l,max}$, more positive torque will be generated in the pre-stall regime. Furthermore, it will also enhance the starting torque. PI for $C_{l,max}$ (W_{Cl}) indicates the percentage of the ratio between the $C_{l,max}$ of certain airfoil with respect to the maximum value of $C_{l,max}$ found among the selected airfoils. Mathematically,

$$W_{Cl} = \frac{C_{l,max,Airfoil}}{C_{l,max,Maximum}} \times 100\% \quad (6.7)$$

Average PI for $C_{l,max}$ (\overline{W}_{Cl}) is determined by averaging the values at RN=100,000 and 300,000.

$$\overline{W}_{Cl} = \frac{W_{Cl, RN=100,000} + W_{Cl, RN=300,000}}{2} \quad (6.8)$$

6.4.5. PI for Roughness Sensitivity

The airfoil should have least amount of roughness sensitivity as SB-VAWTs operate at diversified climatic conditions and its maintainability and performance deteriorate with surface roughness due to dust, dirt, rain or insect debris [Hansen and Butterfield 1993] as highlighted in Section 5.3.7. It has also been described in Section 5.3.7. that analysis of the roughness sensitivity of airfoils can be simulated in XFOIL by imposing fixed transition near to the leading edge portion. To compare the roughness sensitivity of the candidate airfoils for SB-VAWT, a trip is used at 10% chord length downstream of the leading edge at RN=100,000 and 300,000. The results of the simulation at 10% fixed transition are compared with the salient characteristics of these airfoils at free transition. Among all the

aerodynamic parameters, the C_{do} , which is a very important parameter for SB-VAWT, is most affected due to roughness and it increases appreciably with RN. Because of this, change of the C_{do} value between free and fixed transition are used in this analysis to find out the PI for roughness sensitivity. PI for roughness sensitivity ($W_{\text{Roughness}}$) is defined as the percentage of the ratio between the minimum value of change in C_{do} due to roughness found among all the candidate airfoils to that of certain airfoil at the same RN. Mathematically,

$$W_{\text{Roughness}} = \frac{\Delta C_{do, \text{Minimum}}}{\Delta C_{do, \text{Airfoil}}} \times 100\% \quad (6.9)$$

Average PI for roughness sensitivity ($\overline{W}_{\text{Roughness}}$) is determined by averaging the values at RN=100,000 and 300,000.

$$\overline{W}_{\text{Roughness}} = \frac{W_{\text{Roughness}, RN=100,000} + W_{\text{Roughness}, RN=300,000}}{2} \quad (6.10)$$

6.4.6. PI for Drag Bucket

Wide drag bucket is one of the desirable characteristics of VAWTs [Klimas 1985] and increased width of drag bucket is required to maintain performance over a larger range of α [Claessens 2006] as found in Section 5.3.2. In this analysis, width of the drag bucket of the candidate airfoils are determined from the drag polar (C_d - C_l curves) obtained from XFOIL by measuring the change in C_l in the drag bucket. PI for drag bucket (W_{DB}) is defined as the percentage of the ratio between the width of the drag bucket of a certain airfoil with respect to the maximum value found among the candidate airfoils at the same RN. Mathematically,

$$W_{DB} = \frac{\Delta C_{l, \text{Airfoil}}}{\Delta C_{l, \text{Maximum}}} \times 100\% \quad (6.11)$$

Average PI for drag bucket (\overline{W}_{DB}) is determined by averaging the values at RN=100,000 and 300,000.

$$\overline{W}_{DB} = \frac{W_{DB,RN=100,000} + W_{DB,RN=300,000}}{2} \quad (6.12)$$

6.4.7. PI for Minimum Moment Coefficient

According to Kato et. al [1981], pitching moment coefficient (C_m) of a SB-VAWT airfoil should be low (large negative) for high efficiency as discussed in Section 5.3.9. PI for $C_{m,min}$ (W_{Cm}) is defined as the percentage of the ratio between the $C_{m,min}$ of certain airfoil to the minimum value (or the largest negative $C_{m,min}$) found among all the candidate airfoils at the same RN. Mathematically,

$$W_{Cm} = \frac{C_{m,min-Airfoil}}{C_{m,min-Mimumum}} \times 100\% \quad (6.13)$$

Average PI for $C_{m,min}$ (\overline{W}_{Cm}) is determined by averaging the values at RN=100,000 and 300,000.

$$\overline{W}_{Cm} = \frac{W_{Cm,RN=100,000} + W_{Cm,RN=300,000}}{2} \quad (6.14)$$

6.4.8. PI for Deep Stall Angle

As discussed in Section 5.3.6., deep stall has negative influence on the performance of SB-VAWT and it should be postponed to a larger angle of attack [Claessens 2006]. In this analysis, the deep-stall angles of the candidate airfoils are calculated using Equation 5.2 for the upper and lower surfaces of the airfoils. PI for deep stall angle (W_{DS}) is defined as the percentage of the ratio between the deep stall angle of a certain airfoil with respect to the maximum value found among all the candidate airfoils for the same surface (either upper or lower). Mathematically,

$$W_{DS} = \frac{\alpha_{DS,Airfoil}}{\alpha_{DS,Maximum}} \times 100\% \quad (6.15)$$

Average PI for deep stall angle (\overline{W}_{DS}) is determined by averaging the values at upper and lower surfaces of the airfoils.

$$\overline{W}_{DS} = \frac{W_{DS,Upper} + W_{DS,Lower}}{2} \quad (6.16)$$

6.4.9. PI for Airfoil Noise

The noise or sound pressure level (SPL) generated by the airfoil should be kept as low as possible as mentioned in Section 5.3.8. In order to assess the trailing edge noise generated by the candidate airfoils, NAFNoise has been utilized in the present analysis. PI for airfoil noise (\overline{W}_{SPL}) is defined as the percentage of the ratio between the minimum value of SPL among all the candidate airfoils to that found for certain airfoil at the same RN. Mathematically,

$$\overline{W}_{SPL} = \frac{SPL_{Minimum}}{SPL_{Airfoil}} \times 100\% \quad (6.17)$$

6.5. Selection of the Best Prospective Asymmetric Airfoil

After defining the expressions for finding the PI for different desirable aerodynamic characteristics, their values have been determined for the ten selected airfoils. Analysis with PI has been done for two different cases. In the first case, equal weight has been set for all the desirable aerodynamic characteristics. The mathematical expression for this case is:

$$\begin{aligned} W_{Airfoil,Equal} = & \left(\frac{1}{9} * \overline{W}_{Stall} \right) + \left(\frac{1}{9} * \overline{W}_{Cdo} \right) + \left(\frac{1}{9} * \overline{W}_{CUCd} \right) + \left(\frac{1}{9} * \overline{W}_{Cl} \right) + \\ & \left(\frac{1}{9} * \overline{W}_{Roughness} \right) + \left(\frac{1}{9} * \overline{W}_{DB} \right) + \left(\frac{1}{9} * \overline{W}_{Cm} \right) + \left(\frac{1}{9} * \overline{W}_{DS} \right) + \left(\frac{1}{9} * \overline{W}_{SPL} \right) \end{aligned} \quad (6.18)$$

In the second case, the weight has been assigned based on the relative importance of the desirable aerodynamic characteristics. The mathematical expression for this case is:

$$W_{Airfoil, Unequal} = (0.15 * \bar{W}_{Stall}) + (0.15 * \bar{W}_{Cdo}) + (0.15 * \bar{W}_{Cl/Cd}) + (0.15 * \bar{W}_{Cl}) + (0.1 * \bar{W}_{Roughness}) + (0.1 * \bar{W}_{DB}) + (0.1 * \bar{W}_{Cm}) + (0.05 * \bar{W}_{DS}) + (0.05 * \bar{W}_{SPL}) \quad (6.19)$$

Table 6.2 presents the results obtained for the first case where PI of the selected prospective airfoils are based on equal weight. It can be concluded from this table that the performance of LS(1)-0417 is the best. Similar trend has been found in Table 6.3, which shows the PI of selected prospective airfoils based on unequal weight. In this case also, the PI of LS(1)-0417 is the best. The overall ratings of LS(1)-0417 is followed by NACA 4415 and SG6040.

It has also been found in the previous chapter through detailed performance analysis that among all the asymmetric airfoils, the $C_{P,net}$ and $C_{Q,net}$ values of LS-0417 are the best. However, $C_{P,net}$ and $C_{Q,net}$ values of LS-0417 are better than symmetric NACA 0015 up to $\lambda=2.25$ only at $Re=100,000$ and at $Re=300,000$ the situation is even worse and the $C_{P,net}$ values of LS-0417 are lesser than symmetric NACA 0015 for all the tip speed ratios.

6.6. Summary of the Chapter

In this chapter, an attempt has been made to shortlist prospective airfoils based on experimental and analytical airfoil characteristics. Ten prospective airfoils are analyzed through their performance indices. Nine performance indices have been defined in this chapter in light of desirable aerodynamic characteristics to select best performing airfoil. These performance indices are for considering the following aerodynamic characteristics:

- (i) Stall angle at low Reynolds number;

- (ii) Width of the drag bucket;
- (iii) Zero-lift-drag coefficient;
- (iv) C_l/C_d ratio;
- (v) Maximum lift-coefficient;
- (vi) Deep-stall angle;
- (vii) Roughness sensitivity;
- (viii) Trailing edge noise generation; and
- (ix) Pitching moment.

Among all the airfoils, overall rating of NASA LS(1)-0417 has been found to be the best. The overall process of identifying the most promising airfoil in the present study can be better understood from Figure 6.3 which is a modified version of Figure 1.8 with the names of selected airfoils.

Table 6.2: Performance Index of Selected Prospective Airfoils Based on Equal Weight

Airfoil	α_{stall} (degree)	Drag Bucket	C_{D0}	$C_L/C_{D0,\text{max}}$	$C_{L,\text{max}}$	Deep Stall	Roughness Sensitivity	Negative $C_{M,\text{max}}$	SPL (dB)	Performance Index	Overall Rating
LS(1)-0417	82.7	52.7	57.7	72.6	68.0	81.7	100.0	43.1	91.9	72.2	1
NACA 4415	72.3	52.4	72.1	84.1	68.5	74.3	68.2	39.9	99.9	70.2	2
SG6040	82.3	67.6	74.3	83.0	58.6	69.4	61.6	32.6	93.5	69.2	3
S1210	63.3	71.3	18.5	100.0	92.8	60.2	25.6	92.7	97.6	69.1	4
S1223	67.9	28.5	13.0	86.4	100.0	74.9	44.8	100.0	100.0	68.4	5
NLF(1)- 0416	74.8	71.7	78.6	74.7	67.2	62.7	48.4	40.5	90.4	67.7	6
LS(1)- 0417MOD	79.0	41.3	72.9	57.5	68.9	90.8	55.1	40.4	91.8	66.4	7
LS(1)- 0421MOD	92.7	51.7	60.3	62.0	67.7	63.1	71.8	28.5	90.4	65.4	8
NACA 0015	79.3	69.9	100.0	60.5	53.6	82.8	19.3	16.1	94.9	64.1	9
GEMINI	56.3	69.5	92.2	79.6	55.5	62.1	24.0	29.9	94.8	62.6	10

Table 6.3: Performance Index of Selected Prospective Airfoils Based on Unequal Weight

Airfoil	α_{stall} (degree)	Drag Bucket	C_{D0}	$C_L/C_{D,max}$	$C_{L,max}$	Deep Stall	Roughness Sensitivity	Negative $C_{M,max}$	SPL (dB)	Performance Index	Overall Rating
LS(1)-0417	82.7	52.7	57.7	72.6	68.0	81.7	100.0	43.1	91.9	70.4	1
NACA 4415	72.3	52.4	72.1	84.1	68.5	74.3	68.2	39.9	99.9	69.3	2
SG6040	82.3	67.6	74.3	83.0	58.6	69.4	61.6	32.6	93.5	69.1	3
S1210	63.3	71.3	18.5	100.0	92.8	60.2	25.6	92.7	97.6	68.0	4
NLF(1)- 0416	74.8	71.7	78.6	74.7	67.2	62.7	48.4	40.5	90.4	68.0	5
S1223	67.9	28.5	13.0	86.4	100.0	74.9	44.8	100.0	100.0	66.2	6
LS(1)- 0421MOD	92.7	51.7	60.3	62.0	67.7	63.1	71.8	28.5	90.4	65.3	7
LS(1)- 0417MOD	79.0	41.3	72.9	57.5	68.9	90.8	55.1	40.4	91.8	64.5	8
NACA 0015	79.3	69.9	100.0	60.5	53.6	82.8	19.3	16.1	94.9	63.4	9
GEMINI	56.3	69.5	92.2	79.6	55.5	62.1	24.0	29.9	94.8	62.7	10

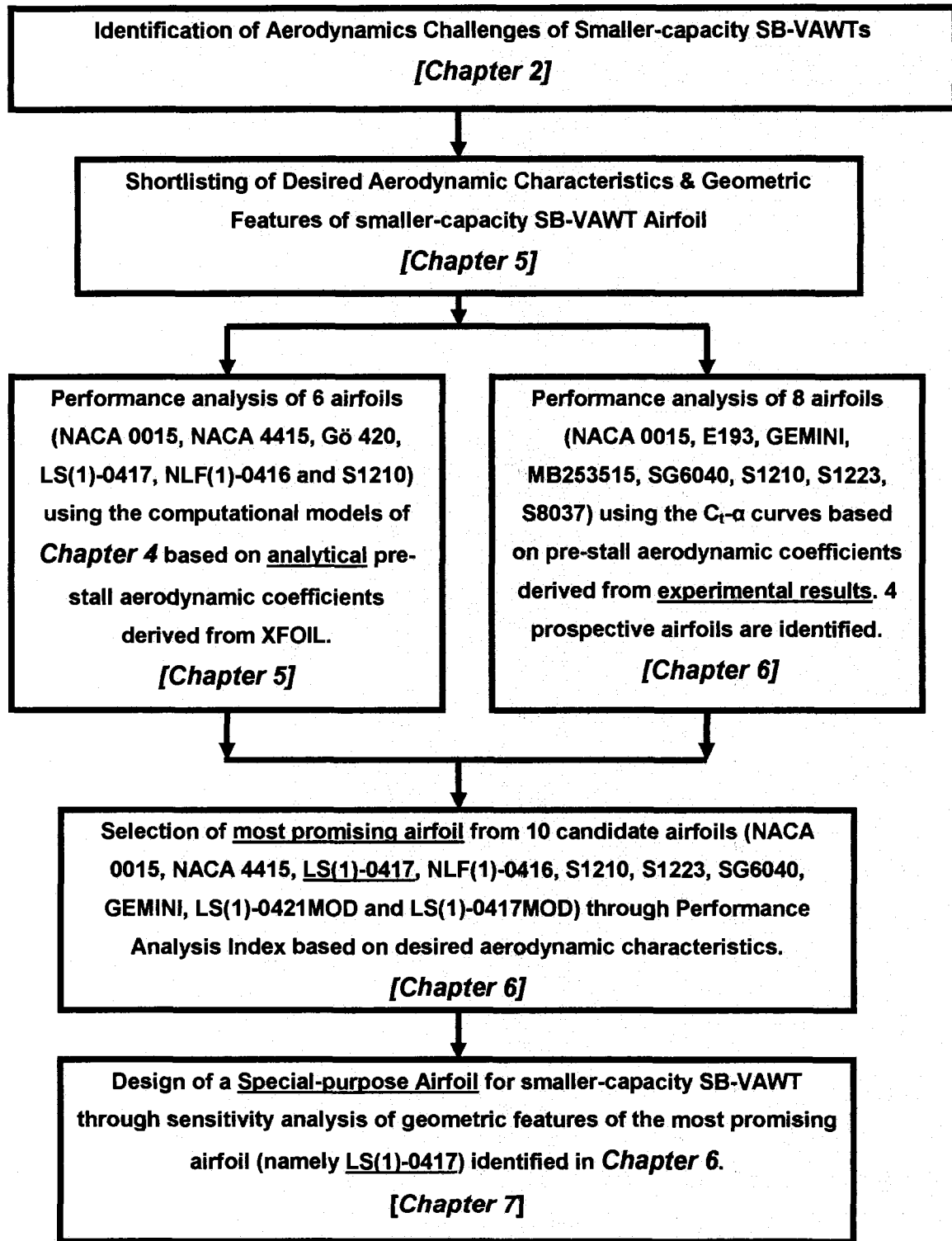


Figure 6.3: Selection Process of the Most-Promising Airfoil for the Design of a Special-Purpose Airfoil

Chapter 7

Design of a Special-purpose Airfoil for Smaller-Capacity SB-VAWT

Ten prospective airfoils are analyzed in the previous chapter by comparing their performance indexes and among all these airfoils, overall rating of NASA LS(1)-0417 has been found to be the best. It has also been found in Chapter 5 through detailed performance analysis that among all the asymmetric airfoils, the $C_{P,net}$ and $C_{Q,net}$ values of LS-0417 are the best. However, $C_{P,net}$ and $C_{Q,net}$ values of LS-0417 are better than symmetric NACA 0015 at $RN=100,000$ only up to $\lambda=2.25$. At $RN=300,000$ the situation is even worse and the $C_{P,net}$ values of LS-0417 are lesser than symmetric NACA 0015 for all the tip speed ratios. So, it will be advantageous to design a special-purpose airfoil in the light of desirable characteristics and geometric features identified in Chapter 5 for self-starting for SB-VAWTs with optimum performance at low RN .

Under these backdrops, an attempt has been made in this chapter to design a special-purpose airfoil by modifying the geometric features of LS-0417 for better performance at both $RN=100,000$ and $300,000$ for wider ranges of λ . For designing this airfoil, the XFOIL (described in Appendix C) and the computational scheme developed in Chapter 4 have been utilized.

7.1. Sensitivity Analysis with Geometric Features of NASA LS(1)-0417

Desirable aerodynamic characteristics identified in Chapter 5 results from the different geometric features of an airfoil as shown in Figure 7.1. So, it is of profound importance to identify the required geometric features and a designer of

small-scale SB-VAWT should consider these features while selecting an airfoil. In this chapter, sensitivity analyses have been made with the main geometric features of NASA LS-0417 using XFOIL. Then, $C_{P,net}-\lambda$ and $C_{Q,net}-\lambda$ curves are produced using the computational scheme (described in detail in Chapter 4) to illustrate their effects on performance of a smaller capacity fixed-pitch SB-VAWT.

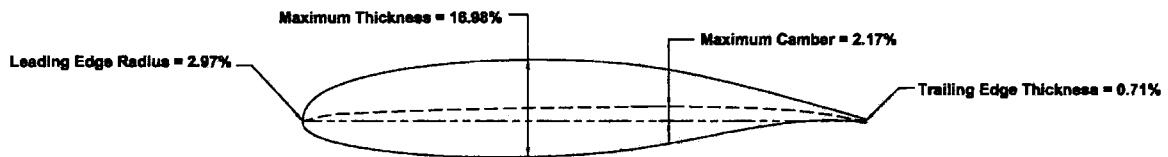


Figure 7.1: Geometric Features of NASA LS(1)-0417

7.1.1. Camber

Computational analysis of Baker [1983] indicated that cambered sections would produce a higher tangential thrust (i.e. torque) over a wider range of α and more energy per “cycle” (i.e. per revolution) than the symmetrical section, and that a VAWT using the slightly cambered GÖ 420 blades would self-start, unlike the same turbine with the symmetrical blades or highly cambered FX 63-137 blades. As discussed in Section 5.4.1., the net advantages of asymmetric airfoils over symmetric ones are: (i) higher lift at low RN; (ii) lesser roughness sensitivity; (iii) higher stall angle; and (iv) large negative pitching moment. However this advantage appears to be outweighed by other disadvantages in the case of highly cambered sections, as will be shown below.

In this section, analyses have been carried out at $RN=100,000$ and $300,000$ by increasing and decreasing the camber of LS(1)-0417 as shown in Figure 7.2(a) to (c). In Figures 7.3 and 7.4, the $C_{P,net}-\lambda$ curves of the selected airfoils with different cambers are shown at $RN=100,000$ and $300,000$. It can be seen from

these figures that the maximum value of $C_{P,net}$ decreases with increase in camber. However, the opposite trend is observed at lower λ values where the problem of self-starting happens.

To understand the effect of camber on SB-VAWTs production of torque, the $C_{Q,net}-\lambda$ curves of the selected airfoils are shown in Figures 7.5 and 7.6. It is clear from these figures that at $Re=100,000$, the values of $C_{Q,net}$ increase with camber up to $\lambda=2.5$ - which is the usual operating region of typical smaller-capacity SB-VAWTs, and beyond this value the opposite is true. At $Re=300,000$ this advantage of increased camber at low λ is negligible. So, from these observations we can conclude that though there is penalty in performance of SB-VAWTs with excessive cambered airfoils, they have positive benefits at lower λ values for eliminating the problem of self-starting.

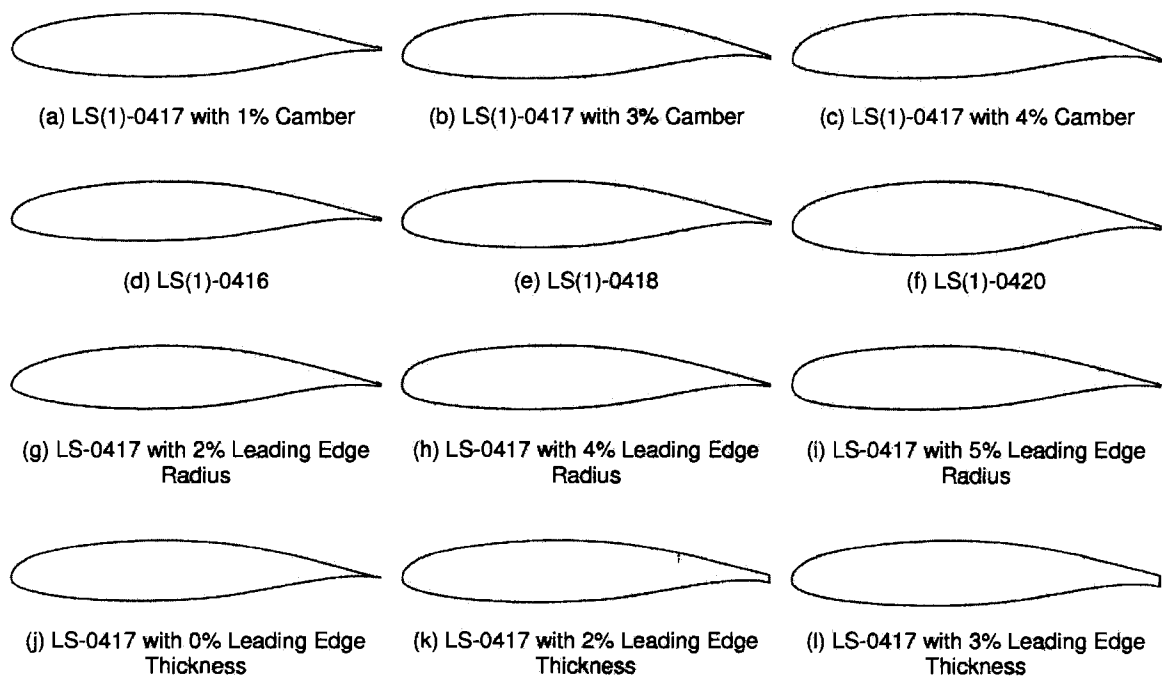


Figure 7.2: Geometry of Candidate Airfoil for Sensitivity Analysis [Islam et. al 2007b]

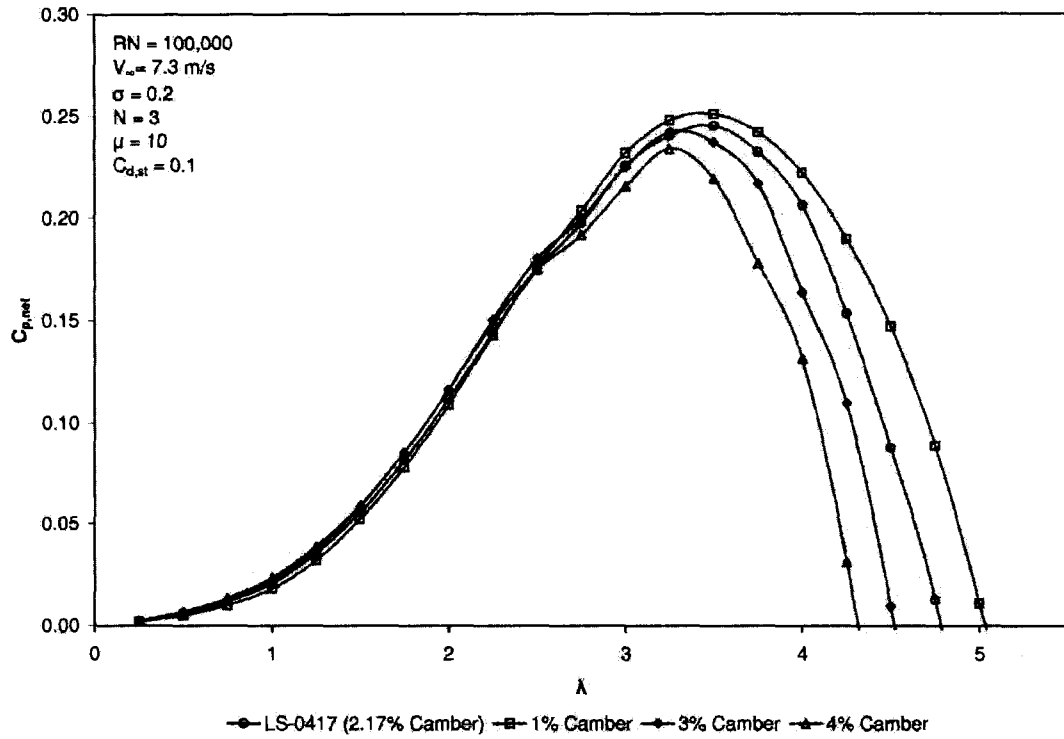


Figure 7.3: Power Coefficients of LS-0417 with Different Cambers at $RN=100,000$ [Islam et. al 2007b]

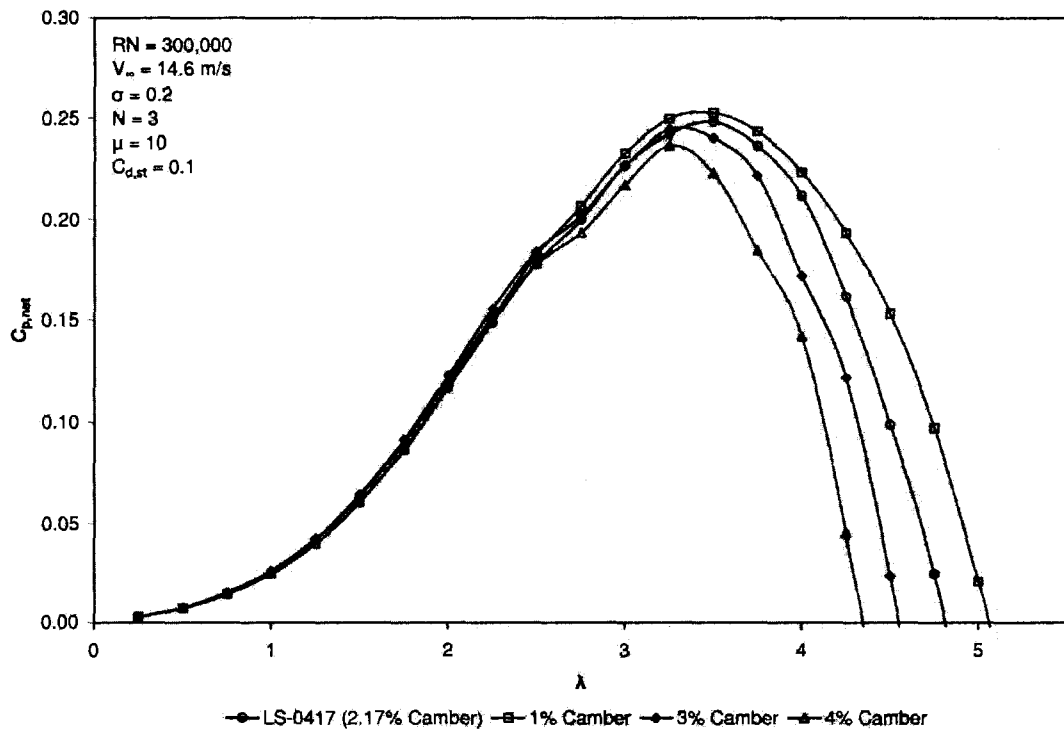


Figure 7.4: Power Coefficients of LS-0417 with Different Cambers at $RN=300,000$ [Islam et. al 2007b]

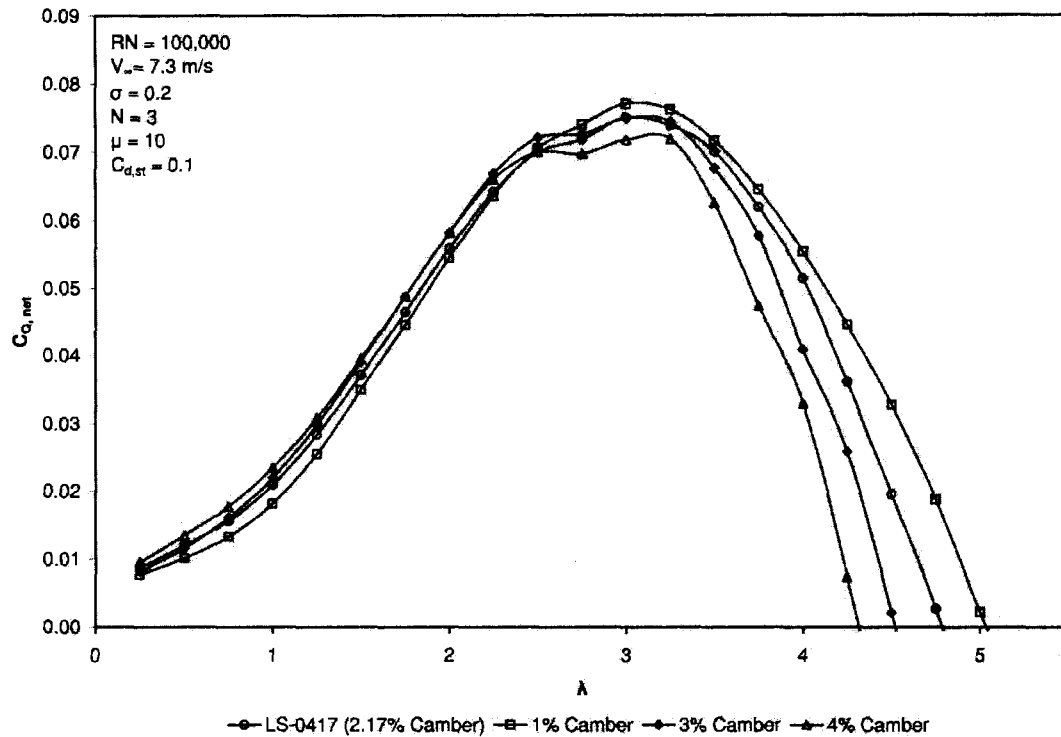


Figure 7.5: Torque Coefficients of LS-0417 with Different Cambers at $RN=100,000$ [Islam et. al 2007b]

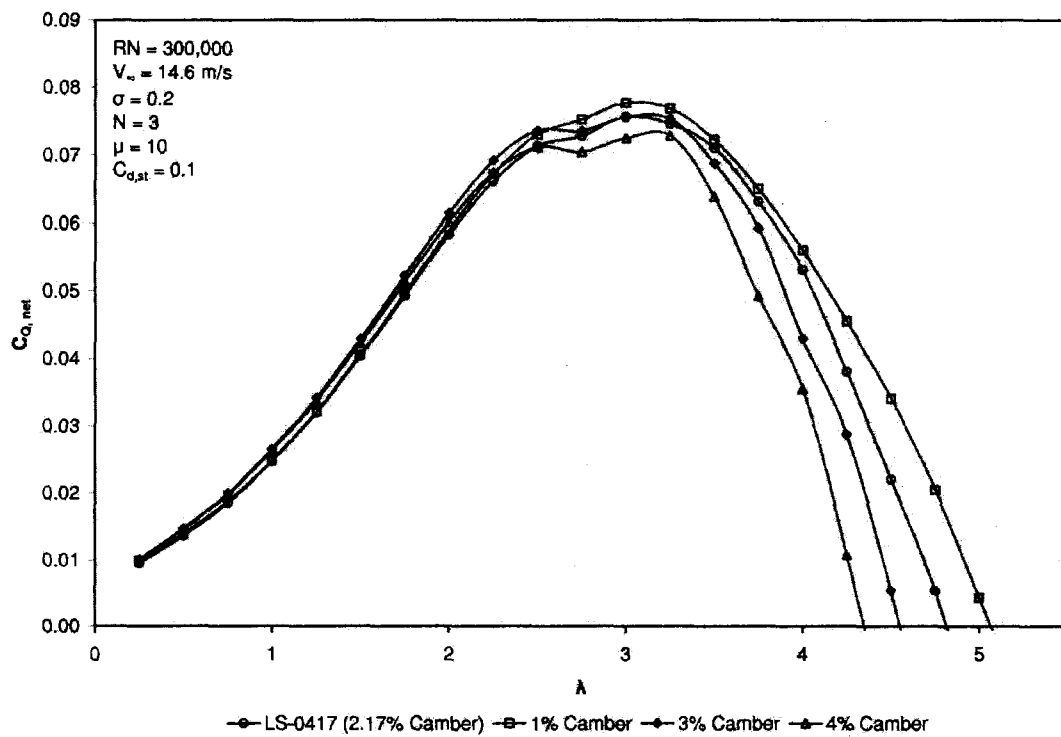


Figure 7.6: Torque Coefficients of LS-0417 with Different Cambers at $RN=300,000$ [Islam et. al 2007b]

7.1.2. Thickness

As discussed in Section 5.4.2., blades with thicker airfoils have at least five advantages for small-scale SB-VAWTs, which are:

- (i) Improvement of performance [Healy 1978a and Angell et. al 1988]
- (ii) Increase in starting torque [Simhan 1994];
- (iii) Increase in width of the drag bucket [Claessens 2006];
- (iv) Lower radiated sound [Parchen et. al 1997]; and
- (v) Improvement of structural strength [Hansen and Butterfield 1993].

Sensitivity analyses have been conducted in this section by varying the maximum thickness (t_{max}) of the LS-0417 ($t_{max}=17\%$). For convenience, the airfoils are renamed based on their thickness as LS-0416 ($t_{max}= 16\%$), LS-0418 ($t_{max}= 18\%$) and LS-0420 ($t_{max}= 20\%$) as shown in Figures 11(d) to (f).

In Figures 7.7 and 7.8, the $C_{P,net}-\lambda$ curves of the selected airfoils are depicted with different thicknesses at $Re=100,000$ and $300,000$ respectively. It can be seen from these figures that the maximum value of $C_{P,net}$ increases up to $t_{max}=18\%$ and beyond this value it starts decreasing. However, at lower λ values the $C_{P,net}$ increases consistently with t_{max} .

The $C_{Q,net}-\lambda$ curves of the selected airfoils with different t_{max} are shown in Figures 7.9 and 7.10. It is found from these figures that the values of $C_{Q,net}$ increase with t_{max} up to $\lambda \approx 3$, and beyond this the effect is not significant up to $t_{max}=18\%$ and further increase in t_{max} decreases the performance. So, it can be understood from this analysis that both the amount of torque and power generated by SB-VAWTs can be increased by using thicker airfoils. However, there is a limit to the benefits to be gained by using very thick airfoils.

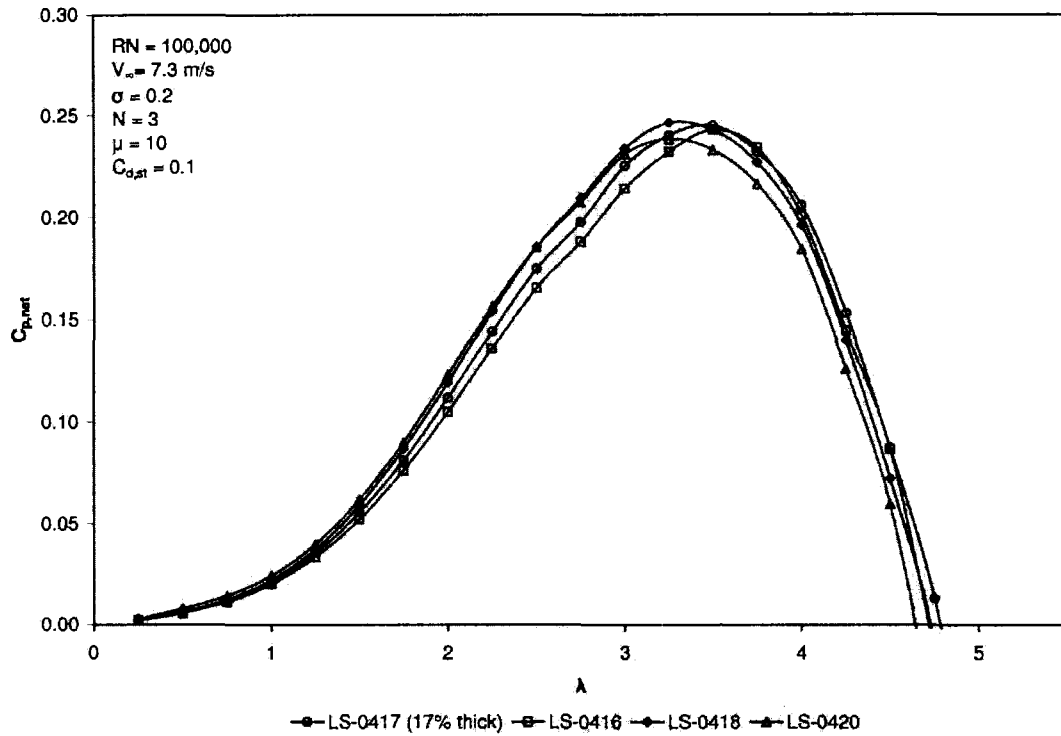


Figure 7.7: Power Coefficients of LS-0417 with Different Thicknesses at $RN=100,000$ [Islam et. al 2007b]

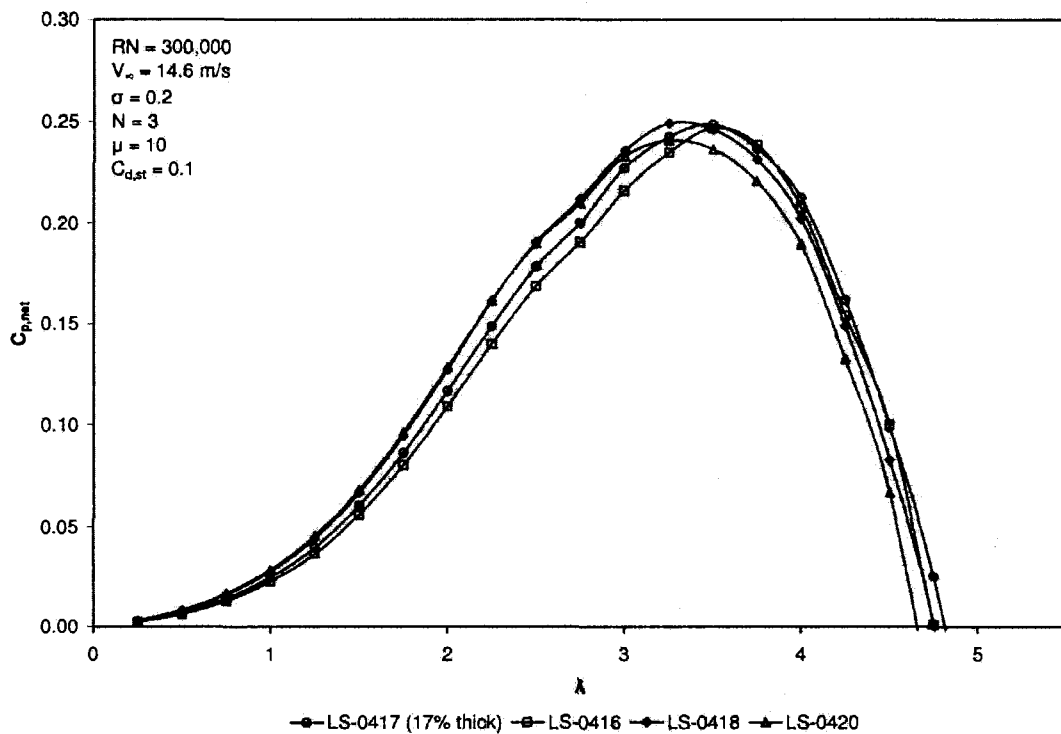


Figure 7.8: Power Coefficients of LS-0417 with Different Thicknesses at $RN=300,000$ [Islam et. al 2007b]

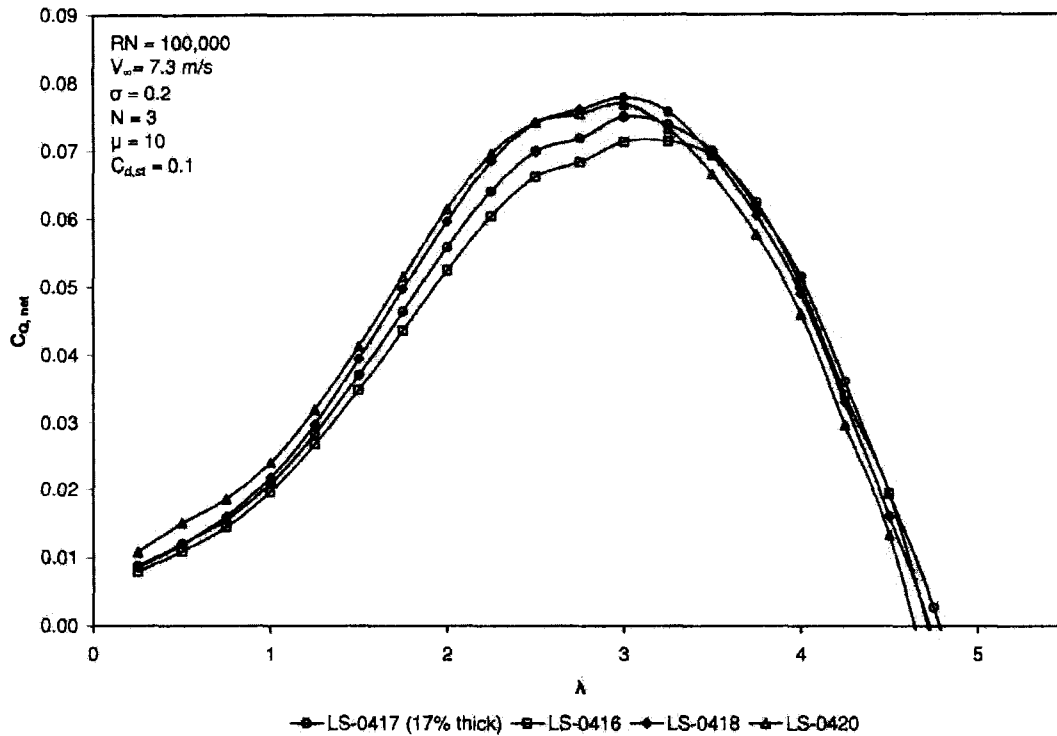


Figure 7.9: Torque Coefficients of LS-0417 with Different Thicknesses at RN=100,000
[Islam et. al 2007b]

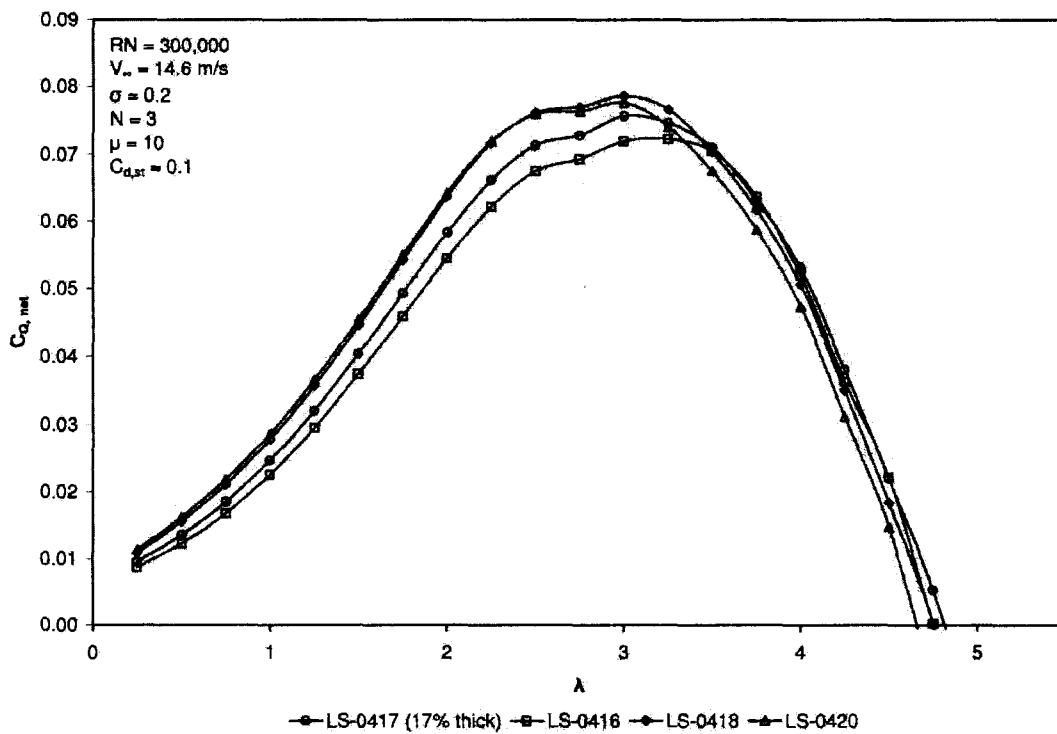


Figure 7.10: Torque Coefficients of LS-0417 with Different Thicknesses at RN=300,000
[Islam et. al 2007b]

7.1.3. Leading Edge

As discussed in Section 5.4.3., larger leading edge radius (R_{LE}) is desirable as they are less sensitive to roughness which is a desirable aerodynamic characteristic for smaller capacity SB-VAWT [Fupeng et. al 2001 and Dereng 1981]. Wind turbines operate under diverse climatic conditions and maintainability and performance deteriorate with surface roughness due to dust, dirt, rain or insect debris. So, the airfoil should have the least amount of roughness sensitivity and from this perspective airfoil with larger R_{LE} is expected to harness more energy by SB-VAWT under dirty blade conditions. Furthermore, deep stall characteristic of an airfoil also depends on leading edge radius. Three new airfoils are constructed by varying the R_{LE} of LS-0417 as shown from Figures 7.2(g) to (i).

In Figures 7.11 and 7.12, the $C_{P,net}-\lambda$ curves of the selected airfoils are depicted at $Re=100,000$ and $300,000$ respectively for different R_{LE} . It can be seen from these figures that for up to $\lambda \approx 4$ the $C_{P,net}$ increases up to $R_{LE}=4\%$ and beyond this value it starts decreasing. Similar trends can be seen in the $C_{Q,net}-\lambda$ curves of the selected airfoils with different R_{LE} as shown in Figures 7.13 and 7.14. So, both the torque and power produced by SB-VAWTs can be increased by using airfoils with larger R_{LE} . However, there is a limit to the benefits as seen here with the LS-0417 airfoil whose R_{LE} can be increased up to 4% without penalty in $C_{P,net}$ and $C_{Q,net}$.

7.1.4. Trailing Edge

It has already discussed in Section 5.4.4. that trailing edge thickness (t_{TE}) has positive benefit for the performance at low Re . According to Sato and Sunada [1995], some of benefits of using blunt airfoil (i.e. an airfoil with trailing edge thickness) at low Re are: (i) the total drag can be reduced; (ii) the maximum lift increased; (iii) the linearity of lift curve with incidences improved; (iv) the

maximum lift-to-drag ratio increased; and (v) airfoil becomes structurally stronger and more rigid.

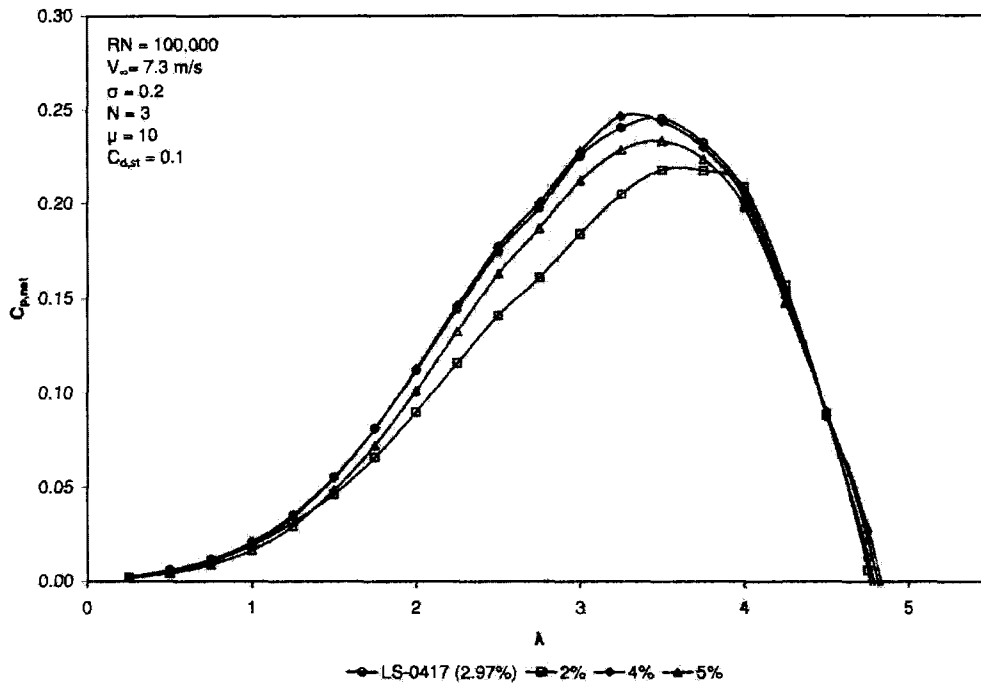


Figure 7.11: Power Coefficients of LS-0417 with Different Leading Edge Radius (R_{LE}) at $RN=100,000$ [Islam et. al 2007b]

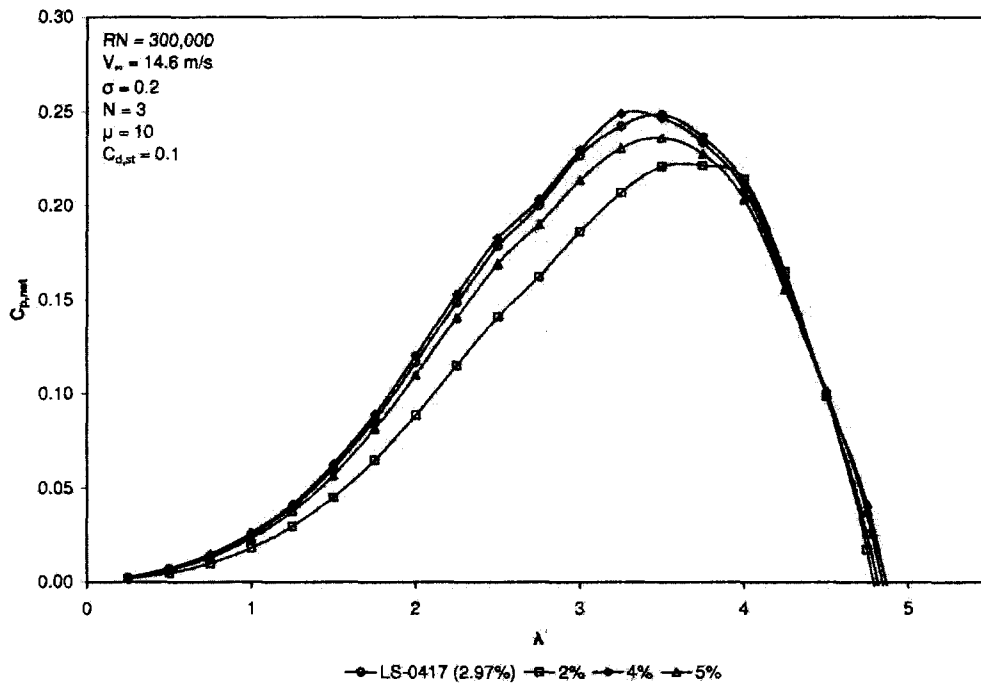


Figure 7.12: Power Coefficients of LS-0417 with Different Leading Edge Radius (R_{LE}) at $RN=300,000$ [Islam et. al 2007b]

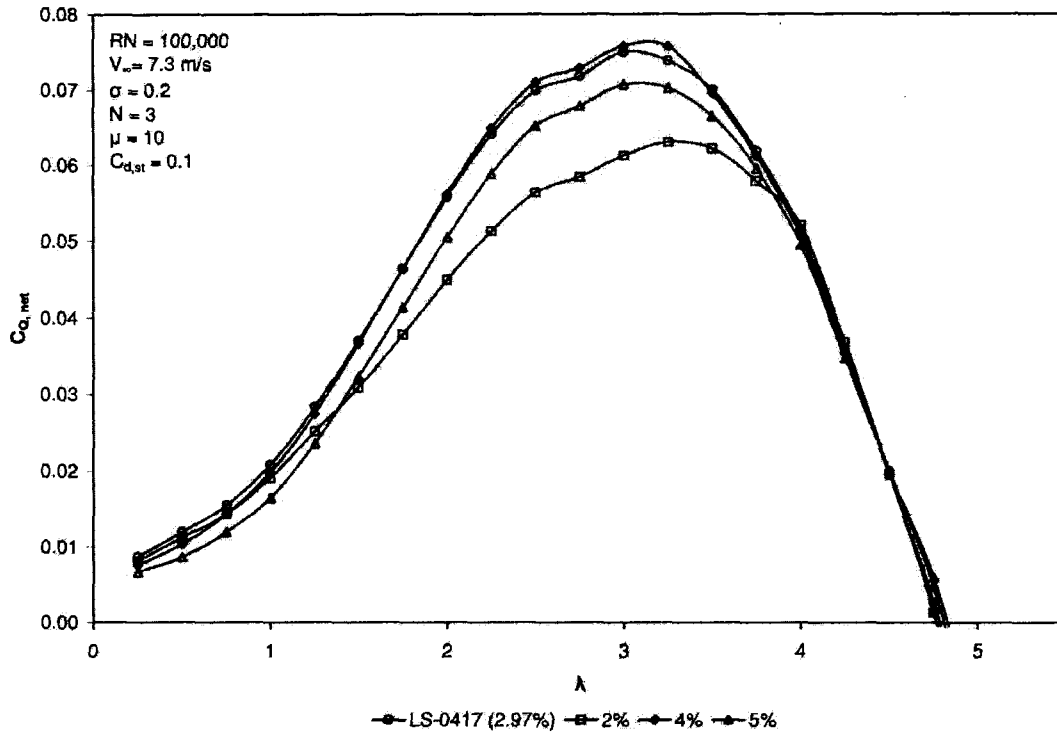


Figure 7.13: Torque Coefficients of LS-0417 with Different Leading Edge Radius (R_{LE}) at $RN=100,000$ [Islam et. al 2007b]

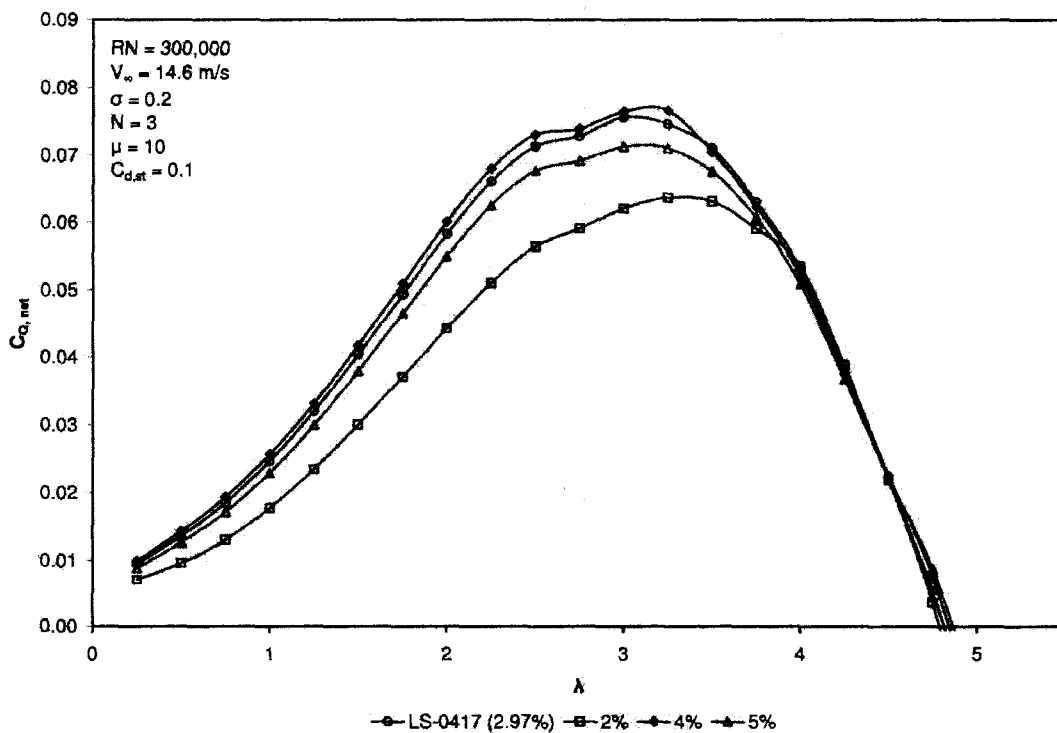


Figure 7.14: Torque Coefficients of LS-0417 with Different Leading Edge Radius (R_{LE}) at $RN=300,000$ [Islam et. al 2007b]

In this section, the variation of trailing edge thickness (t_{TE}) of LS-0417 is investigated by constructing three new airfoils shown in Figure 7.2(j) to (l). In Figures 7.15 and 7.16, the $C_{P,net}-\lambda$ curves of the selected airfoils are presented at $RN=100,000$ and $300,000$ respectively. These figures suggest that the maximum value of $C_{P,net}$ may increase slightly up to $t_{TE}\approx 1\%$ and then it starts decreasing with further increase in t_{TE} at both Reynolds numbers. However, at lower λ values the variation of $C_{P,net}$ is negligible at $RN=100,000$ and slightly changed at $RN=300,000$.

The $C_{Q,net}-\lambda$ curves of the selected airfoils with different t_{TE} are shown in Figures 7.17 and 7.18. It is found from these figures that the values of $C_{Q,net}$ follows the same trends like $C_{P,net}$. So, it is evident that both the torque and power generated by SB-VAWTs can be increased moderately by using airfoils with marginal t_{TE} .

7.2. New Special-Purpose SB-VAWT Airfoil – “MI-VAWT1”

It has been found in the previous section that different geometric features of LS-0417 have profound effect on the performance of SB-VAWTs. In this section, an attempt has been made to design a low RN special-purpose airfoil to generate more torque and power than LS-0417 especially at lower values of λ . The design works used the LS-0417 as a reference airfoil by utilizing the design analysis features of XFOIL and the computational scheme. In the process, the four geometric features (camber, t_{max} , R_{LE} , t_{TE}) are varied in their magnitudes to select optimum values. Finally, the desired airfoil has been designed after going through several trial and errors. This special-purpose airfoil has been named as “MI-VAWT1” and its geometry is shown in Figure 7.19. The coordinates of MI-VAWT1 are given in Appendix D. MI-VAWT1 is 21% thick airfoil with a moderate camber and trailing edge thickness.

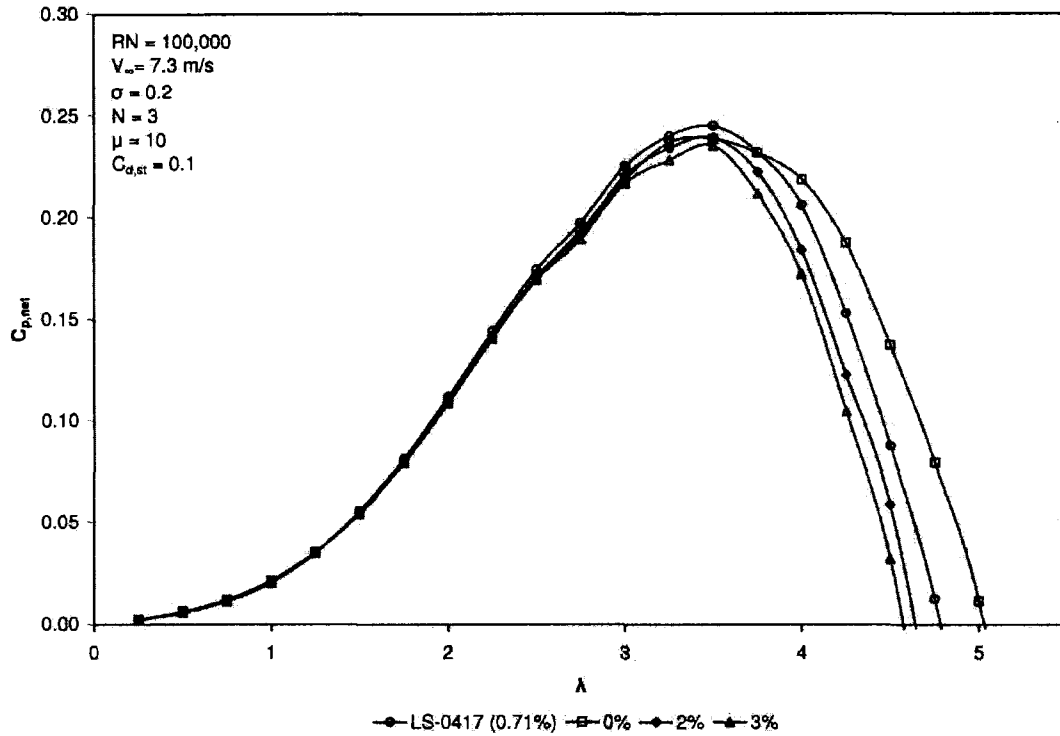


Figure 7.15: Power Coefficients of LS-0417 with Different Trailing Edge Thicknesses (t_{TE}) at $RN=100,000$ [Islam et. al 2007b]

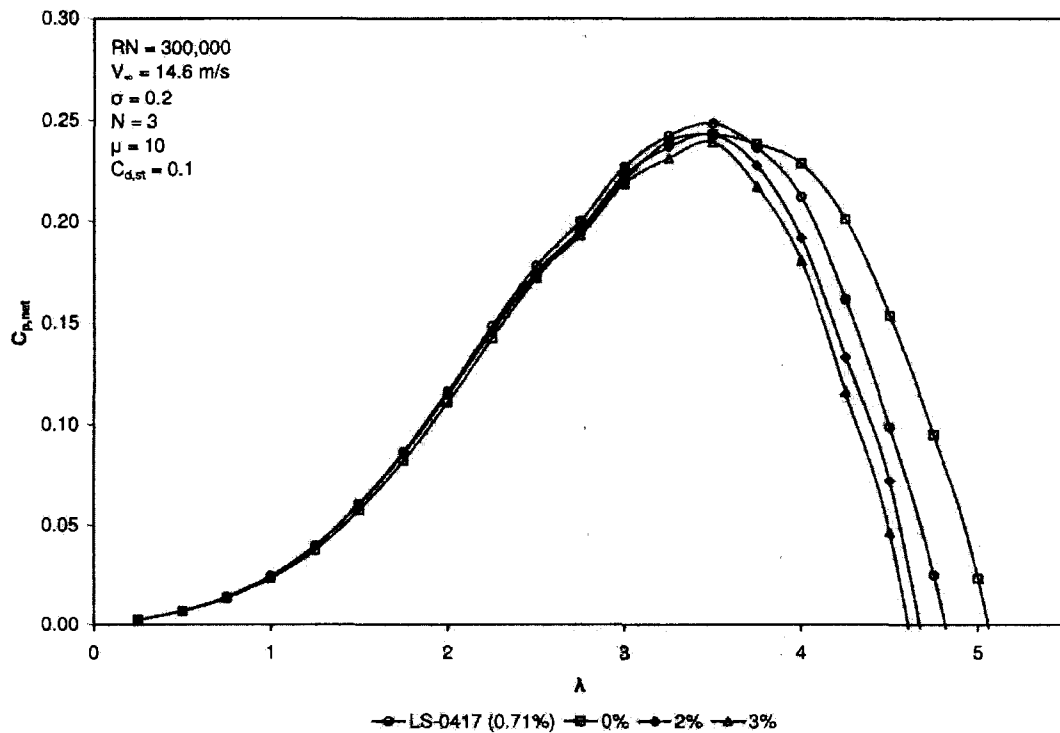


Figure 7.16: Power Coefficients of LS-0417 with Different Trailing Edge Thicknesses (t_{TE}) at $RN=300,000$ [Islam et. al 2007b]

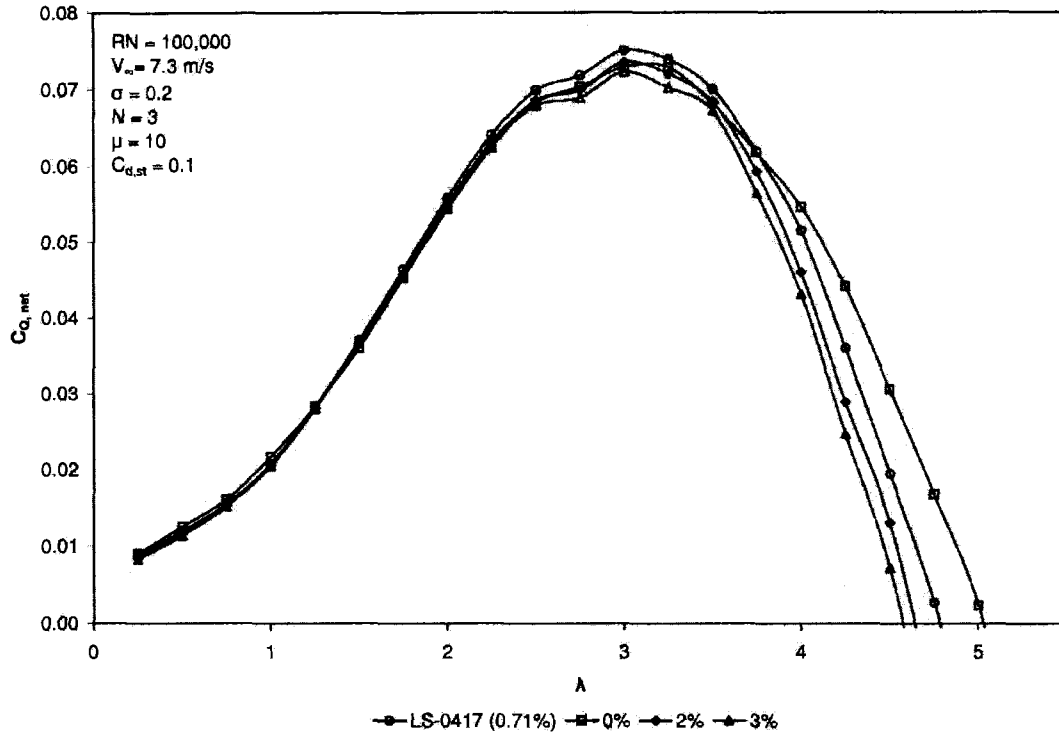


Figure 7.17: Torque Coefficients of LS-0417 with Different Trailing Edge Thicknesses (t_{TE}) at $RN=100,000$ [Islam et. al 2007b]

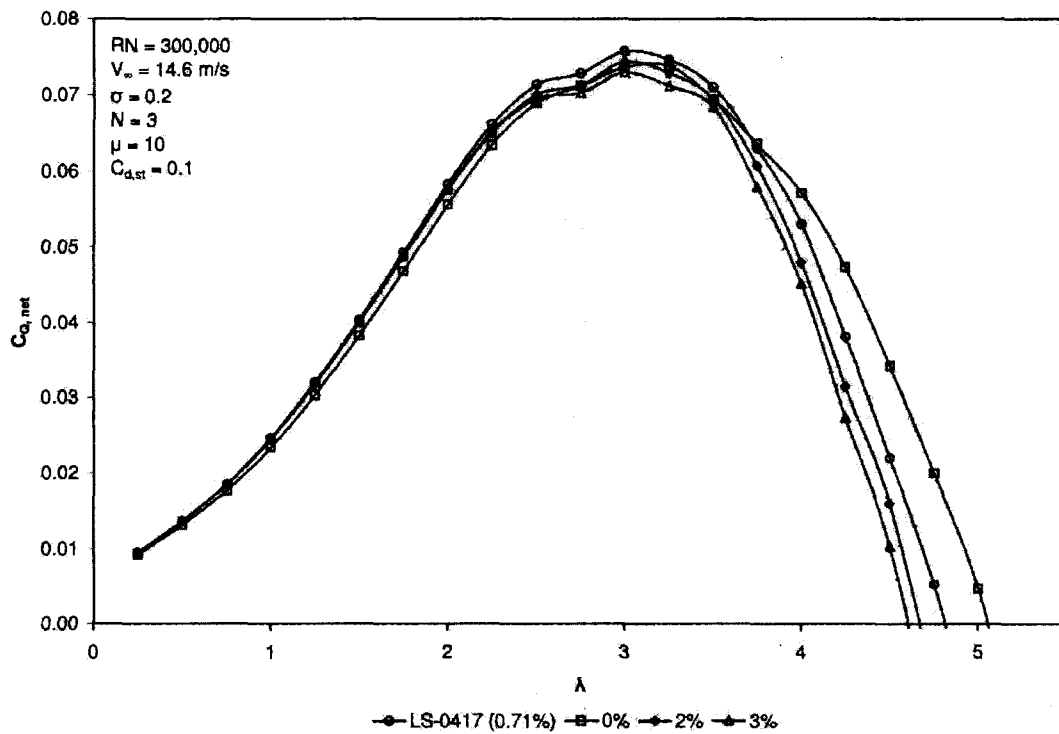


Figure 7.18: Torque Coefficients of LS-0417 with Different Trailing Edge Thicknesses (t_{TE}) at $RN=300,000$ [Islam et. al 2007b]

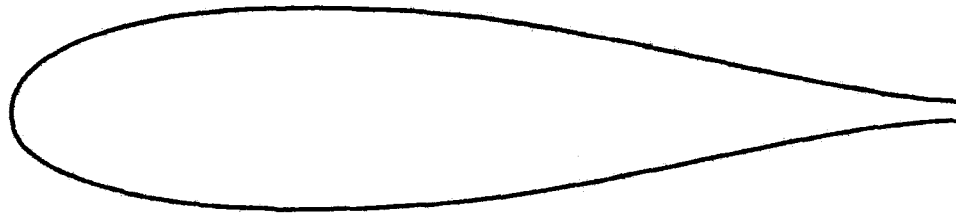


Figure 7.19: Geometry of MI-VAWT1 [Islam et. al 2007b]

In Figures 7.20 to 7.25, the performances of a SB-VAWT with MI-VAWT1 are compared with those of NACA 0015 and LS-0417 at different RN. It can be seen in Figure 7.20 that $C_{p,net}$ of MI-VAWT1 are higher than the other airfoils below $\lambda \approx 3.5$, which are the usual operating points of a SB-VAWT, at $RN=50,000$. Also the $C_{Q,net}-\lambda$ curves illustrated in Figure 7.21 shows the superior performance of MI-VAWT1 up to $\lambda \approx 3.75$. Figure 7.22 shows that $C_{p,net}$ of MI-VAWT1 are higher than the other airfoils below $\lambda \approx 3$ at $RN=100,000$. Also the $C_{Q,net}-\lambda$ curves demonstrated in Figure 7.23 shows superior performance of MI-VAWT1 up to $\lambda \approx 3$. At higher RN values like $RN=300,000$, though MI-VAWT1's performance is much superior to LS-0417 as desired, but its performance is similar to NACA 0015 below $\lambda \approx 2.75$ at $RN = 300,000$ as shown in Figures 7.24 and 7.25.

7.3. Summary of the Chapter

The aim of this chapter has been to design and analyze a special-purpose airfoil suitable for smaller capacity fixed-pitch SB-VAWT which should generate enough torque at low λ and also has reasonable $C_{P,net}$ values. To improve the performance of LS-0417, sensitivity analyses have been conducted with its different geometric features to understand their effects on performance of SB-VAWTs. Subsequently, a special purpose airfoil named "MI-VAWT1" has been designed by utilizing the XFOIL and the computational scheme developed in Chapter 4. It has been found that its performance is superior to that of LS-0417 and NACA 0015 at $RN < 300,000$ and comparable with NACA 0015 at $RN \approx 300,000$.

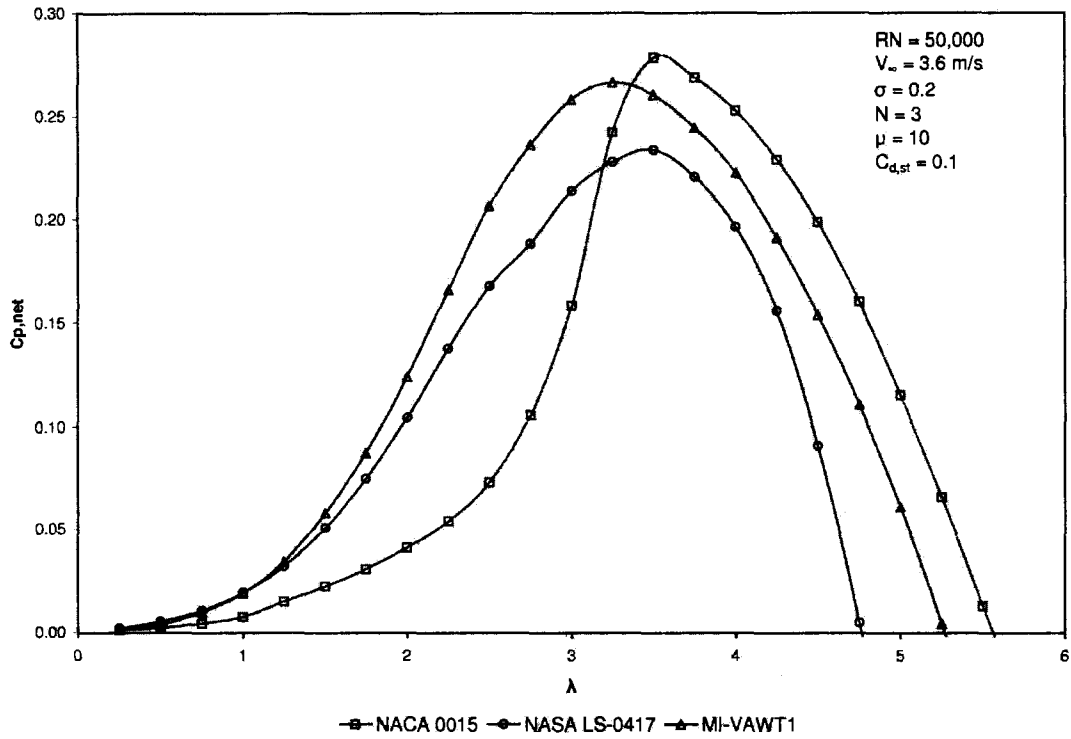


Figure 7.20: $C_{P,net}$ - λ Curves of a SB-VAWT with MI-VAWT1 at $RN=50,000$ [Islam et. al 2007b]

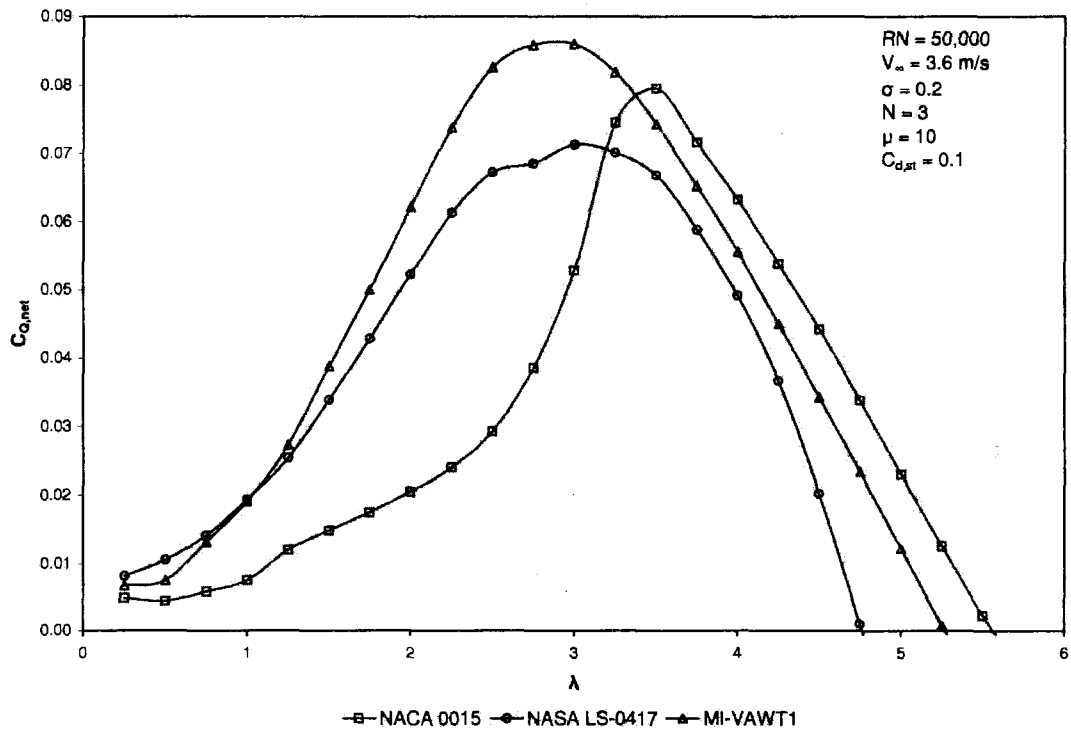


Figure 7.21: $C_{Q,net}$ - λ Curves of a SB-VAWT with MI-VAWT1 at $RN=50,000$ [Islam et. al 2007b]

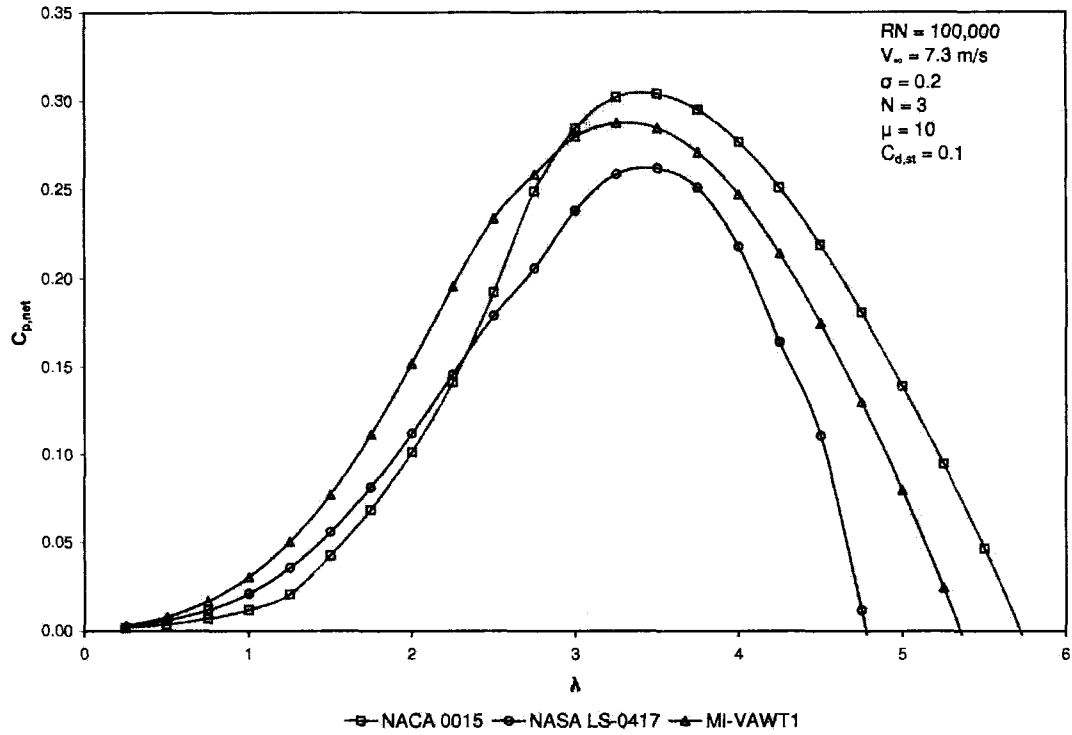


Figure 7.22: $C_{p,net}$ vs λ Curves of a SB-VAWT with MI-VAWT1 at $RN=100,000$ [Islam et. al 2007b]

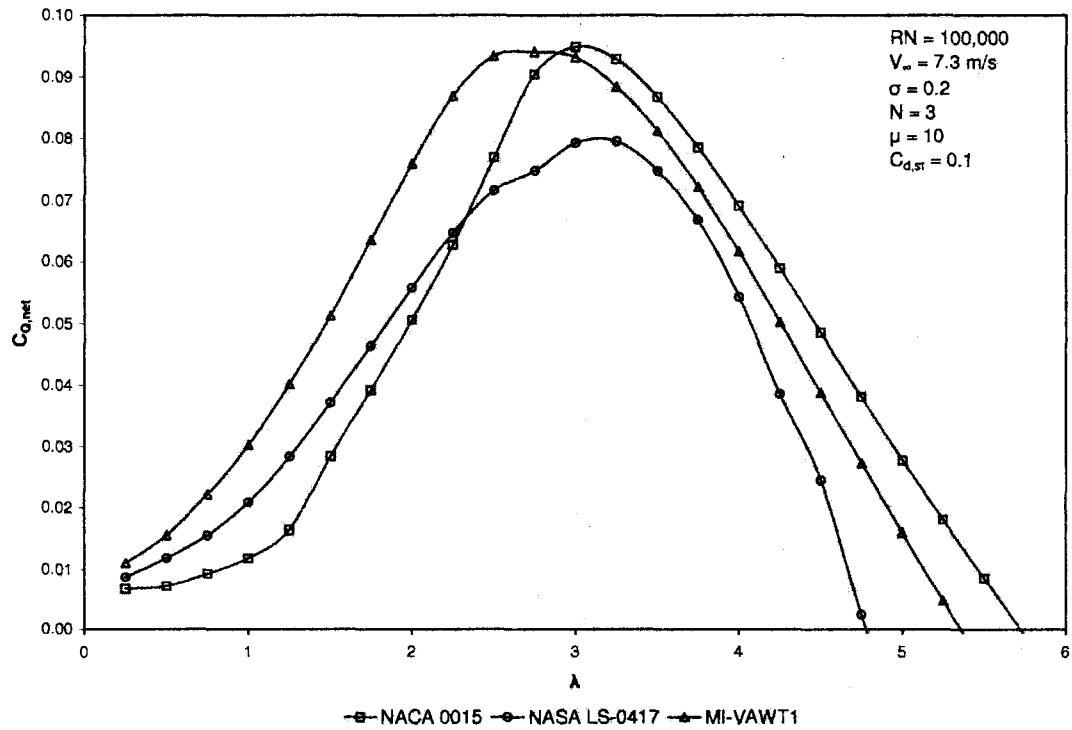


Figure 7.23: $C_{q,net}$ vs λ Curves of a SB-VAWT with MI-VAWT1 at $RN=100,000$ [Islam et. al 2007b]

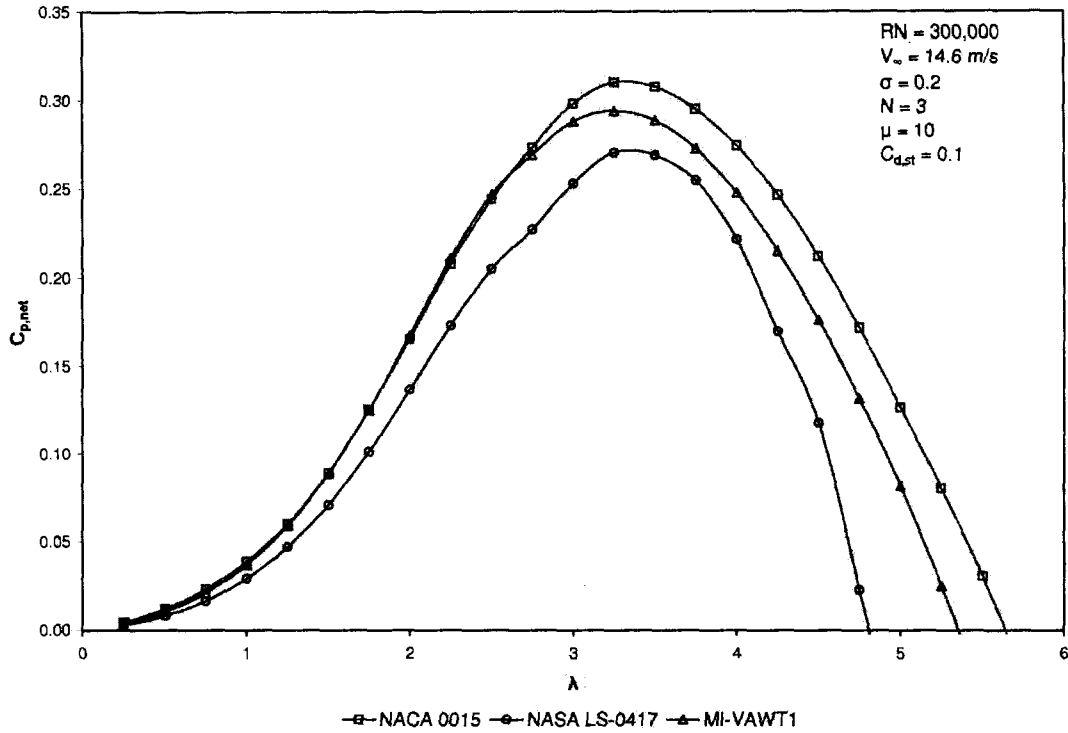


Figure 7.24: $C_{P,net}$ - λ Curves of a SB-VAWT with MI-VAWT1 at $RN=300,000$ [Islam et. al 2007b]

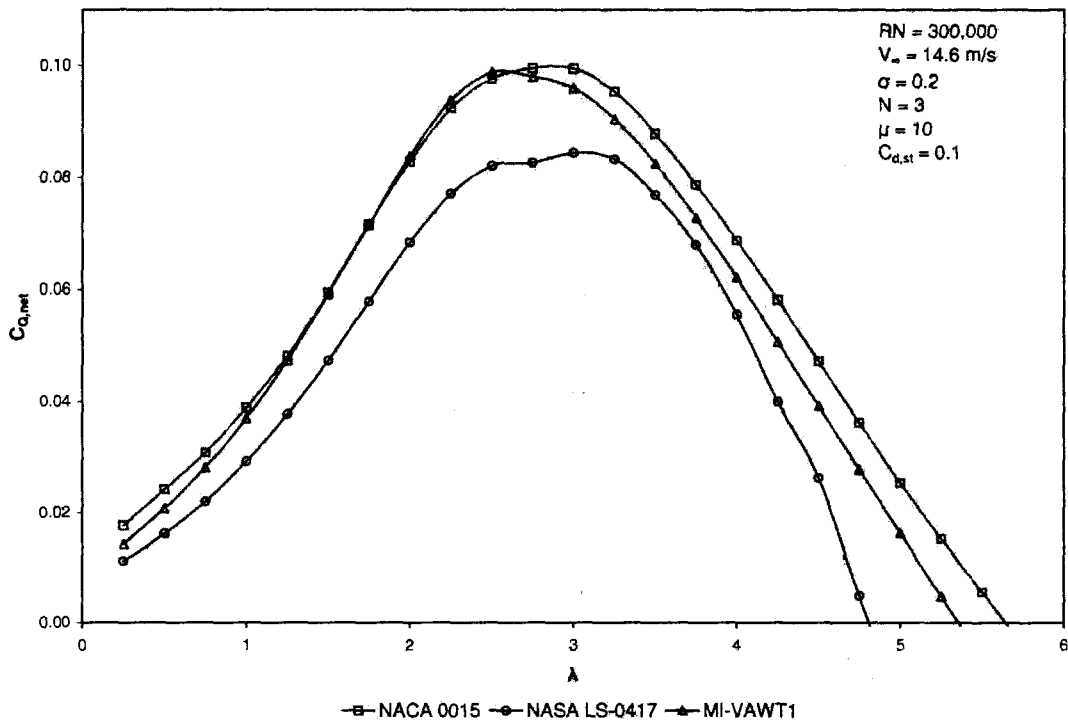


Figure 7.25: $C_{Q,net}$ - λ Curves of a SB-VAWT with MI-VAWT1 at $RN=300,000$ [Islam et. al 2007b]

Chapter 8

Design Analysis of a Smaller-capacity SB-VAWT

An analytical design method is presented in the chapter for a smaller-capacity fixed-pitch SB-VAWT. Different salient design parameters (such as solidity, design power coefficient, design tip speed ratio, design wind speed, cut-out speed, number of blades, blade-section and blade supporting type etc.) are also analyzed. Some innovative design concepts are discussed for improving the performance of a SB-VAWT. Investigations have been made to explore the viability of incorporating wing tip devices to reduce the induced drag of the blades of a SB-VAWT. Analysis has also been done to reduce the parasitic drag of the supporting struts and eventually a new airfoil has been designed which can be utilized as a shape of the struts.

Considering the available design parameters, the present design method gives directions for optimum turbine configurations at variable turbine speed. For design analysis, additional subroutines are written and integrated into the main FORTRAN program which has been developed for the performance analysis using the computational scheme described in Chapter 4. Then, detail sensitivity analyses have been performed for a SB-VAWT equipped with MI-VAWT1. Finally, overall dimensions of a new class of SB-VAWT have been presented based on analytical calculations.

8.1. Design Parameters

As shown in Figure 8.1, fixed-pitch SB-VAWT is one of the simplest types of wind turbines with only three major physical components, namely (a) blade; (b) supporting strut; and (c) central column. The main design parameters related to a smaller-capacity SB-VAWTs are categorized and listed in Table 8.1. It should be mentioned that not all of the parameters are of the same importance for successful final product. Some of the parameters (like choice of airfoil, supporting strut configuration and shape, solidity, blade material) are more sensitive and critical than others. Because of this, detailed sensitivity analyses have been performed with these vital parameters in Section 8.2.

One of the main challenges of wide spread application of smaller-capacity SB-VAWT is to design and develop it in a cost-effective manner. According to Paraschivoiu [2002], *“the overall cost effectiveness of every wind energy conversion system is determined by:*

- (a) Wind turbine manufacturing cost;*
- (b) Amount of energy captures;*
- (c) Site preparation and installation costs;*
- (d) Maintenance costs; and*
- (e) Financing costs.”*

The performance of HAWTs has increased considerably over the past decade which resulted from improved airfoils, variable speed or multi-speed operation and more efficient drive trains [Parashivoiu 2002]. For smaller-capacity fixed-pitch SB-VAWT, all of these factors should also play an important role and deserve serious investigations. The overall cost of the SB-VAWT will mainly depend on the proper choice of the design parameters critically analyzed in the separate sub-headings.

Table 8.1: Different Design Parameters of a SB-VAWT Powered Application

Category	Parameter
Physical Features	<ol style="list-style-type: none"> 1. Blade Airfoil 2. Number of Blade (N) 3. Supporting Struts configuration and shape 4. Central Column
Dimensional	<ol style="list-style-type: none"> 5. Swept Area ($A=HD$) 6. Solidity (Nc/R) 7. Aspect Ratio (H/c) 8. Chord/Radius Ratio (c/R)
Operational	<ol style="list-style-type: none"> 9. Rated Power Output (P_o) 10. Rated Wind Speed (V_{w-d}) 11. Cut-in Speed (V_{cut-in}) 12. Cut-out Speed ($V_{cut-out}$) 13. Power Coefficient (C_{Pd}) 14. Tip Speed Ratio (λ_d) 15. Rotational Speed (ω_d) 16. Pitching of Blade (γ_d)
Balance of System	<ol style="list-style-type: none"> 17. Tower 18. Braking Mechanism 19. Load
Others	<ol style="list-style-type: none"> 20. Material 21. Noise 22. Aesthetic

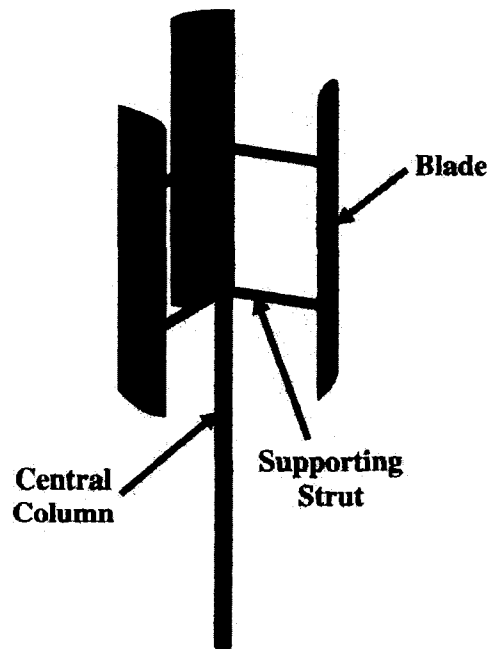


Figure 8.1: The Main Components of a Typical SB-VAWT

8.1.1. Blade Airfoil

The power produced by a SB-VAWT at different wind speeds are largely determined by its blade airfoil. As discussed earlier, symmetrical airfoils (like NACA 0012, 0015, 0018) have historically been chosen for fixed-pitch SB-VAWT because the lift and drag coefficients characteristics are symmetrical about the angle of attack at blade mounting point and the ready availability of performance data. However, as discussed in Chapter 2, the main problem of utilizing these symmetric airfoils is their production of low starting torque at low speed. Though several contemporary variable pitch blade configurations have potential to overcome the starting torque problem but they are quite complicated and impractical for smaller capacity applications.

Among all the design parameters listed in Table 8.1, one of the most important one is the selection of an appropriate blade shape or airfoil. The main emphasis of the present work is to select such an airfoil for cost-effective and efficient SB-VAWT with optimum dimensions. It has been shown in the previous chapters that asymmetric airfoils can produce more torque in the low λ ranges. The aim of Chapters 5 and 6 was to select suitable airfoils based on desirable aerodynamic and geometric features. Subsequently, these tasks lead to design a special-purpose airfoil MI-VAWT1 in Chapter 7. It is one of the main interests of this chapter to find out the design features of a smaller-capacity of a SB-VAWT with this special-purpose airfoil.

8.1.2. Number of Blades

SB-VAWT with a single blade is technically feasible. However a counterweight would be required to balance the mass of the single blade and this counterweight would generate parasitic drag and because forward torque is not produced at all blade positions such a single blade turbine would not self-start [Kirke 1998]. The two-bladed SB-VAWT produces more torque than the single bladed ones, but it can experience severe “butterfly” excitation, which has been responsible for

damaging fatigue stresses in a number of VAWT rotors [Parashivoiu 2002]. However, a three-bladed VAWT rotor is structurally non directional and the response of three blades is more favorable than two blades of the same chord length [Parashivoiu 2002]. The structural dynamics of two and three bladed VAWTs are quite distinct from each other [Parashivoiu 2002]. Parashivoiu [2002] made a comparative study of two and three bladed Darrieus type VAWTs and found that both of these turbines have some advantages and disadvantages. The advantages of two blades VAWTs are: (i) construction cost is lower; (ii) assembly costs are lower; and (iii) strength to weight ratio is better. On the other hand, three-bladed VAWTs have the following advantages: (i) better choice of fabrication technique; (ii) better torque ripple; and (iii) better structural dynamics.

Furthermore, a turbine with three blades tends to run smoothly because of lower fluctuations of energy in each revolution. For three blades SB-VAWTs, cyclic variations in both the torque and the magnitude and direction of the net force on the rotor due to the combined effects of lift and drag on all blades are very much reduced. This is the case because the aerodynamic forces on the blades of a SB-VAWT reach a peak twice per revolution. The aerodynamic forces on two blades 180° apart will peak approximately in phase and will act in approximately the same direction on both blades, leading to potential problems with resonant vibrations in the tower, while those from three blades 120° apart will tend to produce an almost steady force analogous to three phase electrical power [Kirke 1998]. Kirke [1998] suggested that a SB-VAWT requiring greater low speed torque may be designed around three bladed systems at some sacrifice of high speed performance.

8.1.3. Supporting Struts

Supporting struts of SB-VAWTs connect the central rotating column to the blades and they are also important design parameters. They stabilize the blades during survival winds, transfer torque into the central column, reduce operating mean

and fatigue stresses in the blades, and strongly influence some natural frequencies of the rotor [Paraschivoiu 2002]. However, they add to the weight and cost and they generate parasitic drag (as stated in Section 2.3.6) which reduces the net power output. Supporting struts must be strong enough to carry weight, inertial and aerodynamic loads and must also be stiff enough in both flexure and torsion to prevent excessive static and dynamic deflections which would make the turbine appear fragile and might lead to resonant vibrations and fatigue failure.

The design of supporting struts involves a trade-off between aerodynamic and structural requirements. It has already been shown in Section 4.5 that loss of power due to the strut effect is proportional to the cube of the tip speed ratio. So, the length of the supporting struts (i.e. the radius of the turbine) should be as low as possible to reduce the parasitic drag generated by these structures.

8.1.3.1. Types of Blade-supports with Horizontal Struts

The blades of SB-VAWTs can be supported with the horizontal struts in different ways. As shown in Figure 8.2, the three main types of blades supports can be categorized as (i) simple support; (ii) overhang support; and (iii) cantilever support.

To minimize the parasitic drag, cantilever or one horizontal supporting strut per blade is preferred. However, for smaller-capacity SB-VAWT with high blade bending moments due to centripetal acceleration, either simple or overhang supports (which utilize two struts per blade) are preferable. Furthermore, it will be shown later in Section 8.1.7 that blade performance deteriorates as its aspect ratio (μ) decreases. So, it is desirable to use long slender blades for high μ , such long blades generally require two points of support for structural reasons [Kirke 1998].

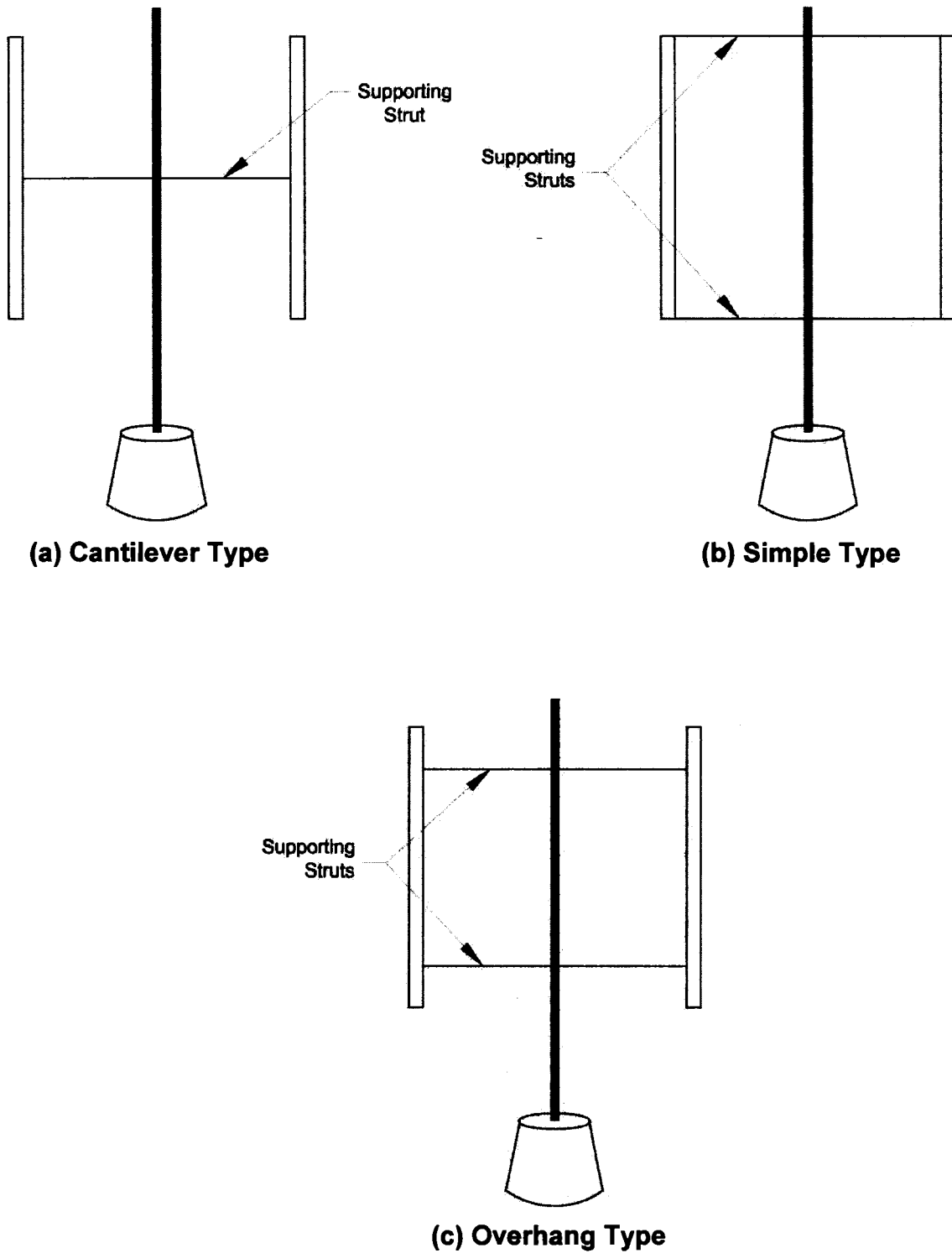


Figure 8.2: Three Different Types of Blade Supports of SB-VAWTs

8.1.3.2. Shape of the Supporting Struts

Different shapes (like rectangular, circular, airfoil etc.) can be utilized as the profile of the supporting struts. However, for aerodynamic reasons a non-lifting airfoil is preferable with a low value of drag coefficient at zero lift (C_{D0}). The value of C_{D0} of the commonly used supporting struts is usually between 0.1 to 0.5 [Kirke 1998]. Based on literature survey, it has been found that only Eppler [1990] designed and tested three thick airfoils dedicated for non-lifting struts. These three airfoils (namely E862, E863 and E864) were designed for Reynolds number of 400,000, 700,000 and 1,200,000 respectively. So, none of these airfoils were designed for applications of a typical smaller-capacity SB-VAWT which operates at RN below 300,000. The lowest RN airfoil among these three is E 862 which is shown in Figure 8.3.

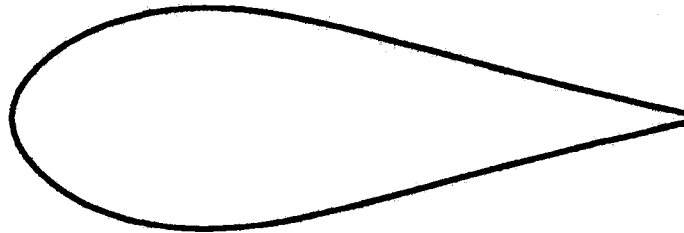


Figure 8.3: Eppler 862 Non-lifting Supporting Strut

Under this backdrop, an attempt has been made in the present research to design a thick non-lifting strut for the RN range below 300,000. The XFOIL has been utilized for this purpose. After conducting detailed analysis, a new airfoil has been designed and named as “MI-STRUT1”. The geometry of MI-STRUT1 is shown in Figure 8.4 and its coordinates are presented in Appendix E. In Figure 8.5, comparison has been made between the C_{D0} of Eppler E862 and MI-STRUT1 at different Reynolds number. It is evident from this figure that C_{D0} values of MI-STRUT1 are lower than E 862 for all the RN and the difference is much greater at $RN < 250,000$. So, based on this study MI-STRUT1 can be considered as a potential candidate for the profile of supporting struts of SB-VAWT for better performance.

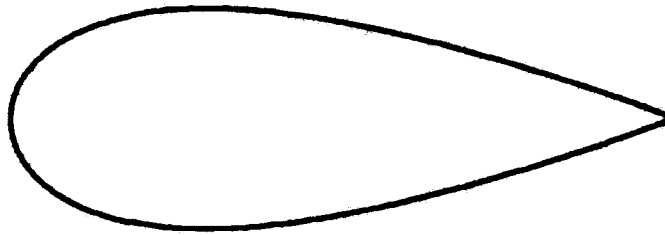


Figure 8.4: Newly Designed MI-STRUT1

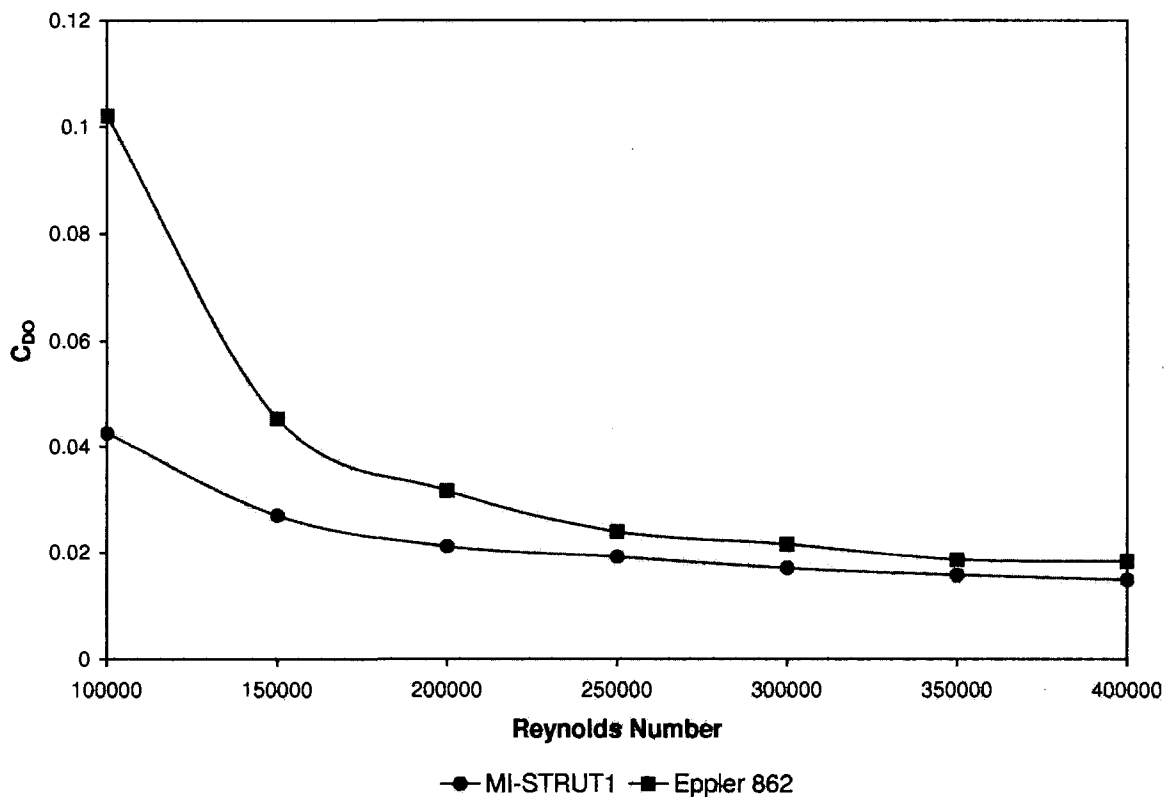


Figure 8.5: Comparison Between the C_{do} of Eppler 862 and MI-STRUT1 at Different Reynolds numbers

In Figures 8.6 and 8.7, $C_{P,net}-\lambda$ curves of a SB-VAWT with MI-VAWT1 blade are illustrated with different shapes of supporting struts at $RN=100,000$ and $300,000$. The values of zero-lift drag coefficient of the different types of struts (denoted as $C_{do,st}$) are shown within the parenthesis. It is evident from Figure 8.6 that the

maximum value of $C_{P,net}$ decreases significantly with the increase of $C_{do,st}$ at $RN=100,000$. It can also be seen from Figure 8.6 that the size of the $C_{P,net}-\lambda$ curve become smaller with increase of $C_{do,st}$ values. The $C_{P,net}$ values at different λ with MI-STRUT1 is much higher than the other two types of strut shapes. Similar trend has been observed from Figure 8.7 for the $C_{P,net}-\lambda$ curves at $RN=300,000$, however the difference between the E862 and MI-STRUT1 is lesser than that of $RN=100,000$. In this case also, the size of the $C_{P,net}-\lambda$ curve become smaller with increasing $C_{do,st}$.

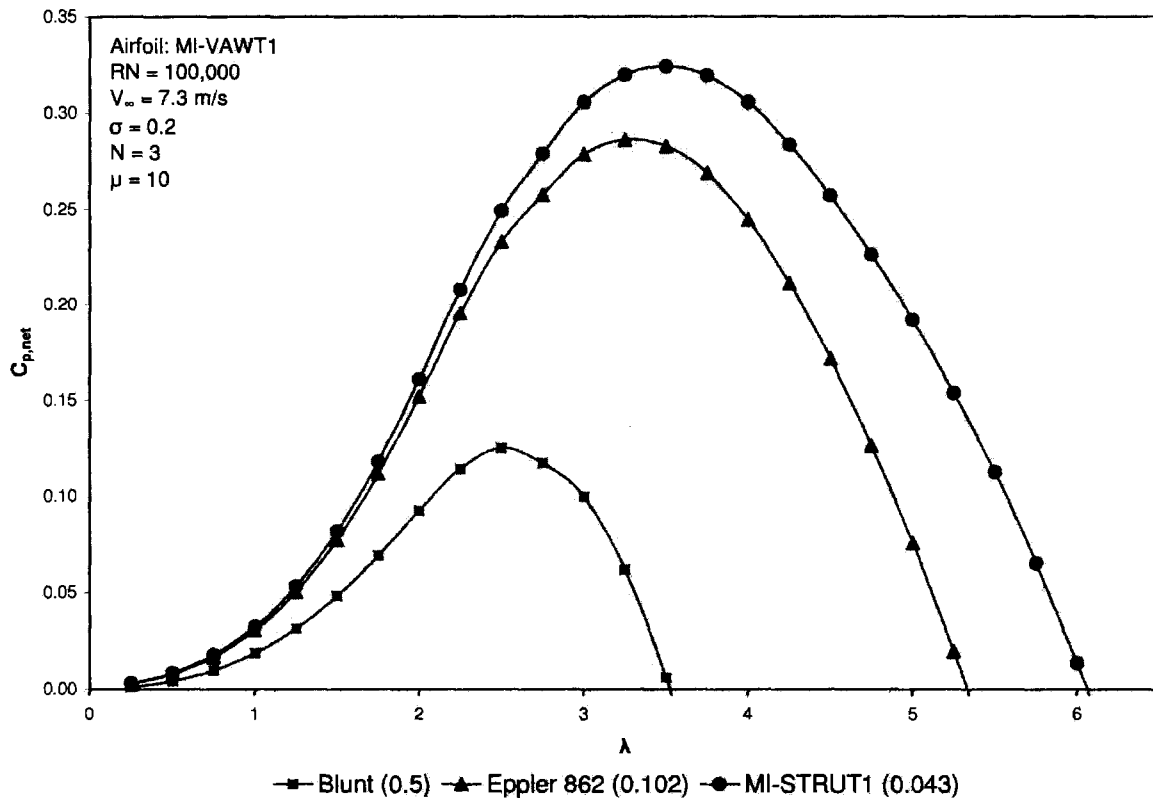


Figure 8.6: $C_{P,net}-\lambda$ Curves of a SB-VAWT with Different Shapes of Supporting Struts at $RN=100,000$

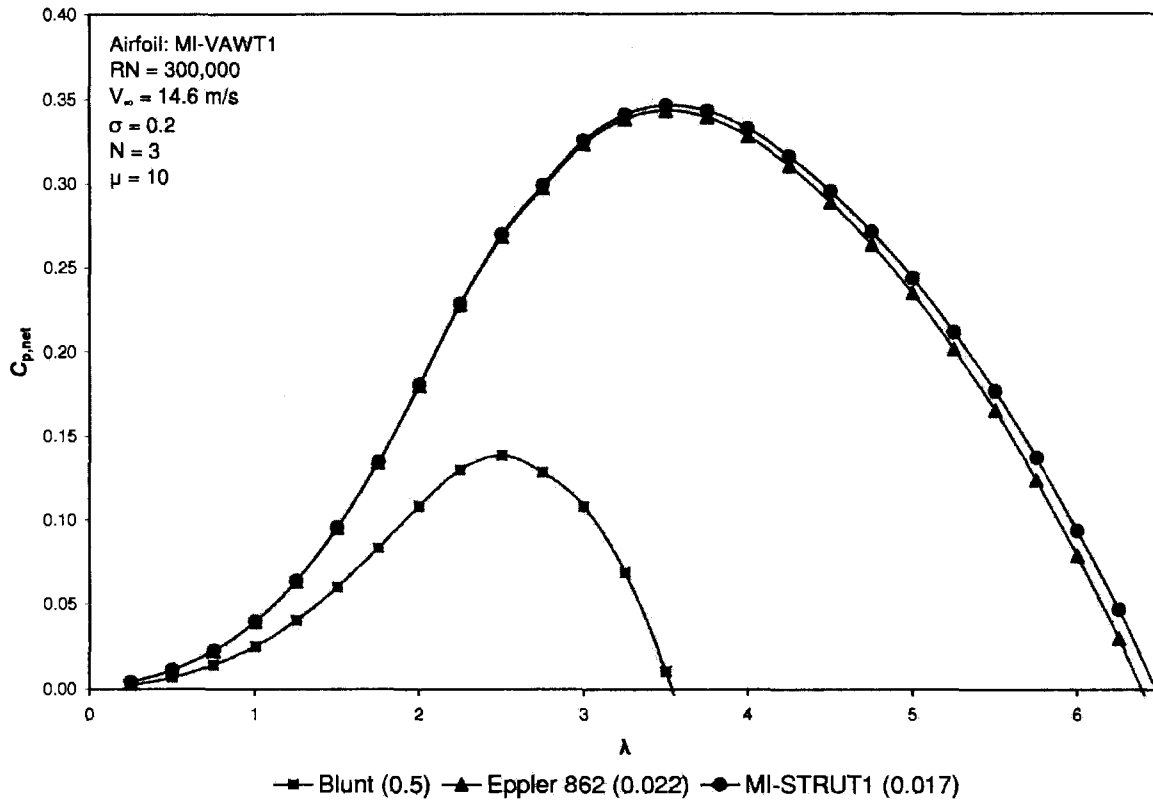


Figure 8.7: $C_{p,net}$ - λ Curves of a SB-VAWT with Different Shapes of Supporting Struts at 300,000

8.1.4. Central Column

The central column of a SB-VAWT is connected with the blades for capturing the energy from the wind. The circular tubes are commonly used as the central column of SB-VAWTs. The diameter of the central column should be judiciously chosen. If the SB-VAWT is situated high above the ground to capture more energy from the wind by extending the rotating central column downwards, larger column diameter might be required for optimum stiffness. The central column can be fabricated from steel tubular columns.

8.1.5. Swept Area

The area through which the rotor blades of a SB-VAWT spins, as seen when directly facing the center of the rotor blades is called the swept area ($A=2RH$).

The power output of a wind turbine is directly related to the swept area of its blades. The larger the diameter of the turbine, the more power it is capable of extracting from the wind. The larger the blades, the stronger they need to be to withstand the higher levels of centrifugal and cyclic varying gravitational loads. Each extra meter of length requires extra strength and adds further to the structures weight and so compounds the problem.

Furthermore, the bending moments across the swept area of the blade can vary considerably with a possible difference of several meters a second in wind speeds between the top and the bottom of the blades rotation. This all adds up to a substantial increase in fatigue, not only in the blade structure but the machines hub, bearing, drive shaft and support tower. So, the swept area of a SB-VAWT should be judiciously chosen after considering all these factors.

8.1.6. Solidity

The SB-VAWT rotor solidity (σ) is defined as the ratio of blade surface area (NcH) to the frontal swept area ($2RH$) that the rotor passes through. It represents one of the key design parameters. σ can be either expressed as " Nc/D " (where D is the diameter of the SB-VAWT) or " Nc/R ". It has been found from the literature that most researchers have used Nc/R as the σ [Kirke 1998] and the same is followed in the present study.

It is evident from the definition of σ that both the weight of the SB-VAWT and manufacturing costs increases with increasing σ . In general, a high solidity SB-VAWT rotor turns slowly and produces high starting torque [Kirke 1998]. So, high solidity turbine has a great advantage of producing higher torque at low tip speed ratios. However, Kirke [1998] found that an increase in solidity has the following drawbacks:

- (i) More material is needed to sweep a given area, so the material and installation costs per unit power output are higher than for a low σ turbine.*

(ii) Maximum efficiency is reached at lower λ , so larger step-up gear ratios are needed for driving most loads, for example generators and centrifugal and helical rotor pumps. This low speed range would of course be an advantage for low speed loads.

(iii) Higher σ fixed pitch VAWTs have a very "peaky" C_p/λ curve, i.e. they operate efficiently over a very narrow range of λ . This is a drawback because when the wind gusts and changes λ the turbine will operate at low efficiency until it can speed up or slow down to track the change in wind velocity, even assuming a well-matched load which adjusts to seek optimum λ (as described in Kirke 1996). Because of its greater blade area a high solidity rotor has greater inertia and will be slow to adjust to the changing wind speed.

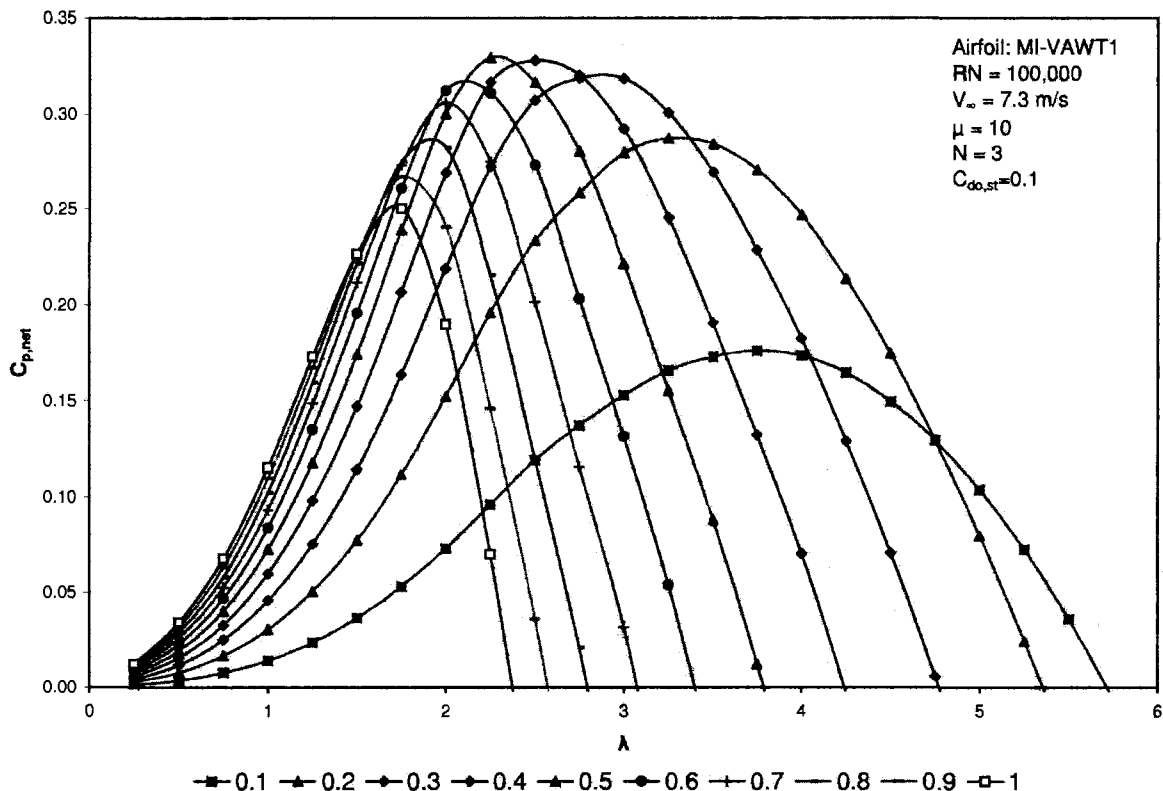


Figure 8.8: Power Coefficients of a Fixed-pitch SB-VAWT at Different Solidities

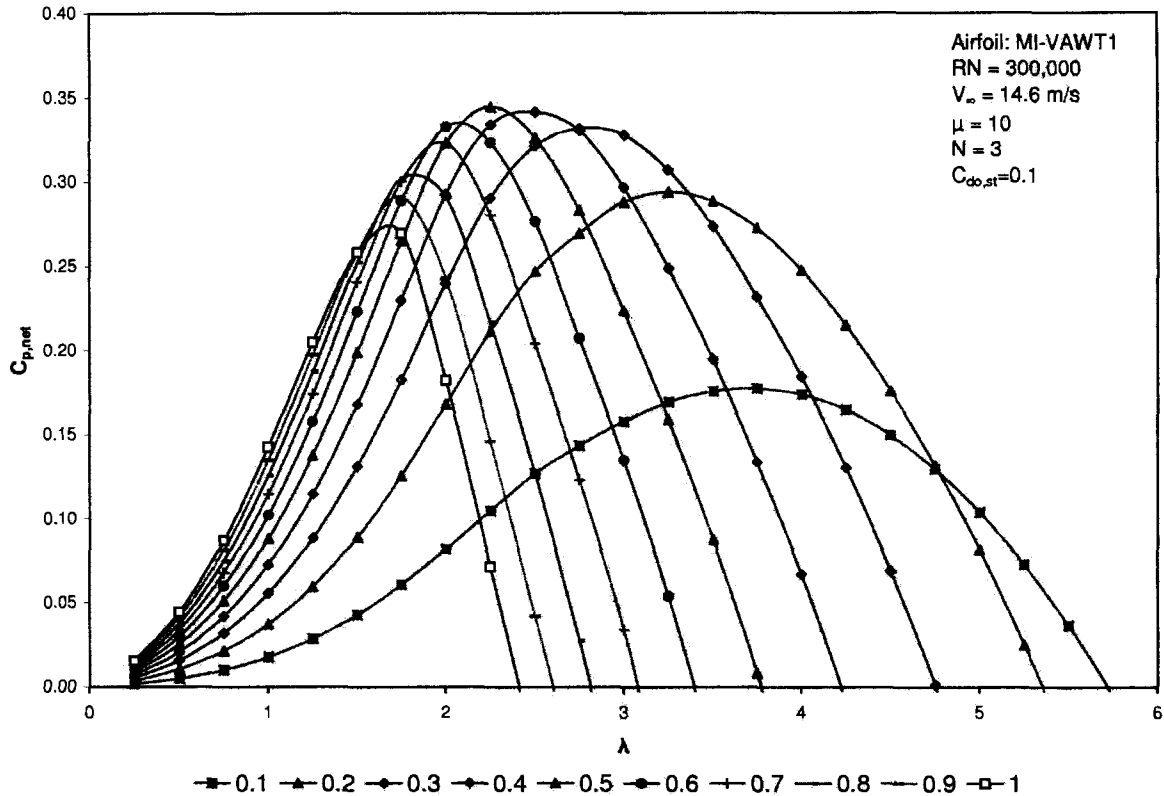


Figure 8.9: Torque Coefficients of a Fixed-pitch SB-VAWT at Different Solidities

In Figures 8.8 and 8.9, $C_{P,net}-\lambda$ curves of a SB-VAWT with MI-VAWT1 blade are shown at different solidities at $RN=100,000$ and $300,000$. It can be seen from Figure 8.8 that the maximum value of $C_{P,net}$ increases with the increase of σ from 0.1 to 0.5. With further increase in σ results in decrease in $C_{P,net}$ values. Also, the shape of the $C_{P,net}-\lambda$ curve becomes sharper with increase of σ which is not desirable. Similar trends have been found at $RN=300,000$ as can be seen from Figure 8.9.

8.1.7. Aspect Ratio (H/c)

It has been reported by Kirke [1998] that to achieve an acceptable peak efficiency, low blade aspect ratio should be avoided and it must be considerably higher than 7.5. It has been observed in the present study that consideration of

finite aspect ratio effect in the calculation reduces the lift/drag ratio, as a result tangential forces decrease and leading to lower power.

Increasing the aspect ratio is one way to increase the swept area for the same chord length and diameter of the SB-VAWT, enabling it to capture more energy. However, the height of the SB-VAWT should be judiciously selected as it will add more blade material. The chord length (c) of the SB-VAWT is related with the bending stresses and aerodynamic loads. The bending stresses are dependent on the square of the c and the aerodynamic loads are dependent on only the first power of c .

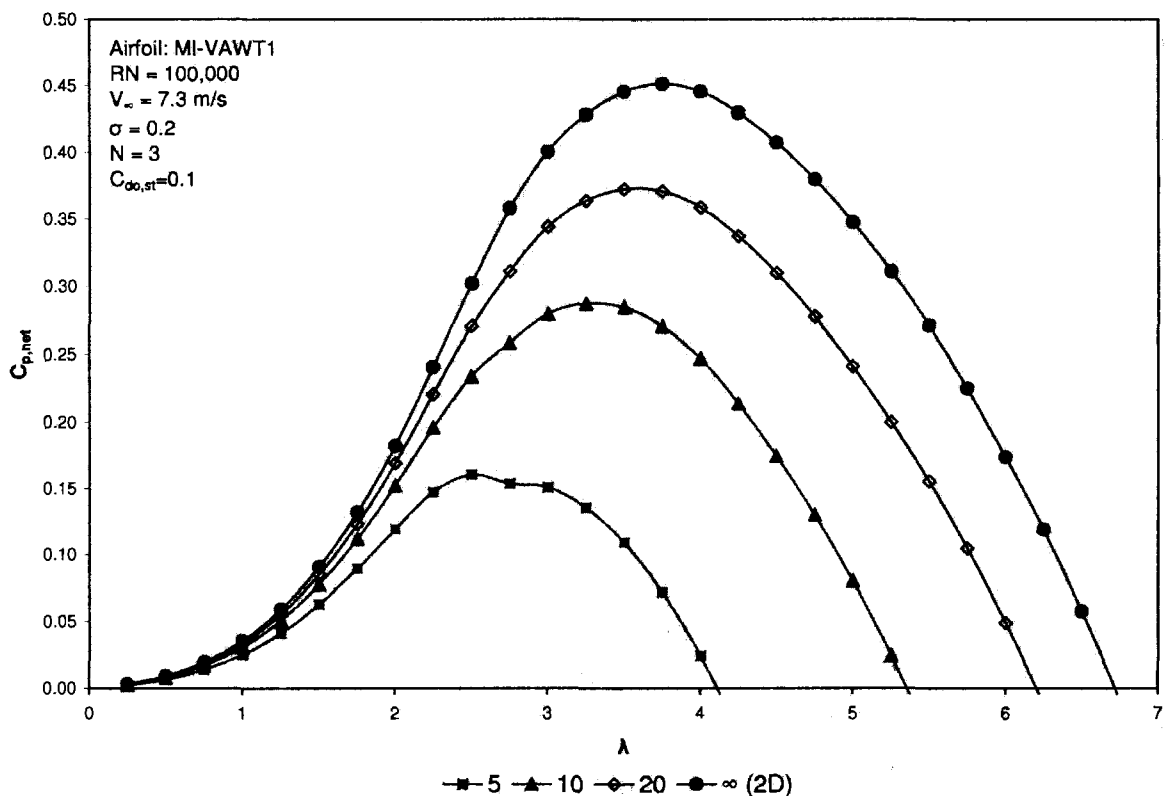


Figure 8.10: $C_{p,net}$ - λ Curves of a SB-VAWT at Different Aspect Ratio

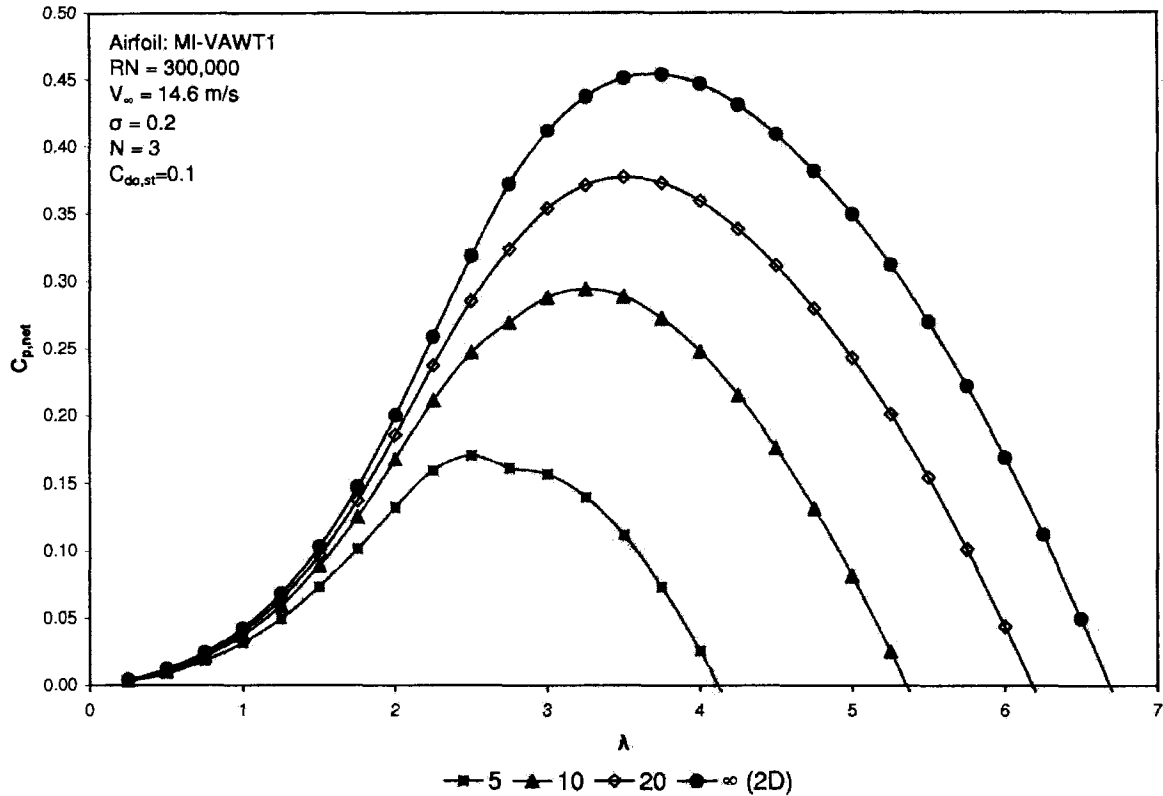


Figure 8.11: $C_{P,net}\lambda$ Curves of a SB-VAWT at Different Aspect Ratio

In Figures 8.10 and 8.11, $C_{P,net}-\lambda$ curves of a SB-VAWT with MI-VAWT1 blade are shown at different aspect ratios. It is shown in Figure 8.10 that the maximum value of $C_{P,net}$ increases with the increase of aspect ratio at $RN=100,000$. The rate of increase in maximum value of $C_{P,net}$ is higher between lower aspect ratios. Same type of variation can also be seen from Figure 8.11 at $RN=300,000$ and the size of the $C_{P,net}-\lambda$ curve become larger with increase of aspect ratio.

8.1.7.1. Wing Tip Devices for SB-VAWT Blades

In recent times, wing tip devices have become a popular technique to increase the aerodynamic performances of lifting wings by reducing the induced drag. As the blades of SB-VAWTs are basically similar to wings, such tip devices has potential application for SB-VAWT blades to increase the aerodynamic performances. The idea behind all these wing tip devices is to diffuse the strong vortices released at the tip and optimize the spanwise lift distribution, while

maintaining the additional moments on the wing within certain limits [Aerodyn 2007]. Over the years, different types of wing tip devices have been investigated and applied in the aerodynamic applications, mainly in the aerospace industries. After literature survey, the following wing devices could be found from the Internet:

- Winglets
- Endplates
- Hoerner Tips
- Tip Tanks
- Tip Sails
- Upswept and Drooped / Raised Wing Tips
- Elliptical Wingtips
- Wing Grids
- Spiroid Tips

Among all these devices, the winglets and endplates are found to be possible candidates for SB-VAWT blades after judging their simplicity, effectiveness and level of advancement. It should however be pointed out that before incorporating these devices with the SB-VAWT blades, further detailed analyses should be performed to assess their net positive contributions.

(a) Winglets:

Winglets represent one of the few effective means of fighting induced drag [Aviation Intranet 2007]. The winglets, as shown in Figure 8.12, are usually mounted on the rear part of the wing (region of lowest pressure) to minimize interference effects. Several theoretical investigations, and later experiments, indicated that the use of vertical lifting surfaces placed at the wing tips produce a beneficial effect on both lift and drag characteristics at the cost of increased bending moment [Aerodyn 2007]. Winglets can be used to produce lower drag and extra lift. Drag reduction rates with winglets can be of the order of 5% [Aerodyn 2007]. According to Boeing [2007], there is added advantage in using a

blended winglet configuration that allows for the chord distribution to change smoothly from the wingtip to the winglet, which optimizes the distribution of the span load lift and minimizes any aerodynamic interference or airflow separation.

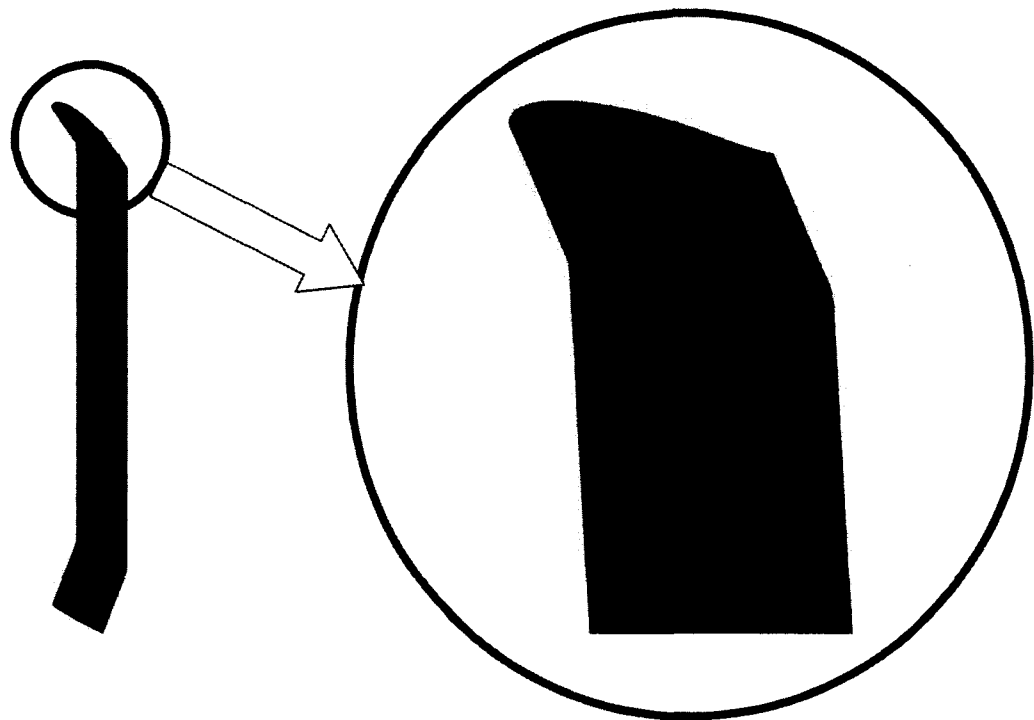


Figure 8.12: MI-VAWT1 Blade with Winglets

(b) Endplates:

Endplates are generally considered a more simple engineering solution than the winglets described above. They are widely used in the airfoil experimental setups to eliminate the wing tip losses. With the endplates attached, it is assumed in these experimentations that the airfoil behaves like a two-dimensional wing.

The endplates, as shown in Figure 8.13, are vertical surfaces added to a wing to redistribute the lift along the span and the effect is strongly increased lift coefficients, against a drag coefficient that decreases by a tiny amount [Aerodyn

2007]. The resulting efficiency of wing (Lift/Drag ratio) is generally greatly improved.

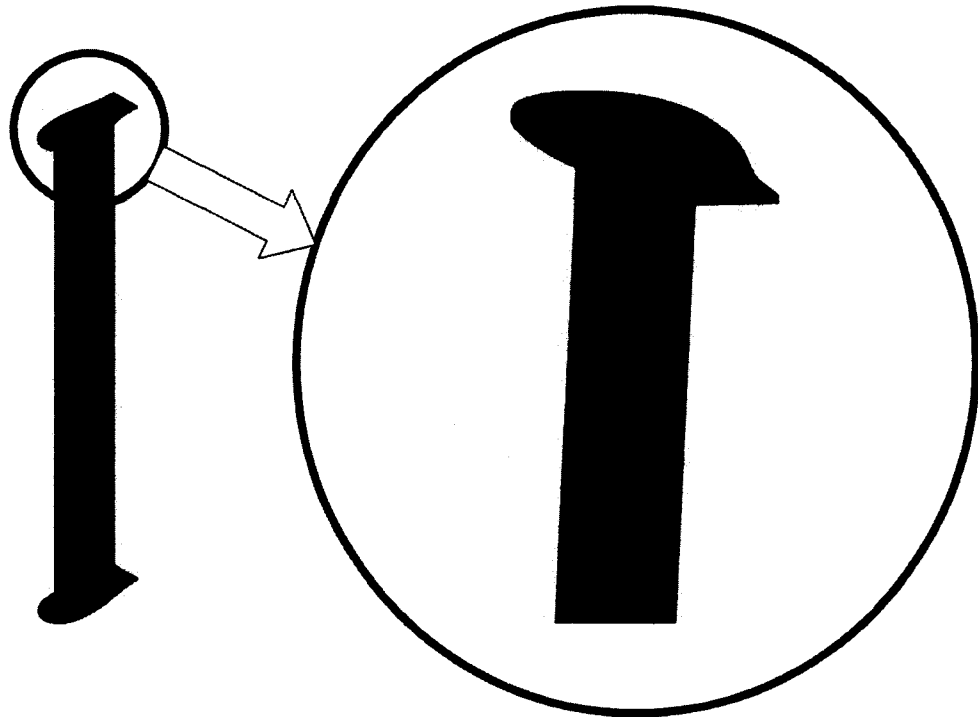


Figure 8.13: MI-VAWT1 Blade with Endplates

8.1.7.2. Elliptical Wings

Apart from the above-mentioned wing tip devices, the induced drag of a wing can also be reduced by fabricating the wing in elliptical shape. An elliptical wing is a wing planform shape (as shown in Figure 8.14), first seen on aircraft in the 1930s, which minimizes induced drag [Wikipedia 2007b]. Elliptical taper shortens the chord near the wingtips in such a way that all parts of the wing experience equivalent downwash, and lift at the wing tips is essentially zero, improving aerodynamic efficiency due to a greater Oswald efficiency number in the induced drag equation [Wikipedia. 2007b]. One of the main barriers of elliptical wings is that the compound curves involved are difficult and more expensive to construct

than the rectangular wings of SB-VAWTs. Before concluding about the viability of elliptical wings, further aerodynamic and economic analyses are required.

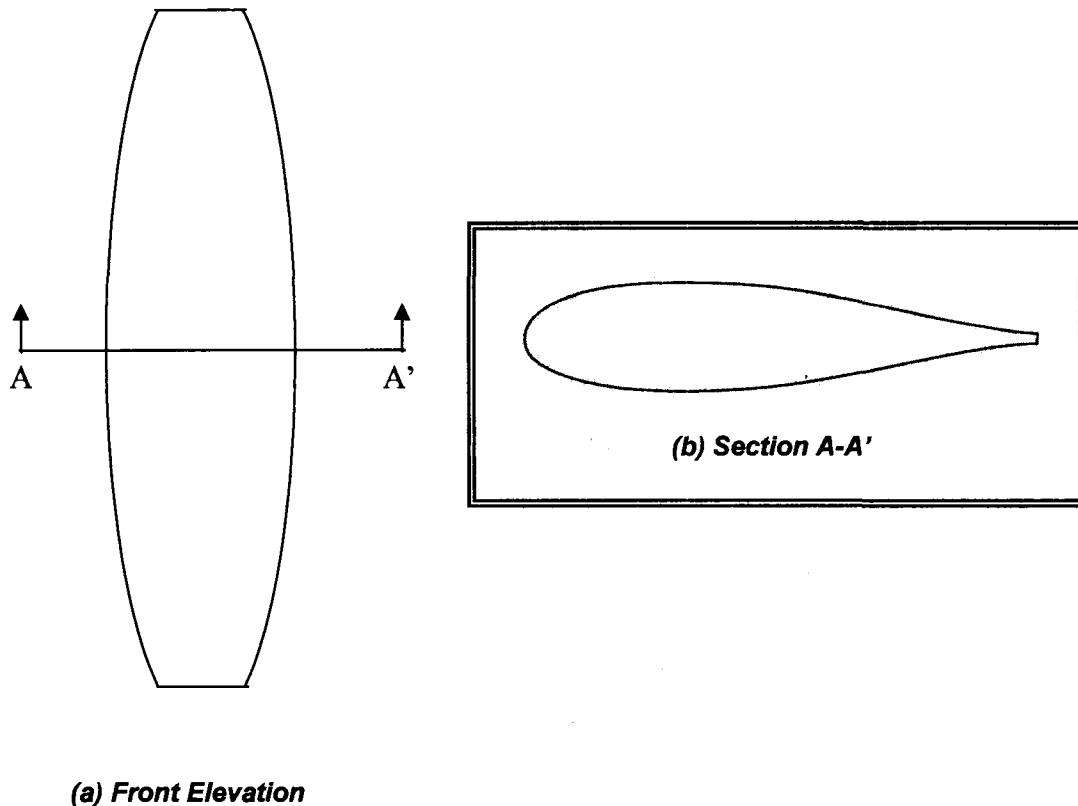


Figure 8.14: Elliptical MI-VAWT1 Blade with Sectional View

8.1.8. Chord-Radius Ratio (c/R)

By definition, the solidity of a SB-VAWT is proportional to its chord to radius. Furthermore, as discussed in detail in Section 2.3.4., the flow curvature effect of a SB-VAWT increases with its chord to radius ratio and under most circumstances it has a detrimental influence on the blade aerodynamic efficiency [Migliore et. al 1980]. So, a much larger c would result in higher c/r (which will increase flow curvature effect) and much heavier blades that would be expensive to build and difficult to handle.

8.1.9. Rated Power Output

The wind turbines like SB-VAWTs are usually designed based on a rated power output which is the nameplate value attained at certain rated wind speed as defined later. The swept area of the turbine is based on the rated power output. The power curve of a wind turbine is a graph that indicates how large the power output will be for the turbine at different wind speeds. A wind turbine power curve is, by international convention, determined by averaging power and wind speed measurements over a fixed time interval, usually ten minutes. The results are then “binned” to produce a graph. The concept of rated power output can be better understood from an illustration of a typical power curve of a 3kW SB-VAWT shown in Figure 8.15.

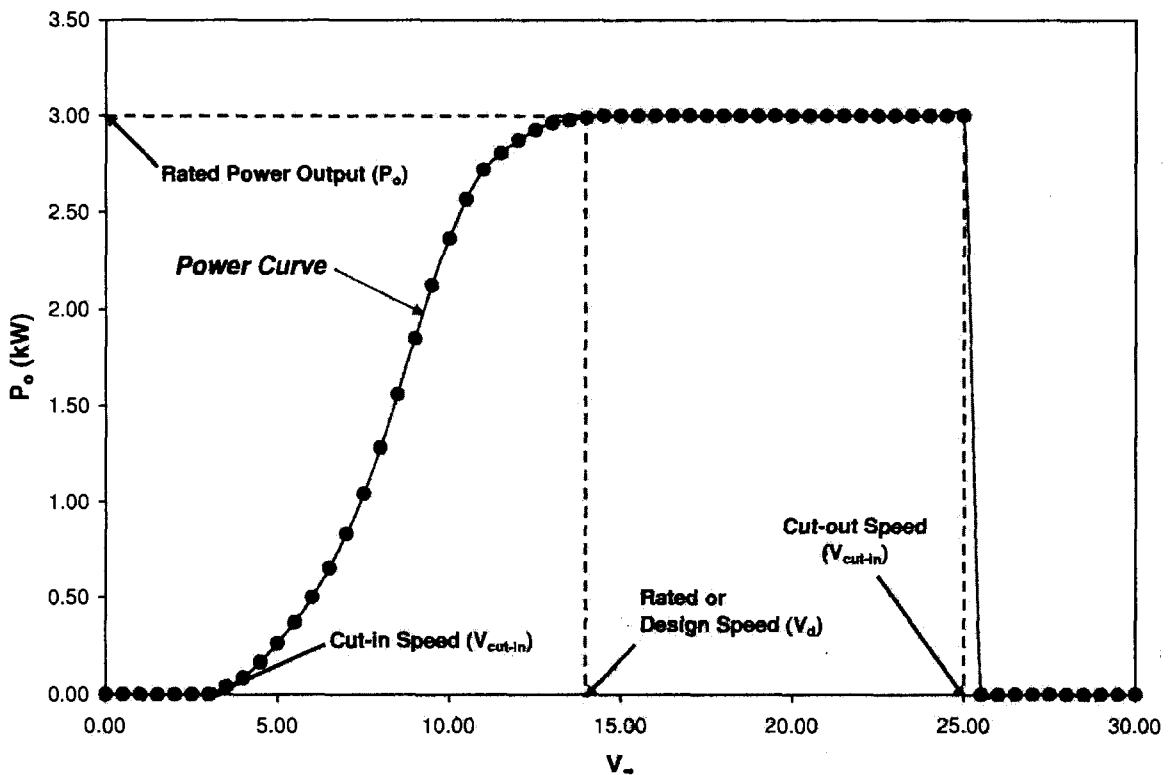


Figure 8.15: Illustration of a Typical Power Curve of a 3kW SB-VAWT

8.1.10. Rated Wind Speed (Design Wind Speed)

The wind speed at which the SB-VAWT produces the rated amount of power is usually defined as the rated or designed wind speed as shown in Figure 8.15. The rated wind speed generally corresponds to the point at which the conversion efficiency is near its maximum. Because of the variability of the wind, the amount of energy a wind turbine actually produces is a function of the capacity factor. The rated wind speed of the typical smaller-capacity SB-VAWTs can vary between 10 to 15 m/s.

8.1.11. Cut-in Speed

Cut-in speed is identified as the lowest speed at which power is produced in the turbine power curve as shown in Figure 8.15. If the turbine's cut-in speed is significantly below a site's average wind speed, problems are inevitable [AWEA 2007]. Also, SB-VAWT should be able to generate enough starting torque at the cut-in wind speed to overcome the drive-train (and gearbox) friction.

8.1.12. Cut-out Speed

The cut-out speed (as illustrated in Figure 8.15) is the wind speed at which the turbine may be shut down to protect the rotor and drive train machinery from damage or high wind stalling characteristics [AWEA 2007]. A wind turbine should be able to withstand the blade stresses at cut-out speed. Normally, the maximum wind speed for operation of the wind turbine is about 25 m/s, i.e., storm conditions, beyond which the rotor is brought to a standstill [Brøndsted et. al 2005]. Based on this, the typical cut-out speed of a smaller-capacity SB-VAWT can be set around 25 m/s.

8.1.13. Power Coefficient

The power coefficient is a non-dimensional number which indicates how efficiently a wind turbine converts the harnessed wind energy to useful electrical

or mechanical energy. The design power coefficient (C_{Pd}) is one of important design parameters. For wind turbines, the C_p - λ curves (usually known as the performance curves) are drawn to select optimum design power coefficient. In Figure 8.16, C_{Pd} is shown in a typical C_p - λ curve.

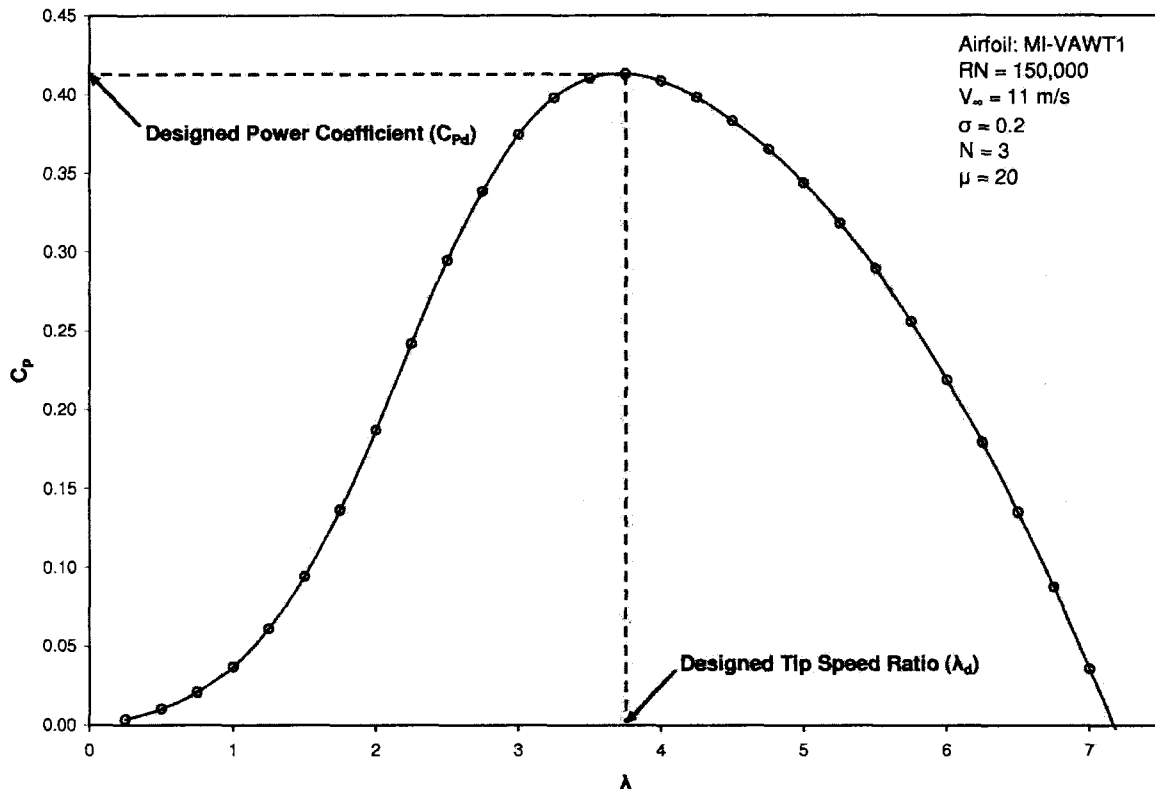


Figure 8.16: Illustration of a Design Power Coefficient and Tip Speed Ratio

8.1.14. Tip Speed Ratio

For wind turbines, the ratio between the rotational speed of the tip of the blade and the actual velocity of the wind is called the tip speed ratio (λ). Usually high tip speed ratio is better, but the value should not be too high so that the machine becomes noisy and highly stressed. The design tip-speed ratio (λ_d) for a wind turbine is usually the ratio of the speed of the tip of a turbine blade for which the power coefficient is at maximum as illustrated in Figure 8.16. The λ_d will

determine how fast one wants the wind turbine to rotate and so it has implications for the load (alternator or other mechanical device) that can be used.

8.1.15. Rotor Speed

The rotor speed is mainly controlled by the wind regime, the solidity, and the machine power rating [Paraschivoiu 2002]. Increasing rotor speed decreases low-speed torque and hence reduces the cost of the drive train. In addition, increased rotor speed enhances the centrifugal force ($m\omega^2$). For a variable speed SB-VAWT, the maximum rotational speed is determined based on design power coefficient (C_{pd}) and tip speed ratio (λ_d).

8.1.16. Blade Pitching

Blade pitching is mostly used to reduce the turbine overspeed thereby preventing structural failure of the turbine at high wind speeds. The pitching mechanism may be of various types: fixed pitching, sinusoidal pitching, combination of fixed and sinusoidal pitching etc. Pitching controls the performance of a turbine significantly. In the present analyses, fixed pitching is considered to be positive for the blade airfoil nose rotating in the outward direction from the blade flight path.

In Figures 8.17 and 8.18, $C_{P,net}-\lambda$ curves of a SB-VAWT with MI-VAWT1 blade are depicted with fixed pitch angles at $RN=100,000$ and $300,000$. It can be observed from Figure 8.17 that with the application of fixed blade pitching the values of $C_{P,net}$ at different λ initially increases between the values of -7 and 3 degrees. Then, with further increase of fixed pitch angle beyond 3 degree result in decrease in the value of $C_{P,net}$ at different λ . From Figure 8.18, similar trends have been observed at $RN=300,000$, i.e. it is seen that the values of $C_{P,net}$ initially increases up to pitch angle of 3 degree and then decreases at higher pitch angles.

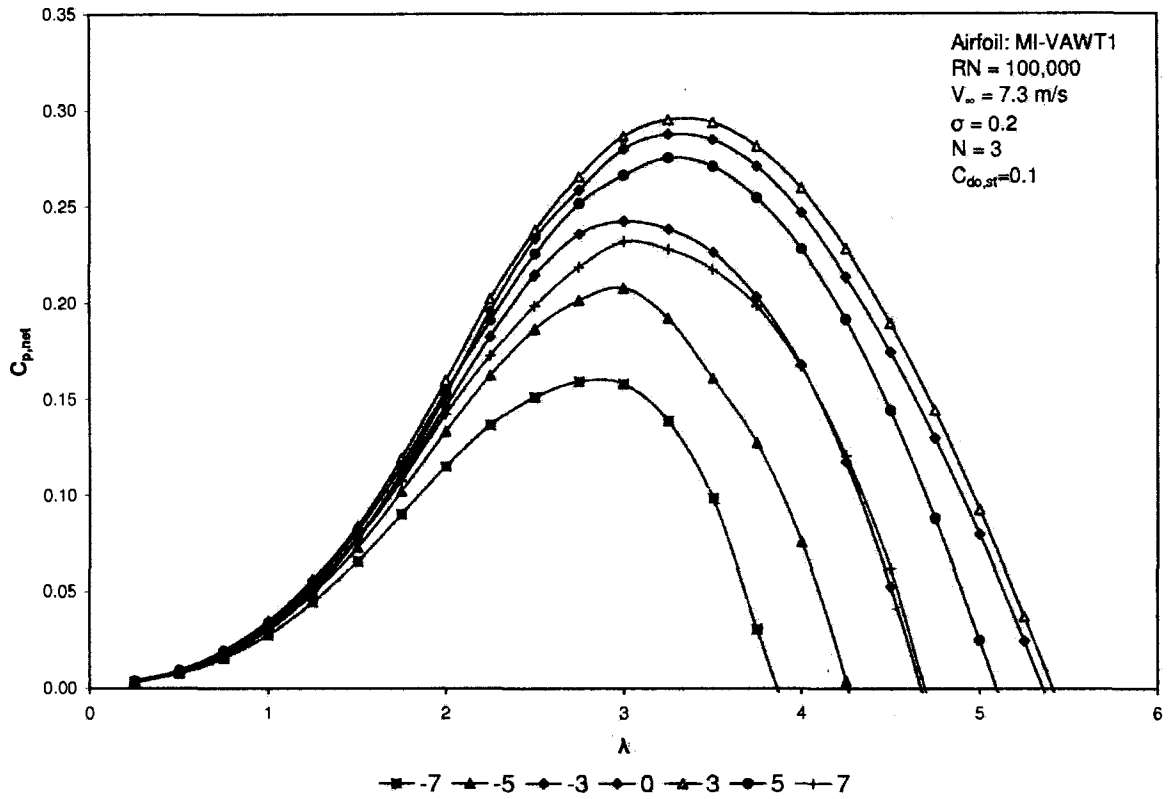


Figure 8.17: $C_{P,net}$ - λ Curves of a SB-VAWT with Different Fixed Pitch Angle

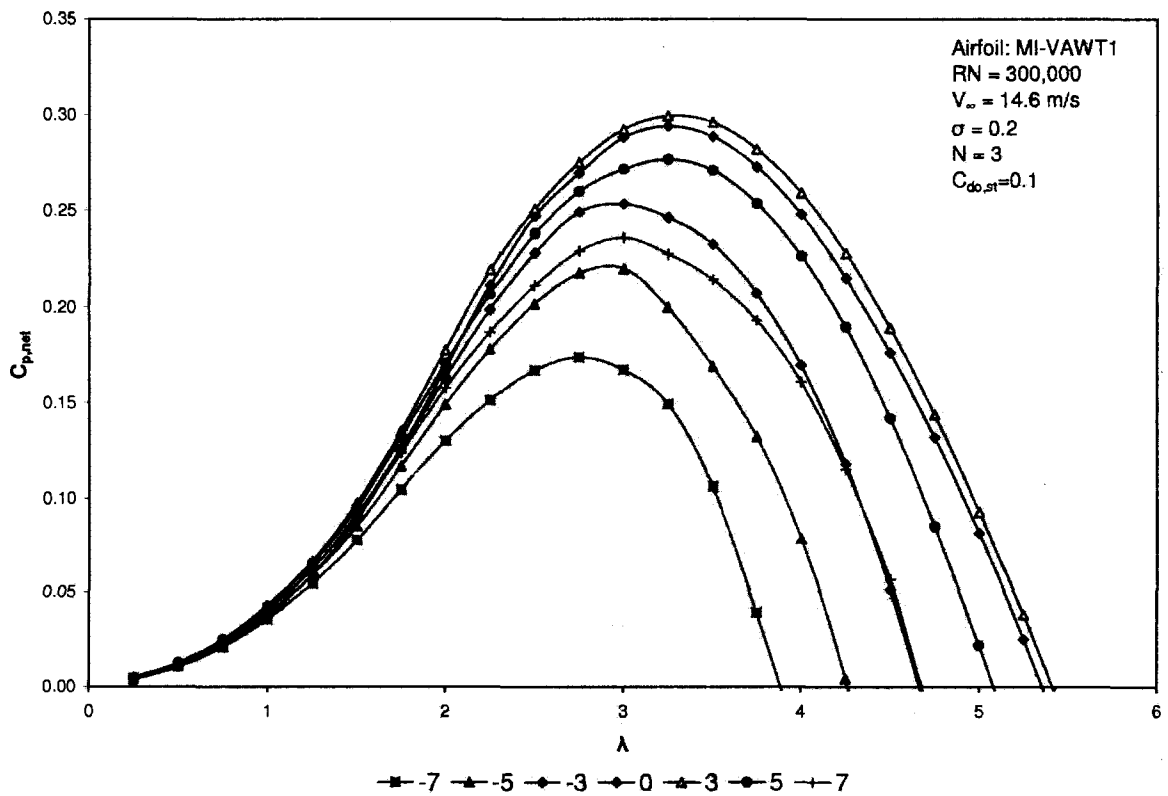


Figure 8.18: $C_{P,net}$ - λ Curves of a SB-VAWT with Different Fixed Pitch Angle

8.1.17. Tower

Additional energy can be captured by a SB-VAWT by increased rotor height that can be considerable in wind regimes with vertical wind shear [Parashivoiu 2002]. Different types of towers (including the lattice type, the guyed tubular type) can be used for housing SB-VAWTs. It should also be pointed out that a set of guy cables seems to be the most efficient method of supporting a tall structure like the steel pole tower hosting a SB-VAWT [Paraschivoiu 2002]. However, Paraschivoiu [2002] also highlighted several disadvantages of guy cables which are:

- Cable foundations are necessary;
- Cable tension must be kept constant;
- Cables are especially awkward on sloping ground;
- Cables must have sufficient clearance from the blades;
- Cables must be angled at 35 degree to the horizontal for keeping maximum stiffness; and
- Transverse oscillations of the cables.

The price of a tower for a wind turbine is generally around 20 per cent of the total price of the turbine and it is therefore quite important for the final cost of energy to build towers as optimally as possible [DWIA 2007b]. According to DWIA [2007b], lattice towers are the cheapest to manufacture, since they typically require about half the amount of steel used for a tubular steel tower with a similar stiffness. It is also possible to construct hybrid type tower which can be fabricated by combining a lattice tower and a guyed tower.

8.1.18. Braking Mechanism

Different types of braking mechanisms can be applied to SB-VAWTs, including (i) mechanical brake and aerodynamic spoiler. Some of the researchers, like Kirke [1998] used an automotive brake drum, shoes and a mechanical (handbrake) linkage which were connected via a cable to a “panic handle” at the base of the

tower of his variable-pitch SB-VAWT so the turbine could be stopped and left stationary when required. Both electrical and mechanical braking systems can be utilized with smaller-capacity SB-VAWTs to allow a controlled emergency stop. For variable speed VAWTs, electrical braking is normally employed [Paraschivoiu 2002].

8.1.19. Type of Loads

It has been discussed in detail in Section 1.4.1 that SB-VAWT can be utilized through different configurations to deliver useful electrical or mechanical energies. Technical aspects of both electric and mechanical loads are also discussed in Section 1.4.1. Furthermore, the different types of applications of SB-VAWTs have been discussed in Section 1.4.2.

8.1.20. Blade Material

One of the most important and critical design parameters for successful smaller-capacity SB-VAWT is selection of the blade material. SB-VAWT blades must be produced at moderate cost for the resulting energy to be competitive in price and the blade should last during the predicted life-time (usually between 20 and 30 years). Though there are many articles and reports available in the public domain on material aspect of HAWTs or curved-bladed VAWTs blades, it was not possible to find any such literature for SB-VAWTs.

The aerodynamic contours of wind turbine blades are formed by the (outer) relatively thin shells and they are supported structurally by a longitudinal beam or by webs, which carry a substantial part of the load on the blade [Brøndsted et. al 2005]. The shape of a typical wind turbine blade in cross section is shown in Figure 8.19. In the subsequent headings, the required materials properties and the available popular materials usually used for wind turbine blades are discussed.

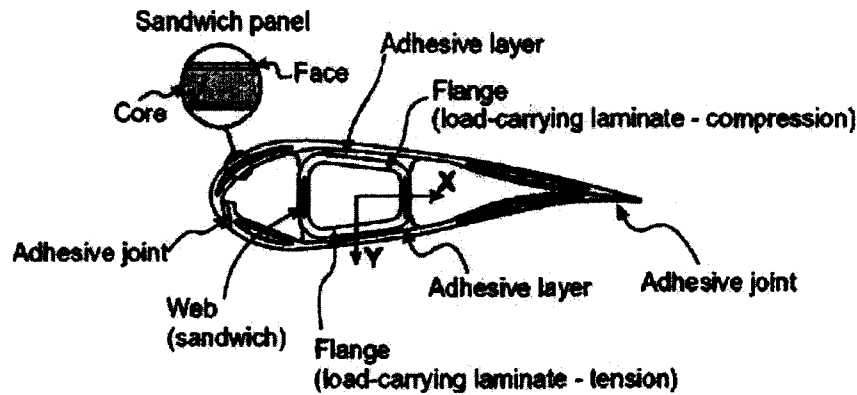


**Figure 8.19: Cross-Section Principle of a Wind Turbine Blade Giving the Nomenclature of the Different Blade Construction Elements [Reprinted, with permission, from the Annual Review of Materials Research, Volume 35 © 2005 by Annual Reviews
www.annualreviews.org]**

8.1.20.1. Required Properties of the Blade Materials

SB-VAWT blades are exposed to diversified load conditions and dynamic stresses are considerably more severe than many mechanical applications as can be seen from Figures 8.20 and 8.21. Based on the operational parameters and the surrounding conditions of a typical SB-VAWT for delivering electrical or mechanical energy, the following properties of the SB-VAWT blade materials are required:

- It should have adequately high yield strength for longer life;
- It must endure a very large number of fatigue cycles during their service lifetime to reduce material degradation;
- It should have high material stiffness to maintain optimal aerodynamic performance;
- It should have low density for reduced amount of gravity and normal force component;
- It should be corrosion resistant;
- It should be suitable for cheaper fabrication methods.
- It must be efficiently manufactured into their final form;
- It should provide a long-term mechanical performance per unit cost;

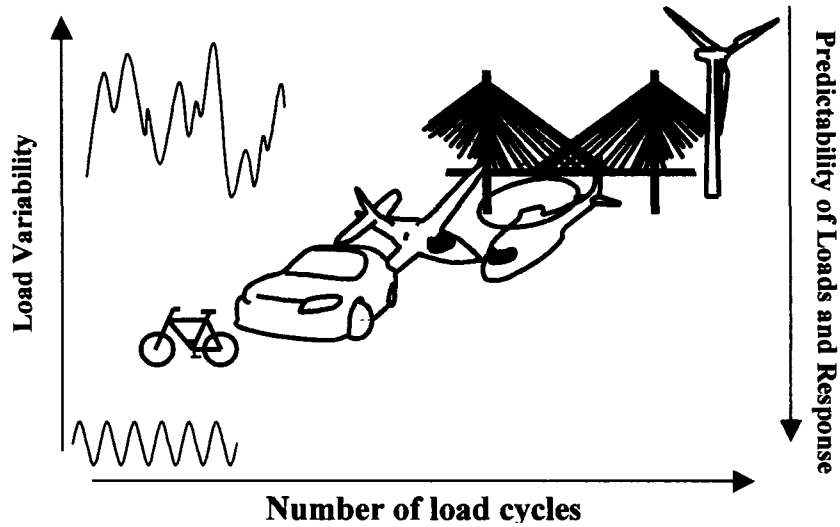


Figure 8.20: Number of Load Cycles of Different Mechanical Applications [Reproduced from Nijssen 2006]

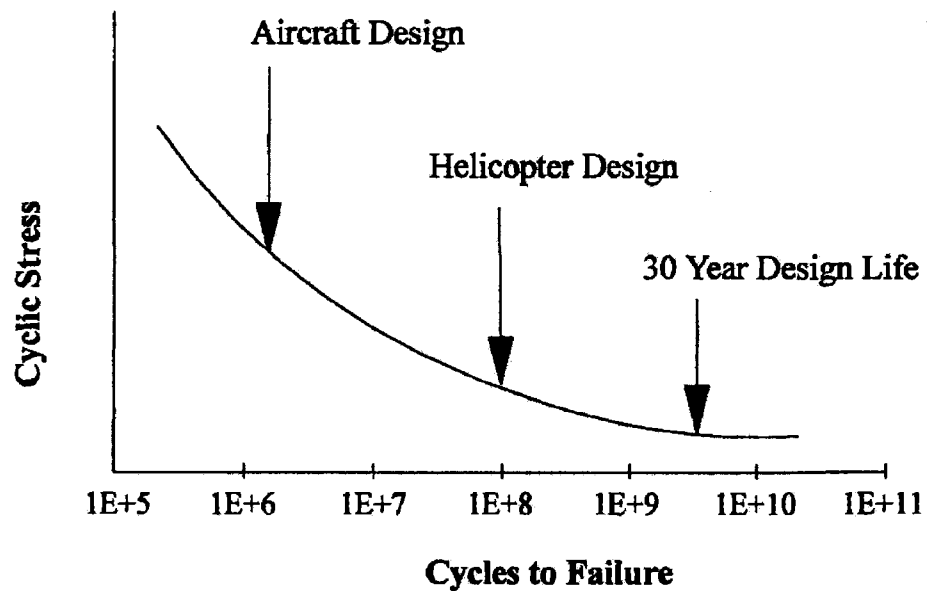


Figure 8.21: Schematic S-N Diagram for Various Fatigue-critical Structures [Sutherland 2000, Copyright John Wiley & Sons Limited. Reproduced with permission]

Among all these requirements, fatigue is the major problem facing both HAWTs and VAWTs and an operating turbine is exposed to many alternating stress cycles and can easily be exposed to more than 10^8 cycles during a 30 year life time [CETC 1995]. The sources of alternating stresses are due to the dynamics

of the wind turbine structure itself as well as periodic variations of input forces [CETC 1995]. An extensive review on the fatigue properties of materials for wind turbines has been done by Sutherland [2000].

8.1.20.2. Prospective Materials

Modern large wind turbine rotor blades (up to 126 m diameter) are made of lightweight pultruded glass-reinforced plastic. The smaller turbine blades are usually made of aluminum, or laminated wood [The Encyclopedia of Alternative Energy and Sustainable Living 2008]. Metals were initially a popular material because they yield a low-cost blade and can be manufactured with a high degree of reliability, however most metallic blades (like steel) proved to be relatively heavy which limits their application in commercial turbines [Sutherland 2000].

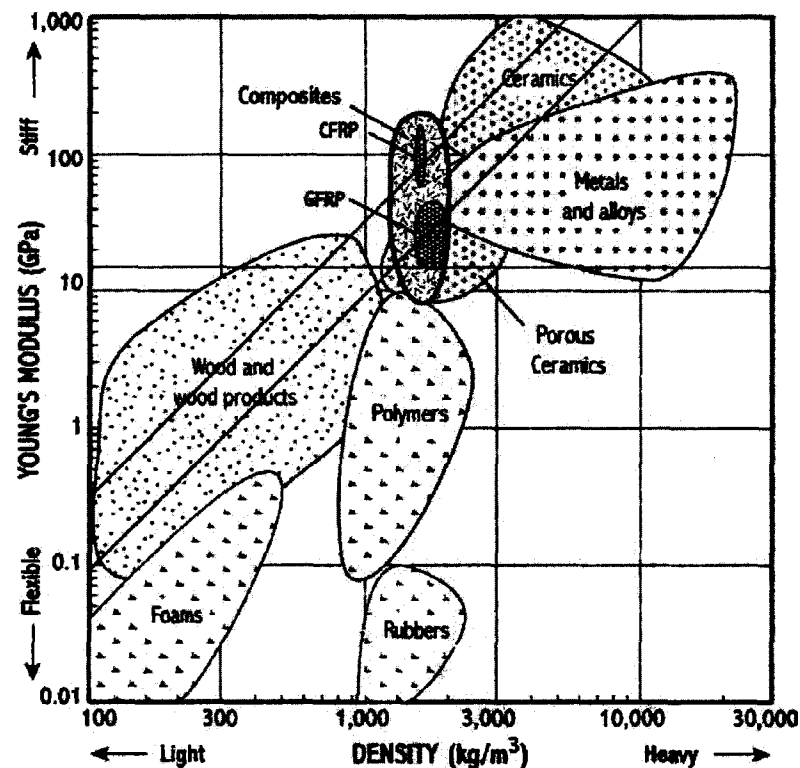


Figure 8.22: Diagram Showing Stiffness versus Density for all Materials [Reprinted, with permission, from the Annual Review of Materials Research, Volume 35 © 2005 by Annual Reviews www.annualreviews.org]

In the past, laminated wood was also tried on early machines in 1977 [Butler and Blackwell 1977]. At present, the most popular materials for design of different types of wind turbines are wood, aluminum and fiberglass composites that are briefly discussed below. In Figure 8.22, stiffness versus density for different types of available materials are shown for illustration purpose.

(a) Wood and Wood Epoxy:

Wood, a naturally occurring composite material, is readily available as an inexpensive blade material with good fatigue properties [CETC 1995]. Wood was a popular wind turbine blade material since ancient time. Wood has relatively high strength-to-weight ratio, good stiffness and high resilience [Sutharland 2000]. Wood and wood epoxy blades have been used extensively by the designer of small and medium sized HAWTs. However, wood does have an inherent problem with moisture stability. This problem can be controlled with good design procedures and quality controlled manufacturing processes. The application of wood to large blades is hindered by its joining efficiency which in many cases has forced designers to examine other materials [Sutharland 2000].

(b) Aluminum:

Aluminum blades fabricated by extrusion and bending are the most common type of VAWT materials. The early blades of Darrieus type VAWTs were made from stretches and formed steel sheets or from helicopter like combinations of aluminum alloy extrusions and fiberglass [Parashivoiu 2002]. It has been reported by Parashivoiu [2002] that the former were difficult to shape into smooth airfoil, while the latter were expensive. The major problem that aluminum alloy for wind turbine application is its poor fatigue properties and its allowable stress levels in dynamic application decreases quite markedly at increasing numbers of cyclic stress applications when compared to other materials such as steel, wood or fiberglass reinforced plastics [CETC 1995].

(c) Fibreglass Composites:

Composites constructed with fibreglass reinforcements are currently the blade materials of choice for wind turbine blades [Sutherland 2000] of HAWT types. This class of materials is called fibreglass composites or fibre reinforced plastics (FRP). In turbine designs they are usually composed of E-glass in a polyester, vinyl ester or epoxy matrix and blades are typically produced using hand-layup techniques. Recent advances in resin transfer moulding and pultrusion technology have provided the blade manufacturers to examine new procedures for increasing the quality of the final product and reducing manufacturing costs [Sutherland 2000]. The characteristics that make composites, especially glass fiber-reinforced and wood/epoxy composites, suitable for wind turbine blades are [NRC 1991]:

- low density;
- good mechanical properties;
- excellent corrosion resistance;
- tailorability of material properties; and
- versatility of fabrication methods.

According to Sutherland [2000] – *“The most significant advancement over this decade is the development of an extensive database for fibreglass composite materials. This database not only provides the designer with basic material properties, it provides guidance into engineering the material to achieve better performance without significantly increasing costs. Some questions have yet to be answered, but research is ongoing. The primary ones are the effects of spectral loading on fatigue behaviour, scaling the properties of non-metallic materials from coupons to actual structures, and environmental degradation of typical blade materials.”*

8.1.20.3. Comparative Analysis between Available Materials

It has been found from literature survey that in recent times both fiberglass-reinforced and wood/epoxy composites have been shown to have the

combination of strength and low material and fabrication costs required for competitive blade manufacture [NRC 1991]. Precise control of airfoil geometry is quite important in providing blades with consistent aerodynamic properties and small variations in outboard airfoil camber ($\pm 1/4$ percent of chord) can lead to substantial aerodynamic imbalance and rotor and turbine life reduction [NRC 1991]. This need for aerodynamic consistency and accuracy has led to the adoption of molding as the fabrication method of choice for both fiberglass and wood/epoxy composites, as it provides control right at the outer aerodynamic surface, which determines the ultimate performance. Both material systems are able to provide the complete range of outboard airfoil shapes currently of interest [NRC 1991].

In mid nineties, a comprehensive investigation on alternative materials for use in medium-size VAWT blades was conducted by W. R. Davis Engineering Ltd for the CANMET Energy Technology Centre (CETC) of Canada [CETC 1995]. It seems that the main focus of this study was curved-type VAWTs. However, significant insight regarding different blade materials can be understood from this study. In this study, consideration was given to parameters of aerodynamic performance, structural capabilities, corrosion, erosion and cost. Six types of blade materials, namely (i) aluminum; (ii) stainless steel; (iii) low carbon steel; (iv) titanium; (v) fibre reinforced composites; and (vi) wood and wood epoxy, were considered in the study. It was found that pultruded FRP is economically more viable than all the materials considered in the study.

In Table 8.2, comparison of the engineering properties of pultruded FRP and extruded Aluminum are shown. The properties of this table are compiled from CETC [1995]. It can be seen from this table that the mechanical strength (ultimate strength, fatigue strength) of the pultruded FRP is significantly better than commonly used Aluminum. Also, comparatively it is lighter in weight. Some of the key findings related to the viability of pultruded FRP blades which came from the CETC [1995] report are:

- *Pultruded fibre reinforced plastic obtained the best rating out of all the materials chosen.*
- *Due to lack of field experience of fibre reinforced materials in the area of VAWT blades a large safety factor would be required.*
- *One method that is becoming quite popular and proving to be very cost effective is pultrusion.*
- *The scores for all the materials except aluminum may be quite conservative due to the fact that the exact processes to manufacture the blades and the behaviour of the blade once in use are fairly unknown. Upon further analysis of these materials may prove to have a substantially better rating than aluminum.*

Pultrusion is a continuous forming process that allows for a very high glass fiber content, which results in a very high strength, yet flexible rotor blade and the basic material strength is in the order of 100,000 psi (689.5 MPa) or approximately twice the strength of low carbon steel [Bergey 2007]. In recent times, pultruded FRP blades have been preferred by one of the leading small HAWT type wind turbine manufacturer like Bergey [Bergey 2007] and a few other small wind energy conversion system [CETC 1995].

Table 8.2: Engineering Properties of Extruded Aluminum and Pultruded FRP

Property	Extruded Aluminum 6061-T6	Pultruded FRP
Ultimate Strength	310 N/mm ²	500 N/mm ²
Fatigue Strength	97 N/mm ² (in 5 X 10 ⁸ cycles)	175 N/mm ² (in 10 X 10 ⁸ cycles)
Density	2700 kg/m ³	1800 kg/m ³
E Modulus	70 X 10 ³ N/mm ²	35 X 10 ³ N/mm ²
Price (Canadian \$/kg)	\$10	\$10 - \$12
Price (Canadian \$/dm ³)	\$28	\$20-\$22

8.1.21. Noise

As SB-VAWTs have prospects to operate in the urban environments, noise emission should be kept as low as possible. It has already been discussed in Section 5.3.8 that the laminar separation bubbles that extend over the trailing edge of the airfoil cause the blades to vibrate and are a source of noise which should be as minimum as possible. Conceptually, as the blade speed of SB-VAWTs is lower than similar capacity HAWTs, the noise generated by them is expected to be lower. This has been validated by a study of Iida et al. [2004] and Iida & Mizuno [2003], who have modelled the aerodynamic sound of a SB-VAWT numerically by using the discrete vortex methods. They managed to capture the complicated wake structure using this method and showed that the SB-VAWT produces less sound than a horizontal axis wind turbine with the same power coefficient at normal operating speed [Iida et al. 2004 and Iida & Mizuno 2003].

8.1.22. Aesthetics

What is aesthetically pleasing is, by definition, an emotional issue [Sagrillo 2007]. Sense of appealing can vary from person to person. However, every effort should be made by the SB-VAWT designers to design the turbine in an attractive fashion. They should be visually unobtrusive and they should be painted in such a manner that they blend in with the environment as much as possible.

8.2. Analytical Tool for Design Analysis of SB-VAWT

After analyzing the main design parameters related to smaller-capacity SB-VAWT in the previous section, an attempt has been made here to perform design analysis with the newly designed MI-VAWT1. Flow diagram of the design procedure is given in Appendix-B. For calculating the performance of the SB-VAWT, the computational scheme described in Chapter 4 is used. The governing

equations for determining the blade stresses for the present design analyses are shown in Appendix-F.

As illustrated in the flow diagram of Appendix-B, the blade stresses are calculated at different azimuth angles for determination of the maximum stress (S_m). S_m is obtained at every skin thickness t_s (as shown in Figure 8.23). The lowest value of S_m in (S_m vs. t_s) distribution is the required blade stress and the corresponding value of t_s is considered as the best thickness. Then, the value of the S_m is compared with the allowable stress (S_a) and it is ensured that S_m is within the range of ($S_a \pm 1$) by altering the aspect ratio of the blade.

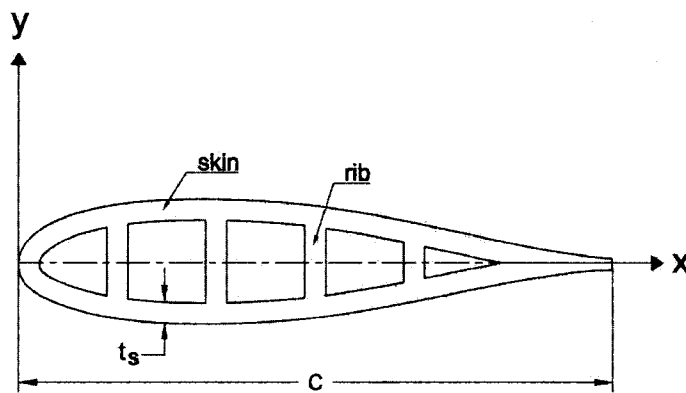


Figure 8.23: MI-VAWT with Skin and Rib Areas

SB-VAWT blades need to be designed for both ultimate loads (based on static strength) and fatigue loads (based on fatigue strength). As wind turbines like SB-VAWTs are fatigue-critical machines, the design of the blades is significantly dictated by fatigue considerations. According to CETC [1995] – the key to successful design rests on the integrity of the design, with specific and detailed consideration of the material being use, the loading conditions anticipated with the specific site of installation and the selection of the best cut-out wind speed of the turbine. Also from structural viewpoint, the dynamic stall is quite significant particularly in the low tip-speed ratio regime where the blade stalls dynamically.

The presence of stall vortices produces critical problems like aero-elastic vibrations and noises from the blades and the fatigue of the blade materials by the unsteady forces [Abramovich 1987].

For the present analyses, Table 8.2 has been used for determining the allowable stresses (S_a) of aluminum and FRP which are being investigated in the present study. The allowable stress for aluminum is selected as 90 N/mm^2 which is below its fatigue strength of 97 N/mm^2 in 5×10^8 cycles. As per suggestion of CECT [1995], a large safety factor of about 3 is used for FRP. The allowable stress for FRP is selected as 170 N/mm^2 which is below its fatigue strength of 175 N/mm^2 in 10×10^8 cycles.

In the present design method, the design point is chosen in the higher tip speed ratio side that corresponds to the peak power coefficient. This is done because the region beyond the peak power coefficient is relatively stable and suitable for smooth operation. It has been observed that executing the codes using the modified Cascade theory yields reasonable computational time.

The type of electric-generator to be chosen for coupling with SB-VAWT depends largely on how the wind turbine energy is utilized. In the present research, the design work is performed with variable turbine speed condition. The ability to operate at variable or multiple speeds is attractive if it can be done economically. This can increase energy capture by 5% to 10% largely depending on the wind regime [Parashivoiu 2002]. Design of a SB-VAWT at variable turbine speed condition is generally done with a view to serving the following purposes:

- It may be used for generating electricity through AC or DC generator;
- It may be applied for water pumping for irrigation; and
- It may be utilized for driving a fan for ventilation.

The design method at variable turbine speed differs slightly from that at constant turbine speed. For the design with variable turbine speed there appear many fixed and variable design parameters as shown in Table 8.3. Based on these parameters, the design works have been carried out in the next section through sensitivity analyses of five fixed design parameters discussed in the previous section, which are:

- (a) Blade material (Aluminum and FRP);
- (b) Solidity (varied between 0.1 and 1);
- (c) Type of blade support (Simple and Overhang);
- (d) Blade airfoil (NACA 0015 and MI-VAWT1); and
- (e) Blade supporting struts shape (Blunt and MI-STRUT1);

Table 8.3: Different Fixed and Variable Parameters Considered in the Design Analyses

Category	Design Parameter	Value
Physical Features	1. Blade Airfoil	Fixed (NACA 0015 or MI-VAWT1)
	2. Number of Blade (N)	Fixed (3)
	3. Supporting Struts type	Fixed (Simple or Overhang type)
	Supporting Struts shape	Fixed (Blunt or MI-STRUT1)
Dimensional	4. Swept Area ($A=2RH$)	Variable
	5. Solidity (Nc/R)	Fixed (Altered from 0.1 to 1)
	6. Aspect Ratio (H/c)	Variable
	7. Chord/Radius Ratio (c/R)	Fixed (Altered from 0.03 and 0.33)
Operational	8. Rated Power Output (P_o)	Fixed (3 kW)
	9. Rated Wind Speed ($V_{=d}$)	Fixed (Altered from 10 to 15 m/s)
	10. Cut-in Speed (V_{cut-in})	Variable
	11. Cut-out Speed ($V_{cut-out}$)	Fixed (25 m/s)
	12. Power Coefficient (C_{Pd})	Variable
	13. Tip Speed Ratio (λ_d)	Variable
	14. Rotational Speed (ω_d)	Variable
	15. Pitching of Blade (γ_d)	Fixed (Fixed pitch angle of zero)
Balance of System	16. Load	Fixed (variable speed)
Others	17. Material	Fixed (Aluminum or FRP)

8.3. Sensitivity Analyses with Selected Design Parameters

To conduct the sensitivity analysis with five different crucial design parameters, the design analysis program has been run by altering certain parameters while keeping the other fixed. The matrix of design parameters for the present sensitivity analyses with these selected design parameters are shown in Table 8.4 for better understanding about the overall approach.

Table 8.4: Matrix of Design Parameters for the Sensitivity Analyses

Design Parameter	Sensitivity Analyses				
	(1) Blade Support Type	(2) Solidity	(3) Blade Material	(4) Blade Airfoil	(5) Blade Supporting Struts Shape
Blade Material	FRP	FRP	(i) Aluminium and (ii) FRP	FRP	FRP
Blade Shape	MI-VAWT1	MI-VAWT1	MI-VAWT1	(i) NACA 0015 and (ii) MI-VAWT1	MI-VAWT1
Blade Support Type	(i) Simple (ii) Overhang and (iii) Overhang with endplates	Overhang with endplates	Overhang with endplates	Overhang with endplates	Overhang with endplates
Blade Supporting Strut Shape	MI-STRUT1	MI-STRUT1	MI-STRUT1	MI-STRUT1	(i) Strut and (ii) MI-STRUT1
Solidity (σ)	0.5	Altered between 0.4 and 1	0.5	0.5	0.5
Wind Speed ($V_{\infty d}$)	Altered between 10 and 15 m/s	10 m/s	Altered between 10 and 15 m/s	Altered between 10 and 15 m/s	Altered between 10 and 15 m/s

8.3.1. Blade Support Type

One of the most important design parameters of SB-VAWT is the type of blade support as discussed in Section 8.1.3.1. In this section, design analyses have been conducted with three types of blade supports, which are (a) Simple (denoted as Type A); (b) Overhang (denoted as Type B); and (c) Overhang with wing tip device (denoted as Type C) to eliminate the finite aspect ratio effect encountered by the blades by minimizing the tip losses. Either concepts of endplate or winglets can be utilized to fabricate a type C SB-VAWT. However, using endplates is expected to be simpler and cheaper option for this kind of novel blades with wing tip device.

The sensitivity analysis is done at different fixed wind speeds, between 10 and 15 m/s for the three types of supports. Results obtained are presented in Table 8.5. It can be seen from Table 8.5(a) that chord, diameter and height of three types of turbines decrease with the increase of wind speed. This happens as a consequence of decreasing swept area because of increasing wind speed for a fixed power coefficient. Among the three types of supports, chord and diameter are lowest for the overhang type support with wing tip device.

In Table 8.5(b), the variation of blade skin thickness (t_s) and the mass per unit height (m_b) are shown. For all the three different types of supports, t_s and m_b are decreasing with wind speed and the values are least for overhang type support with wing tip device. In Table 8.5(c), the variation of design RPM is shown at different design wind speeds. It can be seen that design RPM increases with increase of design wind speed and maximum amount is obtained with Type C. From all these findings, it is clear that the swept area (HD) and required amount of blade materials for obtaining 3kW is least for Type C at different design wind speeds. Furthermore, maximum RPM is also achieved with this type of blade support. These clearly demonstrate the superiority of overhang type support with a wing tip device like endplate.

Table 8.5: Design Analyses of Different Types of Blade Supports

(a) Overall Dimensions of the SB-VAWT at Different Design Wind Speeds

V_{wd} (m/s)	Chord (m)			Diameter (m)			Height (m)		
	Type A	Type B	Type C	Type A	Type B	Type C	Type A	Type B	Type C
10	0.42	0.31	0.27	5.1	3.8	3.3	2.4	3.9	3.7
11	0.37	0.27	0.24	4.4	3.3	2.8	2.1	3.3	3.2
12	0.32	0.24	0.21	3.9	2.9	2.5	1.8	2.9	2.8
13	0.29	0.22	0.19	3.5	2.6	2.2	1.6	2.6	2.5
14	0.26	0.19	0.17	3.1	2.3	2.0	1.4	2.3	2.2
15	0.24	0.18	0.15	2.8	2.1	1.8	1.3	2.1	2.0

(b) t_s and m_b at Different Design Wind Speeds

V_{wd} (m/s)	Skin thickness (m)			Blade Mass per unit Height, m_b (kg/m)		
	Type A	Type B	Type C	Type A	Type B	Type C
10	0.013	0.009	0.008	23.7	12.9	9.8
11	0.011	0.008	0.007	18.0	9.9	7.4
12	0.010	0.007	0.006	13.9	7.8	5.7
13	0.009	0.007	0.006	11.1	6.2	4.5
14	0.008	0.006	0.005	8.9	5.0	3.7
15	0.007	0.005	0.005	7.3	4.1	3.0

(c) λ_d and RMP_d at Different Design Wind Speeds

V_{wd} (m/s)	Design Tip Speed Ratio (λ_d)			Design RPM (RMP_d)		
	Type A	Type B	Type C	Type A	Type B	Type C
10	2.81	3.09	2.83	105.2	157.0	165.1
11	2.81	3.13	2.83	132.6	199.5	209.2
12	2.80	3.15	2.84	164.9	247.5	259.4
13	2.80	3.18	2.84	199.8	302.8	316.2
14	2.80	3.18	2.84	240.2	363.2	379.5
15	2.80	3.19	2.84	284.6	431.2	449.6

8.3.2. Effect of Solidity

It has already been discussed in Section 8.1.6 that value of solidity has profound effect on performance of a SB-VAWT and it is very important to select an appropriate value to obtain optimum performance without requiring excessive blade materials. Design configurations of variable speed SB-VAWT at various solidities are shown in Table 8.6.

In this study, the value of the solidity of the turbine is varied between 0.1 and 1. It can be seen from Table 8.6 that blade chord increases with the increase in solidity, which is obvious as the definition of solidity is Nc/R . Likewise, it is seen that the diameter of the turbine decreases with the increase of solidity ratio. However with the present design approach, with the increase of solidity the height of the turbine increases significantly. It is also found in this table that λ_d , t_s and m_b increase with the increase of solidity, however the value of RPM_d initially increase up to $\sigma=0.3$ and then its value decreases with subsequent increase of σ .

Table 8.6: Sensitivity Analysis with Solidity

σ	A (m ²)	c (m)	D (m)	H (m)	λ_d	RPM _d	t_s (m)	m_b (kg/m)
0.1	14.4	0.1	8.0	1.8	6.3	148.9	0.004	2.4
0.2	11.7	0.2	5.2	2.2	4.7	170.1	0.005	4.0
0.3	11.4	0.2	4.3	2.7	3.9	173.6	0.006	5.9
0.4	11.6	0.2	3.7	3.2	3.3	171.6	0.007	7.9
0.5	12.0	0.3	3.3	3.7	2.8	165.1	0.008	9.8
0.6	12.5	0.3	3.0	4.1	2.5	160.2	0.009	12.0
0.7	13.3	0.3	3.0	4.5	2.5	159.5	0.010	15.6
0.8	16.9	0.4	3.3	5.2	2.5	147.7	0.013	25.2
0.9	15.1	0.4	2.7	5.6	2.0	144.8	0.012	21.3
1	15.9	0.4	2.3	7.0	1.5	123.5	0.011	19.0

8.3.3. Blade Material

In this section, design analyses have been performed with two prospective materials – (a) Aluminum and (b) Pultruded FRP. As mentioned earlier, Aluminum has been extensively used by VAWT manufacturers in the past. Though pultruded FRP has been utilized by HAWT manufacturers, its application with SB-VAWT is not established yet. However, it can be considered as one of the prospective material for SB-VAWT based on the study conducted by CETC [1996] as they are economically attractive and they have a good combination of material properties like: moderate stiffness, high strength, and moderate density.

Design parameters of a variable speed SB-VAWT at different design wind speeds are shown in Table 8.7 for Aluminum and FRP as blade materials. The design wind speed of the turbine is varied between 10 and 15 m/s. It can be seen from Table 8.7 that, different design parameters are behaving in similar fashion like that described in Section 8.3.1 for both blade materials. However, the noticeable difference between the two materials is that values of c , D , t_s and m_b of FRP are lesser than that of Aluminum which is attractive from design point of view. Furthermore, the values of design aspect ratio (H/c) and RPM_d of a SB-VAWT with FRP blades are higher than that of Aluminum.

It should also be stated that, judging from the selected allowable stresses of these two materials, it is expected that FRP will endure 10×10^8 cycles which is double of aluminum's fatigue load cycles (5×10^8) during their lifetime. This is obviously a significant advantage for FRP over aluminum based on their fatigue strength.

Based on all these findings of this section, the superiority of FRP as blade material of SB-VAWT over conventionally used aluminum is clearly demonstrated. Because of this fact, FRP is chosen as the blade material for the remaining sensitivity analyses.

Table 8.7: Design Configurations with Aluminum and FRP

(a) Overall Dimensions of the SB-VAWT at Different Design Wind Speeds

$V_{\rightarrow d}$ (m/s)	Swept Area (m ²)		Chord (m)		Diameter (m)		Height (m)	
	Aluminum	FRP	Aluminum	FRP	Aluminum	FRP	Aluminum	FRP
10	12.1	12.0	0.35	0.27	4.3	3.3	2.8	3.7
11	9.1	9.0	0.31	0.24	3.7	2.8	2.5	3.2
12	7.0	7.0	0.27	0.21	3.2	2.5	2.2	2.8
13	5.5	5.5	0.24	0.19	2.9	2.2	1.9	2.5
14	4.4	4.4	0.21	0.17	2.6	2.0	1.7	2.2
15	3.6	3.6	0.19	0.15	2.3	1.8	1.5	2.0

(b) t_s and m_b at Different Design Wind Speeds

$V_{\rightarrow d}$ (m/s)	Skin thickness (m)		Blade Mass per unit Height, m_b (kg/m)	
	Aluminum	FRP	Aluminum	FRP
10	0.011	0.008	24.8	9.8
11	0.009	0.007	18.5	7.4
12	0.008	0.006	14.2	5.7
13	0.007	0.006	11.3	4.5
14	0.006	0.005	9.0	3.7
15	0.006	0.005	7.4	3.0

(c) λ_d and RMP_d at Different Design Wind Speeds

$V_{\rightarrow d}$ (m/s)	Design Tip Speed Ratio (λ_d)		Design RPM (RMP_d)	
	Aluminum	FRP	Aluminum	FRP
10	2.8	2.8	126.4	165.1
11	2.8	2.8	161.1	209.2
12	2.8	2.8	200.1	259.4
13	2.8	2.8	243.8	316.2
14	2.8	2.8	292.9	379.5
15	2.8	2.8	347.4	449.6

8.3.4. Blade Airfoil

Another critical design parameter for cost effective SB-VAWT is the selection of blade shape or airfoil which has been discussed in detail in Section 8.1.1. One of the most promising airfoil for VAWTs has traditionally been NACA 0015 [Paraschivoiu 2002] which fails to perform well in the low RN and low λ range. As said earlier, the main issue of the present work is to select such an airfoil for cost-effective and efficient SB-VAWT with optimum dimensions and the previous chapters demonstrated that asymmetric airfoils can produce more torque at low speed in the low λ ranges at low RN. The special purpose airfoil MI-VAWT1 has been designed in the previous chapter to fill this gap as much as possible.

In this section, sensitivity analysis is done at different fixed wind speeds, between 10 and 15 m/s for NACA 0015 and MI-VAWT1. The fixed and variable design parameters for this analysis are shown in Table 8.4. Results obtained from the study are presented in Table 8.8. It can be seen from Table 8.8(a) that different design parameters are behaving in same way like that described in Section 8.3.1 for both the blade airfoils. The values of λ_d and RPM_d of a SB-VAWT with MI-VAWT1 blades are slightly lower than that of NACA 0015. However, the noticeable difference between the two airfoils is that values of c , D , t_s and m_b obtained with MI-VAWT1 are lesser than that of NACA 0015 which is attractive from design point of view. It has been established from Figures 7.20 to 7.25 that the performance of newly designed MI-VAWT1 is superior to that of NACA 0015 at low RN and comparable with NACA 0015 at medium RN. It should also be highlighted that the trailing edge and maximum thickness of MI-VAWT1 (21% thick) is higher than NACA 0015 (15% thick) which is expected to give it more structural strength. Based on all these findings of this section, the superiority of MI-VAWT1 as blade airfoil over conventionally used NACA 0015 is demonstrated through this detailed design analysis. Because of these reasons, MI-VAWT1 can be considered as a better candidate as a blade airfoil for a cost-effect SB-VAWT with optimum performance.

Table 8.8: Results of Sensitivity Analysis with Blade Airfoil

(a) Overall Dimensions of the SB-VAWT at Different Design Wind Speeds

$V_{\rightarrow d}$ (m/s)	Swept Area (m ²)		Chord (m)		Diameter (m)		Height (m)	
	NACA 0015	MI-VAWT1	NACA 0015	MI-VAWT1	NACA 0015	MI-VAWT1	NACA 0015	MI-VAWT1
10	11.7	12.0	0.32	0.27	3.8	3.3	3.1	3.7
11	8.8	9.0	0.28	0.24	3.3	2.8	2.6	3.2
12	6.8	7.0	0.24	0.21	2.9	2.5	2.3	2.8
13	5.3	5.5	0.22	0.19	2.6	2.2	2.1	2.5
14	4.3	4.4	0.19	0.17	2.3	2.0	1.8	2.2
15	3.5	3.6	0.18	0.15	2.1	1.8	1.7	2.0

(b) t_s and m_b at Different Design Wind Speeds

$V_{\rightarrow d}$ (m/s)	Skin thickness (m)		Blade Mass per unit Height, m_b (kg/m)	
	NACA 0015	MI-VAWT1	NACA 0015	MI-VAWT1
10	0.010	0.008	11.6	9.8
11	0.008	0.007	8.8	7.4
12	0.007	0.006	6.8	5.7
13	0.006	0.006	5.4	4.5
14	0.006	0.005	4.3	3.7
15	0.005	0.005	3.5	3.0

(c) λ_d and RMP_d at Different Design Wind Speeds

$V_{\rightarrow d}$ (m/s)	Design Tip Speed Ratio (λ_d)		Design RPM (RMP_d)	
	NACA 0015	MI-VAWT1	NACA 0015	MI-VAWT1
10	3.32	2.83	166.1	165.1
11	3.34	2.83	211.3	209.2
12	3.36	2.84	263.4	259.4
13	3.37	2.84	322.1	316.2
14	3.38	2.84	388.1	379.5
15	3.40	2.84	462.5	449.6

8.3.5. Shape of Blade Support

Another area where there is significant room for improving the design of SB-VAWT is the shape of the blade support as discussed in detail in Sections 2.3.6 and 8.1.3.2. It has been discussed that the blade supporting struts which connect the blades with the central rotating column (or rotor) are responsible for generating detrimental parasitic drag which reduce the overall power output. In the conventional SB-VAWTs constructed by different researchers and companies, mainly different blunt profiles (like rectangular or circular) have usually been utilized as the shape of the supporting struts. The value of C_{DO} of these commonly used supporting struts is usually between 0.1 to 0.5 [Kirke 1998]. To reduce this value of C_{DO} , the new airfoil MI-STRUT1 has been proposed in this study which performs better than another streamlined strut, namely E862, especially at low RN range.

In this section, comparison has been made between the design parameters derived for MI-STRUT1 and a conventional blunt object. The average C_{DO} value for MI-STRUT1 and the blunt object are taken as 0.025 and 0.1 respectively. Design analysis is done at different fixed wind speeds, between 10 and 15 m/s for the two blade support shapes. The fixed and variable design parameters for this analysis are shown in Table 8.4. Results obtained are presented in Table 8.9.

It can be seen from Table 8.9 that, different design parameters are behaving in similar fashion like that described in Section 8.3.1 for both the blunt object and MI-STRUT1. However, the manifested difference between the two materials is that values of A , D and m_b of MI-STRUT1 are lesser than that of blunt object which is attractive from design point of view. Furthermore, the values of RPM_d of a SB-VAWT with MI-STRUT1 airfoil as supporting struts shape are higher than that of blunt object at different design wind speeds. So, based on this study MI-STRUT1 can be considered as a potential candidate for the profile of supporting struts of SB-VAWT for better performance.

Table 8.9: Results of Sensitivity Analysis with Blade Support Shape

(a) Overall Dimensions of the SB-VAWT at Different Design Wind Speeds

$V_{\rightarrow d}$ (m/s)	Swept Area (m ²)		Chord (m)		Diameter (m)		Height (m)	
	Blunt	MI-STRUT1	Blunt	MI-STRUT1	Blunt	MI-STRUT1	Blunt	MI-STRUT1
10	12.4	12.0	0.27	0.27	3.3	3.27	3.75	3.66
11	9.3	9.0	0.24	0.24	2.87	2.84	3.25	3.17
12	7.2	7.0	0.21	0.21	2.53	2.51	2.84	2.77
13	5.6	5.5	0.19	0.19	2.25	2.23	2.51	2.45
14	4.5	4.4	0.17	0.17	2.02	2.00	2.24	2.19
15	3.7	3.6	0.15	0.15	1.83	1.81	2.02	1.97

(b) t_s and m_b at Different Design Wind Speeds

$V_{\rightarrow d}$ (m/s)	Skin thickness (m)		Blade Mass per unit Height, m_b (kg/m)	
	Blunt	MI-STRUT1	Blunt	MI-STRUT1
10	0.008	0.008	9.9	9.8
11	0.007	0.007	7.5	7.4
12	0.006	0.006	5.8	5.7
13	0.006	0.006	4.6	4.5
14	0.005	0.005	3.7	3.7
15	0.005	0.005	3.0	3.0

(c) λ_d and RMP_d at Different Design Wind Speeds

$V_{\rightarrow d}$ (m/s)	Design Tip Speed Ratio (λ_d)		Design RPM (RMP_d)	
	Blunt	MI-STRUT1	Blunt	MI-STRUT1
10	2.8	2.8	161.2	165.1
11	2.8	2.8	204.0	209.2
12	2.8	2.8	252.6	259.4
13	2.8	2.8	307.9	316.2
14	2.8	2.8	369.5	379.5
15	2.8	2.8	437.6	449.6

8.4. Specifications of a New Class of SB-VAWT – “MI-VAWT 3000”

After conducting the sensitivity analyses with five key design parameters, a new class of 3kW variable-speed SB-VAWT has been designed and named as “MI-VAWT 3000”. Salient design features of MI-VAWT 3000 are shown in Table 8.10. Figure 8.24 shows the present modified design approach over the conventional one. MI-VAWT 3000 has the following key features which have been selected based on the sensitivity analyses of the previous section:

- The blade airfoil is MI-VAWT1 because of superior performance and overall smaller dimensions;
- The shape of the blade support is MI-STRUT1 to reduce the amount to parasitic drag losses;
- The type of support of the blade is overhang with endplates to eliminate the effect of wing tip losses;
- The blade material is chosen as pultruded FRP for smaller overall dimensions and light-weight blades;
- The solidity has been selected as 0.44 to maximize the power coefficient and to save materials. Also, a 3-bladed SB-VAWT with this value of solidity has a chord/radius (c/R) ratio of 0.15 which is expected to eliminate the effect of flow curvature which usually happens for $c/R \geq 0.18$.

It is very important to note that, the features shown in Table 8.10 are determined through computational investigation and they are preliminary estimations. These features should be verified through further experimental study. It is imperative that a Prototype of MI-VAWT 3000 be fabricated and thorough outdoor experimentation with that prototype be conducted before application. Also, noise and vibration level of MI-VAWT 3000 should be determined. If required, the dimensions of the MI-VAWT 3000 should be optimized for better performance.

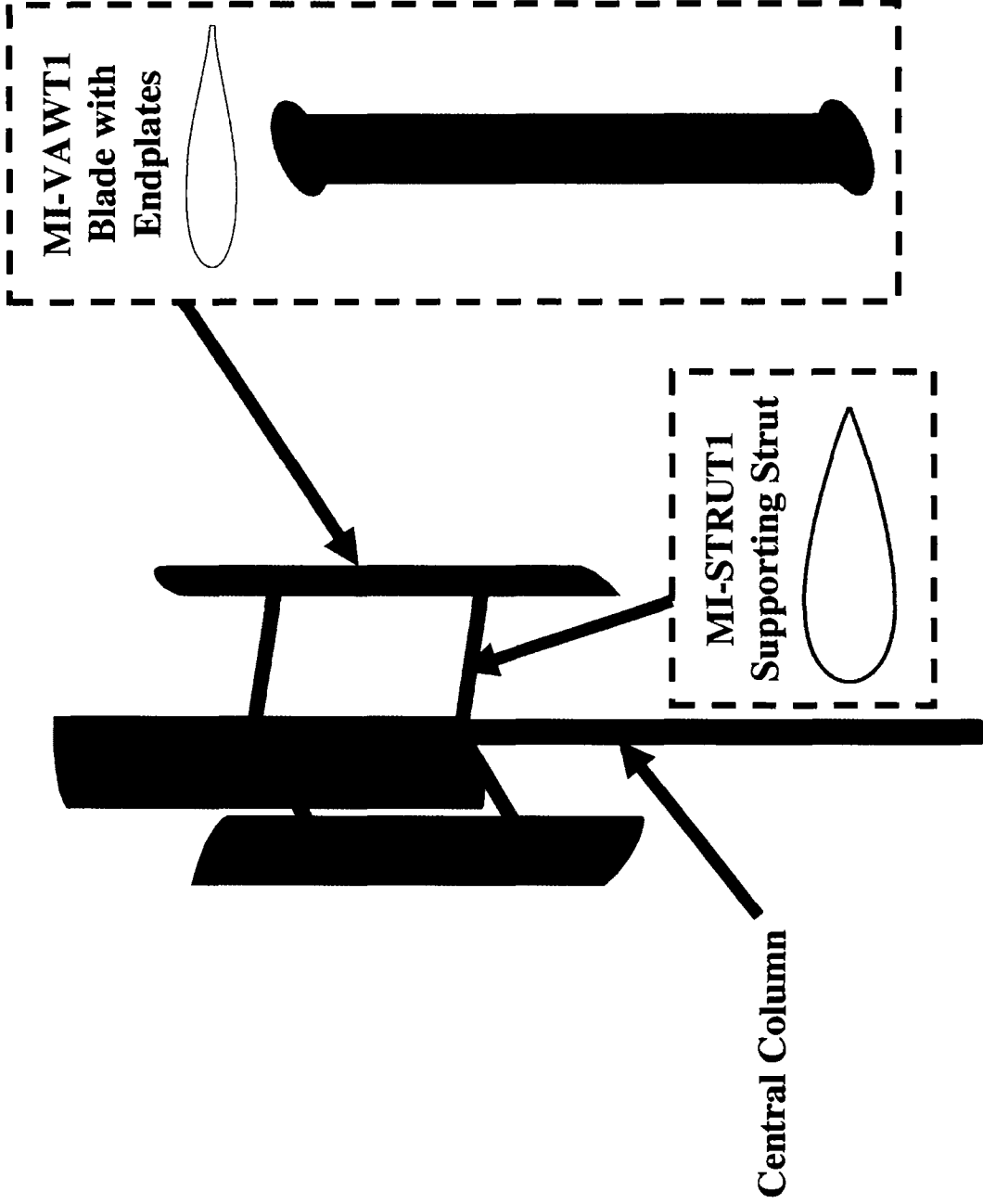


Figure 8.24: SB-VAWT with Three New Design Features

Table 8.10: Specifications of the Salient Design Features of MI-VAWT 3000

Category	Design Parameter	Value
Physical Features	Blade Airfoil	MI-VAWT1
	Design Skin Thickness (t_s)	8 mm
	Number of Blade (N)	3
	Supporting Struts type	Overhang with endplates
	Supporting Struts shape	MI-STRUT1
Dimensional	Swept Area ($A=HD$)	12 m ²
	Chord (c)	27 cm
	Height (H)	3.3 m
	Diameter (D)	3.7 m
	Solidity (Nc/R)	0.44
	Aspect Ratio (H/c)	12.2
	Chord/Radius Ratio (c/R)	0.15
Operational	Rated Power Output (P_o)	3 kW
	Rated Wind Speed (V_{rd})	10 m/s
	Cut-out Speed ($V_{cut-out}$)	25 m/s
	Power Coefficient (C_{Pd})	0.4
	Tip Speed Ratio (λ_d)	2.8
	Rotational Speed (RPM _d)	162
	Pitching of Blade (γ_d)	Fixed pitch angle of zero
Balance of System	Load	Variable speed
Others	Material	Pultruded FRP

In the present study, five design parameter, namely (i) central column; (ii) tower; (iii) braking mechanism; (iv) noise and (v) aesthetics, which have been discussed in Section 8.1 are not been considered and left open. Among these, central column, tower and braking mechanism can be selected from the best practices for cost-effective final product. For better aesthetics, SB-VAWT should be painted with appropriate color to blend smoothly with the surrounding environment.

8.5. Summary of the Chapter

The aim of this chapter was to perform design analyses with a SB-VAWT equipped with newly developed asymmetric airfoil MI-VAWT1 at variable turbine speed condition. 22 design parameters have been identified, which are: (i) blade shape; (ii) number of blade; (iii) supporting struts type and shape; (iv) central column; (v) swept area; (vi) solidity; (vii) aspect ratio; (viii) chord/radius ratio; (ix) rated power output; (x) rated wind speed; (xi) cut-in speed; (xii) cut-out speed; (xiii) power coefficient; (xiv) tip speed ratio; (xv) rotational speed; (xvi) pitching of blade; (xvii) tower; (xviii) braking mechanism; (xix) load; (xx) material; (xxi) noise; and (xxii) aesthetic.

A new non-lifting strut airfoil "MI-STRUT1" has been designed which performs better than another streamlined strut, namely E862. Among all the design parameters, some are quite important for optimum configuration of SB-VAWT. After developing an analytical tool for design analysis of SB-VAWT, sensitivity analyses have been performed with five parameters, which are: (a) blade support type; (b) solidity; (c) blade material; (d) airfoil; and (e) shape of the blade supports. It has been found out from the sensitivity analysis with these parameters that:

- the overhang type support with endplates reduces the overall dimensions of the turbines considerably in comparison to those of the simple and overhang supported turbines without endplates;
- solidity has significant effect on design configurations of a SB-VAWT and it is very important to select an appropriate value to obtain optimum performance without requiring excessive blade materials;
- design features with pultruded FRP as blade material is superior than conventionally used Aluminum;
- from design point of view, performance of MI-VAWT1 as blade airfoil is better than that of conventionally used NACA 0015.

- to reduce the detrimental parasitic drag losses, newly designed MI-STRUT1 can be considered as a potential candidate for the profile of supporting struts of SB-VAWT for better performance;

Based on sensitivity analyses with five design parameters, a new class of 3kW variable-speed SB-VAWTs, named as MI-VAWT 3000 has been designed in this chapter. MI-VAWT 3000 has utilized MI-VAWT1 and MI-STRUT1 as the airfoil for the blade and the supporting struts respectively. It has moderate solidity and has light-weight pultruded FRP as its blade material. Its design configuration is overhang type with endplates which is not a conventional trend for SB-VAWT design. In Table 8.11, comparisons have been made between the conventional approach and the alternative innovative approach adopted in the present study.

Table 8.11: Summary of the Innovative Design Concepts for SB-VAWTs

Concept	Conventional approach	Alternative approach adopted in the present study
Design method	Constant Turbine Speed	Variable turbine speed
Blade airfoil (shape)	Symmetric airfoils like NACA 0012, 0015 and 0018.	Asymmetric airfoil, MI-VAWT1 has been design and applied.
Blade material	Mainly wood or Aluminum	Fibre Reinforced Plastic (FRP)
Solidity	Between 0.2 and 1	Optimized after sensitivity analyses for material savings.
Shape of the horizontal supporting struts	Circular or rectangular shapes	New non-lifting airfoil MI-STRUT1 has been design and applied.
Wing tip devices	Not applied for added complicity	Winglet or endplate are discussed and suggested.
Overall blade geometry	Straight	Alternative elliptical blades are discussed and further aerodynamic and financial analyses are suggested.
Possible loads	Mechanical Pump and Electric generator	Apart from mechanical pump and electric generator, several other loads are suggested (as described in Section 1.4.2).

Chapter 9

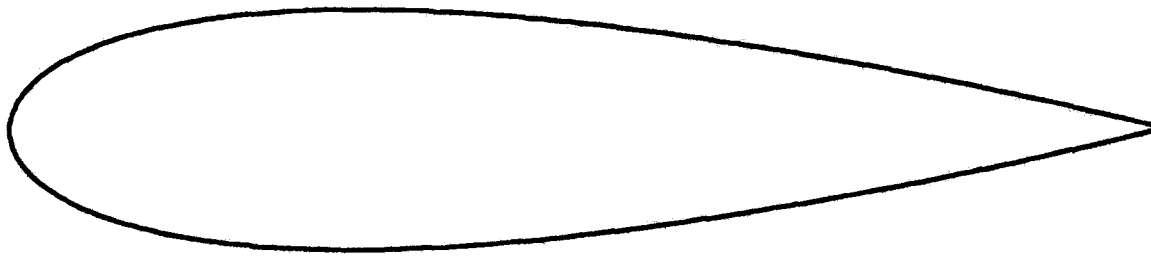
Experimentation of a SB-VAWT Prototype

In order to understand the starting behavior of a smaller-capacity SB-VAWT, a Prototype has been fabricated with both symmetric and asymmetric airfoils. Experimentations have conducted in the outdoor condition. No experimental investigation could be found in the public domain on torque production by a SB-VAWT at no-load condition which is the focus of this experimental work in the present study. To see the effect of solidity, the SB-VAWT prototype has been tested with both two and three blades. The detail of the experimentation process is described in the subsequent headings below.

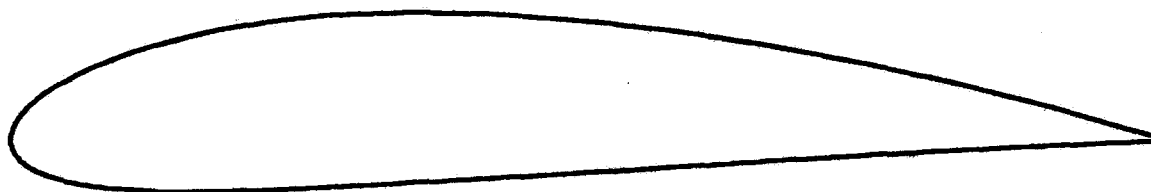
9.1. Fabrication of a SB-VAWT Prototype

In order to conduct the desired experimental investigation, both symmetric (NACA 0021) and asymmetric (NACA 4415) blades have been fabricated which are shown in Figure 9.1. It should be pointed out that NACA 0021 was selected because of its high thickness which is advantageous for higher starting torque. NACA 4415 is a representative of a typical asymmetric airfoil and thus selected as a blade profile for the prototype. No information could be found from the literature on a smaller-capacity fixed-pitch SB-VAWT equipped with either of these two blades.

Close-up picture of the SB-VAWT prototype is shown in Figures 9.2 and 9.3. The prototype was built in such a manner that it can be equipped with both two and three blades. The overall dimensions of the prototype with two different blades are given in Table 9.1. The main components of the SB-VAWT prototype are described in the subsequent headings.



(a) Symmetric NACA 0021 Airfoil



(b) Asymmetric NACA 4415 Airfoil

Figure 9.1: The Selected Symmetric and Asymmetric Airfoils for SB-VAWT Prototype

Table 9.1: Dimensions of SB-VAWT Prototype with Symmetric Airfoil

Design Feature	Symmetric Blade	Asymmetric Blade
Airfoil	NACA 0021	NACA 4415
Height (H)	1.8 m	2 m
Diameter (D)	1.7 m	1.7 m
Chord (c)	0.2 m	0.2 m
Aspect Ratio (H/c)	9	10
HDR (H/D)	1.05	1.18
Solidity (Nc/R)	0.47 for 2 blades and 0.71 for 3 blades	0.47 for 2 blades and 0.71 for 3 blades

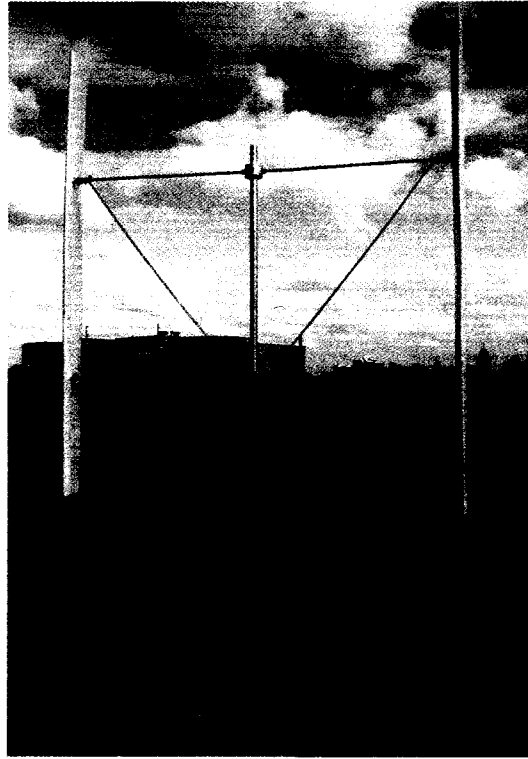


Figure 9.2: SB-VAWT Prototype with 2 Blades

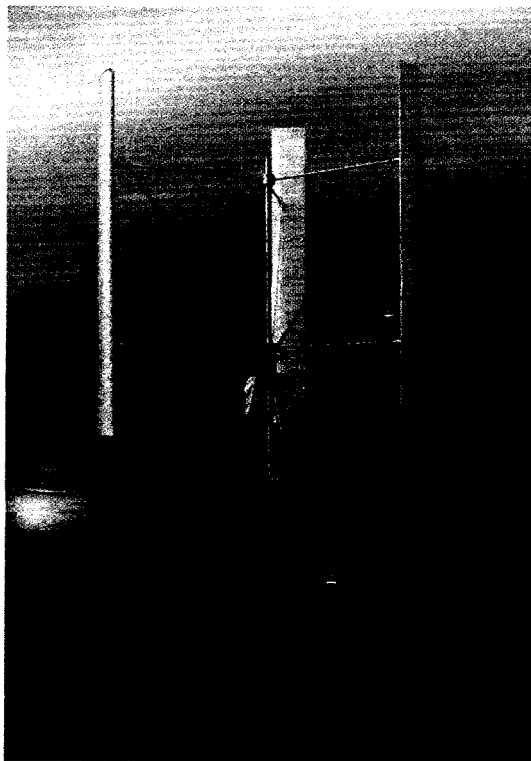


Figure 9.3: SB-VAWT Prototype with 3 Blades

9.1.1. Blades

Initially, at the time of fabricating the main structures (like tower, central shaft, supporting struts etc.) of the SB-VAWT prototype, the three symmetric blades were fabricated. These blades were fabricated by laminating a Styrofoam core (which had a shape of the NACA 0021 airfoil) with fiberglass resin. The Styrofoam core was cut by using hot-wires. However, later on at the time of fabrication of the asymmetric blades, a CNC machine has been utilized for cutting the Styrofoam in the shape of NACA 4415.

The manual blade fabrication process was very tedious and it took considerable amount of time as there are numerous steps in this process. Due to time constraints and non-availability of required instruments, it has not been possible to assess the accuracy of the fabricated blade geometries during this experimental investigation.

Several pictures taken at different stages of the blade fabrication process are shown in Appendix-G. The main steps for blade fabrication in the present case are:

1. Cutting of Styrofoam (Hotwires for NACA 0021 & CNC machine for NACA 4415).
2. Sanding process for smoothing.
3. Painting for safeguarding the Styrofoam from fiberglass resin (a water-based paint has been used).
4. Applying of a releasing agent (Water/Alcohol-based Polyvinyl Alcohol solution of water-soluble, film forming materials)
5. Cutting of fiberglass clothing and spread around the blade core.
6. Applying fiberglass resin along with the hardener.
7. Final sanding process for smoothing.
8. Painting.

9.1.2. Central Shaft

The central shaft of the prototype is made up of Aluminum for its light weight and strength. The diameter and the height of the shaft are 31.75 mm and 2 m respectively. The central rotating shaft has been connected with the tower via two radial ball bearings.

9.1.3. Support Arm

Like the central shaft, the material for the supporting struts is also made up of Aluminum. Each blade was connected with the central shaft via two supporting struts. Additionally, a cross-arm was also added diagonally for extra strength.

9.2. Instrumentation

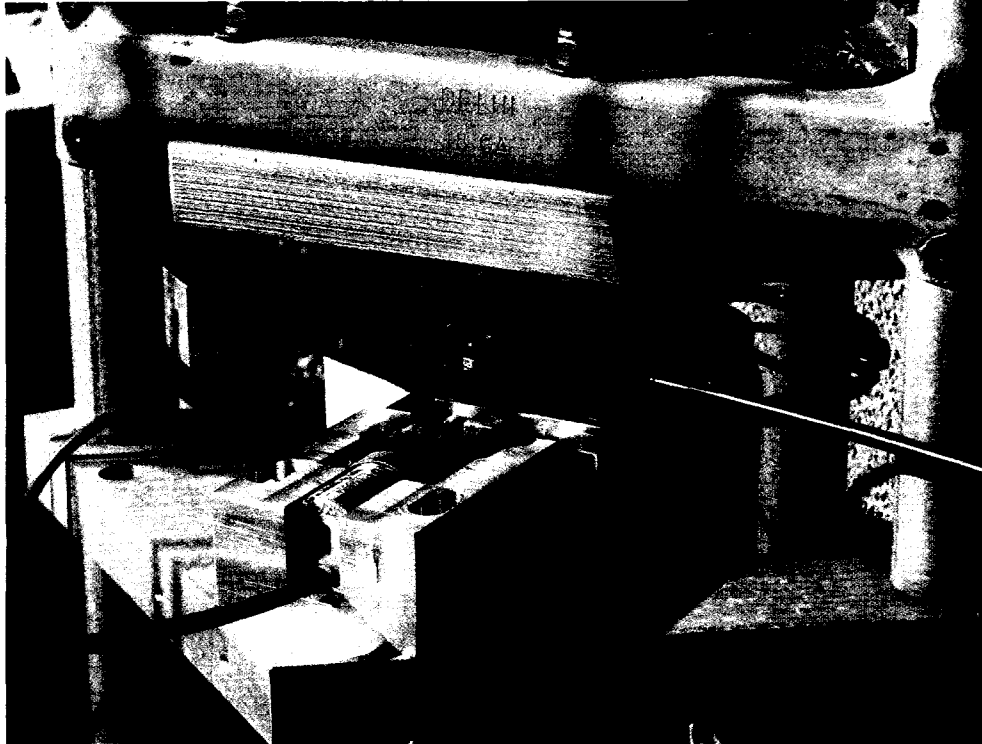
The main objective of the experimentation process is to observe the production of the starting torque by the SB-VAWT prototype. The required instruments for achieving this goal are described below.

9.2.1. Torque

In order to measure the starting torque, a load cell has been used in the present case. The load cell is combined with a braking mechanism and attached at the bottom of the central shaft via a disk. A hand-brake has been used to vary the amount of braking. The assembly of torque measuring instruments is shown in Figure 9.4. The load cell required a signal conditioner and data acquisition system to capture the signals at different intervals.

9.2.2. Wind Speed

An electronic anemometer has been used to log wind speed. Data can be captured at different intervals. The anemometer required an extra tri-pod for mounting it at a suitable height. The anemometer used for the present case is shown in Figure 9.6.



(a) Load Cell & Braking Mechanism



(b) Contact between Brake and Central Shaft via Disk

Figure 9.4: Torque Measurement Setup

9.2.3. Data Acquisition System

An USB-based data acquisition system has been used for capturing data from the load cell. The data acquisition system is shown in Figure 9.5 along with the load-cell signal conditioners.

9.2.4. Notebook Computer

In order to collect data from the USB-based data acquisition system and also from the electronic anemometer, a Pentium-based notebook (laptop) computer has been used which is shown in Figure 9.6.

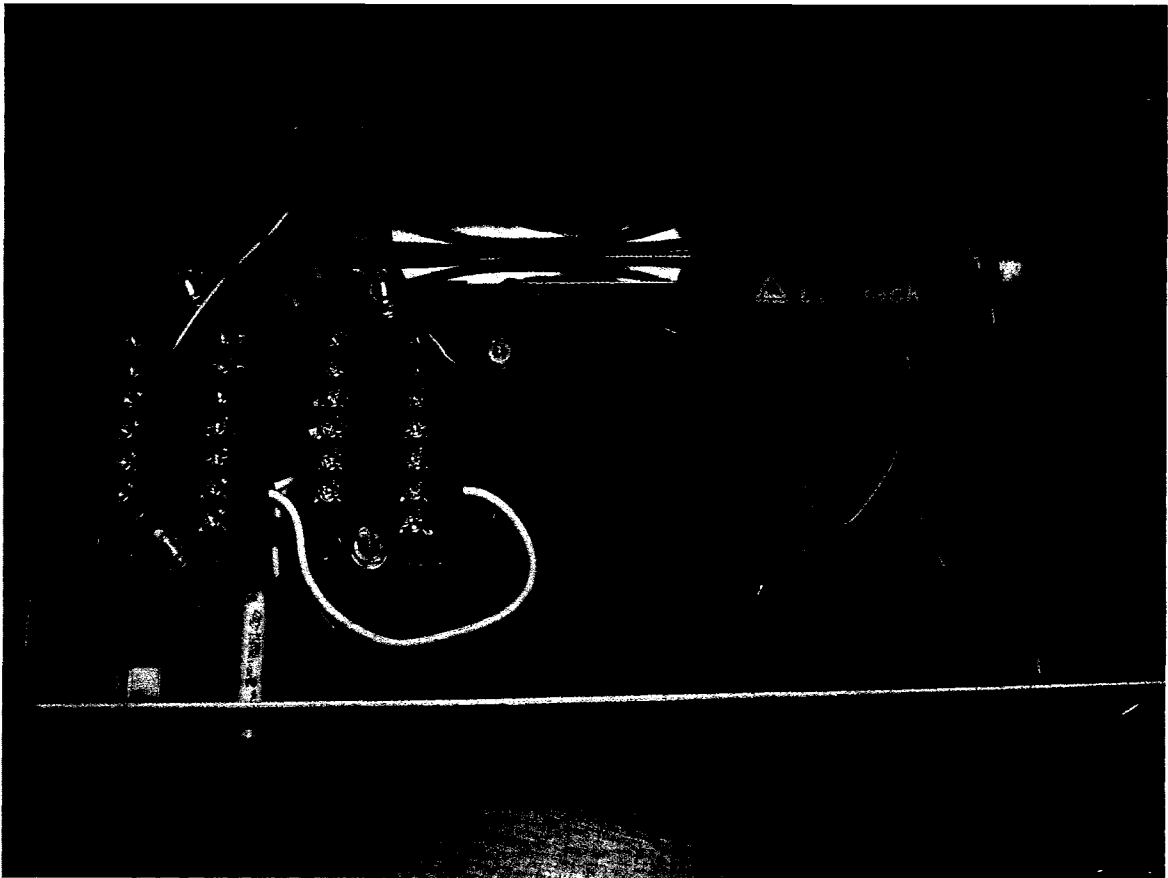


Figure 9.5: Data Acquisition System

9.3. Experimental Setup

The overall experimental setup for measuring the starting torque of the SB-VAWT prototype is shown in Figure 9.6. The prototype has been installed on the roof of the engineering faculty of the University of Windsor. The base of the prototype is located about 17 meters high from the ground level of the University of Windsor campus. The position of the prototype on the roof was selected after much deliberation with least amount of obstacles possible.

Although the prototype was installed on the roof of the building in October 2006, but the candidate could only start acquiring meaningful data of wind velocity and torque between the period of March 2007 and November 2007. The delay of experimentation with the prototype happened because of several reasons, including:

- inclement winter weathers with extended periods of snowfalls.
- longer time for debugging of the instruments;
- calibration process;
- Initial improper siting of the prototype which caused lesser amount of wind velocity harnessed by the prototype; and
- longer than expected time required for fabrication of the NACA 4415 also took considerable amount of time which was beyond expectations.

It should be noted that the amount of wind speed was not appreciable between March and August in Windsor in Ontario, Canada. However, the wind velocity started to increase in the beginning of September 2007 and eventually the maximum amount of 1-minute average wind velocity could be found to be around 6.4 m/s.

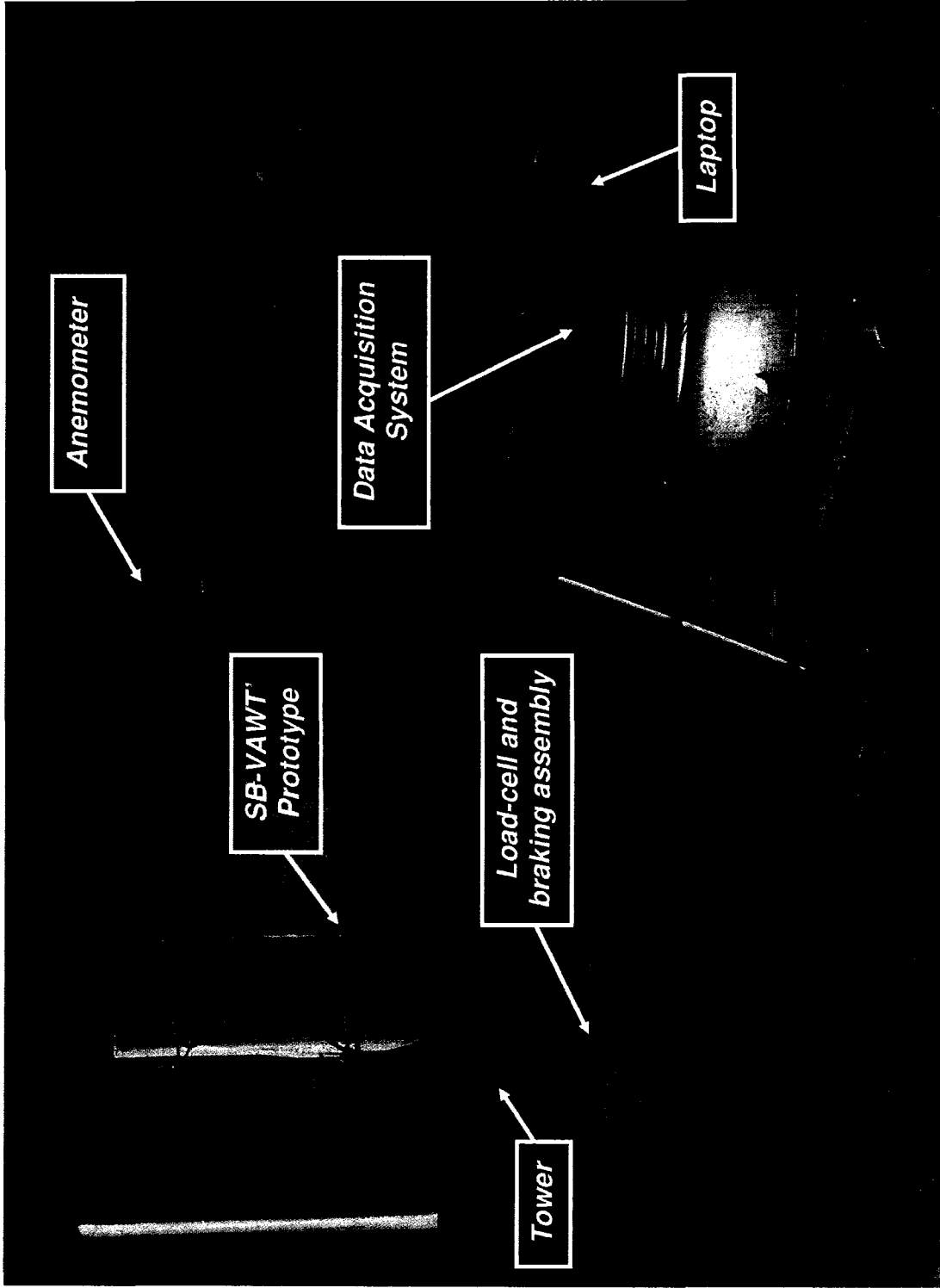


Figure 9.6: Experimental Setup for SB-VAWT Prototype

9.4. Results and Discussions

In order to measure the torque produced by the SB-VAWT prototype during startup from stand-still, the braking mechanism (which is connected directly with the load-cell) has been engaged in full. Then the torque has been measured through the load-cell at an interval of 0.5 second. The wind speed was collected at intervals of 10 to 20 seconds. For producing the plots in this section, the raw datasets of torque and wind speeds have been averaged at 1-minute. Finally, different curves have been produced by curve-fitting of the 1-minute average raw datasets which are shown under relevant headings below. The maximum 1-minute average wind speed was found to be 6.4 m/s (correspond to $RN=87,973$) at the location of the SB-VAWT

9.4.1. Starting Torque at different Wind Speeds

In Figure 9.7, the torque produced by the 2-bladed and 3-bladed SB-VAWT prototype equipped with NACA 0021 airfoil is shown. It can be seen from this figure that as expected, the torque produced by the 3-bladed ($\sigma=0.71$) SB-VAWT is higher than that of 2-bladed ($\sigma=0.47$) SB-VAWT. In Figure 9.8, torque produced by the 2-bladed and 3-bladed SB-VAWT prototype equipped with NACA 4415 is shown. It can be discerned from this figure that similar to NACA 0021, the torque produced by the 3-bladed ($\sigma=0.71$) SB-VAWT is higher than that of 2-bladed ($\sigma=0.47$) SB-VAWT equipped with NACA 4415 airfoil. It should be highlighted that the torque produced by SB-VAWTs should be proportional to the number of blades, but this expectation is not in agreement with the results in Figures 9.9 and 9.10. There can be several reasons for these discrepancies in experimental results. The possible reasons for these are:

- (a) Different orientations of the blades with respect to the incoming wind speeds during the measurements that have been performed at different time of the year under different climatic conditions.
- (b) Inaccuracies of the manually fabricated blades;
- (c) Uncertainties in the measurements;

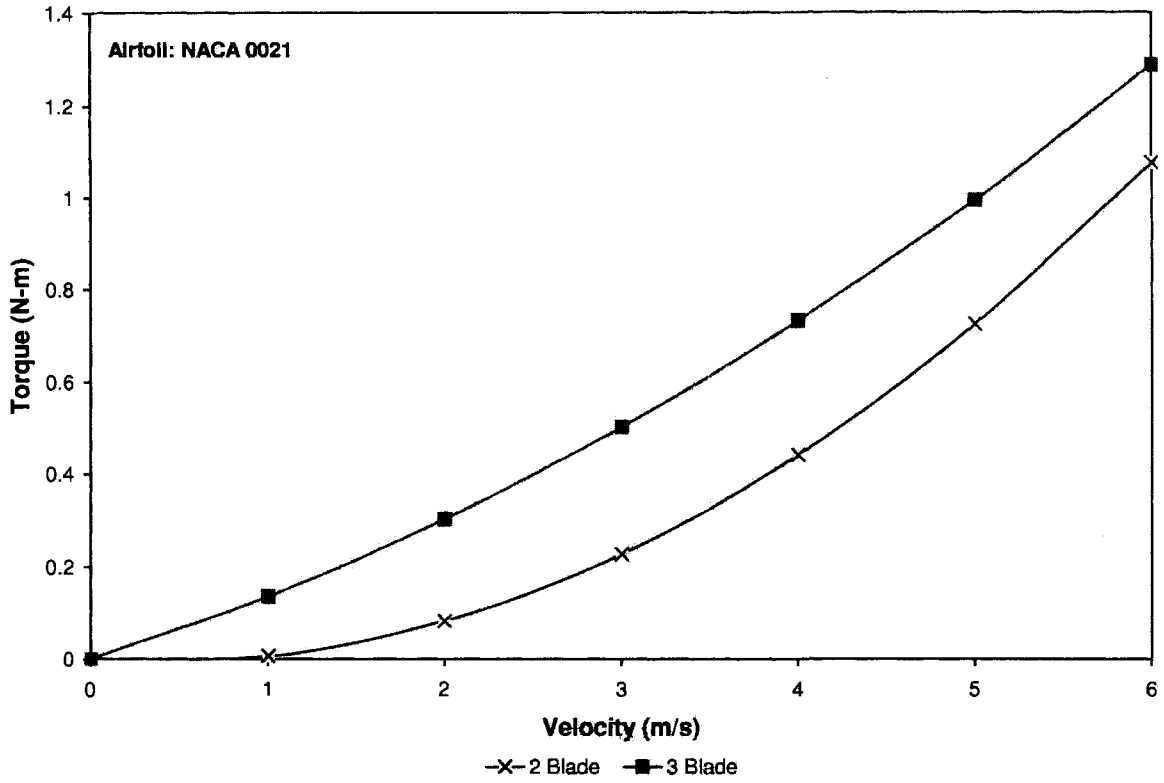


Figure 9.7: Torque Produced by the SB-VAWT Prototype equipped with NACA 0021

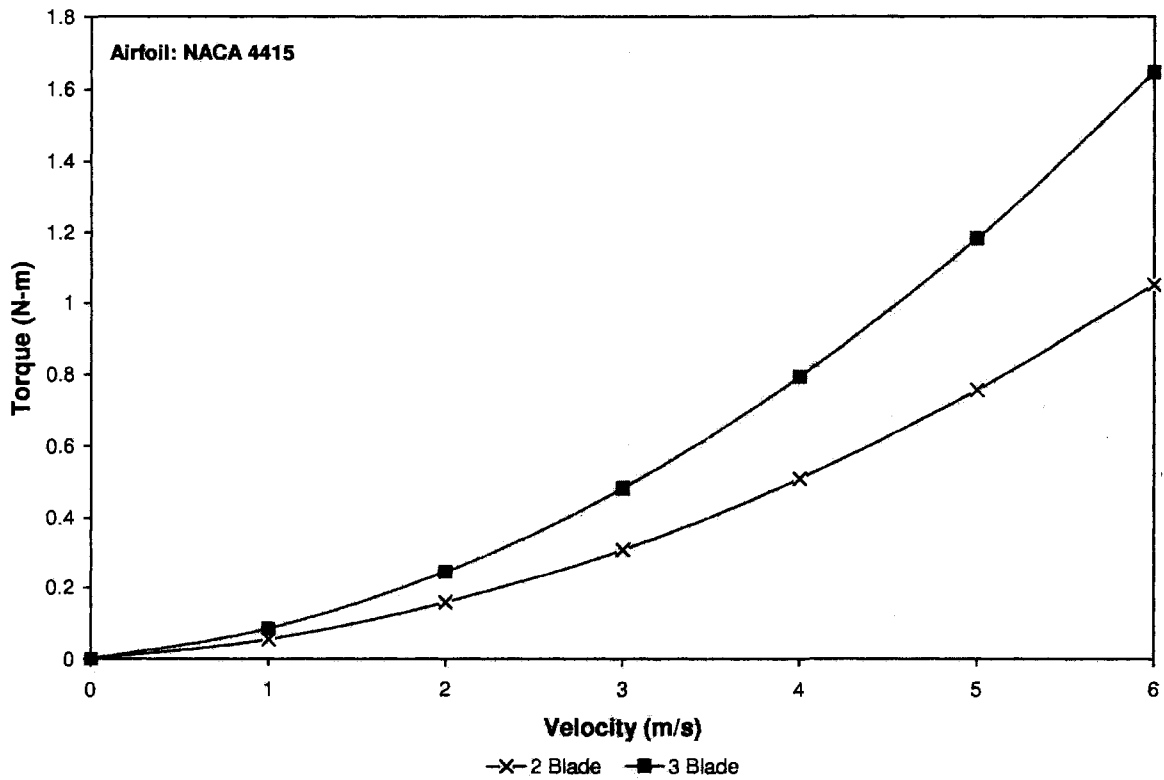


Figure 9.8: Torque Produced by the SB-VAWT Prototype equipped with NACA 4415

It can also be concluded from Figure 9.7 and 9.8 that, low amount of torque is produced by these conventional NACA symmetric and asymmetric airfoils and only a load which requires starting torque in these ranges can be coupled with this type of SB-VAWT.

9.4.2. Comparison of Torque between Symmetric and Asymmetric Airfoils

In Figure 9.9 and 9.10, comparisons have been made between the torque versus wind velocity curves of symmetric NACA 0021 and asymmetric NACA 4415. Figure 9.9 shows the torque production of a 2-bladed SB-VAWT up to wind velocity of 6 m/s with these two types of airfoils. It can be seen from this figure that performance of NACA 4415 is better than NACA 0021 up to the wind speed of 5.5 m/s. Beyond this value, torque production by NACA 0021 is better than NACA 4415.

Figure 9.10 shows the torque versus wind velocity curves of a 3-bladed SB-VAWT with these two airfoils. In this case, performance of NACA 4415 is much better than NACA 0021 airfoil up to wind velocity of 6 m/s and beyond. It can be concluded from these two figures that an asymmetric airfoil like NACA 4415 (15% thick) can produce significantly higher starting torque than a relatively thicker symmetric airfoils like NACA 0021 (21% thick).

9.4.3. Comparison with Computational Results

From Figures 9.11 to 9.14, comparisons have been made between the torque versus wind velocity curves of the experimental results of the SB-VAWT prototype and the computational results obtained from the scheme described in Chapter 4 for symmetric NACA 0021 and asymmetric NACA 4415. Figure 9.11 shows reasonable agreement between the experimental and computational results for a SB-VAWT with 2 NACA 0021 blades. However, in Figure 9.12 the agreement between the experimental and computational results for a SB-VAWT with 3 NACA 0021 blades are not that good.

In the case of a SB-VAWT with 2 NACA 4415 blades as shown in Figure 9.13, the results from computational results are lower than the experimental values for all the wind velocities. Similar trend has been observed in Figure 9.14 which shows the case of a SB-VAWT with 3 NACA 4415 blades. Therefore, for both cases of the asymmetric NACA 4415, the results obtained from the computational model are lower than the experimental values.

As mentioned earlier that the maximum 1-minute average wind velocity in the present analysis is 6.4 m/s which correspond to a Reynolds number of 87,973 at the location of the SB-VAWT where laminar separation is a major problem and a computational model suffers from a significant loss of accuracy which is clear from the comparisons between the experimental and computational results shown in Figure 9.13 and 9.14. However, at higher RN the difference between the results should be less pronounced.

9.5. Summary of the Chapter

In this chapter, the experimental investigation of a smaller-capacity SB-VAWT with both the symmetric and asymmetric airfoils has been carried out. Experimentation has been conducted under in-situ condition. To see the effect of solidities, the prototype has been tested with both two and three blades. It has been found that asymmetric airfoils like NACA 4415 (15% thick) can produce significantly higher starting torque than a relatively thicker symmetric airfoils like NACA 0021 (21% thick) at different solidities. It has also been found that the computational results obtained from the models (described in Chapter 4) agree reasonably for the NACA 0021. But in the case of NACA 4415, the agreement is not appreciable at lower wind velocities.

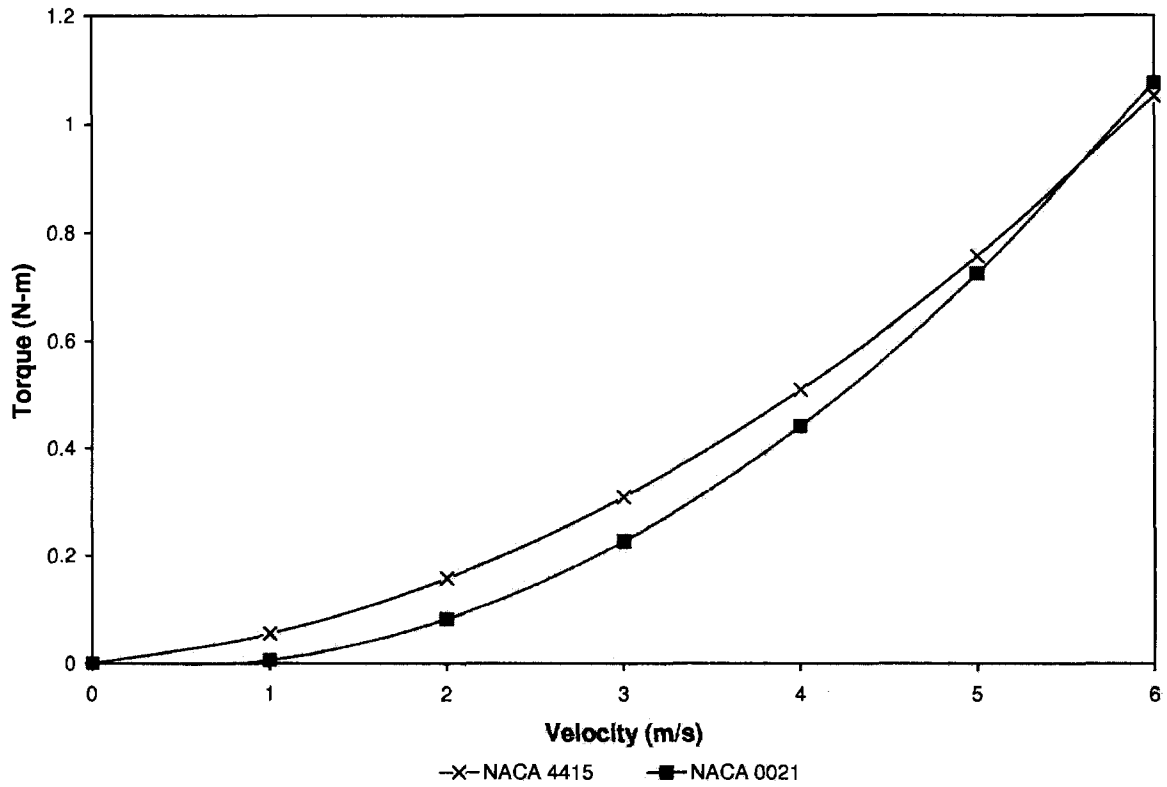


Figure 9.9: Comparison Between NACA 0021 & NACA 4415 equipped with 2-blades

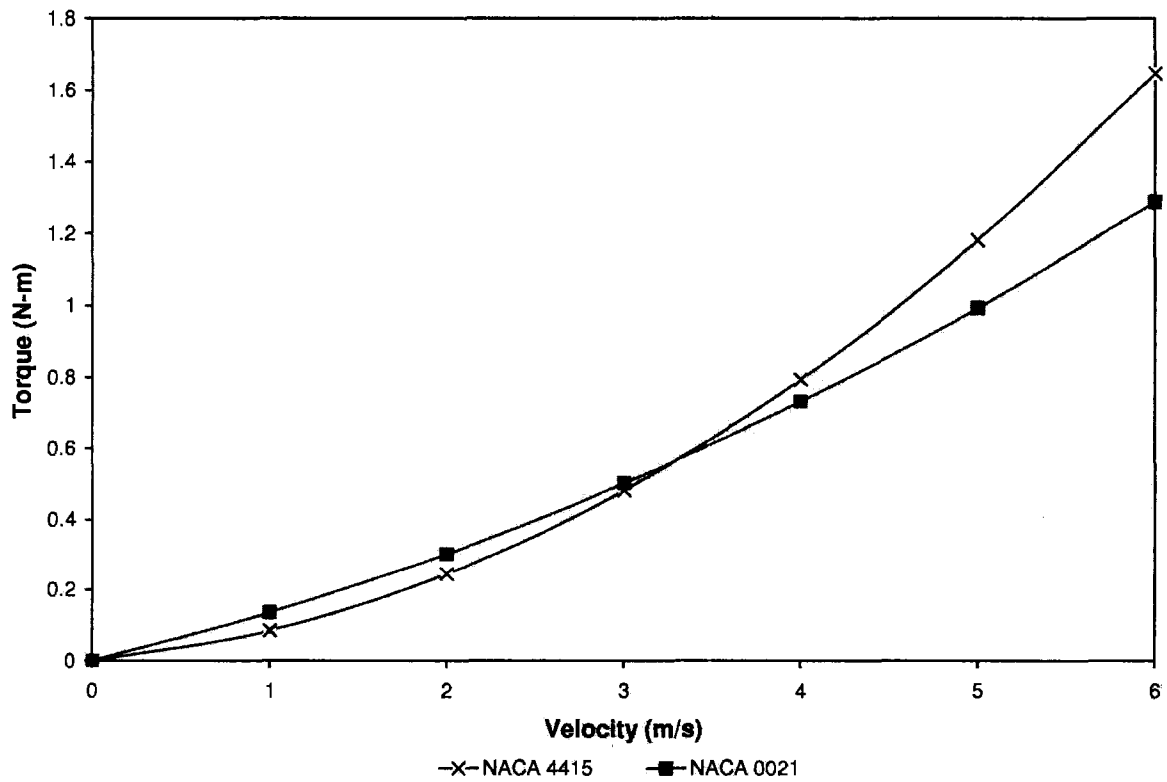


Figure 9.10: Comparison Between NACA 0021 & NACA 4415 equipped with 3-blades

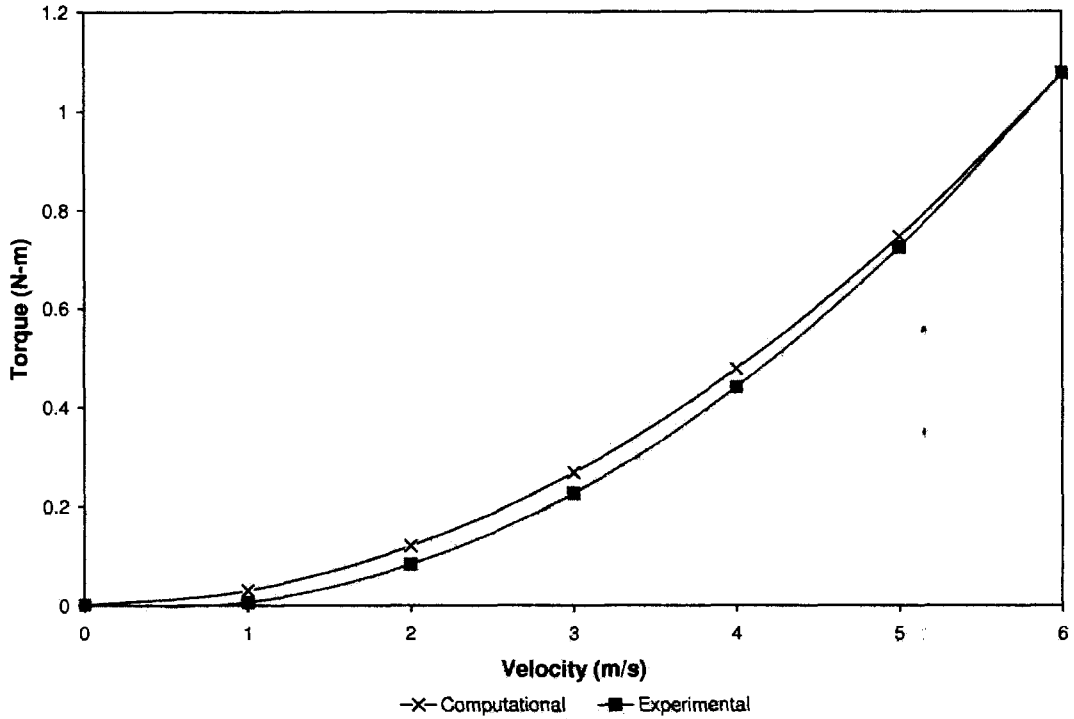


Figure 9.11: Comparison Between the Computational and Experimental Results of SB-VAWT Equipped with 2-blades of NACA 0021

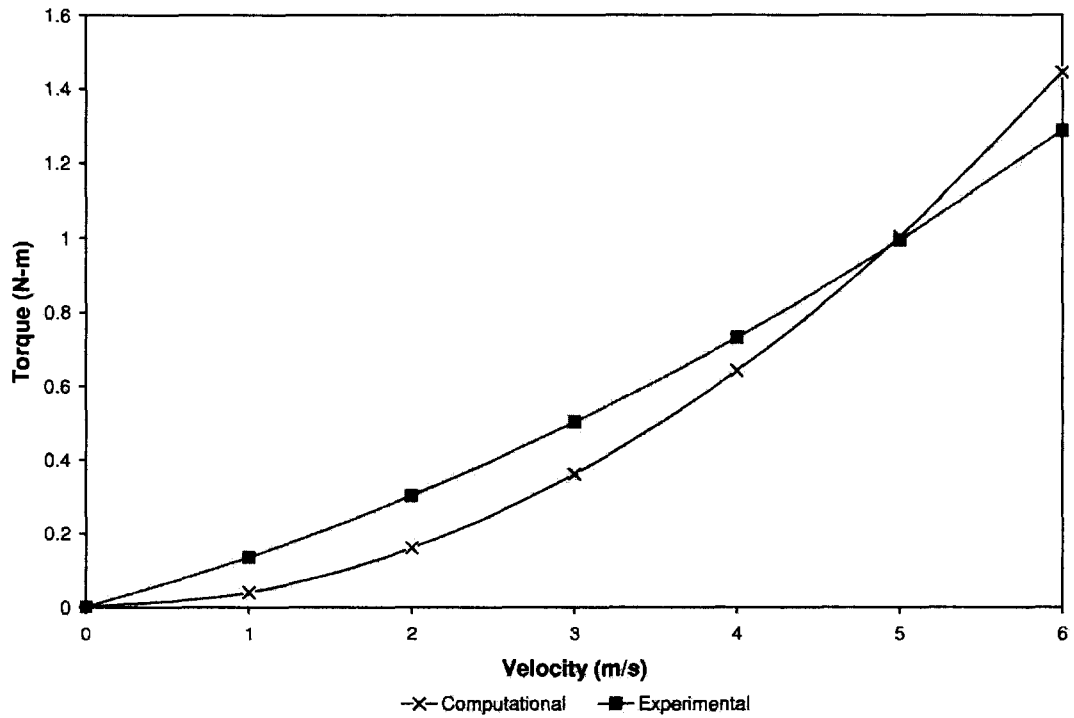


Figure 9.12: Comparison Between the Computational and Experimental Results of SB-VAWT Equipped with 3-blades of NACA 0021

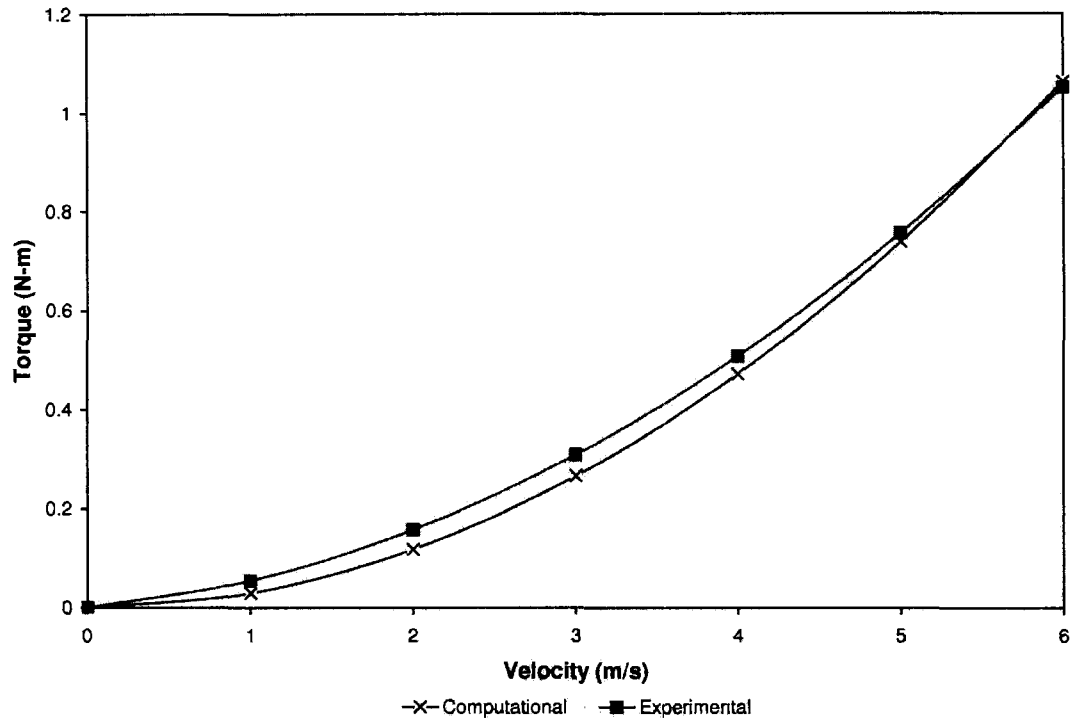


Figure 9.13: Comparison Between the Computational and Experimental Results of SB-VAWT Equipped with 2-blades of NACA 4415

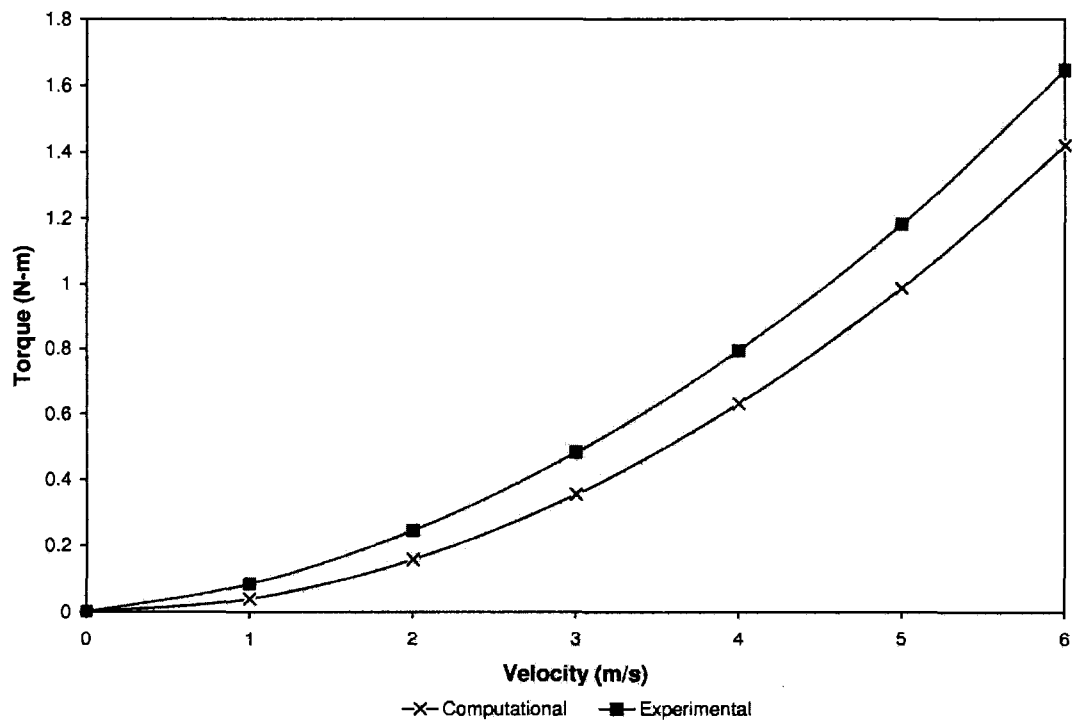


Figure 9.14: Comparison Between the Computational and Experimental Results of SB-VAWT Equipped with 3-blades of NACA 4415

Chapter 10

Concluding Remarks

The present research aimed to perform detail systematic investigative analysis with alternative asymmetric airfoils appropriate for self-starting and better performing smaller capacity fixed-pitch SB-VAWT through critical examination of different aerodynamic factors. In this chapter, conclusions and remarks are drawn based on the research outcomes as described in the preceding chapters. Also, few recommendations are suggested for the future works to foster the development of the research topic which are expected to abate or eliminate the shortcomings of the present research works.

10.1. Research Outcomes

10.1.1. Literature Survey on SB-VAWTs Related Research Activities

- In the past, several universities and research institutions have carried out research activities related to straight-bladed VAWTs and published reports, journal and conference papers. The candidate collected many of these documents and attempted to develop a comprehensive understanding of previous SB-VAWT related research activities, including experimental results from test models and prototypes, aerodynamic theories, special-purpose airfoils designed for SB-VAWT use, and so on.
- Focus of the literature survey are (i) pros and cons of different types of wind turbines, with special emphasis on SB-VAWTs; (ii) major SB-VAWTs related programs; (iii) SB-VAWT aerodynamics; (iv) computational models for design and performance prediction of SB-VAWTs; (v) previously attempted airfoils for

SB-VAWTs; (vi) computational tools for analysis of low-speed airfoils; (vii) SB-VAWT design parameters;

- It has been identified that SB-VAWT is one of the simplest types of wind turbines that can be utilized for an array of applications, including (i) electricity generation; (ii) pumping water; (iii) purifying and/or desalinating water by reverse osmosis; (iv) heating and cooling using vapor compression heat pumps; (v) mixing and aerating water bodies; and (vi) heating water by fluid turbulence. However, in order to apply this type of wind turbine for these prospective applications, a robust design of efficient SB-VAWT with self-starting characteristics is of vital importance.
- SB-VAWTs are potentially more efficient and more economical, but those with fixed pitch straight-blades have hitherto been regarded as unsuitable for stand-alone use due to their lack of starting torque production.
- Conventionally used NACA 4-digit symmetric airfoils are not suitable for smaller capacity SB-VAWTs. Rather, it will be advantageous to utilize a high-lift and low-drag asymmetric thick airfoil suitable for low speed operation typically encountered by SB-VAWT.

10.1.2. SB-VAWT Aerodynamics

- Despite uncomplicated components and easy manufacturing processes, the aerodynamics related to SB-VAWTs is quite complex and needs special considerations.
- SB-VAWTs' performance is affected by several aerodynamic factors which are related with the different structural components and the surroundings.
- One of the most problematic aspects of the complex aerodynamics of SB-VAWTs is that they produce very little starting torque when conventional airfoils are used. One of the main reasons of the inability to self start is due to a band of tip speed ratios below operating condition for which the net amount of energy collected by each blade in each revolution is negative. To achieve self-starting, SB-VAWT blade airfoil must be altered so that a net positive amount of torque is produced at all tip speed ratios up to the operating point.

- The seven main aerodynamic challenges of SB-VAWT are identified as: (i) low RN operation; (ii) post-stall operation; (iii) unsteady effects (like dynamic stall); (iv) rotational effects (like flow curvature); (v) operation of blades in the wake region; (vi) parasitic drag of the supporting struts; and (vii) atmospheric turbulence.
- All these aerodynamic factors collectively make the thorough analysis of SB-VAWT a challenging undertaking and detail analyses of these factors are of great importance for better aerodynamic performance and size of a smaller-capacity SB-VAWT.

10.1.3. Development of Computational Scheme for Performance Analysis of SB-VAWTs

- At present, there are several aerodynamic computational models available for performance analysis of SB-VAWTs and the most widely used models are the double-multiple streamtube model, free-vortex model and the cascade model. Each of these models has their strengths and weaknesses.
- Among all the computational models, the Cascade model, developed by Hirsch and Mandal [1987], is one of the most practical models used for investigating conventionally used two NACA symmetric airfoils (namely NACA 0012 and 0015). This model gives smooth convergence even in high tip speed ratios and for high solidity SB-VAWT with reasonable accuracy.
- A computational scheme, based on different models to consider the main aerodynamic challenges of SB-VAWT, has been developed in Chapter 4, which conforms reasonably well to the experimental results. This modified scheme can be used for performance analysis of SB-VAWT equipped with both symmetric and asymmetric airfoils using the experimental results. This computational scheme can also utilize theoretical aerodynamic coefficients obtained from XFOIL and thus can overcome the lack of expensive experimental results for performance analysis of SB-VAWT.

10.1.4. SB-VAWT Airfoil Desirable Features

- Selection of the airfoil is crucial for better aerodynamic performance and dimensions of a smaller-capacity SB-VAWT.
- Conventionally used archaic NACA 4-digit symmetric airfoils are not appropriate for smaller capacity SB-VAWTs. Rather, it will be advantageous to utilize a high-lift and low-drag asymmetric thick airfoil suitable for low speed operation typically encountered by SB-VAWT.
- Nine aerodynamic features which would contribute to the self-starting and better performance of SB-VAWTs are identified, these are: (i) high stall angle at low Reynolds number, (ii) wide drag bucket, (iii) low zero-lift-drag coefficient, (iv) high C_l/C_d ratio, (v) high maximum lift-coefficient, (vi) delayed deep-stall property, (vii) low roughness sensitivity, (viii) low trailing edge noise generation, and (ix) large negative pitching moment.
- It has been found that the desired airfoil for self-starting SB-VAWT with optimum performance should have camber, higher thickness, large leading edge radius and moderate trailing edge thickness.

10.1.5. Assessment of Previously Attempted Asymmetric Airfoils

- No special-purpose airfoil could be identified from the literature which is designed for the low RN operation. The main emphases for designing the SB-VAWT airfoils were better performance rather than eliminating the starting problem.
- Five asymmetric airfoils, designed mainly for the aviation purposes and are available in the public domain, have been identified as potential candidates for SB-VAWTs. These candidate airfoils are investigated and it has been found that none of these airfoils has all the desirable aerodynamic characteristics or geometric features.
- Detailed performance analyses of a SB-VAWT equipped with five candidate airfoils are further analyzed using the computational models described in Chapter 4 and the results are compared with symmetric NACA 0015, which is

considered as an ideal airfoil for VAWTs. The analyses are carried out at $Re=50,000$, $100,000$ and $300,000$. It has been found that:-

- at $Re=50,000$, $C_{P,net}$ of all the asymmetric airfoils are higher than NACA 0015 in the low tip speed ratios (where the problem with the dead band responsible for self-starting problem occurs with conventional NACA airfoils). However, at $\lambda > 3$ NACA 0015 generates more power.
- Similar trend has been observed at $Re=100,000$ and $C_{P,net}$ of all the asymmetric airfoils are better than NACA 0015. However, at $\lambda > 2.5$ NACA 0015 generates more power.
- At $Re=300,000$, $C_{P,net}$ value of NACA 0015 is higher than all the asymmetric airfoils at all the λ which indicates that the candidate asymmetric airfoils can not perform better than NACA 0015 at $Re \approx 300,000$. Among all the asymmetric airfoils, $C_{P,net}$ values of LS-0417 are the highest up to $\lambda=3.25$.

10.1.6. Selection of a Prospective Airfoils for Self-Starting SB-VAWT

- Nine performance indices have been defined in the present analysis in the light of desirable aerodynamic characteristics to select best performing airfoil. These performance indices are for considering the following aerodynamic characteristics: (i) stall angle at low Reynolds number; (ii) width of the drag bucket; (iii) zero-lift-drag coefficient; (iv) C_l/C_d ratio; (v) maximum lift-coefficient; (vi) deep-stall angle; (vii) roughness sensitivity; (viii) trailing edge noise generation; and (ix) pitching moment.
- Ten prospective airfoils are analyzed in the present study by comparing their performance indices and among all these airfoils, overall rating of NASA LS(1)-0417 has been found to be the best. However, $C_{P,net}$ and $C_{Q,net}$ values of LS-0417 are better than symmetric NACA 0015 at $Re=100,000$ only up to $\lambda=2.25$. At $Re=300,000$ the situation is even worse and the $C_{P,net}$ values of LS-0417 are lesser than symmetric NACA 0015 for all the tip speed ratios.

- Under these backdrops, there is a clear need for designing special-purpose airfoils in the light of desirable characteristics and geometric features for self-starting SB-VAWTs with optimum performance at low RN.

10.1.7. New Special-purpose SB-VAWT Airfoil – “MI-VAWT1”

- To improve the performance of LS-0417, sensitivity analyses have been conducted with its different geometric features to improve the aerodynamic performance. Finally, a new special purpose airfoil named “MI-VAWT1” has been designed in the present study by utilizing the XFOIL and the computational scheme developed in the present research.
- Performance of newly designed special purpose airfoil "MI-VAWT1" is much superior to other prospective asymmetric airfoils and conventionally used NACA 0015 at low RN and low tip speed ratio ranges where the problem of self-starting happens.

10.1.8. New Airfoil for SB-VAWT Supporting Strut – “MI-STRUT1”

- To reduce the detrimental parasitic drag losses, a new airfoil “MI-STRUT1” has been designed for the supporting struts of SB-VAWTs.
- MI-STRUT1 performs better than another popular streamlined strut, namely E862, especially at the low RN range.
- MI-STRUT1 can be considered as a potential candidate for the profile of supporting struts of SB-VAWT for better performance.

10.1.9. Design Analysis

- Twenty two design parameters have been identified, which are: (i) blade shape, (ii) number of blades, (iii) supporting struts type and shape, (iv) central column, (v) swept area, (vi) solidity, (vii) aspect ratio, (viii) chord/radius ratio, (ix) rated power output, (x) rated wind speed, (xi) cut-in speed, (xii) cut-out speed, (xiii) power coefficient, (xiv) tip speed ratio, (xv) rotational speed, (xvi) pitching of blade, (xvii) tower, (xviii) braking mechanism, (xix) load, (xx) material, (xxi) noise, and (xxii) aesthetic.

- An analytical tool has been utilized for the design analysis of SB-VAWT with different fixed and variable design parameters.
- Sensitivity analyses have been performed with five design parameters, which are: (a) blade material, (b) solidity, (c) type of blade support, (d) blade airfoil, and (e) shape of the blade supporting struts. It has been found out from the sensitivity analysis with these parameters that:
 - the overhang type support with endplates reduces the overall dimensions of the turbines considerably in comparison to those of the simple and overhang supported turbines without endplates;
 - solidity has significant effect on design configurations of a SB-VAWT and it is very important to select an appropriate value to obtain optimum performance without requiring excessive blade materials;
 - design features with pultruded FRP as blade material is superior than conventionally used Aluminum;
 - from design point of view, performance of MI-VAWT1 as blade airfoil is superior to that of conventionally used NACA 0015.
 - MI-STRUT1 can be considered as a potential candidate for the profile of supporting struts of SB-VAWT for better performance;

10.1.10. Specification of a New Class of SB-VAWT – “MI-VAWT 3000”

- Based on sensitivity analyses with the five critical design parameters, a new class of 3kW variable-speed SB-VAWT (named as MI-VAWT 3000) has been designed.
- It has MI-VAWT1 and MI-STRUT1 as the airfoil for blade and supporting strut respectively.
- It has moderate solidity and has light-weight pultruded Fibre Reinforced Plastic (FRP) as its blade material.
- Its design configuration is overhang type with wing tip devices.

10.1.11. Experimental Investigation of a SB-VAWT Prototype

- Experimentation has been conducted to investigate the starting torque of a symmetric (NACA 0021) and asymmetric (NACA 4415) airfoils.
- According to the experimental investigation, it has been found that NACA 4415 can produce significantly higher starting torque than a NACA 0021 at two different solidities.

10.2. Recommendations for Further Research Works

- Expressions for considering the natural frequencies can be incorporated in the analytical model for design analysis of SB-VAWTs. Structurally, the SB-VAWT blades and rotor must be a solid unit whose natural frequencies should not coincide with operational frequencies during the operation.
- The computational scheme utilized in the present study for performance prediction and design analysis of SB-VAWTs has not adequately considered the effect of atmospheric turbulence. To quantify its effect, a detailed unsteady CFD analysis can be performed.
- Wind shear may be included in the calculation to see the effect on the turbine performance. It can be important when the turbine is placed close to the ground.
- For assessing the noise generated from MI-VAWT 3000 under different loads, further computational study (similar to Iida et. al 2004 as discussed in Section 8.1.21) can be undertaken.
- Before field application, MI-VAWT 3000 prototype should be fabricated for detailed experimentation to produce power curves. Efforts should be made to identify and quantify the noise and vibration level. If required, the dimensions of the SB-VAWT should be optimized for required optimum performance.
- Detailed experimental work can be undertaken with the SB-VAWT prototype, fabricated in the present study, using the newly designed airfoils (namely MI-VAWT1 & MI-STRUT1) to determine the torque, power output, noise level, vibration etc. at different wind speeds.

References

- [1] Abramovich, H. 1987. Vertical Axis Wind Turbines: A Survey And Bibliography. Wind Engineering. Vol 11, No 6, pp 334-343.
- [2] Advanced Topics in Aerodynamics (Aerodyn). 2007. Wing Tip Devices. URL: http://aerodyn.org/Drag/tip_devices.html (cited December 29, 2007)
- [3] Advanced Topics in Aerodynamics (Aerodyn). 2008. Dynamic Stall. URL: <http://aerodyn.org/Dstall/dstall.html> (cited February 14, 2008)
- [4] Allet, A., Brahim, M.T. and Paraschivoiu, I. 1997. On the Aerodynamic Modeling of a VAWT. Wind Engineering. Vol 21, No 6, pp 351-365.
- [5] American Society of Civil Engineers (ASCE)/Water Pollution Control Federation. 1988. Aeration: a wastewater treatment process. WPCF annual of Practice No. FD-13. WPCF and ASCE, Alexandria, VA, USA.
- [6] American Wind Energy Association (AWEA). 2007. How Does A Wind Turbine's Energy Production Differ from Its Power Production?. URL: <http://www.awea.org/faq/basicen.html#Energy%20output>. (cited December 22, 2007).
- [7] Anderson, J.D. 2001. Fundamentals of Aerodynamics. McGraw-Hill, USA.
- [8] Angell, R.K., Musgrove, P.J. and Galbraith, R.A.M. 1988. Unsteady Wind Tunnel Testing of Thick Section Aerofoils For Use On Large Scale Vertical Axis Wind Turbines. Wind Energy Conversion. 1988: Proceedings of 10th BWEA Conference, London, UK, March 22-24. pp 195-203.
- [9] ASHRAE Journal. 2003. New Turbine Stirs Interest. June. p8.
- [10] Aviation Intranet. 2007. Reducing Induced Drag. URL: <http://selair.selkirk.bc.ca/aerodynamics1/Drag/Page8.html> (cited December 29, 2007)
- [11] Baker, J.R. 1983. Features to Aid or Enable Self-starting of Fixed Pitch Low Solidity Vertical Axis Wind Turbines. Journal of Wind Engineering & Industrial Aerodynamics. Vol15, pp 369-380.

- [12] Beans, E.W. and Jakubowski, G.S. 1983. Method of Estimating the Aerodynamic Coefficients of Wind Turbine Blades at High Angles of Attack. *Journal of Energy*. Vol.7, No.6, Nov-Dec. pp.747-749.
- [13] Berg, D.E. 1983. An Improved Double-Multiple Streamtube Model for the Darrieus Type Vertical-Axis Wind Turbine. *Proceedings of the Sixth Biennial Wind Energy Conference and Workshop, Minneapolis, MN, USA, June*. pp 231-238.
- [14] Bergey. 2007. Bergey Windpower . URL:
http://www.islandearthsolar.com/bergey_wind_power.htm (cited January 1, 2008)
- [15] Blanch, M.J. 2002. Wind energy technologies for use in the built environment. *Wind Engineering*. Vol 26, No 3, pp 125–143.
- [16] Boeing. 2007. Blended Winglets. URL:
http://www.boeing.com/commercial/aeromagazine/aero_17/winglet_story.html (cited December 29, 2007)
- [17] Bravo, R., Tullis, S. and Ziada, S. 2007. Performance Testing of a Small Vertical-Axis Wind Turbine. 21st Canadian Congress of Applied Mechanics, Ryerson University Toronto, Ontario Canada, June.
- [18] Brooks, T., Pope, D., and Marcolini, M. 1989. Airfoil Self-Noise and Prediction. NASA Reference Publication 1218, National Aeronautics and Space Administration, U.S.A.
- [19] Brøndsted, P., Lilholt, H. and Lystrup, A. 2005. Composite Materials For Wind Power Turbine Blades. *Annual Review Material Res.* 2005. Vol 35, pp 505–538.
- [20] Bulteel, D. 1987-88. Centrifugalbeveiliging van een verticale as windturbine. VUB Fakulteit Toegepaste Wetenschappen, Brussels, Belgium.
- [21] Butler, B.L. and Blackwell, B.F. 1977. The Application of Laminated Wooden Blades to a 2-Meter Darrieus type Vertical-Axis Wind Turbine. *SAMPE Quarterly*, Vol 8, No 2, January.

- [22] Canadian Wind Energy Association (CanWEA). 2008. Wind Energy Industry. URL: http://canwea.ca/wind_energy_industry.cfm (cited January 13, 2008)
- [23] CANMET Energy Technology Centre (CETC). 2001. Investigation of Alternative Materials for Use in Mid-Size Vertical Axis Wind Turbine Blades: Materials Assessment. Ontario, Canada.
- [24] CANRen. 2006. Natural Resources Canada. Available online at: <http://www.canren.gc.ca> (cited 11 September 2006).
- [25] Cardona, J.L. 1984. Flow Curvature and Dynamic Stall Simulated with an Aerodynamic Free Vortex Model for VAWT. Wind Engineering. Vol 8, pp 135-143.
- [26] Carmicheal, B.H. 1981. Low Reynolds Number Airfoil Survey. NASA Contractor Report 165803.
- [27] Chappell, M.S. 1986. Wind Energy Research and Development at the National Research Council of Canada. NRCC No. 27459, October 1986, Canada.
- [28] Claessens, M.C. 2006. The Design and Testing of Airfoils for Application in Small Vertical Axis Wind Turbines. Master of Science Thesis, Faculty of Aerospace Engineering, Delft University of Technology, The Netherlands. November.
- [29] Clean Air Renewable Energy Coalition, 2002, Cleaning the Air with Renewable Energy, Briefing Note. Fall 2002.
- [30] The Charles River Radio Controllers (CRRC). 2007. Airfoil Performance Concepts. URL: http://www.charlesriverrc.org/articles/asfwpp/lelke_airfoilperf.htm (cited May 30, 2007)
- [31] Currie, I.G. 1974. Fundamental Mechanics of Fluid. McGraw-Hill.
- [32] Cyberiad, 2007, Airfoil Data, web: <http://www.cyberiad.net/foildata.htm>. (cited May 17, 2007)
- [33] Dahl, K.S. and Fuglsang, P. 1998. Design of the Wind Turbine Airfoil Family RISØ-A-XX. Risø National Laboratory, Roskilde, Denmark. December.

- [34] Dahl, K.S. 1999. Experimental Verifications of the New RISØ-A1 Airfoil Family for Wind Turbines. Proceedings of European Wind Energy Conference 1999. pp 85-88.
- [35] Danish Wind Industry Association (DWIA). 2008a. Turbulence. URL: <http://www.windpower.org/en/tour/wres/turb.htm>. (cited May 8, 2007).
- [36] Danish Wind Industry Association (DWIA). 2008b. Wind Turbine Towers. URL: <http://www.windpower.org/en/tour/wtrb/tower.htm>. (cited December 27, 2007).
- [37] Darrieus, G.J.M. 1931. Turbine Having Its Rotating Shaft Transverse to the Flow of the Current. US Patent No 1835081.
- [38] Decleyre, W. Van Aerschot, D. and Hirsch, Ch. 1981. Effects Of Reynolds Number On The Performance Characteristic Of Darrieus Windmills With Troposkien And Straight Blades. BHRA Fluid Engineering. pp 243-248
- [39] Dereng, V.G. 1981. Fixed Geometry Self Starting Transverse Axis Wind Turbine. United States Patent. Patent No. 4,264,279. April 28.
- [40] Devinant, P., Laverne, T. and Hureau, J. 2002. Experimental Study of Wind-turbine Airfoil Aerodynamics in High Turbulence. Journal of Wind Engineering and Industrial Aerodynamics. Vol 90, pp 689-707.
- [41] Drela, M. 1989. XFOIL: An Analysis and Design System for Low Reynolds Number Airfoils (XFOIL 6.94, 18 December 2001). Low Reynolds Number Aerodynamics, T. J. Mueller (ed.), Lecture Notes in Engineering. Vol 54. Springer-Verlag Berlin, Germany. pp 1–12.
- [42] Drela, M. 2001. XFOIL 6.94 User Guide. MIT Aero & Astro, Harold Youngren, Aerocraft, Inc. 10 December.
- [43] Drela, M. and Giles, M.B. 1987. Viscous-Inviscid Analysis of Transonic and Low Reynolds Number Airfoils. AIAA Journal, Vol 25, No 10, pp 1347-1355.
- [44] Drees, H.M. 1978. The Cycloturbine and its Potential for Broad Application. Proceedings of 2nd International Symposium on Wind Energy Systems, Amsterdam, October. pp E7-81-88.

- [45] Duremberg, C.J. 1979. Unsteady aerodynamics of Vertical Axis Wind Turbines. Proceedings of the 1st British Wind Energy Association workshop, Cranfield, Beds, England, April.
- [46] Eckenfelder, W.W. 1989, Industrial Water Pollution Control, 2nd edition. McGraw Hill, New York, USA.
- [47] Ekaterinaris J.A. and Platzer M.F. 1997. Computational Prediction of Airfoil Dynamic Stall. Progress in Aerospace Science. Vol 33, pp 759–846.
- [48] Eppler, R. and Somers, D. 1980. A Computer Program for the Design and Analysis of Low-Speed Airfoils, NASA TM-80210.
- [49] Eppler, R. 1990. Airfoil Design and Data. Springer-Verlag, Heidelberg, Germany.
- [50] Fujisawa, N. and Shibuya, S. 2001. Observations of Dynamic Stall on Darrieus Wind Turbine Blades. Journal of Wind Engineering and Industrial Aerodynamics. Vol 89, pp 201-214.
- [51] Fanucci, J.B. and Walter, R.E. 1976. Innovative Wind Machines: The Theoretical Performance of a Vertical-axis Wind Turbine. Proceedings of the vertical-axis wind turbine technology workshop, Sandia laboratories, SAND 76-5586, iii-61-95, USA.
- [52] Fell, C. 1985, Desalination Processes and Theory. Proceedings of Australian Water & Wastewater Association, Seminar on Desalination, Adelaide, Australia. June.
- [53] Foellings, F.J. and Smulders, P.T. 1985. Wind Energy and Cooling. Report of Commission of the European Communities. pp 624–628.
- [54] Fupeng, H., Yuhong, L., and Zuoyi, C. 2001. Suggestions for Improving Wind Turbines Blade Characteristics. Wind Engineering. Vol 25, No 2, pp 105-113.
- [55] Gault, D.E. 1957. A Correlation of Low-Speed Airfoil Section Stalling Characteristics with Reynolds Number And Airfoil Geometry. NACA Technical Note 3963, Washington, USA. March.
- [56] Glauert H. 1935. Aerodynamic theory. In: Durand WF, editor. Div. L. Airplane propellers, Vol. 6. Berlin: Springer. pp 324–30.

- [57] Global Wind Energy Council (GWEC). 2008. Continuing Boom in Wind Energy – 20 GW of New Capacity in 2007. URL: <http://www.gwec.net> (cited February 12, 2008)
- [58] Global Energy Concepts. 2003. Market, Cost, And Technical Analysis of Vertical and Horizontal Axis Wind Turbines. Task #2: VAWT vs. HAWT Technology. May.
- [59] Gormont, R.E. 1973. A Mathematical Model of Unsteady Aerodynamics and Radial Flow for Application to Helicopter Rotors. U.S. Army Air Mobility R&D Laboratory, Vertol Division, Philadelphia. USA.
- [60] Grauthoff, M. 1991. Utilization of Wind Energy In Urban Areas – Chance or Utopian Dream? Energy and Buildings, Vol 15–16, pp 517–523.
- [61] Grylls, W., Dale, B., and Sarre, P.E. 1978. A Theoretical and Experimental Investigation into the Variable Pitch Vertical Axis Wind Turbine. Proceedings of 2nd International Symposium on Wind energy Systems, Amsterdam. October. pp E9-101-118.
- [62] Hak, MGE. 1989. Control of Low-Reynolds-Number Airfoils - A Review. Lecture Notes in Engineering, No 54. p 246.
- [63] Hak, M.G.E. 1990. Control of Low-Speed Airfoil Aerodynamics. AIAA Journal, Vol 28, pp 1537–1552.
- [64] Ham, N.D. 1968. Aerodynamic Loading on a Two-dimensional Airfoil during Dynamic Stall. Journal of the AIAA. Vol 6, No. 10. October.
- [65] Ham, N.D. and Garelick, M.S. 1968. Dynamic Stall Considerations in Helicopter Rotor. Journal of the American Helicopter Society. Vol 13, No. 2. April.
- [66] Hannes, R. 2003. HAWT versus VAWT. Refocus July/August.
- [67] Hansen, A. C. and Butterfield, C. P. 1993. Aerodynamics of Horizontal-Axis Wind Turbines, Annual Review of Fluid Mechanics. Vol 25, pp 115-149.
- [68] Healy, J.V. 1978a. The Influence of Blade Thickness on the Output of Vertical Axis Wind Turbines. Wind Engineering. Vol 2, No 1, pp 1-9.
- [69] Healy, J.V. 1978b. The Influence of Blade Camber on the Output of Vertical Axis Wind Turbines. Wind Engineering. Vol 2, No 3, pp 146-155.

- [70] Hepperle, M. 2007. Some Remarks on Experiments, URL: <http://www.mh-aerotoools.de/airfoils/methods.htm#RemarksOnExperiments>. (cited December 21, 2007)
- [71] Hepperle, M. 2008. Design and Analysis of Airfoils. URL: <http://www.mh-aerotoools.de/airfoils/methods.htm> (cited February 14, 2008)
- [72] Hirsch, C. and Mandal, A.C. 1984. Flow Curvature Effect on Vertical Axis Darrius Wind Turbine Having High Chord-Radius Ratio. Proceedings of European Wind Energy Conference, Hamburg, Germany. October. pp 405-410.
- [73] Hirsch, C. and Mandal, A.C. 1987. The Cascade Theory for The Aerodynamic Performance of Darrius Turbines. Wind Engineering. Vol 11, pp 164-175.
- [74] Hoerner, S.F. and Borst, H.V. 1985. Fluid Dynamic Lift. Hoerner Fluid Dynamics, P.O. Box 21992, Bakersfield, CA 93390, USA.
- [75] Holme, O. A. 1976. Contribution to the Aerodynamic Theory of the Vertical Axis Wind Turbine. International Symposium on Wind Energy Systems, September, Cambridge, England. pp C4-55-71.
- [76] Iida, A. and Mizuno, A. 2003. Prediction Of Aerodynamic Noise Radiated From A Vertical-Axis Wind Turbine. Proceedings of the 4TH ASME/JSME Joint Fluids Engineering Conference July 6-10,2003, Honolulu, Hawaii. pp 1-7.
- [77] Iida, A., Mizuno, A., and Fukudome, K. 2004. Numerical Simulation of Aerodynamic Noise Radiated From Vertical Axis Wind Turbines. Technical report, Department of Mechanical Engineering, Kogakuin University, Japan.
- [78] Iida, A., Mizuno, A., and Fukudome, K. 2005. Prediction of Performance of Vertical Axis Wind Turbine With LES. Proceedings of Fluid Engineering Division Conference of Japan Society of Mechanical Engineering in CD-ROM.

- [79] Islam, M., Ting, D. S-K. and Fartaj, A. 2007a. Assessment of Small-Capacity Straight-bladed VAWT for Sustainable Development of Canada. *International Journal of Environment Studies*. Vol 64, No 4, pp 489–500.
- [80] Islam, M., Ting, D. S-K. and Fartaj, A. 2007b. Desirable Airfoil Features for Smaller-Capacity Straight-Bladed VAWT. *Wind Engineering*. Vol 31, No 3, pp 165–196.
- [81] Islam, M., Amin. M.R., Ting, D. S-K. and Fartaj, A. 2007c. Aerodynamic Factors Affecting Performance of Straight-bladed Vertical Axis Wind Turbines. ASME International Mechanical Engineering Congress and Exposition (IMECE) 2007, Seattle, Washington, USA. November. IMECE2007-41346. pp 1-11.
- [82] Islam, M., Ting, D. S-K. and Fartaj, A. 2008a. Aerodynamic Models for Darrieus Type Straight-bladed Vertical Axis Wind Turbines. *Renewable & Sustainable Energy review*, Elsevier. Vol 12, No 4, pp 1087-1109.
- [83] Islam, M., Ting, D. S-K. and Fartaj, A. 2008b. Design of a Special-purpose Airfoil for Smaller-Capacity Straight-Bladed VAWT. *Wind Engineering*. Vol 32, No 1, pp 27–54.
- [84] ITDG. 2006. Wind Electricity Generation. URL: <http://www.itdg.org> (cited September 15, 2006)
- [85] Jacob, E.N. and Sherman, A. 1937. Airfoil Characteristics as Affected by Variations of the Reynolds Number. NACA-TR-586.
- [86] Jesch, L.F. and Walton, D. 1980. Reynolds Number Effects on the Aerodynamic Performance of a Vertical Axis Wind Turbine. Proceedings of 3rd International Symposium on Wind Energy Systems, Lyngby, Denmark, August. pp 323-332.
- [87] Jonkman, J.M. 2003. Modeling of the UAE Wind Turbine for Refinement of FAST_AD. NREL Technical Report. NREL/TP-500-34755. December.
- [88] Kaldlec, E.G. 1982. Characteristics of Future Vertical Axis Wind Turbines. Sandia National Laboratory, New Mexico, USA. November.
- [89] Kato, Y., Seki, K., and Shimizu, Y. 1981a. Vertical Axis Type Wind Power Turbine. United States Patent. Patent No. 4,285,636. August 25.

- [90] Kato, Y., Seki, K., and Shimizu, Y. 1981b. Vertical Axis Wind Turbine Designed Aerodynamically At Tokai University. *Periodica Polytechnica, Mechanical Engineering*. Vol 25, No 1, pp 47-56.
- [91] Kellogg, M.I. and Bowman, W.J. 2004. Parametric Design Study of the Thickness of Airfoils at Reynolds Numbers from 60,000-150,000. 42nd AIAA Aerospace Sciences Meeting and Exhibit, 5-8 January. Reno, Nevada, USA.
- [92] Kentfield, J.A.C. 1996. *The Fundamentals of Wind-driven Water Pumpers*. Gordon & Breach Science, Amsterdam, The Netherlands.
- [93] Kirke, B.K. 1995. Wind Powered Aeration for Wastewater Treatment, Aquaculture And Lake Destratification. *Wind Engineering*. Vol 19, No1, pp 1-12.
- [94] Kirke, B.K. 1998. Evaluation of Self-Starting Vertical Axis Wind Turbines for Stand-Alone Applications. PhD Thesis, Griffith University, Australia.
- [95] Klimas, P.C. 1982. Darrieus Rotor Aerodynamics. *Transactions of ASME Journal. Solar Energy Engineering*. May. Vol 104, pp 102-105.
- [96] Klimas, P.C. 1985. Airfoil Treatments for Vertical Axis Wind Turbines. WINDPOWER '85, San Francisco, CA, USA. August.
- [97] Kuhlman, B. and Kuhlman, B. 1995. *Understanding Polars Without Math. B2Streamlines*, Olalla, WA, USA.
- [98] Laneville, A. and Vittecoq, P. 1986. Dynamic Stall: The Case of The Vertical Axis Wind Turbine, *ASME Journal of Solar Energy Engineering*. Vol 108, pp 140-145.
- [99] Lapin, E.E. 1975. Theoretical Performance of Vertical Axis Wind Turbines. ASME paper, 75-WA/Ener-1, The winter annual meeting, Houston, Texas, USA.
- [100] Larsen, H.C. 1975. Summary of a Vortex Theory for the Cyclogiro. Proceedings of the second U.S. National Conferences on wind engineering research, Colorado state university, V-8-1-3.

- [101] Leishman, J.G. 2002. Challenges in Modeling the Unsteady Aerodynamics of Wind Turbines. ASME 21st ASME Wind Energy Symposium, Reno, NM, USA.
- [102] Lissaman, P.B.S. 1983. Low Reynolds Number Airfoils. Annual Reviews, Fluid Mechanics. Vol 15, pp 223-39.
- [103] Lissaman, P.B.S. 1994. Wind Turbine Airfoils and Rotor Wakes. Wind Turbine Technology, ASME Press, New York, USA. pp 283-323.
- [104] Loth, J.L. and McCoy, H. 1983. Optimization of Darrieus Turbines with an Upwind And Downwind Momentum Model. Journal of Energy. Vol 7, No 4, pp 313-318.
- [105] Lunde, P. 1980. Windmills: From Jiddah to Yorkshire. January/February. Volume 31, Number 1.
- [106] Lyon, C.A., Broeren, P., Giguere, P., Gopalarathnam, A. and Selig, M.S. 1997. Summary of Low-Speed Airfoil Data, Volume 3. SoarTech Publications, Virginia Beach, VA, USA.
- [107] McCrosky, W.J. 1987. A Critical Assessment of Wind Tunnel Results for the NACA 0012 Airfoil. NASA Technical Memorandum 100019, October.
- [108] McGhee, R.J., and Walker, B.S. 1989. Performance Measurements of an Airfoil at Low Reynolds Numbers. Proceeding of the Conference on Low Reynolds Number Aerodynamics, Notre Dame, Indiana, USA, 5-7 June. pp 131-145.
- [109] Mandal, A.C. 1986. Aerodynamics and Design Analysis of Vertical Axis Darrieus Wind Turbines. Ph.D. Dissertation, Vrije Universiteit, Brussel, Belgium.
- [110] Mandal, A.C. and J.D. Burton. 1994. The Effects of Dynamic Stall and Flow Curvature on the Aerodynamics of Darrieus Turbines Applying the Cascade Model. Wind Engineering. Vol 18, No 6, pp 267-282.
- [111] Mandal, A.C. 1994. The Effects of Dynamic Stall and Flow Curvature on the Aerodynamics of Darrieus Turbines Applying the Cascade Model. A Report on Post Doctoral Research In the Renewable Energy and the Environment, Department of Engineering, University of Reading, UK.

- [112] Masse, B. 1981. Description de deux programmes d'ordinateur pour le calcul des performances des charges aerodynamiques pour les eoliennes a axe vertical, IREQ-2379.
- [113] McCroskey, W.J. 1982. Unsteady Airfoils. Annual Review of Fluid Mechanics. Vol 14, pp 285-311.
- [114] Migliore, P.G., Wolfe, W.P. and Fanucci, J. B. 1980. Flow Curvature Effects on Darrieus Turbine Blade Aerodynamics. Journal of Energy. Vol 4, No 2, pp 49-55.
- [115] Migliore, P.G. 1983. Comparison of NACA 6-Series and 4-Digit Airfoils for Darrieus Wind Turbine. Journal of Energy. July-August. Vol 7, No 4, pp 291-292.
- [116] Miley, S.J. 1982. A Catalog of Low Reynolds Number Airfoil Data for Wind Turbine Applications. RFP-3387 VC-60, Rockwell International, February. US Department of Energy, Wind Energy Technology Division, Federal Wind Energy Program.
- [117] Milne-Thompson, L.M. 1973. Theoretical Aerodynamics. 4th Edition, Dover Publications Inc., New York, USA.
- [118] Moriarty, P. 2005. NAFNoise User's Guide. NREL-NWTC, Colorado, USA. July.
- [119] Muniruzzaman, M. and Mandal, A.C. 1993. An Investigation of the effect of Dynamic Stall on Darrieus Turbines Applying the Cascade Model. RERIC International Energy Journal. Vol 15, No 2, pp 111-123.
- [120] Muraca R.J., Stephens M.V., and Dagenhart J.R. 1975. Theoretical Performance of Cross-wind Axis Turbines with Results for a Catenary Vertical Axis Configuration. NASA TMX-72662, USA.
- [121] Maruyama, Y., Shimura, M., Yoshie, R., Wei, R., and Seki, K. 2001. Development of Vertical Axis Wind Turbine with Straight Blades Suitable for Buildings. Proceedings of European Wind Energy Conference (EWEC), Copenhagen, Denmark, July. pp 530-533.

- [122] Nagai, H., Shinoda, J. and Ushiyama, L. 1986. Agricultural Applications of Wind Power in Japan. Proceedings of European Wind Energy Association Conference (EWEC), 7–9 October, Rome, Italy. pp 463–468.
- [123] National Research Council (NRC), Committee on Assessment of Research Needs for Wind Turbine Rotor Materials Technology, 1991. Assessment of Research Needs for Wind Turbine Rotor Materials Technology. URL: http://www.nap.edu/openbook.php?record_id=1824&page=R1 (cited December 22, 2007).
- [124] Natural Resources Canada (NRCan). 2003. Stand-Alone Wind Energy Systems: A Buyer's Guide. Ottawa, Ontario, Canada.
- [125] Natural Resources Canada (NRCan). 2005. Survey of the Small (300W to 300kW) Wind Turbine Market in Canada. NRCan, Ontario, Canada.
- [126] Nijssen, R. 2006. Fatigue Life Prediction and Strength Degradation of Wind Turbine Rotor Blade Composites. PhD Thesis. Aerospace Engineering, Delft University, the Netherlands.
- [127] Noll, R.B. and Ham, N.D. 1980. Analytical Evaluation of the Aerodynamic Performance of a high-reliability Vertical-axis Wind Turbine. Proceedings of AWEA National conference, U.S.A.
- [128] NWTC Design Codes. 2007. FoilCheck. NREL, USA. URL: <http://wind.nrel.gov/designcodes/preprocessors/foilchk/> (cited June 8, 2007).
- [129] Ove Arup & Partners. 2003. Harare International School, Zimbabwe. Zimbabwe.
- [130] Papadopoulos, K. Helmis, C. G. Soilemes, A. T. Papageorgas, P. G. and Asimakopoulos, D. N. 1995. Study of the Turbulent Characteristics of the Near-wake Field of a Medium-sized Wind Turbine Operating in High Wind Conditions. Solar Energy. Vol 55, No 1, pp 61-72.
- [131] Pawsey, N.C.K. 2002. Development and Evaluation of Passive Variable-pitch Vertical Axis Wind Turbines. Doctoral Thesis, The University of New South Wales. November.

- [132] Paraschivoiu, I. 1981. Double-Multiple Streamtube Model for Darrieus Wind Turbines. Second DOE/NASA Wind Turbines Dynamics Workshop, NASA CP-2186, Cleveland, Ohio, February. pp 19-25.
- [133] Paraschivoiu, I. and Delclaux, F. 1983. Double Multiple Streamtube Model with Recent Improvements. Journal of Energy. May-June. Vol 7, pp 250-255.
- [134] Paraschivoiu, I., Delclaux, F., Fraunie, P. and Beguier, C. 1983. Aerodynamic Analysis of the Darrieus Rotor Including Secondary Effects. Journal of Energy. Vol 7, No 5, pp 416-421.
- [135] Paraschivoiu, I. 2002. Wind Turbine Design: With Emphasis on Darrieus Concept. Polytechnic International Press. Montreal, Canada.
- [136] Parchen, R., Bruggeman, J.C. and Dassen, A.G.M. 1997. The Effect of the Blade Thickness of Wind Turbine Blades on the Noise due to Inflow Turbulence. Noise and Vibration Bulletin. July.
- [137] Peace, S. 2003. Why Not Vertical Axis, ReFocus, May-June.
- [138] PSIGATE. 2006. Physical Sciences Information Gateway. URL: http://www.psigate.ac.uk/newsite/physics_timeline.html (cited September 12, 2006).
- [139] Read, S. and Sharpe, D.J. 1980. An Extended Multiple Streamtube Theory for Vertical Axis Wind Turbines. 2nd BWEA Workshop, Cranfield, UK, April. pp 65-72.
- [140] Reid, M.R. 2006, Thin/Cambered/Reflexed Airfoil Development For Micro-Air Vehicles At Reynolds Numbers of 60,000 to 150,000. M.Sc Thesis, Rochester Institute of Technology, Rochester, New York, USA, September.
- [141] Research Group on the Global Future. 2006. Global statistics: urban/rural population, Center for Applied Policy Research, Munich University, Germany. URL: http://www.cap-lmu.de/fgz/statistics/urban_pop.php. (cited September 14, 2006).
- [142] Riegels, F.W. 1961. Aerofoil Sections. Butterworth, London.

- [143] Rohatgi, J. 1996. An Analysis of the Influence of Atmospheric Stability on Vertical Wind Profiles – Its Influence on Wind Energy And Wind Turbines. *Wind Engineering*. Vol 20, No 5, pp 319-332.
- [144] Rohatgi, J. and Barbezier, G. 1999. Wind Turbulence and Atmospheric Stability – Their Effect on Wind Turbine Output. *Renewable Energy*. Vol 16, pp 908-911.
- [145] Sgrillo, M. 2007. Aesthetics Issues and Residential Wind Turbines. URL: http://www.awea.org/faq/sgrillo/ms_aesthetics_0405.html (cited December 31, 2007)
- [146] Sahin, A. D. 2004. Progress and Recent Trends In Wind Energy. *Progress in Energy and Combustion Science*. Vol 30, No 5, pp 501-543.
- [147] Sandia National Laboratory (SNL). 2006. URL: <http://www.sandia.gov/wind>
- [148] Sato, J. and Sunada, Y. 1995. Experimental Research on Blunt Trailing-Edge Airfoil Sections at Low Reynolds Numbers. *AIAA Journal*. November. Vol 33, No 11, pp 2001-2005.
- [149] Savonius, S.J. 1931. The S-Rotor and Its Applications. *Mechanical Engineering*. Vol 53, No 5, pp 333-338.
- [150] Scholz, N. 1977. Aerodynamics of Cascades. Advisory Group for Aerospace Research and Development (AGARD). AGARD-AG-220. Neuilly sur Seine, France.
- [151] Seki, K., Shimizu, Y. and Oshishi, T. 1985. A Study of Aerodynamic Performance and Airfoil for Straight Blade Non-Articulated Vertical Axis Wind and Its Application. *Windpower 85*, San Francisco, CA, USA, August. pp 531-536.
- [152] Seki, K. 2005. Straight Wind Type Wind and Water Turbine. United States Patent. Patent No. 6,974,309 B2. December 13.
- [153] Selig, M.S., Donovan, J.F., and Fraser, D.B. 1989. Airfoil at Low Speeds. Soartech #8, Virginia Beach, VA, USA.
- [154] Selig, M.S., Guglielmo, J.J., Broeren, A.P., and Giguere, P. 1995. Summary of Low-Speed Airfoil Data, Volume 1. SoarTech Publications, Virginia Beach, VA, USA.

- [155] Sharpe, D. J. 1977. A Theoretical and Experimental Study of the Darrieus Vertical Axis Wind Turbine. School of Mechanical, Aeronautical & Production Engineering. Kingston Polytechnic. Research Report. October.
- [156] Sheldahl, R.E. and Blackwell, B.F. 1976. Aerodynamic Characteristics of Four Symmetrical Airfoil Sections Through 180 Degrees Angle of Attack at Low Reynolds Number. Proceedings of the vertical-axis wind turbine technology workshop, Sandia laboratories, SAND76-5586, II-73-106, USA.
- [157] Sheldahl, R.E. and Klimas, P.C. 1981. Aerodynamic Characteristics of Seven Symmetrical Airfoil Sections Through 180-Degree Angle of Attack For Use In Aerodynamic Analysis of Vertical Axis Wind Turbines. Sandia National Labs report SAND80-2114, USA.
- [158] Simhan, K. 1994. A Review Of Calculation Methods For The Determination Of Performance Characteristics of Vertical Axis Wind Energy Converters With Special Reference To The Influence Of Solidity On Starting Characteristics. Proceedings of European Wind Energy Conference, Hamburg, FRG, October. pp 324-331.
- [159] Singh, A., Winoto, S., Shah, D., Lim, K, and Goh, R. 2000. A Computational Study on Airfoils at Low Reynolds Numbers. Proceedings of the ASME Fluids Engineering Division (FED), Vol 253, pp 405-411.
- [160] Smith, B.R. and Swinton, E.A., 1988, Desalination Costs In Australia: A Survey of Operating Plants. Desalination, Vol 70, pp 3–15.
- [161] Atlantic Wind Test Site. 2007. Soft VAWT Project. URL: http://www.awts.pe.ca/soft_VAWT_project.htm
- [162] Somers, D.M. and Maughmer, M.D. 2002. Theoretical Aerodynamic Analyses of Six Airfoils for Use on Small Wind Turbines. Subcontractor Report, National Renewable Energy Laboratory (NREL/SR-500-33295), Golden, Colorado, U.S.A.
- [163] Strickland, J.H. 1976. A Performance Prediction Model for the Darrieus Turbine. International Symposium on Wind Energy Systems, Cambridge, UK, September.

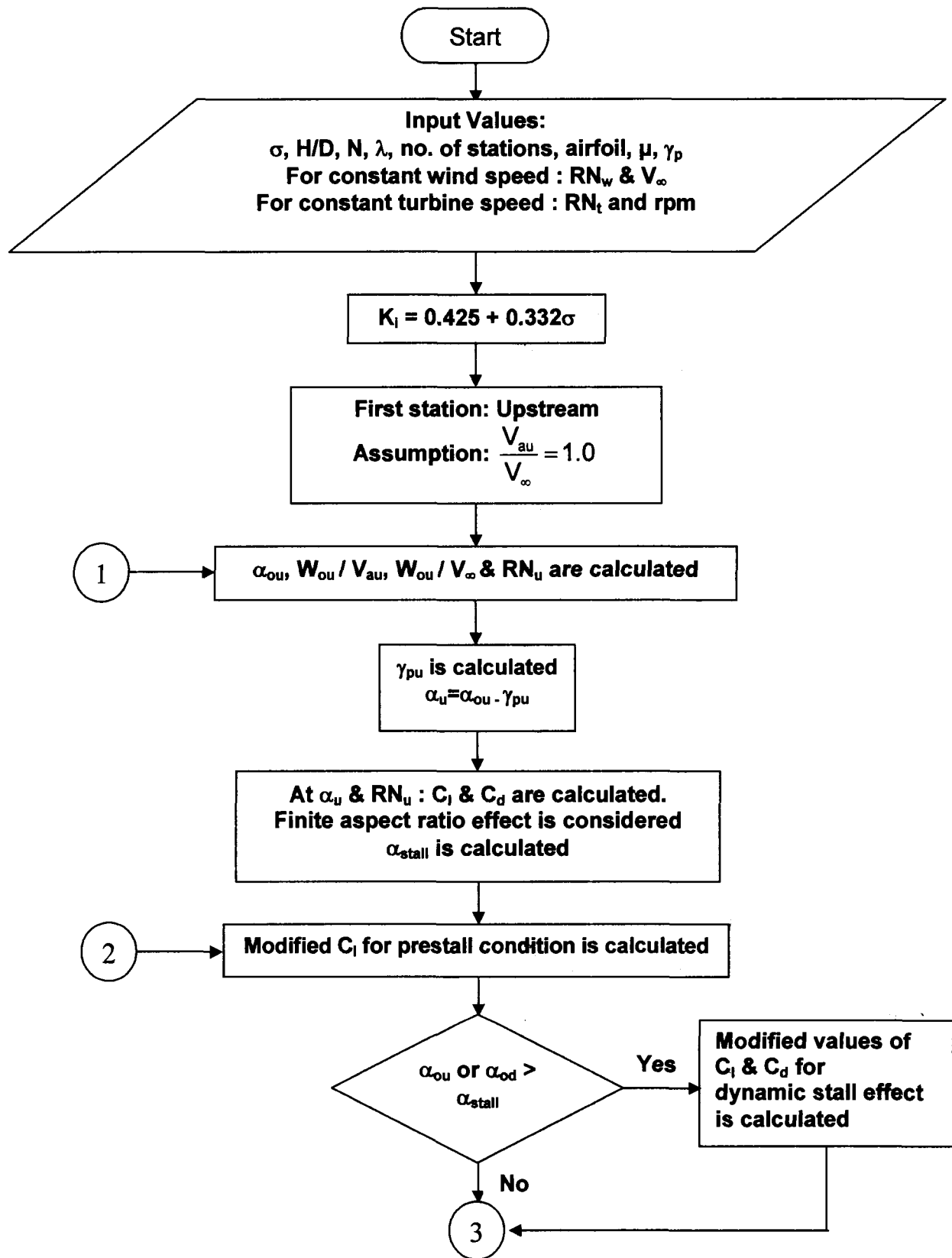
- [164] Strickland, J.H., Webster, B.T., Nguyen, T. 1979. A Vortex Model of The Darrieus Turbine: An Analytical And Experimental Study. *Journal of Fluids Engineering*. December. Vol 101, pp 500-505.
- [165] Strickland, J. B., Webster, B., and Nguyen, T. 1981. A Vortex Model of the Darrieus Turbine: An Analytical and Experimental Study. Technical Report SAND81-7017, Sandia National Laboratory.
- [166] Sutherland, H.J. 2000. A Summary of the Fatigue Properties of Wind Turbine Materials. *Wind Energy*. Vol 3, pp 1-34.
- [167] Tani, I. 1964. Low Speed Flows Involving Bubble Separations. *Progress in Aeronautical Sciences*. Vol 5, pp 70-103.
- [168] Templin, R.J. 1974. Aerodynamic Performance Theory for the NRC Vertical- Axis Wind Turbine. NRC Lab. Report LTR-LA-190, June.
- [169] The Encyclopedia of Alternative Energy and Sustainable Living. 2007. Wind Turbine Blades. URL: http://www.daviddarling.info/encyclopedia/B/AE_blades.html (cited January 1, 2008)
- [170] The Encyclopedia of Alternative Energy and Sustainable Living . 2007. wind turbine rated capacity. URL: http://www.daviddarling.info/encyclopedia/W/AE_wind_turbine_rated_capacity.html. (cited December 25, 2007)
- [171] Timmer, W.A. 2003. Summary of The Delft University Wind Turbine Dedicated Airfoils. *Proceedings of the 2003 ASME wind energy symposium*, Reno, USA. pp 11-21.
- [172] Timmer, W.A. and van Rooy, R.P.J.O.M. 1992. Thick Airfoils for HAWTs. *Journal of Wind Engineering and Industrial Aerodynamics*. May. Vol 39, No 1-3, pp 151-60
- [173] Viterna, L.A. and Corrigan, R.D. 1981. Fixed Pitch Rotor Performance Of Large Wind Turbines. DOE/NASA Workshop on Large Horizontal Axis Wind Turbines, July.
- [174] Vittecoq, P. and Laneville, A. 1983. Aerodynamic Forces For A Darrieus Rotor With Straight Blades: Wind Tunnel Measurements. *Journal of Wind*

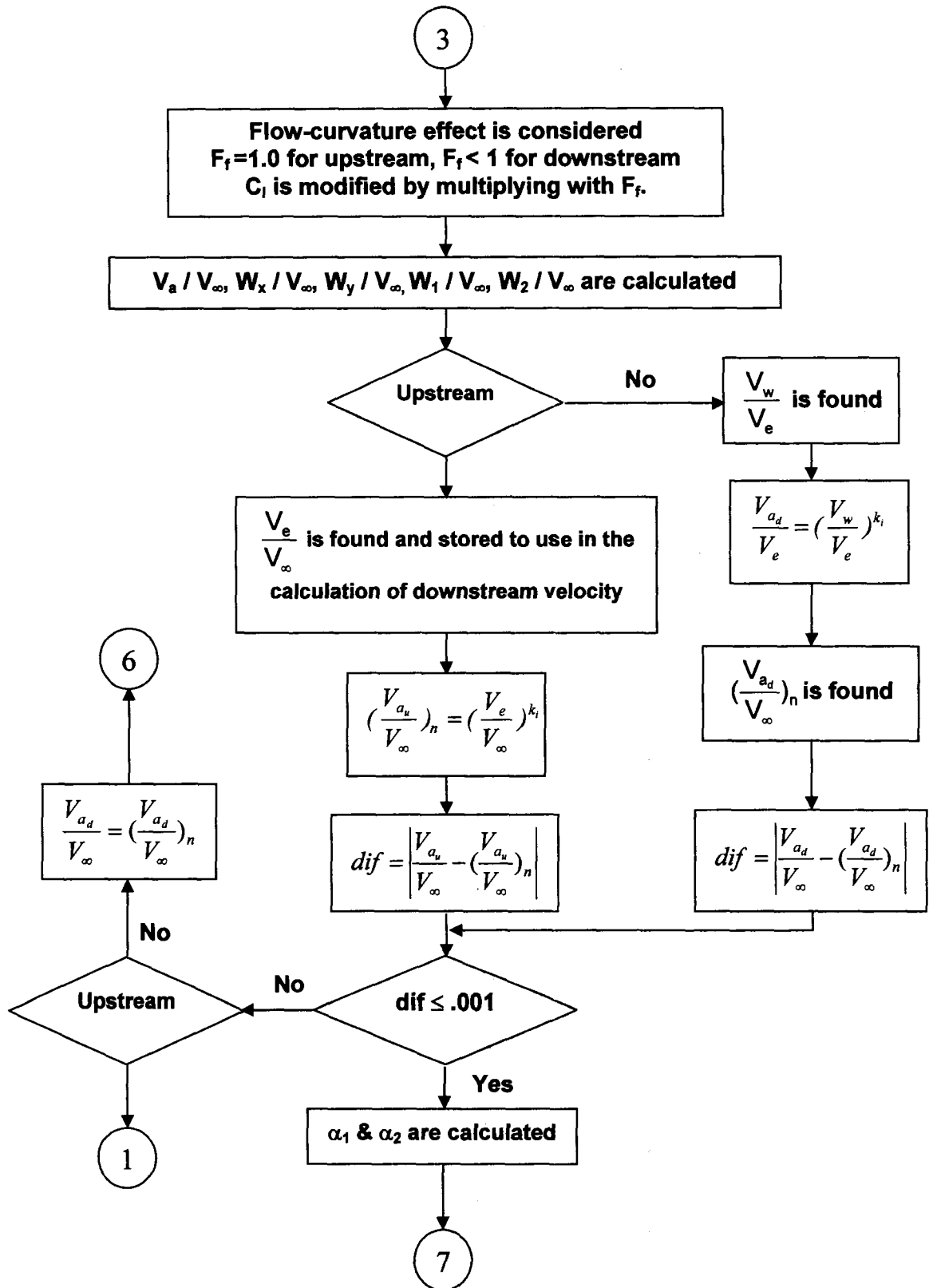
- Engineering and Industrial Aerodynamics. December. Vol 15, No 1-3, pp 381-388.
- [175] Vogel, J. 2005. Wind: A Hard-Blowing History. The Environmental Magazine, Jan-Feb.
- [176] Watson, G.R. 1979. The Self Starting Capabilities of Low Solidity Fixed Pitch Darrieus Rotor. Proceedings of the 1st British Wind Energy Association Workshop, Cranfield, Beds, England, April. pp 32-39.
- [177] Wikipedia. 2007a. Zero-lift Drag Coefficient. URL: http://en.wikipedia.org/wiki/Zero-lift_drag_coefficient (cited March 12, 2007)
- [178] Wikipedia. 2007b. Elliptical wing. URL: http://en.wikipedia.org/wiki/Elliptical_wing (cited December 29, 2007)
- [179] Willmer, A.C. 1979. Low Reynolds Number Tests on the NACA 0015 section. Proceedings of the 1st British wind energy association workshop, England. pp 109-116.
- [180] Wilson, R.E., and Lissaman, P.B.S. 1974. Applied Aerodynamics of Wind Power Machines. Oregon State University, May.
- [181] Wilson, R.E. 1980. Wind-Turbine Aerodynamics. Journal of Wind Engineering and Industrial Aerodynamics. Vol 5, pp 357-372.
- [182] World Commission on Environment and Development (WCED), 1987, Our Common Future. Oxford: Oxford University Press, USA. May.
- [183] XFOIL. 2007. Subsonic Airfoil Development System. URL: <http://web.mit.edu/drela/Public/web/xfoil/> (cited 31 May, 2007).
- [184] You, K.H. and Leng, G., 2003, Renewable Energy in Canada's Remote Communities. Renewable Energy for Remote Communities Program, Natural Resources Canada.
- [185] Zervos, A., Michos, A., Sakellariou, N., and Antoniou, I. 1986. A Two Dimensional Wind Tunnel Study of a Vertical Axis Wind Turbine. Proceedings of European Wind Energy Conference, Rome, Italy. pp 469-474.

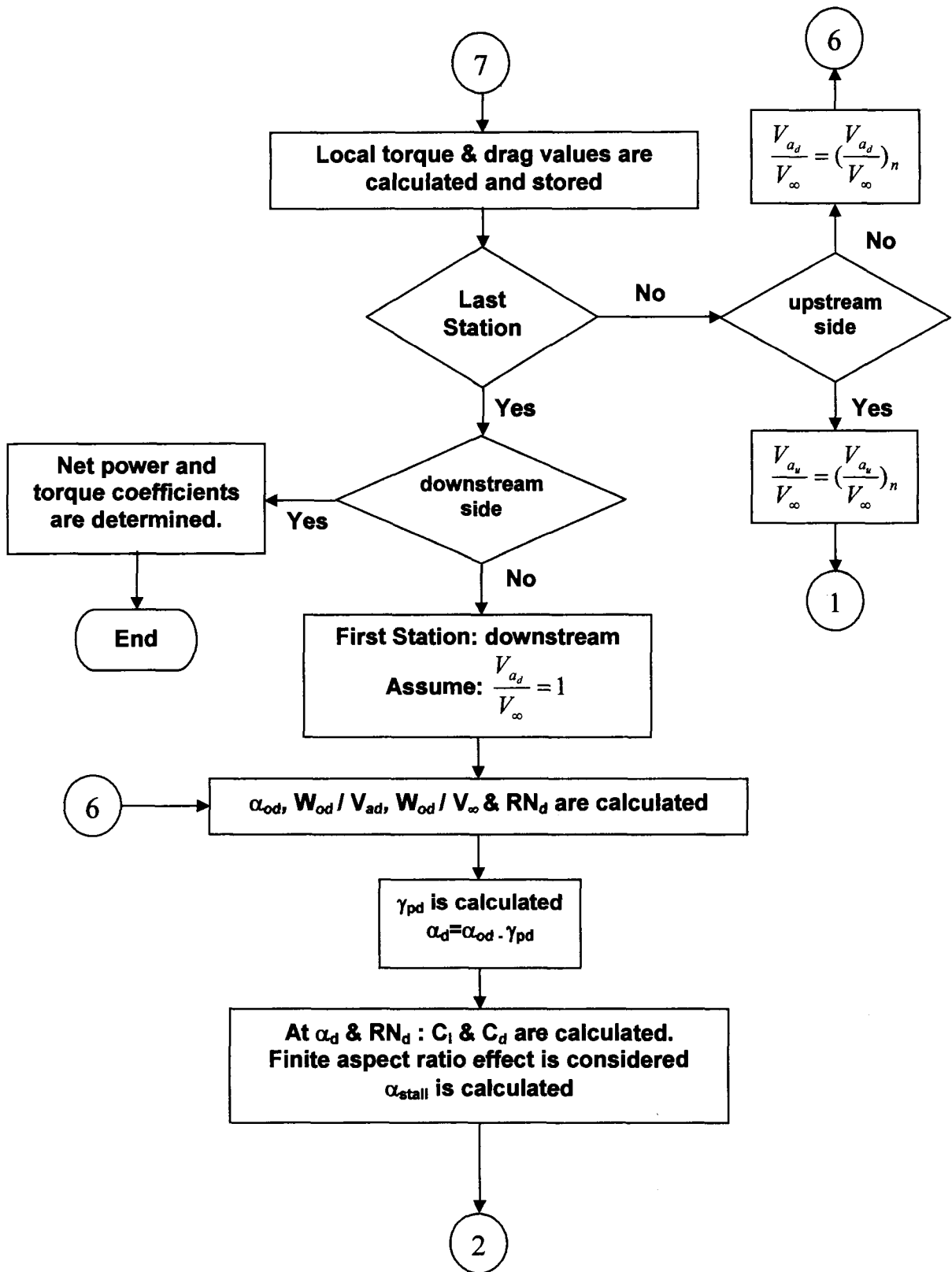
- [186] Zervos, A. 1988a. Aerodynamic Evaluation of Blade Profile for Vertical Axis Wind Turbines. European Wind Energy Conference 1988, Herning, Denmark. June. pp 611-616.
- [187] Zervos, A. 1988b. Aerodynamic Design and Testing of Blade Profiles for Vertical Axis Wind Turbines. Commission of the European Communities. Contractors' meeting, Brussels. pp 309-320
- [188] Zervos, A. 1988c. Aerodynamic Design of Blade Profiles for Vertical Axis Wind Turbines. Euroforum, new energies : Proceedings of an international congress held at Saarbrücken, F.R. Germany, October.
- [189] Zervos, A. and Roucou, R. 1988. Flow Curvature Effects on A Rotating Airfoil. Zeitschrift fur Angewandte Mathematik und Mechanik. Vol 68, No 5, pp 365-368.
- [190] Zervos, A., Morfiadakis, V. and Stefanatos, N. 1989. Testing of Blade Profiles For Vertical Axis Wind Turbines. Proceedings of European Wind Energy Conference (EWEC), Glasgow, Scotland. pp 193-197.
- [191] Zervos, A. and Morfiadakis, E. 1990. Instantaneous Pressure Distribution Measurements on The Blades of A Vertical Axis Wind Turbine. Proceedings of European Wind Energy Conference (EWEC), Madrid, Spain, September. pp 247-251.

APPENDICES

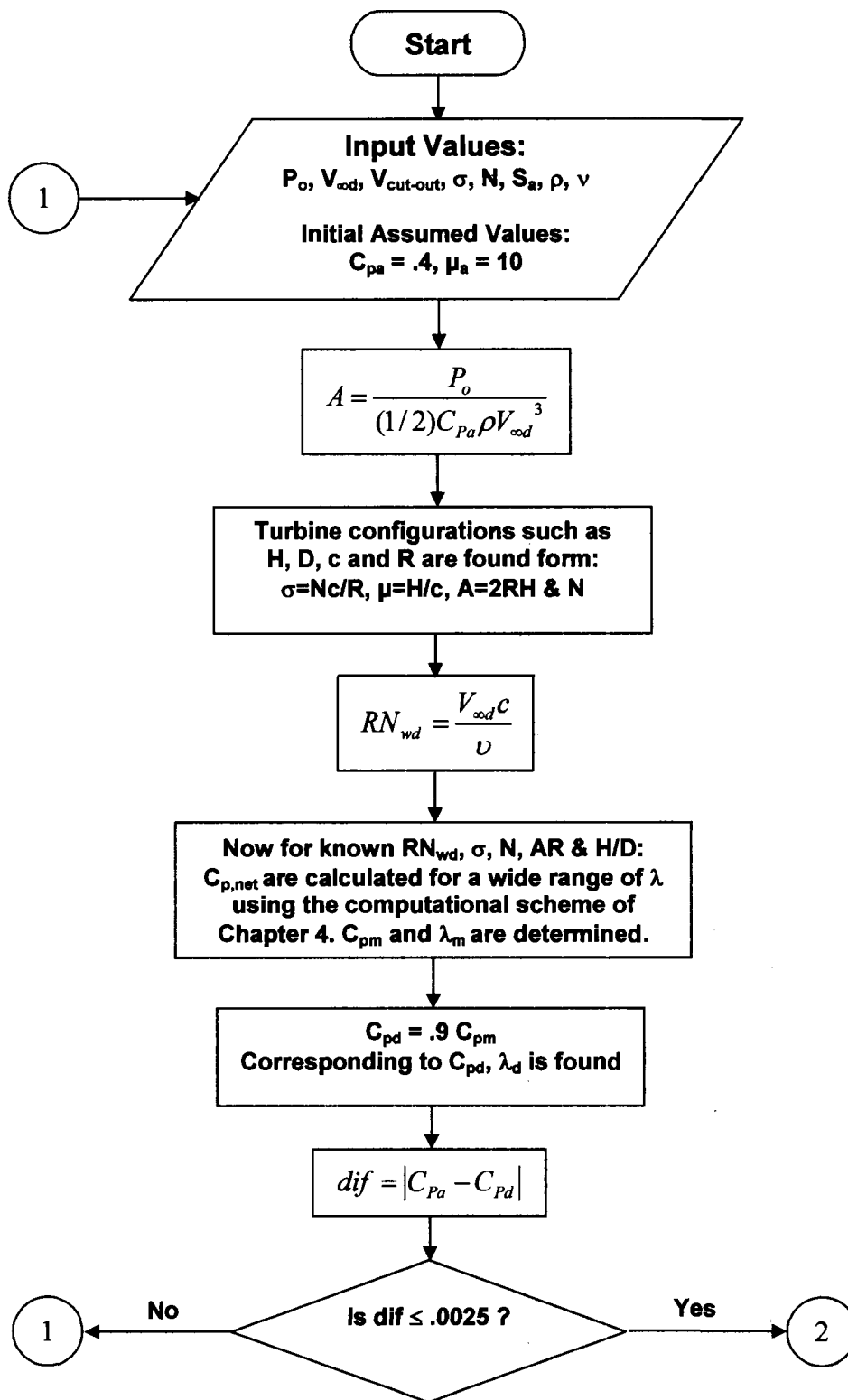
Appendix-A: Flow Diagram of Computational Scheme

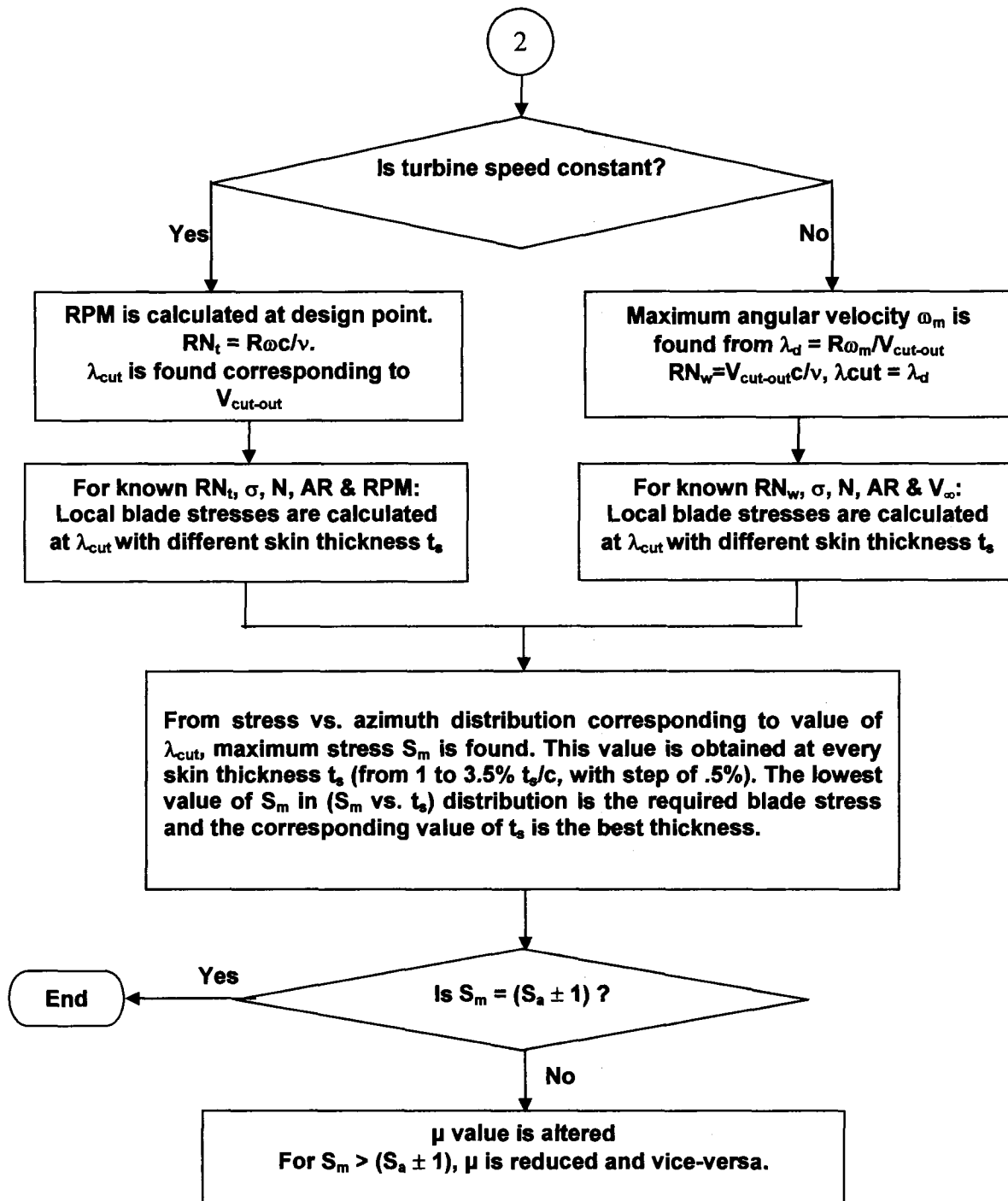






Appendix-B: Flow Diagram of Design Analysis





Appendix C: XFOIL

XFOIL [2007] is a computer program developed by MIT Professor Mark Drela [Drela 1989] for the design and analysis of subsonic isolated airfoils and it has been widely utilized for low RN airfoil analysis by the renowned wind turbine related research organizations including NREL [Somers and Maughmer 2002], Risoe [Dahl and Fuglsang 1998 and Dahl 1999] and Delft University [Timmer and Rooy 1992]. Analytical results obtained from XFOIL conform reasonably with the experimental results.

It has been found from literature survey, among all the tools available in the public domain for analysis & design of low RN airfoils, the performance of XFOIL is one of the best. Moreover, due to availability of attractive frontend packages (like XFLR5, Profili2 etc.), using of XFOIL is much more user friendly and faster than other similar codes like Eppler code (known as PROFIL). Due to these advantageous factors, the candidate selected XFOIL for: (i) to obtain pre-stall airfoil coefficients, and (ii) to perform sensitivity analyses for optimizing the geometric features of a prospective airfoils.

The first version of XFOIL was written by Mark Drela in 1986. The main goal was to combine the speed and accuracy of high-order panel methods with the new fully-coupled viscous/inviscid interaction method used in the ISES code developed by Drela and Giles [Drela, 2001]. A fully interactive interface was employed from the beginning to make it much easier to use than the traditional batch-type CFD codes. Several inverse modes and a geometry manipulator were also incorporated early in XFOIL's development, making it a fairly general airfoil development system. Since version 1.0, XFOIL has undergone numerous revisions, upgrades, and enhancements. These changes mainly originated from perceived shortcomings during actual design use, so XFOIL is now strongly geared to practical airfoil development.

The XFOIL code combines a conformal-mapping method for the design of airfoils with prescribed pressure distributions, a panel method for the analysis of the potential flow about given airfoils, and an integral boundary-layer method. The inviscid formulation is a linear-vorticity stream-function panel method. A general two-dimensional flow field is constructed by the superposition of a free-stream flow, a vortex sheet on the airfoil surface, and a source sheet on the airfoil surface and the wake. The airfoil contour and wake trajectory are discretized into straight panels. Each airfoil panel has a linear vorticity distribution, and each airfoil and wake panel also has a constant source strength associated with it. The source strengths are later related to quantities that define the viscous layer. The system of equations obtained to solve for the vorticity and source strengths is closed with an explicit Kutta condition. An option is included that allows the velocity distribution over a portion of the airfoil to be modified (mixed-inverse problem).

The boundary-layer development and wake are described with a two-equation lagged dissipation integral boundary-layer formulation and an envelope e^n transition criterion. The entire viscous solution is strongly interacted with the incompressible potential flow using a surface transpiration model, which allows the calculation of limited regions of separated flow. The drag is determined from the momentum thickness of the wake far downstream.

C1. General Descriptions of XFOIL

XFOIL is an interactive program for the design and analysis of subsonic isolated airfoils. It consists of a collection of menu-driven routines which perform various useful functions. The salient features of XFOIL are [XFOIL 2007]:

- Viscous (or inviscid) analysis of an existing airfoil, allowing (a) forced or free transition; (b) transitional separation bubbles; (c) limited trailing edge separation; (d) lift and drag predictions just beyond $C_{L,max}$; (e) Karman-Tsien compressibility correction; and (f) fixed or varying Reynolds and/or Mach numbers.

- Airfoil design and redesign by interactive modification of surface speed distributions, in two methods: (a) full-Inverse method, based on a complex-mapping formulation; and (b) mixed-Inverse method, an extension of XFOIL's basic panel method.
- Airfoil redesign by interactive modification of geometric parameters such as (a) max thickness and camber, highpoint position; (b) leading edge radius; (c) trailing edge thickness; (d) camber line via geometry specification; (e) camber line via loading change specification; (f) flap deflection; (g) explicit contour geometry (via screen cursor)
- Blending of airfoils
- Writing and reading of airfoil coordinates and polar save files
- Plotting of geometry, pressure distributions, and multiple polars

C2. Comparison of Results of XFOIL with Experimental Datasets

Over the years, XFOIL has been validated by many researchers in different parts of the world. e.g. results of a comparison study of 3 airfoils at various RN number are presented by Drela and Giles [1987] as validation of XFOIL's prediction capabilities. Analytic and experimental data is presented for LNV109A and RAE 2822 airfoils. Analysis of the LNV109A airfoil at RN value of 250,000, 375,000, 500,000, and 650,000 showed good agreement with experimental results with accurate prediction of laminar separation bubble location, pressure distribution, lift, and drag. A sharp increase in drag below a C_l of 0.9 is predicted which agrees with experimental data. Additional analysis was run for the LA203A airfoil at RN value of 250,000, 375,000, and 500,000. Analytical and experimental results were found to compare well considering the amount of noise in the data. Displacement thickness and momentum thickness were shown to agree well with experimental results, and a large jump in momentum thickness is clearly visible in both the experimental and analytical results [Reid 2006].

An additional study was performed by Singh et. al [2000] to validate XFOIL for RN numbers between 80,000 and 300,000. Four airfoils were chosen because of there

varying shape characteristics and readily available low RN testing data. The airfoils used in the study were the NACA0009, NACA2414, SD7037, and S1223. The XFOIL results were shown to agree well with experimental results for NACA 0009 at $Re = 80,000$ and $100,000$. The NACA 2414, SD7037, and S1223 all showed a tendency for XFOIL to over predict lift and under predict drag consistently at all angles of attack.

Apart from these comparative studies available in the literature, the candidate has also done in-house validations which are shown from Figures C1 to C9. Quite Reasonable correlation can be observed at $Re=200,000$ and above. It has also been observed that at lower Re range $<200,000$, lift coefficients obtained from XFOIL are higher than experimental datasets. Also, the drag coefficient results from XFOIL are lower than experimental datasets. However, since XFOIL is relatively consistent in its over predictions of L/D , similar bias for different types of airfoils can be assumed [Kellogg and Bowman 2004]. Moreover, since in the present study utilizes XFOIL for comparative study, the over predictions at very low Re are not expected to pose a significant inaccuracy for deriving conclusions.

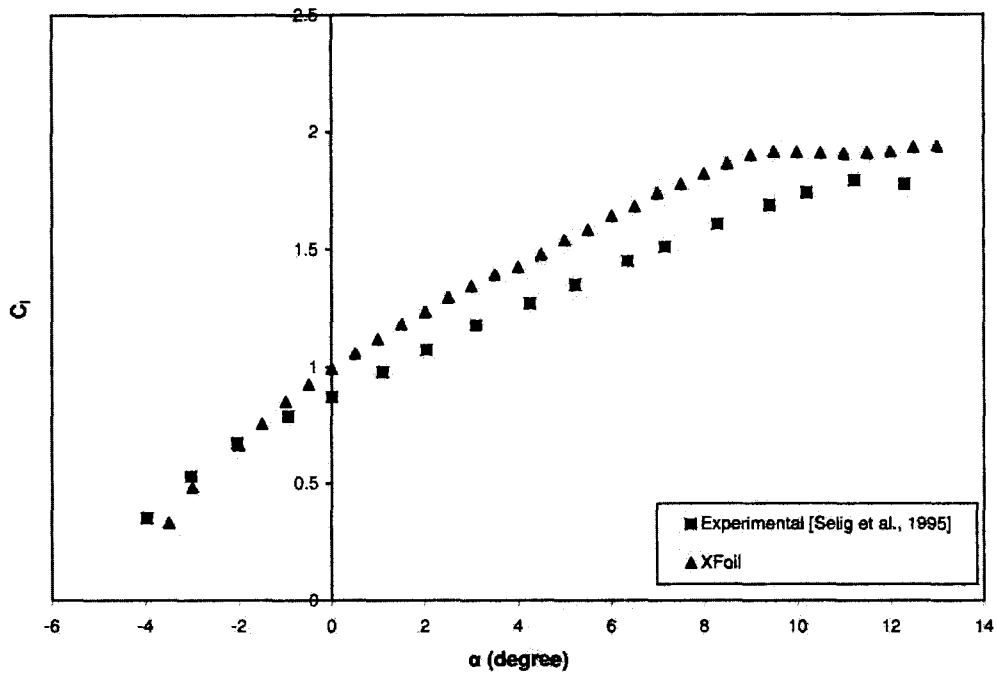
C2.1. Some Comments about Accuracy of Low Re Experimental Results

Some researchers conducting comparative studies were unconvinced that the discrepancy between XFOIL results and experimental measurements was entirely due to inaccuracies in the calculations of XFOIL but were partially due to inaccuracies in the wind tunnel experimentations [Kellogg and Bowman 2004]. It is a known fact that experimental results at low Re ranges are also highly problematic as illustrated by an excellent article by Hepperle [2007]. He has remarked in this article that – “*The scatter of the experimental data is just a matter of fact, caused by the underlying physics*” [Hepperle 2007].

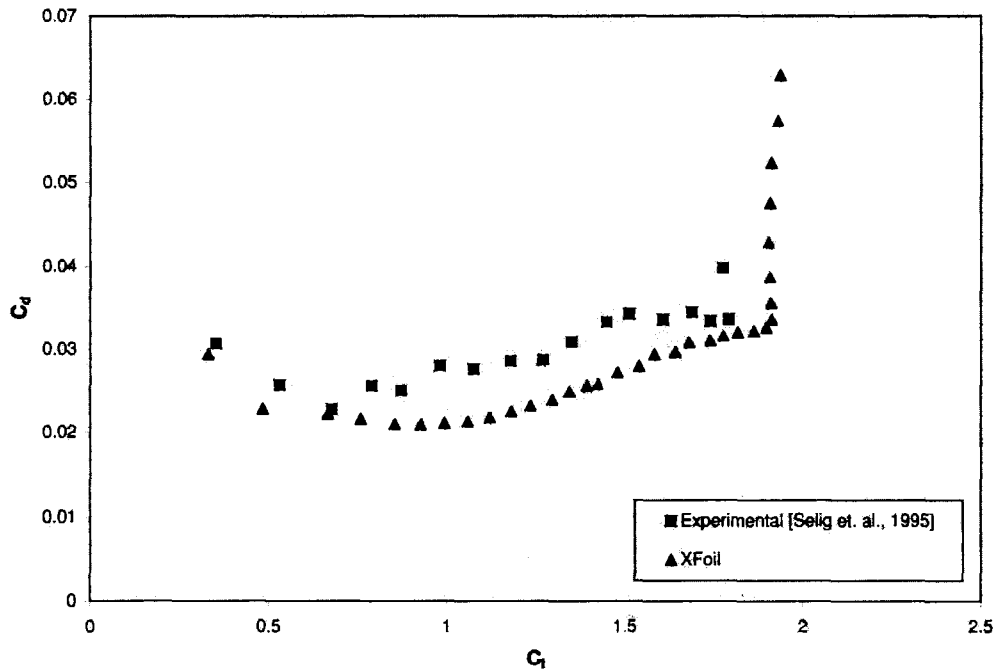
According to McGhee and Walker [1989] - “*Experimental results obtained on various airfoils at low Re in different wind tunnels have shown large differences in airfoil performance ... This is not surprising because of the sensitivity of the airfoil boundary*

layer to free-stream disturbances, model contour accuracy, and model surface roughness. ... At Re of 100,000 or less, the flow phenomena are dominated by the presence of large laminar separation bubbles...".

McCrosky [1987] has shown that even nominally identical sections tested at similar RN in different wind tunnels may give different results [Kirke 1998]. Factors contributing to this variability have been discussed by McGhee and Walker [1989]. The formation of a laminar separation bubble, which markedly affects performance, is sensitive to factors such as surface roughness, inaccuracies in profile, and air turbulence, all of which may vary between a wind tunnel model, a field prototype and a commercially produced turbine [Kirke 1998]. McCrosky [1987] compared all available data for the NACA 0012 section (which is probably the most studied section of all) and concluded that – *“the scatter in the total ensemble of data is unacceptable in the author’s view, and it is not readily apparent which of these results are correct”*.

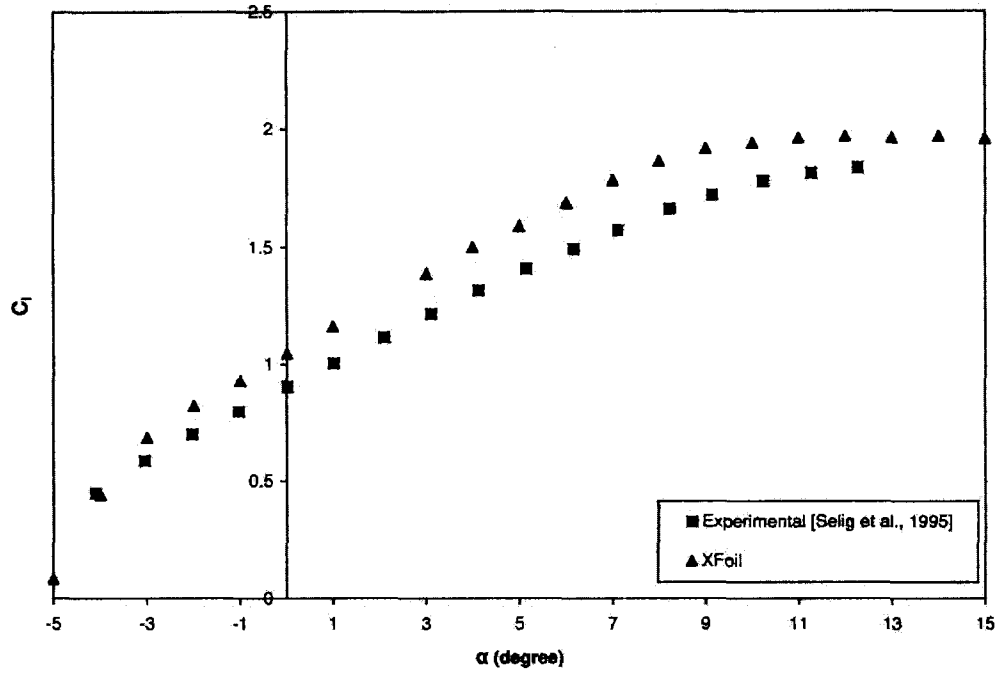


(a) C_l - α Curves

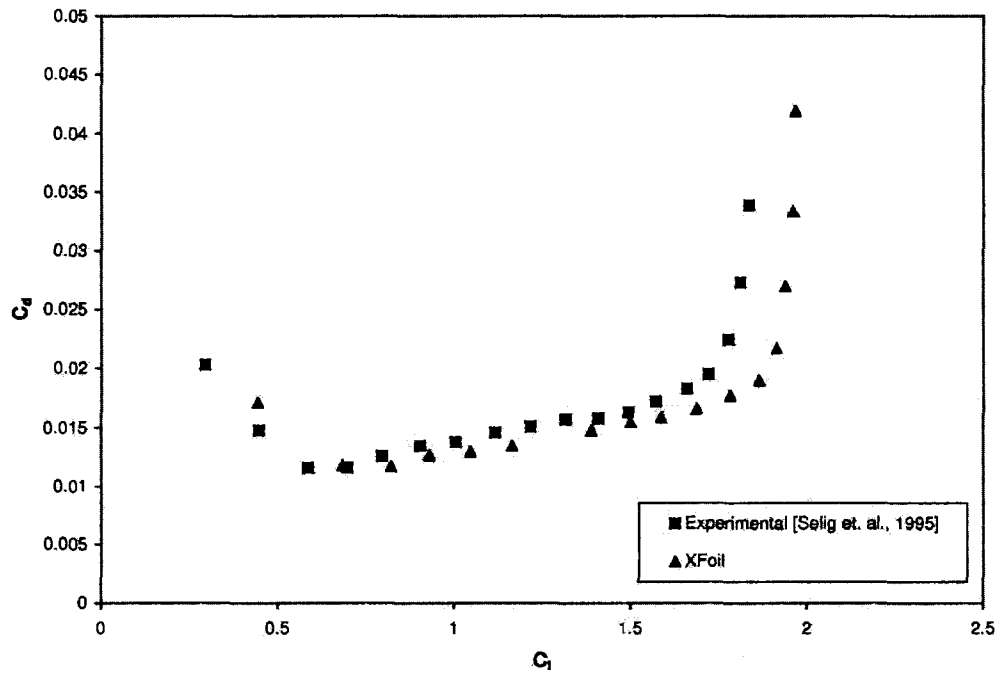


(b) C_d - C_l Curves

Figure C1: Comparison of Experimental Data with XFOIL Results for S1210 at $RN=100,000$

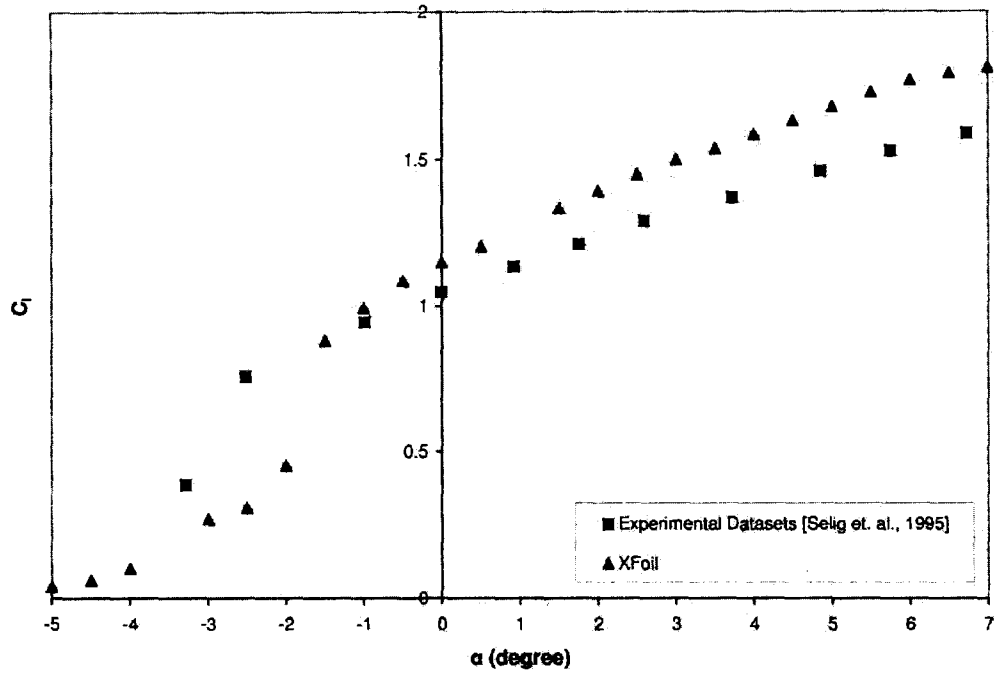


(a) C_l - α Curves

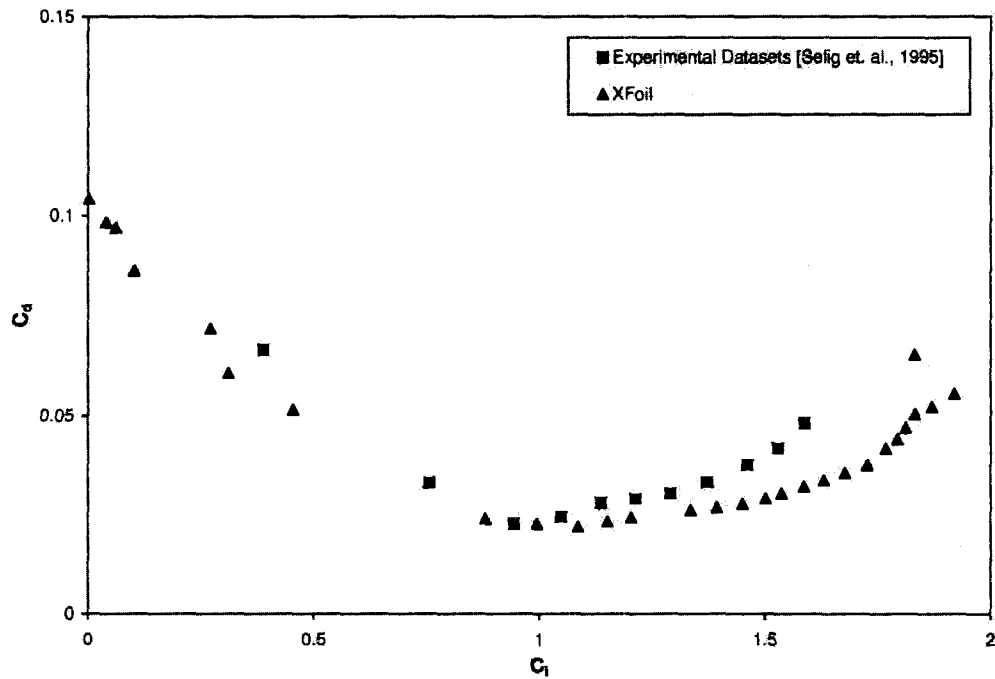


(b) C_d - C_l Curves

Figure C2: Comparison of Experimental Data with XFOIL Results for S1210 at $RN=300,000$

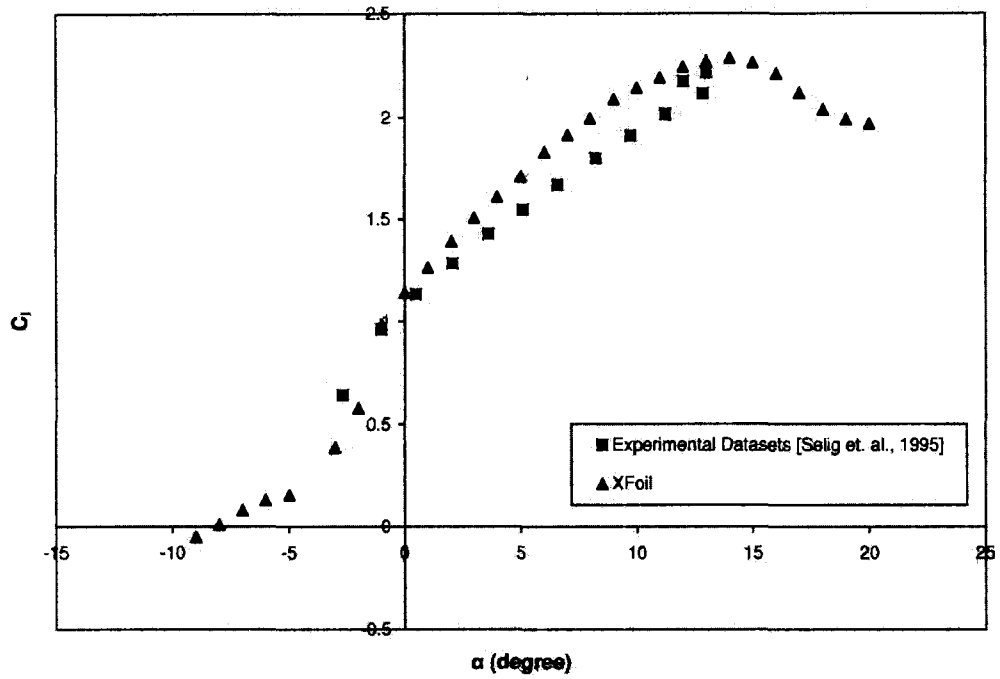


(a) C_l - α Curves

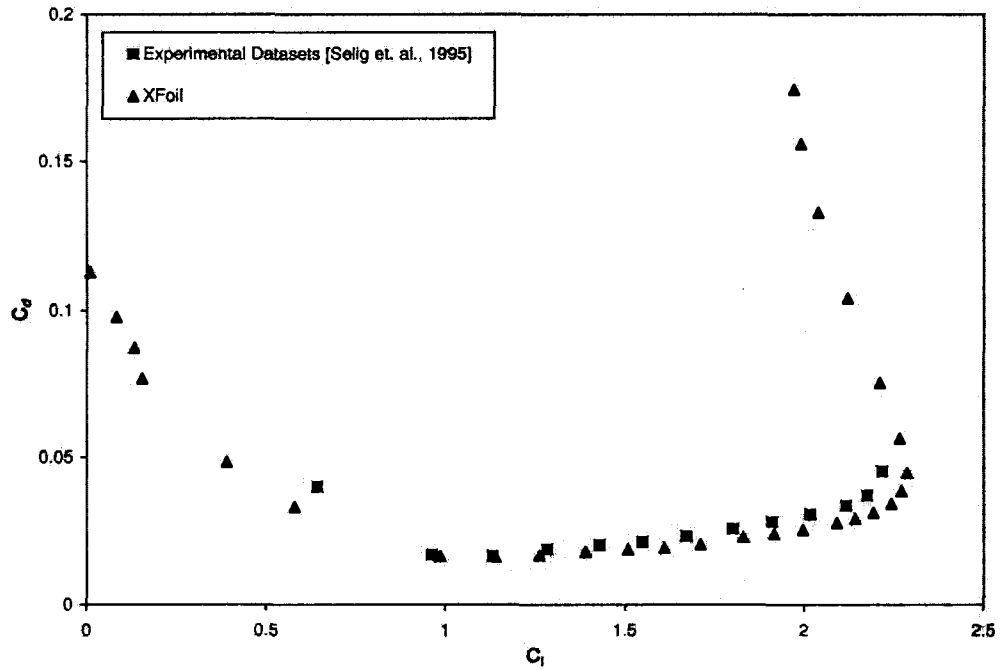


(b) C_d - C_l Curves

Figure C3: Comparison of Experimental Data with XFOIL Results for S1223 at $RN=100,000$

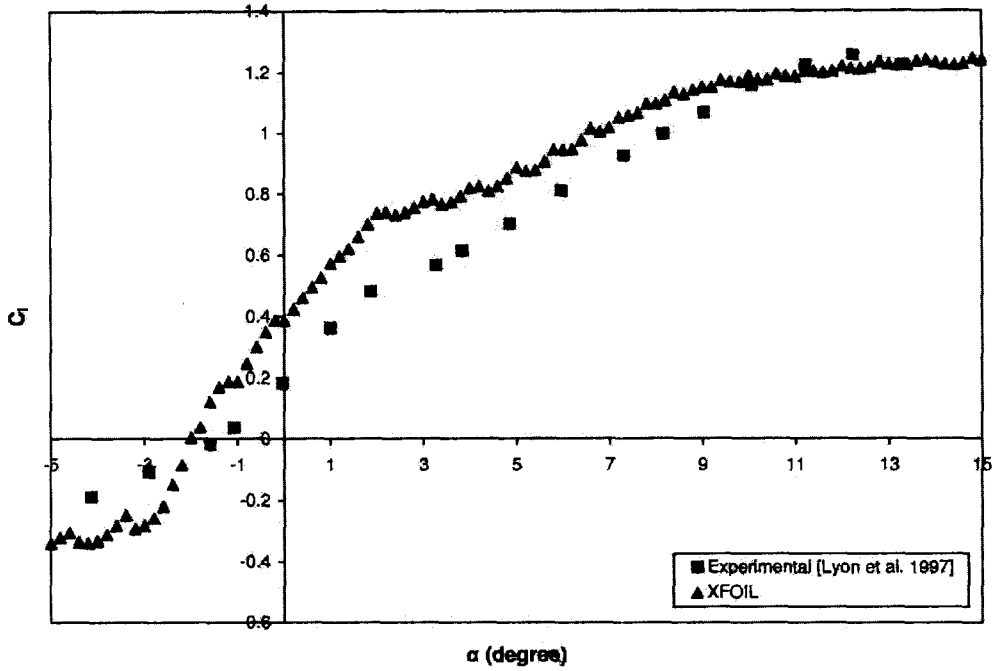


(a) C_l - α Curves

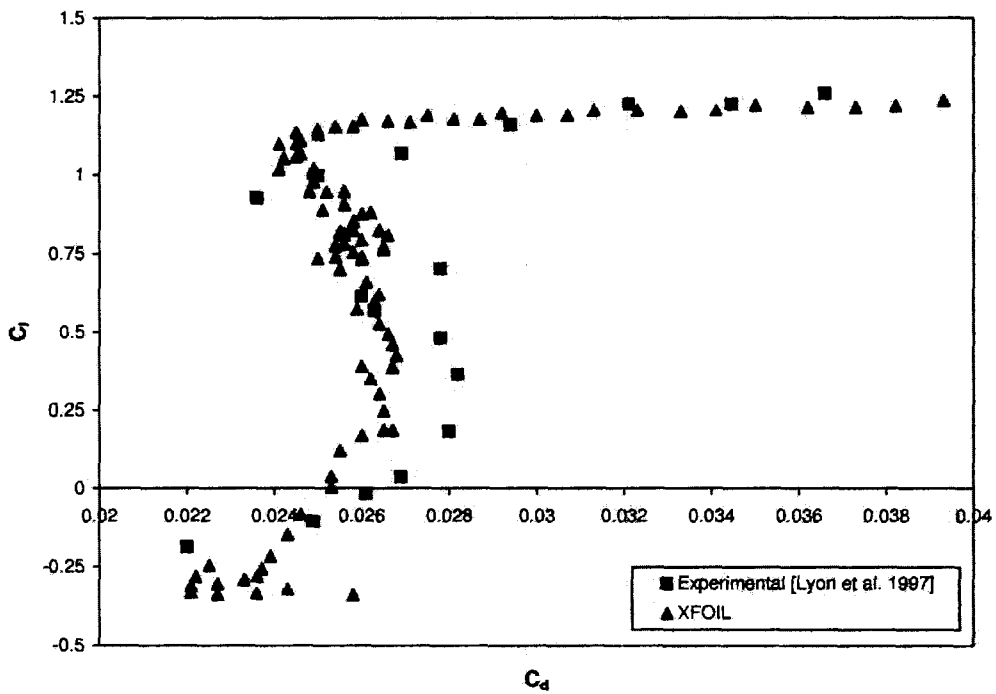


(b) C_d - C_l Curves

Figure C4: Comparison of Experimental Data with XFOIL Results for S1223 at $Re=300,000$

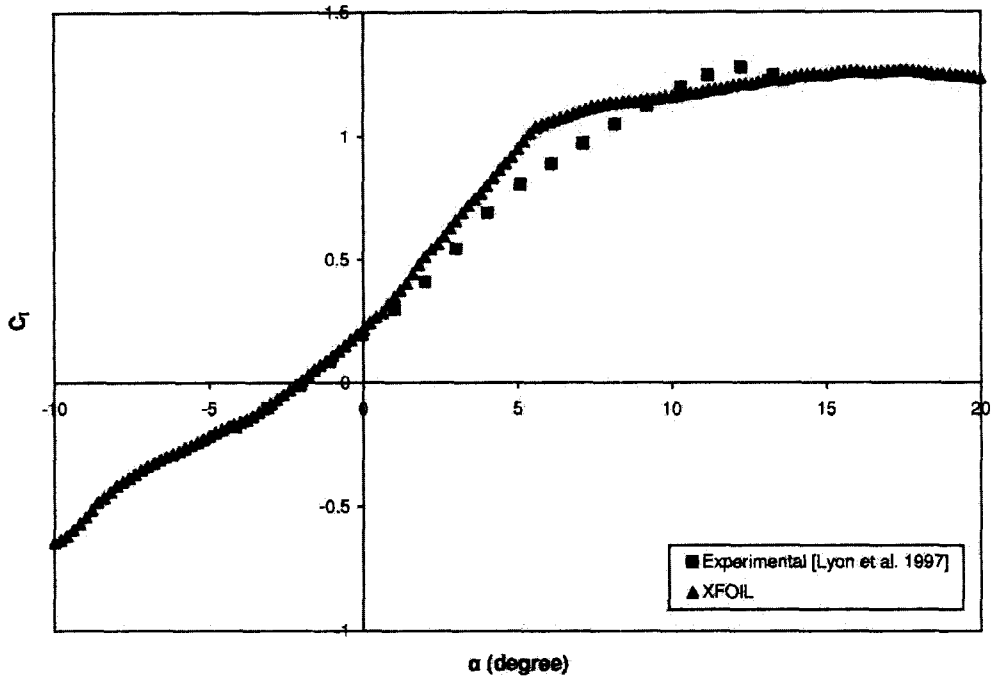


(a) C_l - α Curves

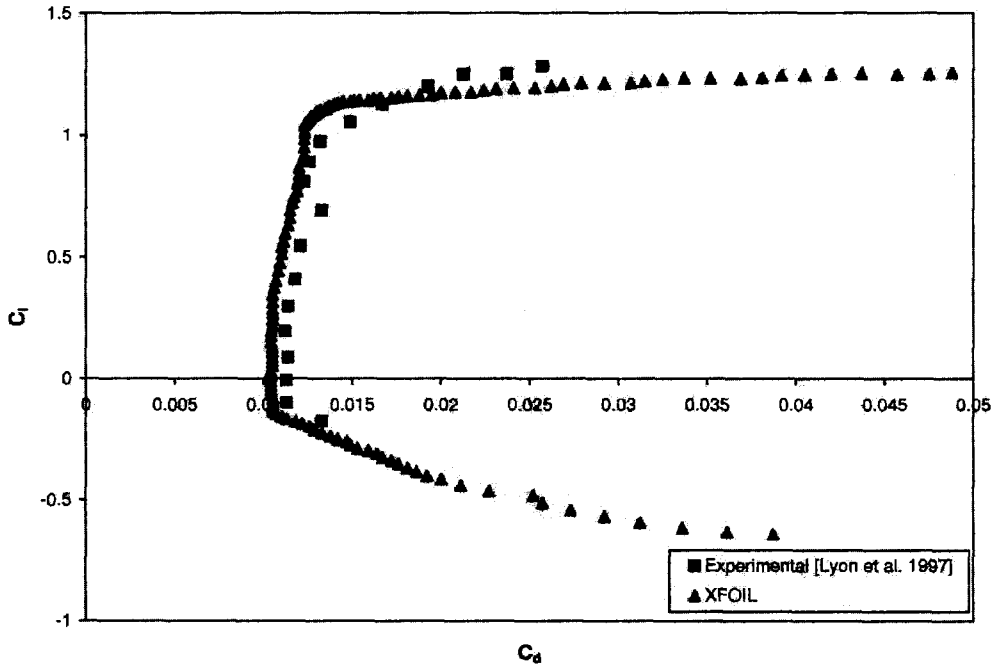


(b) C_d - C_l Curves

Figure C5: Comparison of Experimental Data with XFOIL Results for S8037 at $Re=100,000$

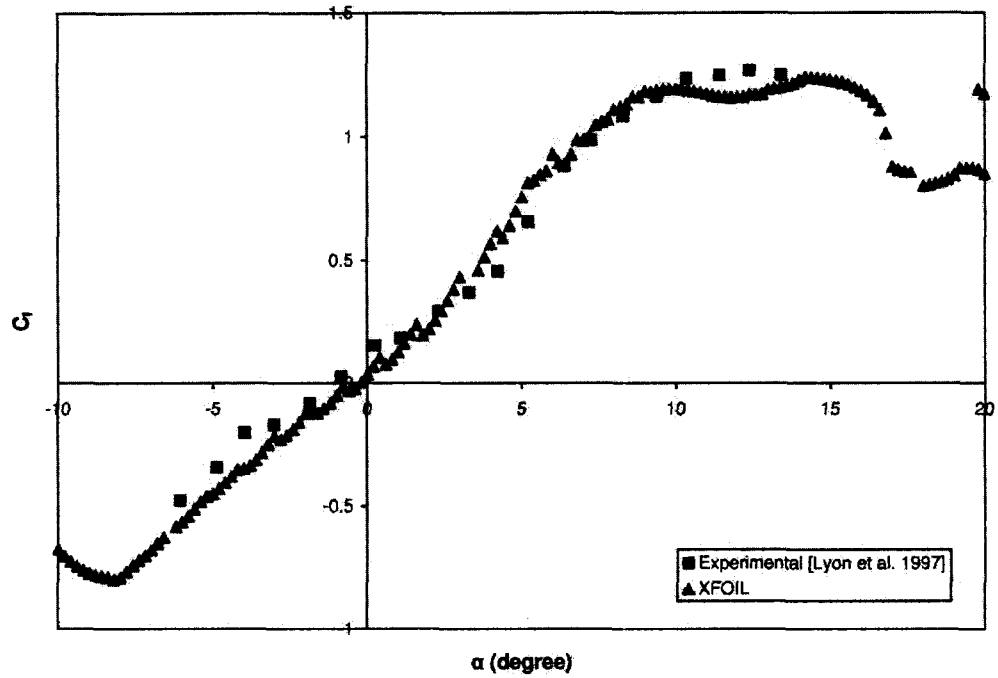


(a) C_l - α Curves

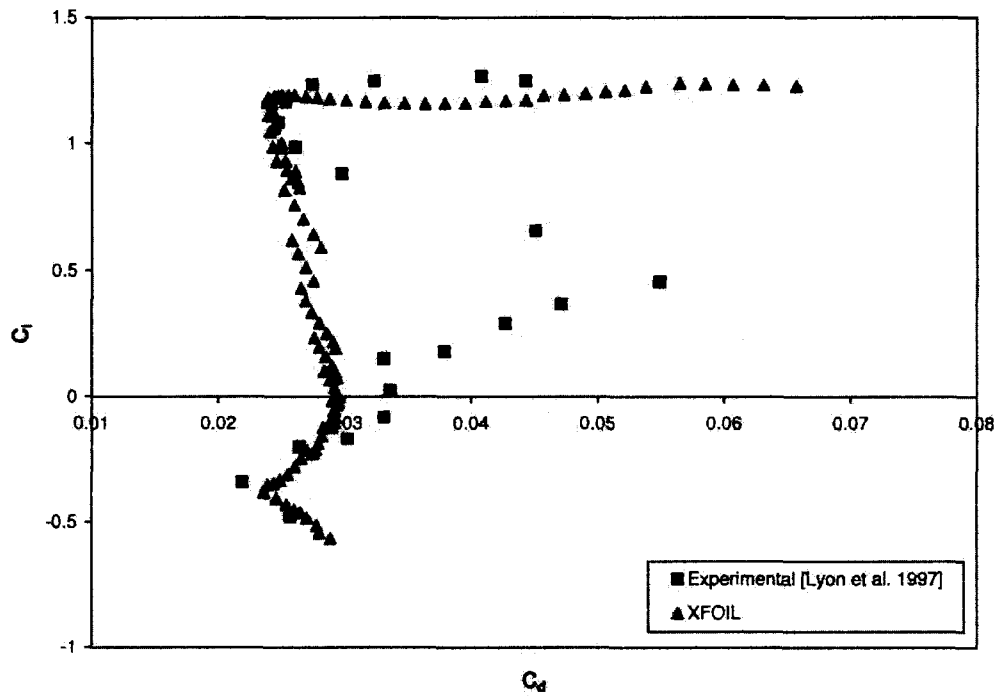


(b) C_d - C_l Curves

Figure C6: Comparison of Experimental Data with XFOIL Results for S8037 at $Re = 300,000$

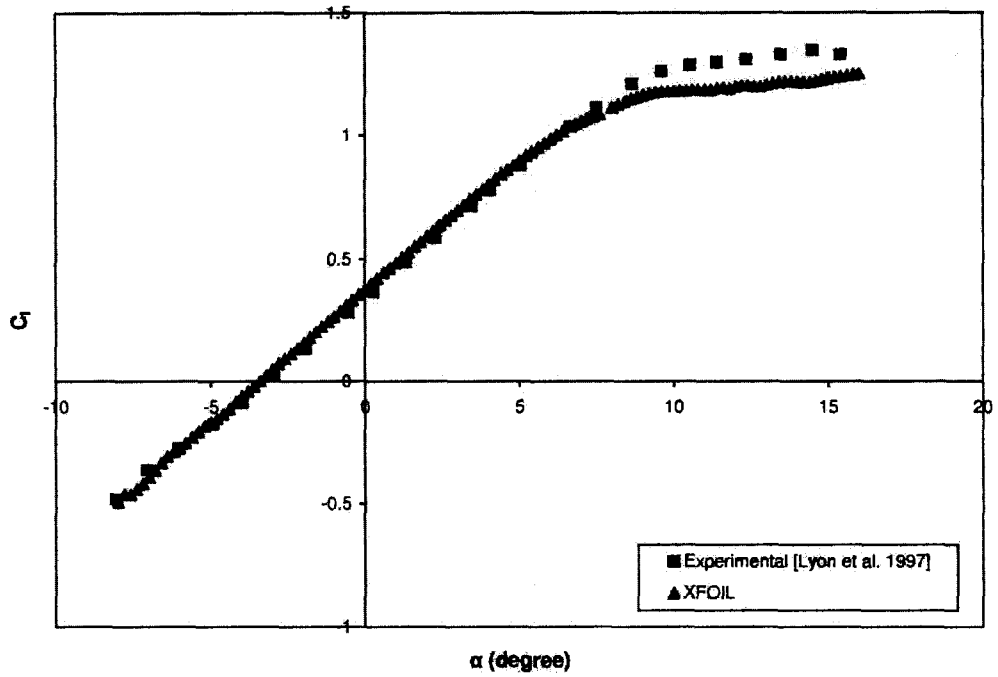


(a) C_l - α Curves

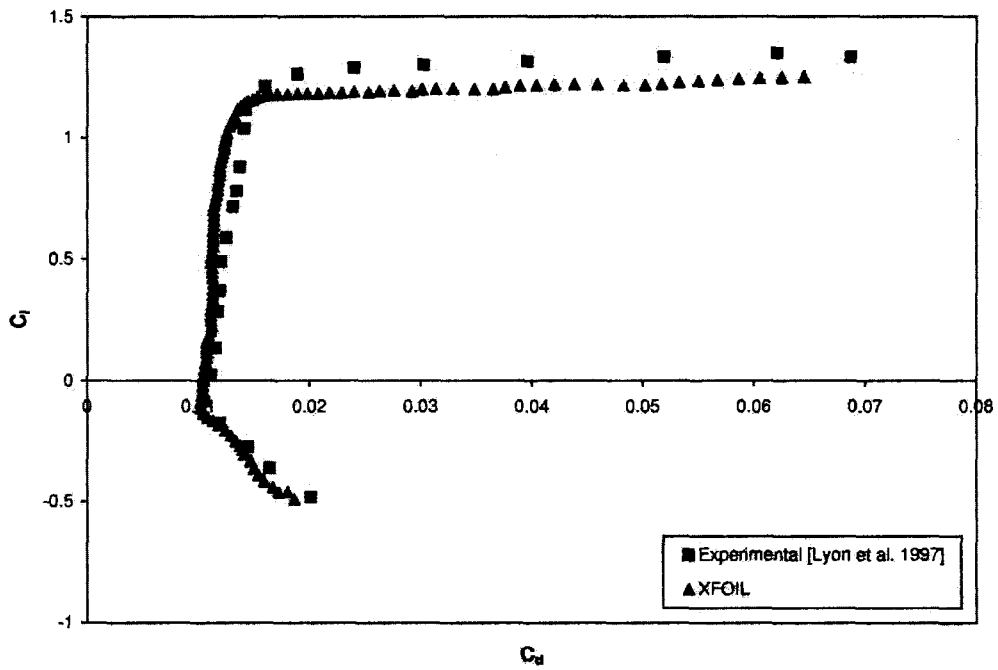


(b) C_d - C_l Curves

Figure C7: Comparison of Experimental Data with XFOIL Results for SG6040 at $Re=100,000$

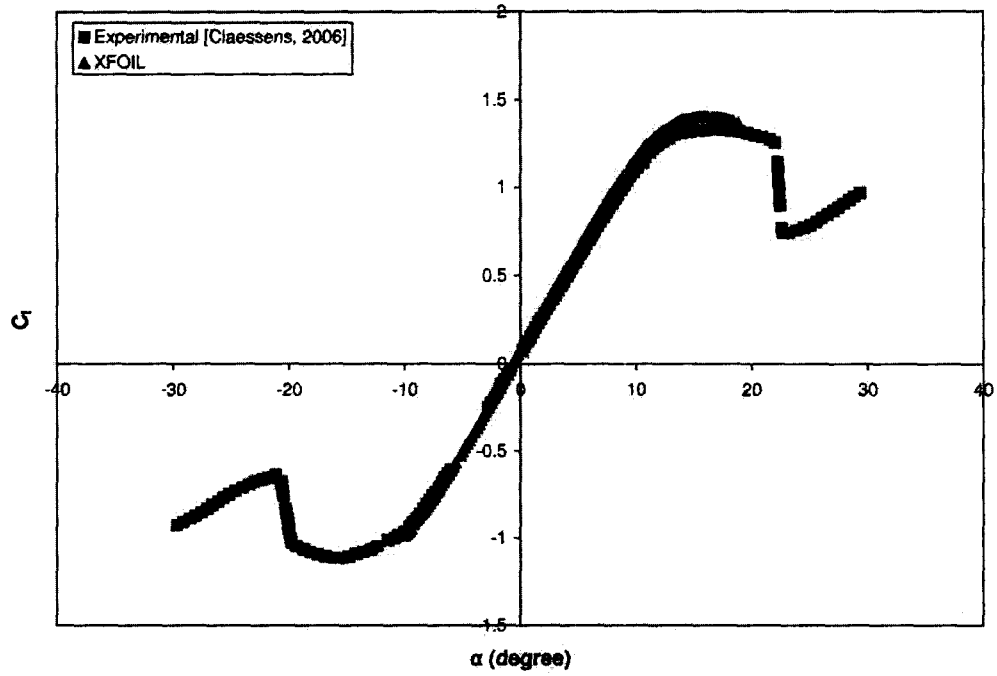


(a) C_l - α Curves

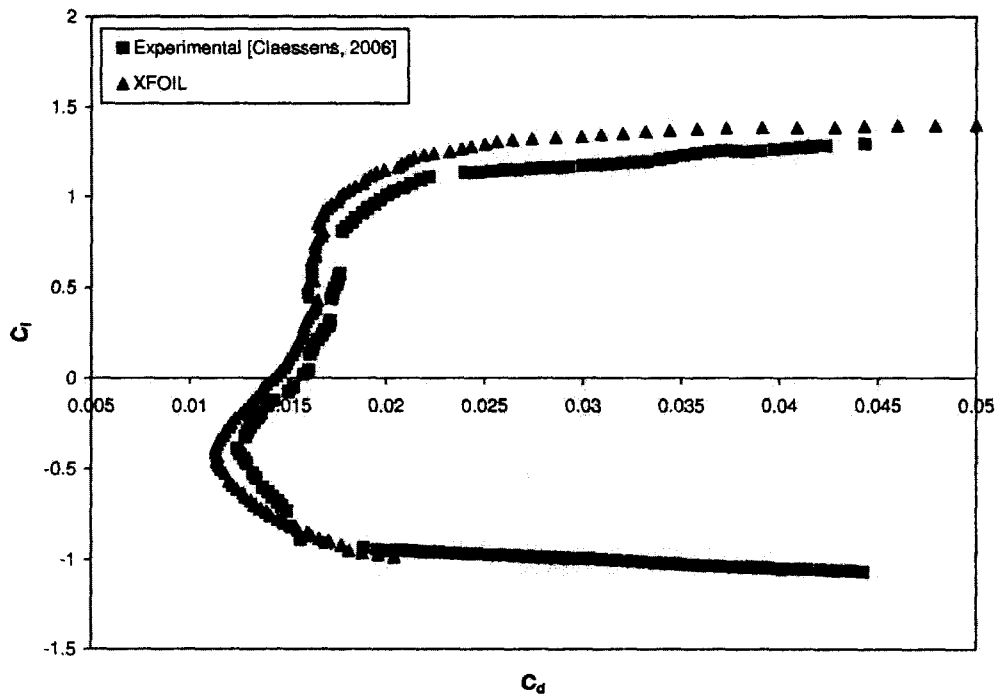


(b) C_d - C_l Curves

Figure C8: Comparison of Experimental Data with XFOIL Results for SG6040 at $Re=300,000$



(a) C_l - α Curves



(b) C_d - C_l Curves

Figure C9: Comparison of Experimental Data with XFOIL Results for DU 06-W-200 at $Re=300,000$

Appendix D: Coordinates of MI-VAWT1

x	y	0.52546	0.09426	0.12462	0.09235	0.00866	0.03162	0.0334	-0.05134	0.21855	-0.09765	0.72679	-0.05119
1	0.00959	0.51247	0.09606	0.11938	0.09109	0.00843	0.02959	0.03569	-0.05272	0.22771	-0.0986	0.74284	-0.04794
0.996	0.00979	0.49968	0.09771	0.1143	0.08979	0.00726	0.02751	0.03805	-0.05408	0.23724	-0.09918	0.75891	-0.04464
0.9872	0.01019	0.48701	0.09921	0.10937	0.08847	0.00612	0.02537	0.0405	-0.05539	0.24715	-0.09968	0.77468	-0.04142
0.98307	0.01089	0.47439	0.10058	0.1046	0.08715	0.00503	0.02323	0.04303	-0.0567	0.25744	-0.10011	0.79007	-0.03833
0.97603	0.01131	0.46175	0.10184	0.1	0.08581	0.00398	0.02107	0.04565	-0.05798	0.26811	-0.10048	0.80508	-0.03541
0.96857	0.01208	0.44906	0.10298	0.09555	0.08448	0.003	0.01889	0.04637	-0.05927	0.27815	-0.10077	0.81969	-0.03262
0.96088	0.013	0.43631	0.10401	0.09128	0.08315	0.00215	0.01698	0.05117	-0.06055	0.29055	-0.10098	0.83377	-0.03
0.95235	0.01405	0.42346	0.10494	0.08717	0.08181	0.00145	0.01442	0.05408	-0.06184	0.30229	-0.10109	0.84719	-0.02754
0.94354	0.01523	0.41054	0.10577	0.08322	0.08048	0.0009	0.01214	0.05707	-0.06314	0.31435	-0.10111	0.85982	-0.02529
0.93417	0.01655	0.39755	0.10649	0.07841	0.07912	0.00049	0.00953	0.06016	-0.06443	0.3267	-0.10105	0.87196	-0.02326
0.92423	0.018	0.38453	0.10713	0.07575	0.07774	0.00021	0.00676	0.06334	-0.06571	0.3393	-0.1009	0.88337	-0.02143
0.91375	0.0196	0.37151	0.10766	0.0722	0.07633	0.00005	0.00396	0.06662	-0.067	0.35209	-0.10065	0.89424	-0.01979
0.90281	0.02133	0.35854	0.10809	0.06878	0.0749	0	-0.00018	0.07	-0.0683	0.36503	-0.10031	0.90461	-0.01832
0.89142	0.02321	0.34569	0.10843	0.06545	0.07341	0.00002	-0.00207	0.07349	-0.06958	0.37805	-0.09988	0.91449	-0.01701
0.87951	0.02528	0.33301	0.10888	0.06223	0.07192	0.00015	-0.00612	0.0771	-0.07087	0.3911	-0.09936	0.92392	-0.01582
0.86701	0.02756	0.32056	0.10883	0.0591	0.07041	0.0004	-0.00873	0.08083	-0.07217	0.40414	-0.09874	0.93292	-0.01476
0.85385	0.03004	0.30837	0.10889	0.05607	0.06888	0.0008	-0.01182	0.08471	-0.07346	0.41714	-0.09803	0.94148	-0.01381
0.84	0.03273	0.2965	0.10885	0.05313	0.06733	0.00135	-0.01437	0.08875	-0.07476	0.43007	-0.09722	0.94959	-0.01296
0.82549	0.03559	0.28495	0.10873	0.05028	0.06579	0.00206	-0.01678	0.09294	-0.07606	0.44292	-0.0963	0.95723	-0.01224
0.81047	0.0386	0.27375	0.10852	0.04732	0.06423	0.00295	-0.01903	0.0973	-0.07734	0.45569	-0.09528	0.96441	-0.01164
0.7951	0.04174	0.26292	0.10822	0.04485	0.06267	0.00397	-0.02117	0.10183	-0.07864	0.46839	-0.09414	0.9712	-0.01115
0.77948	0.045	0.25246	0.10784	0.04228	0.0611	0.00506	-0.02327	0.10653	-0.07995	0.48106	-0.09289	0.97768	-0.01076
0.76365	0.04838	0.24238	0.10739	0.03979	0.0595	0.0062	-0.02536	0.11139	-0.08124	0.49375	-0.09152	0.98394	-0.01048
0.74764	0.05183	0.23267	0.10687	0.03739	0.05789	0.00738	-0.02738	0.1164	-0.08253	0.50651	-0.09001	0.99003	-0.0103
0.73171	0.05524	0.22334	0.10627	0.03507	0.05625	0.00856	-0.02936	0.12158	-0.08379	0.51945	-0.08835	0.99602	-0.01019
0.71603	0.05852	0.21438	0.1056	0.03281	0.05458	0.00982	-0.03125	0.12693	-0.08501	0.53263	-0.08654	0.99898	-0.01017
0.70063	0.06176	0.20577	0.10488	0.03061	0.0529	0.01113	-0.03306	0.13248	-0.08621	0.54611	-0.08457		
0.68548	0.06501	0.19751	0.1041	0.02847	0.0512	0.01253	-0.03479	0.13825	-0.08737	0.5599	-0.08245		
0.67042	0.06817	0.18958	0.10324	0.02638	0.04949	0.01401	-0.03646	0.14425	-0.08851	0.57401	-0.08017		
0.65518	0.07128	0.18197	0.10234	0.02435	0.04778	0.01559	-0.03806	0.15051	-0.08964	0.58843	-0.07774		
0.63978	0.07435	0.17463	0.10139	0.02238	0.04606	0.01726	-0.03962	0.15701	-0.09074	0.60315	-0.07517		
0.62449	0.07733	0.16755	0.10038	0.02049	0.04435	0.01902	-0.04114	0.16374	-0.09181	0.61819	-0.07246		
0.60947	0.08019	0.1607	0.09932	0.01867	0.04262	0.02087	-0.04263	0.17072	-0.09285	0.63354	-0.06961		
0.59474	0.0829	0.15408	0.09823	0.01695	0.04089	0.0228	-0.04411	0.17794	-0.09384	0.64906	-0.06667		
0.58029	0.08547	0.1477	0.0971	0.01531	0.03913	0.02481	-0.04559	0.18543	-0.09477	0.66455	-0.06369		
0.56613	0.08791	0.14158	0.09595	0.01377	0.03734	0.02687	-0.04704	0.19321	-0.09566	0.6799	-0.06065		
0.55226	0.09018	0.1357	0.09478	0.01232	0.0355	0.02889	-0.0485	0.20132	-0.09648	0.6953	-0.05751		
0.53871	0.09231	0.13006	0.09358	0.01095	0.0336	0.03116	-0.04993	0.20976	-0.09725	0.71093	-0.05435		

Appendix E: Coordinates of MI-STRUT1

x	y	0.85771	0.05272	0.45605	0.14504	0.13682	0.14248	0.00056	-0.01102	0.17085	-0.15182	0.54336	-0.13606	0.88915	-0.04253
0.99994	0.00367	0.85215	0.05449	0.48816	0.14641	0.13144	0.14069	0.001	-0.01477	0.17693	-0.15314	0.55122	-0.13445	0.89406	-0.04091
0.99994	0.00369	0.84651	0.05627	0.48027	0.14775	0.12615	0.13683	0.00156	-0.01852	0.18299	-0.15439	0.55906	-0.13282	0.89887	-0.03991
0.99975	0.00376	0.84077	0.05827	0.47239	0.14905	0.12095	0.13691	0.00224	-0.02222	0.18914	-0.15557	0.56689	-0.13115	0.90358	-0.03774
0.99944	0.00388	0.83486	0.05989	0.46451	0.15003	0.11585	0.13492	0.00305	-0.02588	0.19636	-0.15687	0.57471	-0.12947	0.90819	-0.03619
0.999	0.00404	0.82905	0.06172	0.45664	0.15152	0.11085	0.13287	0.00398	-0.0295	0.20166	-0.15771	0.5825	-0.12776	0.9127	-0.03467
0.99844	0.00425	0.82307	0.06356	0.44878	0.15268	0.10594	0.13076	0.00504	-0.03308	0.20803	-0.15868	0.59028	-0.12602	0.9171	-0.03318
0.99776	0.0045	0.81701	0.06542	0.44084	0.15381	0.10113	0.12858	0.00622	-0.03664	0.21447	-0.15957	0.59803	-0.12427	0.9214	-0.03181
0.99695	0.0048	0.81086	0.06729	0.43311	0.15489	0.09642	0.12635	0.00752	-0.04016	0.22089	-0.1604	0.60576	-0.12249	0.9256	-0.03028
0.99602	0.00515	0.80464	0.06917	0.42529	0.15592	0.09181	0.12406	0.00895	-0.04366	0.22757	-0.16115	0.61346	-0.1207	0.92969	-0.02887
0.99496	0.00554	0.79835	0.07106	0.4175	0.1569	0.08731	0.1217	0.01049	-0.04713	0.23422	-0.16183	0.62113	-0.11889	0.93367	-0.0275
0.99378	0.00586	0.79197	0.07296	0.40972	0.15783	0.08289	0.11929	0.01216	-0.05058	0.24084	-0.16244	0.62877	-0.11706	0.93754	-0.02615
0.99248	0.00646	0.78553	0.07487	0.40197	0.1587	0.07786	0.11683	0.01395	-0.05399	0.24772	-0.16298	0.63639	-0.11521	0.94131	-0.02484
0.99105	0.00689	0.77901	0.07679	0.39424	0.15953	0.0744	0.11431	0.01587	-0.05738	0.25457	-0.16345	0.64396	-0.11336	0.94496	-0.02356
0.98951	0.00756	0.77243	0.07871	0.38654	0.1603	0.07031	0.11173	0.0179	-0.06074	0.26148	-0.16384	0.6515	-0.11148	0.94851	-0.02232
0.98784	0.00817	0.76578	0.08064	0.37887	0.16101	0.06633	0.1091	0.02005	-0.06406	0.26844	-0.16417	0.65901	-0.1096	0.95194	-0.02111
0.98605	0.00883	0.75906	0.08257	0.37123	0.16166	0.06246	0.10642	0.02233	-0.06735	0.27547	-0.16443	0.66647	-0.1077	0.95526	-0.01993
0.98413	0.00953	0.75228	0.08451	0.36361	0.16226	0.05869	0.10369	0.02472	-0.0706	0.28255	-0.16482	0.67389	-0.1058	0.95847	-0.0188
0.9821	0.01028	0.74543	0.08645	0.35604	0.16279	0.05504	0.10109	0.02723	-0.07382	0.28969	-0.16478	0.68127	-0.10388	0.96156	-0.01769
0.97995	0.01106	0.73852	0.08839	0.3485	0.16327	0.05149	0.09807	0.02985	-0.077	0.29687	-0.16478	0.6886	-0.10196	0.96454	-0.01663
0.97768	0.01189	0.73156	0.09033	0.34099	0.16388	0.04806	0.09519	0.0326	-0.08013	0.30411	-0.16477	0.69589	-0.10003	0.9674	-0.0156
0.97528	0.01276	0.72455	0.09228	0.33353	0.16403	0.04474	0.09227	0.03544	-0.08323	0.3114	-0.16488	0.70313	-0.0981	0.97015	-0.01462
0.97277	0.01367	0.71745	0.09422	0.32611	0.16431	0.04153	0.08993	0.03844	-0.08629	0.31873	-0.16453	0.71032	-0.09616	0.97277	-0.01387
0.97015	0.01462	0.71032	0.09616	0.31873	0.16453	0.03944	0.08629	0.04153	-0.08943	0.32611	-0.16431	0.71745	-0.09422	0.97528	-0.01276
0.9674	0.0156	0.70313	0.0981	0.3114	0.16468	0.03546	0.08323	0.04474	-0.09227	0.33353	-0.16403	0.72453	-0.09228	0.97768	-0.01189
0.96454	0.01663	0.69589	0.10003	0.30411	0.16477	0.0326	0.08013	0.04806	-0.09519	0.34099	-0.16388	0.73156	-0.09033	0.97995	-0.01106
0.96156	0.01769	0.6886	0.10196	0.29687	0.16478	0.02985	0.077	0.05149	-0.09807	0.3485	-0.16327	0.73852	-0.08839	0.9821	-0.01028
0.95847	0.0188	0.68127	0.10388	0.28969	0.16478	0.02723	0.07382	0.05504	-0.1009	0.35604	-0.16279	0.74543	-0.08645	0.98413	-0.00953
0.95526	0.01993	0.67389	0.1058	0.28255	0.16482	0.02472	0.0706	0.05869	-0.10369	0.36361	-0.16226	0.75228	-0.08451	0.98605	-0.00863
0.95194	0.02111	0.66647	0.1077	0.27547	0.16443	0.02233	0.06735	0.06246	-0.10642	0.37123	-0.16186	0.75906	-0.08257	0.98784	-0.00717
0.94851	0.02232	0.65901	0.1096	0.26844	0.16417	0.02005	0.06406	0.06633	-0.1091	0.37887	-0.16101	0.76578	-0.08064	0.98951	-0.00619
0.94496	0.02356	0.6515	0.11148	0.26148	0.16384	0.01887	0.05738	0.07031	-0.11173	0.38654	-0.1603	0.77243	-0.07871	0.99105	-0.00515
0.94131	0.02484	0.64396	0.11336	0.25457	0.16345	0.01683	0.05399	0.0786	-0.11683	0.39424	-0.15957	0.77901	-0.07679	0.99248	-0.00413
0.93754	0.02615	0.63639	0.11521	0.24772	0.16298	0.01587	0.05058	0.0829	-0.11929	0.40197	-0.1587	0.78553	-0.07487	0.99378	-0.00318
0.93367	0.0275	0.62877	0.11706	0.24094	0.16244	0.0149	0.04713	0.08731	-0.1217	0.40972	-0.15783	0.79197	-0.07296	0.99496	-0.00215
0.92969	0.02887	0.62113	0.11889	0.23422	0.16183	0.01216	0.04511	0.09181	-0.12406	0.4175	-0.1568	0.79835	-0.07106	0.99602	-0.00111
0.9256	0.03028	0.61346	0.1207	0.22757	0.16115	0.00895	0.04366	0.09519	-0.12635	0.42529	-0.15592	0.80576	-0.06917	0.99695	-0.00015
0.9214	0.03171	0.60576	0.12249	0.22099	0.1604	0.00752	0.04016	0.09842	-0.12858	0.43311	-0.15489	0.81086	-0.06729	0.99776	-0.00015
0.9171	0.03318	0.59803	0.12427	0.21447	0.15957	0.00622	0.03664	0.10113	-0.13076	0.44094	-0.15381	0.81701	-0.06542	0.99844	-0.00044
0.9127	0.03467	0.59028	0.12602	0.20803	0.15868	0.00504	0.03308	0.10594	-0.13287	0.44878	-0.15268	0.82307	-0.06356	0.99944	-0.00044
0.90819	0.03619	0.5825	0.12776	0.20166	0.15771	0.00398	0.0295	0.11085	-0.13492	0.45664	-0.15152	0.82905	-0.06172	0.99984	-0.000388
0.90358	0.03774	0.57471	0.12947	0.19536	0.15667	0.00305	0.02588	0.11585	-0.13691	0.46451	-0.1503	0.83496	-0.05989	0.99975	-0.003376
0.89887	0.03931	0.56689	0.13115	0.18914	0.15557	0.00224	0.02222	0.12095	-0.13891	0.47239	-0.14905	0.84077	-0.05807	0.99984	-0.003369
0.89406	0.04091	0.55906	0.13282	0.18299	0.15439	0.00156	0.01852	0.12615	-0.13981	0.48027	-0.14775	0.84851	-0.05627	1	-0.00367
0.88915	0.04253	0.55122	0.13445	0.17693	0.15314	0.001	0.01477	0.13144	-0.14069	0.48816	-0.14641	0.85215	-0.05449		
0.88415	0.04417	0.54336	0.13606	0.17085	0.15182	0.00056	0.01102	0.13682	-0.14248	0.49605	-0.14504	0.85771	-0.05272		
0.87905	0.04584	0.53549	0.13763	0.16816	0.15044	0.00025	0.00727	0.14229	-0.14421	0.50395	-0.14363	0.86318	-0.05087		
0.87385	0.04753	0.52761	0.13918	0.16226	0.14898	0.00006	0.00359	0.14785	-0.14567	0.51184	-0.14218	0.86856	-0.04924		
0.86856	0.04924	0.51973	0.1407	0.15349	0.14746	0	0	0.15349	-0.14746	0.51973	-0.1407	0.87385	-0.04753		
0.86318	0.05097	0.51184	0.14218	0.14785	0.14587	0.00006	-0.00359	0.15922	-0.14898	0.52761	-0.13918	0.87905	-0.04584		
		0.50395	0.14363	0.14229	0.14421	0.00025	-0.00727	0.16504	-0.15044	0.53549	-0.13763	0.88415	-0.04417		

Appendix E: Coordinates of MI-STRUT 1

Appendix F: Determination of Bending Moment and Bending Stress

Derivation techniques of bending moment and bending stress are given in this appendix. Figure F1 shows the forces developed on the turbine blade. F_n and F_t are respectively the aerodynamic normal and the tangential forces. F_n and F_t can be obtained from the equations described in Section 4.1.3.

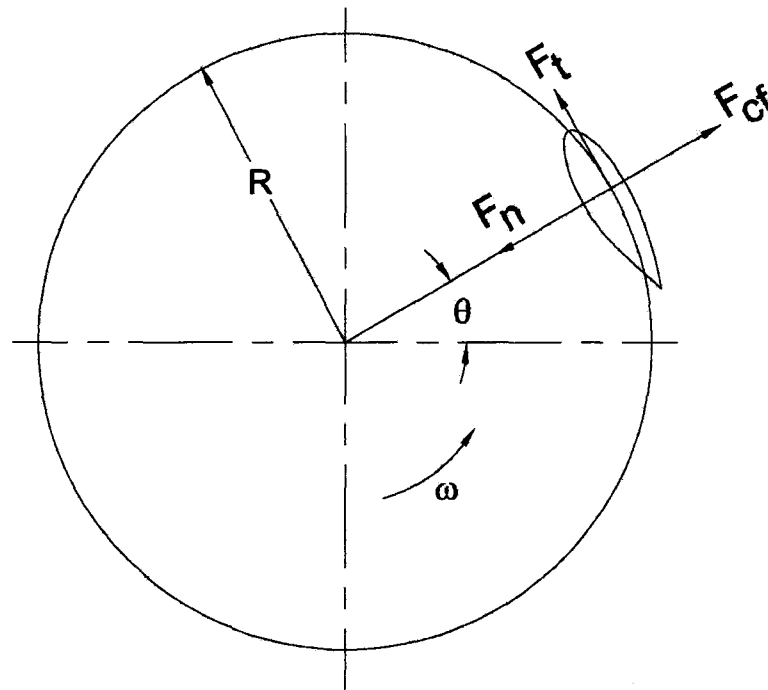


Figure F1: Section of a Straight-Bladed Wind Turbine Showing Forces on the SB-VAWT Blade

F_{cf} is the centrifugal force and it can be expressed as,

$$F_{cf} = m_b \omega^2 R \quad (\text{F.1})$$

where m_b is the blade mass per unit blade length. ω is the angular velocity and R is the radius of the turbine. The directions of the forces as shown in the Figure F1, are

considered to be positive in this analysis. The net normal force on the turbine blade (in the radially outward direction) can be obtained as,

$$F_{net} = F_{cf} - F_n \tag{F.2}$$

F1. Overhang Supported Blades

In this section, calculations are performed considering that the blades are supported like that of an overhang supported beam. In the Figure F2, the bending moment diagram of an overhang-supported beam is shown. The forces on the turbine blade are distributed all over the blade length which is also seen from Figure F2.

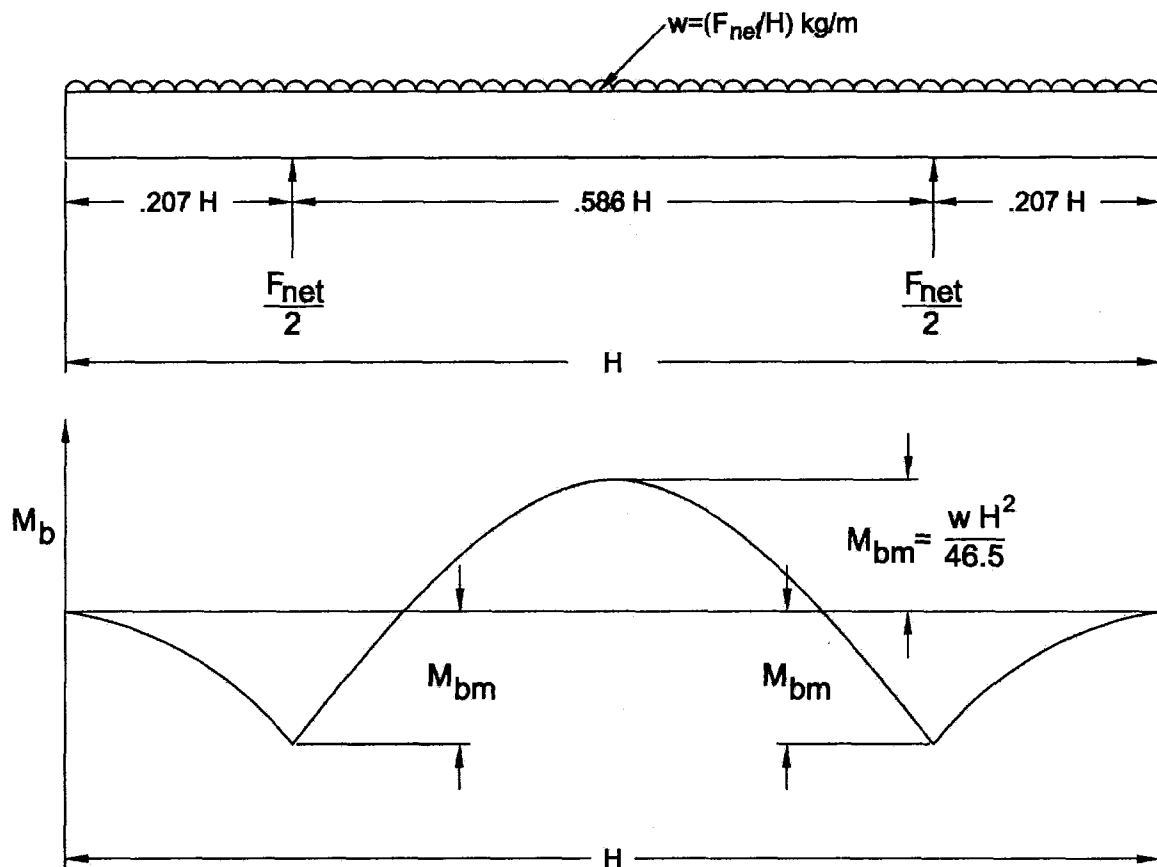


Figure F2: Bending Moment Diagram of an Overhang Supported Beam

The expression of the maximum bending moment can be obtained as,

$$M_{bm} = \frac{wH^2}{46.5} \quad (F.3)$$

where w is the load per unit length of the blade. Introducing the value of $w = F_{net}/H$ in the equation (F.3), one obtains,

$$M_{bm} = \frac{F_{net}H}{46.5} \quad (F.4)$$

where H is the height of the turbine and hence the length of the turbine blade. The maximum bending stress can be found as,

$$S_{bm} = \frac{M_{bm}(t_c c/2)}{I_x} \quad (F.5)$$

where t_c is the maximum blade thickness as a fraction of chord and c is the chord of the blade airfoil. I_x is the area moment of inertia about the chord of the blade airfoil. From the equation (F.4) and (F.5), the expression of the maximum bending stress can be written as,

$$S_{bm} = \frac{F_{net}Hct_c}{93I_x} \quad (F.6)$$

The effect of tangential force on the blade stress is not encountered in this analysis, because this force is negligible in comparison to the net normal force.

F2. Simply Supported Blades

In this section, calculations are performed considering that the blades are supported like that of a simply supported beam. In the Figure F3, the bending moment diagram of a simply-supported beam is shown. The forces on the SB-VAWT blade are distributed all over the blade length, which is also seen from the Figure F3.

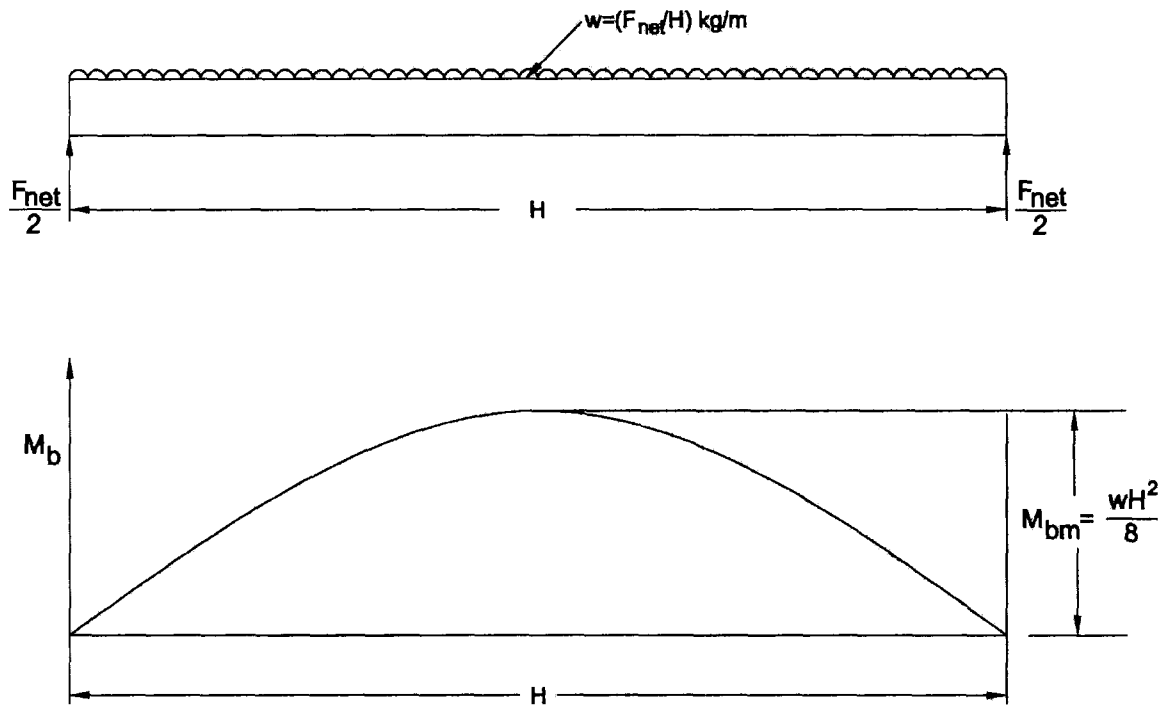


Figure F3: Bending Moment Diagram of a Simply Supported Beam

The mathematical expression of the maximum bending moment can be obtained as,

$$M_{bm} = \frac{wH^2}{8} \quad (\text{F.7})$$

Introducing the value of $w = F_{\text{net}}/H$ in the equation (F.7), one obtains,

$$M_{bm} = \frac{F_{\text{net}}H^2}{8} \quad (\text{F.8})$$

The maximum bending stress can be found as,

$$S_{bm} = \frac{M_{bm}(t_c/2)}{I_x} \quad (\text{F.9})$$

From the equation (F.8) and (F.9), the expression of the maximum bending stress can be written as,

$$S_{bm} = \frac{F_{net} H c t_c}{93 I_x} \quad (\text{F.10})$$

The effect of tangential force on the blade stress is not encountered in this analysis, because this force is negligible in comparison to the net normal force.

Appendix G: Selected Pictures of the Blade Fabrication Process



Figure G1: Cutting of Styrofoam using CNC machine for NACA 4415 Blades

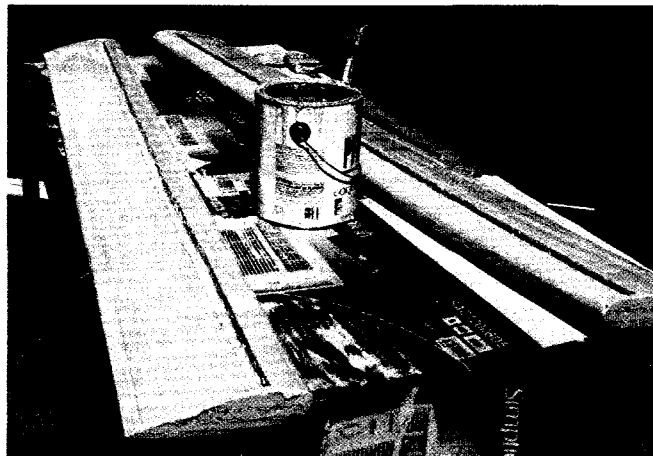


Figure G2: Initial Painting of the Blades with a Water-based Color

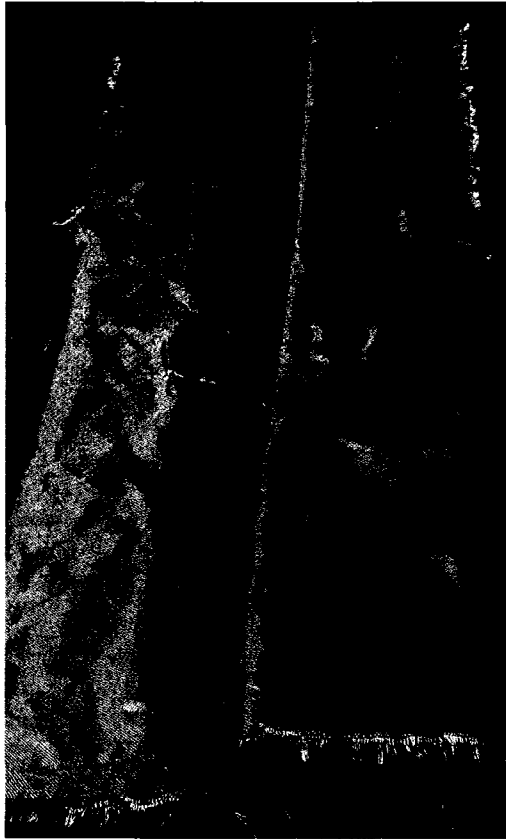


Figure G3: Styrofoam Blade Cores & Fibre Glass Clothing before Lamination Process

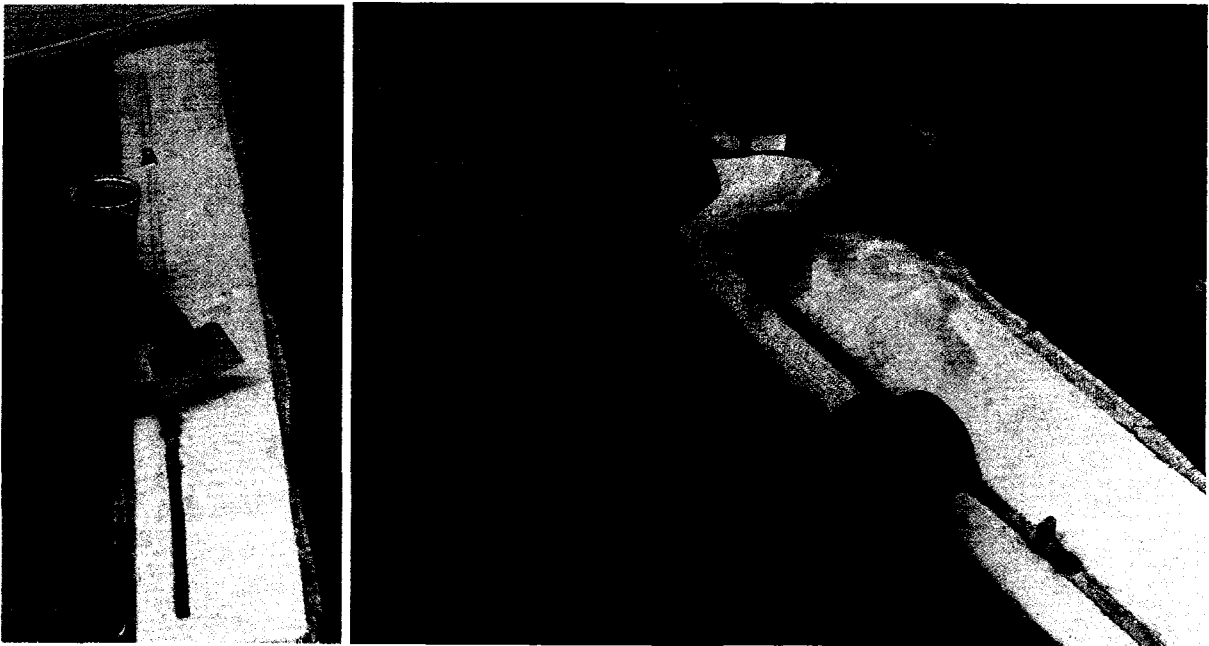


Figure G4: Applying Fiberglass Resin Along With Hardener

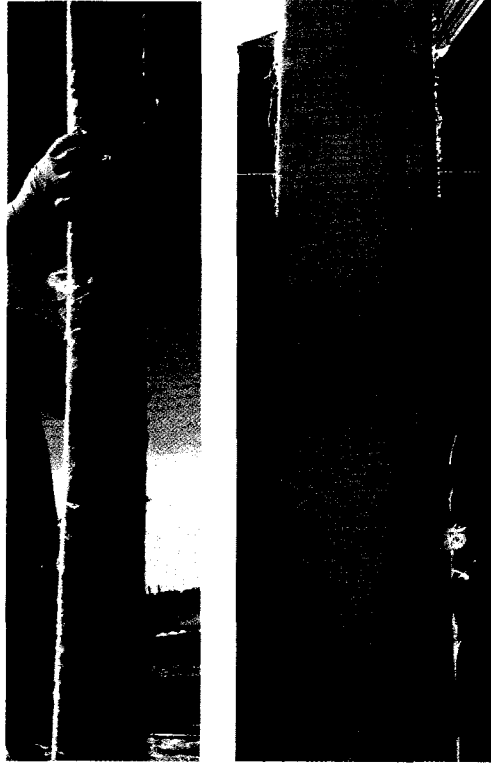


Figure G5: Blades before Sanding Process

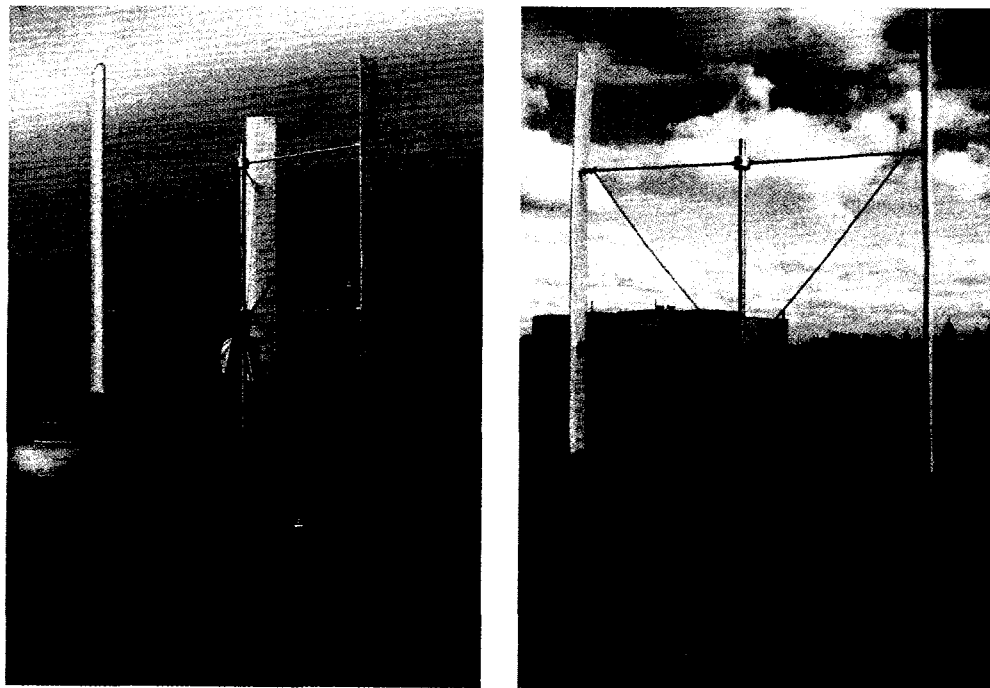


Figure G6: SB-VAWT with the Blades after Final Painting

Vita Auctoris

Mr. Mazharul Islam was born in 1970 in Dhaka, Bangladesh. He obtained his undergraduate degree in Mechanical Engineering in 1993 from Regional Engineering College, Durgapur, India (now known as National Institute of Technology, Durgapur, India). Subsequently, he completed two M.Sc. degrees, the first at the Bangladesh University of Engineering and Technology in 1998, and the second at the University of Oldenburg, Germany in 2001. He started pursuing his PhD in the Department of Mechanical, Automotive & Materials Engineering, University of Windsor, Canada in May 2003.